

# FOURIER TRANSFORM INFRARED SPECTROMETRY

**Second Edition**

**Peter R. Griffiths**  
**James A. de Haseth**

Chemical Analysis: A Series of Monographs on Analytical Chemistry and Its Applications  
J. D. Winefordner, Series Editor

# Fourier Transform Infrared Spectrometry

Second Edition

**PETER R. GRIFFITHS**

University of Idaho  
Moscow, Idaho

**JAMES A. de HASETH**

University of Georgia  
Athens, Georgia



**WILEY-INTERSCIENCE**

A JOHN WILEY & SONS, INC., PUBLICATION



# Fourier Transform Infrared Spectrometry





---

## THE WILEY BICENTENNIAL—KNOWLEDGE FOR GENERATIONS

---

Each generation has its unique needs and aspirations. When Charles Wiley first opened his small printing shop in lower Manhattan in 1807, it was a generation of boundless potential searching for an identity. And we were there, helping to define a new American literary tradition. Over half a century later, in the midst of the Second Industrial Revolution, it was a generation focused on building the future. Once again, we were there, supplying the critical scientific, technical, and engineering knowledge that helped frame the world. Throughout the 20th Century, and into the new millennium, nations began to reach out beyond their own borders and a new international community was born. Wiley was there, expanding its operations around the world to enable a global exchange of ideas, opinions, and know-how.

For 200 years, Wiley has been an integral part of each generation's journey, enabling the flow of information and understanding necessary to meet their needs and fulfill their aspirations. Today, bold new technologies are changing the way we live and learn. Wiley will be there, providing you the must-have knowledge you need to imagine new worlds, new possibilities, and new opportunities.

Generations come and go, but you can always count on Wiley to provide you the knowledge you need, when and where you need it!

**WILLIAM J. PESCE**  
PRESIDENT AND CHIEF EXECUTIVE OFFICER

**PETER BOOTH WILEY**  
CHAIRMAN OF THE BOARD

---

# Fourier Transform Infrared Spectrometry

Second Edition

**PETER R. GRIFFITHS**

University of Idaho  
Moscow, Idaho

**JAMES A. de HASETH**

University of Georgia  
Athens, Georgia



**WILEY-INTERSCIENCE**

A JOHN WILEY & SONS, INC., PUBLICATION

Copyright © 2007 by John Wiley & Sons, Inc. All rights reserved.

Published by John Wiley & Sons, Inc., Hoboken, New Jersey.

Published simultaneously in Canada.

No part of this publication may be reproduced, stored in a retrieval system, or transmitted in any form or by any means, electronic, mechanical, photocopying, recording, scanning, or otherwise, except as permitted under Section 107 or 108 of the 1976 United States Copyright Act, without either the prior written permission of the Publisher, or authorization through payment of the appropriate per-copy fee to the Copyright Clearance Center, Inc., 222 Rosewood Drive, Danvers, MA 01923, (978) 750-8400, fax (978) 750-4470, or on the web at [www.copyright.com](http://www.copyright.com). Requests to the Publisher for permission should be addressed to the Permissions Department, John Wiley & Sons, Inc., 111 River Street, Hoboken, NJ 07030, (201) 748-6011, fax (201) 748-6008, or online at <http://www.wiley.com/go/permission>.

**Limit of Liability/Disclaimer of Warranty:** While the publisher and author have used their best efforts in preparing this book, they make no representations or warranties with respect to the accuracy or completeness of the contents of this book and specifically disclaim any implied warranties of merchantability or fitness for a particular purpose. No warranty may be created or extended by sales representatives or written sales materials. The advice and strategies contained herein may not be suitable for your situation. You should consult with a professional where appropriate. Neither the publisher nor author shall be liable for any loss of profit or any other commercial damages, including but not limited to special, incidental, consequential, or other damages.

For general information on our other products and services or for technical support, please contact our Customer Care Department within the United States at (800) 762-2974, outside the United States at (317) 572-3993 or fax (317) 572-4002.

Wiley also publishes its books in a variety of electronic formats. Some content that appears in print may not be available in electronic formats. For more information about Wiley products, visit our web site at [www.wiley.com](http://www.wiley.com).

Wiley Bicentennial Logo: Richard J. Pacifico

***Library of Congress Cataloging-in-Publication Data:***

Griffiths, Peter R., 1942–

Fourier transform infrared spectrometry / Peter R. Griffiths, James A. de Haseth. – 2nd ed.

p. cm.

ISBN 978-0-471-19404-0

1. Fourier transform infrared spectroscopy. I. de Haseth, James A. II.

Title.

QD96.I5G743 2007

535.8'42–dc22

2006022115

Printed in the United States of America

10 9 8 7 6 5 4 3 2 1

# CONTENTS

## PREFACE

xv

<b>CHAPTER 1</b>	<b>INTRODUCTION TO VIBRATIONAL SPECTROSCOPY</b>	<b>1</b>
1.1.	Introduction	1
1.2.	Molecular Vibrations	3
1.3.	Vibration–Rotation Spectroscopy	6
1.4.	Widths of Bands and Lines in Infrared Spectra	10
1.4.1.	Vibration–Rotation Spectra of Gases	10
1.4.2.	Spectra of Condensed-Phase Samples	11
1.5.	Quantitative Considerations	12
1.5.1.	Beer’s Law	12
1.5.2.	Optical Constants	14
1.6.	Polarized Radiation	15
1.7.	Raman Spectrometry	16
1.8.	Summary	18
<b>CHAPTER 2</b>	<b>THEORETICAL BACKGROUND</b>	<b>19</b>
2.1.	Michelson Interferometer	19
2.2.	Generation of an Interferogram	20
2.3.	Effect of Finite Resolution	26
2.4.	Apodization	30
2.5.	Phase Effects	36
2.6.	Effect of Beam Divergence	41
2.7.	Effect of Mirror Misalignment	46
2.8.	Effect of a Poor Mirror Drive	49
2.9.	Rapid-Scan Interferometers	50
2.10.	Step-Scan Interferometers	53

<b>CHAPTER 3</b>	<b>SAMPLING THE INTERFEROGRAM</b>	<b>57</b>
3.1.	Sampling Frequency	57
3.1.1.	Nyquist Frequency	57
3.1.2.	Conceptual Discussion of Aliasing	58
3.1.3.	Mathematical Discussion of Aliasing	60
3.2.	Aliasing	62
3.3.	Dynamic Range	64
3.3.1.	ADC Specifications	64
3.3.2.	Digitization Noise	66
3.3.3.	Gain Ranging	68
3.3.4.	Chirping	69
3.4.	Analog-to-Digital Converters	71
<b>CHAPTER 4</b>	<b>FOURIER TRANSFORMS</b>	<b>75</b>
4.1.	Classical Fourier Transform	75
4.1.1.	Elementary Concepts	75
4.1.2.	Mathematical Basis	76
4.2.	Fast Fourier Transform	78
4.3.	Phase Correction	85
4.4.	Fourier Transform: Pictorial Essay	88
4.5.	Data Systems	93
<b>CHAPTER 5</b>	<b>TWO-BEAM INTERFEROMETERS</b>	<b>97</b>
5.1.	Michelson-Type Interferometers	97
5.1.1.	Introduction	97
5.1.2.	Drive	97
5.1.3.	Bearings	98
5.1.4.	Fringe Referencing	104
5.1.5.	Dynamic Alignment	110
5.2.	Tilt-Compensated Interferometers	112
5.2.1.	Cube-Corner Interferometers	112
5.2.2.	Other Designs	118
5.3.	Refractively Scanned Interferometers	123
5.4.	Polarization Interferometers	125
5.5.	Step-Scan Interferometers	127
5.6.	Stationary Interferometers	128
5.7.	Beamsplitters	132

5.8. Lamellar Grating Interferometers	138
Appendix: Manufacturers of FT-IR Spectrometers	142
 <b>CHAPTER 6 OTHER COMPONENTS OF FT-IR SPECTROMETERS</b>	 <b>143</b>
6.1. Infrared Radiation Sources for Transmission and Reflection Spectrometry	143
6.1.1. Mid-Infrared Sources	143
6.1.2. Near-Infrared Sources	145
6.1.3. Far-Infrared Sources	146
6.2. Detectors	146
6.2.1. Thermal Detectors	146
6.2.2. Quantum Detectors	148
6.3. Optics	152
6.3.1. Paraboloidal Mirrors	152
6.3.2. Plane Mirrors	155
6.3.3. Ellipsoids, Toroids, and Other Aspherical Mirrors	155
6.4. Spectrometer Design	156
 <b>CHAPTER 7 SIGNAL-TO-NOISE RATIO</b>	 <b>161</b>
7.1. Detector Noise	161
7.2. Trading Rules in FT-IR Spectrometry	164
7.2.1. Effect of Resolution and Throughput on SNR	164
7.2.2. Effect of Apodization	165
7.2.3. Effect of Changing Mirror Velocity	165
7.3. Digitization Noise	166
7.4. Other Sources of Noise	167
7.4.1. Sampling Error	167
7.4.2. Folding	168
7.4.3. Fluctuation Noise	169
7.4.4. Shot Noise	170
7.5. Interferometers Versus Grating Spectrometers	171
7.5.1. Fellgett's Advantage	171
7.5.2. Jacquinot's Advantage	172
7.5.3. Other Factors	173

<b>CHAPTER 8</b>	<b>PHOTOMETRIC ACCURACY IN FT-IR SPECTROMETRY</b>	<b>177</b>
8.1.	Introduction	177
8.2.	Effect of Spectral Resolution	177
8.3.	Effect of Apodization	180
8.3.1.	Triangular Apodization	180
8.3.2.	Norton–Beer Apodization Functions	181
8.4.	100% Lines	181
8.4.1.	Short-Term Performance	181
8.4.2.	Glitches (Nonrandom Noise Sources)	184
8.4.3.	Long-Term Performance	185
8.4.4.	Effect of Sample Diameter and Thickness	186
8.5.	Zero Energy Level	187
8.5.1.	Detector Response Nonlinearity	187
8.5.2.	Changes in Modulation Efficiency	191
8.5.3.	Sampling Effects	193
8.6.	Linearity Between 100% and 0% <i>T</i>	194
<b>CHAPTER 9</b>	<b>QUANTITATIVE ANALYSIS</b>	<b>197</b>
9.1.	Introduction	197
9.2.	Beer’s Law	197
9.3.	Spectral Subtraction	201
9.4.	Linear Least-Squares Fitting Methods	204
9.5.	Classical Least Squares	207
9.6.	Inverse Least-Squares Regression	210
9.7.	Principal Component Analysis	213
9.8.	Principal Component Regression	215
9.9.	Partial Least-Squares Regression	216
9.10.	Validation	217
9.11.	Multivariate Curve Resolution	218
9.12.	General Guidelines for Calibration Data Sets	220
9.13.	Neural Networks	221
<b>CHAPTER 10</b>	<b>DATA PROCESSING</b>	<b>225</b>
10.1.	Baseline Correction	225
10.2.	Interpolation	227
10.3.	Peak Picking	229
10.4.	Spectral Smoothing	232

10.5. Band Fitting	235
10.6. Derivatives of Spectra	237
10.7. Fourier Self-Deconvolution	240
10.8. Spectral Searching	246
<b>CHAPTER 11 CONVENTIONAL TRANSMISSION SPECTROMETRY</b>	<b>251</b>
11.1. Condensed-Phase Samples	251
11.1.1 Window Materials	251
11.1.2 Band Intensities	251
11.1.3 Interference Fringes	253
11.1.4 Trace Analysis	255
11.2. Gas- and Vapor-Phase Samples	256
<b>CHAPTER 12 POLARIZATION</b>	<b>261</b>
12.1. Plane-Polarized Radiation	261
12.2. Circular Polarization	263
12.3. Polarization Modulation	264
12.4. Applications of Linear Dichroism	266
12.5. Vibrational Circular Dichroism	269
<b>CHAPTER 13 SPECULAR REFLECTION</b>	<b>277</b>
13.1. Introduction	277
13.2. Fresnel Reflection from Bulk Samples	277
13.2.1. Fresnel Equations	277
13.2.2. Nonabsorbing Materials	278
13.2.3. Absorbing Materials	279
13.3. Infrared Reflection–Absorption Spectrometry with Metal Substrates	282
13.3.1. Effect of Incidence Angle and Polarization	282
13.3.2. Polarization Modulation	287
13.3.3. Surface Selection Rule	290
13.4. IRRAS with Dielectric Substrates	293
13.5. Transflection	297
13.5.1. Thick Films on Metal Substrates	297
13.5.2. Liquid Sampling for Near-Infrared Spectrometry	300
13.6. Summary	300



<b>CHAPTER 14</b>	<b>MICROSPECTROSCOPY AND IMAGING</b>	<b>303</b>
14.1.	Microsampling with Beam Condensers	303
14.2.	Microscopes	304
14.3.	Diamond Anvil Cells	309
14.4.	Reflection Microscopy	310
14.5.	Hyperspectral FT-IR Imaging	312
14.5.1.	Hyperspectral Imaging with a Step-Scanning Interferometer	312
14.5.2.	Hyperspectral Imaging with a Continuous-Scanning Interferometer	314
14.5.3.	Signal-to-Noise Ratio	316
14.5.4.	Software	318
14.5.5.	Applications of Hyperspectral Imaging	319
<b>CHAPTER 15</b>	<b>ATTENUATED TOTAL REFLECTION</b>	<b>321</b>
15.1.	Introduction	321
15.2.	Theory	322
15.3.	Practical Considerations	327
15.4.	Accessories for Multiple Internal Reflection	329
15.5.	Single-Reflection Accessories	336
15.6.	Infrared Fibers	342
15.7.	Summary	347
<b>CHAPTER 16</b>	<b>DIFFUSE REFLECTION</b>	<b>349</b>
16.1.	Theory of Diffuse Reflection	349
16.2.	Accessories for Diffuse Reflection	353
16.3.	Applications of Mid-Infrared Diffuse Reflection Spectrometry	355
16.4.	Applications of Near-Infrared Diffuse Reflection Spectrometry	358
16.5.	Reference Materials for Diffuse Reflection Spectrometry	361
<b>CHAPTER 17</b>	<b>EMISSION</b>	<b>363</b>
17.1.	Introduction	363
17.2.	Infrared Emission Spectra of Gases	363

17.3. Infrared Emission Spectra of Condensed-Phase Samples	366
17.4. Transient Infrared Emission Spectroscopy	368
 <b>CHAPTER 18 FOURIER TRANSFORM RAMAN SPECTROMETRY</b>	 <b>375</b>
18.1. Introduction	375
18.2. Instrumentation	378
18.2.1. Nd : YAG Laser	378
18.2.2. Filters	380
18.2.3. Collection Optics	381
18.2.4. Interferometer	382
18.2.5. Detector	382
18.2.6. Spectrometer	384
18.3. FT Raman Versus CCD Raman Spectrometry	385
18.4. Applications of FT-Raman Spectrometry	387
18.4.1. Standard Raman Spectroscopy	387
18.4.2. Surface-Enhanced Raman Spectroscopy	389
18.5. Summary	391
 <b>CHAPTER 19 TIME-RESOLVED SPECTROMETRY</b>	 <b>395</b>
19.1. Continuous-Scanning Interferometers	395
19.1.1. Instrumental Considerations	395
19.1.2. Applications	397
19.2. Time-Resolved Measurements Using Step-Scan Interferometers	400
19.2.1. Instrumental Considerations	400
19.2.2. Applications of Time-Resolved Spectroscopy with a Step-Scan Interferometer	402
19.3. Stroboscopic Spectrometry	407
19.4. Asynchronous Time-Resolved FT-IR Spectrometry	408
19.4.1. Instrumental Considerations	408
19.4.2. Application to Liquid-Crystal Orientation Dynamics	412

<b>CHAPTER 20</b>	<b>PHOTOACOUSTIC SPECTROMETRY</b>	<b>415</b>
20.1.	Photoacoustic Spectroscopy of Gases	415
20.2.	Photoacoustic Spectroscopy of Solids with a Rapid-Scanning Interferometer	417
20.3.	Photoacoustic Spectroscopy of Solids with a Step-Scan Interferometer	425
20.3.1.	Phase Modulation	425
20.3.2.	Depth Profiling by Varying the Photoacoustic Phase	428
20.3.3.	Multifrequency Measurements	431
<b>CHAPTER 21</b>	<b>SAMPLE MODULATION SPECTROMETRY WITH A STEP-SCAN INTERFEROMETER</b>	<b>435</b>
21.1.	Dynamic Infrared Linear Dichroism Measured with a Monochromator	435
21.2.	DIRLD Spectrometry with a Step-Scan Fourier Transform Spectrometer	440
21.3.	Two-Dimensional Correlation Plots	448
21.4.	DIRLD Spectrometry with a FT-IR Spectrometry and Digital Signal Processing	454
21.5.	Other Sample Modulation Measurements with Step-Scan Interferometers	458
21.5.1.	Liquid-Crystal Electroreorientation	458
21.5.2.	Infrared Spectroelectrochemistry	460
<b>CHAPTER 22</b>	<b>ATMOSPHERIC MONITORING</b>	<b>463</b>
22.1.	Extractive Atmospheric Monitoring	463
22.2.	Open-Path Atmospheric Monitoring	466
<b>CHAPTER 23</b>	<b>COUPLED TECHNIQUES</b>	<b>481</b>
23.1.	Introduction	481
23.2.	Light-Pipe-Based GC/FT-IR Interfaces	482
23.2.1.	Instrumental Considerations	482
23.2.2.	Spectroscopic Considerations	485
23.2.3.	Chromatogram Construction	486
23.2.4.	Example of GC/FT-IR	490
23.3.	Mobile-Phase Elimination Approaches for GC/FT-IR	491

23.3.1. Introduction	491
23.3.2. Matrix Isolation GC/FT-IR	491
23.3.3. Direct Deposition GC/FT-IR	493
23.4. HPLC/FT-IR Interface	495
23.4.1. Measurements Made with Flow Cells	495
23.4.2. Mobile-Phase Elimination Techniques for HPLC/FT-IR	496
23.5. SFC/FT-IR Interface	500
23.6. TGA/FT-IR	502
23.7. Other Coupled Techniques	504

<b>INDEX</b>	<b>509</b>
--------------	------------



## PREFACE

The advances in the field of Fourier transform infrared (FT-IR) spectrometry in the past 20 years have been quite remarkable. FT-IR spectrometers are installed in just about every analytical chemistry laboratory in the developed world. Actually, we sometimes wonder why so many people still refer to these instruments as FT-IR spectrometers, or more colloquially simply as FTIRs, rather than simply as infrared spectrometers, since almost all mid-infrared spectra are measured with these instruments. We note that scientists who use nuclear magnetic resonance, the other technique that has been revolutionized by the introduction of Fourier transform techniques, no longer talk about FT-NMR, as continuous-wave instruments (e.g., grating monochromators) are a distant memory. Nonetheless, practitioners of infrared spectrometry seem to want to recall the era of grating monochromators, even though the vast majority has never seen one!

This book is the second edition of a volume that was published in 1986. In the past 20 years, an enormous body of work has been published in which the key measurements have been made on FT-IR spectrometers. When we started to write this new edition, it was not our intention to give a compendium of all these applications. Instead, we have tried to give a description of the theory and instrumentation of FT-IR spectrometry as it stands today. Even with this limitation, the material has taken 23 chapters to cover, and we know that a number of topics has been omitted. We ask all our many friends whose work is not referenced in this book for their understanding and forgiveness. All we can say is that had we reviewed all the important and elegant experiments that have been done over the past 20 years, the book would have rivaled the size of the 4000-page-long *Handbook of Vibrational Spectroscopy* that one of us recently coedited. Instead, what we have tried to do is to provide users of FT-IR spectrometers with a reasonably detailed description of how their instruments work and the types of experiments that can be performed even on the less expensive instruments.

At this point we should note that the way that infrared spectroscopy is applied has changed dramatically over the past 20 or 30 years. Whereas infrared spectrometry once played an important role in the structural elucidation of new organic compounds, this task is now largely accomplished by NMR, mass spectrometry and x-ray crystallography. Why, then, is the popularity of infrared spectrometry at an all-time high? The answer is in part to be found in the versatility of this technique and in part in the relatively low cost of the instrumentation. The number of applications for which a careful measurement of the infrared spectrum will yield important qualitative, quantitative, and/or kinetic information is limited only by

the imagination of the user. In the book we have attempted to summarize the types of experiments that can be carried out on FT-IR spectrometers. For most of them, we do not go into great detail. There are a few measurements, however, such as the treatment of dynamic linear dichroism spectra by two-dimensional correlation, where we felt that a more detailed description was needed if it is to be understood by the average reader.

We have attempted to use the correct nomenclature throughout the book. Regrettably, few spectroscopists use correct terminology in their papers and reports. Correct usage for spectroscopic terms has been defined beautifully by John Bertie in a glossary at the end of the *Handbook of Vibrational Spectroscopy*, and we use his recommendations in a consistent manner. The book is largely about the measurement of spectra: hence the title “Fourier Transform Infrared Spectrometry.”<sup>1</sup> Throughout the book we have tried to use the term *wavenumber* when we refer to the abscissa scale of a spectrum in  $\text{cm}^{-1}$ , using the term *frequency* only when referring to the modulation of a signal in hertz. We note that *curve fitting* and *deconvolution* are often (incorrectly) used interchangeably and we have tried to use the terms correctly. We would also note that the verb from which (*de*)*convolution* is derived is (*de*)*convolve* (as in *revolve/revolution* and *evolve/evolution*). Both of us wish to demonstrate that the five years we each spent learning Latin in high school was not misspent!

Measured or measurable parameters end in the suffix *-ance* (e.g., transmittance, absorbance, reflectance). A spectrum that is plotted with one of these parameters as the y-axis can validly be referred to as a *transmittance*, *absorbance*, or *reflectance* spectrum; otherwise, it should be referred to as a *transmission*, *absorption*, or *reflection* spectrum. We particularly note how reflection spectroscopy has fallen into this misuse. Unfortunately, *diffuse reflectance spectroscopy* and *attenuated total reflectance (ATR) spectroscopy* are now part of many spectroscopists’ lexicon. Pedagogy has held sway, however, and we have attempted to use the correct terminology throughout the book. One of us (P.R.G) particularly regrets the poor usage of the term *diffuse reflectance spectroscopy* in his early papers on this subject. He regrets even more that he coined the term *DRIFT* for this technique, as *drift* has all the wrong connotations for any spectroscopic measurement. Shortly after the first papers on DRIFT were published, Bob Hannah of PerkinElmer showed that diffuse reflection infrared spectra could be measured easily on grating spectrometers and coined the acronym *DRUIDS* (diffuse reflection using infrared dispersive spectrometry!). We hope that neither Bob nor Peter is forced to live in acronym hell as result of their transgressions on this planet!

We would also like to note the reason for the hyphen between FT and IR throughout the book. This is to distinguish *Fourier transform infrared spectrometry* from *frustrated total internal reflection*; FTIR is now an infrequently used term for

---

<sup>1</sup>The etymology of the term *spectrometry* is clear, but the meaning of *spectroscopy* is less so as spectra are no longer measured with spectroscopes. In this book we use *spectrometry* to mean the measurement of spectra and *spectroscopy* to mean the science of obtaining qualitative and quantitative information from spectra.

ATR, but nevertheless, this usage was introduced before FT-IR spectrometers became popular.

Finally, we would like to thank the many people who have either supplied material for the various chapters in this book or proofread the work in one of its several drafts. In particular, we would like to thank Richard Jackson, Bruce Chase, Larry Nafie, Rina Dukor, John Chalmers, Milan Milosevic, Neil Overall, and Roger Jones, as well as the members of our research groups, for their comments. We gratefully acknowledge the patience and good grace of the six (count 'em!) Wiley editors who have tried to extract the manuscript from us. Finally, our wives, Marie and Leslie, deserve our unending gratitude for putting up with us over the many years that it has taken to assemble the material for this book.





# INTRODUCTION TO VIBRATIONAL SPECTROSCOPY

## 1.1. INTRODUCTION

Infrared (IR) spectrometry has changed dramatically over the past 40 years. In the 1960s, undergraduate chemistry majors would learn that the primary use of infrared spectrometry was for the structural elucidation of organic compounds. In many large research laboratories, however, the structure of complex molecules is now usually found by a combination of techniques, including two-dimensional nuclear magnetic resonance (NMR), x-ray diffraction, and mass spectrometry, with IR spectrometry playing a less dominant, although still important role. For example, U.S. pharmaceutical companies must still submit IR spectra as part of their application to the Food and Drug Administration as evidence of the putative chemical structure, and in polymer laboratories infrared spectrometry is still used as the primary instrument for the determination of molecular structure.

This is not to imply that molecular structure of simple organic molecules cannot be determined by infrared spectroscopy. In fact, the information that can be deduced from an infrared spectrum is complementary to that of other methods, and infrared spectroscopy provides valuable information that is unattainable by other methods, as is shown in the remainder of the book. More important, however, a plethora of other applications became available with the advent in 1969 of the first commercial mid-infrared Fourier transform spectrometer with better than  $2\text{ cm}^{-1}$  resolution. These include quantitative analysis of complex mixtures, the investigation of dynamic systems, biological and biomedical spectroscopy, microspectroscopy and hyperspectral imaging, and the study of many types of interfacial phenomena. All of these applications (and many more) are described in this book. Furthermore, because of the development of such sampling techniques

as attenuated total reflection (ATR), measurement of the infrared spectra of many types of samples has become quite routine.

The impact of Fourier transform infrared (FT-IR) spectrometers was not recognized immediately. For example, in 1973, Herbert Laitinen, who was the editor of *Analytical Chemistry* at the time, made an analogy with Shakespeare's seven ages of man to define the seven ages of an analytical instrument [1]. These seven ages start with the discovery of the principles of the technique in a physicist's laboratory. After characterization and commercialization of the technique, instruments graduate from the research laboratory to routine measurements, until in their seventh age they are superseded by newer instruments with higher speed, sensitivity, specificity, or resolution. In his 1973 editorial, Laitinen used infrared spectrometry to illustrate an instrument in its seventh age. In fact, the technique was in its second childhood! Let us first consider why FT-IR spectrometers have assumed such a position of dominance for the measurement of infrared spectra.

Survey spectra in the mid-infrared region are often measured at a resolution of  $\sim 4\text{ cm}^{-1}$ . When such spectra between  $4000$  and  $400\text{ cm}^{-1}$  are measured with a prism or grating monochromator, only one  $4\text{-cm}^{-1}$  resolution element in the  $3600\text{-cm}^{-1}$ -wide spectral range of interest is measured at any instant; the remaining 899 resolution elements are not. Thus, the efficiency of the measurement is only about 0.1%. It was typical for survey scans to take several minutes to measure, whereas the measurement of archival-quality spectra (measured at  $1$  to  $2\text{ cm}^{-1}$  resolution) often took at least 30 minutes.

In FT-IR spectrometry, all the resolution elements are measured at all times during the measurement (the *multiplex* or *Fellgett's advantage*). In addition, more radiation can be passed between the source and the detector for each resolution element (the *throughput* or *Jacquinot's advantage*). These advantages are discussed in Chapter 7. As a result, transmission, reflection, and even emission spectra can be measured significantly faster and with higher sensitivity than ever before.

In this book we demonstrate how FT-IR spectrometry can not only be used to measure infrared spectra of the type of samples that have classically been investigated by infrared spectrometers for decades (i.e., gases, liquids, and bulk and powdered solids in milligram quantities), but that interfacial species, microsamples, and trace analytes can now be characterized routinely. Measurement times have been reduced from minutes to fractions of a second; in special cases, reactions taking place in less than a microsecond can be followed. The physical properties of materials can be correlated to the molecular structure by vibrational spectroscopy better than by any other analytical technique. It is probably true to say that during the more than three decades following Laitinen's editorial, infrared spectroscopy has entered and passed from its second childhood into its fifth age. Because of the remarkable advances made in the performance of FT-IR spectrometers, infrared spectrometry has matured to the point that it is used for the solution of a variety of problems from the research lab to the manufacturing floor, and sales of infrared spectrometers are at an all-time high.

The increased popularity of infrared spectrometry and the commercial availability of instruments that are "so simple that a child can operate them" have led to the

unexpected consequence that many operators of FT-IR spectrometers have received little or no formal training in vibrational spectroscopy. To serve these new players in the “FT-IR game” and to help give them a better appreciation of how the measurement of infrared spectra may be optimized, a brief introduction to the origin of vibrational spectra of gases, liquids, and solids is given in the remainder of this chapter. In the rest of the book, we show how FT-IR spectrometers work and how to measure the most accurate and information-rich infrared spectra from a wide variety of samples.

## 1.2. MOLECULAR VIBRATIONS

Infrared spectra result from transitions between quantized vibrational energy states. Molecular vibrations can range from the simple coupled motion of the two atoms of a diatomic molecule to the much more complex motion of each atom in a large polyfunctional molecule. Molecules with  $N$  atoms have  $3N$  degrees of freedom, three of which represent translational motion in mutually perpendicular directions (the  $x$ ,  $y$ , and  $z$  axes) and three represent rotational motion about the  $x$ ,  $y$ , and  $z$  axes. The remaining  $3N - 6$  degrees of freedom give the number of ways that the atoms in a nonlinear molecule can vibrate (i.e., the number of *vibrational modes*).

Each mode involves approximately harmonic displacements of the atoms from their equilibrium positions; for each mode,  $i$ , all the atoms vibrate at a certain characteristic frequency,  $\nu_i$ . The potential energy,  $V(r)$ , of a harmonic oscillator is shown by the dashed line in Figure 1.1 as a function of the distance between the atoms,  $r$ . For any mode in which the atoms vibrate with simple harmonic motion (i.e., obeying Hooke’s law), the vibrational energy states,  $V_{iv}$ , can be described

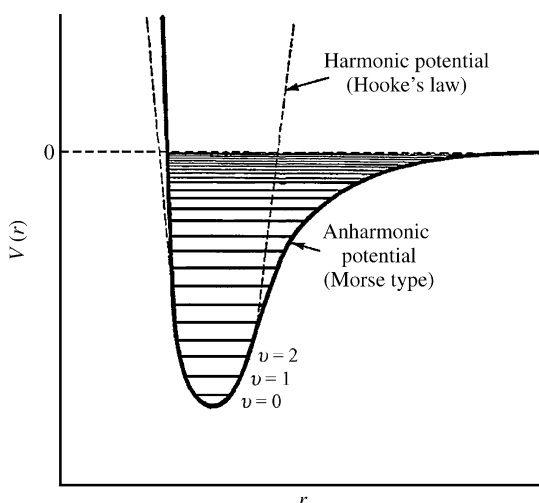


**Figure 1.1.** Potential energy of a diatomic molecule as a function of the atomic displacement during a vibration for a harmonic oscillator (dashed line) and an anharmonic oscillator (solid line).

by the equation

$$V_{iv} = hv_i \left( v_i + \frac{1}{2} \right) \quad (1.1)$$

where  $h$  is Planck's constant,  $v_i$  the *fundamental frequency* of the particular mode, and  $v_i$  the *vibrational quantum number* of the  $i$ th mode ( $v_i = 0, 1, 2, \dots$ ). Note that frequency in units of hertz is usually given the symbol  $\nu$ . Vibrational frequencies are often given in units of wavenumber, the number of waves per unit length. The most common unit of length is the centimeter, in which case the wavenumber has units of  $\text{cm}^{-1}$  and is given the symbol  $\tilde{\nu}$  by many chemists and  $\sigma$  by many physicists. The energy difference for transitions between the ground state ( $v_i = 0$ ) and the first excited state ( $v_i = 1$ ) of most vibrational modes corresponds to the energy of radiation in the mid-infrared spectrum (400 to  $4000 \text{ cm}^{-1}$ ).

The motion of the atoms during the vibration is usually described in terms of the *normal coordinate*,  $Q_i$ . The molecule is promoted to the excited state only if its dipole moment,  $\mu$ , changes during the vibration [i.e., provided that  $(\partial\mu/\partial Q_i) \neq 0$ ]. For molecules with certain elements of symmetry, some vibrational modes may be degenerate, so that more than one mode has a given vibrational frequency whereas others may be completely forbidden. Thus, because of degeneracy, the number of fundamental absorption bands able to be observed is often less than  $3N - 6$ . Because rotation of a linear molecule about the axis of the bond does not involve the displacement of any of the atoms, one of the rotational degrees of freedom is lost and linear molecules have an additional vibrational mode. Thus, the number of modes of a linear molecule is  $3N - 5$ , so that a diatomic molecule ( $N = 2$ ) has a single vibrational mode.

The actual variation of the potential energy as a function of the displacement of the atoms from their equilibrium positions is shown as a solid line in Figure 1.1. From this curve it can be seen that Eq. 1.1 is valid only for low values of the vibrational quantum number and is not valid when  $v_i$  is large. In practice,  $V_{iv}$  must be described using an *anharmonic* (Morse-type) potential function. This behavior is shown in Figure 1.1 as a solid line, and the potential energy is given to a first approximation by the expression

$$V_{iv} = hv_i \left( v_i + \frac{1}{2} \right) + hv_i x_i \left( v_i + \frac{1}{2} \right)^2 \quad (1.2)$$

where  $x_i$  is the *anharmonicity constant*;  $x_i$  is dimensionless and typically has values between  $-0.001$  and  $-0.02$ , depending on the mode.

If the vibrational modes were strictly harmonic, no transitions involving changes in  $v_i$  by more than  $\pm 1$  would be allowed. The effect of anharmonicity is to relax this selection rule (i.e., to allow bands caused by  $|\Delta v_i| > 1$  to become allowed). Thus, overtone ( $\Delta v_i = 2, 3, \dots$ ) and combination ( $\Delta v_i = 1$ ;  $\Delta v_j = 1$ , where  $j$  represents a different mode) bands commonly appear weakly in the mid-infrared spectrum of organic compounds along with bands due to fundamental transitions ( $\Delta v_i = 1$ ).

For many vibrational modes, only a few atoms have large displacements and the rest of the molecule is almost stationary. The frequency of such modes is characteristic of the specific functional group in which the motion is centered and is minimally affected by the nature of the other atoms in the molecule. Thus, the observation of spectral features in a certain region of the spectrum is often indicative of a specific chemical functional group in the molecule. Extensive spectral/structure correlation tables (often known as *Colthup charts*) have been developed to allow chemists to assign one or more absorption bands in a given infrared spectrum to the vibrational mode(s) associated with a certain functional group. These tables may be found in many textbooks on the interpretation of infrared spectra. Other bands involve the significant motion of only a few atoms, yet their frequency varies from one molecule to another containing the particular functional group. These modes are useful to distinguish one molecule from another that contains similar functional groups and hence are often known as *fingerprint bands*.

*Skeletal modes* involve significant displacements of many of the atoms in the molecule. These bands are rarely used to indicate the presence or absence of a specific functional group but again, may be useful to distinguish between structurally similar compounds. The vibrational frequency of skeletal modes is usually quite low. As a result, they absorb long-wavelength radiation that is often below the cutoff of many mid-infrared detectors. The *far-infrared* region of the spectrum ( $10$  to  $400\text{ cm}^{-1}$ ) is rarely used for structural elucidation but contains useful information on the vibration of heavy atoms (especially for inorganic compounds) and/or weak bonds such as hydrogen bonds.

Every molecule has slightly different vibrational modes from all other molecules (with the exception of enantiomers). Thus, the infrared spectrum of a given molecule is unique and can be used to identify that molecule. Infrared spectra give far more detailed information than simply allowing the presence or absence of certain functional groups to be recognized. In the past, many chemists had a solid understanding of how to interpret infrared spectra, but spectral interpretation is starting to become a lost art, in part because of the emergence of nuclear magnetic resonance, mass spectrometry, and x-ray diffraction for this purpose, which are easier to interpret. Although molecular orbital programs are starting to permit infrared spectra of quite complex molecules to be calculated, perfect matching of calculated and measured spectra has yet to be achieved. Today, computer-assisted comparison of the spectra of unknowns to a large number of reference spectra in a database (*spectral, or library, searching*) has become a far more popular way than manual interpretation to find the structure of a molecule from its infrared spectrum. Because of the subtle differences between the spectra of many compounds, the result of a computerized spectral search should never be assumed to give the true identity of a compound without visual comparison by the operator between the best match and the actual spectrum of the unknown.

For most pure compounds, a sample thickness of only about  $10\text{ }\mu\text{m}$  is needed to yield a mid-infrared spectrum for which the bands are neither saturated (maximum transmittance less than 1%) nor so weak that they require ordinate expansion. It is often inconvenient and sometimes impossible to prepare such thin samples. In these

cases, measurement of the *near-infrared* (NIR) spectrum may prove advantageous. Overtone and combination bands are usually much weaker than the fundamental modes from which they are derived. The only exception to this “rule” is when these bands are enhanced by *Fermi resonance*, which occurs when an overtone or combination band absorbs at approximately the same frequency as that of a fundamental mode involving at least one of the same atoms. Although many overtone and combination bands absorb in the mid-infrared region, the first and second overtones ( $\Delta v_i = 2$  and 3) of only the C–H, O–H, and N–H stretching vibrations, or combination bands involving these modes, are found above  $4000\text{ cm}^{-1}$  (i.e., in the NIR region). In the last two decades, NIR spectrometry has become of tremendous importance, in large part because of the very *weakness* of these bands. For samples that are between about 0.1 and 5 mm in thickness, the NIR spectra are often much more appropriate for quantitative, and sometimes even qualitative, analysis than the corresponding mid-infrared spectra of these samples. Furthermore, samples do not have to be mounted in salt cells, sources are more intense, and NIR detectors are more sensitive than mid-infrared detectors. NIR spectra are not as easy to interpret as mid-infrared spectra, but they are very amenable to multivariate statistical analysis of the type that is now becoming common throughout analytical chemistry. Indeed, many of these algorithms were originally developed specifically for the analysis of NIR spectra.

### 1.3. VIBRATION–ROTATION SPECTROSCOPY

One of the greatest strengths of infrared spectrometry is that samples in all phases of matter may be studied. Infrared spectra of gases, liquids, and solids have different characteristics, and it is essential that these differences be understood if spectra of materials in each state are to be measured optimally and to yield the greatest amount of information. For example, the spectra of small molecules in the vapor phase show considerable fine structure because transitions between quantized *rotational energy* levels occur at the same time as vibrational transitions. Similar features are rarely seen in the spectra of larger molecules in the vapor phase (because the individual rotational transitions are too close together to be resolved) or any molecule in the liquid state (because collisions occur at a greater rate than the rotational frequency). The full theory of vibration–rotation spectroscopy is quite complex, and a detailed exposition of this subject is beyond the scope of this chapter, but a brief introduction to vibration–rotation spectroscopy is given below.

The simplest vibration–rotation spectra to interpret are those of diatomic molecules. The rotational energy levels of diatomic molecules are characterized by a single *rotational quantum number*,  $J$ . If the molecule is assumed to be a rigid rotor (i.e., its bond length remains constant no matter how rapidly the molecule rotates), the rotational energy is given by

$$E_J = BJ(J + 1) \quad (1.3)$$

$B$ , called the *rotational constant*, is given by

$$B = \frac{h}{8\pi^2 I c} \quad (1.4)$$

where  $I$  is the moment of inertia of the molecule and  $c$  is the velocity of light. The selection rule for transitions between rotational energy states for linear molecules is

$$\Delta J = \pm 1 \quad (1.5)$$

so that

$$E_J - E_{J-1} = BJ(J+1) - BJ(J-1) = 2BJ \quad (1.6)$$

Thus, for a rigid rotor, the pure rotation spectrum would be comprised of a series of lines with equal spacing of  $2B \text{ cm}^{-1}$ . For most molecules,  $B$  is sufficiently small that the pure rotation spectrum is found in the microwave region of the spectrum; however, for light molecules such as HCl,  $\text{H}_2\text{O}$ , or CO, rotational transitions absorb in the far infrared.

Diatomic molecules, X–Y, have a single fundamental vibrational mode, of wave-number  $\tilde{\nu}_0$ , which is infrared active only if  $X \neq Y$ . For any allowed vibrational transition of a gaseous diatomic molecule, there must be a simultaneous rotational transition; that is,

$$\Delta v_i = \pm 1 \quad \text{and} \quad \Delta J = \pm 1 \quad (1.7)$$

Thus, the vibration-rotation spectrum of a rigid diatomic molecule consists of a series of equally spaced lines above and below  $\tilde{\nu}_0$  that correspond to  $\Delta J = +1$  and  $\Delta J = -1$ , respectively. The series of lines below  $\tilde{\nu}_0$  ( $\Delta J = -1$ ) is known as the *P branch* of the band, while the lines above  $\tilde{\nu}_0$  ( $\Delta J = +1$ ) are known as the *R branch*. Because  $\Delta J \neq 0$ , there is no absorption line at  $\tilde{\nu}_0$ .<sup>1</sup>

In practice, molecules are not rigid rotors, and centrifugal forces cause the length of the bond between X and Y to increase as the angular velocity of the rotating molecule increases. The effect of centrifugal distortion is to increase the moment of inertia, decreasing the rotational constant,  $B$ , at high  $J$ . To a first approximation, the effect of centrifugal distortion is taken care of by adding a second term to Eq. 1.3:

$$E_J = BJ(J+1) - DJ^2(J+1)^2 \quad (1.8)$$

where  $D$  is the *centrifugal distortion constant*. Usually,  $0.1 < B < 10 \text{ cm}^{-1}$  and  $D \sim 10^{-4} \text{ cm}^{-1}$ . Because of the effect of centrifugal distortion, the spacing of the lines in the P branch increases as the distance from  $\tilde{\nu}_0$  increases while that of the lines in the R branch decreases.

<sup>1</sup>There is one exception to this “rule” for diatomic molecules. The fact that nitric oxide has an unpaired electron in its ground state leads to the fact that the transition  $\Delta J = 0$  is allowed.



As molecules become larger and less symmetrical, the spacing of the lines in their vibration–rotation spectra decreases and the spectra become more complex. For a linear molecule such as  $\text{CO}_2$ , the selection rules for each mode depend on the symmetry of the vibration. The symmetric stretching mode of  $\text{CO}_2$  ( $\nu_1$ ) is not active, since  $(\partial\mu/\partial Q) = 0$ . For the antisymmetric stretching mode ( $\nu_3$ ), in which the molecule remains linear throughout the vibration, the selection rules are the same as for diatomic molecules and hence the spectrum has a similar appearance (see Figure 1.2*a*). For the (degenerate) bending mode ( $\nu_2$ ), a vibrational transition

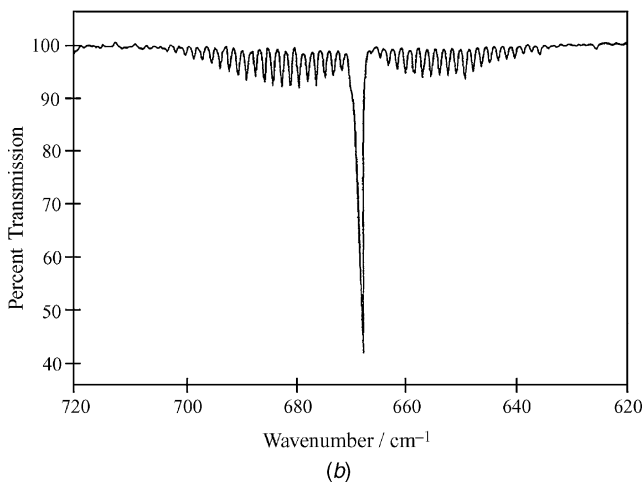
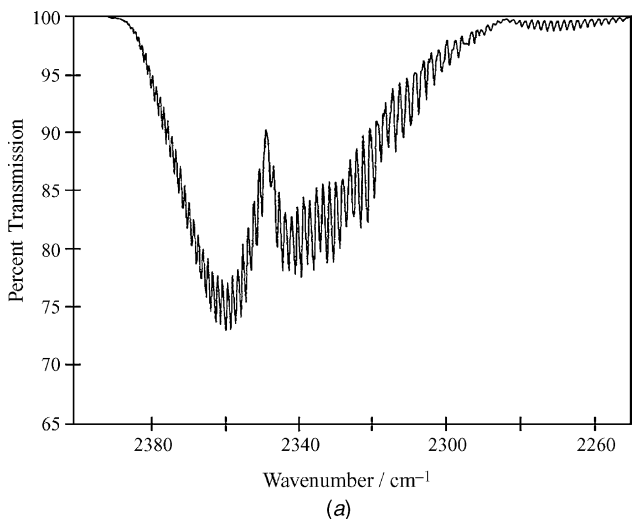


**Figure 1.2.** Infrared active vibration–rotation fundamental bands of carbon dioxide: (a) antisymmetric stretching mode ( $\nu_3$ ) for which the selection rule is  $\Delta\nu_3 = \pm 1$  and  $\Delta J = \pm 1$ ; (b) bending mode ( $\nu_2$ ) for which the selection rules is  $\Delta\nu_2 = \pm 1$  and  $\Delta J = 0, \pm 1$ .

without a simultaneous change in  $J$  is permitted:

$$\Delta v_2 = \pm 1 \quad \text{and} \quad \Delta J = 0, \pm 1 \quad (1.9)$$

Thus, there is a strong line in the spectrum, known as the *Q branch*, corresponding to  $\Delta J = 0$ . The reason that the selection rules are different for these two modes is because different symmetry elements of the linear  $\text{CO}_2$  molecule are lost during these two vibrations.

Linear molecules have two equal principal moments of inertia, corresponding to rotation about the center of mass about two mutually perpendicular axes, with the third principal moment equal to zero. Nonlinear molecules usually have three different moments of inertia. In this case, the vibration-rotation spectrum can be very complex, even for a simple molecule such as water. The rotational fine structure of the H-O-H bending mode of water is shown in Figure 1.3.

The two molecules whose vibration-rotation spectrum is shown in Figures 1.2 and 1.3,  $\text{CO}_2$  and  $\text{H}_2\text{O}$ , are often encountered as interferences when mid-infrared spectra are measured (although the rotational lines in the spectrum of  $\text{CO}_2$  are often unresolved when the spectrometer resolution is  $4 \text{ cm}^{-1}$  or poorer). In fact, it is good practice to eliminate all traces of these molecules in the beam path of an infrared spectrometer by purging the instrument with dry  $\text{CO}_2$ -free air or pure nitrogen gas, as the bands shown in Figures 1.2 and 1.3 will often be seen in the spectra. As noted above, because collisions occur at a greater rate than the rotational frequency of molecules in the liquid state, no rotational fine structure is seen.

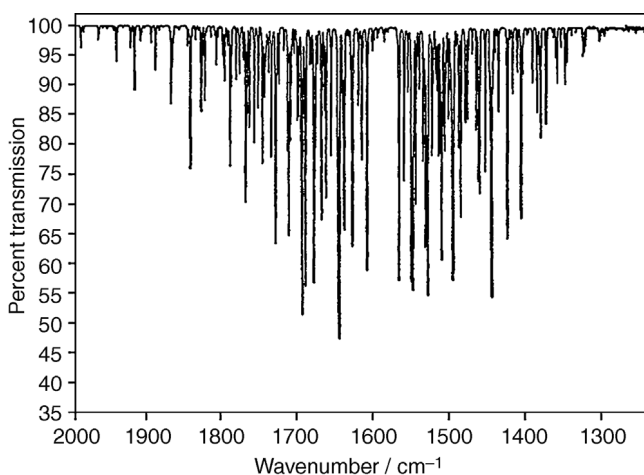


**Figure 1.3.** Vibration-rotation spectrum of the H-O-H bending mode of water vapor.

## 1.4. WIDTHS OF BANDS AND LINES IN INFRARED SPECTRA

### 1.4.1. Vibration–Rotation Spectra of Gases

The shape and width of individual lines in the vibration–rotation spectrum of a gas depend on the gas pressure,  $P$ . For gases at low pressure (typically,  $P < 1$  torr), the shape and width of each spectral line in the width are determined by the Doppler effect (i.e., by the variation of the speed of each molecule in the direction of the beam). The shape of a Doppler-broadened line centered at wavenumber  $\tilde{\nu}_0$  is Gaussian; that is, the absorbance at any wavenumber  $\tilde{\nu}$  is given by

$$A(\tilde{\nu}) = A_0 \exp \left[ \frac{-4 (\ln 2) (\tilde{\nu} - \tilde{\nu}_0)^2}{\gamma_D^2} \right] \quad (1.10)$$

where  $A_0$  is the absorbance at  $\tilde{\nu}_0$ .  $\gamma_D$  is the full width at half-height (FWHH) of the band and is given by

$$\gamma_D = 2 \sqrt{\frac{2(\ln 2) kT}{m}} \frac{v}{c} \quad (1.11)$$

where  $k$  is Boltzmann's constant,  $T$  the temperature (in kelvin),  $v$  the frequency of the transition (in hertz),  $c$  the velocity of light, and  $m$  the mass of the molecule. Since  $m$  is equal to the molecular weight (in grams),  $M$ , divided by Avogadro's number, and frequency,  $v$ , is directly proportional to wavenumber,  $\tilde{\nu}$ , we have

$$\frac{\gamma_D}{\tilde{\nu}} = 7.16 \times 10^{-7} \sqrt{\frac{T}{M}} \quad (1.12)$$

For a line in the H–O–H bending mode of water ( $M = 18 \text{ g} \cdot \text{mol}^{-1}$ ) at  $1500 \text{ cm}^{-1}$ , the Doppler width at room temperature (298 K) is about  $0.0044 \text{ cm}^{-1}$ . Thus, an instrument with very high resolution is needed before Doppler-broadened spectra can be measured accurately.

As the total pressure of the gas is raised above 1 torr, the mechanism of line broadening becomes more dominated by the effect of intermolecular collisions than by the Doppler effect. The shape of lines in collision-broadened spectra is Lorentzian:

$$A(\tilde{\nu}) = A_0 \frac{\gamma_C^2}{\gamma_C^2 + 4 (\tilde{\nu} - \tilde{\nu}_0)^2} \quad (1.13)$$

where  $\gamma_C$ , the FWHH of the collision-broadened line, is directly proportional to the pressure of the gas and increases with the polarity of each component. There are several mechanisms of collision broadening, each of which leads to a slightly different variation of the broadening coefficient with temperature, from  $1/\sqrt{T}$  for hard-sphere collisions to  $1/T$  for dipole–dipole interactions. For many molecules in air at ambient temperature, the collision-broadening coefficient is between  $0.1$  and  $0.2 \text{ cm}^{-1} \cdot \text{atm}^{-1}$ .

Hence for mixtures of an analyte with helium, nitrogen, or air at atmospheric pressure,  $\gamma_C$  of each of the rotational lines is usually between 0.1 and 0.2  $\text{cm}^{-1}$ .

For molecules at pressures between about 1 and 100 torr, the line width is determined by both Doppler and collision broadening. In this case, the shape is given by a convolution of the shapes given by Eqs. 1.10 and 1.13; such a shape is known as a *Voigt profile*. The higher the pressure of the gas, the greater the contribution of collision broadening to the Voigt profile. Voigt profiles cannot be expressed analytically, as they result from the convolution of a Lorentzian and Gaussian shape, but the FWHH is given to a good approximation by

$$\gamma_V = \frac{\gamma_C}{2} + \sqrt{\left(\frac{\gamma_C}{2}\right)^2 + (\gamma_D)^2} \quad (1.14)$$

For large molecules, the spacing of lines in the vibration-rotation spectrum is usually less than 0.1  $\text{cm}^{-1}$ . For such molecules in 1 atm of air or some other inert gas, the line spacing is less than  $\gamma_C$ , so that the lines can never be separated no matter how high the resolution of the spectrometer, and only the band contour can be measured. In this case, the higher the molecular weight of the molecule, the narrower is the band contour. Nonetheless, for most molecules, the FWHH of the band contour is at least 4  $\text{cm}^{-1}$ . For such molecules it is rarely necessary to use a resolution much higher than 4  $\text{cm}^{-1}$  to measure an easily recognizable spectrum, although to obtain a spectrum with minimal distortion of the rotational contour, a somewhat higher resolution should be used.

### 1.4.2. Spectra of Condensed-Phase Samples

Since there is no rotational fine structure in the infrared spectra of liquids, their spectra are much simpler than those of gases. To a good approximation, the shape of bands in the infrared spectra of liquids is Lorentzian (see Eq. 1.13). In practice, the far wings of bands in the spectra of liquids die out somewhat faster than would be given by Eq. 1.13. To model the behavior of bands in the spectra of liquids, bands are sometimes expressed as the sum of Lorentzian and Gaussian bands:

$$A(\tilde{\nu}) = (1 - \alpha)A_0 \frac{\gamma_L^2}{\gamma_L^2 + (\tilde{\nu} - \tilde{\nu}_0)^2} + \alpha A_0 \exp\left[-\frac{(\ln 2)(\tilde{\nu} - \tilde{\nu}_0)^2}{\gamma_G^2}\right] \quad (1.15)$$

where  $\gamma_L$  is the HWHH of the Lorentzian component,  $\gamma_G$  the HWHH of the Gaussian component (usually assumed to be the same), and  $\alpha$  the Gaussian fraction. For many liquids,  $\alpha < 0.1$ . Although complicated, this form is at least analytical, unlike the Voigt profile. An even better description of bands in the spectra of liquids can be made with the use of the classical damped harmonic oscillator model, but this is beyond the scope of this chapter.

The actual widths of absorption bands in the mid-infrared spectra of liquids and solutions depend strongly on the rigidity of the part of the molecule where the

vibrational motion of the molecule is localized. For example, bands associated with aromatic groups often have widths between 2.5 and 5  $\text{cm}^{-1}$ , whereas the FWHH of bands associated with the more flexible alkyl chains is often at least 10  $\text{cm}^{-1}$ . Bandwidths also depend on the polarity of the solvent, with bands of a particular solute in a polar solvent usually being broader than the corresponding bands of the same molecule in a nonpolar solvent. Since water is the most polar solvent, bands of solutes in aqueous solution are usually broader than in any other solvent. When functional groups such as O—H are hydrogen bonded, the width of the stretching bands may be greater than 100  $\text{cm}^{-1}$ . Because the widths of most absorption bands are rarely smaller than 4  $\text{cm}^{-1}$ , it is common for survey spectra of liquids to be measured at a resolution of 4 or 8  $\text{cm}^{-1}$ , whereas high-quality spectra for archival purposes are usually measured at a resolution of 1 or 2  $\text{cm}^{-1}$ . Of course, measurement of a spectrum with a certain signal-to-noise ratio (SNR) takes far longer at a resolution of 1  $\text{cm}^{-1}$  than the corresponding measurement at a resolution of 8  $\text{cm}^{-1}$ . The “trading rules” among resolution, measurement time, and SNR are covered in some detail in Chapter 7.

Few detailed investigations into the shapes and widths of bands in the spectra of solids have been made, but the bands of solids are usually narrower than the corresponding bands of the same molecule in solution because of the restricted motion of the functional groups in the molecules. The shapes of mid-infrared absorption bands of solid compounds are often represented by Eq. 1.15, with no limitation as to the value of the Gaussian fraction,  $\alpha$ .

Because bands in near-infrared spectra are overtones or combinations of fundamentals, the widths of these bands are typically greater than the widths of bands from which they are derived. For example, the FWHH of the first overtone of a C—H stretching band is to a first approximation twice that of the corresponding fundamental. As a result, most NIR spectra of liquids are measured at significantly lower resolution than is the corresponding mid-infrared spectrum.

## 1.5. QUANTITATIVE CONSIDERATIONS

### 1.5.1. Beer’s Law

The Bouguer–Lambert–Beer law (usually called simply *Beer’s law*) is the fundamental law of quantitative spectroscopy and is derived in all elementary textbooks on instrumental analysis. The *transmittance* of any sample at wavenumber  $\tilde{\nu}$  is given by the ratio of the radiant power emerging from the rear face of the sample at that wavenumber  $I(\tilde{\nu})$  to the power of the radiation at the front face of the sample,  $I_0(\tilde{\nu})$ . The transmittance of a pure sample of thickness  $b$  (cm) at wavenumber  $\tilde{\nu}$  is given by Beer’s law as

$$T(\tilde{\nu}) = \frac{I(\tilde{\nu})}{I_0(\tilde{\nu})} = \exp[-\alpha(\tilde{\nu})b] \quad (1.16)$$

where  $\alpha(\tilde{\nu})$  is the *linear absorption coefficient* ( $\text{cm}^{-1}$ ) at  $\tilde{\nu}$ . The *absorbance* of the sample at  $\tilde{\nu}$ ,  $A(\tilde{\nu})$ , is given by the base 10 logarithm of  $1/T(\tilde{\nu})$ :

$$A(\tilde{\nu}) = \log_{10} \frac{1}{T(\tilde{\nu})} = \frac{1}{\ln 10} \alpha(\tilde{\nu}) b \quad (1.17)$$

$(1/\ln 10)\alpha(\tilde{\nu})$  is the *absorptivity* at  $\tilde{\nu}$ ,  $a(\tilde{\nu})$ .

If the sample is a mixture, the absorbance of each component,  $i$ , at concentration,  $c_i$ , is given by Beer's law as

$$\log_{10} \frac{1}{T(\tilde{\nu})} = A_i(\tilde{\nu}) = a_i(\tilde{\nu}) b c_i \quad (1.18)$$

where  $a_i(\tilde{\nu})$  has the units of  $(\text{concentration} \cdot \text{pathlength})^{-1}$ . For  $N$ -component mixtures where more than one component absorbs at  $\tilde{\nu}$ , the total absorbance is given by

$$A(\tilde{\nu}) = \sum_{i=1}^N [a_i(\tilde{\nu}) b c_i] \quad (1.19)$$

Two important points should be raised. First, the absorbance, and not the transmittance, of any component is proportional to its concentration in the sample. Infrared spectra linear in absorbance are rarely measured directly. Before 1980, grating monochromators were routinely used for the measurement of infrared spectra. On these instruments, the ratio of  $I(\tilde{\nu})$  and  $I_0(\tilde{\nu})$  was usually measured, so the usual output of these instruments was a transmittance spectrum. Computers were interfaced to a few infrared grating spectrometers in the 1970s, so that transmittance spectra could be quickly converted to absorbance for quantitative applications. As we will see in Chapter 2, FT-IR spectrometers measure interferograms, from which a single-beam spectrum is calculated. The intensity of the single-beam spectrum,  $B(\tilde{\nu})$ , at any wavenumber  $\tilde{\nu}$  is proportional to the power of the radiation reaching the detector. Thus, to measure the absorbance spectrum of a sample, the ratio of the single-beam spectra of the sample and background is first calculated (to yield the transmittance spectrum), which is then converted to absorbance as shown in Eq. 1.18. It should always be remembered that as the first step of many of the more popular operations in FT-IR spectrometry, including spectral subtraction, multicomponent analysis, and spectral searching, the measured spectrum should always be converted to absorbance.

Second, the effect of reflection loss at the windows of the cell has been neglected in the treatment described above. The refractive index,  $n$ , of most organic samples and windows is about 1.5, so that the reflectance of the front surface is about 4% (see Section 13.2.2). If Beer's law is to be applied accurately, the apparent absorbance caused by reflection loss (0.018 absorbance unit for windows with  $n = 1.5$ ) should first be subtracted from the measured absorbance spectrum.

### 1.5.2. Optical Constants

The fundamental parameters that govern the absorption of radiation are the real and imaginary components of the complex refractive index:

$$\tilde{n}(\tilde{\nu}) = n(\tilde{\nu}) + ik(\tilde{\nu}) \quad (1.20)$$

where  $\tilde{n}(\tilde{\nu})$  is the real refractive index and  $k(\tilde{\nu})$  is the imaginary refractive index at  $\tilde{\nu}$ .  $n(\tilde{\nu})$  is often simply called the *refractive index*.  $k(\tilde{\nu})$  is also sometimes known as the *absorption index* and, incorrectly, as the attenuation index.

For any material,  $n(\tilde{\nu})$  is determined by Snell's law. A few materials have no significant absorption in the mid- and near infrared. Those materials with low refractive index ( $1.45 \leq n \leq 1.6$ ) are useful as windows, whereas those with high refractive index ( $2.4 \leq n \leq 4.0$ ) are frequently used as internal reflection elements (see Chapter 15). For organic and inorganic molecules whose spectra exhibit typical absorption bands, the refractive index changes across the absorption band. A typical refractive index spectrum has the appearance shown in Figure 1.4a. This

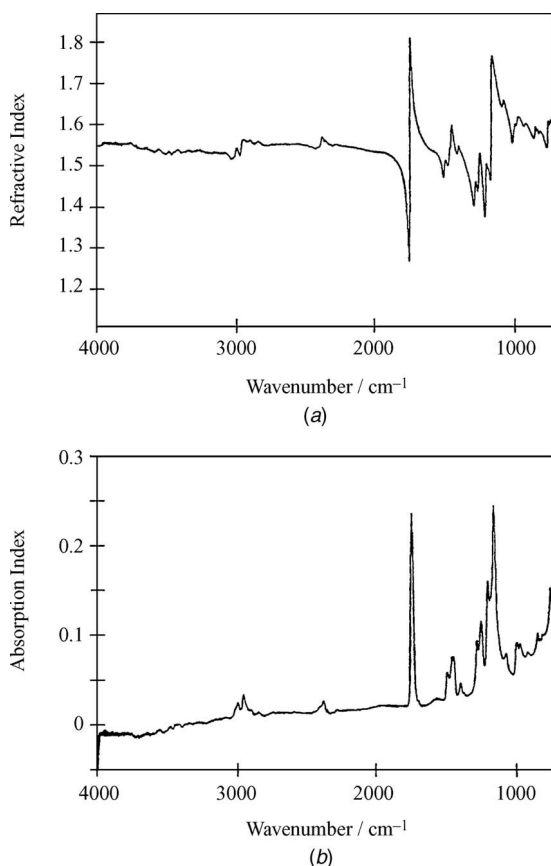


**Figure 1.4.** (a) Refractive index and (b) absorption index spectra of poly(methyl methacrylate).

type of variation in the refractive index across absorption bands is known as *anomalous dispersion*. Outside those regions of anomalous dispersion,  $n$  is fairly constant from the visible through the mid-infrared spectrum.

Like the real refractive index, the imaginary refractive index is also a dimensionless quantity. For pure materials,  $k(\tilde{\nu})$  is given by

$$k(\tilde{\nu}) = \frac{\alpha(\tilde{\nu})}{4\pi\tilde{\nu}} \quad (1.21)$$

where  $\alpha(\tilde{\nu})$  is the linear absorption coefficient defined in Eq. 1.16. A typical absorption index spectrum looks like an absorbance spectrum (see Figure 1.4b). Whereas the transmission spectrum of samples is largely determined by the value of  $k(\tilde{\nu})$  for each band, both of the optical constants  $n(\tilde{\nu})$  and  $k(\tilde{\nu})$  control the reflection of samples, as discussed in Chapter 13.

## 1.6. POLARIZED RADIATION

If a beam of unpolarized electromagnetic radiation is transmitted in the  $z$  direction, the amplitudes of the components of the sinusoidally varying electric field in the  $x$  and  $y$  planes are identical. When the beam is passed through a *polarizer*, the component of the electric field in one plane is transmitted, as described in more detail in Chapter 12. For unoriented samples such as all gases and liquids and isotropic solids, the absorbance of all bands in the spectrum is independent of the orientation of the polarizer. If the molecules in a certain sample are preferentially oriented in a given direction, however, the component of the dynamic dipole moment derivative of each vibrational mode,  $d\mu/dQ$ , in the direction that the radiation is polarized will change as the polarizer is rotated.

Since the largest intensity of each band is observed when the beam is polarized in the direction for which the change in dipole moment for that vibrational mode is greatest, important information on the orientation of samples can be derived by installing a polarizer in the beam. For example, one of the more important applications of the use of polarized light is the measurement of the orientation of the chains in drawn or extruded polymers. A more esoteric application is the estimation of the angle at which surfactants are adsorbed on the surface of water.

Several different types of reflection spectroscopy yield more information when the radiation is polarized. For example, very thin films of molecules adsorbed on the surface of metals only absorb radiation polarized parallel to the plane of incidence. The reflection of light from bulk samples depends on the polarization of the light with respect to the plane of the sample. The effective depth into a sample that can be sensed by internal reflection spectroscopy is also different for radiation polarized perpendicular and parallel to the surface. Polarized radiation may even be used to eliminate interference fringes from the spectra of thin polymer films.

It is hoped that these few examples will give the less experienced reader an indication as to why FT-IR spectroscopy is even more popular today than when it was used primarily as a tool for structural elucidation.



### 1.7. RAMAN SPECTROMETRY

Raman spectrometry is an alternative, and often complementary, way to measure vibrational spectra to infrared spectrometry. In Raman spectrometry the sample is illuminated with a monochromatic beam of radiation of wavenumber  $\tilde{\nu}_0$  (typically, from some type of laser). All of the photons that interact with the sample cause the potential energy of a molecule to be raised to a *virtual state*  $hc\tilde{\nu}_0$  above the ground state, where  $c$  is the velocity of light. Almost immediately most molecules return to the ground state through the emission of a photon of the same wavelength as that of the incident photon. Since the energies of the incident and scattered photons are identical, this process is a form of elastic scattering often referred to as *Rayleigh scattering*. A small fraction of the incident photons drop back to the first excited vibrational state of the  $i$ th vibrational mode of the molecule, so that the energy of the scattered photon is  $hc(\tilde{\nu}_0 - \tilde{\nu}_i)$  i.e., it will be observed at a wavenumber of  $(\tilde{\nu}_0 - \tilde{\nu}_i)$ , where  $\tilde{\nu}_i$  is the wavenumber of the  $i$ th vibrational mode. Since the energies of the incident and scattered photons are different, the scattering is inelastic. This process is known as *Stokes Raman scattering*. Since a given molecule has many different vibrational modes, measurement of the spectrum from  $\tilde{\nu}_0$  to  $(\tilde{\nu}_0 - 4000) \text{ cm}^{-1}$  allows all Raman-active vibrational bands to be measured.

Not all molecules are in the ground vibrational state. A few molecules are in the first excited state of each vibrational mode,  $v_i = 1$ . Neglecting the effect of degeneracy, the Boltzmann population of molecules in the first vibrational state of the  $i$ th mode is given by

$$\frac{N_1}{N_0} = e^{-hc\tilde{\nu}_0/kT} \quad (1.22)$$

where  $N_1$  and  $N_0$  are the numbers of molecules in the first excited state and ground state of the  $i$ th vibrational mode, respectively. When illuminated by a laser, a few molecules in an excited vibrational state can be promoted to a virtual level,  $hc(\tilde{\nu}_0 + \tilde{\nu}_i)$ , and then return to the ground state, resulting in Raman bands at wavenumbers above that of the laser. This process, known as *anti-Stokes scattering*, is much weaker than Stokes scattering for bands above about  $500 \text{ cm}^{-1}$  above  $\tilde{\nu}_0$  (where the Boltzmann population is less than 1%).

The intensity of bands in the Raman spectrum of a compound are governed by the change in *polarizability*,  $\alpha$ , that occurs during the vibration. The intensity of any band in the Raman spectrum is given by the following expression:

$$I_{\text{Raman}} = KI_L(\tilde{\nu}_0 - \tilde{\nu}_i)^4 \left( \frac{d\alpha}{dQ} \right)^2 \quad (1.23)$$

where  $I_L$  is the power of the laser at the sample,  $\tilde{\nu}_0 - \tilde{\nu}_i$  the wavenumber at which the band is measured, and  $d\alpha/dQ_i$  the change in polarizability with the normal coordinate of the vibration. This parameter is the Raman equivalent of absorptivity and is sometimes called the Raman cross section. The constant of proportionality,  $K$ , is

dependent on the optical geometry, collection efficiency, detector sensitivity, and amplification.

Before the mid-1980s, Raman spectroscopy was often considered to be less desirable to infrared absorption spectroscopy for two reasons. First, only one in between  $10^8$  and  $10^{10}$  of the incident photons undergoes Raman scattering. Thus, until about 1985, Raman spectrometry was considered to be a relatively insensitive and/or time-consuming technique. However, the advent of multiplex (usually, Fourier transform) and multichannel (monochromators with array detectors) techniques has greatly increased the sensitivity of modern Raman spectrometry. Of greater difficulty today is the fact that many compounds fluoresce when illuminated by visible lasers, such as by the radiation from an  $\text{Ar}^+$  laser at 488 nm. For some molecules the quantum efficiency for fluorescence with 488-nm radiation can approach 100%, and it is often greater than 0.001%. Even in the latter case, the radiation emitted by luminescence far exceeds the intensity of Raman-scattered radiation. Similarly, fluorescence from a trace molecule with a quantum efficiency approaching 100% can also swamp the Raman signal.

To ameliorate the problem of fluorescence, near-infrared lasers can be used to illuminate the sample. By the use of NIR radiation, the wavelengths used to excite Raman spectra are long enough that most compounds no longer fluoresce. Two types of NIR lasers can be used to measure Raman spectra. The first is the diode laser, with the most popular emitting at  $\sim 785$  or  $\sim 840$  nm ( $12,740$  or  $11,900\text{ cm}^{-1}$ , respectively). Raman spectra generated with NIR diode lasers can be measured using silicon charge-coupled device (CCD) array detectors, which cut on at about  $9500\text{ cm}^{-1}$ , limiting the Raman spectrum to about  $3240$  and  $2500\text{ cm}^{-1}$ , depending on whether a 785- or 840-nm laser is being used.

The other popular NIR laser is the Nd:YAG laser, which emits at  $1064\text{ nm}$  ( $\tilde{\nu}_0 \sim 9400\text{ cm}^{-1}$ ). With this laser, the problem changes from fluorescence to detection. Consider a Raman band due to a C–H stretching mode at  $2950\text{ cm}^{-1}$ . This band must be measured at  $(9400 - 2950)\text{ cm}^{-1}$  (i.e.,  $6450\text{ cm}^{-1}$ ), which is well below the wavenumber at which silicon charge-coupled device (CCD) array detectors cut off. Detectors operating in this region of the spectrum are significantly less sensitive than CCDs. Furthermore, it can be seen from Eq. 1.23 that  $I_{\text{Raman}}$  is proportional to  $(\tilde{\nu}_0 - \tilde{\nu}_i)^4$ . Thus, a Raman band at  $2950\text{ cm}^{-1}$  measured with a 1064-nm Nd:YAG laser would be about 55 times weaker than the same band measured with the 488-nm line of an  $\text{Ar}^+$  laser of equal power. Since CCD array detectors do not respond at  $6450\text{ cm}^{-1}$ , it is not surprising that Fourier transform techniques have been invoked for the measurement of weak Raman signals at such long wavelengths.

There are many reasons why scientists want to measure the Raman spectra of compounds. First, many bands that are weak in the infrared spectrum are among the strongest bands in the Raman spectrum. For example, the S–S and C=C stretching bands are often so weak as to be essentially unrecognizable in the IR spectrum but stick out like the proverbial sore thumb in a Raman spectrum. Second, some Raman bands are found at very characteristic frequencies. For instance, monosubstituted aromatic compounds, together with 1,3-disubstituted and 1,3,5-trisubstituted aromatics, have a very intense band at  $1000\text{ cm}^{-1}$ . This band, along with the presence or absence

of other bands in the infrared and Raman spectrum, can easily identify the substitution pattern of an aromatic ring. Furthermore, samples for Raman spectrometry can be mounted in standard glass tubes, making sample handling far easier for Raman than for infrared spectrometry.

For these reasons, analytical Raman spectrometry has undergone a remarkable rebirth since about 1985. Instruments based on Fourier transform techniques and CCD array detectors are commercially available from a large number of vendors in North America, Europe, and Asia. Like infrared spectrometry, Raman spectrometry has outlived its seventh age, although whether it has matured through its second childhood yet is debatable. Nonetheless, Raman spectrometry is still a vital weapon in a vibrational spectroscopist's arsenal.

### 1.8. SUMMARY

In Chapters 2 to 8 we describe the theory and instrumentation needed for an appreciation of the way that Fourier transform infrared and Raman spectra are measured today. The sampling techniques for and applications of FT-Raman spectrometry are described in Chapter 18. The remaining chapters cover the techniques and applications of absorption, reflection, emission, and photoacoustic spectrometry in the mid- and near-infrared spectral regions.

### REFERENCE

1. H. A. Laitinen, *Anal. Chem.* **45**, 2305 (1973).

## Chapter 2

# THEORETICAL BACKGROUND

### 2.1. MICHELSON INTERFEROMETER

The design of many interferometers used for infrared spectrometry today is based on that of the two-beam interferometer originally designed by Michelson in 1891 [1,2]. Many other two-beam interferometers have subsequently been designed that may be more useful than the Michelson interferometer for certain specific applications. Nevertheless, the theory behind all scanning two-beam interferometers is similar, and the general theory of interferometry is most readily understood by first acquiring an understanding of the way in which a simple Michelson interferometer can be used for the measurement of infrared spectra.

The Michelson interferometer is a device that can divide a beam of radiation into two paths and then recombine the two beams after a path difference has been introduced. A condition is thereby created under which *interference* between the beams can occur. The variation of intensity of the beam emerging from the interferometer is measured as a function of path difference by a detector. The simplest form of the Michelson interferometer is shown in Figure 2.1. It consists of two mutually perpendicular plane mirrors, one of which can move along an axis that is perpendicular to its plane.

Bisecting the fixed mirror and the movable mirror is a *beamsplitter*, where a collimated beam of radiation from an external source can be partially reflected to the fixed mirror (at point F for the median ray) and partially transmitted to the movable mirror (at point M). When the beams return to the beamsplitter, they interfere and are again partially reflected and partially transmitted. Because of the effect of interference, the intensity of each beam passing to the detector and returning to the source depends on the difference in path of the beams in the two arms of the interferometer. The variation in the intensity of the beams passing to the detector and returning to the source as a function of the path difference ultimately yields the spectral information in a Fourier transform spectrometer.

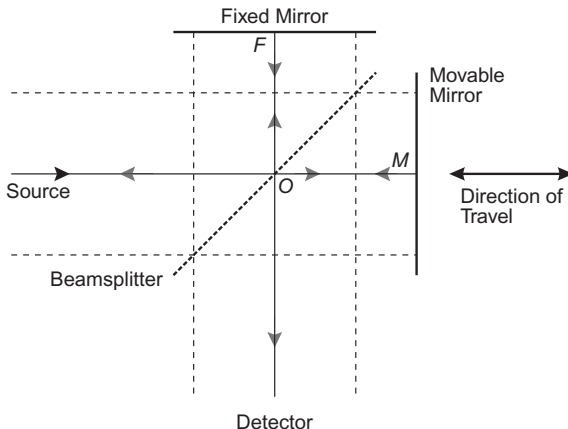


**Figure 2.1.** Michelson interferometer. The median ray is shown by the solid line, and the extremes of the collimated beam are shown by the dashed line.

The beam that returns to the source is rarely of interest for spectrometry, and usually only the output beam traveling in the direction perpendicular to that of the input beam is measured. Nevertheless, it is important to remember that both of the output beams contain equivalent information. The main reason for measuring only one of the output beams is the difficulty of separating the output beam that returns to the source from the input beam. On rare occasions, both output beams are measured with the use of two detectors or by focusing both beams onto the same detector. In other measurements, separate beams can be passed into each arm of the interferometer and the resulting signal measured using one or two detectors.

The movable mirror can either be moved at a constant velocity (*a continuous-scan interferometer*) or be held at equally spaced points for fixed short periods and stepped rapidly between these points (*a step-scan interferometer*). When the mirror of a continuous-scan interferometer is moved at a velocity greater than  $\sim 0.1 \text{ cm} \cdot \text{s}^{-1}$  (the usual case for most commercial instruments), the interferometer is often called a *rapid-scan interferometer*.

## 2.2. GENERATION OF AN INTERFEROGRAM

To understand the processes that occur in a Michelson interferometer better, let us first consider an idealized situation where a source of monochromatic radiation produces an infinitely narrow, perfectly collimated beam. Let the wavelength of the radiation be  $\lambda_0$  (in centimeters) so that its wavenumber  $\tilde{\nu}_0 \text{ (cm}^{-1}\text{)}$  is

$$\tilde{\nu}_0 = \frac{1}{\lambda_0} \quad (2.1)$$

We will denote the source intensity (power) at this wavenumber as  $I(\tilde{\nu}_0)$ . For this example we will assume that the beamsplitter is ideal (i.e., it is a nonabsorbing film whose reflectance and transmittance are both exactly 50%). We first examine the intensity of the beam at the detector when the movable mirror is held stationary at different positions.

The path difference between the beams that travel to the fixed and movable mirrors and back to the beamsplitter is  $2(OM - OF)$  (see Figure 2.1). This *optical path difference* (OPD) is called the *retardation*, and is given the symbol  $\delta$ . Since  $\delta$  is the same for all parallel input beams, such as the two dashed lines shown in Figure 2.1, we can relax our criterion for an infinitely narrow input beam, but ideally it should still remain collimated. (The effect of having an uncollimated beam is discussed in Section 2.6.)

When the fixed and movable mirrors are equidistant from the beamsplitter [i.e., at zero retardation or *zero path difference* (ZPD)], the two beams are perfectly in phase on recombination at the beamsplitter (Figure 2.2a). At this point, the beams interfere *constructively*, and the intensity of the beam passing to the detector is the sum of the intensities of the beams passing to the fixed and movable mirrors. Therefore, all the light from the source reaches the detector at this point and none returns to the source.

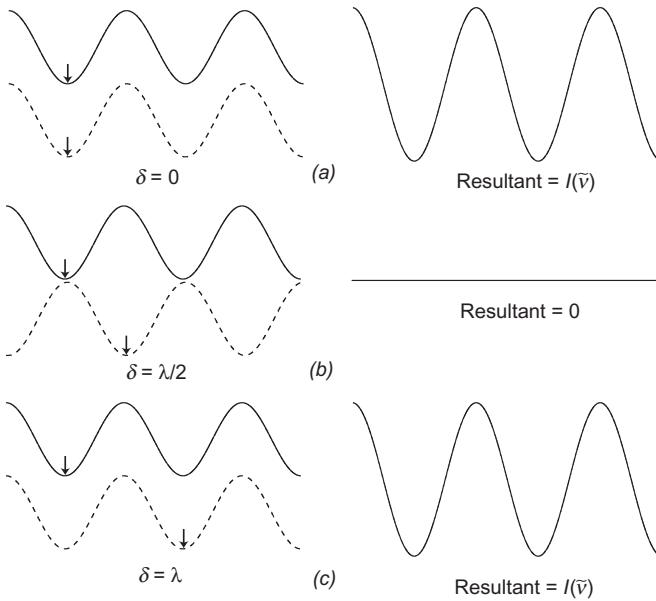


**Figure 2.2.** Phase of the electromagnetic waves from fixed (solid line) and movable (dashed line) mirrors at different values of the optical retardation: (a) zero path difference; (b) path difference of one-half wavelength; (c) path difference of one wavelength. Note that constructive interference occurs for both (a) and (c) and all other retardations of integral numbers of wavelengths.

It is instructive to consider why no radiation returns to the source at ZPD. It is well known that a beam that is reflected by a mirror at normal incidence undergoes a phase change of  $180^\circ$ . The beam that is reflected by an ideal beamsplitter undergoes a phase change of  $90^\circ$ , while the phase of the transmitted beam is unchanged. For the beam that passes to the detector, the beams to the fixed and movable mirrors both undergo a total phase change of  $270^\circ$  and they are therefore in phase on recombination at the beamsplitter. These beams are said to interfere *constructively*. This is not the case for the beam that returns to the source. The beam that travels to the fixed mirror undergoes a phase change of  $90^\circ$  for the first reflection from the beamsplitter, a phase change of  $180^\circ$  for the reflection from the fixed mirror, and a phase change of  $90^\circ$  for the second reflection from the beamsplitter, for a total change of  $360^\circ$ . The beam that travels to the moving mirror, on the other hand, undergoes a phase change of  $180^\circ$  at the mirror, but the phase is unchanged for both transmissions through the beamsplitter. Thus, the two beams are  $180^\circ$  out of phase and are said to interfere *destructively*. Hence, at ZPD the entire power of the incident beam is transmitted to the detector, and no light returns to the source.

If the movable mirror is displaced a distance  $\frac{1}{4}\lambda_0$ , the retardation is now  $\frac{1}{2}\lambda_0$ . The pathlengths to and from the fixed and movable mirrors are therefore exactly one-half wavelength different. On recombination at the beamsplitter, the beams are out of phase and interfere *destructively* (Figure 2.2b). At this point, all the light returns to the source and none passes to the detector. The photons are not destroyed, as is implied by the term *destructive interference*. Photons are a form of energy and hence cannot be created or destroyed. In the case of destructive interference for the beam that passes to the detector, the photons simply travel in a different direction, and that direction is back toward the source in a Michelson interferometer.

A further displacement of the movable mirror by  $\frac{1}{4}\lambda_0$  makes the total retardation  $\lambda_0$ . The two beams are once more in phase on recombination at the beamsplitter, and a condition of constructive interference again occurs for the beam that travels to the detector (Figure 2.2c). For monochromatic radiation, there is no way to determine whether a particular point at which a signal maximum is measured corresponds to zero retardation or a retardation equal to an integral number of wavelengths. If the mirror is moved at constant velocity, the signal at the detector will be seen to vary sinusoidally, and a maximum is registered each time that the retardation is an integral multiple of  $\lambda_0$ . The intensity of the beam at the detector measured as a function of retardation is given the symbol  $I'(\delta)$ . The intensity at any point where  $\delta = n\lambda$  (where  $n$  is an integer) is equal to the intensity of the source  $I(\tilde{\nu}_0)$ . At other values of  $\lambda_0$ , the intensity of the beam at the detector, or *interference record*, is given by

$$I'(\delta) = 0.5 I(\tilde{\nu}_0) \left( 1 + \cos 2\pi \frac{\delta}{\lambda_0} \right) \quad (2.2)$$

or

$$I'(\delta) = 0.5 I(\tilde{\nu}_0) (1 + \cos 2\pi \tilde{\nu}_0 \delta) \quad (2.3)$$

It can be seen that  $I'(\delta)$  is composed of a constant (dc) component equal to  $0.5I(\tilde{\nu}_0)$  and a modulated (ac) component equal to  $0.5I(\tilde{\nu}_0) \cos 2\pi\tilde{\nu}_0\delta$ . Only the ac component is important in spectrometric measurements, and it is this modulated component that is generally referred to as the *interferogram*,  $I(\delta)$ . The interferogram from a monochromatic source measured with an ideal interferometer is given by the equation

$$I(\delta) = 0.5I(\tilde{\nu}_0) \cos 2\pi\tilde{\nu}_0\delta \quad (2.4)$$

In practice, several factors affect the magnitude of the signal measured at the detector. First, it is practically impossible to find a beamsplitter that has the ideal characteristics of 50% reflection and 50% transmission. The nonideality of the beamsplitter must be allowed in Eq. 2.4 by multiplying  $I(\tilde{\nu}_0)$  by a wavenumber-dependent factor of less than unity that represents the relative beamsplitter efficiency (see Section 5.7). Second, most infrared detectors do not have a uniform response at all wavenumbers. In addition, the response of many amplifiers is also strongly dependent on the modulation frequency. It will be seen in Chapter 3 that the amplifier usually contains filter circuits designed to eliminate the signals from radiation outside the spectral range of interest from reaching the detector. It is these filters that cause the amplifier to have a frequency-dependent and hence wavenumber-dependent response (see Section 3.1).

In summary, the amplitude of the interferogram as observed after detection and amplification is proportional not only to the intensity of the source but also to the beamsplitter efficiency, detector response, and amplifier characteristics. Of these factors, only  $I(\tilde{\nu}_0)$  varies from one measurement to the next for a given system configuration, while all the other factors remain constant. Therefore, Eq. 2.4 may be modified by a single wavenumber-dependent correction factor,  $H(\tilde{\nu}_0)$ , so that the ac signal,  $S(\delta)$  (in volts), from the amplifier is

$$S(\delta) = 0.5H(\tilde{\nu}_0)G(\tilde{\nu}_0)I(\tilde{\nu}_0) \cos 2\pi\tilde{\nu}_0\delta \quad (2.5)$$

where  $G(\tilde{\nu}_0)$  is the responsivity of the detector and amplifier (in  $\text{V} \cdot \text{W}^{-1}$ ) for radiation of wavenumber  $\tilde{\nu}_0$ ;  $0.5H(\tilde{\nu})G(\tilde{\nu}_0)I(\tilde{\nu}_0)$  may be set equal to  $B(\tilde{\nu}_0)$ , the single-beam spectral intensity. The simplest equation representing the interferogram is therefore

$$S(\delta) = B(\tilde{\nu}_0) \cos 2\pi\tilde{\nu}_0\delta \quad (2.6)$$

The parameter  $B(\tilde{\nu}_0)$  gives the intensity of the source at a wavenumber  $\tilde{\nu}_0$ , as modified by the instrumental characteristics.

Mathematically,  $S(\delta)$  is said to be the cosine *Fourier transform* of  $B(\tilde{\nu}_0)$ . The spectrum is calculated from the interferogram by computing the cosine Fourier transform of  $S(\delta)$ , which accounts for the name given to this spectrometric technique: *Fourier transform spectrometry*.

In commercially available rapid-scanning Michelson interferometers, the movable mirror is scanned at a constant velocity  $V'$  ( $\text{cm} \cdot \text{s}^{-1}$ ). For these instruments it is



important to understand the way in which the interferogram varies as a function of time,  $S(t)$ , rather than as a function of retardation,  $S(\delta)$ . The retardation  $t$  seconds after the zero retardation point is given by

$$\delta = 2V' t \quad \text{cm} \quad (2.7)$$

Substituting into Eq. 2.6 gives us

$$S(t) = B(\tilde{\nu}) \cos 2\pi\tilde{\nu} \cdot 2V' t \quad (2.8)$$

The units of the abscissa of the interferogram (retardation in centimeters or time in seconds) must always be the inverse of the units of the spectrum (wavenumber in  $\text{cm}^{-1}$  or frequency in hertz, respectively).

For any cosine wave of frequency  $f$ , the amplitude of the signal after a time  $t$  is given by the equation

$$A(t) = A_0 \cos 2\pi f t \quad (2.9)$$

where  $A_0$  is the maximum amplitude of the wave. A comparison of Eqs. 2.8 and 2.9 shows that the frequency  $f_{\tilde{\nu}}$  of the interferogram  $S(t)$  corresponding to the radiation of the wavenumber,  $\tilde{\nu}$  (often known as the *Fourier frequency*), is given by

$$f_{\tilde{\nu}} = 2V'\tilde{\nu} \quad (2.10)$$

There are many other types of two-beam interferometers besides the one originally described by Michelson (see Chapter 5). Many of these interferometers do not vary the path difference between two beams by a single mirror moving at constant velocity. Except for stationary interferometers used for Fourier transform spectroscopy (Section 5.6), an optical element or combination of optical elements is moved so that the optical path difference is changed at a certain rate, known as the optical velocity or OPD velocity,  $V$ . For the Michelson interferometer,  $V = 2V'$ . In general, the Fourier frequency for radiation of wavenumber  $\tilde{\nu}$  is given by

$$f_{\tilde{\nu}} = V\tilde{\nu} \quad \text{Hz} \quad (2.11)$$

In the particular case where the spectrum of a source of monochromatic radiation is to be determined, performing the Fourier transform of a measured interferogram is a trivial operation, since the amplitude and wavelength (or wavenumber) can both be measured directly from the sinusoidal interferogram. If the source emits either several discrete spectral lines or continuous radiation, however, the interferogram is more complex and a computer is required to perform the transform.

When radiation of more than one wavelength is emitted by the source, the measured interferogram is the resultant of the interferograms that correspond to each wavelength. For line sources with very simple spectra, interferograms may be found that repeat themselves at regular intervals of retardation. Some simple spectra and their interferograms are shown in Figure 2.3.

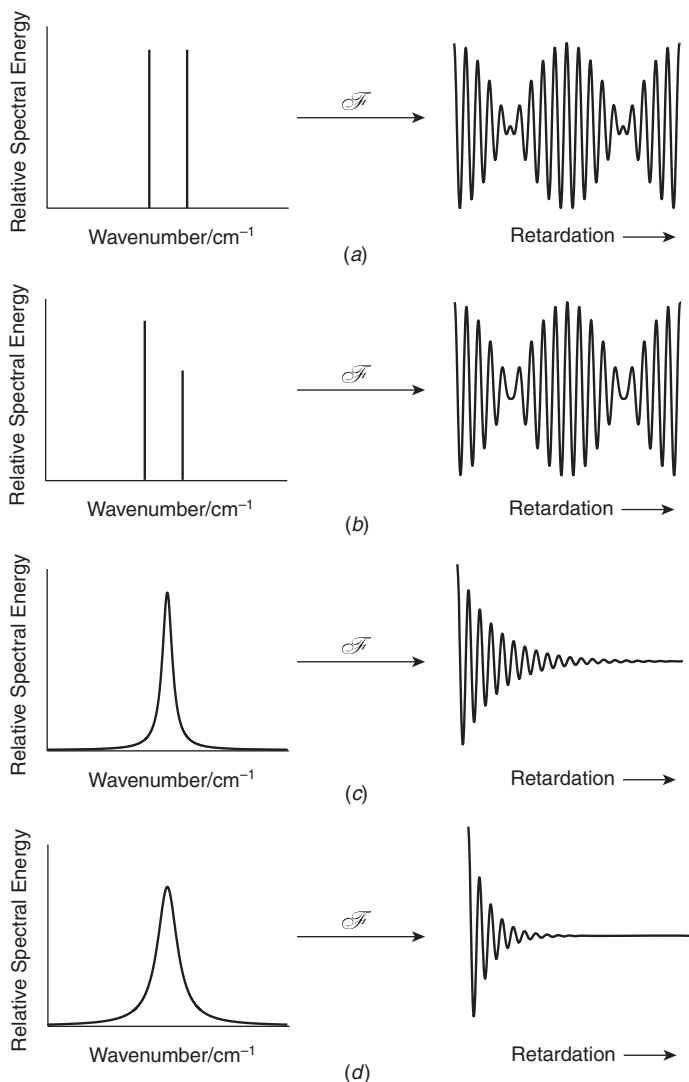


**Figure 2.3.** Simple spectra and interferograms: (a) two infinitesimally narrow lines of equal intensity; (b) two infinitesimally narrow lines of unequal intensity; note that the amplitude of the beat signal in the interferogram never goes to zero; (c) Lorentzian band centered at the mean of the lines in (a) and (b); the frequency of the interferogram is identical to (a) and (b) and the envelope decays exponentially; (d) Lorentzian band at the same wavenumber as (c) but of twice the width; the exponent of the decay for the interferogram has a value double that of the exponent for (c).  $\mathcal{F}$  denotes the Fourier transform.

The curves in Figure 2.3a and b represent the case when two closely spaced lines are examined. It is interesting to note that this was the situation that occurred when Michelson examined the red Balmer line in the hydrogen spectrum [3]. Although he was not able to resolve the high-frequency wave, Michelson observed the envelope,

or visibility curve, of the interferogram. From this visibility curve, he concluded that the Balmer line is actually a doublet. It is now known that this deduction was correct, with the separation of the two lines being 0.014 nm.

The spectra in Figure 2.3*c* and *d* both have Lorentzian profiles and yield sinusoidal interferograms with an exponentially decaying envelope. The narrower the width of the spectral band, the greater is the width of the envelope of the interferogram. For a monochromatic source, the envelope of the interferogram will have an infinitely large width (i.e., it will be a pure cosine wave). Conversely, for broadband spectral sources, the decay is very rapid.

When the source is a continuum, the interferogram can be represented by the integral

$$S(\delta) = \int_{-\infty}^{+\infty} B(\tilde{\nu}) \cos 2\pi\tilde{\nu}\delta d\tilde{\nu} \quad (2.12)$$

which is one-half of a cosine Fourier transform pair, where the other is

$$B(\tilde{\nu}) = \int_{-\infty}^{+\infty} S(\delta) \cos 2\pi\tilde{\nu}\delta d\delta \quad (2.13)$$

It may be noted that  $S(\delta)$  is an *even function*, so that Eq. 2.13 may be rewritten as

$$B(\tilde{\nu}) = 2 \int_0^{+\infty} S(\delta) \cos 2\pi\tilde{\nu}\delta d\delta \quad (2.14)$$

Equation 2.14 shows that in theory one could measure the complete spectrum from 0 to  $+\infty$  (in  $\text{cm}^{-1}$ ) at infinitely high resolution. However, Eq. 2.14 shows that to achieve this, we would have to scan the moving mirror of the interferometer an infinitely long distance, with  $\delta$  varying between 0 and  $+\infty$  cm. The effect of measuring the signal over a limited retardation is to cause the spectrum to have a finite resolution. A more complete description of the effect of measuring the interferogram with a certain limiting retardation is given in the next section. Also, if the Fourier transform were to be performed with the use of a computer, the interferogram would have to be digitized at infinitesimally small intervals of retardation,  $d\tilde{\nu}$ . In practice, the signal must be digitized at finite sampling intervals. The smaller the sampling interval, the greater is the spectral range that can be measured; this problem is discussed in more detail in Section 3.1.

### 2.3. EFFECT OF FINITE RESOLUTION

It is fairly simple to illustrate conceptually how the resolution of a spectrum measured interferometrically depends on the maximum retardation of the scan. As an example, let us consider the case of a spectrum that consists of a doublet, both components of which have the same intensity. Figure 2.4*a* shows the spectrum, and Figure 2.4*b*

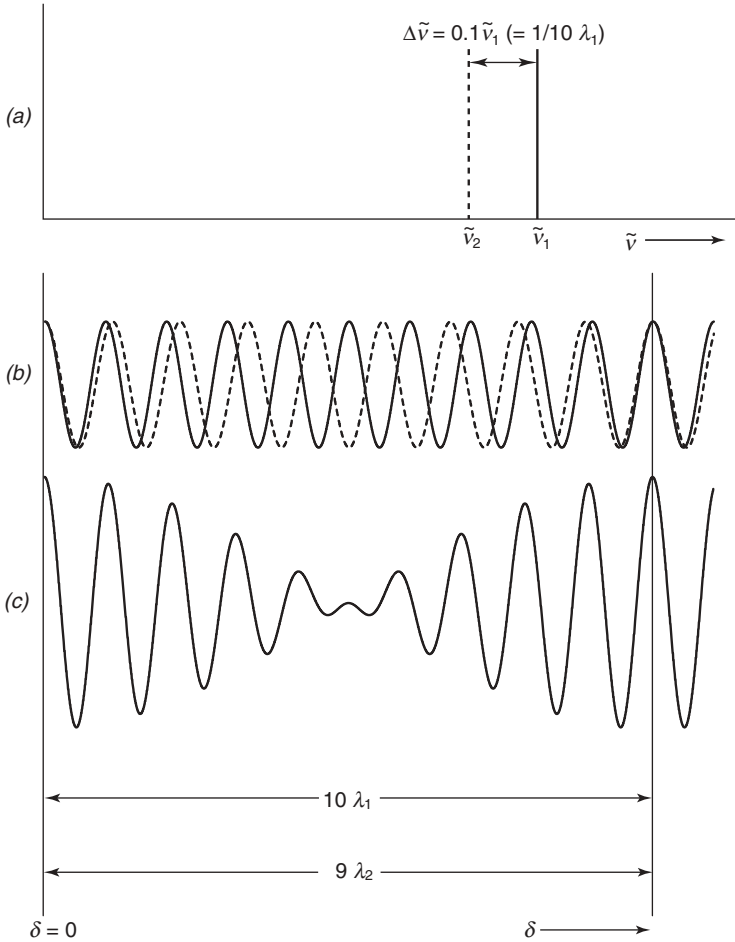


**Figure 2.4.** (a) Spectrum of two lines of equal intensity at wavenumbers  $\tilde{\nu}_1$  (solid line) and  $\tilde{\nu}_2$  (dashed line) separated by  $0.1\tilde{\nu}_1$ ; (b) interferogram for each spectral line shown individually as solid and dashed lines, respectively; (c) resulting interferogram with the first maximum of the beat signal at  $10/\tilde{\nu}_1$ ; to resolve these two spectral lines, it is necessary to generate an optical retardation of at least this value.

shows the interferogram from each line. Figure 2.4c shows the resultant of these curves. This case is equivalent to the upper curve in Figure 2.3.

If the doublet has a separation of  $\Delta\tilde{\nu}(=\tilde{\nu}_1 - \tilde{\nu}_2)$ , the two cosine waves in Figure 2.4b become out of phase after a retardation of  $0.5(\Delta\tilde{\nu})^{-1}$  and are once more back in phase after a retardation of  $(\Delta\tilde{\nu})^{-1}$ . To go through one complete period of the beat frequency, a retardation of  $(\Delta\tilde{\nu})^{-1}$  is therefore required. An interferogram measured only to half this retardation could not readily be distinguished from the interferogram of a source with the profile shown in Figure 2.3c. The narrower the separation of the doublet, the greater is the retardation before the cosine waves become in phase. It is therefore apparent that the spectral resolution depends on

the maximum retardation of the interferometer. Intuitively, it might be concluded that the two lines could just be resolved if the retardation were increased to the point when the two waves became in phase for the first time after zero retardation. In the discussion above it was shown that the two waves become in phase for the first time after the zero retardation point when  $\delta = (\Delta\tilde{\nu})^{-1}$ . Thus, if the maximum retardation of an interferometer is  $\Delta_{\max}$ , the best resolution that could be obtained using this interferometer,  $\Delta\tilde{\nu}$ , is given by

$$(\Delta\tilde{\nu}) = (\Delta_{\max})^{-1} \quad (2.15)$$

Although this conclusion was arrived at intuitively, the answer proves to be approximately correct. The next few paragraphs will show a more rigorous mathematical verification of this conclusion.

By restricting the maximum retardation of the interferogram to  $\Delta$  centimeters, we are effectively multiplying the complete interferogram (between  $\delta = -\infty$  and  $\delta = +\infty$ ) by a truncation function,  $D(\delta)$ , which is unity between  $\delta = -\Delta$  and  $+\Delta$ , and zero at all other points, that is,

$$D(\delta) = \begin{cases} 1 & \text{if } -\Delta \leq \delta \leq +\Delta \\ 0 & \text{if } \Delta > |\delta| \end{cases} \quad (2.16)$$

In view of the shape of this function,  $D(\delta)$  is often called a *boxcar truncation function*. By analogy to Eq. 2.13, the spectrum in this case is given by the equation

$$B(\tilde{\nu}) = \int_{-\infty}^{+\infty} S(\delta)D(\delta) \cos 2\pi\tilde{\nu}\delta \, d\delta \quad (2.17)$$

It can be shown that the Fourier transform (FT) of the product of two functions is the *convolution* of the FT of each function [4]. The effect of multiplying  $S(\delta)$  by the boxcar function  $D(\delta)$  is to yield a spectrum on Fourier transformation that is the convolution of the FT of  $S(\delta)$  measured with an infinitely long retardation and the FT of  $D(\delta)$ . The FT of  $S(\delta)$  is the true spectrum,  $B(\tilde{\nu})$ , while the FT of  $D(\delta)$ ,  $f(\tilde{\nu})$ , is given by

$$\begin{aligned} f(\tilde{\nu}) &= 2\Delta \frac{\sin 2\pi\tilde{\nu}\Delta}{2\pi\tilde{\nu}\Delta} \\ &\equiv 2\Delta \operatorname{sinc} 2\pi\tilde{\nu}\Delta \end{aligned} \quad (2.18)$$

This function is shown in Figure 2.5a. It is centered about  $\tilde{\nu} = 0$  and intersects the  $\tilde{\nu}$  axis at  $\tilde{\nu} = n/2\Delta$ , where  $n = 1, 2, 3, \dots$ , so that the first intersection occurs at a wave-number of  $(2\Delta)^{-1}$ . Mathematically, the convolution of  $B(\tilde{\nu})$  and  $f(\tilde{\nu})$  is described by

$$\begin{aligned} G(\tilde{\nu}) &= B(\tilde{\nu}) * f(\tilde{\nu}) \\ &= \int_{-\infty}^{+\infty} B(\tilde{\nu}') f(\tilde{\nu} - \tilde{\nu}') \, d\tilde{\nu}' \end{aligned} \quad (2.19)$$

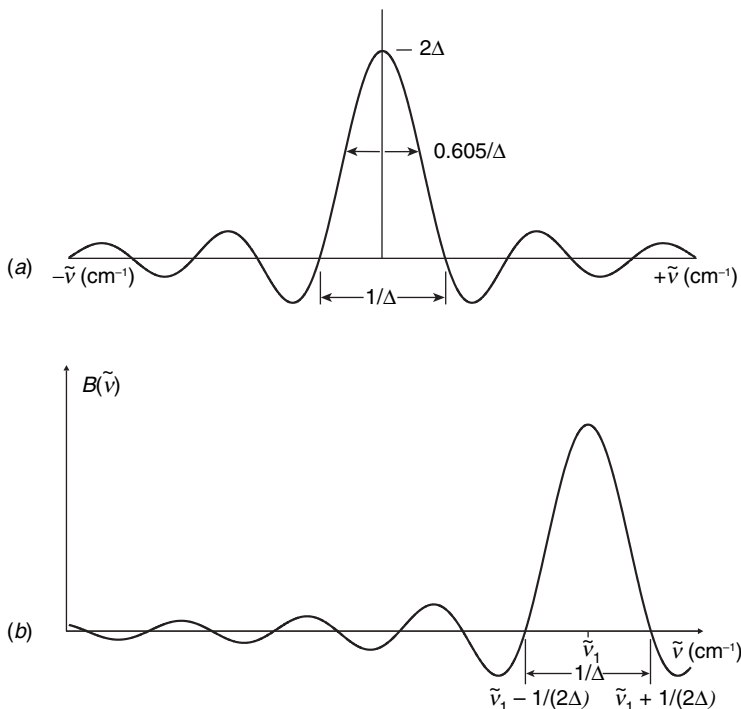


**Figure 2.5.** (a) Fourier transform of a boxcar function of unit amplitude extending from  $+\Delta$  to  $-\Delta$ ; this function has the shape of a  $\sin x/x$  or sinc  $x$ , function. (b) Fourier transform of an unweighted sinusoidal interferogram generated by a monochromatic line at wavenumber  $\tilde{\nu}_1$ ; the maximum retardation for this interferogram was  $\Delta$  centimeters.

To compute the convolution of these two functions, Eq. 2.19 requires that  $f(\tilde{\nu})$  be reversed left to right [which is trivial in this case, since  $f(\tilde{\nu})$  is an even function], after which the two functions are multiplied point by point along the wavenumber axis. The resulting points are then integrated, and the process is repeated for all possible displacements,  $\tilde{\nu}'$ , of  $f(\tilde{\nu})$  relative to  $B(\tilde{\nu})$ . One particular example of convolution may be familiar to spectroscopists who use grating instruments (see Chapter 8). When a low-resolution spectrum is measured on a monochromator, the true spectrum is convolved with the triangular slit function of the monochromator. The situation with Fourier transform spectrometry is equivalent, except that the true spectrum is convolved with the sinc function  $f(\tilde{\nu})$ . Since the Fourier transform spectrometer does not have any slits,  $f(\tilde{\nu})$  has been variously called the *instrument line shape (ILS) function*, the *instrument function*, or the *apparatus function*, of which we prefer the term *ILS function*.

When the sinc function is convolved with a single spectral line of wavenumber  $\tilde{\nu}_1$ , the resulting curve has the formula

$$B(\tilde{\nu}) = 2\Delta B(\tilde{\nu}_1) \text{sinc } 2\pi(\tilde{\nu}_1 - \tilde{\nu})\Delta \quad (2.20)$$

The curve is shown in Figure 2.5*b* and represents the appearance of a single sharp line measured interferometrically at a resolution considerably broader than the half-width of the line.

Since the curve intersects the wavenumber axis at  $(2\Delta)^{-1} \text{ cm}^{-1}$  on either side of  $\tilde{\nu}_1$ , it can be seen that two lines separated by twice this amount, that is, by  $\Delta^{-1} \text{ cm}^{-1}$ , would be completely resolved. The result derived earlier by "intuition" is therefore, indeed, correct. In fact, since two lines separated by  $\Delta^{-1}$  are *completely* (i.e., baseline) resolved, the practical resolution is somewhat better than this value.

Several criteria have been used to define the resolution of spectrometers. The most popular are the Rayleigh criterion and the full width at half-height (FWHH) criterion [5]. The Rayleigh criterion was used originally to define the resolution obtainable from a diffraction-limited grating spectrometer, the ILS of which may be represented by a function of the form  $\text{sinc}^2 x$ . Under the Rayleigh criterion, two adjacent spectral lines of equal intensity, each with a  $\text{sinc}^2 x$  shape, are considered to be just resolved when the center of one line is at the same frequency as the first zero value of the other. Under this condition, the resulting curve has a dip of approximately 20% of the maximum intensity in the spectrum, as shown in Figure 2.6*a*. If the same criterion is applied to a line that has a  $\text{sinc } x$  ILS, however, it is found that the two lines are not resolved, as shown in Figure 2.6*b*.

The FWHH criterion is more useful for monochromators with a triangular slit function than for FT-IR spectrometers. Two triangularly shaped lines of equal intensity and half-width are not resolved until the spacing between the lines is greater than the FWHH of either line [5,6]. The FWHH of a line whose shape is a sinc function given by Eq. 2.18 is  $0.605/\Delta$ , but two lines with  $\text{sinc } x$  lineshapes are not resolved when they are separated by this amount. In practice, a dip of approximately 20% is found when the two lines with a  $\text{sinc } x$  ILS are separated by  $0.73/\Delta$ , as shown in Figure 2.6*c*.

The  $\text{sinc } x$  function is not a particularly useful lineshape for infrared spectrometry in view of its fairly large amplitude at wavenumbers well away from  $\tilde{\nu}_1$ . The first minimum reaches below zero by an amount that is 22% of the height at  $\tilde{\nu}_1$ . If a second weak line happened to be present in the spectrum at the wavenumber of this minimum, it would not be seen in the spectrum computed. One method to circumvent the problem of these secondary minima is through the process known as *apodization*.

## 2.4. APODIZATION

From Section 2.3 we know that when a cosine wave interferogram is unweighted, the shape of the spectral line is the convolution of the true spectrum and a sinc function [i.e., the transform of the boxcar truncation function,  $D(\delta)$ ]. If instead of using the boxcar function, we used a simple triangular weighting function of the form

$$A_1(\delta) = \begin{cases} 1 - \frac{|\delta|}{\Delta} & \text{for } -\Delta \leq \delta \leq \Delta \\ 0 & \text{for } \delta > |\Delta| \end{cases} \quad (2.21)$$

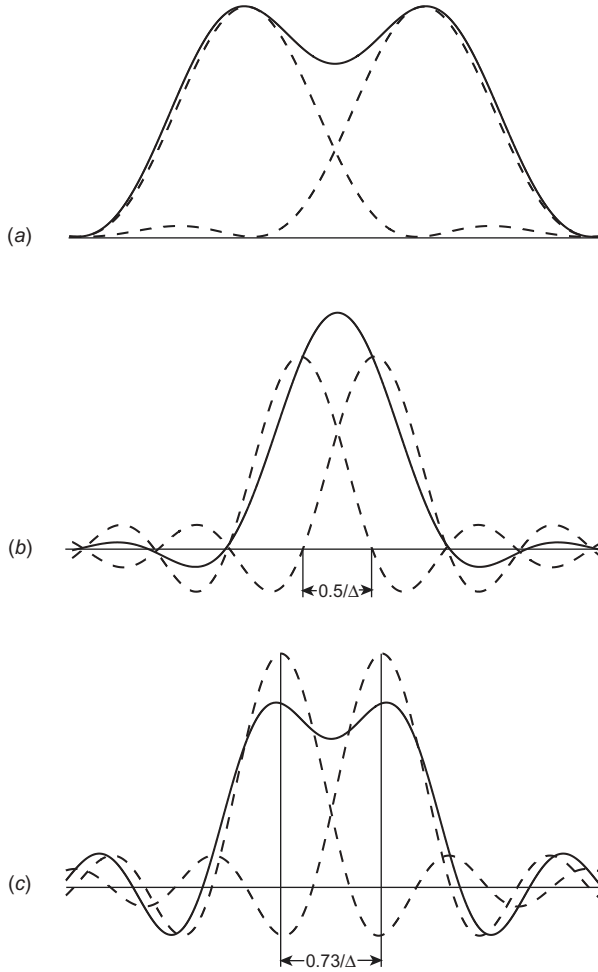


**Figure 2.6.** (a) Resultant of two  $\text{sinc}^2$  functions centered  $1/\Delta$  reciprocal centimeters apart, with each of the individual  $\text{sinc}^2$  functions shown as a dashed line; this condition represented Rayleigh's original definition of resolution for two equally intense lines measured using a diffraction-limited monochromator. (b) Resultant of two sinc functions of equal amplitude centered  $0.5/\Delta$  apart; note that the features are unresolved in the resultant function. (c) Resultant of two sinc functions centered  $0.73/\Delta$  apart; the two features are resolved with a dip of approximately 20%, equivalent to the Rayleigh criterion of resolution for a  $\text{sinc}^2$  function.

the true spectrum would be convolved with the Fourier transform of  $A_1(\delta)$ , and this function would therefore determine the ILS. The Fourier transform of  $A_1(\delta)$  has the form

$$\begin{aligned}
 f_1(\tilde{\nu}) &= \Delta \frac{\sin^2 \pi \tilde{\nu} \Delta}{(\pi \tilde{\nu} \Delta)^2} \\
 &= \Delta \text{sinc}^2 \pi \tilde{\nu} \Delta
 \end{aligned}
 \tag{2.22}$$



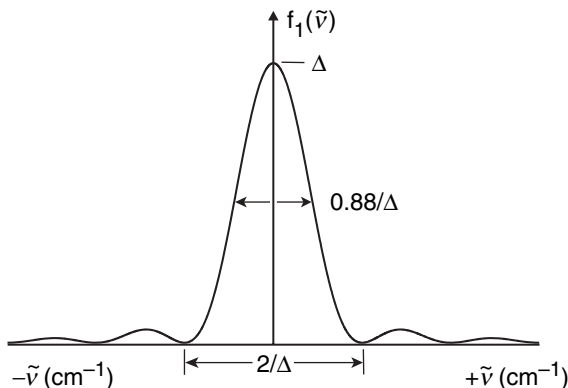


**Figure 2.7.** The  $\text{sinc}^2$  instrument lineshape function computed for triangularly apodized interferograms; note that its full width at half-height is greater than that of the sinc function resulting from boxcar truncation of the same interferogram.

This function is shown in Figure 2.7. As we saw from the discussion of the Rayleigh criterion of resolution, this is also the shape of the ILS function of a diffraction-limited grating monochromator. It can be seen that the amplitude of the sidelobes has been considerably reduced from that of the sidelobes for the sinc function. Suppression of the magnitude of these oscillations is known as *apodization*,<sup>1</sup> and functions such as  $A_1(\delta)$ , which weight the interferogram for this purpose, are known as *apodization functions*.

The function  $A_1(\delta)$ , called a *triangular apodization function*, is a popular apodization function used in Fourier transform infrared spectrometry, which is unfortunate since the triangular apodization function has deleterious effects on the photometric accuracy in a spectrum (see Section 8.3). Nonetheless, for lines separated by  $1/\Delta$ , a 20% dip is found, as shown in Figure 2.6a. If the lines were separated by  $2/\Delta$ , they would be fully resolved (i.e., resolved to baseline). The FWHH for the function  $f_1(\tilde{\nu})$  is  $0.88/\Delta$ , and the lines separated by this amount are just resolved; however, the dip is extremely small, that is, on the order of 1%.

Because of the small differences in resolution that depend on whether or not the interferogram is apodized, the particular apodization function and the resolution criterion that is applied, we prefer to call  $1/\Delta$  the *nominal resolution*.

When an absorbing sample is placed in the beam from a continuous source, the measured interferogram is the sum of the interferogram of the source with no sample present and the interferogram due to the sample. Because energy is being absorbed by the sample, these two interferograms are  $180^\circ$  out of phase. The effect of apodization may be considered separately for the source and sample interferogram. The interferogram due to a broadband continuous source has the appearance of an intense spike at zero retardation about which can be seen modulations that die

<sup>1</sup>The word *apodization* refers to the suppression of the sidelobes (or feet) of the ILS; the word is apocryphally derived from the Greek term  $\acute{\alpha}\pi\delta\delta\omicron\zeta$  (without feet).

out rapidly to an unobservably low amplitude. On the other hand, the interferogram caused by a sample with narrow absorption lines will show appreciable modulation even at large retardations. When the measured interferogram is triangularly apodized, the background spectrum due to the source is usually affected imperceptibly since its interferogram has very little information at high retardation. Interferograms of very broad absorption bands also decay very quickly (see Figure 2.3), and if the maximum retardation is much greater than the reciprocal of the FWHH, apodization will have little effect on these bands. For narrow spectral lines measured with the maximum retardation less than the reciprocal of the FWHH, the shape of the lines will be approximately the same as the shape of the instrument line shape function. When the interferogram is not apodized, the lines will have a  $\text{sinc } x$  shape, and when the interferogram is weighted with a triangular apodization function, the lines will have a  $\text{sinc}^2 x$  shape.

Any function that has a value of unity at  $\delta = 0$  and decreases with increasing retardation will serve as an apodization function. Kauppinen et al. [7] have given explicit forms for a variety of common apodization functions. These are reproduced, together with the equation for the corresponding ILS function, in Figure 2.8. Also given in these figures is the FWHH,  $\Delta\tilde{\nu}_{1/2}$ , and the relative magnitude of the strongest sidelobe to the central lobe,  $s$ . As a general rule, it can be seen that the narrower  $\Delta\tilde{\nu}_{1/2}$  is, the greater is  $s$ . There are exceptions to this “rule.” For example, if the triangular squared function (Figure 2.8d) is compared to the Gaussian function (Figure 2.8h), it can be seen that the  $\Delta\tilde{\nu}_{1/2}$  for the ILS computed from the Gaussian function is less than that for the triangular squared function and that sidelobe suppression is also superior.

Several general studies on apodization functions have been carried out. For example, Filler [8] investigated a variety of trigonometric functions, and Norton and Beer [9] tested over 1000 functions of the general form

$$A(\delta) = \sum_{i=0}^n C_i \left[ 1 - \left( \frac{\delta}{\Delta} \right)^2 \right]^i \quad (2.23)$$

They found that there is a distinct empirical boundary relation between  $\Delta\tilde{\nu}_{1/2}$  and  $s$  (see Figure 2.9). Functions could be found with a wider FWHH and larger sidelobe amplitude than the boundary relation; others approached the boundary, but none was found that decreased both the FWHH and the sidelobe amplitude beyond the boundary conditions. Three preferred functions, dubbed Norton–Beer weak, medium, and strong, were suggested, for which the FWHH of the ILS function was 20, 40, and 60%, respectively, greater than that of the sinc function at the same nominal resolution, with all three giving ILS functions with  $\Delta\tilde{\nu}_{1/2}$  and  $s$  close to the boundary conditions. The three ILS functions are shown in Figure 2.10, and the coefficients  $C_i$  for each are shown in Table 2.1.

One other popular apodization function is the Happ–Genzel function, given by

$$A(\delta) = 0.54 + 0.46 \cos \pi \frac{\delta}{\Delta} \quad (2.24)$$

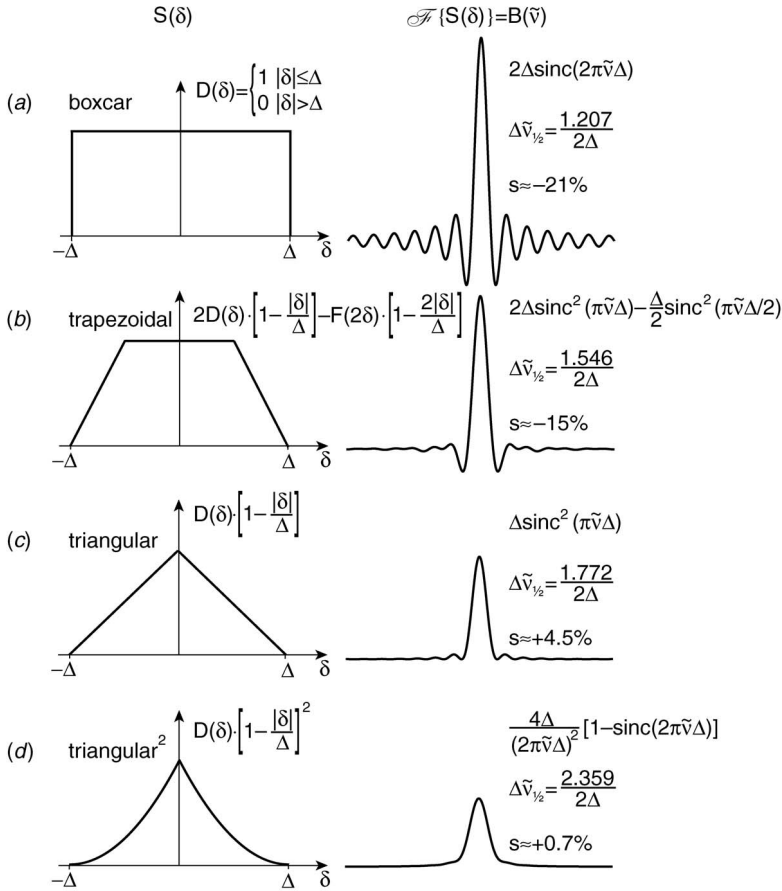


**Figure 2.8.** Series of apodization functions and their corresponding instrument lineshape functions: (a) boxcar truncation; (b) trapezoidal; (c) triangular; (d) triangular squared; (e) Bessel; (f) cosine; (g)  $\text{sinc}^2$ ; (h) Gaussian apodization. In each case the equations representing the shapes of the apodization and ILS functions are given, together with the full width at half-height,  $\Delta\tilde{\nu}_{1/2}$ , and the amplitude of the largest sidelobe  $s$ , as a percentage of the maximum excursion. (Redrawn from [7], by permission of the Optical Society of America; copyright © 1981.)

The FWHH of the ILS function given by the Happ–Genzel function is close to that of the Norton–Beer strong apodization function. Another common function that strongly suppresses the sidelobe amplitude is the Blackman–Harris function,

$$\begin{aligned}
 A(\delta) = & 0.35875 - 0.48829 \cos\left(2\pi \frac{\delta}{\Delta}\right) + 0.14128 \cos\left(4\pi \frac{\delta}{\Delta}\right) \\
 & - 0.01168 \cos\left(6\pi \frac{\delta}{\Delta}\right)
 \end{aligned} \tag{2.25}$$

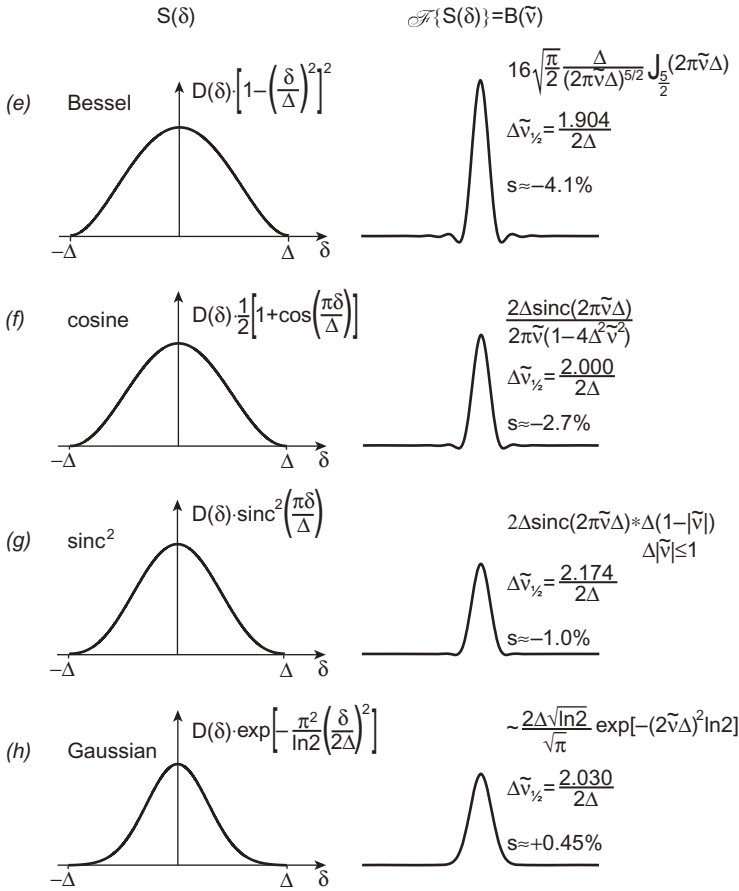
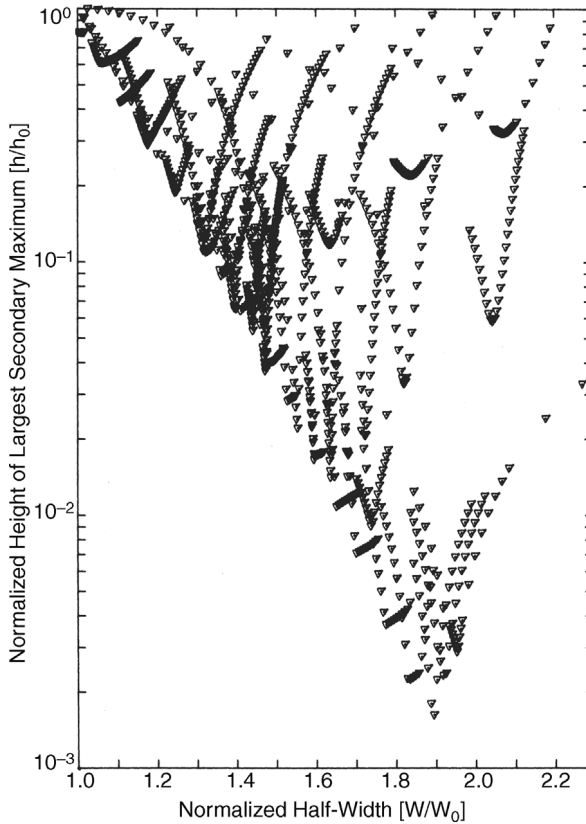


Figure 2.8. (continued)

The FWHH of this function is even wider than that of the Norton–Beer strong function and so in general is not recommended. (A similar function is the Blackman function that uses the first three terms instead of four, but the coefficients are different.)

In general, it is advisable to use some type of apodization for FT-IR spectrometry when the spectrum contains features that are narrower than the nominal resolution. When the bandwidths of the spectral lines are broader than the resolution, apodization serves as a smoothing function but otherwise degrades the spectral quality because of the loss in resolution. The specific function that should be used for a given application depends on the experiment being performed. If good quantitative accuracy is required, the Norton–Beer medium or Happ–Genzel functions can be recommended. A more complete discussion of the effect of apodization functions on absorption spectra can be found in Sections 8.2 and 8.3.



**Figure 2.9.** Normalized height of the largest secondary lobe for a series of apodization functions studied by Norton and Beer ( $S$ , from Figure 2.8) as a function of their half-width relative to the corresponding sinc function. (Reproduced from [9], by permission of the Optical Society of America; copyright © 1977.)

## 2.5. PHASE EFFECTS

Up to this point, it has been assumed that Eqs. 2.12 and 2.14 give an accurate representation of the interferogram. In practice, an additional term often has to be added to the *phase angle*,  $2\pi\tilde{\nu}\delta$ , to describe the actual measured interferogram. Corrections to the phase angle may arise because of optical, electronic, or sampling effects; two common examples that lead to a change in the cosine term of these equations may be cited:

1. If we make use of the fact that the interferogram as represented in Eq. 2.12 is symmetrical about  $\delta = 0$  but the first data point is actually sampled before the zero retardation point, at  $\delta = -\varepsilon$  the interferogram takes the form

$$S(\delta) = \int_0^{+\infty} B(\tilde{\nu}) \cos 2\pi\tilde{\nu}(\delta - \varepsilon) d\tilde{\nu} \quad (2.26)$$

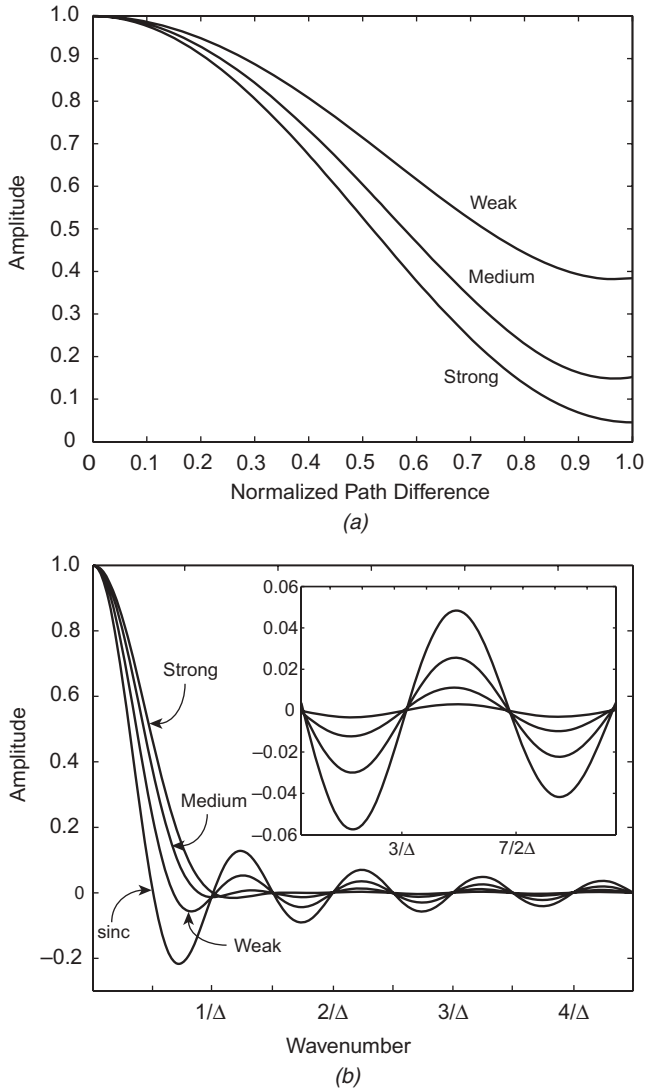


**Figure 2.10.** (a) Weak, medium, and strong apodization functions proposed by Norton and Beer; (b) corresponding lineshape functions with the sinc function shown for reference.

**Table 2.1. Coefficients  $C_i$  for the Norton–Beer Apodization Functions**

	$C_0$	$C_1$	$C_2$	$C_3$
Boxcar	1	0	0	0
Weak	0.384093	-0.087577	0.703484	0
Medium	0.152442	-0.136176	0.983734	0
Strong	0.045335	0	0.554883	0.399782

2. Electronic filters designed to remove high-frequency noise from the interferogram (see Section 3.2) have the effect of putting a wavenumber-dependent phase lag,  $\theta_{\tilde{\nu}}$ , on each cosinusoidal component of the interferogram, and the resulting signal is given by

$$S(\delta) = \int_0^{+\infty} B(\tilde{\nu}) \cos(2\pi\tilde{\nu}\delta - \theta_{\tilde{\nu}}) d\tilde{\nu} \quad (2.27)$$

Since any cosine wave  $\cos(\alpha - \beta)$  can be represented by

$$\cos(\alpha - \beta) = \cos \alpha \cos \beta + \sin \alpha \sin \beta \quad (2.28)$$

the addition of a second term to the phase angle,  $2\pi\tilde{\nu}\delta$ , has the effect of adding sine components to the cosine wave interferogram. Two properties of sine and cosine waves are important in this respect:

$$\begin{aligned} \text{(a)} \quad & \cos \varphi \text{ and } \sin \varphi \text{ are orthogonal} \\ \text{(b)} \quad & \cos \varphi - i \sin \varphi = \exp(-i\varphi) \end{aligned} \quad (2.29)$$

where  $i$  is the imaginary number  $\sqrt{-1}$ . In light of this relationship (Euler's equation), Eq. 2.27 may be rewritten in the transcendental exponential notation [10] as

$$S(\delta) = \int_0^{+\infty} B(\tilde{\nu}) \exp(-2\pi i \tilde{\nu} \delta) d\tilde{\nu} \quad (2.30)$$

For this representation,  $S(\delta)$  and  $B(\tilde{\nu})$  are said to be linked through the *complex Fourier transform*. To recover  $B(\tilde{\nu})$  from  $S(\delta)$ , the inverse complex transform

$$B(\tilde{\nu}) = \int_{-\infty}^{+\infty} S(\delta) \exp(2\pi i \tilde{\nu} \delta) d\delta \quad (2.31)$$

is performed.

The fundamental properties of  $i$ , that is,

$$i^2 = -1 \quad \text{and} \quad i^{-1} = -i$$

allow this shorthand notation to accommodate the symmetry of the sine and cosine functions while preserving their orthogonality. This notation also helps to explain

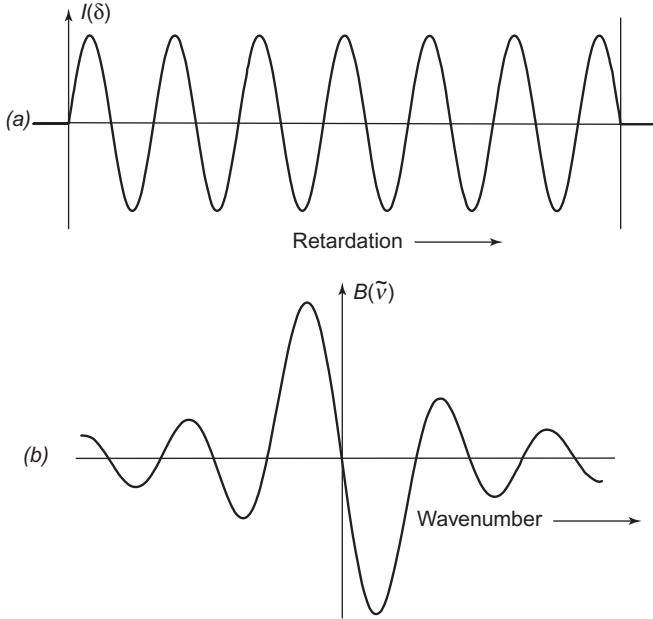


**Figure 2.11.** (a) Sine wave interferogram; (b) result of performing the cosine Fourier transform on this interferogram.

why the component of the spectrum computed with the use of the cosine Fourier transform is often called the *real part* of the spectrum,  $\text{Re}(\tilde{v})$ , whereas the component computed using a sine transform is called the *imaginary part*,  $\text{Im}(\tilde{v})$ . This is discussed in greater detail in Section 4.3.

The cosine Fourier transform of a truncated sine wave has the form shown in Figure 2.11. In general, the shape of the ILS is intermediate between this function and the sinc function that results from the cosine transform of a truncated cosine wave. The process of removing these sine components from an interferogram, or removing their effects from a spectrum, is known as *phase correction*.

If there were simply a sampling error in the collection of the interferogram, the phase spectrum would be linear, but in general the phase spectrum contains higher-order terms, for example,

$$\theta_{\tilde{v}} = A + B\tilde{v} + C\tilde{v}^2 + \dots \quad (2.32)$$

In this case there is no point at which all the wavelengths are exactly in phase and the interferogram is said to be *chirped*. For most interferograms, the amount of chirping is small, but in a few unusual cases,  $\theta_{\tilde{v}}$  can vary rapidly (see Section 3.2). Figure 2.12 shows an interferogram that exhibits a small amount of chirping.

A more detailed discussion of phase correction is given in Chapter 4. At this point it is sufficient to say that if the phase angle  $\theta_{\tilde{v}}$  in an interferogram measured with a continuous broadband source varies only slowly with wavenumber (as is





**Figure 2.12.** Typical interferogram of a blackbody-type source in the region of the centerburst measured by a rapid-scanning interferometer. The slight asymmetry indicates a very small amount of chirping.

usually the case), the phase spectrum (i.e., the variation of  $\theta_{\tilde{\nu}}$  with  $\tilde{\nu}$ ) may be computed from a region of the interferogram measured symmetrically on either side of the zero retardation point, or *centerburst*. (Interferograms measured with approximately equal retardations on both sides of ZPD are usually known as *double-sided interferograms*.) For high-resolution measurements, however, it is rarely feasible to measure full double-sided interferograms. In this case,  $\theta_{\tilde{\nu}}$  is calculated only at very low resolution, by starting data collection a short distance to the left of the centerburst, at  $-\Delta_1$ , and continuing until the desired resolution has been attained, that is, to a point such that  $\delta = +\Delta_2$ , where  $(\Delta_2)^{-1}$  is the resolution desired for the spectrum and  $(\Delta_1)^{-1}$  is the resolution desired for the phase spectrum. (Interferograms measured with a short retardation on one side of the ZPD and a much longer retardation on the other are usually known as *single-sided interferograms*.) The short double-sided region of the interferogram from  $-\Delta_1$  to  $+\Delta_1$  is used to calculate the phase spectrum by computing the sine and cosine transforms and applying the relationship

$$\theta_{\tilde{\nu}} = \arctan \frac{\text{Im}(\tilde{\nu})}{\text{Re}(\tilde{\nu})} \quad (2.33)$$

Most modern FT-IR spectrometers that operate at a resolution of  $1 \text{ cm}^{-1}$  or poorer collect full double-sided interferograms (i.e., they are measured from  $-\Delta_2$  to  $+\Delta_2$ ). In this case, the phase spectrum is calculated from the entire interferogram, hence no approximations are made in the calculation of  $\theta_{\tilde{\nu}}$ . Chase [11] demonstrated the improvement in photometric accuracy when symmetrically double-sided interferograms are acquired. The advantage of collecting a double-sided

interferogram lies not only in the accuracy at which the phase spectrum is calculated (and hence the improved photometric accuracy of the spectrum), but the signal-to-noise ratio (SNR) is also improved in comparison to single-sided measurements, as the data on either side of the centerburst are redundant except for the noise and collection of these data twice leads to an improvement in the SNR by  $\sqrt{2}$ . (Of course, the measurement time has also been doubled.)

## 2.6. EFFECT OF BEAM DIVERGENCE

In Section 2.2 it was stated that the beam that passes through the interferometer must be perfectly collimated. In practice, a perfectly collimated beam can only be generated from an infinitesimally small source, in which case no signal would be measured by the detector. To measure a signal at the detector, a source of finite size must be used and the beam is no longer collimated. In this section the limits on source size are discussed, so that a beam with the largest possible solid angle may be passed through the interferometer to give the highest signal without any degradation to the resolution.

If the light from an extended monochromatic source is passed through a Michelson interferometer, circular interference fringes, known as Hadinger fringes, are produced in the plane of the image of the source [12] (e.g., the detector position). This effect is shown schematically in Figure 2.13. The distance between successive maxima is largest at zero retardation and their spacing shrinks with increasing retardation. As the retardation increases, the intensity of the signal at any point in this plane changes sinusoidally. If the entire beam were measured by the detector, there would be no overall change of intensity with retardation, and no interferogram would be able to

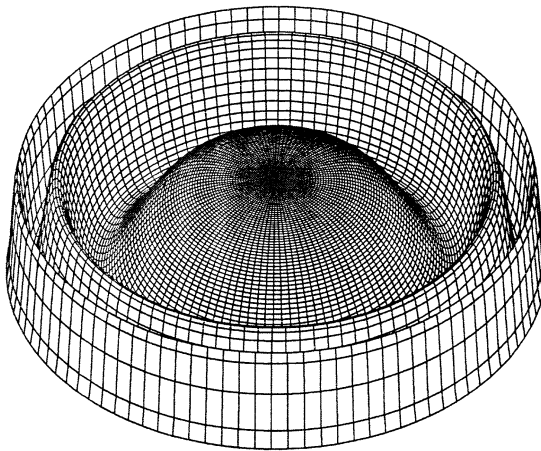


**Figure 2.13.** Fringe pattern seen at the focus of a monochromatic beam from a source of finite size. Only the central light fringe must be observed in Fourier transform spectrometry or the resolution of the spectrum will be degraded.

be recorded. Thus, an aperture at a plane of the source image, often known as the *Jacquinot stop*, limits the area of the beam at the detector so that only the central fringe of the interferogram is measured (see Chapter 6). In low-resolution FT-IR spectrometers, the detector itself is the limiting aperture and a Jacquinot stop is not needed.

This can be viewed in a simple way so that approximate quantitative relationships can be found. Consider the effect of a noncollimated beam of monochromatic light of wavelength  $\lambda$  passing through the interferometer with a divergence half-angle  $\alpha$ . At zero retardation, the path difference between the central ray that passes to the fixed and movable mirrors is zero, and there is also no path difference for the extreme rays. Thus, there will be constructive interference for both beams. Let the movable mirror now be moved a distance  $l$  (Figure 2.14). The off-axis ray follows a path to point A. When the mirror is at zero retardation, the ray follows path 1, and after the mirror has been moved, it follows path 2. Beyond point B on path 1 and point C on path 2, the paths of the two rays are equivalent. For the ray that follows path 1, the pathlength AB is given by

$$AB = 2l \tan \alpha \sin \alpha \quad (2.34)$$

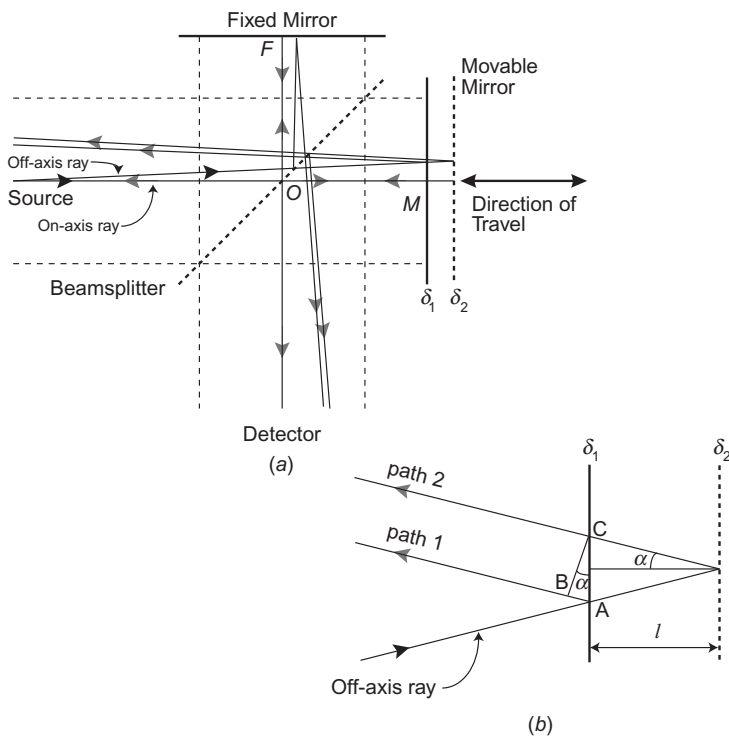


**Figure 2.14.** (a) Diverging beam passing through a Michelson interferometer; (b) expanded schematic of where the diverging beam strikes the moving mirror. The beam at retardation  $\delta_1$  is shown as path 1, and the beam at retardation  $\delta_2$  is shown as path 2.

or with a simple trigonometric identity,

$$AB = 2l \frac{\sin^2 \alpha}{\cos \alpha} \quad (2.35)$$

For the beam that follows path 2, the pathlength AC is given by

$$AC = \frac{2l}{\cos \alpha} \quad (2.36)$$

Therefore, the path difference,  $\Delta$ , is

$$\begin{aligned} \Delta &= AC - AB \\ &= \frac{2l}{\cos \alpha} - 2l \frac{\sin^2 \alpha}{\cos \alpha} \\ &= 2l \cos \alpha \end{aligned} \quad (2.37)$$

It may be surprising to note that the path difference for the extreme ray is shorter than for the on-axis, or central, ray, which has a path difference of  $2l$ . Hence, the path difference,  $x$ , between the central and extreme rays is

$$x = 2l(1 - \cos \alpha) \quad (2.38)$$

The series expansion for a cosine function is

$$\cos \alpha = 1 - \frac{\alpha^2}{2!} + \frac{\alpha^4}{4!} - \frac{\alpha^6}{6!} + \dots$$

If  $\alpha$  is small,

$$1 - \cos \alpha \sim \frac{1}{2} \alpha^2$$

Therefore,

$$x \sim 2l \cdot \frac{1}{2} \alpha^2 = l \alpha^2 \quad (2.39)$$

since  $\cos \alpha$  is approximately equal to 1.

As  $l$  increases, the extreme ray will be out of phase with the central ray for the first time when

$$x = \frac{1}{2} \lambda$$

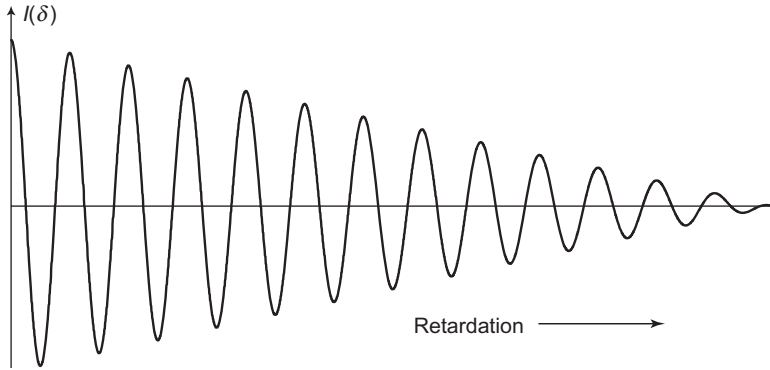


**Figure 2.15.** Appearance of the interferogram of a beam of monochromatic radiation diverging rapidly as it passes through the interferometer.

At this point, the fringe contrast at the detector disappears completely, and any further increase in  $l$  will add no further information to the interferogram (Figure 2.15). This retardation ( $2l$ ) gives the highest resolution  $\Delta\tilde{\nu}$  achievable with this half-angle  $\alpha$  for a wavelength  $\lambda$  or a wavenumber  $\tilde{\nu}(=\lambda^{-1})$ . By Eq. 2.15,  $(2l)^{-1}$  is equal to the resolution ( $\Delta\tilde{\nu}$ ). Fringe contrast would obviously have been lost at a shorter retardation if  $\tilde{\nu}$  were increased. Therefore, if a resolution of  $\Delta\tilde{\nu}$  is to be achieved at all wavenumbers in a spectrum measured between 0 and  $\tilde{\nu}_{\max}$   $\text{cm}^{-1}$ , the greatest beam half-angle,  $\tilde{\nu}_{\max}$ , that can be passed through the interferometer is given by

$$l\alpha^2 = \frac{\alpha^2}{2(\Delta\tilde{\nu})} = \frac{1}{2\tilde{\nu}_{\max}}$$

Therefore,

$$\alpha_{\max} = \left( \frac{\Delta\tilde{\nu}}{\tilde{\nu}_{\max}} \right)^{1/2} \quad (2.40)$$

The *maximum solid angle* that can be tolerated is therefore

$$\Omega_{\max} = 2\pi\alpha^2 = 2\pi \frac{\Delta\tilde{\nu}}{\tilde{\nu}_{\max}} \quad \text{steradians} \quad (2.41)$$

The effect of having a large solid angle is similar to the effect of apodization. For this reason, it has been called *self-apodization* [13].

From Eq. 2.41 it can be seen that the solid angle of the beam passing through the interferometer must be reduced every time the resolution is increased (i.e.,  $\Delta\tilde{\nu}$  is decreased). This is usually accomplished by reducing the diameter of the Jacquinot stop that is mounted at the beam focus.

Besides setting a limit on the achievable resolution, beam divergence also has the effect of shifting the wavenumber of a computed spectral line from its true value. Consider the interferograms due to the central and extreme rays from a monochromatic source. The apparent wavelength of the interferogram for the extreme ray is shorter than that of the central ray (Figure 2.14). For a particular divergence half-angle  $\alpha$ , the path difference between the central and extreme rays at a retardation  $\Delta$  is given by Eq. 2.39 as

$$x = \frac{1}{2} \alpha^2 \Delta \quad (2.42)$$

Between  $\delta = 0$  and  $\Delta$ , there are  $n$  maxima in the (cosine) interferogram for the central ray, where

$$\Delta = n\lambda = \frac{n}{\tilde{\nu}} \quad (2.43)$$

For the extreme ray, there is a decreased retardation  $(\Delta - x)$ , and the effective wavelength of this ray is therefore changed to a value  $\lambda'$ , where

$$\Delta - x = n\lambda' = \frac{n}{\tilde{\nu}'} \quad (2.44)$$

Combining Eqs. 2.43 and 2.44 and substituting for  $x$  from Eq. 2.42, we obtain

$$\frac{\tilde{\nu}'}{\tilde{\nu}} = \frac{\Delta}{\Delta - x} = \frac{1}{1 - \alpha^2/2} \quad (2.45)$$

If  $\alpha$  is small,

$$\frac{\tilde{\nu}'}{\tilde{\nu}} = 1 + \frac{1}{2} \alpha^2$$

so that

$$\tilde{\nu}' = \tilde{\nu} \left( 1 + \frac{1}{2} \alpha^2 \right) \quad (2.46)$$

To a first approximation, the wavenumber of the line computed from this interferogram,  $\tilde{\nu}''$ , is the mean of the wavenumbers of the central and extreme rays, that is,

$$\begin{aligned} \tilde{\nu}'' &\sim \frac{\tilde{\nu} + \tilde{\nu}'}{2} = \tilde{\nu} \left( 1 + \frac{\alpha^2}{4} \right) \\ &= \tilde{\nu} \left( 1 + \frac{\Delta \tilde{\nu}}{4 \tilde{\nu}_{\max}} \right) \end{aligned} \quad (2.47)$$

A more complete derivation of this wavelength shift [14,15] leads to a calculated shift of twice the magnitude given in Eq. 2.47, since the extreme rays have a larger contribution than the central rays to the total signal.

Two further conclusions may be drawn from this discussion. Most modern interferometers incorporate a laser to permit the interferogram to be digitized at equal intervals of retardation (see Chapters 3 and 5). If the reference laser is even slightly misaligned (which it usually is), or the divergence of the infrared beam is greater than that of the laser beam (which it always is), a small wavenumber shift is introduced. Thus, the great wavenumber accuracy of a Fourier transform spectrometer may be lost, although the abscissa will still be very precise (i.e., repeatable). Nevertheless, since the shift always varies linearly with  $\bar{\nu}$ , it is a simple matter to correct for the shift by changing the value of the laser wavenumber entered into the Fourier transform programs by an appropriate amount after calibration against a suitable sample. It may also be noted that the instrument should be recalibrated each time the laser is changed or removed from the interferometer.

Similarly, any time the average divergence angle of the beam passing through the interferometer is changed, the wavenumber scale will shift slightly. This effect will occur any time the diameter of the limiting aperture (which may be the Jacquinot stop, the detector, the sample, or the sampling accessory) is changed. In a few commercially available spectrometers, this change in the abscissa scale is compensated in the instrument's software. A small shift in the wavenumber scale will also be introduced when a sample cell that is smaller than the open beam of the spectrometer is inserted into the sample compartment or a sampling accessory. Similar effects can be observed if sampling accessories are misaligned. The presence of a shift is easily detected in subtraction experiments (see Chapter 9), since absorption bands can never be compensated precisely but rather, show up as a "derivative-shaped" residual in the difference spectrum. To avoid this effect, the sample and reference cells must both be larger than the beam or geometrically identical. Errors in the wavenumber scale will also be introduced if the beam is deflected by wedged windows or sample [16], and more severe errors will occur if a sample of small diameter is not held at the center of the beam [17].

## 2.7. EFFECT OF MIRROR MISALIGNMENT

The quality of spectra measured on a Michelson interferometer depends both on the alignment of the fixed mirror relative to the moving mirror and on how accurately the plane of the moving mirror is maintained during the scan. These effects are discussed in this section and Section 2.8, respectively.

If the moving mirror is held at a different angle than the fixed mirror relative to the plane of the beamsplitter, the image of the beam to the moving mirror will hit the plane of the detector at a different position than the beam that traveled to the fixed mirror (see Figure 2.16). Consider the concentric rings forming the image of an extended source at the detector (Figure 2.13). If the images from the fixed and moving mirrors are not centered at the same point on the detector, fringe contrast

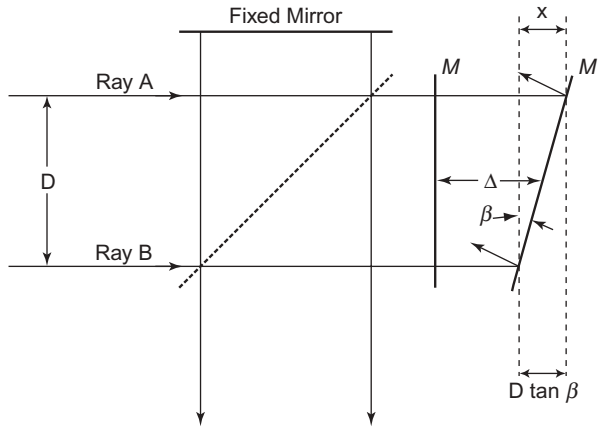


**Figure 2.16.** Effect of changing the plane of the moving mirror of an interferometer during a scan. Rays A and B represent the extreme rays of the collimated beam passing through the interferometer, and  $\beta$  is the angle by which the plane of the moving mirror tilts.

can be drastically reduced. Since the diameter of any ring is dependent on the wavelength of the radiation, short-wavelength radiation from a polychromatic source will be affected more than long-wavelength radiation.

This effect is illustrated in Figure 2.17. Single-beam spectra of a continuous source are shown for which the two mirrors in the interferometer are (a) well aligned, (b) in fair alignment, and (c) badly aligned. As the alignment of the fixed mirror is degraded, the signal at the high wavenumber (and hence the SNR)

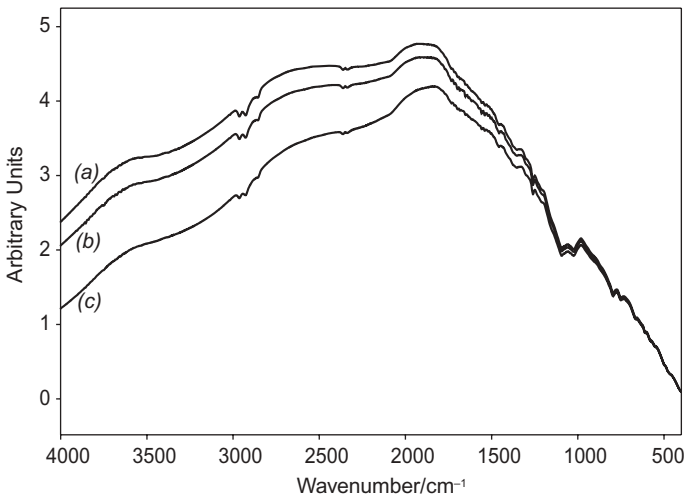


**Figure 2.17.** Single-beam spectra measured (a) with the fixed mirror of the interferometer in good alignment with the moving mirror, (b) with the fixed mirror slightly out of alignment, and (c) with the fixed mirror well out of alignment.



decreases concomitantly. When the interferometer is badly out of alignment, all the information at high wavenumber is lost. To obtain good spectra at short wavelengths, it is vital that the mirrors of the interferometer are maintained in alignment.

For some *slow-scanning interferometers* designed for far-infrared spectrometry ( $\tilde{\nu}_{\max} < 400\text{ cm}^{-1}$ ), the interferogram is often perfectly symmetrical when the interferometer is in good alignment. As the alignment deteriorates, not only does the amplitude of the signal at zero retardation decrease but the interferogram also becomes asymmetrical. This behavior demonstrates that the zero-phase difference point no longer occurs at the same path difference for all wavelengths.

For rapid-scanning interferometers, the interferogram is always slightly chirped, so these interferometers should not be aligned using the symmetry of the interferogram as a guide. To align a rapid-scanning interferometer, the moving mirror should be scanned repetitively about ZPD and the fixed mirror is adjusted to give the maximum signal. To check that the alignment is good, it is advisable to have a reference single-beam spectrum at hand taken with the same source, beamsplitter, and detector measured when it is known that the alignment was good, for example, immediately after installation of the spectrometer. Alignment at any other time is tested by calculating the ratio of the single-beam spectrum stored after realigning the interferometer to the “good” stored reference spectrum. If the ratio at low wavenumber is approximately 100% but is substantially lower at higher wavenumber, there is a high probability that the alignment of the interferometer is still not optimal (see Figure 2.18). It should be noted that the same effect can also be observed if the source temperature has decreased from the time the original reference spectrum was measured, but usually this is less likely. If the ratio spectrum is flat but at less than 100%, there is a good possibility that the spectrometer optics (but not the interferometer) are out of alignment.

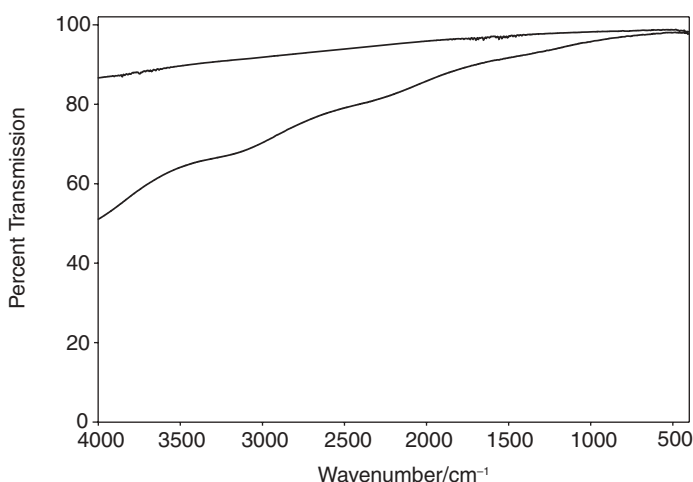


**Figure 2.18.** Ratio of spectra (b) (upper trace) and (c) (lower trace) to spectrum (a) in Figure 2.17.

Alignment of the interferometer mirrors is almost invariably needed when the beamsplitter is changed. It is also needed at infrequent intervals to improve the performance when the energy at high frequency in the spectrum appears to have decreased; some modern spectrometers perform this task automatically. Alignment is generally performed by adjusting the plane of a fixed mirror or the plane of the beamsplitter so that the angle between the plane of the fixed mirror and the plane of the beamsplitter is exactly the same as that for the moving mirror.

## 2.8. EFFECT OF A POOR MIRROR DRIVE

The quality of the drive mechanism of the moving mirror ultimately determines whether a certain interferometer can be used to measure a spectrum with a resolution that corresponds to the reciprocal of the maximum retardation of the interferometer. The resolution of a Fourier transform spectrometer is determined by the maximum retardation only if the planes of the mirrors remain in good alignment throughout the entire scan and if the beam that passes through the interferometer is sufficiently collimated.

The effect of a drive mechanism that does not allow the plane of the moving mirror of the interferometer to maintain its angle relative to the plane of the beamsplitter is somewhat analogous to the effect of beam divergence discussed in Section 2.6. In the case of the poor mirror drive, however, an optical path difference is generated between the two extreme rays of the beam passing through the interferometer rather than a path difference between the extreme rays and the central ray.

Let us consider the effect of a mirror tilt of  $\beta$  radians on a collimated beam of radiation of wavelength  $\lambda$  and diameter  $D$  (in centimeters) (see Figure 2.16). The increase in retardation,  $x$ , for the upper ray (A) over the lower ray (B) is

$$x = 2D \tan \beta \quad (2.48)$$

If  $\beta$  is small,

$$x = 2D\beta \quad (2.49)$$

Loss of fringe modulation will start to become apparent when  $x \sim 0.1\lambda$ . Thus, to ensure that no degradation of resolution occurs during the scan,

$$x < \frac{\lambda_{\min}}{10} = \frac{1}{10\tilde{\nu}_{\max}}$$

that is,

$$\beta < \frac{1}{20D\tilde{\nu}_{\max}} \quad (2.50)$$

where  $\tilde{\nu}_{\max}$  is the highest wavenumber in the spectrum. For a mid-infrared spectrometer with  $D = 5$  cm and  $\tilde{\nu}_{\max} = 4000$   $\text{cm}^{-1}$ ,  $\beta$  must therefore be less than  $2.5$   $\mu\text{rad}$  throughout the entire scan. Misalignment of the moving mirror with respect to the fixed mirror by this amount will lead to a loss of resolution. The *routine* achievement of such small tolerances over long retardations is one of the significant factors that has led to the rapid development of Fourier transform infrared (FT-IR) spectrometry since 1970.

If the resolution is found to have been degraded because of mirror tilt, the effect may be minimized by reduction of the diameter of the beam. For example, if the desired resolution is not attained above  $2000$   $\text{cm}^{-1}$  in an interferometer with  $D = 5$  cm, the beam may be apertured down to a diameter of  $2.5$  cm. When the area of the beam is so reduced, however, the amount of energy that reaches the detector is reduced in proportion to the area of the beam, that is, by a factor of 4, and the SNR of the spectrum would also be reduced by this amount.

## 2.9. RAPID-SCAN INTERFEROMETERS

Rapid-scan interferometers account for almost all the FT-IR spectrometers currently in use. In these instruments the moving mirror travels at a constant velocity (usually greater than  $0.1$   $\text{mm} \cdot \text{s}^{-1}$ ) during each scan. In a typical experiment the SNR of the spectrum is improved by repeated measurement and co-addition of the interferograms. Whereas the signal adds coherently, the measurement noise does not, as it is random and hence increases only with the square root of the number of scans,  $N$ ; thus, the SNR increases with  $\sqrt{N}$ . This process is known as *signal averaging*.

To permit accurate phase correction, the moving mirror must start data collection at a point before the interferogram centerburst, or zero path difference (ZPD), usually at the maximum retardation for the resolution required for double-sided interferograms. The mirror then moves through ZPD to the maximum retardation on the other side of the interferogram for the desired resolution. The interferogram is sampled at a constant retardation interval determined by the Nyquist criterion as described in Chapter 3. When the maximum desired retardation has been reached, the moving mirror is decelerated and its direction is reversed. In some interferometers the moving mirror is returned as rapidly as possible to a retardation well before where the first data point of the previous scan was acquired, to allow it to speed up to the appropriate constant velocity so that another scan may be collected. Hence the moving mirror completes a second cycle where it begins from rest at some level of retardation before data collection is initiated and passes through ZPD and onto the point of maximum retardation. The moving mirror is stopped and returned to its initial position. This process is repeated as often as needed to achieve the desired SNR.

A schematic diagram of retardation and mirror velocity versus time is shown in Figure 2.19. This operation is not very efficient as a considerable time in the cycle is not used for the collection of data but is used to decelerate the moving mirror,

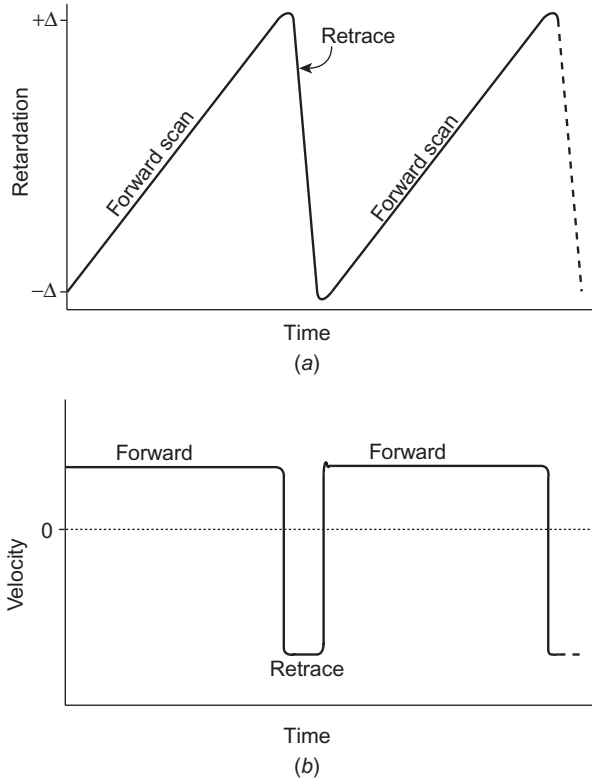


**Figure 2.19.** (a) Retardation versus time for a unidirectional rapid-scanning interferometer where the mirror speed is relatively slow during data collection, then resets rapidly for the next scan; (b) velocity scan that corresponds to (a). The speed in the reset direction is greater than that for scanning.  $-\Delta$  and  $+\Delta$  indicate the limits of retardation at the beginning and end of travel, respectively.

turn it around, and bring it back up to constant velocity for data collection. The actual fraction of the time spent in the measurement of the interferogram depends on the data collection velocity, the rapidity with which the interferometer mirror may be stopped and reversed, the reset speed, and the resolution of the interferogram. This fraction is specified by the *duty cycle efficiency*, which is the ratio of the active data acquisition time per scan to the time between the start of successive scans. As the velocity of the moving mirror increases, the time during which data are acquired per scan decreases and the time required to turn around the moving mirror increases. Thus, the duty cycle efficiency decreases as the mirror velocity is increased. For low-resolution scans made with a high optical velocity, the duty-cycle efficiency rarely exceeds 25%.

In many contemporary interferometers, the duty cycle efficiency is improved by collecting data in both directions, or bidirectionally. In this case, interferograms are collected in both the forward and reverse directions. Of course, the speed

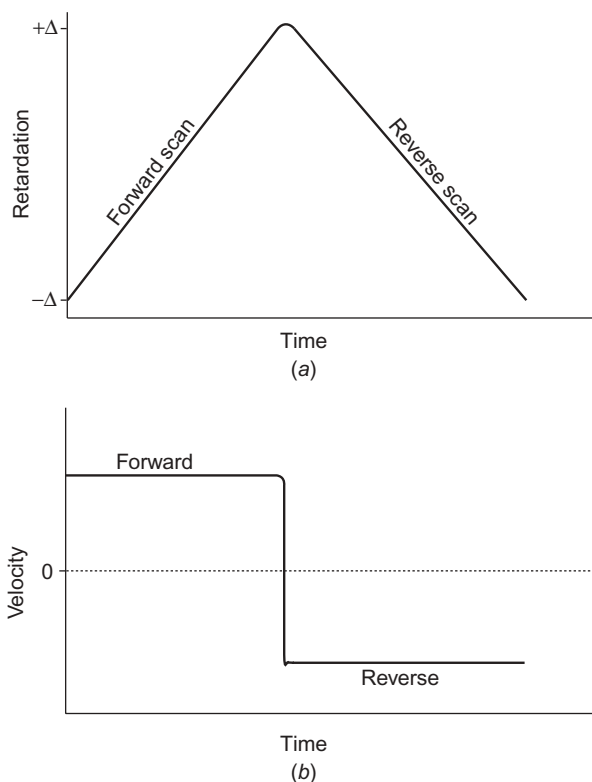


**Figure 2.20.** Retardation (a) and velocity (b) versus time for a bidirectional rapid-scanning interferometer. The speed of the moving mirror in both directions is the same.

of the moving mirror for the forward and reverse scans must be the same. Schematic diagrams of the retardation and velocity are shown in Figure 2.20. The duty cycle is more efficient as data collection is accomplished throughout a greater portion of the entire cycle. In this instance, the interferograms acquired in the forward and reverse scans must be signal-averaged in separate files. In an optical sense the two sets of interferograms are identical, but electronic filters in the amplifier circuitry for the infrared detector add a direction-dependent phase error. Consequently, the two sets of interferograms are independently transformed to spectra and then the spectra are co-added. This is not a serious problem, as computer memory and storage are inexpensive and the additional transformation time is negligible. At least one manufacturer of interferometers has been able to correct for the direction-dependent phase error and allow the co-addition of forward and reverse interferograms.

Any interferometer in which the mirror moves at a constant velocity and the beam is not modulated by an external chopper or by phase modulation (see Section 20.3)

may be classified as a rapid-scan interferometer. The optical velocities of rapid-scan interferometers range from approximately  $0.1$  to  $6.0 \text{ cm} \cdot \text{s}^{-1}$ . For some experiments, such as photoacoustic spectrometry (PAS), the slowest scan speed may be slightly less than  $0.1 \text{ cm} \cdot \text{s}^{-1}$ , whereas in other experiments, where the sample is changing very rapidly,  $V$  may exceed  $6.0 \text{ cm} \cdot \text{s}^{-1}$ .

With many rapid-scan interferometers, it is possible to vary the scan velocity of the moving mirror. The scan speed is sometimes reported as a frequency rather than the actual physical or optical velocity. When an interferometer scans at a constant velocity, the frequency of each wavelength in the spectrum is different, as shown in Eq. 2.10. It is sometimes simpler to reference the scan velocity to a single wavelength, and the wavelength chosen is usually that of the reference laser, which is often a HeNe laser (see Chapters 3 and 5). The wavelength of a HeNe laser is  $632.8 \text{ nm}$ , so that its wavenumber is  $\sim 15,800 \text{ cm}^{-1}$ . In this case, the scan “speed” is often given simply as  $5 \text{ kHz}$ . A physical scan speed of  $0.16 \text{ cm} \cdot \text{s}^{-1}$  ( $V = 0.32 \text{ cm} \cdot \text{s}^{-1}$ ) generates a HeNe frequency of  $\sim 5 \text{ kHz}$ . This scan speed is typical for a room-temperature detector such as a deuterated triglycine sulfate (DTGS) pyroelectric detector. On the other hand, a mercury–cadmium–telluride (MCT) detector requires a faster optical velocity, on the order of  $2.6 \text{ cm} \cdot \text{s}^{-1}$ , or a HeNe frequency of about  $40 \text{ kHz}$ . (Detectors are discussed in Section 6.2). Use of the HeNe frequency to specify the scan speed has the advantage that there is no ambiguity as to whether the scan speed is a physical or optical velocity.

## 2.10. STEP-SCAN INTERFEROMETERS

There are experiments for which rapid-scan interferometers are not well suited. These experiments include depth profiling by photoacoustic spectrometry (Section 20.3), hyperspectral imaging (Section 14.5), fast time-resolved spectrometry

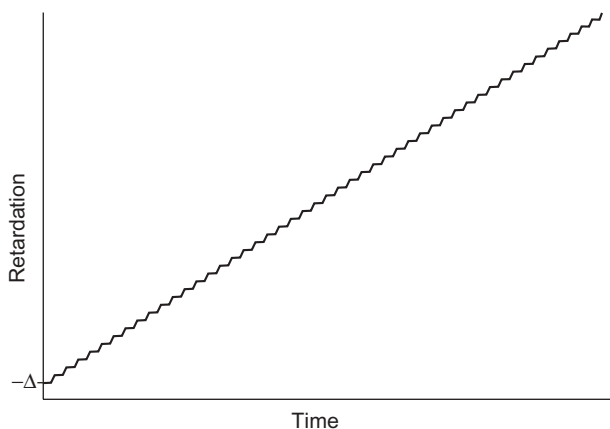


**Figure 2.21.** Retardation versus time for a step-scanning interferometer. The velocity of the moving mirror is zero at each step and the mirror moves very quickly between steps.

(Section 19.2), and sample-modulation measurements (Chapter 21). For PAS the change in frequency of each wavelength leads to a different penetration depth in a rapid-scan interferometer. In the other experiments mentioned, rapid-scan systems simply prove to be impractical. For these measurements, *step-scan interferometers* may prove to be beneficial. In a step-scan interferometer, the moving mirror is moved in discrete steps and halt the mirror at each retardation at which the interferogram is sampled. In a practical sense, there is no difference between a rapid-scan interferometer and a step-scan interferometer. In a conventional experiment, both produce identical data at the same signal-to-noise ratio. In a step-scan system, the moving mirror is usually scanned only once, but the retardation may be held constant for a long enough time that the data may be signal-averaged at each step. When rapid- and step-scan experiments are compared, the total time at each retardation step is the same for the step-scan and co-added rapid-scan experiments. Figure 2.21 shows a schematic of the retardation of the mirror versus time. The efficiency of most step-scanning interferometers is quite high, as the time between steps is very low compared to the time spent collecting data. Step-scanning interferometers are discussed in more detail in Section 5.5.

## REFERENCES

1. A. A. Michelson, *Philos. Mag.* **31**, 256 (1891).
2. A. A. Michelson, *Light Waves and Their Uses*, University of Chicago Press, Chicago, 1902 (reissued in paperback, Phoenix Edition, 1961).
3. A. A. Michelson, *Studies in Optics*, University of Chicago Press, Chicago, 1927 (Phoenix Edition, 1962).
4. R. N. Bracewell, *The Fourier Transform and Its Applications*, 3rd ed., McGraw-Hill, New York, 2000.
5. J. D. Ingle and S. R. Crouch, *Spectrochemical Analysis*, Prentice Hall, Englewood Cliffs, NJ, 1988, p. 71.
6. P. R. Griffiths, Resolution and instrument line shape, in *Handbook of Vibrational Spectroscopy*, J. M. Chalmers and P. R. Griffiths, Eds., Wiley, Chichester, West Sussex, England, 2002, Vol. 1, p. 241.
7. J. K. Kauppinen, D. J. Moffatt, D. G. Cameron, and H. H. Mantsch, *Appl. Opt.* **20**, 1866 (1981).
8. A. H. Filler, *J. Opt. Soc. Am.* **54**, 762 (1964).
9. R. H. Norton and R. Beer, *J. Opt. Soc. Am.* **66**, 259 (1976); erratum: **67**, 419 (1977).
10. C. T. Foskett, The Fourier transform and related concepts: a first look, in *Transform Techniques in Chemistry*, P. R. Griffiths, Ed., Plenum Press, New York, 1978.
11. D. Chase, *Appl. Spectrosc.* **36**, 240 (1982).
12. E. V. Lowenstein, Fourier spectroscopy: an introduction, in *Aspen International Conference on Fourier Spectroscopy, 1970*, G. A. Vanasse, A. T. Stair, Jr., and D. J. Baker, Eds., U.S. Air Force, L. G. Hanscom Field, Bedford, MA, 1971, Vol. AFCRL-71-0019, p. 3.

13. E. G. Coddling and G. Horlick, *Appl. Spectrosc.* **27**, 85 (1973).
14. J. Chamberlain, in *The Principles of Interferometric Spectroscopy*, G. W. Chantry and N. W. B. Stone, Eds., Wiley, Chichester, West Sussex, England, 1979.
15. A. E. Martin, Infrared interferometric spectrometers, in *Vibrational Spectra and Structure*, J. R. Durig, Ed., Elsevier, Amsterdam, The Netherlands, 1980.
16. T. Hirschfeld, *Anal. Chem.* **51**, 495 (1979).
17. J. Chamberlain, *Infrared Phys.* **11**, 25 (1971).





## Chapter 3

# SAMPLING THE INTERFEROGRAM

### 3.1. SAMPLING FREQUENCY

#### 3.1.1. Nyquist Frequency

It was shown in Eqs. 2.12 and 2.13 that to compute the complete spectrum from 0 to  $\infty \text{ cm}^{-1}$ , the interferogram would have to be sampled at infinitesimally small increments of retardation. That is, of course, impossible, as an infinite number of data points must be collected and computer storage space would be exhausted. Even if these data could be collected, the Fourier transform would take forever to be computed. Obviously, interferograms must be sampled discretely. Just how often the interferogram should be sampled is a problem that has been solved mathematically.

Any waveform that is a sinusoidal function of time or distance can be sampled unambiguously with a sampling frequency or wavenumber greater than or equal to twice the bandpass of the system [1]. Under this condition, which is known as the *Nyquist criterion*, the analog signal may be digitized *without any loss of information*. Consider the case of a spectrum in which the highest wavenumber that reaches the detector is  $\tilde{\nu}_{\text{max}}$ . The frequency of the cosine wave in the interferogram that corresponds to  $\tilde{\nu}_{\text{max}}$  is  $V\tilde{\nu}_{\text{max}}$ , where  $V$  is the optical velocity (from Eq. 2.11); therefore, the interferogram must be digitized at a frequency of  $2V\tilde{\nu}_{\text{max}}$  hertz or once every  $(2V\tilde{\nu}_{\text{max}})^{-1}$  seconds. This is equivalent to digitization of the signal at retardation intervals of  $(2\tilde{\nu}_{\text{max}})^{-1}$  centimeters. It is better to design a system where the signal is sampled at equal intervals of retardation rather than at equal intervals of time because if the mirror velocity varies only slightly during the scan, the signal is still sampled at the correct interval. With this type of sampling, only gross deviations in mirror velocity can cause deleterious effects in the computed spectrum [2].

### 3.1.2. Conceptual Discussion of Aliasing

The effect of disobeying the Nyquist criterion is illustrated by the waves in Figure 3.1. Each of these waves is sampled at a frequency that has been selected so that the corresponding amplitudes are the same for the waves in Figure 3.1*a* and *b*, as represented by the vertical lines. In Figure 3.1*a*, the sine wave has a frequency of  $f$  and is sampled at a frequency of  $2f$  (i.e., this wave is sampled at the highest possible frequency). Thus,  $2f$  is the Nyquist frequency. In Figure 3.1*b* the frequency of the sine wave is  $f - f_1$ . This sinusoid is digitized more than twice per wave and is therefore sampled correctly. The sinusoid in Figure 3.1*c* has a frequency of  $f + f_1$ , and it can be seen that at the points it is digitized, the values are exactly the same as they are in Figure 3.1*b*. Thus, when the signal is sampled with a frequency of  $2f$ , it is impossible to distinguish between waves of frequency  $f + f_1$  and  $f - f_1$ . Therefore, the sampled waveform will produce a feature at  $f_{\max} - f_1$  after computation, although there may never have been a feature at that frequency originally.

It can also be seen that a higher-frequency wave (in fact, many higher-frequency waves) can be drawn through the data points in Figure 3.1*c* (see Figure 3.2). It is a property of discrete Fourier transform mathematics that the true wavenumber of the signal cannot be determined unequivocally unless precautions are taken to ensure that all frequencies are less than  $f_{\max}$ . In FT-IR spectrometry it is therefore most important to limit the highest Fourier frequency in the signal that is passed to the analog-to-digital converter (ADC). The shortest wavelength that reaches the detector can be restricted by an appropriate optical filter, although this is rarely done in

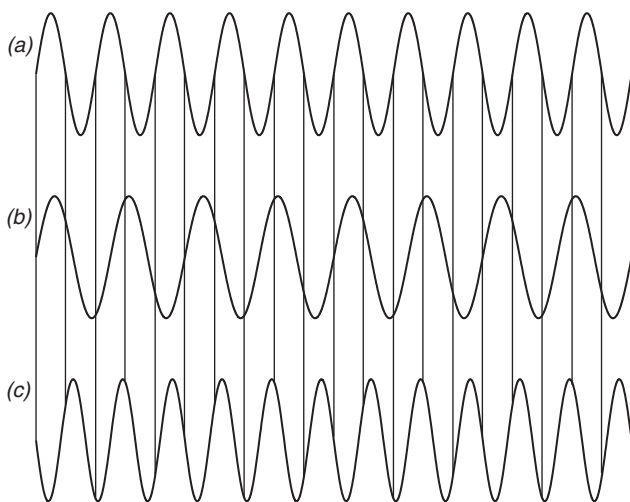


**Figure 3.1.** (a) Sine wave sampled at exactly twice its frequency; (b) lower-frequency wave sampled at the same frequency as in (a); (c) sine wave of higher frequency than the wave in (a) and sampled at the same frequency. Note that the sampling amplitudes in (b) and (c) are identical.

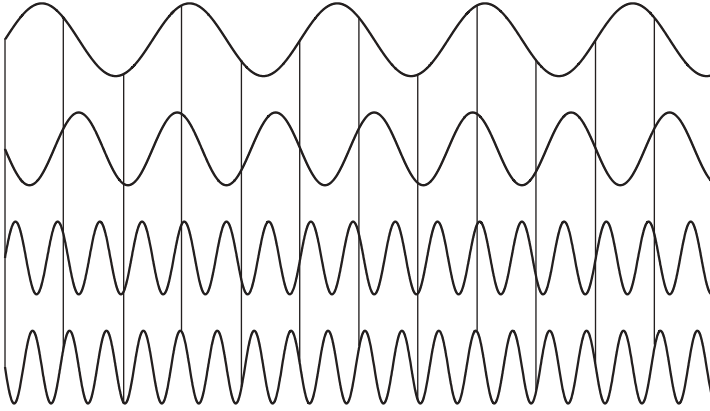


**Figure 3.2.** Multiple sine waves, all with identical amplitudes at the sampling frequency shown in Figure 3.1.

practice. More commonly, the frequency range of the signal and noise is restricted by a low-pass electronic filter.

It is important to consider how the Nyquist sampling criterion affects the spectrum. If the sampling frequency of a wave is  $2F$ , all the frequencies below  $F$  will be transferred through the sampling process unambiguously. On the other hand, a feature whose frequency is higher than  $F$  will appear at a frequency below  $F$ . This phenomenon is known as *folding* or *aliasing*. Figure 3.3 shows a spectrum in schematic form where  $2F$  is the sampling frequency. Three features,  $R$ ,  $S$ , and  $T$ , are shown in the schematic spectrum.  $R$  occurs in the normal bandpass of 0 to  $F$  and is not folded as it is sampled correctly under the Nyquist criterion;  $S$  is folded from the region  $F$  to  $2F$  to  $S'$ ;  $T$  is folded from the region  $2F$  to  $3F$  down in frequency to  $T'$  and then to  $T''$ . It can be seen that there is no way to distinguish which of the features is real and which arises because of folding. Thus, if the sampling frequency is  $2F$ , any frequency region in bandwidth  $F$  can be examined.

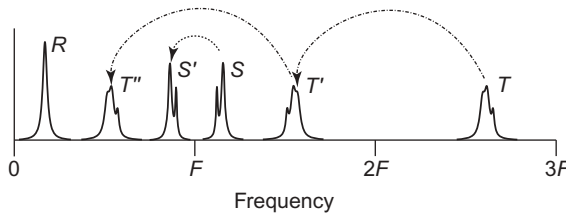


**Figure 3.3.** Spectrum with three features,  $R$ ,  $S$ , and  $T$ .  $R$  is within the appropriate bandwidth for sampling, 0 to  $F$ , and it is not folded.  $S$  is in the bandwidth  $F$  to  $2F$  and it is folded to  $S'$ .  $T$  is in the bandwidth  $2F$  to  $3F$ , and it is folded to  $T'$  in the region  $F$  to  $2F$ , as well as to  $T''$  in the 0 to  $F$  region.

### 3.1.3. Mathematical Discussion of Aliasing

It is a property of Fourier transform mathematics that multiplication in one domain is equivalent to convolution in the other. (Convolution has already been introduced with regard to apodization in Section 2.3.) If we sample an analog interferogram at constant intervals of retardation, we have in effect multiplied the interferogram by a repetitive impulse function. The repetitive impulse function is in actuality an infinite series of Dirac delta functions spaced at an interval  $1/x$ . That is,

$$\text{III}_{1/x}(\delta) = \frac{1}{x} \sum_{n=-\infty}^{\infty} \kappa\left(\delta - \frac{n}{x}\right) \quad (3.1)$$

where  $\kappa$  is the Dirac delta function and  $\text{III}_{1/x}(\delta)$ <sup>1</sup> is the Dirac delta comb as a function of retardation  $\delta$ . Figure 3.4a shows a Dirac delta comb, where the up arrows indicate the impulses. The Fourier transform of the Dirac delta comb is another Dirac delta comb of period  $x$  as opposed to  $1/x$ ; that is,

$$\text{III}_x(\tilde{v}) = x \sum_{n=-\infty}^{\infty} \kappa(\tilde{v} - nx) \quad (3.2)$$

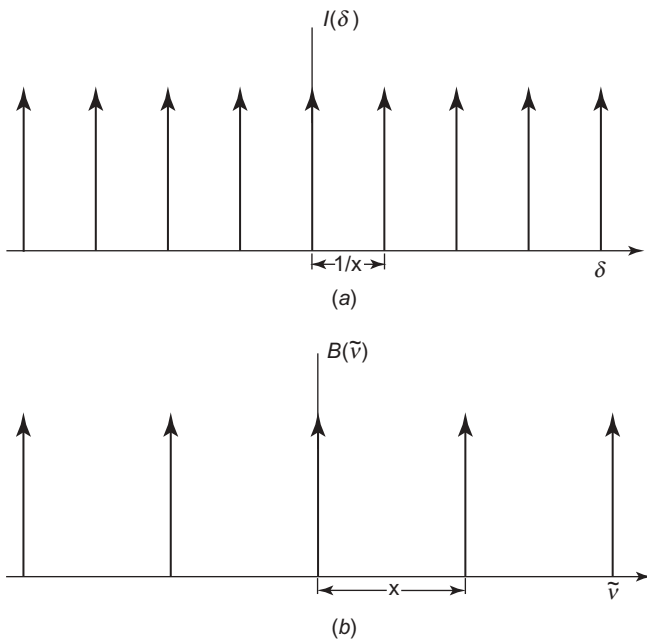


**Figure 3.4.** (a) Dirac delta comb (or Shah function) of period  $1/x$ ; (b) its Fourier transform, another Dirac comb of period  $x$ .

<sup>1</sup>III is the cyrillic character *shah*.

Figure 3.4*b* illustrates the Dirac delta comb as a function of wavenumber,  $\tilde{\nu}$ . The function in Eq. 3.2 is an infinite series. We multiply the analog interferogram with the Dirac delta comb of Eq. 3.1, and consequently, the Fourier transform of the interferogram (i.e., the spectrum) is convolved with the transformed comb (see Section 2.3). The effect of this convolution is to repeat the spectrum *ad infinitum*. If the spectrum covers the bandwidth 0 to  $\tilde{\nu}_{\max}$ , the transformed Dirac delta comb must have a period of at least  $2\tilde{\nu}_{\max}$ ; otherwise, the spectra will overlap as a result of the convolution. In other words,

$$x > 2\tilde{\nu}_{\max} \quad (3.3)$$

and

$$\frac{1}{x} \leq (2\tilde{\nu}_{\max})^{-1} \quad (3.4)$$

This process is illustrated in Figure 3.5. Figure 3.5*a* shows a discretely sampled  $\text{sinc}^2$  function sampled at a retardation of  $(2\tilde{\nu}_{\max})^{-1}$ , and Figure 3.5*b* shows its Fourier transform. As can be seen clearly, there is no overlap of the resulting spectra (triangular functions, in this case). If the sampling frequency were decreased so that the signal were sampled at  $(\tilde{\nu}_{\max})^{-1}$ , the transformed spectra, which are necessarily

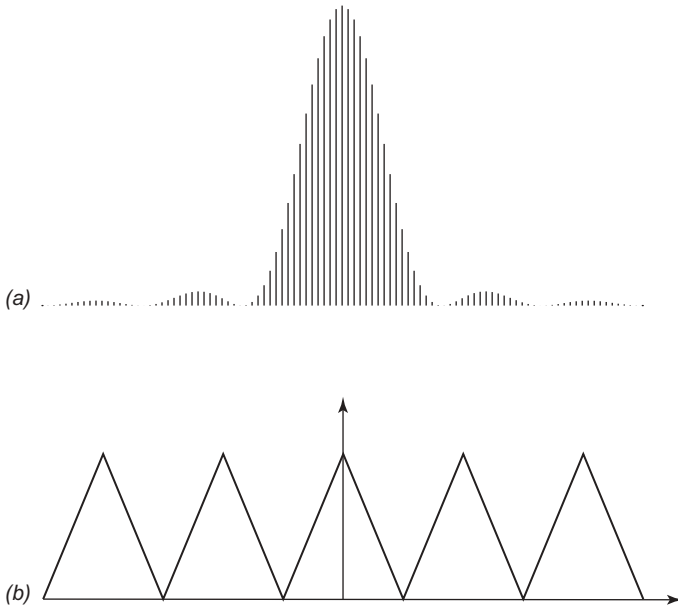


**Figure 3.5.** (a) Discretely sampled  $\text{sinc}^2$  function; (b) its Fourier transform, a series of triangle functions.

convolved with the spectral domain Dirac delta comb, would overlap and spectral features would appear at incorrect wavenumbers.

### 3.2. ALIASING

Aliasing has great importance for high-resolution spectrometry or other experiments where large data sets may be recorded or very rapid computation times are required. When the bandwidth of the spectrum is limited with an optical or electronic filter, a lower sampling frequency could be used than if the complete spectrum from zero to  $\tilde{\nu}_{\max}$  were measured. Filtering the signal in this way cuts down the number of data points that must be collected for a given retardation and the computation time required for the Fourier transform. For rapid-scan interferometers, however, the collection time is not reduced, as the full retardation of the interferometer at that resolution must still be used. With step-scan interferometers, the scan time can be reduced as the number of sampling positions is reduced.

In summary, when the entire spectrum from zero to  $\tilde{\nu}_{\max}$  is required at a resolution of  $\Delta\tilde{\nu}$ , the number of points to be sampled,  $N_s$ , is given by

$$N_s = \frac{2\tilde{\nu}_{\max}}{\Delta\tilde{\nu}} \quad (3.5)$$

If the spectral range is restricted to fall between a minimum wavenumber  $\tilde{\nu}_{\min}$  and a maximum wavenumber  $\tilde{\nu}_{\max}$ , the number of points required is

$$N_s = \frac{2(\tilde{\nu}_{\max} - \tilde{\nu}_{\min})}{\Delta\tilde{\nu}} \quad (3.6)$$

One very important fact must be remembered when sampling considerations are being discussed. A data system cannot distinguish between signal and noise, so that any noise whose frequency falls outside the range  $V\tilde{\nu}_{\max} - V\tilde{\nu}_{\min}$  will be treated in the same fashion as any real signal outside the range and will be folded back into the spectrum. Thus, the noise between  $\tilde{\nu}_{\min}$  and  $\tilde{\nu}_{\max}$  will increase. It is therefore most important to restrict the bandpass of the amplifier so that only the wavenumber range of interest is amplified and all the other electrical frequencies (whether they correspond to signal or noise) are filtered out. In practice, it can be quite difficult to design an electronic filter with a very sharp cutoff, so generally a somewhat higher sampling frequency than required by  $\tilde{\nu}_{\max}$  and  $\tilde{\nu}_{\min}$  is used. For example, many mid-infrared FT-IR spectrometers use a HeNe laser for wavenumber calibration and interferogram sampling (Section 5.1.4). Even though  $\tilde{\nu}_{\max}$  for mid-infrared spectrometry is  $4000 \text{ cm}^{-1}$ , the Nyquist frequency is usually  $0.5\tilde{\nu}_{\text{HeNe}}$  or  $\sim 7900 \text{ cm}^{-1}$ . In this way, any noise that is folded back into the spectrum is folded back into a region above  $4000 \text{ cm}^{-1}$  where there is no useful spectral information.

An example of a real system where these factors have been brought into consideration may be found in commercial FT-IR spectrometers that collect high-resolution

spectra. As discussed above, a lower sampling frequency than necessary for a bandwidth of 0 to  $\tilde{\nu}_{\max}$  can be employed for a bandwidth  $\tilde{\nu}_{\min}$  to  $\tilde{\nu}_{\max}$ . In this case, optical and electronic filters may be used to restrict the bandpass of the detector output. Because many mid-infrared FT-IR spectrometers use a HeNe laser to measure the optical retardation of the interferometer, the normal sampling interval is 632.8 nm. Multiples of this HeNe wavelength are used to keep the number of sampling points to a minimum. Thus, in mid-infrared spectrometry, the sampling interval is 632.8 nm, which corresponds to a minimum wavelength of  $2 \times 632.8$  nm, which in turn is equivalent to a maximum (Nyquist) wavenumber of  $\sim 7900$   $\text{cm}^{-1}$ . If a sampling interval of  $2 \times 632.8$  nm is used, the spectral bandpass must not exceed  $\sim 3950$   $\text{cm}^{-1}$ , that is, a minimum wavelength of  $4 \times 632.8$  nm. For a high-resolution spectrum, the number of data points can be greatly reduced by using a large sampling interval, or as it is sometimes called, a high *undersampling ratio*.

In practice, current computers have sufficient memory, storage, and computing speed to make restricting the bandpass and increasing the sampling interval unnecessary for all but the highest-resolution spectra. There are experiments, however, where undersampling and aliasing can still be of great use. For example, huge data sets are collected in two-dimensional hyperspectral imaging spectrometry with an infrared microscope, a focal plane array detector, and a step-scan interferometer (see Section 14.5). For a simple system with a  $64 \times 64$  element focal plane array, the data sets can become formidable. Even at a resolution of 8  $\text{cm}^{-1}$  and an undersampling ratio of 4 (a bandpass of 0 to 3950  $\text{cm}^{-1}$ ), the raw data set of 4096 (i.e.,  $64 \times 64$ ) spectra will occupy 28.4 Mbytes. To compute all these spectra is not very time consuming, as all 4096 transforms can be completed in under a minute. Nonetheless, the data collection may be as long as 40 minutes. If the spectral bandpass can be reduced from a range of 3950 to 0  $\text{cm}^{-1}$  to the range of 1975 to 988  $\text{cm}^{-1}$ , the undersampling ratio can be set to 16. Hence, only one out of the four steps required previously is recorded and the data collection can be reduced to approximately 10 min. In addition, the total amount of data will be reduced to about 7 Mbytes. Such time differences become even more important as the size of the focal plane arrays is increased. Under the same conditions a  $256 \times 256$  focal plane array detector will lead to collection times of more than 10 hours. A reduction of the data acquisition time to under 3 hours at an undersampling ratio of 16 becomes very attractive.

To effect high undersampling ratios, an optical filter must be placed in the beam path to restrict the bandpass to the region of interest. Optical filter design is sufficiently good that regions outside the bandpass are completely eliminated. Before the design of excellent optical filters, electronic filters were implemented to augment the optical filtering, but this approach is not appropriate when interferograms are measured on a step-scan interferometer. As stated above, electronic filters do not have sharp cutoffs; hence they cannot be used in lieu of optical filters, and their use is obviated by the current specifications of optical filters.

Most near-infrared (NIR) spectra are measured from 2500 to 1100 nm (4000 to 9100  $\text{cm}^{-1}$ ). To record a spectrum over this range, the interferogram must be sampled twice per wavelength of the HeNe laser interferogram to give a bandpass



of  $\sim 15,800$  to  $0 \text{ cm}^{-1}$ . In this case, interferograms are sampled at every zero crossing of the HeNe interferogram rather than once per wavelength ( $\lambda_{\text{HeNe}}$ ). To achieve a constant sampling interval of  $0.5\lambda_{\text{HeNe}}$ , it is important that the HeNe interferogram not be biased or distorted; otherwise, the sampling interval will alternate between slightly shorter and slightly longer than  $0.5\lambda_{\text{HeNe}}$  and the spectrum will include some rather subtle artifacts.

Another important aspect to be considered is any possible nonlinearity of the detection system where the amplitude of high-intensity signals is reduced. The worst case is found when the signal exceeds the maximum allowed input voltage to analog-to-digital converters (ADCs), in which case the signal is said to be *clipped*. An interferogram is the sum of many sinusoids, but a clipped interferogram begins to resemble a square wave near the centerburst. It was stated that any waveform must be digitized at twice the bandpass of the system so that the signal may be recovered completely. If the harmonics of the signal are generated in the detection system, deleterious effects may occur. Such is the case of a square wave, which can be expressed as a series:

$$\sin x + \frac{1}{3} \sin 3x + \frac{1}{5} \sin 5x + \dots$$

If the harmonics are outside the bandwidth allowed by the sampling frequency, they will naturally be folded into the real spectrum, thereby causing either spurious lines to appear (in the case of a line spectrum) or photometric inaccuracy (when the source is continuous). This phenomenon is explained in greater detail in Section 8.5.1.

### 3.3. DYNAMIC RANGE

#### 3.3.1. ADC Specifications

In Section 3.2 we discussed how often the interferogram should be digitized; in this section we discuss to what accuracy the *amplitude* of the signal should be sampled. In view of the fact that the intensity of the interferogram at zero retardation represents the summation of the amplitudes of all the waves in the interferogram, the signal-to-noise ratio (SNR) at this point can be extremely high when an incandescent broadband source is being measured. On the other hand, the SNR in the regions of the interferogram well displaced from zero retardation can be very low.

To give an example of the range of the signals found in interferometry, consider the case of the interferogram of an incandescent blackbody source generated by a rapid-scanning interferometer and detected by a mid-infrared pyroelectric bolometer such as DTGS (see Chapter 6). The ratio of the intensity of the signal to zero retardation to the root-mean-square (rms) noise level (often called the *dynamic range*) can often be higher than  $10^5:1$ . State-of-the-art sample-and-hold ADCs have a resolution of 18 bits, which means that the signal can be divided up into

a maximum of  $2^{18}$  (262,144) levels. (Most commercial sample-and-hold ADCs are limited to 16 bits; thus, the signal can be divided to a maximum of  $2^{16}$  or 65,536 levels.) Thus, if the dynamic range of the interferogram is 100,000, only the two least significant bits of the ADC would be used to digitize the noise level. If the dynamic range of the interferogram were, say, an order of magnitude higher, the noise level would fall below the least significant bit of the ADC, and real information would be lost from the interferogram.

This example illustrates an important point for the sampling of interferograms in that at least 1 or 2 bits of the ADC should be sampling detector noise. If no detector noise is seen, the inaccurate sampling of the interferogram can lead to the generation of another type of noise in the spectrum called *quantization*, or *digitization*, noise. The source of digitization noise is illustrated in Figure 3.6, where it can be seen that there is a difference between the sampled values of the waveform and the true values. This is equivalent to noise in the signal and will obviously transform into spectral noise.

For a spectrum measured between  $\tilde{\nu}_{\max}$  and  $\tilde{\nu}_{\min}$  at a resolution of  $\Delta\tilde{\nu}$ , there are  $M$  resolution elements, where

$$M = \frac{\tilde{\nu}_{\max} - \tilde{\nu}_{\min}}{\Delta\tilde{\nu}} \quad (3.7)$$

Let us consider what spectral dynamic range can be accommodated by a 16-bit ADC. A 16-bit ADC has a resolution of  $2^{16}$  (65,536), but at least 1 bit is needed for noise, so the effective resolution is  $2^{15}$  (32,768). A mid-infrared spectrum that has a bandpass of  $3600\text{ cm}^{-1}$  ( $4000$  to  $400\text{ cm}^{-1}$ ) and is recorded at a resolution of  $4\text{ cm}^{-1}$ , has 900 resolution elements ( $3600/4$ ). If the spectrum is assumed to have the same intensity at all wavenumbers, the dynamic range of the interferogram can be approximated by the square root of the number of resolution elements ( $M^{1/2}$ ) multiplied by the dynamic range of the spectrum. Thus, the dynamic range of the spectrum is the resolution of the ADC ( $\sim 30,000$ ) divided by  $M^{1/2}$  (30),

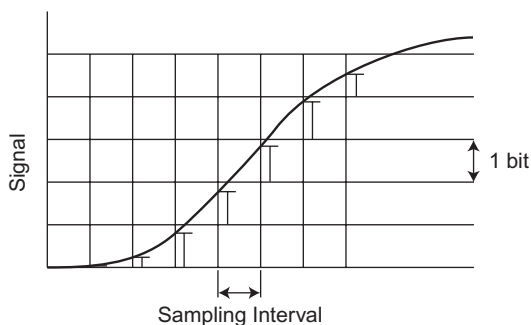


**Figure 3.6.** Effect of poor digitization accuracy. The difference between the actual and sampled signals is shown for each data point. This error can be considered to be approximately equivalent to peak-to-peak detector noise of  $\frac{1}{2}$  bit.

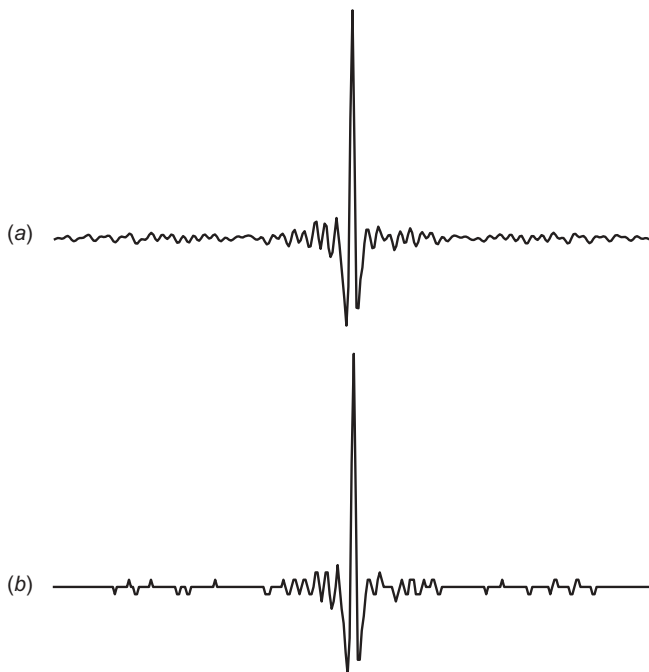


**Figure 3.7.** (a) Interferogram of polystyrene with a 16-bit ADC; (b) interferogram of the same sample with a 6-bit ADC.

or 1000:1. Interferograms measured on some commercial Fourier transform spectrometers can exceed this spectral dynamic range; hence, a 16-bit ADC may not be adequate to record the spectrum.

The effect of grossly insufficient resolution of an ADC can be fairly easily understood by comparing the same interferogram measured with a 16- and a 6-bit ADC. These interferograms are shown in Figure 3.7*a* and *b*. It can easily be seen that most of the later points in the interferogram have a value of zero. The only data points that influence the spectrum are those at low retardation, thus explaining the decreased resolution of spectra measured with an ADC of low dynamic range. Because the spectrum is measured at such low resolution, the band intensity is also reduced (see Section 8.2).

### 3.3.2. Digitization Noise

Even when a pyroelectric bolometer (such as DTGS) is used for these measurements, the dynamic range of an interferogram from an incandescent source measured using a single scan of a rapid-scanning interferometer sometimes does not allow weak spectral features to be seen. For instance, for a spectrum with  $\Delta\tilde{\nu} = 2\text{ cm}^{-1}$  and  $\tilde{\nu}_{\text{max}} = 4000\text{ cm}^{-1}$  measured with a single scan and digitized with a 16-bit ADC, any feature in this spectrum absorbing less than 0.1% of the

radiation would be missed. To improve the SNR achievable in the interferogram, signal-averaging techniques must be used.

If the noise level in any waveform is much smaller than the least significant bit of the ADC, signal averaging will not improve the SNR of the signal-averaged waveform over the single-scan case, since the same value of any point will be measured for each scan. This leads to the odd situation that it is conceivably possible to obtain a greater spectral SNR ultimately from an interferogram of small dynamic range than from one of high dynamic range. It has been suggested that *noise injection*, the addition of noise with a limited bandwidth, or a single incoherent sinusoidal wave outside the frequency range of interest but below the folding frequency, can be added to the interferogram [3]. This raises the instantaneous signal so that it will be digitized accurately, and signal averaging will allow the true value to be approached (Figure 3.8). The band of noise frequencies must be outside the range of modulation frequencies imposed by the interferometer. Remembering that the highest Fourier frequency in the interferogram is  $2V_{\text{max}}$  (see Section 2.2), it is apparent that the lowest frequency in the band of injected noise must be greater

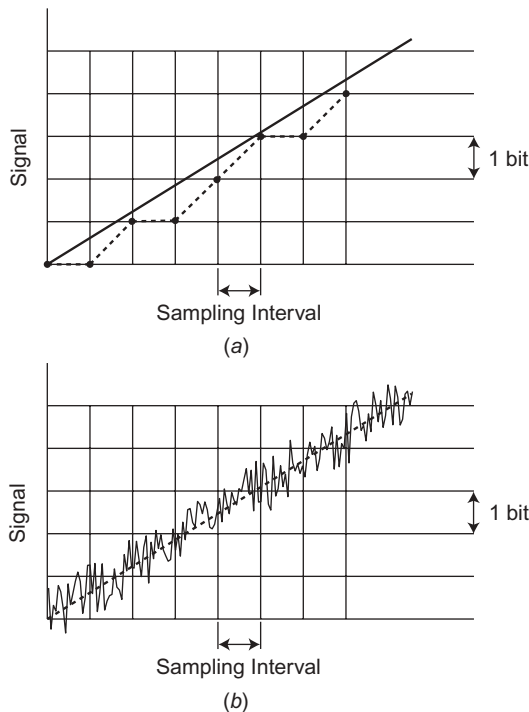


**Figure 3.8.** Effect of digitizing a signal with an ADC of limited dynamic range for signal-averaging systems. For a noise-free signal [solid line in (a)], the same value of the signal is measured each scan, and the apparent signal after one scan or many signal-averaged scans is the same (dashed line). If the peak-to-peak noise level is greater than the least significant bit [solid line in (b)], signal averaging is successful and the final signal (dashed line) is a much closer approximation of the true values than if no noise were present.

than this frequency. The highest frequency in the noise band should be less than the Nyquist frequency (i.e., one-half of the sampling frequency).

Alternatively, noise could be injected between 0 and  $2V\tilde{\nu}_{\min}$  if there is a large enough frequency band to permit this to be achieved. One way that has been proposed of injecting noise into the interferogram is through the leakage of 60-Hz line frequency into the signal. For mid-infrared measurements using KBr optics ( $\tilde{\nu}_{\min} = 400 \text{ cm}^{-1}$ ) with a rapid-scanning interferometer having a mirror velocity of  $1.6 \text{ mm s}^{-1}$ ,  $2V\tilde{\nu}_{\min} = 128 \text{ Hz}$ ; therefore, the 60-Hz line frequency would fall in an ideal region provided that higher harmonics are not present. When achieved successfully, noise injection has the effect of randomly changing the least significant bit of the ADC without reducing the SNR of the spectrum between  $\tilde{\nu}_{\min}$  and  $\tilde{\nu}_{\max}$ . This technique is incorporated in at least one commercial FT-IR spectrometer.

### 3.3.3. Gain Ranging

A technique that is now used almost universally with sample-and-hold ADCs to increase the dynamic range of the interferogram is the use of a *gain-ranging amplifier*, where the gain is switched in the time interval between two adjacent sample points that are a certain distance either side of zero retardation by a factor  $g$ , where  $g = 2^N$  and  $N$  is an integer; thus,  $g = 2, 4, 8$ , etc. (Figure 3.9). In the simplest gain-ranging amplifiers, the gain is switched once on either side of the centerburst, and the wings of the interferogram are typically amplified by a factor of 8 more than the region around the centerburst. In this way, the region of low dynamic range away

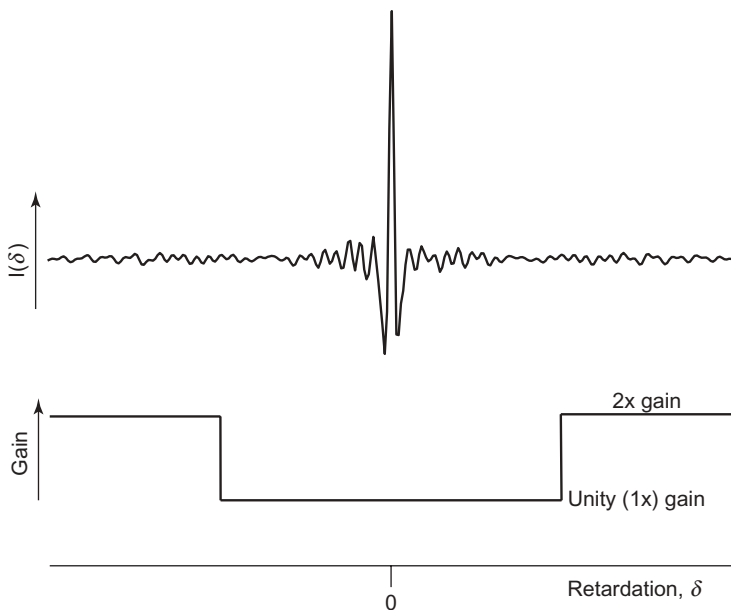


**Figure 3.9.** Action of a gain-ranging amplifier.

from zero retardation can be amplified and therefore sampled more accurately than if such an amplifier were not used [4].

Although the SNR of the interferogram may be larger than the dynamic range of the ADC in the small region around the centerburst, the much wider region outside the centerburst, which is important for the detection of weak narrow bands, is sampled adequately. After the desired number of co-added interferograms have been measured in this way, all data points in the wings of the interferogram (outside the gain-ranging *radius*) are divided by  $g$  in order that the entire interferogram is converted to the same effective gain before the Fourier transform. This procedure increases the dynamic range of the ADC by almost  $N$  bits, with a corresponding increase in the SNR of the spectrum.

Hirschfeld [5] suggested that an even better way to apply the concept of gain ranging is to use a series of steps approximating the envelope of the interferogram. He showed that when gain ranging is applied in this manner, the improvement in gain ranging over the case when no gain ranging is applied is

$$\frac{\text{SNR}_{\text{GR}}}{\text{SNR}} = \sqrt{2} \left[ \int (\log_2 g) + 1 \right] \quad (3.8)$$

This multistep approach is being used in several commercial FT-IR spectrometers. Only with efficient gain ranging can the SNR of FT-IR spectra measured with a pyroelectric detector and 16-bit ADC come close to the theoretical value.

### 3.3.4. Chirping

In all the interferograms discussed to date, there is a very large signal at one point (zero retardation) since each wavelength is in phase (or very close to it) at this point. It is possible to modify the interferogram such that each wavelength has its own origin, thus avoiding the large central fringes that normally occur. This distribution of interferogram origins may be accomplished by placing a flat optical element into the beam in the interferometer between the fixed mirror and the beamsplitter [6]. Since the refractive index of all materials varies with wavelength to a greater or lesser extent, as shown in Figure 3.10, the zero-phase difference point for each wavelength will be different. Figure 3.11 illustrates the effect on the interferogram of placing an optical element in one beam of the interferometer, yet the spectrum can be recovered completely [7]. The same effect can be accomplished by constructing the beamsplitter either so that the thicknesses of the substrate and compensator plates (see Section 5.7) are different or that these plates are made from different materials. In either case, there is no single path difference at which all wavelengths are in phase to produce a central fringe, so that the dynamic range is reduced while Fellgett's advantage (Section 7.5.1) is retained. Whereas at one time chirping seemed to be a promising way of keeping the dynamic range of the digitizer as low as possible, the only time that chirping has been applied beneficially is for satellite-borne interferometers from which data must be telemetered to Earth. Furthermore, apodization of chirped interferograms

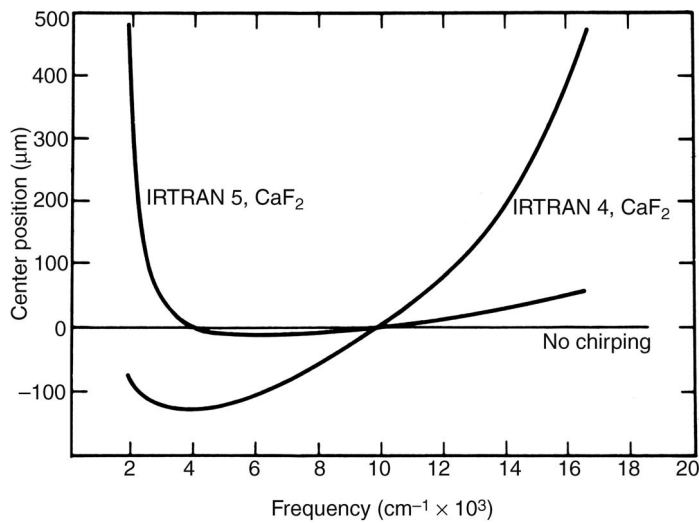


**Figure 3.10.** Dispersion of the zero-path-difference location for two possible chirping configurations. (Reproduced from [6], by permission of the author.)

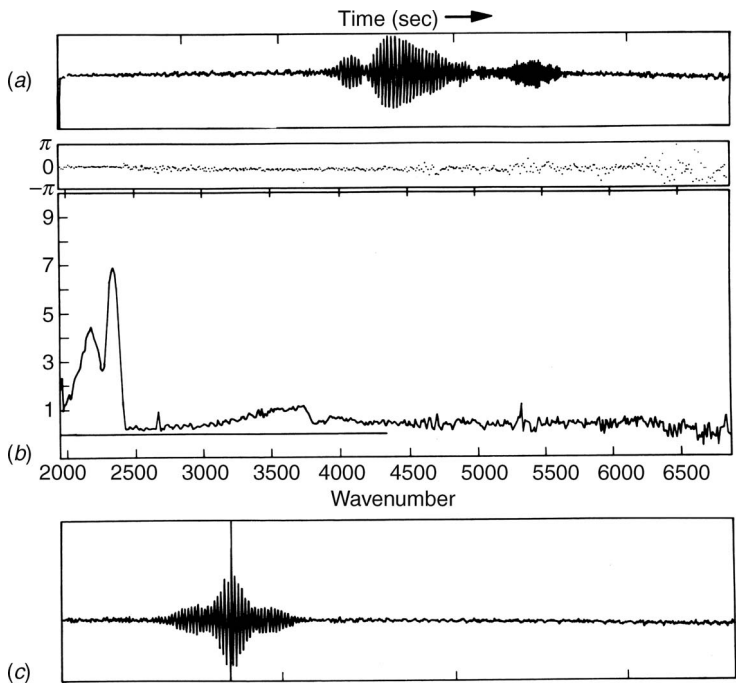


**Figure 3.11.** (a) Chirped interferogram; (b) phase-corrected spectrum of the source calculated from this interferogram; (c) almost completely unchirped interferogram reconstructed from this spectrum. (Reproduced from [7], by permission of the Society for Applied Spectroscopy; copyright © 1974.)

requires two-dimensional functions; that is, apodization becomes a function of retardation and wavelength, which unnecessarily complicates the operation [3].

### 3.4. ANALOG-TO-DIGITAL CONVERTERS

Since the early days of FT-IR spectrometry, instruments have used standard sample-and-hold analog-to-digital converters. Sample-and-hold ADCs are somewhat limited in their ability to digitize data. It becomes prohibitively costly to produce sample-and-hold ADCs with both an increased number of bits, or quantization levels, and a high sampling frequency. Sample-and-hold ADCs digitize a signal by successive approximation. As discussed above, the interferogram is sampled at the zero crossings of the laser interferogram. When the laser interferogram reaches the appropriate value (zero), a signal is sent to the ADC and the voltage of the interferogram at that instant is stored in the ADC; that is, it is sampled and held. The ADC operation works by successive approximation circuitry to digitize the voltage value. Basically, this is a “binary chop” approximation. A test voltage is set to the midpoint of the allowed voltage range. A determination is made to determine if the captured voltage is above or below the test value. If it is above the test value, for example, a new test voltage is set midway between the old test voltage and the maximum voltage. The test is repeated and a determination is made as to whether the held voltage is above or below the new test point. Once that determination is made, a new test voltage is set midway between the former test voltage and the limit of the former interval. At each step the interval is decreased by one-half, and a test is undertaken to determine if the held voltage is above or below the test point. In a small number of steps any voltage can be determined within the resolution of the ADC.

Fast sample-and-hold ADCs are expensive to produce, because as the digitization rate increases, the operations have to be completed more rapidly. As the number of bits increases, more operations have to be done in the time before a new voltage is captured. Nonetheless, many instrument vendors continue to use sample-and-hold ADCs in their instruments. The technology is extremely reliable and very well understood. Sample-and-hold ADCs are appropriate for fast detectors such as mercury cadmium telluride bolometers, provided that a sampling rate of greater than 400 kHz is not needed.

Some vendors, however, have taken advantage of a newer, less costly technology developed for the video and audio industries. The explosion of inexpensive devices for multimedia entertainment has required the development of digital-to-analog converters (DACs) to convert digital media to sound and visual output, and ADCs to record multimedia information on digital media. This problem has been solved with the use of *sigma-delta* ( $\Sigma$ - $\Delta$ ) ADCs. *Sigma-delta* refers to the method of operation, specifically, a summation-comparison methodology. Brault [8] was the first to report the use of a  $\Sigma$ - $\Delta$  ADC in an FT-IR spectrometer.

A  $\Sigma$ - $\Delta$  ADC is essentially a 1-bit converter. It is the manner in which this 1-bit converter is used that makes these devices sufficiently fast and still allow digitization with a large number of quantization levels (bits). The  $\Sigma$ - $\Delta$  ADC is basically



composed of a modulator and a digital filter. The modulator is simply a difference amplifier, an integrator, and a comparator, which is the 1-bit ADC. An input signal is continuously fed into the difference amplifier and the output is sent to an integrator. The integrated signal is sent to a comparator that compares the integrated signal to a reference voltage. The output from the comparator is simply a high (“1”) or low (“0”) signal. This output is fed to the digital filter as well as back to the difference amplifier through a switch that indicates whether the signal was high or low (this switch is in effect a 1-bit DAC). The level of the voltage from the feedback DAC indicates whether the signal being fed into the ADC is higher or lower than what was registered from the comparator. Basically, the feedback loop tells if the input signal is larger or smaller than the feedback voltage. If it is larger, the modulator put out a series of 1’s (bigger input voltage); if it is smaller, it puts out more 0’s (smaller input voltage). The stream of data bits comprises a computer word indicative of the magnitude of the signal.

One of the major differences of the  $\Sigma$ - $\Delta$  ADC over sample-and-hold technology is that there is no event-related triggering of the data.  $\Sigma$ - $\Delta$  ADCs can operate in the megahertz range and complete 1-bit digitizations at that rate, although most  $\Sigma$ - $\Delta$  ADCs that are used for FT-IR spectroscopy operate at a rate of less than 200 kHz. The device is regulated (or essentially triggered) by a clock that maintains a constant sampling rate. The input voltage is constantly fed into the ADC and it is sampled at the clock rate, not at the zero crossings of the laser interferogram. As no perfect correlation between the frequency of the laser interferogram and an independent ADC clock can be guaranteed,  $\Sigma$ - $\Delta$  ADCs are sampled at a much higher frequency than is necessary for sample-and-hold devices. The data can be reduced to the standard laser modulation frequency computationally.

Oversampling, sampling the  $\Sigma$ - $\Delta$  ADC much faster than necessary, is actually inherent to the high performance of these devices. All ADCs have an inherent noise associated with the digitization process. It is a result of the quantization of the signal (i.e., it is measured in discrete steps); hence, there is an error between the true analog value and the measured digitized value. As the quantization levels are small, noise causes the measured values to fluctuate between different quantization levels as discussed in Section 3.3. Fortunately, the digitization noise is independent of the sampling frequency or the signal level; hence, the noise is distributed across the bandpass of the entire signal. If the bandpass of the signal is increased by raising the Nyquist frequency, the noise is evenly distributed across the entire bandpass, and the noise at any given frequency is lower. Part of the function of  $\Sigma$ - $\Delta$  ADC is to “shape” the noise with the integrator and digital filter that follow the modulator. Noise-shaping filters the data so that most of the noise is moved to higher frequencies. The real signal that is needed usually falls in the low-frequency region (e.g., 120 to 1200 Hz for a typical interferogram measured with a DTGS detector); if the noise is forced to a higher-frequency region (above 1200 Hz) the signal in the bandpass of interest is cleaner. This operation can be enhanced by the addition of more integrators and 1-bit feedback DACs in the modulator. At the time of this writing  $\Sigma$ - $\Delta$  ADCs are available with fifth-order comparators (five integrators and five feedback DACs) and have digitization levels of 24 bits. These ADCs are

capable of digitizing signals to full resolution at 192 kHz, although most operate at half this rate. The manufacturers claim that the ADCs have more than 21 effective bits; that is, fewer than 3 bits are consumed by noise. This is a considerable improvement over older sample-and-hold ADCs that are financially viable up to 16 bits; but quantization noise limits their range. As discussed above, gain-ranging increases the effective bit path, but typically to no more than 18 bits.

It is important that the infrared interferogram be sampled correctly with respect to the laser reference interferogram. If there were not an appropriate correlation between the two signals, one of the advantages of FT-IR spectrometry—the advantage in wavenumber precision that these instruments have over scanning monochromators, sometimes known as the *Connes advantage*—would be lost. Most  $\Sigma$ - $\Delta$  ADCs are made for the stereo industry, and consequently, they typically have two input channels (although some systems have up to eight input channels for “surround” sound). The laser signal is input to one channel and the interferogram is input to the other. As shown in Figure 3.12, both are digitized at the same rate and time by the ADC clock. The output signals are typically an order of magnitude

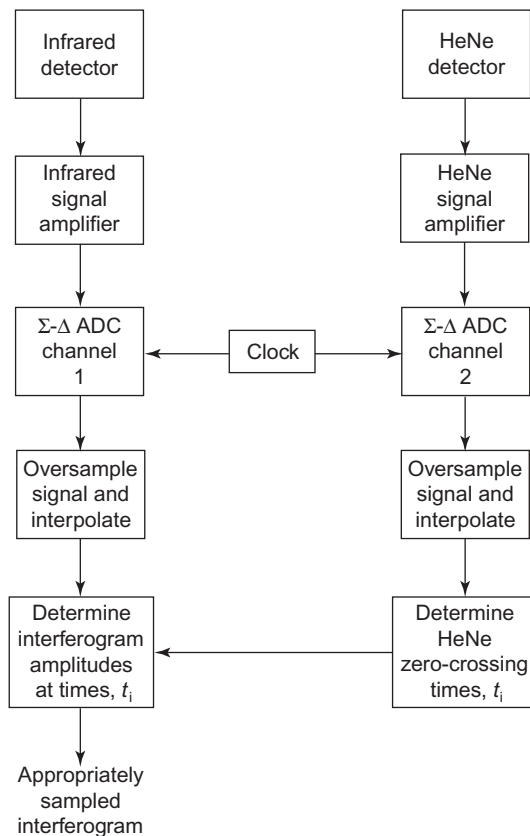


**Figure 3.12.**  $\Sigma$ - $\Delta$  ADC signal processing diagram for the laser and interferogram signals.

oversampled (a typical  $\Sigma$ - $\Delta$  ADC rate is 96 kHz). From the oversampled laser and interferogram signals, data can be extracted at the laser fringe zero crossings, and interpolation of both signals is undertaken if necessary to recover the data at exactly the correct retardation values. Technically, the interferogram can be digitized at any frequency as long as it is sampled consistent with the Nyquist criterion, so this operation may seem superfluous. Nonetheless, it must be remembered that the HeNe laser is a de facto wavelength standard, and most FT-IR spectrometers report spectra recorded on this scale. If a different sampling interval were used, it would be extremely difficult to compare spectra from one instrument to another, which is especially important for spectral subtraction and searching.

One last note about  $\Sigma$ - $\Delta$  ADCs is that the interpolation of the oversampled data really requires a specialized processor, usually in the form of a digital signal processor (DSP). These are processors originally developed for the telecommunications industry that can be programmed to execute a single task very rapidly. DSPs are being connected directly to  $\Sigma$ - $\Delta$  ADCs, and the entire apparatus may be mounted in the detector electronics. In this way the signal from the detector is digital, not analog, and hence the signal is not subject to electromagnetic radiative noise, which results in spectra with a reduced noise level when the SNR of the interferogram is very high.

Sigma-delta ADCs are not a universal panacea, as they still only acquire data no faster than 200 kHz. Although this appears to be fast, both the interferogram and the laser signal have to be oversampled by as much as an order of magnitude. Hence the actual digitization rate is equivalent to only 20 kHz for a sample-and-hold ADC. At the present time this limits the use of these high-bit ADCs to slower data acquisition rates.

## REFERENCES

1. H. Nyquist, *AIEE Trans.* **617**, 644 (1928).
2. A. S. Zachor, I. Coleman, and W. G. Mankin, Effects of drive nonlinearities in Fourier spectroscopy, in *Spectrometric Techniques*, G. A. Vanasse, Ed., Academic Press, New York, 1981, Vol. II, p. 128.
3. L. Mertz, *Transformations in Optics*, Wiley, New York, 1965.
4. T. Hirschfeld, Quantitative IR: a detailed look at the problems involved, in *Fourier Transform Infrared Spectroscopy*, J. R. Ferraro and L. J. Basile, Eds., Academic Press, New York, 1979, Vol. 2, p. 193.
5. T. Hirschfeld, *Appl. Spectrosc.* **33**, 525 (1979).
6. G. F. Hohnstreiter, T. P. Sheahan, and W. Howell, Michelson interferometer-spectrometer for on-board space vehicle measurements, in *Aspen International Conference on Fourier Spectroscopy, 1970*, G. A. Vanasse, A. T. Stair, Jr., and D. J. Baker, Eds., U.S. Air Force, L. G. Hanscom Field, Bedford, MA, 1971, Vol. AFCRL-71-0019, p. 243.
7. T. P. Sheahan, *Appl. Spectrosc.* **28**, 283 (1974).
8. J. W. Brault, *Appl. Opt.* **35**, 2891 (1996).

# FOURIER TRANSFORMS

## 4.1. CLASSICAL FOURIER TRANSFORM

### 4.1.1. Elementary Concepts

In Chapters 2 and 3 the various factors for the generation of an interferogram were discussed. In this chapter the techniques for computing the spectrum from this digitized interferogram are described.

Prior to 1966, spectroscopists who measured spectra interferometrically used the same basic algorithm for their computations. This involved the use of what is now known as the *classical, conventional, or discrete Fourier transform*. Although it is true that few people today use this algorithm in view of the substantial time advantages to be gained by use of the fast Fourier transform technique (described in Section 4.2), an understanding of the conventional Fourier transform leads to a better comprehension of more advanced techniques.

The concept of the classical Fourier transform is fairly simple to understand. As an example, let us consider the case of a long-cosine-wave interferogram digitized at equal intervals. To perform the classical Fourier transform, we simply multiply each point by the corresponding point of an analyzing cosine wave of unit amplitude and add the resultant values. For each analyzing wave whose frequency is *different* from that of the cosinusoidal interferogram, the sum will be zero (i.e., the two waves are orthogonal). If the frequencies of the interferogram and the analyzing wave are the same, the resultant will be a large positive number, since at each point that the interferogram takes a positive value, the analyzing wave will also be positive, and vice versa. The magnitude of the sum will be proportional to the amplitude of the cosine wave interferogram.

For an analyzing wave whose frequency is very close to that of the monochromatic interferogram, it requires greater retardation for the resultant to take a zero value than for analyzing waves whose frequencies are well separated from that of the interferogram. In fact, if the frequency of the analyzing wave is gradually increased from that of the interferogram, it is not too difficult to visualize that the resultant will decrease from the large positive magnitude discussed in the

preceding paragraph, pass through zero to a negative value, and then oscillate between negative and positive values whose amplitude decreases as the frequency difference between the interferogram and analyzing wave increases. This oscillatory pattern is described mathematically by the sinc function shown in Figure 2.5b. The greater the retardation over which the interferogram is sampled, the higher is the frequency of this oscillation; that is, the narrower is the FWHH of the sinc function and the higher is the spectral resolution.

The way in which *phase errors* are introduced during the transform may also be understood conceptually from the example above. For example, if the sinusoidal interferogram was  $180^\circ$  out of phase with the analyzing cosine wave ( $\theta_v = \pi$  in Eq. 2.27), then at each retardation the interferogram has a positive value, the analyzing wave will be negative, and vice versa. Therefore, the product of the interferogram and analyzing wave will be negative for each data point, and the resultant will be equal in magnitude but opposite in sign to the case when  $\theta_v = 0$ . Obviously, correction for phase errors is important if photometrically accurate spectra are to be calculated.

#### 4.1.2. Mathematical Basis

Let us now consider the classical Fourier transform from a more mathematical basis by considering the case of a symmetrical interferogram that has been measured from the zero retardation point [1]. The integral

$$B(\tilde{\nu}) = \int_{-\infty}^{+\infty} S(\delta)A(\delta) \cos 2\pi\tilde{\nu}\delta d\delta \quad (4.1)$$

where  $A(\delta)$  represents any truncation or apodization function previously referred to as  $D(\delta)$  and  $A_1(\delta)$ ,  $A_2(\delta)$ , and so on (Section 2.4), can be written as

$$B(\tilde{\nu}) = 2 \int_0^{+\infty} S(\delta)A(\delta) \cos 2\pi\tilde{\nu}\delta d\delta \quad (4.2)$$

because of the symmetry of the interferogram about the point of zero retardation.

It was stated in Section 3.1 in the discussion of the Nyquist sampling criterion that if the signal were digitized with a small enough interval between data points, no information from the analog signal would be lost. The maximum sampling interval  $h$  is given by

$$2h = (\tilde{\nu}_{\max} - \tilde{\nu}_{\min})^{-1} \quad (4.3)$$

If the interferogram has been sampled correctly, we can replace the integral of Eq. 4.2 by a summation and calculate the intensity  $B'(\tilde{\nu}_1)$  at any wavenumber  $\tilde{\nu}_1$ . Let the retardation at any sampling point be given by  $n\tilde{h}$ , where  $n$  is an integer, and let

$S_a(n)$  be the value of the interferogram measured at this point:

$$B'(\tilde{\nu}_1) = S_a(0) + 2S_a(1) \cos 2\pi\tilde{\nu}_1 h + 2S_a(2) \cos 2\pi\tilde{\nu}_1 \cdot 2h \\ + \cdots + 2S_a(N-1) \cos 2\pi\tilde{\nu}_1 (N-1)h \quad (4.4)$$

where  $N$  is the total number of points sampled.

$$B'(\tilde{\nu}) = S_a(0) + 2 \sum_{k=1}^{N-1} S_a(k) \cos 2\pi\tilde{\nu}_1 kh \quad (4.5)$$

The summation in Eq. 4.5 is performed for all wavenumbers of interest in the spectrum. It need not, however, be carried out for all wavenumbers from  $\tilde{\nu}_{\max}$  to  $\tilde{\nu}_{\min}$ .

Even for fairly short spectral ranges, the computing time involved for this operation can be quite high, especially if each cosine term required is calculated from a series. Cosine tables can be stored in the computer memory, but this does not provide an adequate solution. It has been found that a successful method of circumventing this problem is by the use of recursion relationships, whereby a value for  $\cos 2\pi\tilde{\nu}_1 kh$  can be calculated from the value of  $\cos 2\pi\tilde{\nu}_1 h$ . In this way, only one cosine value has to be calculated for each spectral wavenumber. The Chebyshev recursion formula,

$$\cos(p+1)x = 2 \cos x \cos px - \cos(p-1)x \quad (4.6)$$

is the one used most frequently. It has been shown that if the cosines are calculated to six significant figures, the difference between the value computed by a series expansion and the values obtained from 12,000 iterations is less than 1 in 50,000. The first cosine,  $\cos 2\pi\tilde{\nu}_1 h$ , is computed with a series formula, and all the cosines that follow are computed with a recursion formula for each new value  $\tilde{\nu}_1$ . Each of the values of  $S_a(k) \cos 2\pi\tilde{\nu}_1 kh$  is added to the sum, and the resulting number is proportional to the value of  $B'(\tilde{\nu}_1)$ .

If a double-sided interferogram has been collected and the centerburst is near the middle of the interferogram, the summation in Eq. 4.5 may be replaced by the summation

$$|B'(\tilde{\nu}_1)| = \left\{ \left[ \sum_{k=-N/2}^{(N/2)-1} S_a(k) \cos 2\pi\tilde{\nu}_1 kh \right]^2 + \left[ \sum_{k=-N/2}^{(N/2)-1} S_a(k) \sin 2\pi\tilde{\nu}_1 kh \right]^2 \right\}^{1/2} \quad (4.7)$$

The sine values are calculated with the use of another recursion formula also attributed to Chebyshev:

$$\sin(p+1)x = 2 \sin px \cos x - \sin(p-1)x \quad (4.8)$$

The summation of Eq. 4.7 produces the *magnitude* spectrum of  $B'(\tilde{\nu}_1)$ , denoted  $B(\tilde{\nu}_1)$ . The magnitude spectrum will exhibit no phase error, but the effect of noise on the spectrum is nonlinear, as all noise will be positive and increases as the signal decreases.

If there are  $N$  points in the interferogram, let us consider how many operations are required during the computation of a single-sided cosine transform. For each spectral point  $\tilde{\nu}_j$ , we perform  $N$  multiplications for  $S_a(k) \cos 2\pi\tilde{\nu}_j kh$ . To add the values, we must do  $N - 1$  additions, so that a total of  $2N$  operations is needed for each wavenumber  $\tilde{\nu}_j$ . To examine the complete spectrum, we must compute the spectrum at  $\frac{1}{2}N$  wavenumber values at least. Thus, a total of approximately  $N^2$  operations are needed for the conventional Fourier transform, not counting the time required to compute the cosine value.

If the double-sided complex transform is performed, the number of operations increases. For each value of  $\tilde{\nu}_j$ , we now perform  $N$  multiplications for  $S_a(k) \cos 2\pi\tilde{\nu}_j kh$ , and  $N$  multiplications are required for  $S_a(k) \sin 2\pi\tilde{\nu}_j kh$ . Then  $N - 1$  additions must be made for the cosine transform and  $N - 1$  for the sine transform, so a total of approximately  $4N$  operations must be made for each wavenumber. If the full bandwidth of the spectrum is to be examined at the same resolution as the single-sided spectrum, twice as many data points must be taken so the number of operations is increased to  $8N$ . The number of output points is the same as for the single-sided case, so that  $4N^2$  operations are required. This number does not include the time required for the cosine, sine, square, and square root calculations required for each value of  $\tilde{\nu}_j$ .

As the number of points to be calculated increases beyond about 10,000, the calculation time for a spectrum can become prohibitive, even for very fast present-day computers, for which that computation can take many hours. Prior to the development of fast, readily available computers, this problem was especially annoying and did not appear to be resolvable until about 1966. At that time, Forman [2] published a paper on the application of the fast Fourier transform technique to Fourier spectrometry. This technique had been described in the literature by Cooley and Tukey [3] one year earlier. This algorithm extended the use of Fourier transform spectrometry to encompass high-resolution data in all regions of the infrared spectrum. It is described in the next section.

## 4.2. FAST FOURIER TRANSFORM

The fast Fourier transform (FFT) is an algorithm that was described by Cooley and Tukey [3] in which the number of necessary computations is drastically reduced when compared to the classical Fourier transform. To understand the algorithm, the interferogram and the spectrum should be regarded as the complex pair [4]

$$S(\delta) = \int_{-\infty}^{+\infty} B(\tilde{\nu}) e^{i2\pi\tilde{\nu}\delta} d\tilde{\nu} \quad (4.9)$$

$$B(\tilde{\nu}) = \int_{-\infty}^{+\infty} S(\delta) e^{-i2\pi\tilde{\nu}\delta} d\delta \quad (4.10)$$

where Eq. 4.9 is the complex inverse Fourier transform of the spectrum to produce the interferogram. This is an alternative form of Eq. 2.27.

The point of departure for the FFT from the continuous Fourier transform is the discrete Fourier transform (DFT). The DFT of an interferogram of  $N$  points to produce a spectrum of  $N$  points may be written as<sup>1</sup>

$$B(r) = \sum_{k=0}^{N-1} S_0(k) e^{-i2\pi rk/N} \quad r = 1, 2, \dots, N-1 \quad (4.11)$$

where  $B(r)$  is the spectrum expressed at discrete wavenumbers  $r$ . Let us define a parameter  $W$  such that

$$W = e^{-i2\pi/N} \quad (4.12)$$

Upon substitution of this value of  $W$  in Eq. 4.11, we obtain

$$B(r) = \sum_{k=0}^{N-1} S_0(k) W^{rk} \quad (4.13)$$

From this equation it can be seen that each discrete value of  $B(r)$  requires  $N$  complex multiplications and  $N-1$  complex additions. Since there are  $N$  terms of  $B(r)$ ,  $N^2$  complex multiplications are required, as stated in Section 4.1. The FFT is based on the idea that Eq. 4.13 can be expressed in general matrix form, and that matrix can be factored in a manner that will reduce the overall number of computations.

The Cooley–Tukey algorithm is general and can be applied to any Fourier transform, but the computation is greatly simplified if  $N$  is a base 2 number, that is,  $N = 2^\alpha$ , where  $\alpha$  is a positive integer. The factorization procedure may be demonstrated easily for the case when  $N = 4 = 2^2$ . In this example, Eq. 4.13 becomes

$$B(r) = \sum_{k=0}^3 S_0(k) W^{rk} \quad r = 0, 1, 2, 3 \quad (4.14)$$

which may be expressed more fully as

$$\begin{aligned} B(0) &= S_0(0)W^0 + S_0(1)W^0 + S_0(2)W^0 + S_0(3)W^0 \\ B(1) &= S_0(0)W^0 + S_0(1)W^1 + S_0(2)W^2 + S_0(3)W^3 \\ B(2) &= S_0(0)W^0 + S_0(1)W^2 + S_0(2)W^4 + S_0(3)W^6 \\ B(3) &= S_0(0)W^0 + S_0(1)W^3 + S_0(2)W^6 + S_0(3)W^9 \end{aligned} \quad (4.15)$$

<sup>1</sup>This equation is identical to Eq. 4.5 if  $h = 1/N$ .



The set of equations 4.15 may be expressed as a matrix multiplication:

$$\begin{vmatrix} B(0) \\ B(1) \\ B(2) \\ B(3) \end{vmatrix} = \begin{vmatrix} W^0 & W^0 & W^0 & W^0 \\ W^0 & W^1 & W^2 & W^3 \\ W^0 & W^2 & W^3 & W^6 \\ W^0 & W^3 & W^6 & W^9 \end{vmatrix} \begin{vmatrix} S_0(0) \\ S_0(1) \\ S_0(2) \\ S_0(3) \end{vmatrix} \quad (4.16)$$

or, more compactly,

$$\mathbf{B}(r) = \mathbf{W}^{rk} \mathbf{S}_0(k) \quad (4.17)$$

Several simplifications can be applied immediately to reduce the number of computations. Most obviously, knowing that  $W^0 = 1$  saves computation of seven exponentials. Two other simplifications, which are less obvious, are based on the cyclic nature of the exponential term  $W$  ( $W$  is an exponential function of  $2\pi$ ). First,

$$W^M = W^{\text{mod}(M,N)} \quad (4.18)$$

where  $\text{mod}(M,N)$  is the integer function equal to  $M - (M/N)N$ . Recall that in integer arithmetic  $M/N$  produces a truncated quotient, so the mod function calculates the remainder after division. The proof of Eq. 4.18 is straightforward. If  $M = nN + k$ , where  $M$ ,  $n$ ,  $N$ , and  $k$  are all integers, then

$$\begin{aligned} W^M &= e^{-i2\pi M/N} = e^{-i2\pi(nN+k)/N} \\ &= e^{-i2\pi k/N} e^{-i2\pi n} = e^{-i2\pi k/N} \\ &= W^{\text{mod}(M,N)} \end{aligned}$$

Therefore, Eq. 4.16 may be further reduced by substituting  $W^{\text{mod}(rk,N)}$  for  $W^{rk}$ ; thus,

$$\begin{vmatrix} B(0) \\ B(1) \\ B(2) \\ B(3) \end{vmatrix} = \begin{vmatrix} 1 & 1 & 1 & 1 \\ 1 & W^1 & W^2 & W^3 \\ 1 & W^2 & W^0 & W^2 \\ 1 & W^3 & W^2 & W^1 \end{vmatrix} \begin{vmatrix} S_0(0) \\ S_0(1) \\ S_0(2) \\ S_0(3) \end{vmatrix} \quad (4.19)$$

The second cyclic property of  $W$  is

$$\begin{aligned} W^{k+N/2} &= e^{-i2\pi(k+N/2)/N} \\ &= e^{-i2\pi k/N} e^{-i\pi} = -e^{-i2\pi k/N} \\ &= -W^k \end{aligned} \quad (4.20)$$

Thus, Eq. 4.19 may be reduced further by substituting  $-W^1$  for  $W^3$  and  $-W^0 (= -1)$  for  $W^2$ . Although the DFT can be greatly simplified by these substitutions and only  $\frac{1}{2}N$  complex terms need to be calculated, the DFT still requires  $N^2$  multiplications for the complete calculation of  $B(r)$ .

If we consider Eq. 4.14, we see that both  $k$  and  $r$  can be represented as binary numbers, specifically 2-bit binary numbers. For  $N = 4$ ,

$$\begin{aligned} k = 0, 1, 2, 3 \text{ (decimal)} & \quad \text{or} \quad k = (k_1, k_0) = 00, 01, 10, 11 \text{ (binary)} \\ r = 0, 1, 2, 3 \text{ (decimal)} & \quad \text{or} \quad r = (r_1, r_0) = 00, 01, 10, 11 \text{ (binary)} \end{aligned}$$

Thus,

$$k = 2k_1 + k_0 \quad \text{and} \quad r = 2r_1 + r_0$$

where  $k$  and  $r$  are the base 10 representations of the two numbers. With  $k$  and  $r$  expressed as binary numbers, Eq. 4.14 can be rewritten

$$B(r_1, r_0) = \sum_{k_0=0}^1 \sum_{k_1=0}^1 S_0(k_1, k_0) W^{(2r_1+r_0)(2k_1+k_0)} \quad (4.21)$$

When Eq. 4.14 is rewritten, it must contain a summation sign for each bit in the binary number. The FFT is based on factorization of the DFT, but the exponential term  $W$  is not as yet in the appropriate form; thus,

$$\begin{aligned} W^{(2r_1+r_0)(2k_1+k_0)} &= W^{(2r_1+r_0)2k_1} W^{(2r_1+r_0)k_0} \\ &= W^{4r_1k_1} W^{2r_0k_1} W^{(2r_1+r_0)k_0} \\ &= W^{2r_0k_1} W^{(2r_1+r_0)k_0} \end{aligned} \quad (4.22)$$

Equation 4.21 can be written

$$B(r_1, r_0) = \sum_{k_0=0}^1 \sum_{k_1=0}^1 S_0(k_1, k_0) W^{2r_0k_1} W^{(2r_1+r_0)k_0} \quad (4.23)$$

At this point, the DFT has been factorized into the FFT form. To effect the FFT, it is necessary only to calculate each summation individually. The inside summation is evaluated first, and the result is used to calculate the outside summation. The inside summation is

$$S_1(r_0, k_0) = \sum_{k_1=0}^1 S_0(k_1, k_0) W^{2r_0k_1} \quad (4.24)$$

which may be expanded to

$$\begin{aligned}
 S_1(0,0) &= S_0(0,0) + S_0(1,0)W^0 \\
 S_1(0,1) &= S_0(0,1) + S_0(1,1)W^0 \\
 S_1(1,0) &= S_0(0,0) + S_0(1,0)W^2 \\
 S_1(1,1) &= S_0(0,1) + S_0(1,1)W^2
 \end{aligned} \tag{4.25}$$

Based on the cyclic properties of  $W$  as explained above (see Eq. 4.20),  $S_1(0,0)$  and  $S_1(1,0)$  may be calculated simultaneously as

$$\begin{aligned}
 S_1(1,0) &= S_0(0,0) + S_0(1,0)W^2 \\
 &= S_0(0,0) - S_0(1,0)W^0
 \end{aligned} \tag{4.26}$$

Equation 4.25 shows that  $S_1(1,0)$  differs from  $S_1(0,0)$  only by the sign of the second term. Thus, for  $S_1(0,0)$  an addition is performed, and for  $S_1(1,0)$  a subtraction is performed. Figure 4.1a is a schematic shorthand notation for the summation in Eq. 4.24. The schematic is read by interpreting the symbols near the head and tail of the arrows. For example,  $S_1(0,1) = S_1(1_{10}) = S_0(1_{10}) + S_0(3_{10})W^0$ , where the subscript 10 indicates that the numbers are to the base 10. The  $S_1(1_{10})$  and  $S_1(3_{10})$  are linked by a dual-node-pair arrow, which indicates that they are calculated simultaneously, as all their terms are identical. This summation has required only one complex term to be calculated ( $W^0$ ) and two multiplications.

The outside summation uses the results of the inside summation, or  $S_1(r_0, k_0)$ ; then

$$S_2(r_0, r_1) = \sum_{k_0=0}^1 S_1(r_0, k_0) W^{(2r_1 + r_0)k_0} \tag{4.27}$$

Similar to Eq. 4.24, this summation can be enumerated:

$$\begin{aligned}
 S_2(0,0) &= S_1(0,0) + S_1(0,1)W^0 \\
 S_2(0,1) &= S_1(0,0) + S_1(0,1)W^2 \\
 S_2(1,0) &= S_1(1,0) + S_1(1,1)W^1 \\
 S_2(1,1) &= S_1(1,0) + S_1(1,1)W^3
 \end{aligned} \tag{4.28}$$

Figure 4.1b shows the schematic from Figure 4.1a with the computations from Eq. 4.27 added. Again only two complex multiplications in the second summation have been performed, which gives a total of four from the FFT algorithm as opposed to the  $16 N^2$  for the DFT. In general, the FFT requires only  $\frac{1}{2}N$  complex multiplications and  $N(N-1)$  complex additions. The ratio of DFT operations to

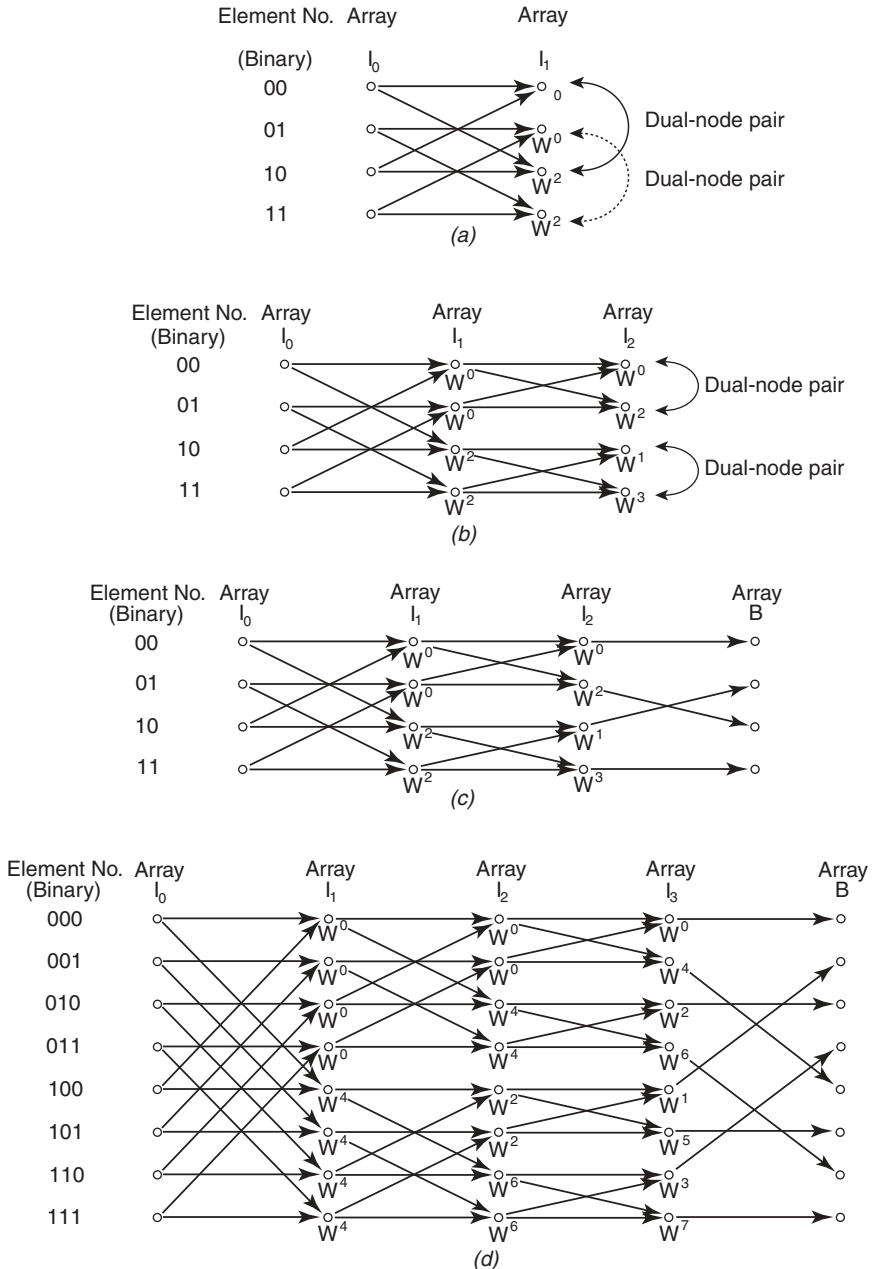


**Figure 4.1.** Schematic shorthand notation for the FFT procedure: (a) representation for Eq. 4.24 that is interpreted by the convention that the data point at the head of the arrows is the sum of the data at the tails of the arrows; a term  $W$  may be near one of the arrowheads and the data point at the tail of that arrow is multiplied by the  $W$  term prior to addition; (b) representation for Eqs. 4.24 and 4.27; (c) full schematic for a four-data-point FFT, including bit unscrambling; (d) eight-point FFT representation.

FFT operations can be attributed to the complex multiplications; hence,

$$\frac{N^2}{N\alpha/2} = \frac{2N}{\alpha} \quad (4.29)$$

Clearly, as  $N$  increases, the efficiency of the FFT increases dramatically.

The FFT does not end with the second summation in Eq. 4.27 for the case  $N = 4$ . The spectral datum  $B(r) = B(r_1, r_0)$  is not equal to  $S_2(r_0, r_1)$ . The only difference between the two data vectors is that the bits in the subscripted variables have been reversed; that is, the elements of  $B$  have the bits in the order  $r_1, r_0$ , whereas  $S_2$  has the bits in the order  $r_0, r_1$ . It is a simple matter to unscramble the bits to produce the desired result. Figure 4.1c shows the full schematic for the FFT of Eq. 4.14.

The general case, where  $N = 2^\alpha$ , requires that the DFT be factored into summations. The flow graph schematic for the FFT of an interferogram where  $N = 2^3 = 8$  is shown in Figure 4.1d. This flow graph illustrates that the FFT has more steps, but in the evaluation of each element of each array, only one complex multiplication and one complex addition are required.

It is interesting to note that there are several canonic forms of the FFT algorithm. If the original input data are scrambled according to the bit reversal algorithm, the spectrum can be computed in place. In a real sense, the procedure of the FFT is reversed, and the flow graph of this canonic form would begin with the dual-node pairs adjacent and end with the pairs  $\frac{1}{2}N$  elements apart. The results are identical, but the procedure varies. The latter canonic form has been used by Connes [5]. These two canonic forms of the Cooley–Tukey algorithm are termed *decimation in time* because some alternative derivations imply that the number of samples is reduced.

The other two canonic forms of the FFT algorithm are based on the Sande–Tukey algorithm [6]. This algorithm factors the DFT in  $r$  as opposed to  $k$ , leading to a *decimation in frequency* procedure. All four forms produce identical results and involve the same number of operations, although two of the forms (the Cooley–Tukey form with the input data scrambled, and the Sande–Tukey form with the input data in natural order) are computationally more efficient. The reason that these forms are more computationally efficient is that the  $W$  terms are calculated in order, and hence storage of those terms and the concomitant reading and writing to memory becomes unnecessary. In general, the FFT can be performed on any size array as long as the number of data points in the interferogram is an integer power of 2. Consequently, all commercial FT-IR instruments collect interferograms that are  $2^\alpha$  data points in length.

Advantage can be taken of the fact that interferograms are real functions and thus there is no imaginary input as the imaginary portion is zero. Computer space can be conserved through exploitation of this characteristic. Algorithms exist whereby a real input array of  $N$  points is Fourier transformed to give real and imaginary spectral domain arrays of  $\frac{1}{2}N$  points each. Because the spectral domain arrays are symmetric, all the information is present in one-half (or  $\frac{1}{2}N$  points) of

the array. A complex FFT requires  $2N$  data locations in computer memory, whereas a real function FFT requires only  $N$ . More important than the space saving, the number of operations in the FFT computation is reduced by approximately 2.

The FFT remains a very important algorithm, even with present-day computational hardware. A single low-resolution interferogram may be computed in a few seconds using the discrete Fourier transform, but computational times become unacceptable when higher-resolution interferograms are computed to spectra, or multiple interferograms are computed in succession. Still, advances have been made on computing hardware to speed data acquisition and reduce overhead on computations, and a brief discussion of these advances is presented in Section 4.5.

Appropriate transformation of interferograms to produce accurate spectra is not restricted to Fourier transform algorithms, and one of the additional procedures, phase correction, is presented in the following section.

### 4.3. PHASE CORRECTION

The sources of phase error have been presented in Section 2.5, where it was stated that the phase angle  $\theta_v$  is usually a function of wavenumber. It should also be noted that phase is a complex quantity; that is, it has real and imaginary parts.

When a recorded interferogram  $S(\delta)$  is transformed to produce a spectrum  $B'(\tilde{v})$ , a complex Fourier transform must be used unless the interferogram is symmetric. Hence, from Eq. 4.10,

$$B'(\tilde{v}) = \int_{-\infty}^{+\infty} S(\delta) e^{-i2\pi\tilde{v}\delta} d\delta \quad (4.30)$$

After transformation,  $B'(\tilde{v})$  is calculated by the complex addition

$$B'(\tilde{v}) = \text{Re}(\tilde{v}) + i \text{Im}(\tilde{v}) \quad (4.31)$$

where  $\text{Re}(\tilde{v})$  and  $\text{Im}(\tilde{v})$  are the real and imaginary parts of  $B'(\tilde{v})$ , respectively. If  $S(\delta)$  is symmetrically sampled (i.e., there is an equal number of points on both sides of the centerburst), we may calculate the magnitude spectrum of  $B'(\tilde{v})$ , which is denoted  $|B'(\tilde{v})|$ :

$$|B'(\tilde{v})| = \sqrt{\text{Re}(\tilde{v})^2 + \text{Im}(\tilde{v})^2} \quad (4.32)$$

The magnitude spectrum exhibits zero phase error but has noise nonlinearities. The magnitude (Eq. 4.32) and complex spectra (Eq. 4.31) are related by the phase angle  $\theta_v$ :

$$B'(\tilde{v}) = |B(\tilde{v})| e^{i\theta_v} \quad (4.33)$$

The complex spectrum  $B'(\tilde{\nu})$  contains all the spectral information, but it is dispersed into two complex planes by the phase. The magnitude spectrum  $|B(\tilde{\nu})|$  is a real (in the complex sense) representation of the spectrum, but it is only the absolute value of that representation. The true spectrum  $B(\tilde{\nu})$ , which is also real, lacks the noise nonlinearities of the magnitude spectrum. The object of phase correction is to produce the true spectrum  $B(\tilde{\nu})$ . Since  $\theta_{\tilde{\nu}}$  usually varies slowly with wavenumber, it is possible to factor  $e^{i\theta_{\tilde{\nu}}}$  from Eq. 4.33. In this case,

$$\begin{aligned} B(\tilde{\nu}) &= B'(\tilde{\nu})e^{-i\theta_{\tilde{\nu}}} \\ &= \text{Re}(\tilde{\nu})\cos \theta_{\tilde{\nu}} + \text{Im}(\tilde{\nu})\sin \theta_{\tilde{\nu}} \end{aligned} \quad (4.34)$$

When  $e^{i\theta_{\tilde{\nu}}}$  is transposed from one side to the other of Eq. 4.33, only the real terms are retained from the trigonometric expansion because the true and amplitude spectra are real functions. Equation 4.34 represents a phase correction algorithm for double-sided interferograms.

As was stated above, the phase angle is, in practice, a slowly varying function with wavenumber; therefore,  $\theta_{\tilde{\nu}}$  does not need to be measured to a high resolution. The phase angle may be adequately calculated from a short, symmetrically sampled interferogram and subsequently applied to a much higher resolution spectrum. Of course, when this is done, the phase angle spectrum must be interpolated to the same resolution as the amplitude spectrum from the whole interferogram. Equation 4.34 holds in this case. Therefore, an asymmetrically sampled interferogram can be collected as long as there is a short symmetrically sampled portion that will provide the phase angle. This method of phase correction was developed by Mertz [7,8]. Regardless, most modern instruments record double-sided interferograms and the entire symmetrically sampled interferogram is used for phase correction, at least when  $\Delta\tilde{\nu} \geq 1 \text{ cm}^{-1}$ . In general, it is better to use the entire double-sided interferogram for calculation of the phase, and this does not cost any additional computation time. The phase angle is calculated as:

$$\theta_{\tilde{\nu}} = \arctan \frac{\text{Im}(\tilde{\nu})}{\text{Re}(\tilde{\nu})} \quad (4.35)$$

where  $\text{Re}(\tilde{\nu})$  and  $\text{Im}(\tilde{\nu})$  are the real and imaginary parts of the complex transform, respectively. The complex Fourier transform (DFT or FFT) is performed on the entire interferogram after apodization (Section 2.4). Before the phase correction can be performed (Eq. 4.34), the phase angle spectrum  $\theta_{\tilde{\nu}}$  is interpolated, if necessary, to bring it to the same resolution as the resolution of the entire interferogram.

A second method of phase correction, which was developed by Forman et al. [9], is mathematically equivalent to the Mertz method but is performed in the interferogram domain. Recalling that a multiplication in one domain is a convolution in the other, phase correction may be accomplished by taking the inverse Fourier transforms of the two right-hand terms of Eq. 4.34 and convolving them to produce a

phase-corrected interferogram. The inverse Fourier transform of  $B'(\tilde{\nu})$ ,

$$J'(\delta) = \int_{-\infty}^{+\infty} B'(\tilde{\nu}) e^{i2\pi\tilde{\nu}\delta} d\tilde{\nu} \quad (4.36)$$

yields  $J'(\delta)$ , which is the recorded signal. Similarly,

$$\theta_{\delta} = \int_{-\infty}^{+\infty} e^{-i\theta\tilde{\nu}} e^{i2\pi\tilde{\nu}\delta} d\tilde{\nu} \quad (4.37)$$

where  $\theta_{\delta}$  is the complex Fourier transform of the phase angle spectrum. The two functions to be convolved (Section 2.3) may be of different dimensions; therefore, no interpolation of  $\theta_{\delta}$  is necessary. The phase-corrected interferogram,  $J(\delta)$ , is then

$$\begin{aligned} J(\delta) &= \int_{-\infty}^{+\infty} J'(\delta') \theta(\delta - \delta') d\delta' \\ &= J'(\delta) * \theta_{\delta} \end{aligned} \quad (4.38)$$

where  $*$  denotes convolution and  $\delta'$  is the displacement variable.

The phase-corrected interferogram is symmetric and is thus an even function. A complex Fourier transform is not necessary, and only a cosine Fourier transform need be used. Chase [10] has found, however, that the Mertz method is not as accurate as the Forman method, not because of the phase correction itself, but because it leads to artifacts if single-sided rather than double-sided interferograms are collected. If single-sided interferograms are recorded, the error in the Mertz method can be significant, as the error can be greater than 1% transmission, particularly in the vicinity of spectral bands. The Mertz method is by far the more computationally efficient of the two methods, due to the high computational requirements of a convolution.

An interesting aspect of the Forman method is the opportunity to include numerical filtering. Because  $\theta_{\tilde{\nu}}$  is a quotient,  $\theta_{\tilde{\nu}}$  is not defined where there is no signal and there is only noise. In these regions of no signal,  $\theta_{\tilde{\nu}}$  varies wildly because of the noise and no useful information can be obtained. Thus, by necessity the phase-angle spectrum must be zeroed outside the signal bandwidth. This amounts to truncation of the bandpass of both the phase-angle spectrum and the spectrum itself after convolution because the phase-angle bandpass is carried through the convolution. This property may be used to some advantage.

If a high-resolution spectrum is collected, the number of data points in the interferogram can be large ( $10^6$  is not uncommon). Undersampling (Section 3.2) may be used to examine a restricted spectral region, but appropriate optical filters, and possibly electronic filters, are required. Effective sampling can be achieved by numerical filtering. The entire interferogram is collected at the normal sampling interval



and the phase-angle spectrum is calculated. Rather than the inverse Fourier transform of the entire bandpass being computed, the bandpass of the phase-angle spectrum is restricted to the region of interest. The only stipulation is that the restricted bandpass is an integer fraction of the total bandpass. Convolution of the measured interferogram with the restricted bandpass complex Fourier transform of the phase angle produces a symmetric interferogram with an effective oversampling. If the restricted bandpass is one-sixtieth of the total bandpass, the effective oversampling is a factor of 60 and only every sixtieth data point need be retained during the collection of the interferogram, as the convolution is carried out in real time. The spectrum is calculated with a cosine Fourier transformation. A huge reduction in storage space and transform computation time is achieved and no electronic or optical filter is required. This method of data reduction has been described by Bell [11], and at least one commercial FT-IR spectrometer vendor implemented this technique at one time [12].

Phase correction may not always be possible. As stated above, the phase-angle spectrum is defined only where a signal exceeds the noise, which may not be the case for discrete emission spectra. In this instance, a double-sided interferogram must be collected and the magnitude spectrum computed. Discrete emission spectra are not commonly encountered in infrared spectrometry but occur in the ultraviolet-visible region for atomic emission spectrometry.

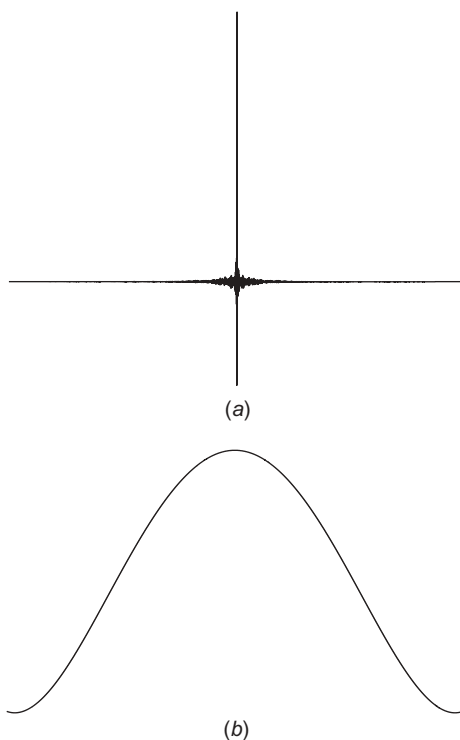
One final aspect of interferogram transformation is concerned with the choice of the origin of the interferogram. During computation it is common practice to shift the interferogram so that the first data point corresponds to the largest datum of the centerburst, and the points that preceded the centerburst are shifted to the end of the interferogram signal. Hence, the interferogram has maxima at the extrema and approaches zero in the center. This shift is performed after apodization, just before transformation. The reason for this shift is to reference the phase angle to the zero phase, that is, to the centerburst. A very thorough treatment of apodization and phase correction may be found elsewhere [13].

#### 4.4. FOURIER TRANSFORM: PICTORIAL ESSAY

The nuances of a practical computational technique are often not clear from a discussion of the theory. With this in mind, an example of the Fourier transformation of an interferogram into a spectrum is illustrated for each step of the procedure. Only the Mertz method is shown, as this is the method commonly in use in commercial instrumentation. There is little reason to use the Forman method unless numerical filtering is to be applied.

The Fourier transformation of an interferogram by the Mertz method is illustrated in Figure 4.2. Figure 4.2*a* is a double-sided interferogram of polystyrene. This interferogram is somewhat chirped so that some phase error can be expected upon direct transformation. The first step is to apply an apodization function, in this case the Norton–Beer medium function, which is shown in Figure 4.2*b*. After the arrays in Figure 4.2*a* and *b* are multiplied together, the data are shifted about the

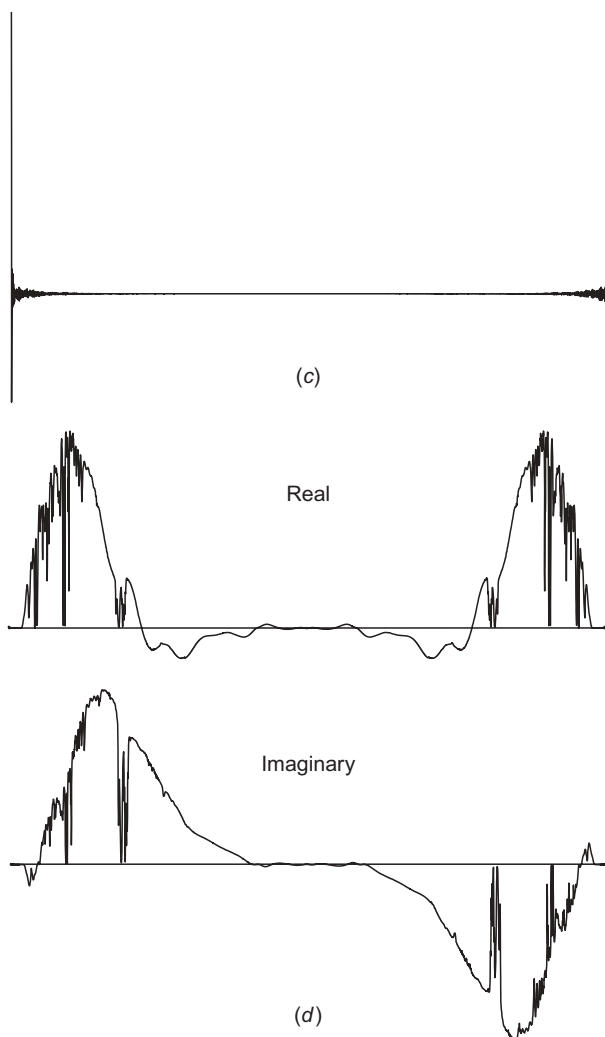
maximum value to reference the function as close to zero phase as possible (see Figure 4.2c). This double-sided interferogram is used to calculate the phase curve as well as the spectrum. Upon complex Fourier transformation of the function in Figure 4.2c, both the real and imaginary portions of the phase curve are produced, as the original interferogram has both cosine and sine components. The real and imaginary parts of the phase curve are shown in Figure 4.2d. In these curves, the central point is at the highest wavenumber of the bandpass ( $7900\text{ cm}^{-1}$  for this spectrum) whereas the two endpoints correspond to  $0\text{ cm}^{-1}$ . The actual phase curve (Figure 4.2e) is calculated using Eq. 4.35. The cosine and sine functions are calculated from the phase curve and are shown in Figure 4.2f. Only one-half of each curve of Figure 4.2f has been retained since each half is a mirror image of the other



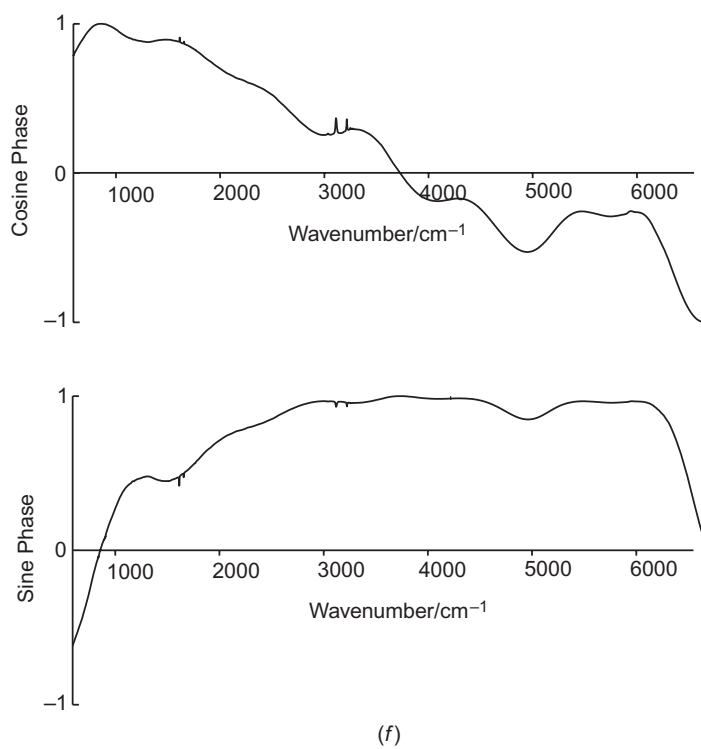
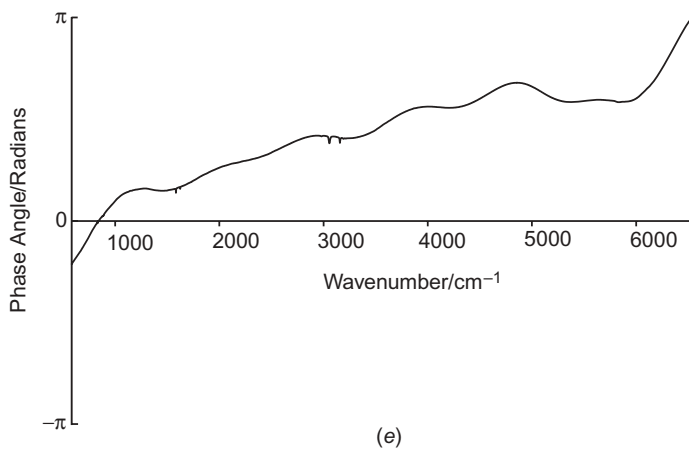
**Figure 4.2.** Pictorial essay of transformation and phase correction by the Mertz method: (a) double-sided interferogram of a polystyrene film; (b) Norton-Beer medium apodization function for the interferogram; (c) product of the interferogram in (a) with the apodization function in (b); the interferogram is shifted for zero phase; (d) real and imaginary portions of the complex FFT of the interferogram in (c); (e) phase curve calculated from the data in (d); (f) cosine and sine functions of the phase curve; (g) products of the curves in (d) and (f); the real spectrum is multiplied by the cosine phase curve and the imaginary spectrum is multiplied by the sine phase curve; (h) sum of the spectra in (g); (i) transmittance spectrum after the single-beam spectrum in (h) is ratioed against a single-beam reference spectrum. (*Continued*)

and no information is lost when one half is discarded. It should also be noted that the phase curve has a value of zero where the phase is not defined. These regions where the phase is not defined are those regions outside the spectral bandwidth, that is, at wavenumbers greater than approximately  $6400\text{ cm}^{-1}$  and less than  $450\text{ cm}^{-1}$  for mid-infrared measurements. The cosine- and sine-phase curves have been plotted only for the defined region  $450$  to  $6400\text{ cm}^{-1}$ .

The corresponding data in Figure 4.2*d* and *f* are multiplied together to produce the curves in Figure 4.2*g*. Addition of the real and imaginary parts (Figure 4.2*h*)



**Figure 4.2.** (continued)

**Figure 4.2.** (continued)

produces the single-beam phase-corrected spectrum. The results of Figure 4.2*g* and *h* come from the application of Eq. 4.34. A similar procedure is carried out with a reference interferogram (no sample in the infrared path), and the ratio of the two single-beam spectra is calculated to produce the phase-corrected transmittance spectrum (Figure 4.2*i*).

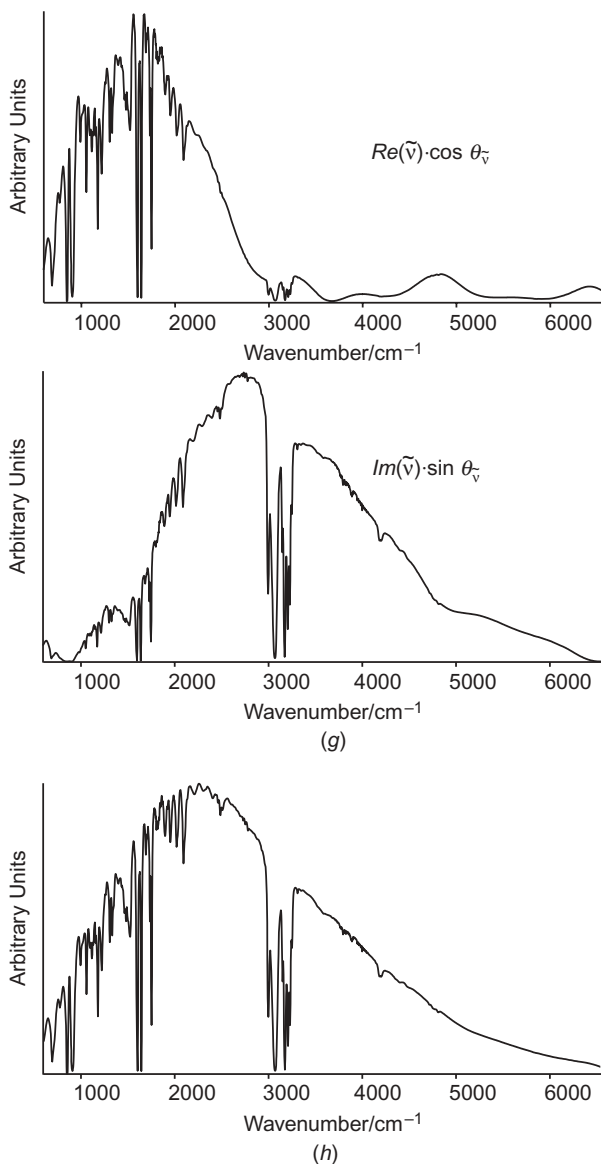


**Figure 4.2.** (continued)

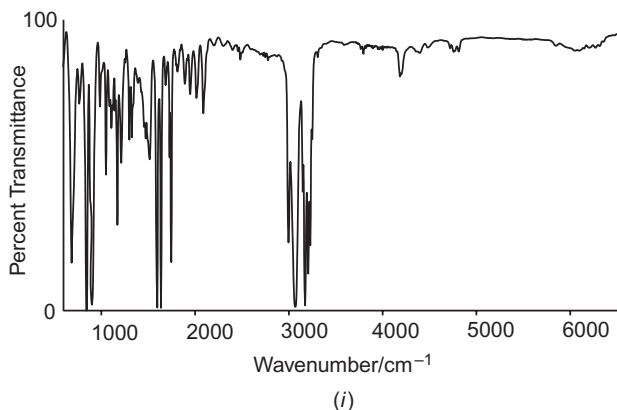


**Figure 4.2.** *(continued)*

#### 4.5. DATA SYSTEMS

Until the early 1990s most commercial FT-IR spectrometers had dedicated, proprietary computers. Personal computers (PCs) had been available for several years, and there was considerable pressure on the manufacturers of spectrometers to abandon the proprietary model and shift to the ubiquitous PCs. Most users of spectrometers did not realize that the decision to keep proprietary computer systems was not motivated by profit, but rather by necessity. In the early 1990s, PCs reached processor (CPU) speeds as high as 33 MHz, which was as fast as the proprietary computers. What was missed was that PCs were designed as business machines, and little allowance was made for real-time data acquisition. That is, the PC was not designed to collect large amounts of data directly from a spectrometer or any other scientific instrument. Although the PCs had good CPU speeds, the actual data bus remained rather slow, at about 5 MHz. Higher bus speeds were required, and for most applications the required speed was about 8 MHz. The proprietary computers had the same bus speeds as the CPU; that is, bus speeds were as high as 33 MHz. This meant that the data could be transferred from an instrument and into memory at a much faster rate than could be accomplished on a PC. The rate at which a spectrometer could collect data and send it to the computer easily exceeded the bus speed of a PC, particularly if an MCT detector were to be used and the scan velocity of the moving mirror was rather high.

Because of pressure from customers, manufacturers abandoned the proprietary computer and did move to PCs, but only when bus speeds approached 8 MHz. Early on, for some spectrometers, this necessitated specialized interface cards for the PCs that could buffer data from the spectrometer and supply it to the PCs at a rate that was acceptable to the PC. It should be noted, however, that this was of some benefit to the manufacturers, as the design of interface cards was considerably simpler and less expensive than the design of proprietary computers. It was not a panacea, however, and problems did arise. Not all PC manufacturers adhere to industry standards,

and various peripherals and programs can interfere with the operation of spectrometer interface cards. These interface cards may incorporate proprietary data transfer protocols or may rely on standard communications technologies, such as RS-232c serial communications or GPIB (IEEE-488) 8-bit parallel protocols.

As the technology for PCs progressed, the bus speed rose, and at the time of this writing has reached 1066 MHz for dual-core CPUs; single-core systems are limited to 800 MHz. This made the specifications on interface cards less stringent, and newer technologies, such as the universal serial bus (USB), have made it possible to eliminate the interface card entirely for some models of spectrometers. Although early USB devices (USB 1.1) typically operated at  $12 \text{ Mbits} \cdot \text{s}^{-1}$ , USB 2.0 has increased the data transfer rates to  $480 \text{ Mbits} \cdot \text{s}^{-1}$ . Some instrument manufacturers, but not FT-IR spectrometer manufacturers at the time of this writing, have used Ethernet connections for interfaces. These communication speeds are typically 100 to 300 MHz (CAT5e cabling), but technology is in place to make the communications much faster, and some current Ethernet interfaces will support communication speeds of up to 1 GHz (CAT6). If greater speed is needed, optical fibers can operate at several GHz.

Computers require data interrupts to service the vast number of processes that occur in modern computers. For example, each time a disk reads or writes, an interrupt signal is sent to the processor to inform it of the need to acquire or supply data. The processor must halt other less important processes for the disk operations to complete. Early systems often had as many as 64 interrupt levels, so that many different tasks could be undertaken simultaneously. These interrupts made programming and design difficult, and as PCs were designed as business machines that were to control little hardware, initially only eight interrupts were provided. That number has risen to only 16 today. Many of the interrupts are needed for system tasks. This shortage led to several interface problems for spectrometer manufacturers, but the newer technologies, such as USB and Ethernet, do not require additional interrupts, and interfacing has again become simpler and more reliable.

Despite the fact that communications have become faster, it does not mean that the need for specialized hardware has been totally eliminated. Emphasis has now shifted to technologies that increase the speed of Fourier transforms, either by doing the Fourier transforms directly or by doing some preprocessing of data. Digital signal processing (DSP) hardware has been incorporated into some spectrometers for these purposes. The advantages of these specialized hardware devices is being overshadowed, however, by the very rapid increase in computer speed. As desktop computers have gone well past the 3-GHz barrier, and PC communications buses have gone to 800 MHz and beyond, the need for such specialized devices has diminished.

## REFERENCES

1. J. Connes, *Rev. Opt.* **40**, 45 (1961); English translation as Document AD-409869, Clearinghouse for Federal Scientific and Technical Information, Cameron Station, VA.
2. M. L. Forman, *J. Opt. Soc. Am.* **56**, 978 (1966).

3. J. W. Cooley and J. W. Tukey, *Math. Comput.* **19**, 297 (1965).
4. E. O. Brigham, *The Fast Fourier Transform and Its Applications*, Prentice Hall Facsimile Edition, Englewood Cliffs, NJ, 1988.
5. J. Connes, Computing problems in Fourier spectroscopy, in *Aspen International Conference on Fourier Spectroscopy, 1970*, G. A. Vanasse, A. T. Stair, Jr., and D. J. Baker, Eds., U.S. Air Force, L. G. Hanscom Field, Bedford, MA, 1971, Vol. AFCRL-71-0019, p. 83.
6. W. M. Gentleman and G. Sande, *AFIPS Proc.* **29**, 563 (1966).
7. L. Mertz, *Transformations in Optics*, Wiley, New York, 1965.
8. L. Mertz, *Infrared Phys.* **7**, 17 (1967).
9. M. L. Forman, W. H. Steel, and G. A. Vanasse, *J. Opt. Soc. Am.* **56**, 59 (1966).
10. D. Chase, *Appl. Spectrosc.* **36**, 240 (1982).
11. R. J. Bell, *Introductory Fourier Transform Spectroscopy*, Academic Press, New York, 1972.
12. ABB Bomem, Inc., 585 Charest Boulevard, East, Québec, Québec G1K 9H4, Canada.
13. J. E. Bertie, Apodization and phase correction, in *Analytical Applications of FT-IR to Molecular and Biological Systems*, J. R. Durig, Ed., D. Reidel, Dordrecht, The Netherlands, 1980, p. 25.





## Chapter 5

# TWO-BEAM INTERFEROMETERS

### 5.1. MICHELSON-TYPE INTERFEROMETERS

#### 5.1.1. Introduction

As noted in Chapter 2, the simplest type of two-beam interferometer is the one designed by Michelson over 100 years ago [1]. Today there are many different designs of interferometers and almost as many companies manufacturing them. The companies that exist at the time of this writing are listed in the appendix to this chapter. Many of these companies have been acquired by larger companies, so that their names have changed more than the basic design of their interferometers. When we refer to specific instruments, we use the company's name at the time the instrument was introduced, if this is appropriate, but generally try to use the current company name.

In its most popular manifestation, the Michelson interferometer consists of a fixed and a moving plane mirror with a beamsplitter held at an angle bisecting the planes of these two mirrors (see Figure 2.1). (The design of the beamsplitter is covered later in this chapter.) Each mirror must be flat to better than one-tenth of the shortest wavelength in the spectrum being measured ( $\lambda_{\min}$ ). The angle between the mirrors is usually  $90^\circ$ , but other angles are equally feasible. For example, in many of the interferometers marketed by Bio-Rad (now Varian) and Bruker Optics, this angle is  $60^\circ$ . Smaller angles than  $90^\circ$  allow the size of the beamsplitter to be reduced without decreasing the diameter of the beam passing through the interferometer, thereby reducing the manufacturing cost of the interferometer, or conversely, permitting higher optical throughput at the same cost.

#### 5.1.2. Drive

The moving mirror in most interferometers is driven by an electromagnetic transducer that operates on principles that are identical to the voice-coil transducer

installed in most loudspeakers. The coil is wrapped around the shaft on which the mirror is mounted, and the shaft passes through a circular magnet. As the current passing through the coil is increased, the magnetic field that is generated interacts with the field of the permanent magnet, which produces a force that drives the shaft forward or backward. The force produced by the voice-coil mirror drive is simply the product of the field strength of the permanent magnet, the length of the winding and the current passing through the coil. In most conventional FT-IR spectrometers, the maximum force that can be developed is on the order of 1 or 2 N. For many mirror systems, the mass that must be moved is between 50 and 500 g. The combined effect of the low maximum force that can be applied to the mirror and the high mass of the mirror and its associated mount limit the rate at which the velocity of the moving mirror can be increased to its desired value. The highest practical physical velocity at which the mirror can be translated with an acceptable duty-cycle efficiency (see Section 5.1.4) is about  $10 \text{ cm} \cdot \text{s}^{-1}$ , but speeds of between  $0.1$  and  $6 \text{ cm} \cdot \text{s}^{-1}$  are more common.

### 5.1.3. Bearings

The drive for the moving mirror must, of course, allow the mirror to be moved far enough to enable the maximum resolution to be attained. At any time during this motion, the plane of the moving mirror must not tilt by an amount that will cause the optical path difference (OPD) for the ray that is reflected from one edge of the moving mirror to differ from the OPD for the ray reflected from the diametrically opposite edge by more than about  $\lambda_{\min}/10$  (Section 2.8). To achieve this level of precision, the moving mirror in most of the earlier interferometers used for mid- and near-infrared spectrometry (as well as one or two contemporary instruments) was driven on an *air bearing*. In most air bearings used in these interferometers, the maximum distance between the piston and the cylinder was between about 2 and  $5 \mu\text{m}$ . Because the lubricant was air (typically, at a pressure of about 2 atm), the frictional drag was minimal and the drive was extremely smooth.

The cylinder of the bearing should cover the shaft over the full mirror travel. For measurements made at a resolution of  $0.1 \text{ cm}^{-1}$ , where the moving mirror of a Michelson interferometer travels 5 cm, a 10-cm-long air bearing should be used. If the spacing between the air bearing and the shaft is  $2 \mu\text{m}$ , the maximum possible tilt along the entire drive is  $20 \mu\text{rad}$ , although in practice the tilt is significantly lower than this. To achieve this level of performance for measurements made at fairly high resolution, it is obvious that both the cylinder and shaft must be exceptionally straight.

In any image-forming system such as the optics of an FT-IR spectrometer, the optical throughput (see Section 2.7) of the beam is fixed by two limiting apertures, the entrance pupil and the field stop. The *aperture stop* limits the diameter of the beam at each optical component, while the *field stop* determines the size and shape of the image. In an FT-IR spectrometer, the aperture stop is usually decided by the diameter of the beamsplitter or one of the larger mirrors in the optical path. However, in one instrument, a variable aperture, called the *beamsplitter stop* or

*B-stop*, is located at a conjugate focus to the beamsplitter and acts as the aperture stop.

All FT-IR spectrometers with a resolution better than  $1\text{ cm}^{-1}$  have a field stop located at a focus located between the source and the interferometer. The function of this aperture is to ensure that the maximum half-angle of the beam passing through the interferometer does not exceed  $(\Delta\tilde{\nu}/\tilde{\nu}_{\max})^{1/2}$  radians (see Eq. 2.40). This aperture has been called the *Jacquinot stop* (or *J-stop*) to recognize the fact that Pierre Jacquinot first realized that the optical throughput of a Fourier transform spectrometer is greater than that of a monochromator operating at the same resolution when the aperture stops in each instrument are identical [2]. In many low-resolution FT-IR spectrometers, there is no J-stop and the detector acts as the field stop. For the modulation efficiency of the interferometer to be high, the optical path difference from any point in the source plane to any point in the field plane should be equal to the OPD at any other point. If this is not so, either the aperture stop or the field stop must be made sufficiently small that the variation in OPD across the beam is less than  $\lambda_{\min}/10$ .

Steel [3] has described several of the factors that affect the performance of two-beam interferometers. He introduced four parameters, *shear*, *shift*, *tilt*, and *lead*, to describe errors in the motion of the interferometer mirror. The origin of these parameters is shown schematically in Figure 5.1, which shows two rays through the interferometer that connect a point  $(\xi, \eta)$  at the source to a point  $(u', v')$  in the field plane. These rays leave the source with direction cosines  $(l_1, m_1, n_1)$  and  $(l_2, m_2, n_2)$  and arrive in the field planes with direction cosines  $(l'_1, m'_1, n'_1)$  and  $(l'_2, m'_2, n'_2)$ . The images of each plane as seen from the other are shown in Figure 5.2. Because there is one image for each of the two beams, each image is doubled. These two images may be separated laterally and/or longitudinally. Either separation can cause a difference in the direction of a pair of rays. For the beamsplitter images, the

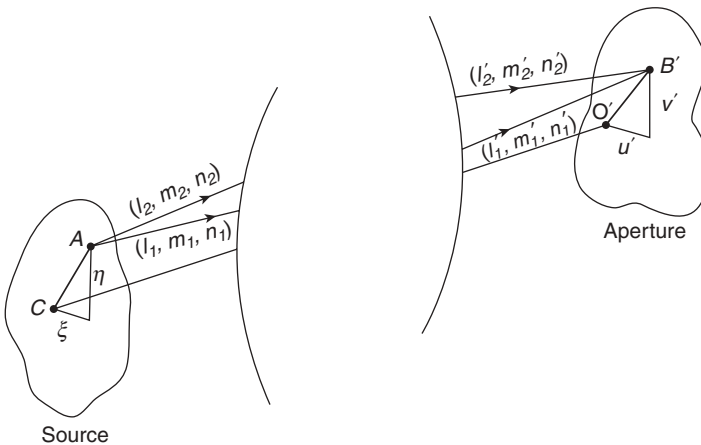


**Figure 5.1.** Positions at reference planes and directions of rays. (Reproduced from [3].)

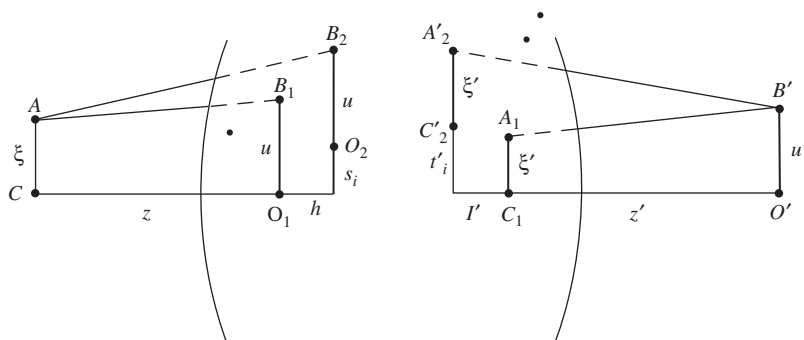


**Figure 5.2.** One section of Figure 5.1, showing the images of each plane as seen from the other. (Reproduced from [3].)

lateral separation is the shear,  $s$ , and the longitudinal separation is the shift,  $h$ . For the field images, these are the tilt,  $t'$ , and the lead,  $l'$ .

The biggest potential drawback to a single-bearing design for a Michelson interferometer is the possibility of tilt. A second cause of error is motion about the drive direction (the *roll axis*) which will cause a tilt if the plane of one mirror does not coincide with that of the image of the other. In one of the early low-resolution rapid-scanning interferometers, the roll motion was restrained through the use of springs mounted on the rear end of the mirror drive. In another, the roll motion was prevented by a stainless-steel extension attached to the moving mirror assembly that slid over a bar coated with polytetrafluoroethylene (PTFE). A better way to prevent the mirror from rotating is the use of a dual-bearing design. However, because the bearings can bind, an additional motion in a direction perpendicular to the direction of the drive can be set up in dual-bearing interferometers if a small lateral force is applied. Mirror roll has also been reduced in other interferometers by using rectangular bearings.

An important problem with interferometers with an air bearing drive is the need for a reliable source of compressed air. The typical flow rate of air through the bearing is  $\sim 3 \text{ L} \cdot \text{min}^{-1}$ . Thus, if a gas cylinder is used to supply the air, it takes only about a day before the cylinder must be replaced. A more permanent air supply is obtained by drawing some of the dry air from the spectrometer into a small compressor, the output of which is fed into the bearing.

The first interferometer incorporating an air-bearing drive was the Block Engineering Model 296. This interferometer was the one used in the first commercial mid-infrared FT-IR spectrometer designed for laboratory use, the Digilab FTS-14 [4]. This instrument was introduced in 1969 and was followed a few years later by the Model 7199 spectrometer made by Nicolet Analytical Instruments which also featured an air-bearing drive. Both of these early FT-IR spectrometers were too large to be placed on a lab bench and the compressor was mounted inside the instrument's cabinetry. Over the next 10 or 15 years, the optics and electronics of FT-IR spectrometers became far more compact and bench-top instruments became commonplace. Since compressors are noisy and occupy too much bench space,

an alternative type of drive to the air bearing was required for these instruments. Many different drives are incorporated in today's Michelson interferometers. These have been described in some detail by Jackson [5], and several of the figures shown in this chapter are reproduced from his excellent article. Although the mechanical design of the drives used in Michelson interferometers, and indeed many different interferometer designs, may be quite different, it may be stressed that all of them are good enough to allow the specifications of the particular instrument to be met.

One of the first drives not to use an air bearing was the *porch swing design* first described by Walker and Rex [6]. Their design is shown schematically in Figure 5.3. The key to this type of drive is the fact that the mirror pivot mounts are slightly eccentric, allowing the plane of the mirror surface to remain parallel throughout the scan. Although such a drive is not suitable for high-resolution measurements, it is possible to maintain the tilt angle below  $5 \mu\text{rad}$  for an OPD up to  $\sim 0.25 \text{ cm}$  ( $\Delta\tilde{\nu} = 4 \text{ cm}^{-1}$ ).

*Flex-pivot bearings* are designed to provide rotational motion, but can be modified to provide translational motion when combined with a porch-swing drive. A cutaway diagram showing the principle of operation of a flex-pivot bearing is shown in Figure 5.4 [5]. The curved arrows indicate the rotation of one section relative to the other. Flex-pivots consist of two interlocking cylinders, A and B, which are not in contact with each other but are connected by flexure plates. The two cylinders can rotate relative to each other over limited deflection angles, with very little shift of the center of motion. Provided that the bearing is not loaded excessively and an OPD of greater than  $2 \text{ cm}$  is not required, these bearings give good performance and have exceptionally long lifetimes.

Several of the early low-resolution FT-IR spectrometers sold by Nicolet incorporated flex-pivot drives, and the interferometer made by Midac has a porch-swing drive by which a resolution of up to  $0.5 \text{ cm}^{-1}$  can be achieved [7]. The major

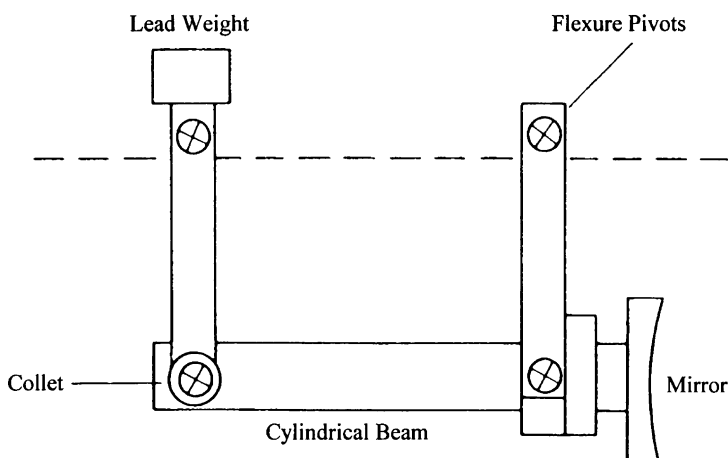
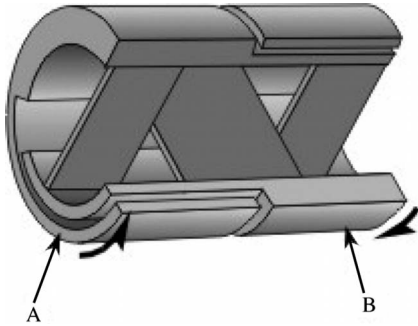
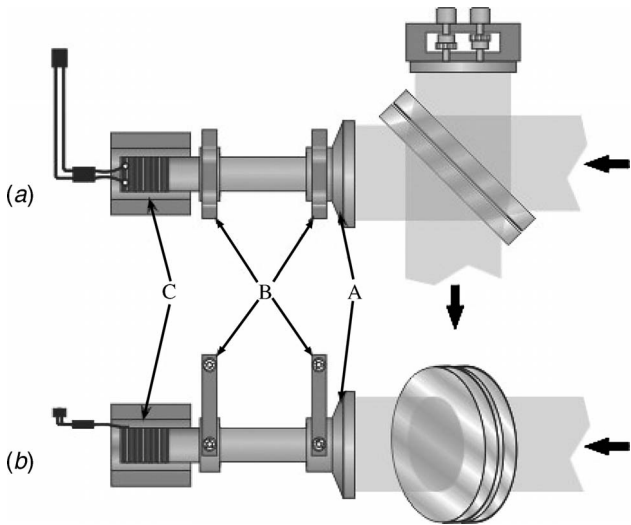


Figure 5.3. Porch-swing interferometer.



**Figure 5.4.** Principle of operation of a flex-pivot bearing. The curved arrows indicate rotation of one section relative to the other. (Reproduced from [5], by permission of John Wiley & Sons, Ltd.; copyright © 2002.)

components of the Midac interferometer are shown in Figure 5.5. The moving mirror and mirror carriage, A, are suspended from the interferometer block by two H-shaped swing arms, B. The arms are attached to the interferometer block and the mirror carriage at eight pivot points. The interferometer block, arms, and mirror carriage form the arms of a parallelogram, so that when current is applied to the voice coil, C, the mirror swings backward and forward. Although this motion will introduce some shear, the fact that the interferometer mirrors are planar means that this shear does not have a deleterious effect.



**Figure 5.5.** Midac interferometer: (a) plan view; (b) side view. The direction of the radiation is given by the solid arrows. (Reproduced from [5], by permission of John Wiley & Sons, Ltd.; copyright © 2002.)

Other mirror drives, such as the ones now used by Thermo Electron and Varian, are characterized by their simplicity and innovation. For example, the bearing assembly used in many Varian interferometers includes a fixed glass rail, a rigid movable carriage that carries the moving mirror and the drive coil, and a mechanism for keeping the carriage in contact with the rail [8]. The glass rail has two optically flat faces that define a horizontally flat line of intersection. Regions of the carriage have plastic surfaces that provide a low-friction bearing interface for contacting the flat surfaces of the rail. To improve stability and reduce the possibility of any transverse movement, the carriage is pushed downward by an overlying glass plate with a downward-facing flat surface. A spring-loaded plastic element is mounted on the top of the carriage. This element contacts, and slides along, the flat glass surface and transmits a downward force to the carriage.

The drive in several of the interferometers made by Thermo Electron consists of a cylindrical glass bearing with a precision-ground piston fabricated from a graphite composite running down the center of the tube [9]. The design of the interferometer used in their Avatar spectrometer is shown in Figure 5.6. The moving mirror is attached to a flexure diaphragm, D, to a piston, E, that is mounted in graphite composite bushings, F. This assembly fits inside a glass tube, G, to very close tolerances. The clearance and tolerances of the piston and the glass cylinder are such that when the mirror moves at a high speed, the piston rides on a small cushion of air that is trapped between the graphite and the glass. Thus, the performance characteristics of these interferometers are similar to those of traditional air-bearing interferometers. A unique feature of this interferometer design is that the permanent magnet, H, is attached to the moving mirror while the voice coil, I, is fixed. Extra coils can then be used to pivot the moving mirror about a point in the center of the flexure ring. These coils are used for dynamic alignment (see Section 5.1.5). It is

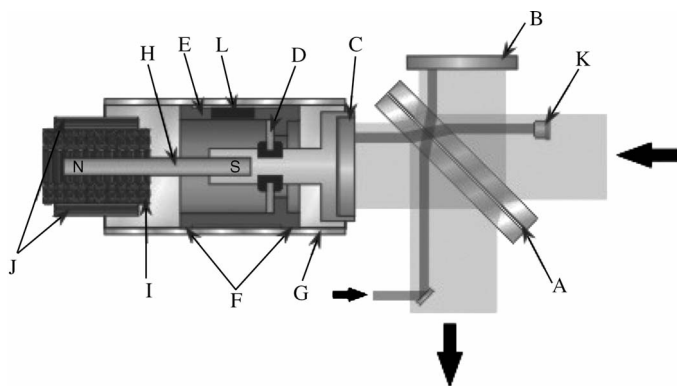


**Figure 5.6.** Interferometer used in the Thermo Nicolet Avatar spectrometer. The direction of the radiation is given by the solid arrows. A, beamsplitter; B, fixed mirror; C, moving mirror; D, flexure diaphragm; E, piston; F, graphite composite bushings; G, glass tube; H, permanent magnet; I, voice coil; J, extra coils to pivot the moving mirror about the center of the flexure ring; K, quadrant detector; L, small permanent magnet to eliminate roll of the moving mirror. (Reproduced from [5], by permission of John Wiley & Sons, Ltd.; copyright © 2002.)



also worthy of note that even though static friction is always greater than dynamic friction, the composition of the graphite composite from which the piston has been fabricated has been chosen so that the bearing can be started and stopped with minimal static friction. This bearing is therefore equally applicable to conventional rapid-scan interferometers and step-scan interferometers of the type discussed in Section 5.5.

#### 5.1.4. Fringe Referencing

For interferograms to be added coherently (a process sometimes known as *co-adding* or *signal averaging*), corresponding data points in each interferogram must be acquired at exactly the same retardation. To achieve this goal, at least one other interferogram is measured along with the signal interferogram that is used to trigger the analog-to-digital converter (ADC). In all contemporary FT-IR spectrometers, a narrow monochromatic beam of radiation, usually from a helium–neon (HeNe) laser, is passed through the interferometer together with the infrared beam. Whereas the interferogram of a broadband source such as a Globar has a well-defined centerburst, the interferogram of a monochromatic source is sinusoidal and hence changes sign twice per wave at the *zero crossings*. In many instruments, mid-infrared interferograms are digitized once per wave, at one of these zero crossings. The wavenumber of a HeNe laser,  $\tilde{\nu}_{\text{HeNe}}$ , is  $\sim 15,800 \text{ cm}^{-1}$ ; hence the Nyquist wavenumber for mid-infrared measurements is about  $7900 \text{ cm}^{-1}$ . Since the near-infrared (NIR) spectrum extends beyond  $7900 \text{ cm}^{-1}$ , NIR interferograms must be sampled at least at every zero crossing (twice per wave), in which case the Nyquist wavenumber is  $15,800 \text{ cm}^{-1}$ . Some instruments allow sampling at even shorter intervals, usually by doubling the frequency of the laser interferogram electronically. For example, for the spectrometer on which the high-resolution ultraviolet spectrum shown in Figure 5.7 was measured, the free spectral range was  $63,200 \text{ cm}^{-1}$ .

In Chapter 3 it was noted that the performance of FT-IR spectrometers can be limited by the dynamic range of the ADC. Most of the instruments made in the 1990s were equipped with 16-bit ADCs, with sampling being triggered at the zero crossings of the laser interferogram. Since the signal-to-noise ratio (SNR) at the centerburst was often greater than the dynamic range of the ADC, it was common practice to extend the dynamic range by means of gain ranging (see Section 3.3.3). After data acquisition is complete, the low-gain region of the interferogram is multiplied by a factor that is exactly equal to the ratio of the gains used to amplify each part of the interferogram. In this way, every point is recorded at the same amplification. If this factor is not selected correctly, the noise level of the spectrum will be slightly increased and artifacts are sometimes seen in the baseline.

Obviously, this problem would be alleviated if ADCs of higher dynamic range were used. Although 18-bit ADCs are commercially available, they are typically slower and more expensive than their 16-bit counterparts. A relatively recent development has been the introduction of the sigma–delta ADCs (see Section 3.4). These devices have an effective dynamic range of about 21 bits but sample the signals from the infrared and laser detectors simultaneously at equal intervals of time rather

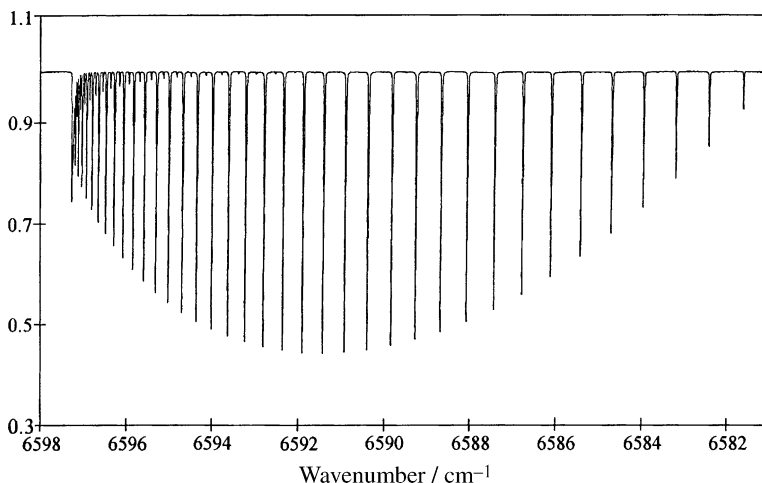


**Figure 5.7.** Atomic emission spectrum of platinum measured at a resolution of  $0.11\text{ cm}^{-1}$ , showing the performance of a Bruker 120 HR spectrometer operating in the ultraviolet with a Nyquist wavenumber of  $\sim 63,200\text{ cm}^{-1}$ . The resolving power for this spectrum is  $4.7 \times 10^6$  and the measurement time was 24 hours. (Reproduced by permission of Bruker Optics.)

than OPD. To calculate the signal at equal intervals of OPD, the infrared signal at the laser zero crossings is calculated before the Fourier transform is performed, most commonly using an algorithm described by Brault [10]. Although the use of sigma-delta ADCs affects the electronic and software designs of modern FT-IR spectrometers, it has very little impact on the mechanical design of the interferometer.

For a Michelson interferometer, the rate of change of retardation is twice the mechanical velocity of the mirror. This parameter is often known as the *optical velocity*,  $V$ , and has the units of centimeters (retardation) per second. Some FT-IR vendors specify the velocity of the moving mirror in their interferometer in terms of its mechanical velocity and some in terms of its optical velocity. (*Note:* Users should make sure which of these two parameters is in fact specified.) Still others specify the optical velocity in terms of the corresponding modulation frequency of the laser interferogram; although a few commercial interferometers no longer use HeNe lasers, we will denote the frequency of the laser interferogram as  $f_{\text{HeNe}}$ .

Assuming that one interferogram point is being sampled each wave of the laser interferogram, the *sampling frequency* is equal to  $f_{\text{HeNe}}$  and is given by the product of  $V$  and  $\tilde{\nu}_{\text{HeNe}}$ . If the optical velocity of the moving mirror is  $0.30\text{ cm} \cdot \text{s}^{-1}$ , the sampling frequency is  $0.30 \times 15,800\text{ Hz}$ , or  $4.74\text{ kHz}$ , and the Nyquist frequency is  $2.37\text{ kHz}$ . It is therefore essential that all contributions to the signal having a frequency above  $2.37\text{ kHz}$  are filtered out either electronically or optically before the interferogram is digitized. Because the highest wavenumber is  $4000\text{ cm}^{-1}$ , the highest frequency of interest in the interferogram is  $1.20\text{ kHz}$ . Thus, as much of the signal as possible above  $\sim 1.50\text{ kHz}$  should be removed with a low-pass electronic filter to avoid any deleterious effects of folding. Filters with a very sharp cutoff

(sometimes known as “brick-wall filters”) introduce high-frequency oscillations of the phase in the region of the cutoff frequency. It is for this reason that some manufacturers use slower filters and sample at higher frequency than  $f_{\text{HeNe}}$  when measuring mid-infrared spectra. Some manufacturers then apply digital filtering to the sampled interferogram to minimize aliasing.

For coherent signal-averaging (co-adding) interferograms, the first data point in every interferogram must be acquired at exactly the same point. The original laser-referenced interferometers used a clever way to achieve this goal. A narrow beam of light from a bright source of visible light was passed through the interferometer along with the laser beam. In some interferometers, these two beams were passed through a separate *reference interferometer* that shared its mirror drive with the main interferometer through which the collimated infrared beam was passed. An example of such an interferometer is shown schematically in Figure 5.8.

The infrared, laser, and white-light interferograms were measured by separate detectors. All three interferograms are shown in Figure 5.9. Because the wavelengths of visible light are so much shorter than the wavelengths of infrared radiation, the centerburst of the white-light interferogram is much sharper than that of the infrared interferogram. The sampling electronics were designed to sense each zero crossing of the laser interferogram and to use each positive- and/or negative-going zero crossing to trigger the ADC. They also sensed when the white-light interferogram reached a certain threshold voltage,  $V_t$ , near its centerburst. After the voltage of the white-light interferogram exceeded  $V_t$ , the infrared interferogram was digitized at each subsequent zero crossing of the laser interferogram (or every second, third, or fourth zero crossing, depending on the desired value of the Nyquist wavenumber). The centerburst of the white-light interferogram was set to occur shortly before that of the infrared interferogram (as shown in Figure 5.8) by adjusting the position of the fixed mirror of the reference interferometer. Interferograms sampled in this manner are said to be acquired in the *single-sided mode*.

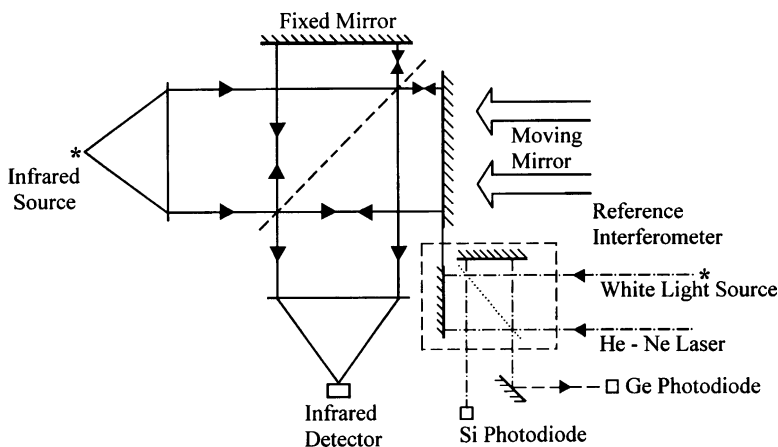


**Figure 5.8.** Interferometer, incorporating a separate reference interferometer for the laser and white channels.

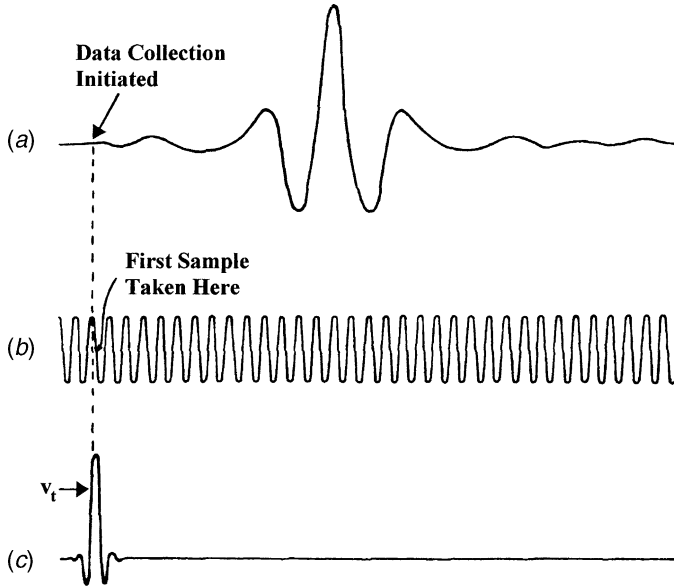


**Figure 5.9.** Interferograms measured using an interferometer of the type shown in Figure 5.8, showing the signals measured by (a) an infrared detector, (b) a laser detector, and (c) a white-light detector. Note that the reference interferometer is positioned so that the centerburst of the white-light interferogram occurs before that of the infrared interferogram. When the amplitude of the white-light interferogram exceeds the threshold voltage,  $V_t$ , data acquisition is initiated at the next zero crossing of the laser interferogram.

The measurement of interferograms with an instrument equipped with a white-light reference interferometer has several disadvantages. First, the position of the fixed mirror of the reference interferometer cannot be adjusted easily; thus, the length of the short interferogram before the centerburst must remain constant and cannot be changed as the maximum retardation (i.e., the spectral resolution) is varied. Second, the Mertz phase correction algorithm yields the highest photometric accuracy when the centerburst is in the center of the scan (i.e., when the interferogram is sampled *double-sided*) [11]. Third, because the centerburst of the white-light interferogram must always occur before the centerburst of the infrared interferogram, data can only be acquired when the moving mirror of the interferometer is traveling in one direction. Thus, at the end of each scan made with an interferometer similar to the one in Figure 5.4, the moving mirror had to be turned around, retraced rapidly beyond the centerburst of the white-light interferogram, accelerated once again, and controlled so that its velocity is constant by the time the centerburst of the white-light interferogram had been reached again. This resulted in a very poor *duty cycle efficiency*,  $\xi$ , where  $\xi$  is defined as the ratio of the time that data are actually being acquired to the total time from the start of the first scan to the end of the last. It can readily be understood why  $\xi$  rarely exceeded 0.5 (50%) for unidirectional interferometers operating single-sided at low resolution.

The use of a white-light reference had one final disadvantage. If the alignment of the reference interferometer drifted slightly, it was not uncommon for the white-light and laser interferograms to drift slightly with respect to each other. If the drift was sufficiently large, the laser fringe at which data acquisition was initiated would change from one scan to the next and signal averaging would no longer be coherent.

All the disadvantages of a white-light interferogram were eliminated when computers became fast enough that the position of the moving mirror could be monitored continually throughout the forward and reverse scans, and in the early 1980s *fringe counting* replaced use of the white-light interferogram. However, as originally implemented, fringe counting had a problem that occurred when the direction in which the mirror was moving was reversed. This problem was caused by the fact that the mirror velocity is zero at the exact point when the mirror changed directions, so that it is difficult to know which direction the mirror is traveling near the turnaround point. Furthermore, if the laser interferogram is near its maximum or minimum amplitude when the mirror is near the turn-around point, even a small vibration could cause a given fringe to be counted more than once, and the data system would lose the fringe count.

Several interferometer manufacturers devised clever ways to retain the fringe count during turnaround of the moving mirror. Some of these methods are based on insertion of a quarter-wave retardation plate in the laser beam, so that two laser interferograms, A and B, are measured, with one phase-retarded by one-fourth of a wave with respect to the other. If the mirror moves in one direction, A leads B, and if it moves in the other direction, B leads A. By feeding both signals into a comparator circuit, it is possible to know exactly when the direction of the mirror travel changes. Furthermore, if the laser interferogram is near its maximum or minimum amplitude at the turnaround point, the other is close to a zero crossing, so that the system is far less sensitive to the effects of vibration.

Besides triggering the ADC, the laser interferogram is also used to provide a signal that allows the velocity of the moving mirror to be controlled accurately. For this purpose, the frequency of the laser interferogram is compared to a sinusoid of known frequency,  $f_{\text{ref}}$ . If  $f_{\text{HeNe}} > f_{\text{ref}}$ , the voltage to the voice coil must be reduced to slow down the moving mirror; similarly, if  $f_{\text{HeNe}} < f_{\text{ref}}$ , the velocity of the mirror must be increased. If the mirror velocity varies by much more than 0.1%, the SNR of the spectrum is degraded (see Section 7.4.1). Thus accurate control of the mirror velocity has an important impact on the performance of an FT-IR spectrometer.

Finally, the frequency of the laser interferogram is a secondary standard for measuring the frequencies of each sinusoidal wave in the infrared interferogram. Thus, it was common to read that the wavenumbers of sharp lines in FT-IR spectra are known to the same accuracy as the wavenumber of the HeNe laser. Indeed, many brochures have given the wavenumber *accuracy* of FT-IR spectra as being better than  $0.01 \text{ cm}^{-1}$ . This claim is usually unwarranted, for two reasons. First, the divergence angle of the infrared beam passing through the interferometer is larger than that of the HeNe laser. Thus, the wavenumber of each band in the

infrared spectrum will be shifted from its true value (see Section 2.6). Second, the diameter of the beam focus in the sample compartment can be reduced by the sample or sampling accessory, a condition known as *vignetting*. In this case the effective divergence angle in the interferometer is changed and a wavenumber shift is introduced. Until recently, however, it was believed that the wavenumber *precision* (i.e., reproducibility) was no worse than  $0.01 \text{ cm}^{-1}$ , even though the accuracy was poorer than this.

This situation was questioned in 1998, when Weis and Ewing showed that the wavenumber of unstabilized HeNe lasers of the type that are installed in most commercial FT-IR spectrometers can vary by up to  $0.3 \text{ cm}^{-1}$  ( $\pm 0.15 \text{ cm}^{-1}$ ) because of mode hopping and changes in the length of the laser cavity with temperature [12]. Such changes in the laser wavenumber could lead to shifts in the wavenumber scale of approximately  $\pm 0.04 \text{ cm}^{-1}$  in the mid-infrared spectrum and even greater shifts at shorter wavelengths. Jackson [13] also found that shifts of  $0.05 \text{ cm}^{-1}$  occur in practice, but does not agree with Weis and Ewing's conclusion that these shifts are due completely to mode hopping in the laser. A HeNe laser has a gain curve with a typical FWHH of 1400 MHz centered at 473.61254 THz. Underneath the gain curve are several cavity resonance modes, each with a FWHH of  $\sim 1 \text{ MHz}$ . The mode spacing is given by  $c/2L$ , where  $c$  is the velocity of light and  $L$  is the length of the laser cavity (typically, about 15 cm). Thus,  $\Delta f \approx 1 \times 10^9 \text{ Hz}$ . A typical HeNe laser used in benchtop FT-IR spectrometers has two to three modes under the gain curve. If the temperature of the cavity is not held at a constant value, the frequency of the cavity modes can vary, leading to an instability in its frequency. The shift in wavelength of a cavity mode,  $\Delta\lambda$ , is given by

$$\Delta\lambda = \frac{\Delta L}{L}\lambda \quad (5.1)$$

where  $\Delta L$  is the change in the length of the laser cavity. For the type of glass used in most HeNe lasers, the change in wavelength of the laser as a result of temperature variation is  $\sim 2.5 \times 10^{-3} \text{ nm} \cdot \text{K}^{-1}$ . Since the gain curve does not move, the maximum instability cannot be more than the gain curve, or about  $\pm 1400 \text{ MHz}$ . This is a fractional instability of  $\sim 3 \times 10^{-6}$ , or  $\pm 0.047 \text{ cm}^{-1}$ . Thus, less than half of the wavenumber instability of an FT-IR spectrometer is caused by mode hopping of the laser as the temperature of the room changes. The rest is probably caused by such effects as changes in the angle of the laser through the interferometer and changes in the refractive index of air caused by thermal effects [14]. Whatever the cause of the wavenumber instability observed, it is somewhat greater than the value of  $\pm 0.01 \text{ cm}^{-1}$  usually specified by most manufacturers.

Although it has been an almost universal practice to include fringe referencing in interferometers to permit interferogram co-addition since the early 1970s, increases in computer speed have made this practice unnecessary. Some manufacturers have eliminated optics or electronics to determine the position of the moving mirror and have instead settled for always moving the mirror to its maximum retardation. The mirror scans constantly from one extreme to the other and the laser signal is used

simply for sampling (see Chapter 3). At the end of each scan the centerburst is located by software and the interferogram is truncated to the appropriate retardation. Phase correction is applied and the interferogram is transformed to the single-beam spectrum. This in turn is ratioed to the appropriate background spectrum, and the percent transmission or absorbance spectrum is calculated. All this is accomplished within one scan cycle of the interferometer. Spectra are co-added instead of interferograms. The operation is as accurate as the co-addition of interferograms, but elimination of the added hardware to position the mirror for coherent data collection provides a significant cost savings. Of course, this method is only practical for low-resolution spectrometers ( $\geq 4\text{ cm}^{-1}$ ), where the duty-cycle efficiency is not too adversely affected by not scanning a shorter distance for the lower-resolution measurements.

### 5.1.5. Dynamic Alignment

None of the bearings described in Section 5.1.3 is suitable for retardations much greater than 20 cm ( $\Delta\tilde{\nu} < 0.05\text{ cm}^{-1}$ ). The fabrication of an interferometer with minimal tilt over very long mirror travels has caused the designers of high-resolution FT-IR spectrometers to come up with some innovative designs. Many of the solutions have involved the use of optical methods of tilt compensation, such as the cube-corner or cat's-eye interferometers (described in Section 5.2). One approach, known as *dynamic alignment*, allows standard Michelson interferometers to achieve an optical path difference of up to 5 m. The original developments on dynamic alignment were carried out by Buijs et al. [15], and the high-resolution spectrometers made by the company that Buijs originally founded, Bomem Corporation (now ABB), are all based on this principle. (In fact, some Bomem spectrometer models were called the DA-3, DA-6, and the DA-8, where DA stands for "dynamic alignment.") The instruments from several manufacturers of medium-resolution FT-IR spectrometers, including Thermo Electron, Varian, and Shimadzu, are now based on the dynamic alignment approach.

In a typical dynamically aligned interferometer, the beam from the HeNe laser is either split into three or simply expanded up to  $\sim 1\text{ cm}$  in diameter. The beam is passed through the beamsplitter and focused on three separate detectors, as shown in Figure 5.10 (as three separate laser beams instead of an expanded beam). If the plane of the moving mirror remains parallel throughout the scan, the three sinusoidal interferograms remain exactly in phase. Tilting of the moving mirror causes a difference in the phase of these three interferograms. This phase difference is sensed and corrected in real time. The alignment of the fixed mirror (usually), the moving mirror, or the beamsplitter may be changed in one of several different ways. Bomem uses a lever-arm system, Varian uses piezoelectric transducers, and Thermo Electron uses electromagnetic actuators. The method that is used in the Thermo Electron Avatar spectrometer (described in Section 5.1.3) can be seen in Figure 5.6. In this instrument, extra voice coils allow the moving mirror to be pivoted about a point in the center of the flexure ring. The HeNe laser beam is expanded and measured by a quadrant detector. The angle of the moving mirror

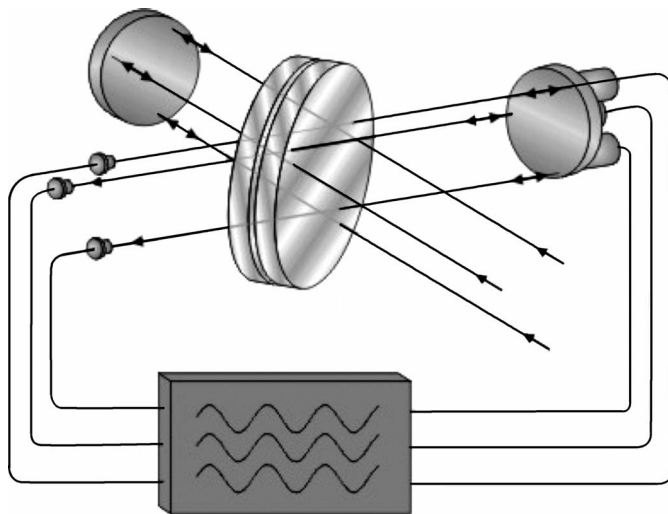


**Figure 5.10.** Path of three parallel laser beams through a dynamically aligned Michelson interferometer. The beams are detected by three separate detectors, and the signals from the detector are fed to three actuators that control the alignment of one of the mirrors. (Reproduced from [5], by permission of John Wiley & Sons, Ltd.; copyright © 2002.)

is adjusted by a feedback mechanism that depends on the phase difference between the sinusoidal interferograms that are measured by the four detectors.

No matter which system is used to adjust the plane of the interferometer mirror, the adjustment must be carried out sufficiently quickly that if only the infrared signal is examined, the interferometer appears to remain in perfect alignment throughout the scan. It should be recognized, however, that in order for any phase difference between the laser interferograms to be sensed, the interferometer must already have gone slightly out of alignment. Thus, it is probably true to say that dynamic alignment can never be quite as effective as a really smooth drive for a Michelson interferometer; however, Varian does employ dynamic alignment on their research-grade air bearing interferometers. Because the piezoelectric transducers or electromagnetic actuators serve other purposes, such as controlling the OPD if the interferometer is used in the step-scanning mode (see Section 5.5), the plane of the mirror in several top-of-the-line FT-IR spectrometers is kept constant by dynamic alignment.

Dynamic alignment is more effective the longer the wavelengths in the infrared spectrum. In the NIR and visible spectrum, the Fourier frequencies in the interferogram start to approach  $f_{\text{HeNe}}$  and the time required to sense the phase difference between the three laser interferograms becomes a significant fraction of the period of the laser interferogram ( $1/f_{\text{HeNe}}$ ). Nonetheless, dynamic alignment is a highly effective technique for high-resolution spectroscopy in all spectral regions. It is also very effective for quantitative measurements in the mid-infrared region, especially when the spectrometer must be housed in a location where the temperature



can vary by several degrees, as the spectrometer is likely to change alignment with temperature. However, if a dynamically aligned interferometer is used for the quantitative near-infrared analysis of minor components in complex mixtures using a multivariate technique such as partial least squares (PLS) regression (see Section 9.9), it may be necessary to add several factors to the PLS model to compensate for the small changes in the interferogram introduced by the dynamic alignment process [16].

Even dynamic alignment cannot compensate for the effect of a bad bearing design. For example, Beckman Instruments, one of the two leading manufacturers of infrared grating spectrometers in the 1960s and 1970s, tried to make their entry into the field of FT-IR spectrometry with a dynamically aligned interferometer, the bearing of which involved intimate contact of a circular piston and cylinder, both of which had ground-glass surfaces. These surfaces often tended to bind, causing velocity errors that were too large to be compensated by dynamic alignment. It is a comment on the power of market economics that Beckman did not last very long in the field of FT-IR spectrometry!

## 5.2. TILT-COMPENSATED INTERFEROMETERS

### 5.2.1. Cube-Corner Interferometers

One way to minimize the effect of tilt in a Michelson interferometer is to replace the plane mirrors by retroreflectors that return the beam along a path that is parallel to that of the incident beam. The simplest example is a roof retroreflector, where two plane mirrors are mounted at  $90^\circ$ . The way in which a roof retroreflector functions can be seen in Figure 5.11. When the pair of mirrors is tilted by any angle in the plane of the page, the reflected beam is always parallel to the incident beam (even though it may be slightly displaced). In practice, the two-dimensional roof retroreflector is of little use for FT-IR spectroscopy because if the roof were tilted out of the plane of the page by an angle  $\alpha$ , the angle between the incident and return beams is  $2\alpha$  and the effect of the tilt is increased. However, the *cube-corner retroreflector*, where three plane mirrors are mounted with their planes mutually perpendicular, is the three-dimensional equivalent of the roof and compensates for tilt in any direction [17].

Several commercial interferometers incorporate cube-corner retroreflectors, including the spectrometers marketed by Jasco, MKS (formerly On-Line Technology), and Shimadzu, and some of the spectrometers made by ABB, Bruker, and Thermo Electron. The moving optical element on all Mattson interferometers is driven on high-precision roller bearings, which probably would not give a sufficiently accurate drive for a plane-mirror Michelson interferometer but are perfectly adequate when cube corners are used. Although in most commercial interferometers cube-corner retroreflectors are used at relatively low resolution ( $\Delta\tilde{\nu} > 0.5 \text{ cm}^{-1}$ ), these devices are also used by Bruker in their very high resolution Model IFS 120 HR spectrometer. A maximum retardation of over 6 m can be achieved with

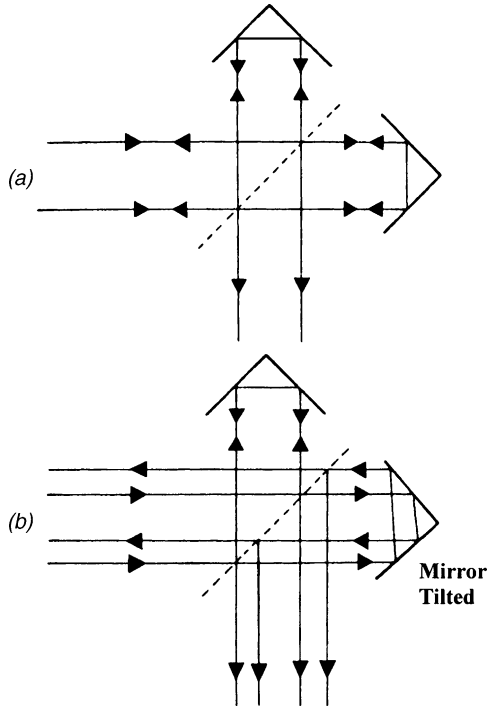


**Figure 5.11.** Principle of a corner retroreflector: (a) both retroreflectors are in good alignment, so there is no essential difference from the case of a plane-mirror Michelson interferometer; (b) one of the retroreflectors is tilted, but the output beams are still parallel, unlike the case for a plane-mirror Michelson interferometer. The concept of the “roof” retroreflector shown here can be extended into three dimensions through the use of cube corners.

the interferometer used in this instrument, allowing unapodized spectra of narrow lines to be measured with a FWHH of  $\sim 0.001 \text{ cm}^{-1}$  and a resolving power of better than  $10^6$ . In the Bruker IFS 120 HR interferometer, the primary bearing is a carriage that rides on two hard steel bars. The bushings on the carriage are made of PTFE for low friction, and the bars are polished and very straight. The carriage is pulled up and down the rails by a pretensioned steel cable. On the carriage is a secondary drive, comprising a voice coil and a porch-swing bearing design. The secondary drive is used for all low-resolution measurements, and to compensate for velocity errors in the main drive during high-resolution scans. Examples of spectra measured with this spectrometer at a resolution of  $0.001 \text{ cm}^{-1}$  in the far infrared and  $0.01 \text{ cm}^{-1}$  in the near infrared are shown in Figures 5.12 and 5.13, respectively.

Even though cube corners largely eliminate the effect of tilt, lateral displacements produce a shear that has a similar effect on the interferogram. In practice, it is easier to meet the tolerance on lateral displacements than on tilts, so that retroreflectors have a definite experimental advantage over plane mirrors for a given drive. Steel [3] has suggested a combination of a movable cube corner and stationary plane mirrors that introduces neither shear nor tilt. An interferometer based on this principle, shown

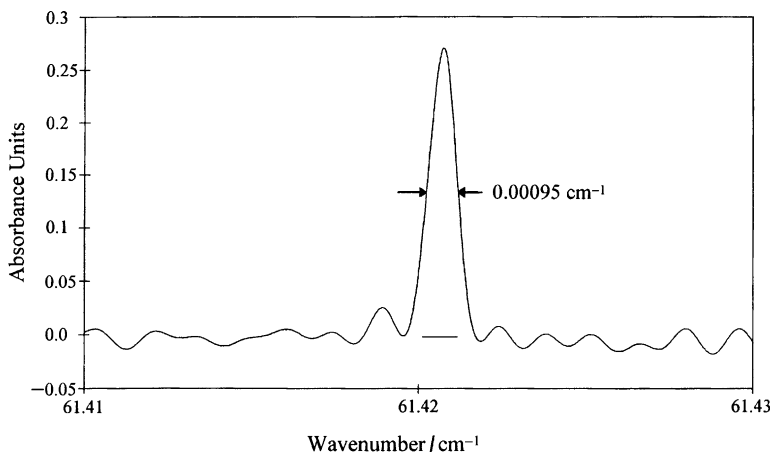


**Figure 5.12.** Unapodized spectrum of a pure rotational transition of CO measured at a nominal resolution of  $0.00125\text{ cm}^{-1}$  on a Bruker 120 HR. (Reproduced by permission of Bruker Optics.)

schematically in Figure 5.14, was introduced by Analect Instruments (now Applied Instrument Technologies Division of Hamilton Sundstrand) but is no longer sold by this company. Since the alignment of a plane mirror may change slowly over time, it is logical that the same combination of cube corner and plane mirror should be used in both arms of the interferometer, and an interferometer based on this principle was introduced by Oriel Corp in 1997.

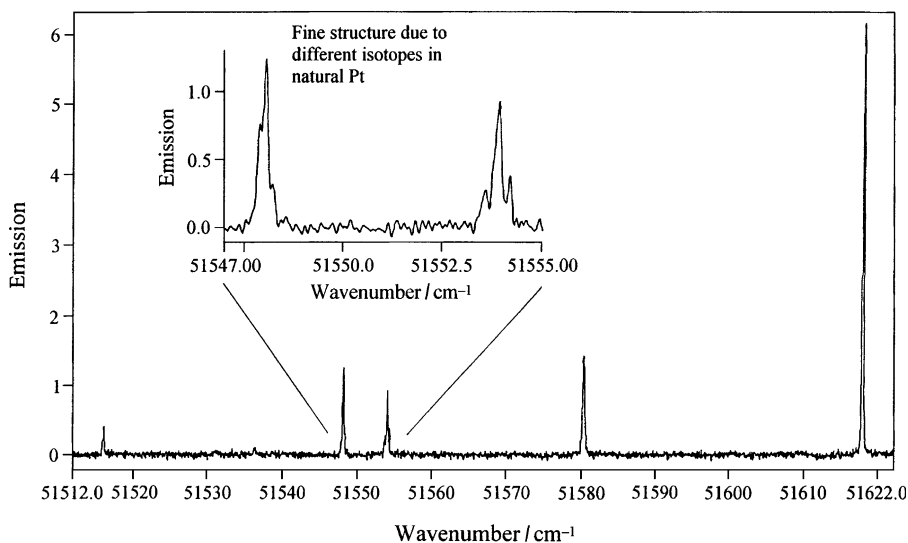


**Figure 5.13.** Near-infrared spectrum of  $\text{N}_2\text{O}$  measured at a resolution of  $0.01\text{ cm}^{-1}$  on a Bruker 120 HR equipped with an InSb detector. (Reproduced by permission of Bruker Optics.)

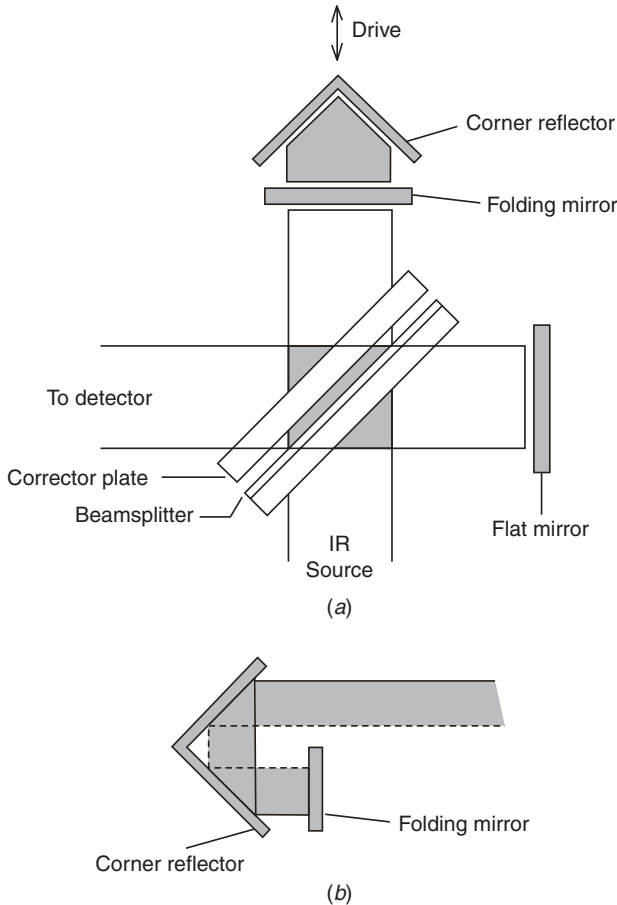


**Figure 5.14.** Anallect Multisept interferometer, incorporating the design described by Steel [3]: (a) plan view; (b) side view. (Originally reproduced by permission of the Anallect Instruments Division of Laser Precision Corporation.)

An interesting variation on this design that eliminates the problem of shear was patented by On-Line Technologies (now part of MKS) (see Figure 5.15). One arm of their interferometer incorporates the same moving cube corner/plane mirror pair seen in Figure 5.14. The other side of the plane mirror is used for the second beam. The double-sided mirror ensures that the beams that are reflected from its surface remain parallel to each other, further minimizing the effect of tilt and shear. Because these components provide both tilt and shear immunity, their precise position on an interferometric scale is not important and they may be mounted flexibly on a frame to isolate them from thermal, mechanical, and gravitational stresses that may be introduced by the frame. The self-compensation in the cube corner makes the system immune to tilt and shear inaccuracies in the mirror drive. The

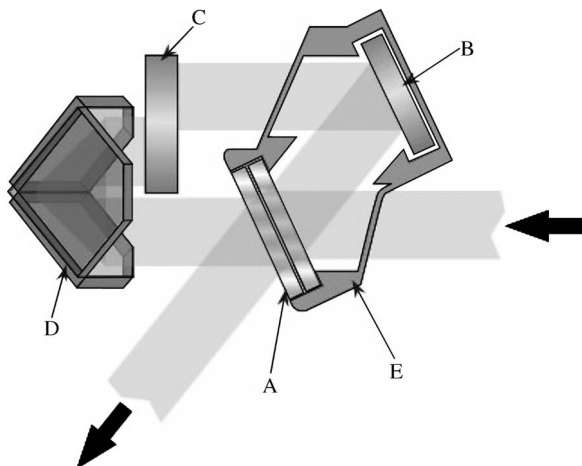


**Figure 5.15.** Construction of an interferometer manufactured by On-Line Technologies. Radiation hits the beamsplitter (A) and is reflected to a cube-corner retroreflector (D) onto one side of a moving double-sided mirror (C). The beam that is transmitted through the beamsplitter is reflected from a fixed mirror (B) to the other side of the moving double-sided mirror (C). (Reproduced from [5], by permission of John Wiley & Sons, Ltd.; copyright © 2002.)

cube-corner retroreflector is attached to the top of a flexing parallelogram that is allowed to change shape by the flexure pivots in each corner so that the cube-corner moves parallel to its original position. A dynamic balance is achieved by mounting the parallelogram by flexures E and F at the midpoints of the parallelogram ends and by proper location of the centers of gravity of the top and bottom.

The few disadvantages of the cube-corner interferometer can also be ameliorated by a clever modification known as the double-pendulum interferometer, first described by Rippel and Jaacks in 1987 [18]. In this interferometer, shown schematically in Figure 5.16, the two cube-corner retroreflectors are rigidly coupled so that a displacement of  $x$  leads to an OPD of  $4x$ . Because of the rotating motion of the pendulum structure, the interferometer is insensitive to tilt and shear and is only sensitive to changes in torque. ABB-Bomem applies this design in their MB series instruments. These instruments have proved their worth under a variety of conditions, including severe vibration. In fact, the first time the authors saw a Bomem MB-100 spectrometer, it was operating on top of an unbalanced clothes drier! Monitoring industrial processes seems almost trivially simple by comparison.

Bruker has designed a variation of the double-pendulum interferometer that reduces the effect of shear in comparison to the double-pendulum design of the Bomem interferometer. The major differences from the standard double-pendulum design are the inclusion of a flat folding mirror in each arm of the interferometer and the fact that the center of mass of the pendulum coincides with the pendulum axis (see Figure 5.17). The folding mirrors permit a very compact design and allow the interferometer to be aligned without having to adjust the beamsplitter or one of the moving optical elements. Alignment of a stationary mirror is possible in some

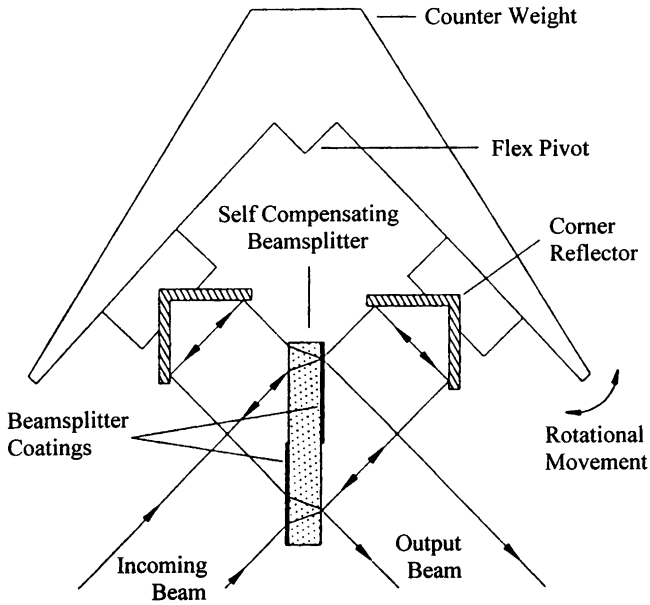


**Figure 5.16.** Double-pendulum interferometer of the type first described by Rippel and Jaacks [18] and used by ABB-Bomem in their MB series instruments.

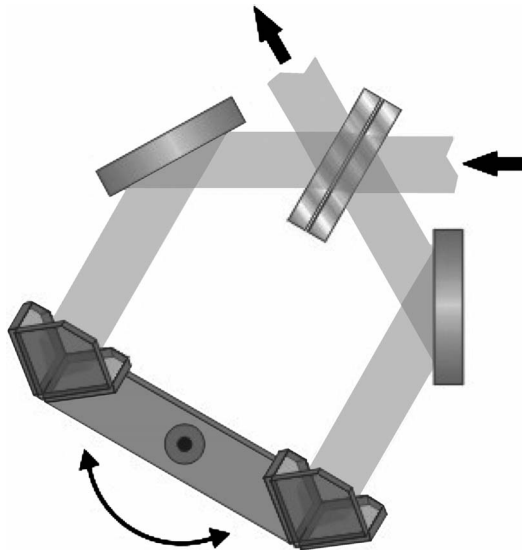


**Figure 5.17.** Double-pendulum interferometer used in many of the instruments manufactured by Bruker. (Reproduced from [5], by permission of John Wiley & Sons, Ltd.; copyright © 2002.)

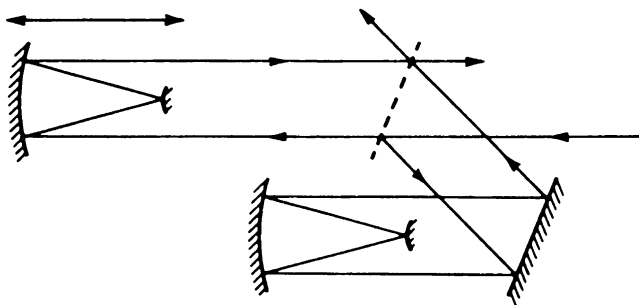


**Figure 5.18.** Cat's-eye interferometer employed in many early high-resolution interferometers made by Connes and other French spectroscopists. (Reproduced from [3].)

double-pendulum designs that use retroreflectors and flat mirrors, but in this case the clear aperture is only half the area of the retroreflector. Placing the center of mass within the pendulum axis eliminates unwanted torque on the bearing and makes the interferometer relatively immune to velocity errors caused by vibration since the pendulum is symmetric about the axis and external forces tend to affect both arms equally. The bearing itself consists of two flex pivots that are spatially separated on the same axis (the pendulum axis). This design provides very high rigidity, except in the desired rotational axis, so that mirror shear effects are eliminated. The effect of mirror tilt is, of course, eliminated through the use of cube corners.

The use of cube-corner retroreflectors has the disadvantage of requiring quite delicate initial alignment and introducing some polarization effects (although the greatest source of polarization is generally the beamsplitter; see Section 5.7). To get around these problems, *cat's eyes* have been used as retroreflectors in high-resolution FT-IR spectrometers. These devices usually consist of a concave (often paraboloidal) mirror with a convex spherical mirror to image the beamsplitter back on itself at zero retardation. The principle of the cat's-eye interferometer is shown in Figure 5.18. Many of the first high-resolution FT-IR spectrometers made in France in the 1960s and 1970s by Pierre Connes [19] (and subsequently by several scientists who received their training in his laboratory [20,21]) incorporated cat's-eye retroreflectors. The remarkable data measured on these instruments attests to the success of the cat's eyes in compensating for the effect of mirror tilt.

### 5.2.2. Other Designs

Perkin-Elmer (now PerkinElmer) (PE) Corporation designed several types of tilt-compensated interferometers for their FT-IR spectrometers. All of these interferometers operate on a similar principle, which was first described by Sternberg and James in 1964 [22]. In these interferometers, two or more mirrors are mounted on a common base plate which is rotated to give rise to the path difference in two arms of the interferometer.

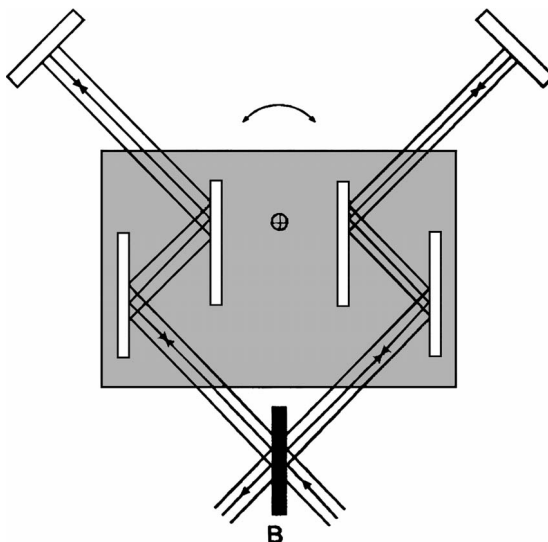


**Figure 5.19.** Principle of the interferometer incorporated in the PerkinElmer GX spectrometer.

For example, the interferometer in the PE Spectrum GX (and previously in the PE System 2000 and Spectrum 2000) spectrometers is represented schematically in Figure 5.19. Four plane mirrors are mounted on a *tilt table*. As this table is rotated, the optical path is increased in one arm of the interferometer and decreased in the other. Each beam is reflected from the fixed plane mirror at  $90^\circ$  and returns to the beamsplitter along exactly the same path. Any misalignment of the tilt table will cause each beam to be affected in the same way, so the effect of the tilt of the mirrors on the tilt table is compensated. Although the effect of thermal expansion of the rotating assemblies is compensated, expansion of the optical bench on which the stationary plane mirrors of these interferometers are mounted is not. If the angle between the stationary mirrors changes, some misalignment of the interferometer can result.

An interferometer, known as a *periscope interferometer*, was installed originally in all instruments in the PE Model 1600 series and has formed the basis of their Paragon 1000, Spectrum 1000, and Spectrum 1 series spectrometers. The path difference in this interferometer is generated by tilting a pair of mirrors, B and C, shown in Figure 5.20. The other plane mirrors (A, D, E, and F) are all fixed. The effect of tilt in the moving element is compensated by the fact that the beams passing to and from the stationary mirror follow the same path, so that any errors introduced on the outward path are compensated on the return path. Since the PE spectrometers comprising the periscope interferometer outsold all other FT-IR spectrometers in the 1990s, it is apparent that the customers of these instruments agree that this interferometer is very stable for a long time.

In an excellent paper [23], Kauppinen et al. discuss a series of related interferometers in which complementary reflections from two flat mirrors in each arm



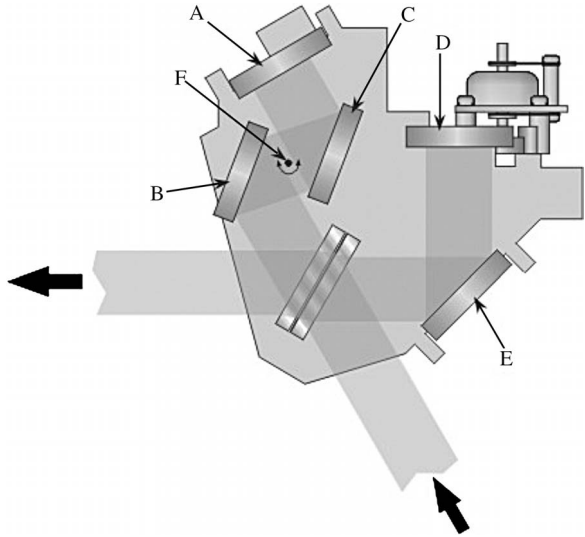


**Figure 5.20.** Interferometer incorporated in the PerkinElmer Spectrum 1 spectrometers. (Reproduced from [5], by permission of John Wiley & Sons, Ltd.; copyright © 2002.)

of the interferometer ensure that a final reflection from a plane mirror is at normal incidence. The interferometer shown in Figure 5.20 is one example of such a device. Kauppinen’s group proposed and demonstrated a variant illustrated in Figure 5.21, which also uses planar reflectors with rotational motion. It is optically

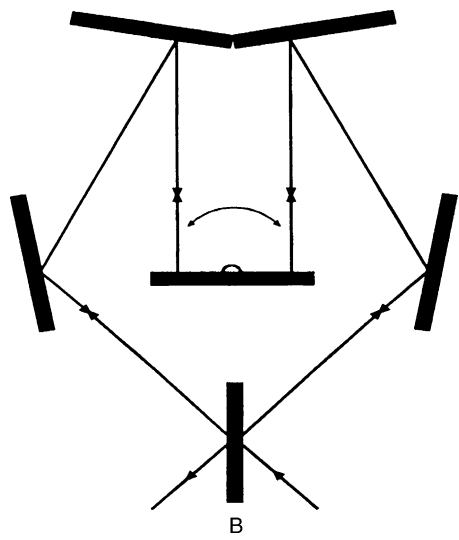


**Figure 5.21.** Interferometer designed by Kauppinen et al. (Reproduced from [23], by permission of the Optical Society of America; copyright © 1995.)

equivalent to the interferometer shown in Figure 5.20 but with the advantage that it is quite compact and resistant to deformation by thermal and mechanical stress.

A successful variant of this principle where the OPD is introduced by rotating a refractive element has been designed by Mold and Turner of PerkinElmer Ltd. [24,25]. When tested in comparison with several other tilt-compensated interferometers, this instrument had better resistance to the effects of tilt and shear than that of any other instrument tested. For example, the modulation efficiency of this interferometer in the near infrared did not change by more than 0.1% when the temperature was changed by more than 5°C [26]. This instrument has one fairly important disadvantage, however, in that it is far more expensive instrument to build than competitive designs and has not been introduced commercially.

None of the interferometers discussed previously in this chapter can be used to obtain spectra in less than about 40 ms at a resolution that is adequate for studying condensed-phase samples (e.g.,  $4\text{ cm}^{-1}$ ) since they all use a reciprocating mirror motion. As the mirror velocity is increased, the turnaround time, the time required to retard the mirror, turn it around, and accelerate it back to its operating speed, increases relative to the active scanning time. In other words, the duty cycle efficiency of the measurement decreases. For a Michelson interferometer to measure an interferogram over an OPD of 0.25 cm in 1 ms, the optical velocity is  $250\text{ cm}\cdot\text{s}^{-1}$ , and the force required to turn around a mirror weighing at least 30 g is well over 100 N. Thus, to achieve very high scan rates, it is necessary that the moving optical element rotate completely rather than in a reciprocating motion in the manner of the interferometers shown in Figures 5.19, 5.20, and 5.21.

Haschberger and Tank [27] described one approach to generating a path difference by rotating optical elements by rotating a cube-corner retroreflector mounted off-axis, as shown in Figure 5.22. Any beam impinging on the reflector will be reflected antiparallel to the incident beam, regardless of the rotation angle or shear offset. The main advantage of this design is its excellent tilt and shear compensation. An instrument based on this principle, known as the MIROR (Michelson interferometer with rotating retroreflector), has been made by the Deutschen Zentrum für Luft- und Raumfahrt. This instrument has a maximum OPD of 10 cm and can measure 180 interferograms per minute at a nominal resolution of  $0.1\text{ cm}^{-1}$ . Because the spinning retroreflectors are intrinsically unbalanced, however, it is probable that an interferometer based on this principle could not achieve complete rotations in a few milliseconds.

This limitation has been overcome in an interesting design that has been proposed and demonstrated by Manning [28] in which the optical path difference is generated by the rotation of a plane mirror in one arm of the interferometer, as shown in Figure 5.23. In order that a path difference is generated as the mirror rotates, the two regions at which the beam hits this mirror must be at different distances from the mirror's center. The fixed arm of the interferometer is of the Steel design (see Figure 5.14) for compactness and thermal stability. This rather complicated interferometer is also tilt and shear compensated. The rotating mirror is balanced by shaving an appropriate amount of material from its thicker edge. Once this mirror has reached its full angular velocity, the drive motor needs only

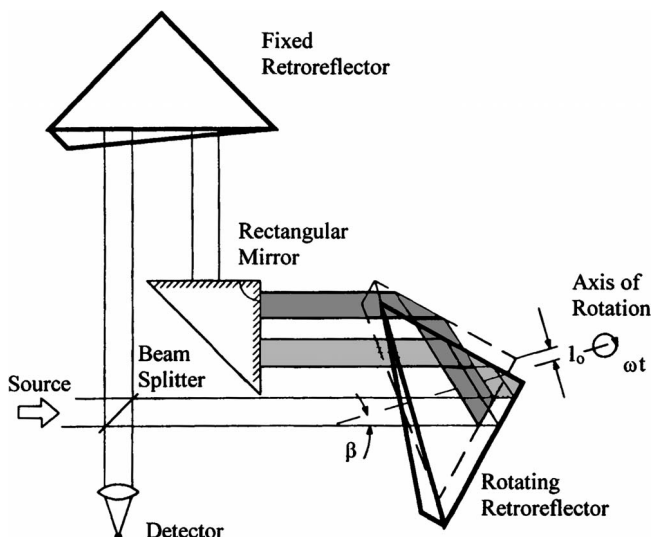


**Figure 5.22.** Interferometer described by Haschberger and Tank [27] in which the OPD is generated by rotating a cube-corner retroreflector mounted off-axis. (Reproduced from [27], by permission of the Optical Society of America; copyright © 1993.)

to supply enough power to maintain its speed, thus overcoming the main drawback of interferometers involving a reciprocating motion. Two interferograms with a maximum OPD of  $\sim 0.16$  cm are measured for each rotation of the mirror. Provided that the atmosphere around the interferometer is evacuated, angular velocities of

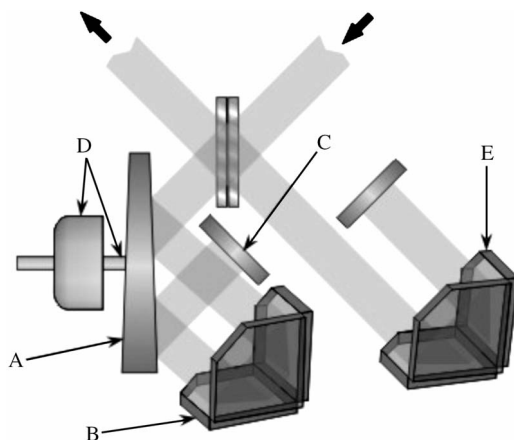


**Figure 5.23.** Rotating interferometer marketed by Manning Applied Technology. The beam passing through the beamsplitter reflects from the inner part of a beveled rotating mirror, A, to a cube corner, B, where it is reflected to the outer part of mirror A and hence to a plane mirror, C. The beam reflected from C returns along the same path to the beamsplitter. The beveled mirror is driven by the motor, D. As mirror A rotates, the OPD changes sinusoidally with time, with two interferograms being generated for each rotation of the mirror. (Reproduced from [5], by permission of John Wiley & Sons, Ltd.; copyright © 2002.)

30,000 rpm are possible with this instrument, enabling up to 1000 scans per second to be measured in principle. In its current manifestation, the infrared and laser interferograms are sampled simultaneously at 4 MHz, so that  $6\text{-cm}^{-1}$  resolution spectra are measured once every 5 ms, the speed of the ADC being the main factor that limits the rate at which interferograms can be acquired. Since advances in ADC technology are made every year, it seems only a matter of time before this instrument will be able to measure 1000 scans per second.

### 5.3. REFRACTIVELY SCANNED INTERFEROMETERS

Although most spectrometric measurements are made with small sources or samples, there are certain types of emission measurements where the source can be quite large. In particular, for measurements of twilight and night airglow, the source is very extensive and extremely weak. Thus, the SNR of the interferogram could be improved if the solid angle of the beam passing through the interferometer could be increased without sacrificing resolution. The reason that the acceptance angle for a given resolution has to be kept below a certain angle was discussed in Section 2.7. If some means of making the OPD invariant with the divergence angle of the incident beam was available, a greater throughput from an extended source could be allowed and hence a greater SNR attained.

A technique suggested by Bouchareine and Connes [29] accomplishes such *field widening* to the first order by using prisms in place of the usual mirrors in a Michelson interferometer, as shown in Figure 5.24. The back sides of the prisms are silvered and the interferometer is aligned in the same way as a typical Michelson interferometer. Instead of obtaining differential pathlengths by moving one mirror parallel with the rays of light that impinge on it, in the field-widening approach a prism is moved parallel, with its apparent mirror position inserting more material in one beam to effect an increase in retardation. *Apparent mirror position* refers to the apparent position of the coated back surface of the prism, looking through the optical material. Thus, the direction of the drive is perpendicular to the light rays. It can be shown that provided that the prism has the correct dimensions and is properly aligned, the retardation is independent of the incident angle, so that angles larger than  $(\Delta\tilde{\nu}/\tilde{\nu}_{\max})^{1/2}$  radians can be tolerated. To allow the solid angle of the beam to be increased in this manner, prisms giving wavelength distortions of less than  $\lambda/10$  across the full travel of the prism are required. The prisms are quite large. For example, for measurements in the visible region of the spectrum, the wedge angle of the quartz prisms is  $\sim 8^\circ$  and the retardation  $\delta$  achieved by moving one prism a distance of  $x$  centimeters is only  $0.21x$  centimeters.

Maintaining accurate positioning of the prism over the entire length of a scan required to yield a  $1\text{-cm}^{-1}$  resolution spectrum presented a real problem in stability. The base of the interferometer had to be constructed of granite and the optical carrier was made of stainless steel and invar, the low-expansion coefficient of which is close to that of granite and quartz. Nonetheless, the sensitivity of measurements of extended sources made with this type of interferometer could be up to 20 times

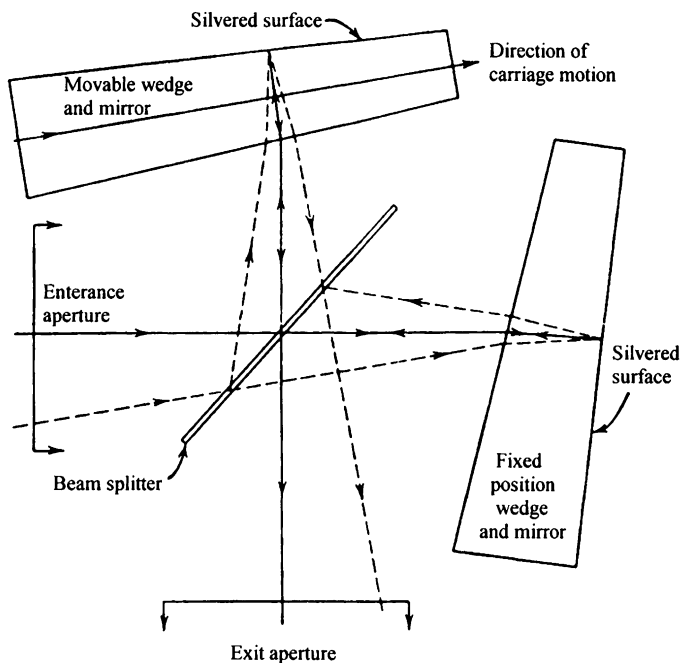


**Figure 5.24.** Field-widened interferometer designed by Bouchareine and Connes [29]. The movable rear-silvered mirror is translated in a direction perpendicular to that of a conventional Michelson interferometer, so that the OPD is increased by increasing the distance traveled through the prism. (Originally reproduced from [29], by permission of the author.)

higher than that of the spectrum of the same source measured with a standard Michelson interferometer.

The principle of moving a refractive optical element instead of a mirror also lies behind the design of the Transept or Doyle interferometer, designed by Doyle at Analect Instruments and now marketed by Applied Instrument Technologies Division of Hamilton Sundstrand [30]. The design of this interferometer is shown in Figure 5.25. Note that the substrate and compensator plate of the beamsplitter are wedge shaped, and the compensator plate is scanned to increase the optical path in one arm of the interferometer. The use of cube corners reduces the criticality of motion control and position measurement of the moving element and reduces the amount of angular alignment needed for the bearing. Because of its design, this interferometer achieves a modest amount of field widening, with an improvement over a conventional Michelson interferometer by a factor approximately equal to  $n^2$ , where  $n$  is the refractive index of the moving wedge. This allows the aperture of the interferometer to be reduced without a loss of optical throughput. Like the field-widened interferometer of Bouchareine and Connes, however, the moving wedge must be translated much more than the retardation. For a wedge angle of  $10^\circ$ , the wedge must be moved about four times farther than the moving mirror of a Michelson interferometer to achieve the same OPD.

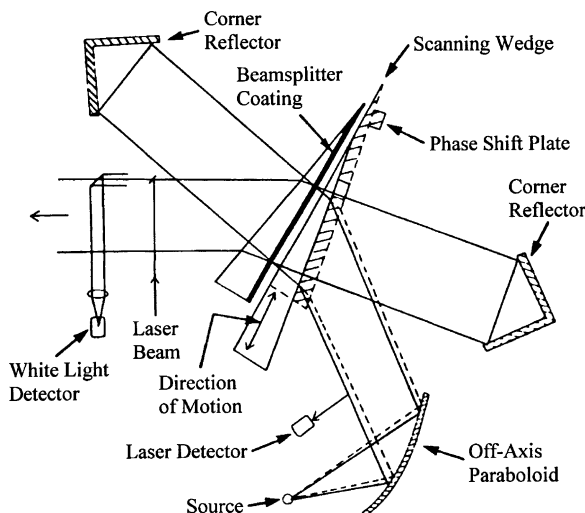


**Figure 5.25.** Refractively scanned interferometer designed by Doyle. (Originally reproduced by permission of the Analect Instruments Division of Laser Precision Corporation.)

One potential disadvantage of refractively scanned interferometers is the effect of dispersion on the wavenumber accuracy. However, the variation of  $n$  with wave-number is known and this effect can be compensated accurately by the appropriate software. This disadvantage is more than offset by the fact that the stationary cube corners in each arm of the interferometer give it a remarkable immunity from the effects of tilt and shear. As a result, this interferometer is often used for process monitoring by FT-IR spectrometry. This interferometer has been installed as the key component of process monitors in well over 100 plants.

Refractively scanned interferometers are by no means new. Jamin described such an interferometer as early as 1856 [31]. In a superb monograph entitled *Transformations in Optics*, that was published over 40 years ago [32], Mertz remarked that the output beam of a folded Jamin interferometer, shown in Figure 5.26, has remarkable immunity to the effects of tilt and shear. (In fact, only beam  $O_2$  has such immunity, but that is enough.) Mertz apparently had a premonition of potential problems with the folded Jamin design, however, as he noted that the angular acceptance for such interferometers was not known. Ray-tracing calculations have subsequently shown that although the acceptance angle in the plane of the figure is at least as high as that of a Michelson interferometer, the acceptance angle in the perpendicular plane is essentially zero away from ZPD [26].

#### 5.4. POLARIZATION INTERFEROMETERS

Several types of interferometer have been described that are based on the properties of polarized radiation. The first instrument based on this principle was designed for

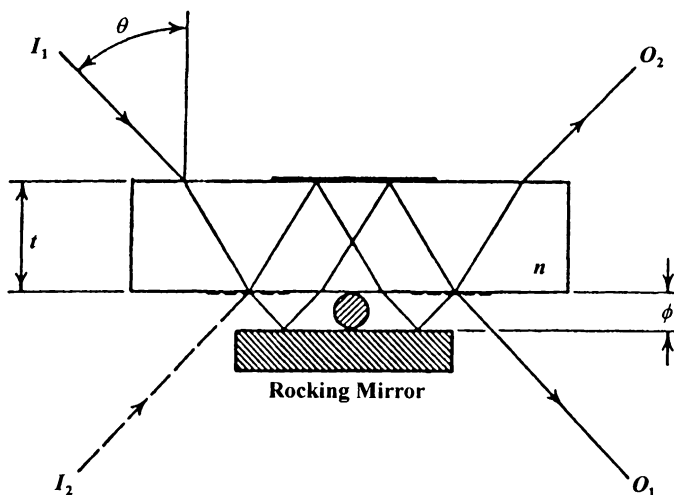


**Figure 5.26.** Jamin interferometer, where the OPD is introduced by rotating the rocking mirror. (Reproduced from [32], by permission of John Wiley & Sons; copyright © 1965.)

far-infrared spectroscopy by Martin and Puplett [33] and can be most readily understood from the diagram shown in Figure 5.27. A collimated beam is plane polarized at  $P_1$  in the plane at  $45^\circ$  to the normal of this page. It is then divided by a flat wire-grid polarizer,  $D_1$ , into beam A, polarized with its electric vector normal to the paper, and B, polarized at  $90^\circ$  to A. A and B are then recombined at the wire grid,  $D_2$ , and the combined beam finally passes through polarizer  $P_2$ , the axis of which may be either parallel or perpendicular to  $P_1$ .

For a monochromatic source, the beam is elliptically polarized after recombination at  $D_2$ , with an ellipticity varying with increasing path difference between A and B. After  $P_2$ , the beam is plane polarized with an amplitude that varies periodically with path difference. For an unpolarized light source, the intensity is given by exactly the same expression as the interference record for a Michelson

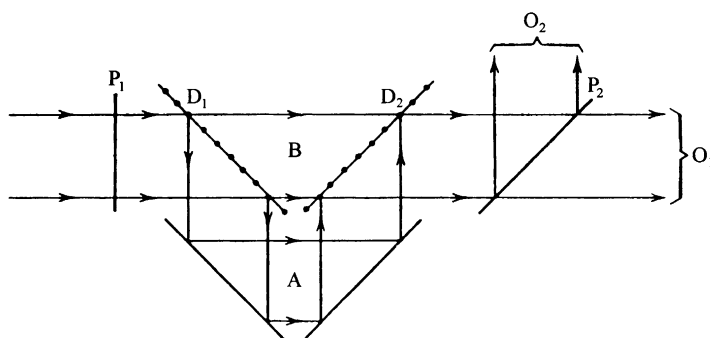


**Figure 5.27.** Martin-Puplett interferometer.

interferometer (Eq. 2.3) if  $P_1$  and  $P_2$  are oriented in parallel. If  $P_1$  and  $P_2$  are crossed, the sign in Eq. 2.3 is changed (i.e., the behavior is the same as for the beam that returns to the source for a Michelson interferometer). Interferometers based on this concept have very high efficiency for far-infrared spectrometry and have been used for measurements from 2 to  $700\text{ cm}^{-1}$  [34].

There is only one polarization interferometer that is commercially available today and that is the one originally made for near-infrared spectrometry by Bühler Instruments and Bran + Luebbe, now marketed by Büchi [35]. In this spectrometer, the radiation from a halogen source is polarized before being passed to two birefringent prisms, one of which is fixed and the other of which moves. The output from these prisms is passed to an analyzing polarizer where the interferogram is generated. The principle of operation of the Bühler interferometer is not dissimilar to that of the Martin–Puplett interferometer, but the instrumental tolerances are far stricter. For a detailed discussion of polarization interferometers, the book edited by Polavarapu [36] is strongly recommended.

## 5.5. STEP-SCAN INTERFEROMETERS

There are several types of measurements for which standard rapid-scanning interferometers may be inappropriate. These include hyperspectral imaging (Section 14.5), high-speed time-resolved spectrometry (Section 19.2), photoacoustic spectroscopy (Section 20.3), and sample modulation spectroscopy (Chapter 21). For these measurements it is necessary to hold the optical path difference constant while a measurement is made, after which the OPD is rapidly advanced to the next sampling position and then held constant once again for the next measurement. This process is repeated until all the data needed to obtain the interferogram are acquired. Such interferometers are called *step-scan interferometers*.

Many measurements of far-infrared spectra made in the 1960s were carried out using primitive step-scan interferometers, where the mirror position was controlled by a shaft encoder. The high-resolution step-scan interferometers built in the late 1960s and 1970s by Pierre Connes and his school in France, used largely for near-infrared spectrometry, involved a far more sophisticated drive mechanism, as might be expected in light of the fact that the position of the interferometer mirrors had to be controlled to about 100 times finer tolerances because of the difference in wavelengths in the near and far infrared. The step-scan interferometers that are commercially available today are closely related to the latter type of interferometer. However, unlike the Connes-type interferometers, most contemporary interferometers, after a few simple changes, can also be used in the rapid-scanning mode.

The SNR of spectra measured interferometrically is determined in part by how accurately the position of the moving mirror is known (see Eq. 7.12). Many measurements made using a step-scan interferometer require the OPD to be held constant to better than 1 nm (just a few atomic diameters!). To achieve this goal, the interference record from the HeNe laser must be measured. The points that correspond to the zero crossings of the laser interferogram are the points where the slope



of the interference record is the steepest. Thus, any changes in OPD are sensed far more accurately by holding the movable mirror constant at this position than, say, at the point where the slope of the interference record is zero. The way that this is achieved by each of the manufacturers of step-scan interferometers at the time of this writing is slightly different. Suffice it to say that each of them (Bruker, Varian, and Thermo-Electron) achieves the specification that the root-mean-square positional uncertainty is better than 1 nm.

Ideally, time-resolved and imaging measurements require that the OPD be held precisely constant at each sampling point. On the other hand, for photoacoustic and most sample modulation measurements, the position of one of the interferometer mirrors is varied sinusoidally with an amplitude of one, two, or more wavelengths of the HeNe laser by a piezoelectric transducer while the average position is held constant at each sampling point. This mode of operation is called *phase modulation*.

For phase-modulation measurements, the detector signal is demodulated (either using a lock-in amplifier or by digital signal processing) to obtain the amplitude of the detector signal at each sampling point. The signals that are in phase with and  $90^\circ$  out of phase (quadrature) to the phase modulation are both demodulated and the values of the amplitudes of the in-phase and quadrature signals are stored at each sample point. For a monochromatic line measured by an ideal interferometer, the conventional interference record is a biased cosine wave (see Eq. 2.3). For low-amplitude phase modulation, the corresponding signal is the first derivative of the interference record. Thus, for an ideal phase-modulated interferometer measuring a line source, the interferogram is a sine wave centered about zero, rather than a cosine wave. In any event, the spectrum from phase-modulated interferograms can be obtained by taking the complex Fourier transform of the interferogram.

## 5.6. STATIONARY INTERFEROMETERS

Some interferometers have been designed where the beam is dispersed across a linear array detector so that the interferogram is measured simply by reading the signal at each detector element without scanning any type of optical element. Such *stationary interferometers* are very attractive, as there are no moving parts and hence they are not susceptible to velocity errors.

The design of most stationary interferometers is based on the common-path, or Sagnac [37,38], interferometer. Okamoto et al. [39] reported a design based on the Sagnac interferometer that is shown in Figure 5.28. Other interferometers involving a similar design had been described previously in papers by Stroke and Funkhouser [40], Yoshihara and Kitada [41], and Kamiya et al. [42]. These interferometers have been used for a variety of applications where the signal is low but have not been used for conventional mid- or near-infrared spectrometry where spectra must be measured with a very high SNR. One possible reason for this is that it is unlikely that stationary interferometers have the same stability as scanning interferometers since the position of the beam at each pixel is so sensitive to the angle between the mirrors  $M_1$  and  $M_2$ .

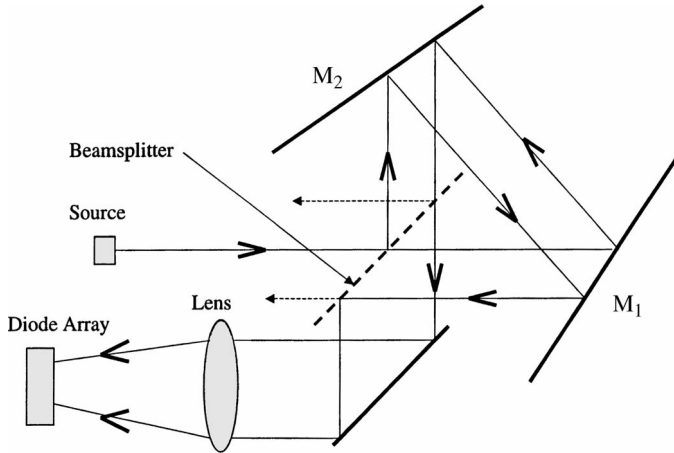


**Figure 5.28.** Typical design of a Sagnac interferometer.

Rafert et al. [43] and Dierking and Karim [44] have reported monolithic designs for the common-path interferometer that should minimize this problem. These devices are shown schematically in Figures 5.29 and 5.30, respectively. Rafert's design can accept an angle of  $8^\circ$  in the plane of the interferometer, and in the perpendicular plane the acceptance angle can be as large as  $16^\circ$  (although this may be difficult to achieve in practice). Thus, this interferometer allows significant field widening with respect to a Michelson interferometer with a beamsplitter of equal area. The expected gain in SNR is rarely achieved in practice, however. For example, Dierking and Karim [44] showed spectra of a low-pressure mercury lamp and a light-emitting diode measured in equal times on their instrument and a conventional spectroradiometer, for which the SNR and resolution of the spectra measured on each instrument are approximately equal. Results such as this suggest that from the standpoint of sensitivity, there is no major advantage to using a monolithic Sagnac interferometer.

Little has been published concerning the sensitivity and instability of stationary interferometers. Where spectra have been shown, their quality appears to be poorer than that of analogous data measured on scanning interferometers (and sometimes even monochromators), in terms of both SNR and resolution. There are several possible reasons for the low sensitivity of these instruments. First, since the interference record rather than the interferogram is being measured, the responsivity of every pixel of the detector must be identical (to better than  $\sim 10$  ppm). In practice, this specification is extremely hard to achieve, so the variation in pixel response must first be measured and then be corrected digitally. Furthermore, with high incident light levels, the response of any quantum detectors will almost certainly be nonlinear, leading to photometric errors (see Section 8.6). The final and most fundamental concern relates to the problem of *multiplicative noise*, caused by the fact that the interference record (i.e., the dc and ac signals) is measured by a stationary interferometer, whereas only the ac signal is measured by a rapid-scanning

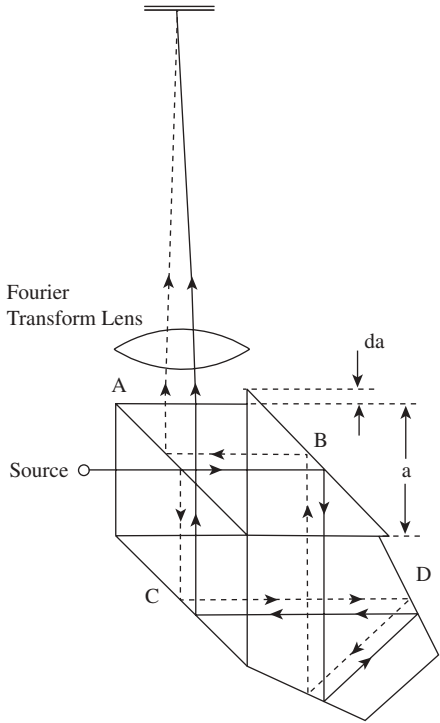


**Figure 5.29.** Monolithic common-path interferometer designed by Rafert et al. (Reproduced from [43], by permission of the Optical Society of America; copyright © 1995.)

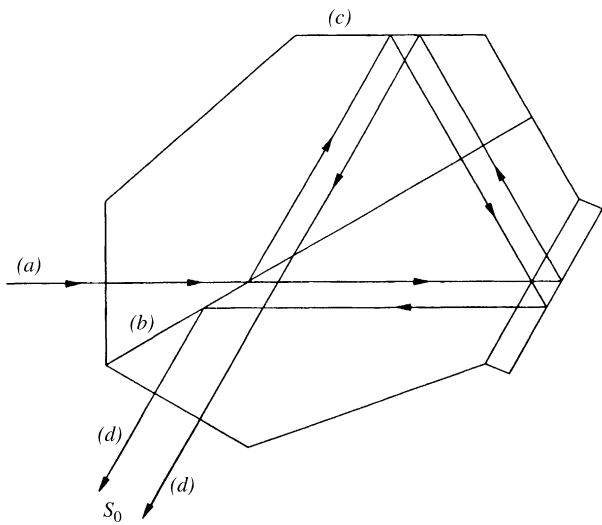


**Figure 5.30.** Monolithic common-path interferometer designed by Dierking and Karim. (Reproduced from [44], by permission of the Optical Society of America; copyright © 1996.)

interferometer. For conventional measurements (where a noise level of less than 1 milliabsorbance unit is usually desired), the stability of every component of the common-path interferometer must be better than 10 ppm if multiplicative noise is to be avoided. With rapid-scanning interferometers this problem is ameliorated because the dc component is filtered out and the dynamic range in the wings of an interferogram is *much* less than that of an interference record.

The two most important factors that would lead to multiplicative noise are short-term variations in the integrated intensity of the source and variation of the responsivity of the detector elements with temperature. The temperature of each of these components would have to be controlled to the point that both the source intensity and detector responsivity would need to be stable to better than 10 ppm. The positions of every mirror and/or lens in the optical train and the concentration of water vapor would also have to be controlled carefully. Thus, in practice there are very few applications where the use of a stationary interferometer would seem to be beneficial in the laboratory. One area where they may be advantageous is for satellite sensing, where the high readout speed of array detectors would allow the spectrum of very small areas of Earth to be measured, and the use of a two-dimensional array detector would allow spatial and spectral resolution to be attained simultaneously. It should be noted, however, that stationary interferometers are limited in their resolution, especially at the longer wavelengths. The problem lies in the available sizes of one- or two-dimensional arrays. At the short wavelengths, such as the visible or short-wavelength near infrared ( $\lambda < 1.25 \mu\text{m}$ ), reasonably large arrays are economically attractive and technically feasible. As the wavelength becomes longer, linear arrays beyond 1024 pixels are not available at the time of this writing, to the best knowledge of the authors. Even if the centerburst were placed at one end of the array, which would preclude double-sided phase correction, the resolution would only be about  $16 \text{ cm}^{-1}$ .

There are more subtle problems associated with interferometers of this type. Retardation is dependent on dispersion of the beam from the optical center of the interferometer. Unfortunately, this is not a linear function and retardation increases rapidly with dispersion. As a consequence, the interferogram may be sampled appropriately at the optical center of the interferometer, but at the extremes of the dispersion, the sampling interval is too large. This is a serious effect from which even relatively low-resolution stationary interferometers suffer. To complicate matters even more, the effect of dispersion is wavelength dependent, and longer wavelengths are affected to a greater extent than short wavelengths. For example, in some designs of stationary interferometers for long-wavelength measurements ( $1.1 < \lambda < 2.5 \mu\text{m}$ ), a 512-pixel linear array would be expected to yield a resolution of about  $64 \text{ cm}^{-1}$  if the centerburst were placed in the center of the array. In practice, the actual resolution ranges from about 160 to  $200 \text{ cm}^{-1}$ .

Stationary interferometers that are used for two-dimensional imaging have the added criterion that the detector array must be aligned exactly with the entrance slit to the interferometer. An imaging stationary interferometer has a slit instead of a circular aperture. If the slit and the array are not aligned exactly, the interferograms are spread across more than one row or column of the array detector and serious data loss occurs.

## 5.7. BEAMSPLITTERS

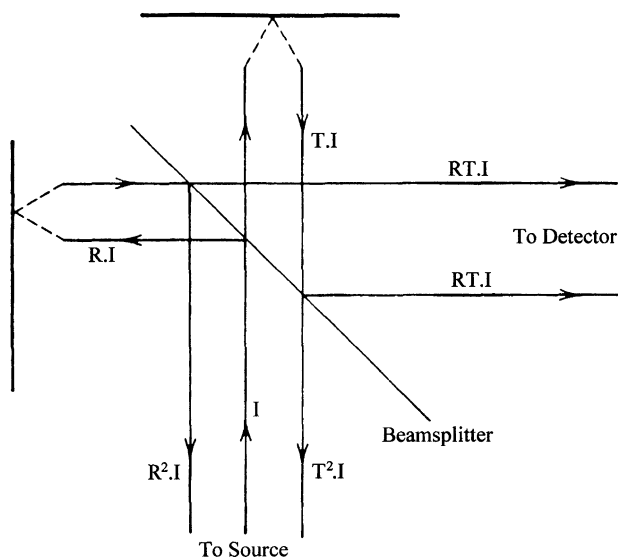
The performance of the beamsplitter is of vital importance to the successful operation of most FT-IR spectrometers and we consider the design and performance of beamsplitters in this section. Consider a beam of monochromatic radiation at wavenumber,  $\tilde{\nu}$ , entering a two-beam interferometer. Let the intensity of the radiation be  $I(\tilde{\nu})$  and let the reflectance and transmittance of the beamsplitter be  $R_{\tilde{\nu}}$  and  $T_{\tilde{\nu}}$ , respectively. For a beamsplitter that absorbs no radiation,  $R_{\tilde{\nu}} + T_{\tilde{\nu}} = 1$ . As mentioned in Section 2.2, an ideal beamsplitter is one for which  $R_{\tilde{\nu}}$  and  $T_{\tilde{\nu}}$  are equal to 0.5 across the entire spectrum that is measured. Usually, however, either  $R_{\tilde{\nu}}$  or  $T_{\tilde{\nu}}$  is slightly greater than 0.5, which has the effect of reducing the beamsplitter efficiency.

Figure 5.31 shows the intensity of the various beams in the interferometer *if no interference effects occur*. The intensity of the beam transmitted to the detector (the dc component of the interference record; see Section 2.2),  $2R_{\tilde{\nu}}T_{\tilde{\nu}}$ , is always less than  $(R_{\tilde{\nu}}^2 + T_{\tilde{\nu}}^2)$ , except when  $R_{\tilde{\nu}} = T_{\tilde{\nu}} = 0.5$ , which is the case of the ideal beamsplitter. In order that there be no energy loss at the beamsplitter, the sum of the intensities of the beam passing to the detector and the beam returning to the source must be equal to  $I(\tilde{\nu})$ . This is easily verified as follows:

$$2R_{\tilde{\nu}}T_{\tilde{\nu}}I(\tilde{\nu}) + (R_{\tilde{\nu}}^2 + T_{\tilde{\nu}}^2)I(\tilde{\nu}) = (R_{\tilde{\nu}}^2 + 2R_{\tilde{\nu}}T_{\tilde{\nu}} + T_{\tilde{\nu}}^2)I(\tilde{\nu}) \quad (5.2)$$

$$= (R_{\tilde{\nu}} + T_{\tilde{\nu}})^2 I(\tilde{\nu}) \quad (5.3)$$

$$= I(\tilde{\nu}) \quad (5.4)$$



**Figure 5.31.** Modified ray diagram of a Michelson interferometer in which the beams traveling in opposite directions have been separated for clarity. If radiation of intensity  $I$  enters the interferometer, the dc intensity of the beam transmitted to the detector is  $2RTI$  and the dc intensity of the beam returning to the source is  $(R^2 + T^2)I$ .

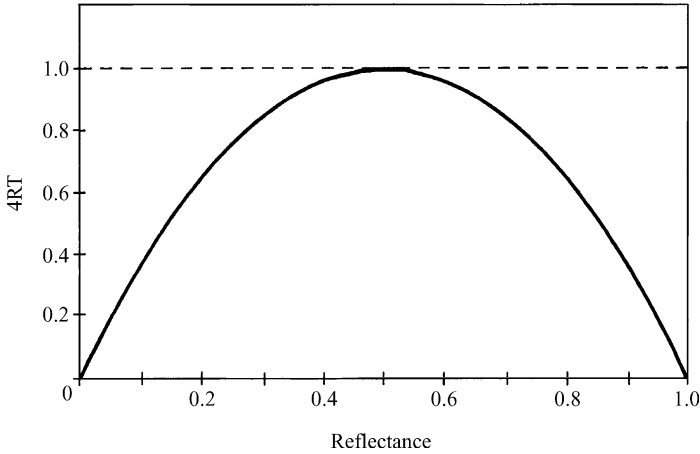


**Figure 5.32.** Variation of the beamsplitter efficiency,  $4RT$ , with reflectance,  $R$ , assuming that the beamsplitter does not absorb any of the incident radiation. Provided that  $0.28 \leq R \leq 0.72$ , the beamsplitter efficiency exceeds 80%.

Unlike the dc component, the modulated (ac) component of the interference record must be identical for both beams (by the principle of conservation of energy). Since  $2R_{\tilde{v}}T_{\tilde{v}} \leq (R_{\tilde{v}}^2 + T_{\tilde{v}}^2)$ , it should not be too surprising that the amplitude of the ac component of both beams is  $(2R_{\tilde{v}}T_{\tilde{v}})I(\tilde{v})$ .

The beamsplitter efficiency,  $\eta(\tilde{v})$ , is defined as  $4R_{\tilde{v}}T_{\tilde{v}}$ . The variation of  $\eta(\tilde{v})$  with  $R_{\tilde{v}}$  for a nonabsorbing beamsplitter is shown in Figure 5.32. It can be seen that  $\eta(\tilde{v})$  is equal to unity (100%) when  $R_{\tilde{v}} = T_{\tilde{v}} = 0.5$ , which was the case for the ideal beamsplitter discussed in Section 2.2. Provided that  $0.28 \leq R_{\tilde{v}} \leq 0.72$ , the beamsplitter efficiency exceeds 80%. The practical achievement of efficiencies this high across the entire spectral range is one of the major accomplishments of beamsplitter manufacturers.

The reflectance of materials is governed by the Fresnel equations, which give  $R_p$ , the reflectance of radiation whose electric field is polarized parallel to the plane of incidence ( $p$ -polarization) and  $R_s$ , the reflectance of radiation whose electric field is polarized perpendicular to the plane of incidence ( $s$ -polarization) as

$$R_p = \frac{\tan^2(\theta - \theta')}{\tan^2(\theta + \theta')} \quad (5.5)$$

$$R_s = \frac{\sin^2(\theta - \theta')}{\sin^2(\theta + \theta')} \quad (5.6)$$

where  $\theta'$  is the angle of refraction inside the material.

The type of material from which good beamsplitters are made should have a fairly high refractive index. An obvious candidate is germanium, for which the refractive index,  $n$ , is  $\sim 4.0$ . For germanium at  $45^\circ$  incidence ( $\theta = 45^\circ$ ,  $\theta' = 10^\circ$ ),

$R_p = 0.24$  and  $R_s = 0.49$ , so that  $\eta_p = 0.73$  and  $\eta_s \sim 1.00$ . Thus, even though germanium is a good material for  $s$ -polarized radiation, its efficiency for  $p$ -polarized radiation is a little low. This is why beamsplitters polarize the beam in interferometers. The situation is even worse for films of low refractive index. For example, the refractive index of poly(ethylene terephthalate) (PET),<sup>1</sup> which is commonly used as the beamsplitter for far-infrared measurements, is about 1.69. Thus, when  $\theta = 45^\circ$ ,  $\theta' = 24.7^\circ$ , in which case  $R_p = 0.019$  and  $R_s = 0.136$  ( $\eta_p = 0.075$  and  $\eta_s \sim 0.47$ ).

The ideal material for a beamsplitter would have a refractive index greater than 5. For example, if  $n = 5.0$  and  $\theta = 45^\circ$ ,  $R_p = 0.56$  and  $R_s = 0.32$ , so that  $\eta_s = 0.98$  and  $\eta_p = 0.87$ . Even if materials could be found with such high refractive indices could be found, their refractive index would have to be constant across the entire spectral range if all wavelengths are to be in phase at the same point. (The effect of dispersion on the interferogram has been called *chirping*; see Section 2.5.)

Despite the arguments made in the two preceding paragraphs, germanium, silicon, and PET were commonly used in the fabrication of beamsplitters. The trick is to make use of the interference fringes generated by thin films of these materials. Interference fringes are caused by multiple internal reflections in parallel-sided thin films and cause the reflectance to change from the values calculated from the Fresnel equations. For FT-IR spectrometry, the film thickness is selected such that the first fringe covers the spectral range of interest. PET is generally used as a self-supporting film for far-infrared measurements, whereas Ge and Si are usually deposited on flat substrates of low refractive index, such as KBr.

Let us first consider self-supporting thin-film (pellicle) beamsplitters of thickness  $d$ . Chamberlain et al. [45] have shown that the beamsplitter efficiencies for parallel and perpendicular polarized radiation are given by

$$\eta_p = \frac{4R_p T_p^2 E}{(T_p^2 + R_p E)^2} \quad (5.7)$$

$$\eta_s = \frac{4R_s T_s^2 E}{(T_s^2 + R_s E)^2} \quad (5.8)$$

where

$$T_p = (1 - R_p)^2 \quad (5.9)$$

$$T_s = (1 - R_s)^2 \quad (5.10)$$

and

$$E = 4 \sin^2(2\pi d \tilde{\nu} \cos \theta') \quad (5.11)$$

$$\equiv 4 \sin^2 \varepsilon \quad (5.12)$$

<sup>1</sup>PET is usually known by its trade names Mylar in the United States and Melinex in Europe.

where

$$\varepsilon = 2\pi d \tilde{\nu} \cos \theta' \quad (5.13)$$

The relative beamsplitter efficiency of a film for unpolarized incident radiation is simply given by the average of the values for parallel and perpendicular polarized radiation:

$$\eta = 0.5(\eta_p + \eta_s) \quad (5.14)$$

From Eqs. 5.7 and 5.8 it is seen that  $\eta(\tilde{\nu})$  will take a zero value when  $E$  is zero: that is, when  $\varepsilon = m\pi$ , where  $m = 0, 1, 2, \dots$ . Similarly,  $\eta(\tilde{\nu})$  will exhibit a maximum when  $m = \frac{1}{2}, \frac{3}{2}, \frac{5}{2}$ , and so on. The efficiency of any beamsplitter is zero at  $0 \text{ cm}^{-1}$  and returns to zero when  $\varepsilon = \pi$ . Thus, the wavenumber at which this minimum value of  $\eta$  is seen,  $2\nu_0 \text{ cm}^{-1}$ , is given by

$$2\tilde{\nu}_0 = (2nd \cos \theta')^{-1} \quad (5.15)$$

Between 0 and  $2\tilde{\nu}_0$ , the variation of  $\eta(\tilde{\nu})$  with  $\tilde{\nu}$  is symmetrical about  $\tilde{\nu}_0$ , although the actual shape of the curve is dependent on the values of  $n$  and  $\theta$ , since it is these two parameters that determine the internal reflectance in the film.

For thin films of low-refractive-index materials, the maximum reflectance,  $R_0$ , is usually found midway between  $0 \text{ cm}^{-1}$  and the location of the first minimum. Figure 5.33 shows the efficiency of a PET film as a function of  $\varepsilon$ . It can be seen

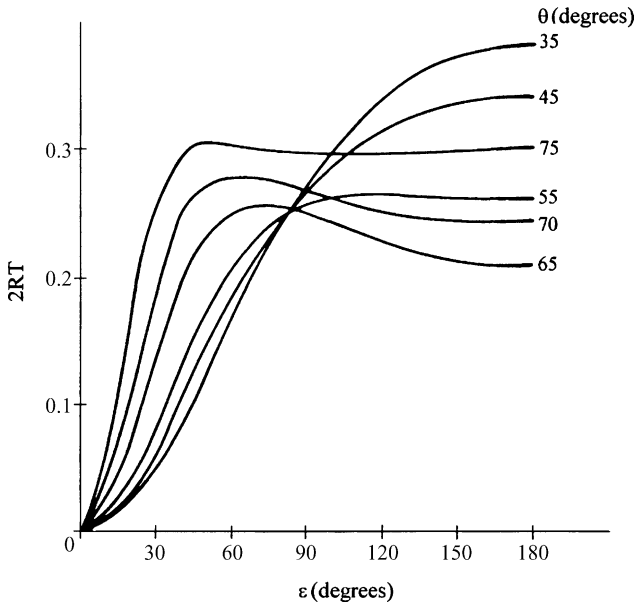


**Figure 5.33.** Variation of  $2RT$  with  $\varepsilon$  for different angles of incidence for a Mylar film. (Originally reproduced from [45], by permission of Elsevier Publishing Co.; copyright © 1966.)



**Table 5.1. Spectral Range as a Function of the Thickness of PET Films**

Film Thickness ( $\mu\text{m}$ )	Spectral Range ( $\text{cm}^{-1}$ )
6.25	80–450
12.5	40–220
25.5	20–100
50	12–50
100	8–25

that  $\eta(\tilde{\nu})$  never exceeds 0.7, primarily because of the low single-surface reflectance at  $\theta = 45^\circ$  for parallel ( $R_p = 0.02$ ) and perpendicular ( $R_s = 0.14$ ) polarized radiation. Many of the earliest far-infrared FT-IR spectrometers were equipped with PET beamsplitters, despite their low efficiency. Even today, many interferometers for far-infrared spectrometry still use this material. Table 5.1 shows the thickness of PET beamsplitters used for far-infrared spectrometry. It can be seen that the spectral range over which PET beamsplitters can be used is short, so the thickness of the film must be optimized depending on the spectral region of interest. PET beamsplitters are also quite microphonic, picking up any vibrations that are transmitted by the optical bench. When the film vibrates, the interferogram becomes unstable, which results in decreased sensitivity and poorer baselines.

With all these disadvantages, it is surprising that PET has been the material of choice as a far-infrared beamsplitter. Several other materials have been tested, including metal mesh and germanium. Germanium has good transmission throughout the far infrared and does not need to be used as a thin film to achieve a reflectance of  $\sim 50\%$ . Furthermore, the refractive index of germanium is fairly constant across the far infrared, so that chirping is not a major problem. With this in mind, two manufacturers have developed proprietary beamsplitters for far-infrared spectrometry. Nicolet developed a far-infrared beamsplitter that is comprised of a solid germanium plate that has a significantly higher efficiency than PET beamsplitters, while Bruker use a germanium film deposited on PET which has a higher efficiency than 6- $\mu\text{m}$  PET over the entire spectral range from 700 to  $20\text{ cm}^{-1}$ .

For measurements in the mid- and near-infrared, the thickness of self-supporting beamsplitters would have to be so thin that the film would be extremely fragile. Instead, materials of high refractive index are vapor-deposited on flat substrates. The transmission of the substrate is an important factor in the determination of the spectral range that can be covered. For example, if the substrate is KBr, spectra can be measured down to  $400\text{ cm}^{-1}$ . If longer wavelengths are of interest, the use of CsI is called for. The substrate must be flat to one-tenth the wavelength of the shortest wavelength of interest. Fortunately, the materials that are used for near-infrared measurements are harder than those used for mid-infrared spectroscopy. The most common substrates are listed in Table 5.2. All these materials have significant dispersion across the spectral range of interest. To avoid chirping, therefore, a compensator plate of exactly the same thickness and material as the substrate is needed.

**Table 5.2. Common Beamsplitter Substrates Used in FT-IR Spectrometry**

Substrate	Spectral Range (cm <sup>-1</sup> )
Quartz	Vacuum UV to 3,300
Calcium fluoride	14,500–1,200
Potassium bromide	14,000–400
Cesium iodide	6,400–200

Calculations of the beamsplitter efficiency of deposited films are more complex than for unsupported films, since the refractive index of the substrate and compensator plates must be taken into account. Sakai [46] has reported the efficiency of a beamsplitter comprised of a thin film of silicon on a CaF<sub>2</sub> substrate with a compensator plate of the same thickness (see Figure 5.34). This figure shows the average of the curves for  $\eta_s$  and  $\eta_p$ . It can be seen that the efficiency exceeds 0.8 for wavenumbers between about  $0.3\tilde{\nu}_0$  and  $1.7\tilde{\nu}_0$ , where  $\tilde{\nu}_0$  is the center wavenumber of the spectral range for which the beamsplitter is designed. The corresponding curve for Ge on KBr is quite similar. If this beamsplitter were to be used for measurements between, say, 400 and 4400 cm<sup>-1</sup>, the film would be deposited at a thickness such that  $\tilde{\nu}_0 \approx 2400$  cm<sup>-1</sup>. The beamsplitter efficiency would exceed 80% between

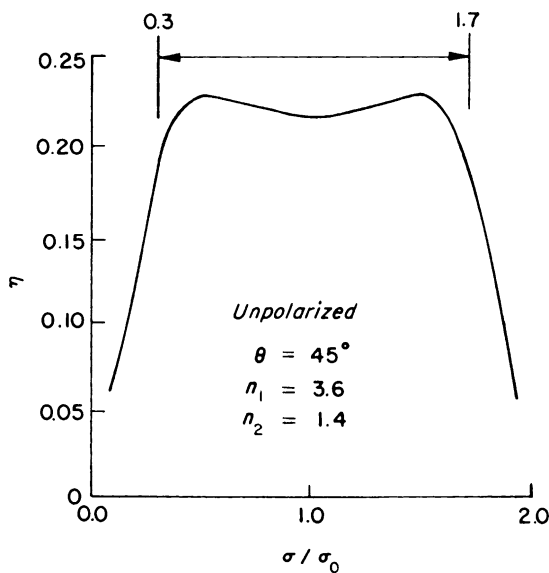


**Figure 5.34.** Variation of  $RT (= \eta)$  with wavenumber,  $\tilde{\nu}$  or  $\sigma$ , normalized to the center wavenumber,  $\tilde{\nu}_0$  or  $\sigma_0$ , for a silicon film ( $n_1 = 3.6$ ) on a calcium fluoride substrate ( $n_2 = 1.4$ ) with a CaF<sub>2</sub> compensator plate of the same thickness, with  $\theta = 45^\circ$ , calculated for the first “hoop” of the beamsplitter efficiency curve. (Originally reproduced from [46], by permission of the author.)

about  $720$  and  $4080\text{ cm}^{-1}$ , but would fall off rapidly outside this range. Thus, it is not uncommon for the performance of many of the earlier mid-infrared FT-IR spectrometers that incorporated Ge/KBr beamsplitters to be quite low, below  $600\text{ cm}^{-1}$ .

To improve the situation, many manufacturers of FT-IR spectrometers use multilayer beamsplitters where as many as 15 or more different layers are deposited sequentially on the substrate to increase the spectral coverage. At least one manufacturer has reported the development of a beamsplitter that can be used for both mid- and near-infrared measurements with an efficiency that is greater than 30% between  $10,000$  and  $400\text{ cm}^{-1}$ . The peak efficiency of these wide-range beamsplitters is, to a certain extent, sacrificed to obtain such wide coverage. However, having a single beamsplitter that can be used for the measurement of mid-infrared, near-infrared, and Raman spectra is attractive to labs on a relatively limited budget.

## 5.8. LAMELLAR GRATING INTERFEROMETERS

Despite their obvious advantages over grating monochromators for far-infrared spectrometry, Michelson interferometers still exhibit certain disadvantages for very far infrared spectrometry. The main disadvantage of the Michelson interferometer as it is conventionally used for far-infrared spectrometry is the low efficiency and limited spectral range given by the Mylar beamsplitter. On the other hand, the type of interferometer known as a lamellar grating interferometer can have an efficiency close to 100% and can operate over a wide spectral range for far-infrared spectrometry [47].

Unlike the Michelson interferometer, in which the amplitude of the radiation is divided at the beamsplitter, the lamellar grating interferometer uses the principle of wavefront division. It consists of two sets of parallel interleaved mirrors, one set that can move in a direction perpendicular to the plane of the front facets, with the other set fixed, as shown in Figure 5.35. Thus, when a beam of collimated radiation is incident onto this grating, half the beam will be reflected from the front facets, whereas the other half will be reflected from the back facets. By moving one set of mirrors, the path difference between the two beams can be varied so that an interferogram is generated. It can be seen from Figure 5.36 that essentially all the radiation from the source reaches the detector, so that the efficiency of the lamellar grating interferometer can approach 100%.

In practice, however, the efficiency falls off at high and low wavenumbers. The theoretical efficiency of a lamellar grating interferometer compared with that of a Michelson interferometer using a PET beamsplitter is shown in Figure 5.36. The cutoff at low wavenumber,  $\tilde{\nu}_L$ , is caused by the cavity effect, by which the modulation of waves for which the electric vector is parallel to the sides of the cavity starts to decrease;  $\tilde{\nu}_L$  is equal to  $(0.3a)^{-1}$ , where  $a$  is the grating constant. The reduction in efficiency at high wavenumbers,  $\tilde{\nu}_C$ , is caused by waves diffracted at the grating (which can be considered as a series of long rectangular slits) being canceled at the exit aperture;  $\tilde{\nu}_C$  is equal to  $F/aS$ , where  $F$  is the focal length of the collimator and  $S$

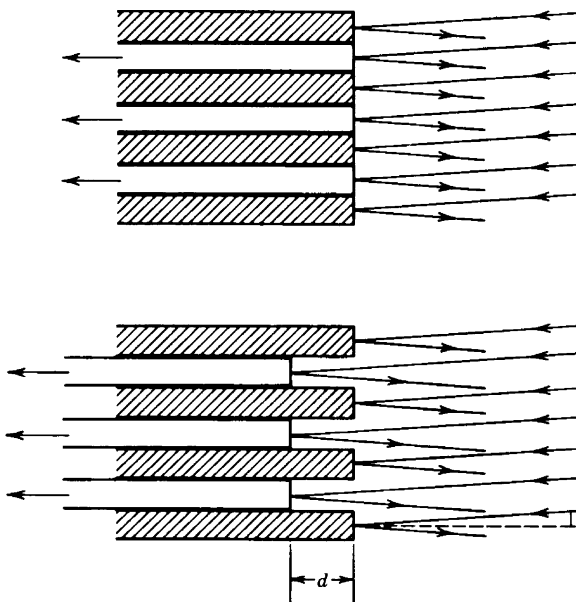


**Figure 5.35.** Principle of the lamellar grating interferometer. Radiation reflected from the movable facets travels a distance of  $2d/\cos \alpha$  farther than the radiation reflected from the stationary (shaded) facets.

is the diameter of the exit aperture. While the optical and mechanical properties of lamellar grating interferometers preclude their use much above  $150\text{ cm}^{-1}$ , they have been used successfully from  $150\text{ cm}^{-1}$  to as low as  $1.5\text{ cm}^{-1}$ . Although a lamellar grating interferometer was once available commercially, none is currently

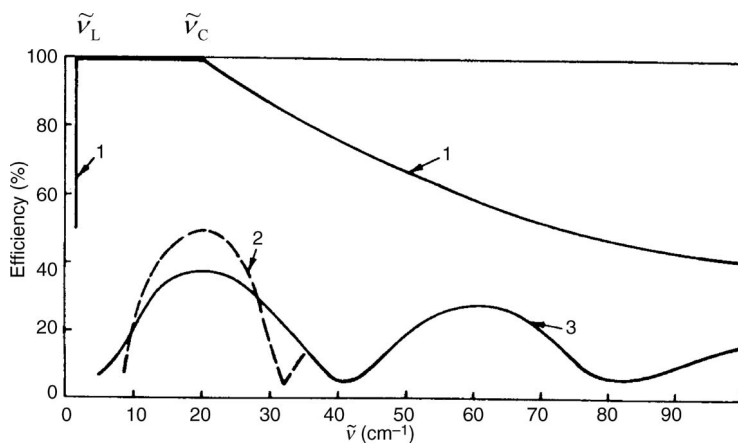


**Figure 5.36.** Comparison of the theoretical efficiency of a lamellar grating interferometer (1) and a Michelson interferometer equipped with a metal mesh beamsplitter (2) and a  $100\text{-}\mu\text{m}$  PET beamsplitter (3). (Reproduced from [47], by permission of the Optical Society of America; copyright © 1964.)

sold and spectroscopists interested in the region below  $100\text{ cm}^{-1}$  are probably better advised to use one of the recently developed terahertz spectrometers, by which far-infrared spectra can be measured at higher SNR values than by either Michelson or lamellar grating interferometers.

## REFERENCES

1. A. A. Michelson, *Philos. Mag.* **31**, 256 (1891).
2. P. Jacquinot, *Rep. Prog. Phys.* **XXIII**, 295 (1960).
3. W. H. Steel, Interferometers for Fourier spectroscopy, in *Aspen International Conference on Fourier Spectroscopy, 1970*, G. A. Vanasse, A. T. Stair, Jr., and D. J. Baker, Eds., U.S. Air Force, L. G. Hanscom Field, Bedford, MA, 1971, Vol. AFCRL-71-0019, p. 43.
4. R. Curbelo and C. Foskett, An automated interferometer spectrometer: real-time data acquisition and on-line computation to  $0.5\text{ cm}^{-1}$ , in *Aspen International Conference on Fourier Spectroscopy, 1970*, G. A. Vanasse, A. T. Stair, Jr., and D. J. Baker, Eds., U.S. Air Force, L. G. Hanscom Field, Bedford, MA, 1971, Vol. AFCRL-71-0019, p. 221.
5. R. S. Jackson, Continuous-scanning interferometers for mid-infrared spectroscopy, in *Handbook of Vibrational Spectroscopy*, J. M. Chalmers and P. R. Griffiths, Eds., Wiley, Chichester, West Sussex, England, 2002, Vol. 1, p. 264.
6. R. P. Walker and J. D. Rex, Interferometer design and data handling in a high-vibration environment, Part I: Interferometer design, in *Multiplex and/or High Throughput Spectroscopy*, G. A. Vanasse, Ed., Society of Photo-Optical Instrumentation Engineers, Bellingham, WA, 1979, Vol. 191, p. 88.
7. G. L. Auth, Ruggedized compact interferometer requiring minimum isolation from mechanical vibrations, U.S. patent 4,693,603 (assigned to MIDAC Corporation, Costa Mesa, CA, September 15, 1987).
8. R. Curbelo and D. C. Brown, Interferometer bearing assembly, U.S. patent 4,828,367 (assigned to Bio-Rad Laboratories Inc., Hercules, CA, May 9, 1989).
9. J. M. Coffin, Interferometer of an infrared spectrometer with dynamic moving mirror alignment, U.S. patent 5,883,712 (assigned to Nicolet Instrument Corporation, Madison, WI, March 16, 1999).
10. J. W. Brault, *Appl. Opt.* **35**, 2891 (1996).
11. D. Chase, *Appl. Spectrosc.* **36**, 240 (1982).
12. D. D. Weis and G. E. Ewing, *Anal. Chem.* **70**, 3175 (1998).
13. R. S. Jackson, Bruker Optics, personal communication to P. R. Griffiths (1998).
14. C. J. Manning and P. R. Griffiths, *Appl. Spectrosc.* **51**, 1092 (1997).
15. H. L. Buijs, D. J. W. Kendall, G. Vail, and J.-N. Bérubé, Fourier transform infrared hardware developments, in *1981 International Conference on Fourier Transform Infrared Spectroscopy*, H. Sakai, Ed., Society of Photo-Optical Instrumentation Engineers, Bellingham, WA, 1981, Vol. 289, p. 322.
16. M. S. Benak, Rio Grande Medical Technologies, Inc. (now InLight Solutions, Inc.), personal communication to P. R. Griffiths (1998).
17. M. V. R. K. Murty, *J. Opt. Soc. Am.* **50**, 83 (1960).

18. H. Rippel and R. Jaacks, Performance data of the double pendulum interferometer, in *Recent Aspects of Fourier Transform Spectroscopy*, special issue of *Mikrochim. Acta [Wien]*, G. Guelachvili, R. Kellner, and G. Zerbi, Eds., Springer-Verlag, Vienna, Austria 1988, Vol. III, p. 303.
19. J. Connes and P. Connes, *J. Opt. Soc. Am.* **56**, 896 (1966).
20. M. Cuisenier and J. Pinard, *J. Phys.* **28**, (1967).
21. G. Guelachvili and J.-P. Maillard, Fourier Spectroscopy from  $10^6$  samples, in *Aspen International Conference on Fourier Spectroscopy, 1970*, G. A. Vanasse, A. T. Stair, Jr., and D. J. Baker, Eds., U.S. Air Force, L. G. Hanscom Field, Bedford, MA, 1971, Vol. AFCRL-71-0019, p. 151.
22. R. S. Sternberg and J. F. James, *J. Sci. Instrum.* **41**, 225 (1964).
23. J. Kauppinen, I. K. Salomaa, and S. M. Aaronson, *Appl. Opt.* **34**, 6081 (1995).
24. A. Turner and H. M. Mould, EU patent EP 0 681 166 A1 (assigned to Perkin-Elmer Limited, Beaconsfield, Buckinghamshire, England, November 8, 1995).
25. A. Turner and H. M. Mould, Interferometer having combined beam splitter compensator plate, U.S. patent 5,808,739 (assigned to Perkin-Elmer Ltd., Beaconsfield, Buckinghamshire, England, September 15, 1998).
26. R. G. Messerschmidt, at the time with Rio Grande Medical Technologies, Inc. (now InLight Solutions, Inc.), personal communication to P. R. Griffiths (1998).
27. P. Haschberger and V. Tank, *J. Opt. Soc. Am. A* **10**, 2338 (1993).
28. C. J. Manning, Smoke and mirrors: ultra-rapid-scan FT-IR spectrometry, in *Fourier Transform Spectroscopy: 11th International Conference, 1997*, J. A. de Haseth, Ed., American Institute of Physics, Woodbury, NY, 1998, Vol. 430, p. 84; Manning Applied Technology, 419 South Main Street, P.O. Box 265, Troy, ID 83871.
29. P. Bouchareine and P. Connes, *J. Phys. Radium* **24**, 134 (1963).
30. W. M. Doyle, B. C. McIntosh, and W. L. Clarke, *Appl. Spectrosc.* **34**, 599 (1980).
31. J. Jamin, *C. R. Acad. Sci. (Paris)* **42**, 482 (1856).
32. L. Mertz, *Transformations in Optics*, Wiley, New York, 1965.
33. D. H. Martin and E. Puplett, *Infrared Phys.* **10**, 105 (1969).
34. P. A. R. Ade, A. E. Costley, C. T. Cunningham, C. L. Mok, G. F. Neill, and T. J. Parker, *Infrared Phys.* **19**, 599 (1979).
35. E. W. Ciurczak, *Spectroscopy* **20**(2), 68 (2005).
36. P. L. Polavarapu, Ed., *Principles and Applications of Polarization-Division Interferometry*, Wiley, New York, 1998.
37. G. Sagnac, *C. R. Acad. Sci.* **157**, 708 (1913).
38. G. Sagnac, *C. R. Acad. Sci.* **157**, 1410 (1913).
39. T. Okamoto, S. Kawata, and S. Minami, *Appl. Opt.* **23**, 269 (1984).
40. G. W. Stroke and A. T. Funkhouser, *Phys. Lett.* **16**, 272 (1965).
41. K. Yoshihara and A. Kitada, *Jpn. J. Appl. Phys.* **7**, 116 (1967).
42. K. Kamiya, K. Yoshihara, and K. Okada, *Jpn. J. Appl. Phys.* **7**, 1129 (1968).
43. J. B. Rafter, R. G. Sellar, and J. H. Blatt, *Appl. Opt.* **34**, 7228 (1995).
44. M. P. Dierking and M. A. Karim, *Appl. Opt.* **33**, 84 (1996).
45. J. E. Chamberlain, G. W. Chantry, F. D. Findlay, H. A. Gebbie, J. E. Gibbs, N. W. B. Stone, and A. J. Wright, *Infrared Phys.* **6**, 195 (1966).

46. H. Sakai, Consideration of the signal-to-noise ratio in Fourier spectroscopy, in *Aspen International Conference on Fourier Spectroscopy, 1970*, G. A. Vanasse, A. T. Stair, Jr., and D. J. Baker, Eds., U.S. Air Force, L. G. Hanscom Field, Bedford, MA, 1971, Vol. AFCRL-71-0019, p. 19.
47. P. L. Richards, *J. Opt. Soc. Am.* **54**, 1474 (1964).

#### APPENDIX: MANUFACTURERS OF FT-IR SPECTROMETERS

Currently	Originally	In Between	URL <sup>a</sup>
ABB Bomem	Bomem	Hartmann and Braun	<a href="http://www.abb.com">http://www.abb.com</a>
Bruker Optics			<a href="http://www.brukeroptics.com">http://www.brukeroptics.com</a>
Büchi Labortechnik			<a href="http://www.buchi.com">http://www.buchi.com</a>
Designs and Prototypes			<a href="http://www.designsandprototypes.com">http://www.designsandprototypes.com</a>
Deutschen Zentrum für Luft- und Raumfahrt			<a href="http://www.caf.dlr.de/caf/mf-ev">http://www.caf.dlr.de/caf/mf-ev</a>
Grabner Instruments			<a href="http://www.grabner-instruments.com">http://www.grabner-instruments.com</a>
Hamilton Sundstrand	Analect	Laser Precision/ Orbital	<a href="http://www.hs-ait.com">http://www.hs-ait.com</a>
Horiba			<a href="http://www.jp.horiba.com">http://www.jp.horiba.com</a>
JASCO			<a href="http://www.jascoinc.com">http://www.jascoinc.com</a>
Manning Applied Technology			<a href="http://www.appl-tech.com">http://www.appl-tech.com</a>
Mettler Toledo	ASI Applied Systems		<a href="http://www.mt.com/autochem">http://www.mt.com/autochem</a>
Midac			<a href="http://www.varianinc.com">http://www.varianinc.com</a>
MKS	On-Line Technologies		<a href="http://www.mksinst.com">http://www.mksinst.com</a>
Newport Oriel	Oriel		<a href="http://www.newport.com/oriel/">http://www.newport.com/oriel/</a>
PerkinElmer	Perkin-Elmer		<a href="http://www.perkinelmer.com">http://www.perkinelmer.com</a>
Shimadzu			<a href="http://www1.shimadzu.com">http://www1.shimadzu.com</a>
Smith's Detection	Sensir		<a href="http://www.smithsdetection.com">http://www.smithsdetection.com</a>
Surface Optics Corp			<a href="http://www.surfaceoptics.com">http://www.surfaceoptics.com</a>
Thermo Electron	Mattson		<a href="http://www.thermo.com">http://www.thermo.com</a>
Thermo Electron	Nicolet		<a href="http://www.thermo.com">http://www.thermo.com</a>
Varian	Digilab	Bio-Rad, Digilab LLC	<a href="http://www.varianinc.com">http://www.varianinc.com</a>

<sup>a</sup>This may not be the exact URL for the company's FT-IR products, but it is a simple matter to find it from here (usually under "Products").

Other companies that formerly made FT-IR spectrometers but (to the best of our knowledge are no longer involved in this field) include Beckman Instruments, Block Engineering, Bran + Luebbe, Bühler Instruments, Carson Alexiou, Chelsea Instruments, Coderg, Grubb Parsons, Hewlett-Packard, Idealab, JEOL, J. J. Lloyd, Polytec, Queen Mary Instruments, Research and Industrial Instruments Corp. (RIIC), and Unicam.

# OTHER COMPONENTS OF FT-IR SPECTROMETERS

## 6.1. INFRARED RADIATION SOURCES FOR TRANSMISSION AND REFLECTION SPECTROMETRY

### 6.1.1. Mid-Infrared Sources

The ideal source of continuous mid-infrared radiation is a high-temperature blackbody. The spectral energy density at wavenumber  $\tilde{\nu}$  from a blackbody source at temperature  $T$ ,  $U_{\tilde{\nu}}(T)$ , is given by the Planck equation, which is discussed in greater detail in Section 7.1. Plots of  $U_{\tilde{\nu}}(T)$  against wavenumber for a blackbody held at several different temperatures are shown in Figure 6.1. The actual spectral energy density of any infrared source is the product of its emissivity,  $\varepsilon(\tilde{\nu})$ , and the blackbody spectral energy density. At first glance, one might think that the source temperature should be as high as possible to maximize the value of  $U_{\tilde{\nu}}(T)$ . This is not always the case, however. For example, the temperature of a tungsten filament in a standard incandescent light bulb is close to 3000 K, but tungsten filaments are sealed in a glass bulb so that they can be operated under a high vacuum. Since glass does not have good transmission characteristics in the mid-infrared, simple light bulbs are never used as mid-infrared sources, and any source for this spectral region must operate in direct contact with the atmosphere. This factor alone severely limits the highest temperature at which mid-infrared sources may operated.

While the temperature, and hence the spectral energy density (see Chapter 7), of an incandescent mid-infrared source should be as high as possible to maximize the signal-to-noise ratio (SNR) of the spectrum, several other factors besides temperature must also be taken into account. These include the lifetime and stability of the source, the possibility of saturating the detector or amplifier (see Section 8.6.1), and the possibility of overloading the analog-to-digital converter (ADC) (see Section 3.2).

The most common mid-infrared source used in FT-IR spectrometers is a resistively heated silicon carbide rod, commercially known as a *Globar*. The typical



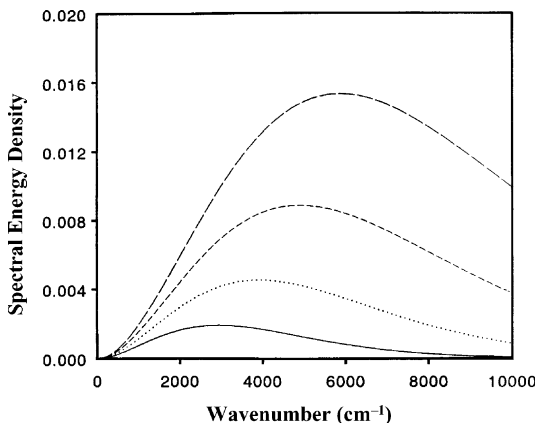


**Figure 6.1.** Spectral energy density of blackbody sources at 1500, 2000, 2500, and 3000°C. The temperature of many sources used for mid-infrared spectrometry is  $\sim 1500^{\circ}\text{C}$ , while the temperature of many near-infrared sources is  $\sim 3000^{\circ}\text{C}$ .

temperature at which a Globar is operated is  $\sim 1300\text{ K}$ . In the past, Globars were always water-cooled to avoid overheating the electrical contacts, but several other ceramic sources are now available that can be run without the need for a source of cooling water; however, these are generally operated at a lower temperature.

Several early FT-IR spectrometers were equipped with simple resistively heated *wire coils*, such as *nichrome* or *Kanthal*. These sources did not require water cooling but had a lower operating temperature and poorer emissivity than a Globar, and are rarely used today. Another time-tested, albeit also now rarely used mid-infrared source is the *Nernst glower*. Nernst glowers are fabricated from a mixture of refractory oxides and can be run several hundred degrees hotter than a Globar. The main disadvantage of the Nernst glower is the fact that the emissivity of the oxides from which it is composed,  $\epsilon(\tilde{\nu})$ , is quite low above  $2000\text{ cm}^{-1}$ . If only the region below  $2000\text{ cm}^{-1}$  is of interest, the Nernst glower is obviously a better source than a Globar. On the other hand, if the entire mid-infrared spectrum is to be measured with a Nernst glower, the SNR at high wavenumber will be low.

It is noteworthy that when the full radiant power from a Globar is measured with a standard deuterated triglycine sulfate (DTGS) detector (see Section 6.2), the SNR of the interferogram at the centerburst can approach 100,000 (see Chapters 3 and 7). Thus, for many measurements made with a standard FT-IR spectrometer equipped with a DTGS detector and a 16-bit ADC with a gain-ranging amplifier, there is usually no need for a better source than a Globar. If the energy transmitted through the sample and associated optics is low, however, the more energy emitted by the source, the better.

Some sources that are significantly hotter than a Nernst glower have been reported. For example, Su et al. [1] and Keiderling [2] have reported  $30 \times 8\text{ mm}$  carbon-rod sources that operate at  $\sim 3\text{ kW}$  and have a 2500-K color temperature when operating at maximum voltage. These sources have a typical lifetime of

one month and are relatively expensive to fabricate since they require water cooling. They are, however very inexpensive to replace. The sources originally reported by Keiderling were actually designed for a dispersive instrument, but another variant of this type of source was recently reported by Herceg et al. [3]. This source can operate at temperatures as high as 3000 K but in light of its short lifetime at this temperature is usually operated at between 2200 and 2300 K. The spectral energy density (see Section 7.1) at  $3100\text{ cm}^{-1}$  of a graphite source at  $2000^{\circ}\text{C}$  is about three times higher than that of a Globar at  $1300^{\circ}\text{C}$ . Herceg et al. [3] have shown that the SNR of reflection-absorption spectra (see Section 13.3) measured on an FT-IR spectrometer increases by approximately this factor in practice.

It should be noted that these sources are different from the carbon arcs that were at one time used for movie projectors and in spotlights, in which a discharge is formed between two electrodes. The latter sources are extremely bright ( $\sim 6000\text{ K}$  color temperature), but the rod has to be fed into the arc continually since the carbon gets ablated away continuously. Carbon arcs do not need a window (although flushing to lower ozone buildup might be beneficial), whereas carbon rods must usually be sealed under  $\text{N}_2$  or Ar to avoid combustion.

For FT-IR *microspectrometry*, the ideal source for mid-infrared measurements would be very small, both to match the sample size and because the beam can then be focused on a very small detector (see Section 7.1). Because light losses can be quite large in IR microscopes, an ideal source for FT-IR microspectrometry would be about 1 mm in diameter, operate at a temperature of at least 2000 K, and have a high emissivity across the spectrum. Unfortunately, no source yet fulfills these criteria for laboratory measurements.

A few interesting sources for future FT-IR spectrometers have been reported in the past 10 years, including the synchrotron and free electron laser (FEL) [4]. Using the radiation from a synchrotron beam line, spectra of samples as small as  $10\text{ }\mu\text{m}$  in diameter (the diffraction limit) may be measured with very high SNR in times as short as 1 second. Obviously the use of these sources requires the spectroscopist to travel to a synchrotron or FEL facility with a mid-infrared beam line equipped with a FT-IR microspectrometer. Such facilities are available in several countries and can be used at minimal cost provided that the potential user can make a good case for the measurement.

### 6.1.2. Near-Infrared Sources

It can be inferred from Figure 6.1 that near-infrared (NIR) sources should be run at significantly higher temperatures than mid-infrared sources. Since glass and quartz are transparent across the entire NIR region, this goal can be met through the use of a simple and inexpensive tungsten-filament light bulb or quartz-tungsten-halogen (QTH) lamp. Provided that these sources are run at less than their specified operating voltage, they are also very long lived. QTH lamps are more intense than tungsten light bulbs, but this intensity may sometimes lead to problems of digitization noise and response nonlinearity, as discussed above. On the other hand, for several important contemporary applications of FT-NIR spectrometry, such as skin measurements

using fiber-optic probes, either the sample or sampling optics can attenuate the beam from the source by as much as 99.9%. The greater the attenuation, the greater is the need for the more intense source. In such cases, the use of QTH lamps is all but mandatory. In practice, the choice of a NIR source should be based on the photon flux required for the interferogram to fill the ADC at the centerburst.

### 6.1.3. Far-Infrared Sources

The spectral energy density of blackbody sources is always very low below  $200\text{ cm}^{-1}$  (see Figure 6.1) and the problem of measuring far-infrared spectra is compounded by the fact that the emissivity of both Globars and Nernst glowers is much less than unity in the far infrared. The usual source that is used for far-infrared spectrometry is a high-pressure mercury lamp. The emissivity of the hot quartz envelope of this source is  $\sim 1$  above  $100\text{ cm}^{-1}$ . Below  $100\text{ cm}^{-1}$ , quartz starts to become transparent, so that  $\epsilon(\tilde{\nu} \ll 1)$ . On the other hand, the intensity of the radiant energy emitted from the plasma inside the bulb is significantly higher than that emitted by a standard Globar in this spectral region. High-pressure mercury lamps are, therefore, the standard source used for far-infrared FT-IR spectrometry.

## 6.2. DETECTORS

### 6.2.1. Thermal Detectors

Infrared detectors can be divided into two types: thermal detectors and quantum detectors. Thermal detectors operate by sensing the change in temperature of an absorbing material. Their output may be in the form of an electromotive force (e.g., thermocouples), a change in the resistance of a conductor (e.g., bolometers) or semiconductor (e.g., thermistor bolometers), or the movement of a diaphragm caused by the expansion of a gas (e.g., pneumatic detectors). All of the above types of thermal detectors have been used for mid-infrared measurements over the past century. They all have drawbacks for FT-IR spectrometry, however, since each has a response time of several milliseconds, which is too long for the high frequencies generated by today's FT-IR spectrometers.

If the interferometer mirror speed is such that the optical velocity is  $0.316\text{ cm} \cdot \text{s}^{-1}$  (HeNe laser frequency of  $5\text{ kHz}$ ),  $4000\text{-cm}^{-1}$  radiation is modulated at  $\sim 1.25\text{ kHz}$  (see Eq. 2.11). Thus, the response time of a detector for FT-IR spectrometry must be less than  $1\text{ ms}$ . Although several cryogenically cooled detectors have response times this low, the only mid-infrared detectors that have an appropriate combination of high speed, reasonably good sensitivity, low cost, good linearity, and operation at or near room temperature are the *pyroelectric bolometers*.

These detectors incorporate as their heat-sensing element ferroelectric materials that exhibit a large spontaneous electrical polarization at temperatures below their Curie point. If the temperature of ferroelectric materials is changed, the degree of polarization also changes. If electrodes are placed on opposite faces of a thin slice

of material to form a capacitor, this change in polarization may be observed as an electrical signal. When the polarization changes, the charges induced on the electrodes can either flow as a current through a circuit of relatively low impedance or produce a voltage across the slice if the external impedance is comparatively high. Note that these detectors produce a signal only when the temperature of the element changes and are not very useful for measuring temperatures that do not change.

The sensing element of the pyroelectric detectors used in most of the original rapid-scanning FT-IR spectrometers was *triglycine sulfate* (TGS). The Curie temperature,  $T_c$ , of TGS is only about 39°C. If the temperature of a pyroelectric detector exceeds its Curie temperature, its response drops to zero. In this case the element must be repolarized before it can be reused. Even though the electronics of most modern FT-IR spectrometers incorporate automatic “repoling” of pyroelectric detectors, it was found that *deuterated triglycine sulfate* (DTGS) has a higher Curie temperature than TGS ( $T_c \sim 49^\circ\text{C}$ ) and replaced TGS in about 1980. More recently, the properties of *deuterated l-alanine-doped triglycine sulfate* (DLATGS) have been found to be even more suitable for FT-IR, and many contemporary instruments are equipped with a DLATGS detector. Another type of pyroelectric bolometer that has been installed in a few inexpensive FT-IR spectrometers is *lithium tantalate*. Because of their extensive use in burglar alarms,  $\text{LaTiO}_3$  detectors are very inexpensive; however, their sensitivity is about three times lower than that of DTGS detectors, which more than offsets their cost advantage for most applications.

The pyroelectric element is usually mounted so that the thermal resistance between the element and its surroundings is large and the thermal time constant is consequently long. The thermal circuit can be represented by an electrical analog comprising a capacitance shunted by a large resistance. The voltage responsivity of a pyroelectric detector to a modulated change in temperature of frequency  $f$  (hertz) is given by

$$R_v = \frac{p(T)R_E}{\rho C_p d [1 + (2\pi f R_E C_E)^2]^{1/2}} \quad (6.1)$$

where  $p(T)$  is the pyroelectric coefficient at temperature  $T$ ,  $R_E$  the feedback or load resistance,  $\rho$  the density of the crystal,  $C_p$  its specific heat,  $d$  the spacing between electrode surfaces, and  $C_E$  the effective capacitance. The capacitive element is essentially noise-free and the long thermal time constant leads to low thermal noise. In fact, the noise performance attainable with DTGS pyroelectric bolometers is dominated by the noise performance of its associated amplifiers. For wide bandwidths, such as those encountered in rapid-scanning FT-IR spectrometers, Johnson noise in the load resistor dominates. A more detailed discussion of the factors governing signal-to-noise ratio is given in Chapter 7.

To a good approximation,  $R_v$  is proportional to  $1/f$ . For a rapid-scanning interferometer, therefore, the optical velocity  $V$  should be as low as possible. Two factors usually determine the value of  $V$  when a DTGS detector is being used. First,  $V$  must be high enough that the SNR of the interferogram at the centerburst is

approximately equal to the dynamic range of the ADC. If  $V$  is too low, the SNR will exceed the dynamic range of the ADC and hence will be too high to permit valid signal averaging. In practice,  $V$  is usually set so that the electrical line frequency (60 Hz in the United States) and its first harmonic fall below the signal caused by the lowest wavenumber in the spectrum ( $400\text{ cm}^{-1}$ ). If  $V = 0.316\text{ cm} \cdot \text{s}^{-1}$ , any “glitch” in the spectrum due to unfiltered 60-Hz line frequency would fall at  $60/0.316$ , or  $190\text{ cm}^{-1}$ , and an interference at the first harmonic of this frequency (e.g., due to fluorescent lighting) would be seen at  $380\text{ cm}^{-1}$ . If the line voltage has any appreciable square-wave character, however, higher harmonics of 60 Hz will still be seen in the mid-infrared spectrum. It should also be noted that the high-frequency response characteristics of some DGTS and DLATGS detectors have been improved to the point that  $V$  can be increased to about  $0.5\text{ cm} \cdot \text{s}^{-1}$ , further reducing their susceptibility to digitization noise and interference by the electrical line frequency and its harmonics.

### 6.2.2. Quantum Detectors

The alternative method of detecting infrared radiation depends on the interaction of radiation with the electrons in a solid, causing the electrons to be excited to a higher energy state (e.g., from a valence band to a conduction band of a semiconductor). These effects depend on the quantum nature of radiation, and detectors based on this principle are usually called *quantum detectors*. The energy of each photon is directly proportional to its wavenumber, and a transition from one state to another will occur only if the wavelength of the radiation is less than some critical value  $\lambda_{\text{max}}$ . The sensitivity of quantum detectors usually increases with wavelength (up to the cutoff), as the number of photons for a given amount of energy increases. Since the output is controlled by the number of electrons excited, the output voltage also rises with wavelength. When the wavelength approaches  $\lambda_{\text{max}}$ , however, the response drops off precipitously. This behavior is in contrast to that of thermal detectors, where the response per watt is constant.

To use quantum effects for the detection of radiation, it is necessary to be able to excite electrons from one state to another state that has different electrical properties. One way is by photoemission, where electrons are given enough energy to escape from the surface and flow through a vacuum to produce an electrical current. Phototubes and photomultipliers fall into this category. Because high energies are required to release electrons from a photoemissive surface, this effect can only be used in the ultraviolet, visible, and near-infrared (to  $\sim 1\text{-}\mu\text{m}$ ) regions.

Semiconductor detectors are often used in the mid- and near-infrared. These detectors are generally *p-n* junction semiconductors. Semiconductors are so called because they have a relatively small bandgap between the valence and conduction bands of the material. If electrons can be promoted from the valence band to the conduction band, the material will pass a current. In semiconductor detectors, the energy of a photon is greater than the bandgap and promotes an electron from the valence band to the conduction band. The ensuing current is used to register the detection of the photons. Typically, these detectors are comprised of

two doped semiconductors. *Doping* is the addition of a small concentration of an element that either has more electrons than the native semiconductor (*n*-type, or donor, semiconductors which are electron-rich), or fewer electrons (*p*-type, or acceptor, semiconductors, which are electron deficient). The regions where electrons are deficient are commonly known as *holes*. When the two semiconductor types are joined at a junction or interface, the electrons and holes migrate to the other side until a charge is built up across the interface that impedes any more diffusion of electrons or holes. The region close to the interface becomes depleted at the steady state. When a photon with a greater energy than the bandgap strikes the detector, electrons are generated in the conduction band and the number of holes increases in the valence band. Recombination of the electrons and holes is prevented by a potential applied to the detector. Only when a photon strikes the photodetector is current passed. Quantum detectors that operate in this manner include PbS, PbSe, and InSb. Other quantum detectors include II–VI combinations of semimetals, that is, mixtures of metals from groups II and VI of the periodic table. One such detector is mercury cadmium telluride (MCT,  $\text{Hg}_{1-x}\text{Cd}_x\text{Te}$ ), a mixture of HgTe and CdTe. The ratio of the blend leads to the bandpass of the detector.

The very low energy of the photons that must be sensed by mid-infrared photodetectors has the consequence that electrons can be excited by random thermal agitation of the solid, which gives rise to noise in the output. Noise is also generated by leakage of current through the detector from the photoconductive or photovoltaic circuit used to bias the detector. Cooling reduces both these sources of noise. The sensitivity of infrared detectors is usually given in terms of their *specific detectivity*,  $D^*$  (see Section 7.1); the higher the  $D^*$ , the higher the sensitivity of a given detector. Plots of  $D^*$  against wavelength for a number of different photodetectors are shown in Figure 6.2. For a given material, the higher the sensitivity and the lower the value of  $\lambda_{\min}$  required, the lower the temperature to which the detector must be cooled. Some detectors, such as PbS and PbSe, are usually operated at about  $-20^\circ\text{C}$ , and thermoelectric (TE) cooling is sufficient. On the other hand, most of the more popular quantum detectors that respond to mid-infrared radiation, including MCT and InSb, are usually cooled to 77 K with liquid nitrogen ( $\text{LN}_2$ ). Where exceptionally high sensitivity is required, detectors are cooled to the temperature of liquid helium (4.2 K). The very high sensitivity of liquid-helium-cooled detectors, such as copper-doped germanium, often means that the surroundings must be cooled to the temperature of liquid nitrogen ( $\text{LN}_2$ ) to minimize the noise generated by randomly emitted photons.

Mercury cadmium telluride detectors are by far the most commonly used photodetectors for mid-infrared spectrometry. The  $D^*$  of MCT detectors is strongly dependent on their composition but is typically about 10 to 50 times greater than that of DTGS. The wavelength at which they cut off is usually only slightly longer than the wavelength of their maximum response,  $\lambda_{\max}$ .  $\text{LN}_2$ -cooled MCT detectors are commonly classified as narrowband ( $\lambda_{\max} \sim 12 \mu\text{m}$ ), midband ( $\lambda_{\max} \sim 16 \mu\text{m}$ ), and wideband ( $\lambda_{\max} \sim 22$  to  $24 \mu\text{m}$ ) detectors, although any value of  $\lambda_{\max}$  between about 12 and  $24 \mu\text{m}$  may be specified. MCT detectors can be manufactured with

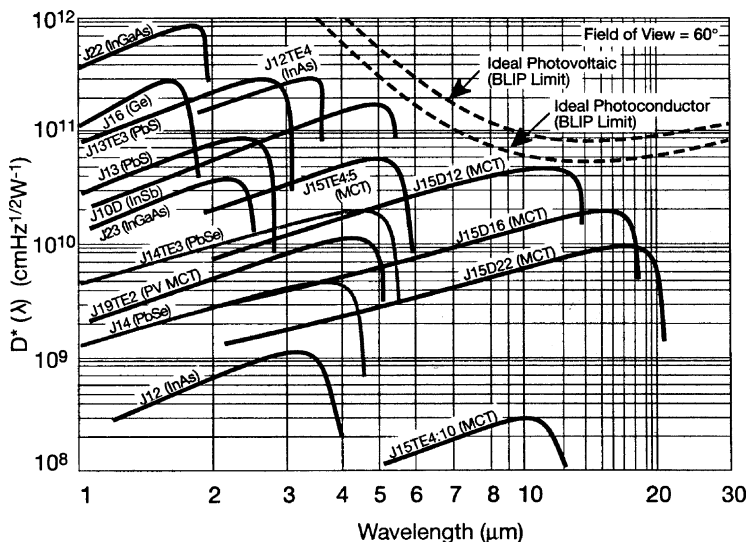


**Figure 6.2.** Plots of  $D^*$  (specific detectivity; see Chapter 7) as a function of wavelength for several photodetectors made by one manufacturer. The detectors marked J15D12, J15D16, and J15D22 are MCT detectors. The last two digits refer to the cutoff wavelength, so these detectors are narrowband, midband, and wideband MCT detectors. If the product code includes the letters TE, the detectors are thermoelectrically cooled; otherwise, they are cooled with  $\text{LN}_2$ . Other detectors whose performance is shown on this plot include PbS, PbSe, InSb, InAs, InGaAs, and Ge. (Courtesy of Judson Technologies.)

long-wave cutoffs as great as  $33\ \mu\text{m}$ , but the  $D^*$  of these detectors is little better than that of pyroelectric detectors. Narrowband MCT detectors have the highest peak detectivity ( $D^* \sim 4 \times 10^{10}\ \text{cm} \cdot \text{Hz}^{1/2} \cdot \text{W}^{-1}$ ) and wideband detectors the lowest ( $D^* \sim 5 \times 10^9\ \text{cm} \cdot \text{Hz}^{1/2} \cdot \text{W}^{-1}$ ). In Figure 6.2, J15D12, J15D16, and J15D22, respectively, are examples of response curves for narrow-, mid-, and wideband MCT detectors that operate at 77 K. There is obviously a price in sensitivity to pay for extending the cutoff of MCT detectors. Note also that MCT detectors can be cooled either by a small Stirling engine that can reduce the temperature of the detector element to 77 K or, if operation at higher temperature is adequate, they can be thermoelectrically (TE) cooled. In the case of the detector-labeled J15TE4:5 in Figure 6.2, the peak  $D^*$  is not significantly higher than that of the  $\text{LN}_2$ -cooled narrowband MCT detector, even though  $\lambda_{\text{max}}$  is considerably shorter. Similarly, J15TE4:10 is little more sensitive than a DTGS detector.

The choice of which type of MCT detector to use should be based on several considerations. First, the nature of the vibrational modes to be measured must be considered. For a narrowband detector,  $\lambda_{\text{max}} \sim 13.3\ \mu\text{m}$  ( $\tilde{\nu}_{\text{min}} \sim 750\ \text{cm}^{-1}$ ), the C—H out-of-plane bending bands in the spectra of aromatic molecules that can be used to determine the substitution pattern often absorb below the cutoff. These bands will be seen with a midband MCT detector. Conversely, many important bands in the spectra of minerals will not be seen, even with a midband detector.

The next consideration is whether exchanging a DTGS detector for MCT will actually lead to an increased SNR in practice. For example, the dynamic range of a 16-bit ADC may be only just sufficient to accurately digitize typical interferograms measured with a DTGS detector in the region of the centerburst (see Sections 3.3 and 7.3). In this case, simply changing to a more sensitive detector will not lead to an increase in sensitivity. Second, the linear dynamic range of MCT detectors is quite limited and the effect of measuring interferograms with a nonlinear detector is to degrade the photometric accuracy severely (see Section 8.6.1). Thus, MCT detectors should be used only when the signal that is being measured is too low to allow adequate spectra to be measured with a DTGS detector.

When an MCT detector is already installed in the spectrometer and a sample with high transmittance is to be measured, important time may be wasted by switching to a DTGS detector to avoid the effects of the type described above. If this is the case, an MCT detector can be used, *but the beam must be attenuated both so that the sensitivity is not limited by the dynamic range of the ADC and to ensure that the response of the detector is linear*. There are several ways to attenuate the beam of an FT-IR spectrometer. The most popular (but worst, in the opinion of the authors) is to reduce the diameter of the J-stop. In this case, the diameter of the focused beam at the detector element is reduced but the photon flux density of the beam is not and the effect of nonlinearity (see Figure 8.7) is usually still apparent in the spectrum. A better way to attenuate the beam is to reduce the diameter of the beamsplitter stop, or B-stop, that is, to reduce the size of the virtual image of the beamsplitter; however, few commercial FT-IR spectrometers are designed with B-stops. The final way is to place a screen somewhere in the beam, preferably where it is collimated or approximately so, such as at the entrance to the sample compartment. Screening the beam or reducing the diameter of the B-stop reduces both the photon flux and the photon flux density of the beam at the detector, and either method is to be preferred over reducing the diameter of the J-stop.

Unlike the case for thermal detectors, the sensitivity of many quantum detectors increases as the modulation frequency increases. The  $D^*$  of a typical photoconductive MCT detector reaches its maximum value at a modulation frequency of  $\sim 1$  kHz and remains approximately constant to  $\sim 1$  MHz. Thus, for mid-infrared spectra ( $\tilde{\nu}_{\max} = 4000 \text{ cm}^{-1}$ ) measured with an MCT detector on a rapid-scanning interferometer, the optical velocity,  $V$ , could be as high as  $250 \text{ cm} \cdot \text{s}^{-1}$ . This implies that the frequency of the laser interferogram,  $f_{\text{HeNe}}$ , will be at least 4 MHz. No analog-to-digital converters that can be triggered externally (e.g., at the zero crossings of the laser interferogram) at such a high rate are commercially available, although this situation may well change in the future. In practice, many standard FT-IR spectrometers equipped with an MCT detector operate with  $V \geq 6.3 \text{ cm} \cdot \text{s}^{-1}$  ( $f_{\text{HeNe}} \geq 100 \text{ kHz}$ ).

MCT detectors may be operated in the photoconductive (PC) or photovoltaic (PV) mode, with PC operation being the more common. PV-MCT detectors are used when the response time of the measurement must be very short. Because the  $D^*$  of most PC-MCT detectors is approximately constant between modulation frequencies from 1 kHz to 1 MHz, it is difficult to drive the interferometer mirror



fast enough that the high-frequency cutoff is exceeded. The only time that the high-frequency cutoff of PC-MCT detectors may present a problem is for time-resolved measurements of reactions taking place in less than 1  $\mu\text{s}$  (see Section 19.2). For probing very fast reactions, PV-MCT detectors are generally used, since these detectors have a response time of about 10 ns, which is at least an order of magnitude faster than PC-MCT detectors.

As noted above, electrons can be excited into the conduction band of a semiconductor detector by photons emitted from the surroundings. The greater the gap between the valence and conduction bands, the shorter is  $\lambda_{\text{min}}$ . Because the energy emitted by black and gray bodies near ambient temperature decreases with wavenumber, the sensitivity of detectors increases as the bandgap increases. The value of  $D^*$  at the wavelength of their maximum sensitivity,  $\lambda_{\text{max}}$ , is approximately equal to the *background limit for infrared photons* (BLIP) for each detector for a field of view (fov) of about  $60^\circ$ . As shown in Figure 6.2, the BLIP for PV detectors is about a factor of 2 higher than that of PC detectors. Because the ambient photon flux decreases as the fov of a given detector decreases,  $D^*$  can be increased by restricting the fov. It may be noted that even though the  $D^*$  of the detector may be increased by decreasing the fov, the optical throughput (*étendue*), and hence the signal-to-noise ratio of the spectrum, may well be reduced (see Section 7.1).

Many detectors are available for FT-NIR spectrometry, as can be seen from Figure 6.2. Besides MCT, the most common  $\text{LN}_2$ -cooled quantum detectors are InSb, InAs, Ge, and InGaAs. The most popular thermoelectrically cooled detectors are MCT, InAs, InGaAs, PbSe, PbS, Ge, and Si, and several of these detectors (especially InGaAs) operate with good sensitivity at room temperature. Although the result of operating MCT detectors at a higher temperature than  $\text{LN}_2$  is to reduce the value of  $\lambda_{\text{min}}$ , there is often a surprisingly small difference in the  $D^*$  values of NIR detectors operating at 77 K and  $\sim 250$  K because the photon flux from the surroundings to the detector decreases as  $\lambda_{\text{min}}$  decreases.

## 6.3. OPTICS

### 6.3.1. Paraboloidal Mirrors

In laboratory FT-IR spectrometers, the radiation emitted by the source is collected and collimated, passed through the interferometer, brought to a focus in the sample compartment and refocused onto the detector. The beam from the source is usually collimated with an off-axis segment of a paraboloidal mirror before it is passed through the interferometer. To appreciate why this type of mirror is needed, the properties of the corresponding two-dimensional conic section, the *parabola*, should be examined. Any line parallel to the axis of a parabola is reflected through its focus (see Figure 6.3). Rotation of the parabola about its axis creates a *paraboloid*. Thus, any collimated beam of radiation parallel to the axis of a paraboloid will also be reflected through its focus.

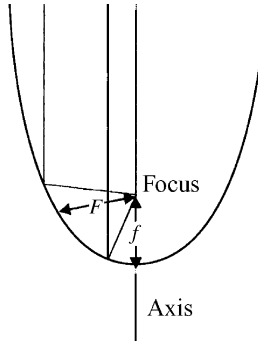


**Figure 6.3.** Typical parabola, with focal length  $f$ . For the off-axis section shown on this figure, the effective focal length is  $F$ .

Paraboloidal mirrors are used in two ways in FT-IR spectrometers. Any beam emanating from a focus may be collimated by a paraboloidal mirror. For example, radiation from the infrared source is collimated by a paraboloidal mirror before being passed through the interferometer. Alternatively, a collimated beam may be focused by a paraboloidal mirror (e.g., the collimated light emerging from the interferometer is focused at the center of the sample compartment by such a mirror). It is rare that the central ray of the collimated beam coincides with the axis of the paraboloid; thus, the segments of the paraboloidal mirrors used in FT-IR spectrometers are usually referred to as *off-axis parabolds*.

The true focal length of a paraboloid is the distance between its focus and vertex ( $f$  in Figure 6.3). For an off-axis paraboloid, however, it is more useful to specify its effective focal length (EFL), which is the distance between the *center of the segment* and the focus. If the two lines drawn parallel to the axis in Figure 6.3 represent the extreme rays of a collimated beam, the EFL of the paraboloid for this beam is  $F$ . The magnification of an image by an off-axis paraboloid depends on its EFL. Consider the two paraboloids, A and B, with EFLs equal to  $F_A$  and  $F_B$  (see Figure 6.4).

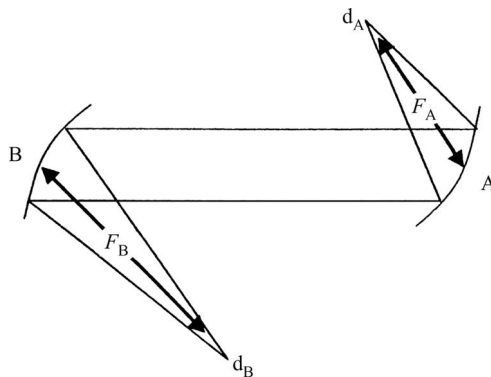


**Figure 6.4.** Two off-axis parabolas, A and B, with effective focal lengths,  $F_A$  and  $F_B$ , respectively. The ratio of the diameter of the foci,  $d_A/d_B$ , is equal to  $F_A/F_B$ .

The diameter of the image at the focus of mirror A,  $d_A$ , is given to a first approximation by

$$d_A = \frac{d_B F_A}{F_B} \quad (6.2)$$

where  $d_B$  is the diameter of the image at the focus of mirror B. Thus, mirrors with long focal lengths lead to larger images than those of short focal-length mirrors.

The EFL of a particular off-axis paraboloid depends on its function in the spectrometer. This is illustrated by the very simple spectrometer design shown in Figure 6.5. The EFL of the mirror used to collect the source radiation must be short in order that the collection efficiency be as high as possible. On the other hand, the EFL of the paraboloid used to bring the beam to a focus in the sample compartment is usually much longer than that of the source mirror because the compartment must be large enough that bulky sampling accessories can be installed. Two examples can be cited where mirrors of very short focal length are needed. The first is for infrared microspectrometry, where the diameter of samples being investigated is much smaller than that of the capillary films, sealed liquid cells, and KBr pellets conventionally used in infrared spectroscopy. Thus, the focal length of the objective in an infrared microscope must be much smaller than that of the mirrors bringing

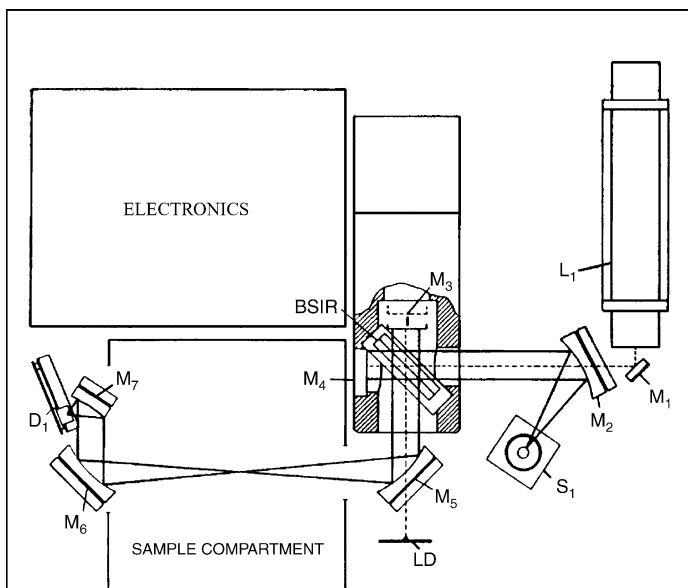


**Figure 6.5.** Optics of a very simple FT-IR spectrometer;  $S_1$ , source;  $L_1$ , HeNe laser;  $M_1$ , plane mirror;  $M_2$ ,  $M_5$ ,  $M_6$ , and  $M_7$ , off-axis paraboloids of varying focal lengths;  $M_3$ , moving interferometer mirror;  $M_4$ , fixed interferometer mirror; BSIR, beamsplitter;  $D_1$ , detector. Note that mirrors  $M_2$  and  $M_5$  have a hole drilled through so that the laser beam can pass to the laser detector, LD.

the beam into the sample compartment. The second relates to the detector fore-optic. The noise equivalent power of infrared detectors is inversely proportional to the square root of their area (see Eq. 7.1), so that the size of the detector element should be as small as possible. To create this very small image, the EFL of the detector mirror must be very short, so that all the light that passes through the sample is focused onto a detector with the smallest possible size.

A truly collimated beam can only be produced from a point source. Since the area of a point source is zero, no light emerges from a point source, and in practice a source of finite size must be used. The effect of a source of finite area is to cause the “collimated” beam that passes through the interferometer to diverge slightly and to allow enough photons to reach the detector so that an acceptable signal-to-noise ratio (SNR) is attained. If the source is too large, the spectral resolution is degraded. It was seen from Eq. 2.40 that to maintain a resolution of  $\Delta\tilde{\nu}$  across the spectrum, the half angle of the beam passing through the interferometer,  $\alpha_{\max}$ , cannot exceed  $(\Delta\tilde{\nu}/\tilde{\nu}_{\max})^{1/2}$  radians, where  $\tilde{\nu}_{\max}$  is the highest wavenumber in the spectral range of interest. Ideally,  $\alpha_{\max}$  should have the largest possible value consistent with the resolution at which the spectrum is being measured. To achieve this goal, the radiation from the source of most medium- or high-resolution FT-IR spectrometers ( $\Delta\tilde{\nu} < 1 \text{ cm}^{-1}$ ) is passed through a variable aperture, known as the *Jacquinot stop*, as described in Section 5.1. The higher the resolution desired, the smaller is the diameter of the J-stop. The effect of the J-stop diameter on the signal-to-noise ratio of the spectrum is discussed in detail in Chapter 7.

For low-resolution spectrometers ( $\Delta\tilde{\nu} \geq 2 \text{ cm}^{-1}$ ),  $\alpha_{\max}$  is usually so great that all the light allowed by Eq. 2.40 cannot be focused onto the detector. In this case, the detector element itself acts as the limiting aperture and there is no need to install a J-stop in the optics. As a result, the optics of low-resolution FT-IR spectrometers can be as simple as those of the instrument shown in Figure 6.5.

### 6.3.2. Plane Mirrors

The other optics that may be found in FT-IR spectrometers include plane, ellipsoidal, toroidal, and aspherical mirrors. The primary purpose of *plane mirrors* in FT-IR spectrometers is simply to ensure that the optical bench is as compact as possible. In practice, gold-coated mirrors often have a reflectance of about 0.98. An optical path with 20 mirrors, each with a reflectance of 0.98, has a transmittance of  $0.98^{20}$ , or 67%. If the reflectance of each mirror is 95%, the overall efficiency would be only 36%. Thus, the number of plane and other mirrors should be kept as small as possible, and gold coating should be applied whenever high optical efficiency is desired.

### 6.3.3. Ellipsoids, Toroids, and Other Aspherical Mirrors

Ellipses have two foci, and any line passing through one focus is reflected through the second one (see Figure 6.6). Ellipsoids are created by rotating an ellipse about its major axis (i.e., the axis containing the two foci). A cone of light emanating

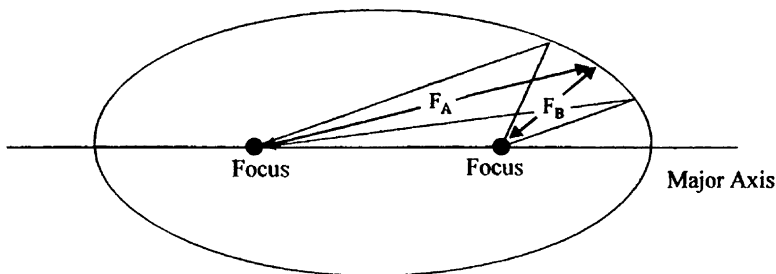


**Figure 6.6.** Ellipse with two effective focal lengths,  $F_A$  and  $F_B$ . As for the two parabolas shown in Figure 6.4, the ratio of the diameter of the foci,  $d_A/d_B$ , is equal to  $F_A/F_B$ .

from one focus of an ellipsoid is reflected to the other focus. Thus, it is always possible to replace the two paraboloids taking the beam from the sample compartment to the detector in the design shown in Figure 6.5 by a single off-axis segment of an ellipsoid (again, this is usually known as an *off-axis ellipsoid*). The distances between each focus of an off-axis ellipsoid and its center are its two effective focal lengths,  $F_A$  and  $F_B$  (see Figure 6.6), and the magnification is again given by Eq. 6.2. For most ellipsoids used in FT-IR spectrometers, one of the focal lengths is usually from two to six times longer than the other. Occasionally, optical designs have been reported where a focusing mirror with two approximately equal focal lengths is needed. Ellipsoids are rarely used in this case and sections of *toroidal* (doughnut-shaped) mirrors are used instead.

When off-axis segments of paraboloidal and ellipsoidal mirrors are configured so that the beam is reflected through an angle much greater than  $30^\circ$ , or when the diameter of the beam at a focus is large, the beam can become aberrated; this effect is sometimes known as *coma*. Coma can be minimized by the computer design of a mirror for a particular application, followed by diamond turning. The surface of a computer-designed aspherical mirror is usually similar to the corresponding paraboloid or ellipsoid, but the differences are often enough to yield significantly higher performance for instruments of very high optical throughput.

#### 6.4. SPECTROMETER DESIGN

As we have seen several times in this book, the half-angle of the collimated beam passing through the interferometer beam must be less than  $(\Delta\tilde{\nu}/\tilde{\nu}_{\max})^{1/2}$  radians. This angle is controlled by the *limiting aperture* of the instrument. When the maximum retardation allowed by a given interferometer is 1 cm or less ( $\Delta\tilde{\nu} \geq 1 \text{ cm}^{-1}$ ), the limiting aperture is usually the detector, whereas for measurements at higher resolution, the beam divergence must be controlled by the J-stop.

For FT-IR spectrometers that do not require the use of a J-stop, a simple off-axis paraboloidal segment is used to collect and collimate the beam from the source. For higher-resolution instruments, a slightly more complicated optical arrangement is

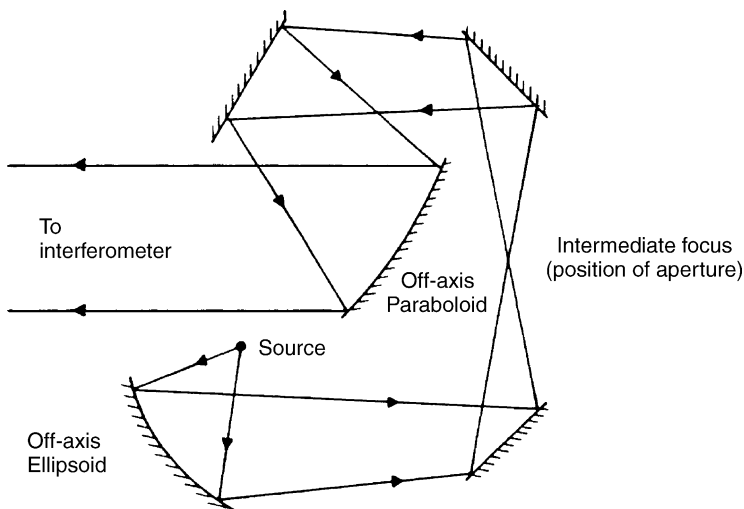


**Figure 6.7.** Typical source optics that incorporate a Jacquinot stop at the intermediate focus.

needed to collect the beam from the source, focus it at the J-stop, and collimate the input beam to the interferometer. A typical optical arrangement is shown in Figure 6.7. Here an ellipsoidal mirror is used to collect the beam from the source and refocus it at the J-stop, where an adjustable iris is located. Since the resolution and spectral range are usually specified by the operator, the diameter of this iris is often controlled automatically by the instrument's computer. A paraboloidal mirror collimates the beam after it has passed through the limiting aperture. An instrument equipped with a Jacquinot stop that can generate spectra at higher resolution is shown in Figure 6.8.

The optics of a commercial low-resolution FT-IR spectrometer were shown in Figure 6.5. The differences between this instrument and the one shown in Figure 6.8 are immediately apparent. First and foremost, no J-stop is used on the low resolution instrument. The radiation from the source is directly collimated with a single off-axis paraboloid before being modulated by the interferometer. The focal length of the source paraboloid is short (about 7 cm), so that as much of the radiation emitted by the source as possible can be collected. On the other hand, the modulated radiation is focused at the center of the sample compartment by a paraboloid of relatively long focal length ( $\sim 25$  cm), so that large sampling accessories can be mounted in the sample compartment. The shorter the focal length of this mirror, the smaller the diameter of the focused beam but the less versatile is the spectrometer. The beam from a HeNe laser is also sometimes passed through the sample compartment to facilitate the alignment of the sample or sampling accessory. (*Note:* This is not the same laser as that used in the interferometer.) After the infrared beam is passed through the sample, it is focused on the detector either by two paraboloidal mirrors (as shown in Figure 6.4) or one ellipsoidal mirror. In either case, the mirror(s) have one long and

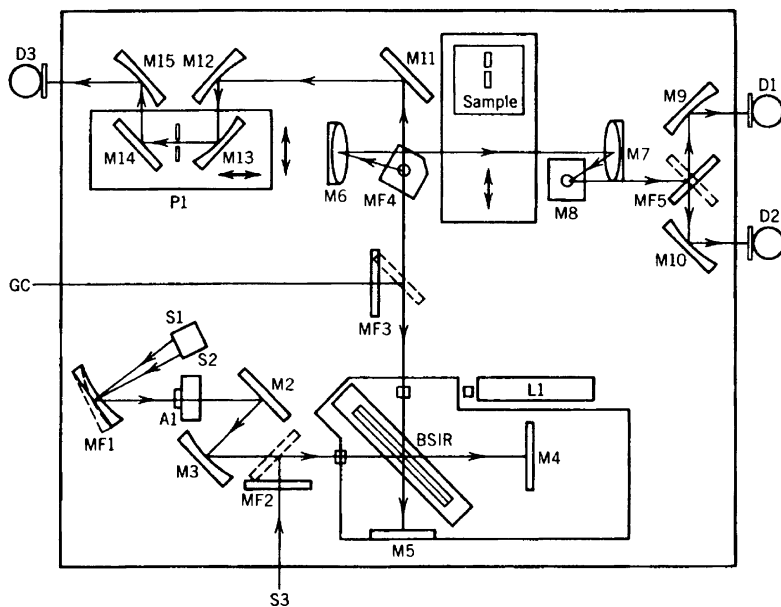


**Figure 6.8.** Optics of the Nicolet Model 60-SX FT-IR spectrometer (now obsolete). Sources can be located at S<sub>1</sub>, S<sub>2</sub>, and/or S<sub>3</sub>; detectors can be located at D<sub>1</sub>, D<sub>2</sub>, and/or D<sub>3</sub>; M signifies a fixed mirror; MF signifies a flip mirror; A<sub>1</sub> is a Jacquinot stop.

one short focal length. The long focal length is needed to allow the beam to emerge from the sample compartment. The short focal length is needed so that the image of the beam at the detector, and hence the detector itself, is as small as possible. The focal length is usually selected so that the focused beam fills the detector exactly.

Some sampling accessories [e.g., infrared microscopes (see Chapter 14) and gas chromatography interfaces (see Chapter 23)] are too big to fit in even the largest sample compartment. In these cases, the accessories are mounted outside the instrument and the modulated beam is directed to them by means of a switchable mirror (often known as a *flip mirror*). It is very rare that the beam is returned to the detector mounted inside the instrument, so a second detector is usually a component of accessories that are mounted outside the spectrometer in the *external beam*. Several contemporary instruments are also equipped with flip mirrors to direct the beam to different possible internal beam paths, in one or more of which a different accessory may be mounted permanently. In this way, the user can switch rapidly from one type of measurement to another, making optimal use of a single spectrometer.

Water vapor in the beam of FT-IR spectrometers is a major source of interference. Thus, the optical bench should ideally either be purged with dry air or evacuated completely. Some low-resolution spectrometers are hermetically sealed and desiccated, so that the only humid air is in the sample compartment. These instruments are adequate if the spectra of conventional films, KBr disks, and solutions

are of interest, since the spectra rarely require ordinate expansion. However, any time the ordinate scale must be expanded, the presence of weak lines in the spectrum of atmospheric water vapor can mask absorption features due to minor, but important components. The intensity of lines due to atmospheric water vapor must always be much less than the intensity of the bands of interest, and it is incumbent on the operator to ensure that the instrument is always purged adequately. Two sources of dry  $\text{CO}_2$ -free air may be cited. The ideal source is the boil-off gas from liquid nitrogen cylinders. This gas may be free in labs that use large volumes of  $\text{LN}_2$  but is quite expensive if the  $\text{LN}_2$  is purchased solely for purging the spectrometer. If  $\text{LN}_2$  boil-off is unavailable, the most economical source of dry air is a regenerating dryer. Keeping dryers functioning well frequently takes more effort than keeping the spectrometer operational, and the importance of removing all oil droplets from the input to these dryers cannot be overstressed.

The presence of carbon dioxide is usually not quite as detrimental as water vapor because  $\text{CO}_2$  absorbs in less important spectral regions for most applications. Nonetheless, the best spectra are acquired by purging the instrument with  $\text{CO}_2$ -free air. Some regenerating driers produce  $\text{CO}_2$ -free air. The flow rate of the purge gas through the spectrometer should be enough to reduce the level of  $\text{H}_2\text{O}$  and  $\text{CO}_2$  to an acceptably low level within about a minute after the sample has been loaded into the spectrometer. However, the flow rate should not be too high, because microphonic noise can be introduced into the spectrum.

Many older FT-IR spectrometers, and a few contemporary ones, are equipped with a pair of flip mirrors that direct the beam through the front and back of the sample compartment, in a fashion analogous to the “sample” and “reference” beams of a double-beam grating spectrometer. This design allowed the beam to be switched from one channel to the other every 10 or 20 scans, so that the scans from each channel are signal averaged. The partial pressure of water vapor in the spectrometer changes relatively slowly while the spectrometer is being purged, so that the intensity of the lines due to atmospheric  $\text{H}_2\text{O}$  and  $\text{CO}_2$  changes at about same rate in the sample and reference single-beam spectra. When the transmittance spectrum is calculated by ratioing these two spectra, the features caused by  $\text{H}_2\text{O}$  and  $\text{CO}_2$  are, in principle, eliminated. In practice, however, the paths of the beams through these two channels are often different enough to cause small spectral shifts (see Section 2.6). If this is the case, derivative-shaped residuals are seen in the resulting transmittance spectrum.

In general, the best way to eliminate the effect of atmospheric  $\text{H}_2\text{O}$  and  $\text{CO}_2$  is always to remove these molecules before the measurement of any spectrum. If there are still some features caused by the absorption of water vapor in the spectrum, they may sometimes be eliminated by subtraction of a reference spectrum of water vapor measured with the same resolution and apodization from the spectrum. However, it should be remembered that changes in either the optical throughput or the alignment between the measurement of the reference and sample spectra will cause a wavenumber shift (see Section 2.6), leading to the same type of derivative-shaped residual lines as discussed above.



### REFERENCES

1. C. N. Su, V. J. Heintz, and T. A. Keiderling, *Chem. Phys. Lett.* **75**, 157 (1980).
2. T. A. Keiderling, Vibrational circular dichroism: comparison of techniques and practical considerations, in *Practical Fourier Transform Infrared Spectroscopy*, J. R. Ferraro and K. Krishnan, Eds., Academic Press, San Diego, CA, 1990, p. 203.
3. E. Herceg, H. Celio, and M. Trenary, *Rev. Sci. Instrum.* **75**, 2545 (2004).
4. G. P. Williams, Synchrotron and free electron laser sources of infrared radiation, in *Handbook of Vibrational Spectroscopy*, J. M. Chalmers and P. R. Griffiths, Eds., Wiley, Chichester, West Sussex, England, 2002, Vol. 1, p. 341.

# SIGNAL-TO-NOISE RATIO

## 7.1. DETECTOR NOISE

An FT-IR spectrometer is used optimally when detector noise exceeds all other noise sources and is independent of the signal level. This is the usual case for mid-infrared spectrometry but may not be so for shorter wavelengths. The sensitivity of mid-infrared detectors is commonly expressed in terms of the *noise equivalent power* (NEP) of the detector, which is the ratio of the root mean square (rms) noise voltage,  $V_n$ , in  $V \cdot \text{Hz}^{-1/2}$ , to the voltage responsivity,  $R_v$ , of the detector, in  $V \cdot W^{-1}$ . It is effectively a measure of the optical power that gives a signal equal to the noise level; thus, the smaller the NEP, the more sensitive is the detector. The NEP is proportional to the square of the detector area,  $A_D$ , with the constant of proportionality being known as the specific detectivity,  $D^*$ ; that is,

$$D^* = \frac{(A_D)^{1/2}}{\text{NEP}} \quad \text{cm} \cdot \text{Hz}^{1/2} \cdot \text{W}^{-1} \quad (7.1)$$

(The unit  $\text{cm} \cdot \text{Hz}^{1/2} \cdot \text{W}^{-1}$  is sometimes called the Jones.) The *noise power*,  $N'$ , observed in a measurement  $t$  (seconds) is given by

$$N' = \frac{\text{NEP}}{t^{1/2}} \quad \text{W} \quad (7.2)$$

To determine the signal-to-noise ratio (SNR) obtainable in any measurement, we must know not only the noise power but also the power of the signal. The *spectral brightness* i.e., the power flow per unit area per wavenumber per steradian at wavenumber  $\tilde{\nu}$  from a blackbody source at temperature  $T$  is given by the Planck equation:

$$U_\nu(T) = \frac{C_1 \nu^3}{\exp(C_2 \nu/T) - 1} \quad \text{W sr}^{-1} \cdot \text{cm}^2 \cdot \text{cm}^{-1} \quad (7.3)$$

where  $C_1$  and  $C_2$  are the first and second radiation constants, having the values

$$C_1 = 2hc^2 = 1.191 \times 10^{-12} \text{ W cm}^{-2} \cdot \text{sr} \cdot (\text{cm}^{-1})^4 \quad (7.4)$$

$$C_2 = \frac{hc}{k} = 1.439 \text{ K} \cdot \text{cm} \quad (7.5)$$

where  $k$  is Boltzmann's constant.

The power received at a detector through any optical system is determined by the *optical throughput*, or *étendue*, of that system, that is the product of the area of the beam,  $A$ , and its solid angle at the limiting aperture,  $\Omega \cdot \text{sr}$ . For an optimally designed FT-IR spectrometer, the throughput is determined by the area of the mirrors of the interferometer and the maximum allowed solid angle, given by Eq. 2.41. The power,  $S'$ , transmitted to a detector through an interferometer at a resolution  $\Delta\tilde{\nu}$  and operating at a throughput  $\Theta$  with an efficiency  $\xi$  in the unit wavenumber interval is given by

$$S' = U_v(T) \Theta \Delta\tilde{\nu} \xi \quad (7.6)$$

Thus, the SNR of a spectrum measured with a two-beam interferometer is given by

$$\text{SNR} = \frac{S'}{N'} = \frac{U_v(T) \Theta \Delta\tilde{\nu} t^{1/2} \xi}{\text{NEP}} \quad (7.7)$$

$$= \frac{U_v(T) \Theta \Delta\tilde{\nu} T^{1/2} D^* \xi}{A_D^{1/2}} \quad (7.8)$$

It has been noted in Chapters 2 and 6 that, in practice, the throughput can be limited either by the maximum allowed solid angle of the beam or by the physical constraints of the optics, especially the size of the detector or the  $f$ -number of the detector foreoptics. The latter criterion is often encountered for low-resolution measurements where the beam through the interferometer can subtend a large solid angle. When the area of the detector limits the throughput, let us denote the throughput by  $\Theta_D$ , where  $\Theta_D$  is equal to the product of the solid angle of the beam being focused on the detector,  $\Omega_D$  (in steradians), and the detector area,  $A_D (\text{cm}^2)$ .  $\Omega_D$  is given to a good approximation by [1]

$$\Omega_D = 2\pi(1 - \cos \alpha_M) \quad (7.9)$$

where  $\alpha_M$  is the maximum half-angle of convergence achievable from the detector foreoptics and rarely exceeds  $45^\circ$ ; thus,  $\Omega_D$  is usually less than 2 sr.

When the solid angle of the beam through the interferometer is determined by the maximum wavenumber of interest in the spectrum,  $\tilde{\nu}_{\text{max}}$ , and the desired resolution,  $\Delta\tilde{\nu}$ , the solid angle of the beam through the interferometer,  $\Omega_I$ , is given by

$$\Omega_I = \frac{2\pi \Delta\tilde{\nu}}{\tilde{\nu}_{\text{max}}} \quad \text{sr} \quad (7.10)$$

so that

$$\Theta_I = \frac{2\pi A_M \Delta \tilde{\nu}}{\tilde{\nu}_{\max}} \quad \text{sr} \quad (7.11)$$

where  $A_M$  is the area of the interferometer mirrors being illuminated.

To determine whether  $\Theta_I$  or  $\Theta_D$  should be used in Eq. 7.8, both parameters should be calculated and the smaller one used. This is fairly easily done and will be illustrated using the parameters of one commercial FT-IR spectrometer:

$$A_D = 0.04 \text{ cm}^2 \text{ (2-mm-square detector)}$$

$$A_M = 19.6 \text{ cm}^2 \text{ (5-cm-diameter mirrors)}$$

$$\Delta \tilde{\nu} = 1 \text{ cm}^{-1} \text{ (arbitrarily)}$$

$$\tilde{\nu}_{\max} = 4000 \text{ cm}^{-1} \text{ (for mid-infrared spectrometry)}$$

$$\Omega_D = 1.5 \text{ sr (f/1 condensing optics)}$$

Thus,

$$\Theta_D = (0.04) \times (1.5) = 0.06 \text{ cm}^2 \cdot \text{sr}$$

$$\Theta_I = 2\pi(19.6) \left( \frac{1}{4000} \right) = 0.03 \text{ cm}^2 \cdot \text{sr}$$

Since  $\Theta_I < \Theta_D$ , the throughput for  $1\text{-cm}^{-1}$  resolution measurements is limited by the maximum-allowed divergence of the beam through the interferometer rather than by the detector foreoptics. For measurements at  $2\text{-cm}^{-1}$  resolution (on this particular spectrometer),  $\Theta_I = \Theta_D = 0.06 \text{ cm}^2 \cdot \text{sr}$ , and this value is used in the following paragraph.

It is instructive to calculate the theoretical SNR of a typical commercial FT-IR spectrometer that operates with a 2-mm DTGS detector ( $D^* = 2 \times 10^8 \text{ cm} \cdot \text{Hz}^{1/2} \cdot \text{W}^{-1}$ ) with an optical throughput of  $0.06 \text{ cm}^2 \cdot \text{sr}$ . We will assume that the spectrometer is equipped with a blackbody source operating at  $1100^\circ\text{C}$  ( $1373 \text{ K}$ ); from Eq. 7.3, the spectral brightness of this source at, say,  $1000 \text{ cm}^{-1}$  is calculated to be  $6.4 \times 10^{-4} \text{ W sr}^{-1} \cdot \text{cm}^2 \cdot \text{cm}^{-1}$ . We will also assume that measurements are performed at  $4\text{-cm}^{-1}$  resolution in a measurement time of 1 s. In most commercial FT-IR spectrometers, the overall optical efficiency is about 10% ( $\xi = 0.10$ ). Substitution in Eq. 7.8 yields the remarkably high value of  $7.7 \times 10^4$ . The performance of FT-IR spectrometers is usually estimated by measuring the noise level on the *100% line*, (i.e., the spectrum that is measured from the ratio of two identical spectra). The root-mean-square noise level on the 100% line calculated from the ratio of two 1-second spectra obtained under these conditions should be 0.002%. The peak-to-peak noise level is typically five times greater than the rms value, so this would be expected to be on the order of 0.01%. Even though such high performance is pushing the limits of conventional analog-to-digital converters

(see Chapter 3), the very best commercial FT-IR spectrometers on the market come close to achieving this performance.

For any instrument, the optimum performance is found when the detector is exactly filled by the image of the source while the beam passes through the interferometer with the maximum allowed throughput (i.e., when  $\Theta_I = \Theta_D$ ). At this point, the optics are said to be *throughput matched*. Any further increase in the solid angle of the beam passing through the interferometer would result in the area of the source image at the detector exceeding  $A_D$ , in which case the effective throughput is constant at  $\Theta_D$ . The throughput of most low-resolution FT-IR spectrometers is limited by the detector foreoptics unless the diameter of the sample is less than that of the beam at the sample focus. These instruments always operate with a *constant throughput*,  $\Theta_D$ , with  $\Theta_D \leq \Theta_I$  for all resolution settings.

Spectrometers capable of higher resolution ( $\Delta\tilde{\nu} < 1 \text{ cm}^{-1}$ ) are usually equipped with a Jacquinot stop. The J-stop is located at an intermediate focus in the source optics (see Figures 6.9 and 6.10) to reduce the solid angle of the beam to the value given by Eq. 7.10. Measurements at high resolution are therefore measured with *variable throughput*,  $\Theta_I$ , which must be decreased as the spectral resolution increases (i.e.,  $\Delta\tilde{\nu}$  decreases).

## 7.2. TRADING RULES IN FT-IR SPECTROMETRY

### 7.2.1. Effect of Resolution and Throughput on SNR

The relationships among signal-to-noise ratio, resolution, and measurement time have been called the *spectroscopic trading rules*. In FT-IR spectrometry, the trading rules can be best understood from Eq. 7.8. Let us first consider the effect on the noise level of the 100% line as the retardation at which measurements made on a rapid-scanning interferometer is increased. We will assume initially that measurements are taken under the *constant throughput criterion* and that the velocity of the moving mirror is unchanged. In this case, not only do  $U_{\tilde{\nu}}(T)$ ,  $D^*$ ,  $\xi$ , and  $A_D$  remain constant but  $\Theta$  does, too. If the resolution is improved by a factor of 2 (i.e.,  $\Delta\tilde{\nu}$  is halved) and the measurement time,  $t$ , is unchanged, the SNR decreases by a factor of 2; thus, the noise level on the 100% line doubles. To regain the original SNR, the measurement time must be increased by a factor of 4, since  $\text{SNR} \propto t^{1/2}$ .

For measurements made under the *variable throughput criterion*, a greater penalty is paid for increasing the resolution. In this case not only is  $\Delta\tilde{\nu}$  halved, but so is  $\Theta$  (see Eq. 7.11). Thus, the SNR is reduced by a factor of 4 (i.e., the noise level of the 100% line is quadrupled). In this case, the measurement time must be increased by a factor of 16 to regain the original SNR.

The discussion above considers only the effect of changing the resolution on the noise level of the 100% line; the effect of changing the resolution on the intensity of spectral features should also be considered. If  $\Delta\tilde{\nu}$  is much narrower than the FWHH of the features in the spectrum, changing the resolution has a minimal effect on the intensity of these features. This would be the case for many condensed-phase

spectra if the resolution is changed from  $2\text{ cm}^{-1}$  to  $1\text{ cm}^{-1}$ . On the other hand, if  $\Delta\tilde{\nu}$  is much larger than the FWHH of the spectral features, as it often is when resolved lines in the vibration–rotation spectrum are measured, increasing the resolution will result in a narrowing of the line and a concomitant increase in its peak absorbance. Surprisingly for a spectrum comprised of weak, narrow lines, degrading the resolution by a factor of 2 will have no effect on the SNR of the lines. In this case, the width of a narrow line will double and its peak absorbance will be halved. Since both the peak absorbance of each line and the noise level on the 100% line are halved, the SNR remains approximately constant. On the other hand, if  $\Delta\tilde{\nu}$  is much less than the FWHH of the spectral features, the measured peak absorbance is effectively unchanged. Doubling the resolution (halving  $\Delta\tilde{\nu}$ ) will cause the baseline noise to be increased by a factor of 2 or 4, depending on whether the spectrum was measured under the constant or variable throughput criterion and the SNR of the bands is reduced by the same factor. It is therefore advisable not to measure the spectra of compounds with relatively broad bands at high resolution.

### 7.2.2. Effect of Apodization

For all the results derived above, it has been assumed that the interferograms were not multiplied by an apodization function. It should be recognized, however, that the process of apodization affects both the resolution and the noise level of FT-IR spectra. Perhaps the simplest example of how apodization affects the SNR of a spectrum is to compare the effect of changing from boxcar truncation to triangular apodization. The information near the centerburst determines the shape of the single-beam spectrum, and this low-resolution spectrum is largely unchanged when the interferogram is multiplied by an apodization function. Low-spatial-frequency noise (see Section 10.4) and very broad bands are also unaffected by apodization. Conversely, the sinusoids due to narrow bands take much longer to decay and are therefore far more attenuated when the spectral data are apodized. Similarly, high-spatial-frequency noise is also attenuated on apodization. In summary, apodization is simply a type of smoothing operation. On the average, the rms noise on the spectrum is decreased by a factor of  $\sqrt{3}$  for triangular apodization in comparison to boxcar truncation [2]. The more rapidly an apodization function decays, the greater will be its effect on the spectrum. For example, the Norton–Beer “strong” apodization function will smooth the spectrum significantly more than the corresponding “weak” function. Apodization is discussed further in Section 8.3.

### 7.2.3. Effect of Changing Mirror Velocity

The effect of changing the scan speed of a rapid-scanning interferometer may also be inferred from Eq. 7.8. If  $D^*$  does not change with modulation frequency, doubling the mirror velocity will simply halve the measurement and reduce the SNR by a factor of  $\sqrt{2}$ . Doubling the number of scans will recover the SNR of the original measurement.

Unfortunately, this simple treatment is rarely valid in practice, since the  $D^*$  value of most detectors varies with the modulation frequency,  $f$ , of the radiation being measured (see Chapter 6). With pyroelectric detectors,  $D^*$  varies approximately as  $f^{-1/2}$ ; thus if the speed of the moving mirror is halved while keeping the measurement time constant, the SNR will increase. Conversely,  $D^*$  of most quantum detectors usually increases as  $f$  increases up to some maximum value ( $\sim 1$  kHz for photoconductive MCT detectors). It then remains approximately constant as the modulation frequency is increased, and finally drops off at frequencies above 1 MHz. Since it is rare that interferometers are operated at scan speeds that modulate the incident radiation at frequencies greater than 1 MHz, operating at high scan speeds when an MCT detector is employed is usually beneficial.

Several other factors must also be taken into account when examining the impact of changing the velocity of the moving mirror on SNR. For example, the *duty-cycle efficiency* of the interferometer should not change greatly as the scan speed is varied. The duty cycle efficiency is defined as the ratio of the time during which the interferogram is actually being acquired to the time between successive scans. This parameter usually deteriorates at high scan speeds, because the amount of time required to turn the moving mirror around and accelerate it to a constant velocity increases slightly as the mirror speed increases, but the time taken to scan over a given retardation drops. Thus when an MCT detector is being used, increasing the mirror velocity above a certain level does not necessarily yield the full benefit in SNR expected from the detector specifications.

Similarly, the full benefit of *reducing* the scan speed when a DTGS detector is being used is not always realized. In this case, the SNR at the interferogram centerburst can become so large that it exceeds the dynamic range of the ADC, in which case the digitization noise (see Section 7.3) exceeds the detector noise. For many FT-IR spectrometers equipped with pyroelectric detectors, the mirror velocity is set at a value so that the SNR at the centerburst is just less than the dynamic range of the ADC. It may also be noted that the mirror velocity is usually set at a sufficiently high value to avoid low-frequency noise, which may be caused by vibrations of the building or the components on the optical bench. Finally, the scan speed should be kept high enough that the longest wavelength in the spectrum is modulated above the electrical line frequency (60 Hz in the United States), or else “glitches” may be seen in the spectrum (see Section 8.4.2).

### 7.3. DIGITIZATION NOISE

For valid signal averaging, the peak-to-peak noise of the interferogram should always exceed the least significant bit of the analog-to-digital converter (ADC) [i.e., the dynamic range of the ADC should exceed the SNR of the interferogram at the centerburst (see Section 3.3)]. This criterion is not easy to accomplish with modern FT-IR spectrometers. For example, in Section 7.1 it was shown that the SNR of a  $4\text{-cm}^{-1}$  spectrum measured with a DTGS detector in 1 s may be as large as  $8 \times 10^4$ . The SNR of the corresponding interferogram is even higher. For

example, for a boxcar spectrum (i.e., a single-beam spectrum of constant intensity across the wavenumber range of interest ( $\tilde{\nu}_{\max}$  to  $\tilde{\nu}_{\min}$ ) and zero intensity outside this range) with  $M$  resolution elements, the SNR at the centerburst of interferogram is  $\sqrt{M}$  times higher than the SNR of the spectrum. For example, if  $\tilde{\nu}_{\max} = 4000 \text{ cm}^{-1}$ ,  $\tilde{\nu}_{\min} = 400 \text{ cm}^{-1}$ , and  $\Delta\tilde{\nu} = 4 \text{ cm}^{-1}$ , then  $M = 900$ . If the average SNR of the spectrum is  $1 \times 10^4$ , the SNR at the interferogram centerburst is about  $3 \times 10^5$ . The dynamic range of a 16-bit ADC is  $2^{15}$  (i.e.,  $\sim 3 \times 10^4$ ). It is certainly not surprising that the SNR of a one-scan,  $4\text{-cm}^{-1}$  spectrum measured on FT-IR spectrometers manufactured between the mid-1980s and mid-1990s was about  $10^3$  (0.1% noise on the 100% line) as it was limited by the dynamic range of the ADCs used at that time.

This ADC-limited performance has been exceeded in more recent FT-IR spectrometers because of three factors: the use of *gain-ranging amplifiers*, the development of sample-and-hold ADCs with larger dynamic range than  $2^{16}$ , and the advent of the sigma-delta ADC, which are discussed in detail in Chapter 3. When efficient gain ranging is applied to an interferogram, the signal-to-noise ratio of an FT-IR spectrum measured with a pyroelectric detector can now approach the theoretical level.

## 7.4. OTHER SOURCES OF NOISE

### 7.4.1. Sampling Error

As discussed in Section 3.1, sinusoidal signals should be sampled at equal intervals with a frequency at least twice that of the highest-frequency wave (the Nyquist criterion). The effect of sampling the interferogram at unequal intervals of retardation with a random error is equivalent to adding noise to the signal, as illustrated in Figure 7.1. For an rms positional error  $\Delta x$ , the maximum SNR able to be achieved

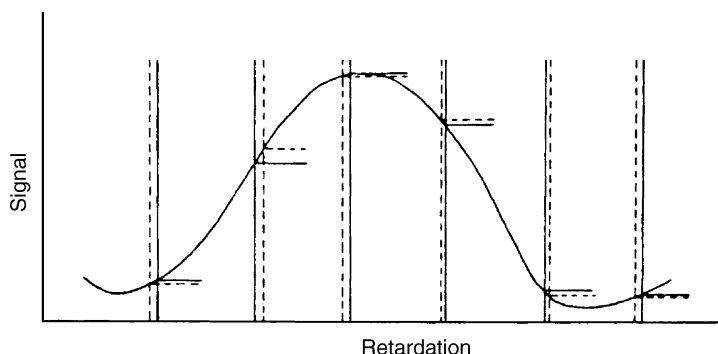


**Figure 7.1.** Simulated interferogram sampled at equally spaced intervals (solid vertical lines) and unequally spaced intervals (dashed lines). The difference between the ordinate values of the correctly and incorrectly sampled interferograms is equivalent to noise superimposed on the true interferogram. The error is dependent on both the difference between the correct and actual sampling positions and the slope of the interferogram at each point.



in the spectrum was given by Hirschfeld [1] as

$$\text{SNR}_{\text{max}} = \frac{4}{\Delta x \tilde{\nu}_{\text{max}}} \quad (7.12)$$

To achieve a SNR of  $10^5$  in the mid-infrared spectrum ( $\tilde{\nu}_{\text{max}} = 4000 \text{ cm}^{-1}$ ), the positional error must be less than  $10^{-8} \text{ cm}$  ( $1 \text{ \AA}$ ) (i.e., about one atomic diameter!). It is a testimony to the power of laser referencing that this specification is easily met by all commercial FT-IR spectrometers.

A second-order phenomenon may become important if the optical velocity of the moving mirror is not precisely constant throughout the scan, even though the interferogram is sampled at exactly equal intervals of retardation. If the mirror velocity,  $V$ , is exactly constant, radiation from a monochromatic source of wavenumber,  $\tilde{\nu}_0$ , will appear as a single sinc function in the spectrum. On the other hand, if the mirror velocity is varying sinusoidally [i.e., it may be represented as  $V(1 + a \sin 2\pi ft)$ ], the resulting spectrum will show small sidebands at wavenumbers of  $\tilde{\nu}_0 \pm f/V$  on either side of the main band. The larger the value of  $a$ , the greater will be the amplitude of the sidebands. If the mirror velocity varies randomly about the central value  $V$ , this effect will be manifested as noise, with the greatest noise amplitude occurring at  $\tilde{\nu}_0$ . For spectra of a continuous source, the noise will be dispersed throughout the spectrum and the effect of a variable mirror velocity is simply to decrease the SNR. Noise caused by variations in the mirror velocity has been treated in some detail by Zachor and Aaronson [3], and this type of noise is often referred to as *Zachor–Aaronson noise*. Zachor–Aaronson noise can be minimized by ensuring that the electronic filters through which the infrared and laser interferograms are passed are identical [4].

### 7.4.2. Folding

We have seen in Sections 3.1 and 3.2 that if the interferogram is sampled at a frequency of  $f_s$ , it is critical that the signals from all wavenumbers above  $0.5f_s/V \text{ cm}^{-1}$  and noise with a frequency greater than  $0.5f_s$  hertz must be prevented from reaching the ADC, to avoid folding. It should be recognized that electronically, signal and noise at a given frequency cannot be distinguished. Thus, noise in the region of the spectrum above the Nyquist frequency will also fold back into the spectrum. It is therefore important that the cutoff of the low-pass electronic filter be set to an appropriate value. For mid-infrared spectrometry, the Nyquist wavenumber is usually one-half the wavenumber of the HeNe laser ( $0.5\tilde{\nu}_{\text{HeNe}} \sim 7900 \text{ cm}^{-1}$ ), while the highest wavenumber of interest in the spectrum rarely exceeds  $4000 \text{ cm}^{-1}$ . Provided that the electronic filter completely eliminates the signal and noise from all frequencies above about  $0.75\tilde{\nu}_{\text{HeNe}}V$  to zero, the noise (and photometric accuracy) below  $4000 \text{ cm}^{-1}$  is not degraded by folding.

The closer the high-wavenumber end of the spectrum is to the Nyquist frequency, the faster must be the filter cutoff. So-called “brick-wall” filters have been designed, but they tend to affect the phase of the signal near the Nyquist frequency to a far

greater extent than do slower filters. Thus, care has to be taken to ensure that phase correction is done correctly in order that there is no degradation of the photometric accuracy of the spectrometer.

### 7.4.3. Fluctuation Noise

If the intensity of the signal varies, due either to fluctuations of the source output, the detector response, or to changes in the refractive index of the atmosphere between the source and the detector (*scintillation*), noise will be seen over the frequency range at which these fluctuations occur. Unlike the types of noise we have considered to date, which are additive, fluctuation noise is *multiplicative* and is much more serious for Fourier spectrometry.

When fluctuation noise is greater than detector noise, the changes caused by the fluctuations may negate the multiplex advantage [5]. The SNR of spectra measured in the presence of fluctuation noise has been given by Hirschfeld [1] as

$$\text{SNR} = \frac{f(\tilde{\nu}) \Delta\tilde{\nu} \xi t^{1/2}}{a^2 + b^2(\tilde{\nu}_{\max} - \tilde{\nu}_{\min}) F^{*2}} \quad (7.13)$$

where  $f(\tilde{\nu})$  is the spectral energy density function,  $\Delta\tilde{\nu}$  the resolution,  $\xi$  the spectrometer efficiency,  $t$  the measurement (as discussed at the start of this chapter),  $a$  the detector noise,  $b$  the relative fluctuation amplitude, and  $F^*$  the average value of  $f(\tilde{\nu})$ .

In the absence of fluctuation noise, the multiplex advantage of FT-IR spectrometry over a single-channel dispersive spectrometer with the same optical throughput and efficiency (often referred to as *Fellgett's advantage*) is given by the square root of the number of resolution elements in the spectrum,  $M$ , where  $M = (\tilde{\nu}_{\max} - \tilde{\nu}_{\min})/\Delta\tilde{\nu}$ .

For a boxcar spectrum, where  $F^* = f(\nu)$ , the Fellgett advantage in the presence of fluctuation noise is given by

$$F_g = \left( \frac{1 + g^2}{M^{-1} + M_g^2} \right)^{1/2} \quad (7.14)$$

where  $g$  is the ratio of fluctuation noise to detector noise in each resolution element:

$$g = \frac{bF^* \Delta\tilde{\nu}}{a} \quad (7.15)$$

The multiplex advantage is canceled completely when  $F_g = 1$ , which occurs when  $g = M^{1/2}$ .

Hirschfeld has shown the effects of various values of the relative fluctuation amplitude  $b$  on spectra measured with a SNR of 100 as  $M$  varies; his conclusions are summarized in Figure 7.2. It can be seen that very small fluctuations (so small that they cannot conveniently be measured electronically) cause the SNR to be

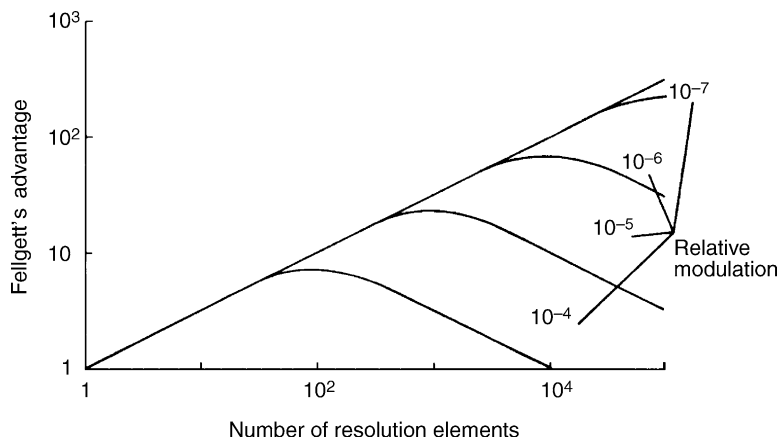


**Figure 7.2.** Effect of multiplicative noise on Fellgett's advantage as a function of the number of resolution elements for a spectral SNR of 100 and several different values of the relative fluctuation amplitude. (Reproduced from [1], by permission of Academic Press; copyright © 1979.)

degraded. Hirschfeld has suggested that reduction in the fluctuation noise is a major cause of the “5 o'clock effect,” that is, the performance of some FT-IR spectrometers improving in the evening when many external perturbations are shut down.

No single technique will compensate completely for the effects of fluctuation noise. The best way to minimize this effect is to use a scan speed that causes the infrared wavelengths to be modulated at frequencies outside the frequency range of the perturbations. Atmospheric scintillation is rarely observed at frequencies much above 500 Hz, so these effects are rarely seen in the mid-infrared spectrum when the mirror velocity is greater than about  $1 \text{ cm} \cdot \text{s}^{-1}$ . On the other hand, fluctuation noise can be a major problem when the scan speed is very low, as it is with FT-Raman spectrometry (see Chapter 18) and step-scanning interferometers (see Section 5.5). The possible causes of fluctuation noise in step-scan FT-IR spectrometry have been discussed in some detail by Manning and Griffiths [6].

#### 7.4.4. Shot Noise

The advantages of Fourier transform spectrometry over the use of a scanning monochromator (often referred to as *dispersive spectrometry*) is fully valid only when the detector noise is independent of the power of the radiation incident on the detector. When the detector is photon shot-noise limited [as it generally is for a photomultiplier tube (PMT), and often is for other sensitive detectors used in the near-infrared, visible, and ultraviolet spectral regions], the noise level is proportional to the square root of the incident power. For a boxcar spectrum, this means that shot noise is proportional to the square root of the number of resolution elements in the spectrum,  $M^{1/2}$ . This disadvantage therefore precisely offsets Fellgett's advantage when continuous broadband sources are employed. It should also be

noted that Jacquinot's advantage (see Section 7.5) is reduced by the ratio of the square root of the throughputs of the interferometer and monochromator. The effect of shot noise is the main reason why Fourier spectrometry was never popular for measurements of ultraviolet and visible spectra. Indeed, with the availability of charge-coupled-device (CCD) array detectors with quantum efficiencies that approach 100%, the only reason to use two-beam interferometers for the measurement of UV-visible spectra is the wavenumber precision afforded by the reference laser.

Hirschfeld [7] proposed that for atomic emission spectrometry (AES), where discrete lines are observed, shot noise will be distributed across the entire spectrum. Thus, weak emission lines may be buried under the noise generated by strong atomic lines. Even though AES performed with an FT spectrometer often gives lower SNR than the corresponding measurement carried out with an échelle grating and charge-coupled-device array detector, the very high wavenumber precision of the FT instrument has led some practitioners to use FT spectrometers for AES. For the measurement of an atomic emission spectrum that consists of a few weak and no intense lines, the distribution of shot noise would appear to be an advantage. In one of the few experiments in which this hypothesis might be checked, however, Horlick et al. [8] found that the noise level in the region of an isolated emission line (as estimated by the standard deviation of several measurements of its peak intensity) was substantially greater than the baseline noise. The source of this noise is probably related to the fluctuations of the source.

Until 1985, it was also believed that the very strong line due to Rayleigh scattering would always lead FT-Raman spectrometry to yield poorer spectra than a scanning monochromator with a PMT. The development of very sharp notch filters to eliminate the Rayleigh line while transmitting the Raman bands negated this argument, and FT spectrometry is a powerful approach to the measurement of Raman spectra with near-infrared excitation, as described in Chapter 18.

## 7.5. INTERFEROMETERS VERSUS GRATING SPECTROMETERS

### 7.5.1. Fellgett's Advantage

The two fundamental benefits of Fourier transform over grating spectrometry are the multiplex (Fellgett) and throughput (Jacquinot) advantages. The multiplex advantage, which was discussed in Section 7.4.3, results from the capability to measure spectral information from all wavelengths simultaneously. An analogous advantage is found for all Fourier transform techniques over the corresponding single-channel measurement [e.g., FT-NMR (nuclear magnetic resonance) over continuous-wave NMR spectrometry]. The multiplex advantage can be stated in two ways:

1. For spectra measured in the same time at the same resolution, optical throughput and efficiency, the SNR of a spectrum measured on an FT-IR

spectrometer exceeds the SNR of an identical spectrum measured on a grating spectrometer by the square root of the number of resolution elements in the spectrum,  $\sqrt{M}$ .

2. To measure such spectra with the same SNR, the dispersive spectrum must be measured  $M$  times longer than the FT spectrum. This can be a significant improvement. For example, for a mid-infrared spectrum measured at a resolution of  $4 \text{ cm}^{-1}$ ,  $M = 900$ . Assuming that it takes 15 minutes to measure this spectrum on a grating spectrometer, it would only take 1 second to measure the same spectrum on an FT-IR spectrometer.

### 7.5.2. Jacquinot's Advantage

The maximum optical throughput of a Fourier spectrometer is

$$\Theta_I = \frac{2\pi A_M \Delta\tilde{\nu}}{\tilde{\nu}_{\max}} \quad \text{cm}^2 \cdot \text{sr} \quad (7.16)$$

where  $A_M$  is the effective area of the interferometer mirrors. The throughput of a grating spectrometer operating in first order is

$$\Theta_G = \frac{h A_G \Delta\tilde{\nu}}{f a \tilde{\nu}^2} \quad \text{cm}^2 \cdot \text{sr} \quad (7.17)$$

where  $h$  is the slit height,  $A_G$  the effective area of the grating,  $f$  the focal length of the collimating mirror, and  $a$  the grating constant. The ratio of the throughputs of these two spectrometers (Jacquinot's advantage) is, therefore [9],

$$\frac{\Theta_I}{\Theta_G} = \frac{2\pi A_M f a \tilde{\nu}^2}{A_G h \tilde{\nu}_{\max}} \quad (7.18)$$

This equation shows that Jacquinot's advantage increases as  $\tilde{\nu}^2$  if neither the beamsplitter nor the grating is changed during the measurement. However, since most commercial grating spectrometers incorporate automatic grating interchanges (usually, at  $2000$  and  $667 \text{ cm}^{-1}$ ), the grating constant may change at these wavenumbers. Jacquinot's advantage is shown for two commercial mid-infrared spectrometers operating at  $2 \text{ cm}^{-1}$  resolution in Figure 7.3. It can be seen that  $\Theta_I$  is substantially superior to  $\Theta_G$  over much of the spectrum, but toward the far infrared the use of an optimized grating makes Jacquinot's advantage quite small.

For FT-IR spectrometers where the throughput is limited by the detector foreoptics (the constant throughput case discussed in Section 7.2), Jacquinot's advantage may be considerably less than the value calculated from Eq. 7.18. For example, if the resolution is changed from  $2 \text{ cm}^{-1}$  to  $8 \text{ cm}^{-1}$ , the throughput of the grating spectrometer can increase by a factor of 16 while  $\Theta_I$  remains unchanged [9].

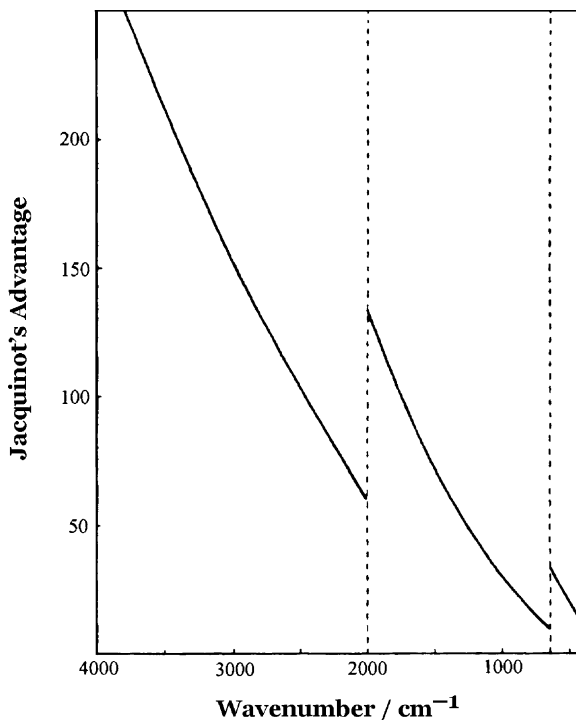


**Figure 7.3.** Calculated variation of Jacquinot's advantage between a Digilab FTS-14 FT-IR spectrometer and a Beckman Model 4240 grating spectrometer, both operating at  $2\text{ cm}^{-1}$  resolution. The dashed lines indicate the grating changes for the monochromator. (Reproduced from [9], by permission of the Society for Applied Spectroscopy; copyright © 1977.)

### 7.5.3. Other Factors

Combining the values of Fellgett's and Jacquinot's advantages, FT-IR spectrometers should be about 2000 times more sensitive than grating spectrometers that operate in the mid-infrared. In practice, however, smaller values are found. To understand why this is the case, we must consider other components in these spectrometers. The same types of source are used in both types of instruments, so we will neglect any discussion of this component. This cannot be said of the detector, however.

A typical value for the NEP of a thermocouple used in a grating spectrometer with a 15-Hz chopper is  $1 \times 10^{-10} \text{ W} \cdot \text{Hz}^{-1/2}$ . This number increases (i.e., deteriorates) rapidly as the chopping frequency increases, so higher chopping rates are rarely used. Thermocouples are never installed in rapid-scanning FT-IR spectrometers because of the deleterious effects of reducing the mirror velocity (see Section 7.2.3).

The typical NEP of a DTGS detector for a modulation frequency of 15 Hz is  $2 \times 10^{-9} \text{ W} \cdot \text{Hz}^{-1/2}$  [i.e., about 20 greater (i.e., worse) than that of a thermocouple].

Furthermore, the NEP of pyroelectric detectors increases with modulation frequency (although not as rapidly as that of the thermocouple). The mirror speed for many FT-IR spectrometers equipped with DTGS detectors is  $1.58 \text{ mm} \cdot \text{s}^{-1}$ , which corresponds to a laser modulation frequency of 5 kHz. The ratio of the NEP of a pyroelectric detector of an FT-IR spectrometer operating at this scan speed to that of a thermocouple in a grating spectrometer with a 15-Hz chopper is shown in Figure 7.4. Comparing the data in Figures 7.3 and 7.4, it can be seen that the “detector disadvantage” of mid-infrared Fourier transform spectrometry largely offsets the Jacquinot advantage [9]. Thus, the practical advantage of FT-IR spectrometers equipped with DTGS detectors over grating spectrometers equipped with a thermocouple detector is given simply by Fellgett’s advantage (i.e., a time advantage of  $(\tilde{\nu}_{\text{max}} - \tilde{\nu}_{\text{min}})/\Delta\tilde{\nu}$  for measurements made at the same SNR or an SNR advantage of  $[(\tilde{\nu}_{\text{max}} - \tilde{\nu}_{\text{min}})/\Delta\tilde{\nu}]^2$  for measurements made in the same time).

The efficiency of a diffraction grating can approach 85% at the wavelength for which it is optimized. Nonetheless, the efficiency falls off quickly on either side of

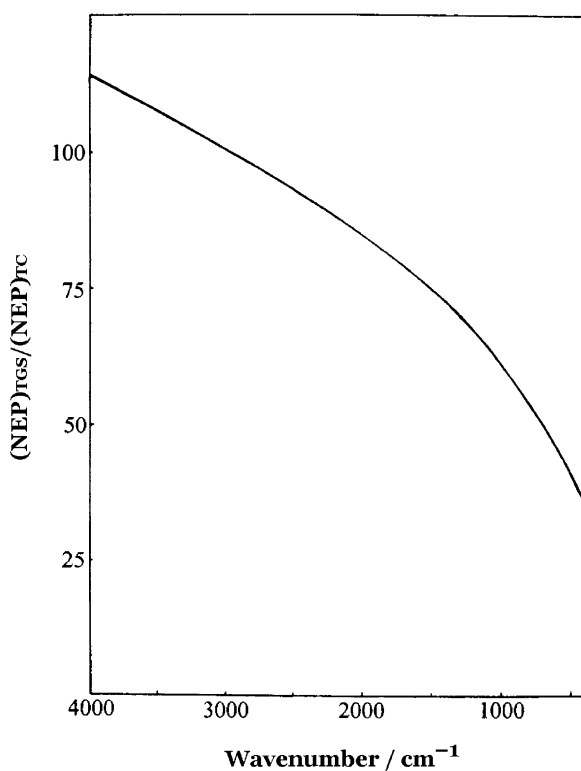


**Figure 7.4.** Ratio of the NEPs of a triglycine sulfate pyroelectric bolometer of the type used on early FT-IR spectrometers and a thermocouple of the type used on grating spectrometers. The mirror velocity for the interferometer was  $1.58 \text{ mm} \cdot \text{s}^{-1}$  (5-kHz laser frequency). (Reproduced from [9], by permission of the Society for Applied Spectroscopy; copyright © 1977.)

this wavelength. Conversely, the efficiency of beamsplitters (especially multilayer beamsplitters) remains high over much of the spectrum (as discussed in Section 5.6). Thus, a comparison of the efficiency of gratings and beamsplitters favors FT-IR spectrometry.

A good description of all the factors contributing to the efficiency of an FT-IR spectrometer has been reported by Mattson [10]. He measured the effect of several different parameters that include beamsplitter efficiency, Fresnel losses at the substrate and compensator plate, reflection losses at the mirrors, radiation obscured by the mounting hardware for the HeNe laser, the emissivity of the source, and losses caused by imperfect optical alignment. He calculated the overall efficiency ( $\xi$  in Eq. 7.8) as being 0.096. This value is in accord with the value of 0.10 used in Section 7.1 to estimate the SNR of a commercial FT-IR spectrometer.

## REFERENCES

1. T. Hirschfeld, Quantitative IR: a detailed look at the problems involved, in *Fourier Transform Infrared Spectroscopy: Applications to Chemical Systems*, J. R. Ferraro and L. J. Basile, Eds., Academic Press, New York, 1979, Vol. 2, p. 193.
2. T. Hirschfeld, personal communication to P. R. Griffiths (1970).
3. A. S. Zachor and S. M. Aaronson, *Appl. Opt.* **18**, 68 (1979).
4. L. M. Logan, Signal-to-noise enhancement of Fourier transform spectroscopy (FTS) by electrical filter compensation of slide velocity errors, in *Multiplex and/or High Throughput Spectroscopy*, G. A. Vanasse, Ed., Society of Photo-Optical Instrumentation Engineers, Bellingham, WA, 1979, Vol. 191, p. 110.
5. T. Hirschfeld, *Appl. Spectrosc.* **30**, 234 (1976).
6. C. J. Manning and P. R. Griffiths, *Appl. Spectrosc.* **51**, 1092 (1997).
7. T. Hirschfeld, *Appl. Spectrosc.* **30**, 68 (1976).
8. G. Horlick, R. H. Hall, and W. K. Yuen, Atomic emission spectrochemical measurements with a Fourier transform spectrometer, in *Fourier Transform Infrared Spectroscopy: Techniques Using Fourier Transform Interferometry*, J. R. Ferraro and L. J. Basile, Eds., Academic Press, New York, 1982, Vol. 3, p. 37.
9. P. R. Griffiths, H. J. Sloane, and R. W. Hannah, *Appl. Spectrosc.* **31**, 485 (1977).
10. D. R. Mattson, *Appl. Spectrosc.* **32**, 335 (1978).





## Chapter 8

# PHOTOMETRIC ACCURACY IN FT-IR SPECTROMETRY

### 8.1. INTRODUCTION

Many factors affect the photometric accuracy of Fourier transform spectrometers. They include the effect of resolution and apodization on the spectrum, the reproducibility of the single-beam spectra, the accuracy of the zero level, and the linearity of the transmittance ( $T$ ) scale. Several spectrometer manufacturers have observed that the 100% line on their instruments may be reproduced to better than 0.1% and, as a result, have claimed that their instruments are *accurate* to 0.1% $T$ . This is not necessarily the case, however, as we show below.

### 8.2. EFFECT OF SPECTRAL RESOLUTION

No matter what type of spectrometer is used, a measured spectrum is always slightly different from the true spectrum because of the measurement process, and it is important to recognize that instrumental effects often determine how well Beer's law is obeyed for any chemical system. For example, when a monochromator is used to measure a spectrum, the true spectrum is convolved with the spectrometer's slit function. The effect of this convolution is to decrease the intensity and increase the width of all bands in the spectrum. The convolution of Lorentzian absorption bands with a triangular slit function was reported over 50 years ago in a classic paper by Ramsay [1]. Ramsay defined a *resolution parameter*,  $\rho$ , as the ratio of the full width at half-height (FWHH) of the slit function to the true FWHH of the band. He showed how the measured, or apparent, absorbance,  $A_{\text{peak}}^a$ , at the peak of a Lorentzian band varied as a function of the true peak absorbance,  $A_{\text{peak}}^t$ , and the resolution parameter. Not surprisingly, Ramsay showed that as  $\rho$  approaches zero (infinitely high resolution), the band is measured with increased accuracy.

In the absence of chemical or instrumental effects, Beer's law tells us that the true peak absorbance of each band of any component of a mixture,  $A_{\text{peak}}^t$ , is directly proportional to the concentration of a given component of a mixture. If Beer's law is to be obeyed in practice (in the absence of chemical effects), a plot of the apparent, or measured, peak absorbance,  $A_{\text{peak}}^a$  versus  $A_{\text{peak}}^t$  must be linear, but  $A_{\text{peak}}^a$  need not necessarily be equal to  $A_{\text{peak}}^t$ . In this case the slope of a plot of  $\log A_{\text{peak}}^a$  versus  $\log A_{\text{peak}}^t$  must be unity. Ramsay showed that for spectra measured on a grating spectrometer with a triangular slit function, this criterion was fulfilled for all values of  $\rho$  provided that  $A_{\text{peak}}^t$  is less than about 0.7. On the other hand, at very high values of  $A_{\text{peak}}^t$ , the slope of plots of  $\log A_{\text{peak}}^a$  versus  $\log A_{\text{peak}}^t$  approached 0.5, indicating that  $A_{\text{peak}}^a$  is proportional to  $(A_{\text{peak}}^t)^{1/2}$  when the true peak absorbance is significantly greater than 1. Surprisingly, this behavior was predicted even for  $\rho < 0.2$ . In summary, for spectra measured on a grating monochromator, Beer's law is obeyed in practice only when the true peak absorbance is less than about 0.7 for all reasonable values of the resolution. We will see that this conclusion is sometimes, but not always, also true for FT-IR spectrometers.

Anderson and Griffiths [2] examined the corresponding behavior for Lorentzian bands measured with a FT-IR spectrometer. They defined the *nominal resolution* of the spectrometer as the reciprocal of the maximum retardation, so that in this case  $\rho$  is equal to the reciprocal of the product of the maximum retardation,  $\Delta_{\text{max}}$ , and the true FWHH of the band. Plots of  $\log A_{\text{peak}}^a$  versus  $\log A_{\text{peak}}^t$  for spectra

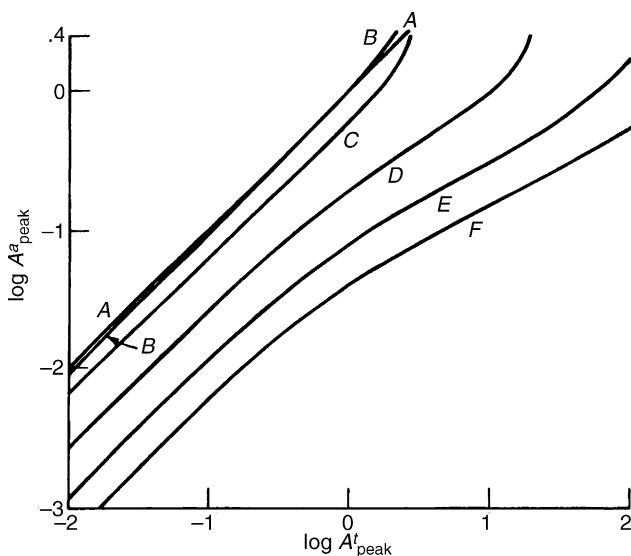


**Figure 8.1.** Variation of the measured, or apparent, absorbance,  $A_{\text{peak}}^a$ , at the peak of a Lorentzian band as a function of the true peak absorbance,  $A_{\text{peak}}^t$ , plotted on a logarithmic scale for Lorentzian bands measured with no apodization (boxcar truncation). A,  $\rho = 1.0$ ; B,  $\rho = 3$ ; C,  $\rho = 10$ ; D,  $\rho = 25$ ; E,  $\rho = 50$ . (Reproduced from [2], by permission of the American Chemical Society; copyright © 1975.)

measured without apodization are reproduced in Figure 8.1. It can be seen that Beer's law is always obeyed (i.e., the slope of this plot is equal to unity) by relatively weak bands ( $A'_{\text{peak}} < \sim 0.7$ ), but not for more intense bands; however, the behavior is strongly dependent on the way in which the interferograms are apodized.

The main cause of the deviation from ideal Beer's law behavior seen in Figure 8.1 is the fact that the single-beam spectrum of the sample is the product of the single-beam spectrum of the background and the transmittance spectrum of the sample. Thus when unapodized spectra are measured on a FT-IR spectrometer, the transmittance spectrum *and not the absorbance spectrum* is convolved with the sinc ILS function (see Section 2.3). As  $A'_{\text{peak}}$  increases, the shape of bands in the transmittance spectrum becomes progressively less Lorentzian. When  $A'_{\text{peak}} > 3$ , convolution of bands in the transmittance spectrum with the sinc ILS function introduces sidelobes to the spectrum. To illustrate this effect, transmittance spectra measured with  $\rho = 1$  and  $A'_{\text{peak}} = 2, 3, 4$ , and 5 (minimum percent transmission = 1, 0.1, 0.01, and 0.001%, respectively) are shown in Figure 8.2. When  $A'_{\text{peak}} = 1$ , the sidelobes are not apparent, but it can be seen that  $A^a_{\text{peak}} > A^t_{\text{peak}}$ , which helps to explain the positive deviation from Beer's law behavior in Figure 8.1 when  $\rho = 1$ .

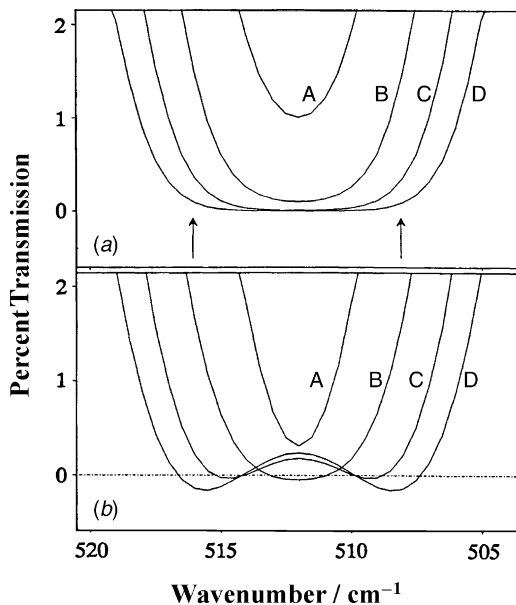


**Figure 8.2.** (a) Ordinate expanded transmittance spectra for A,  $A'_{\text{peak}} = 2$ ; B,  $A'_{\text{peak}} = 3$ ; C,  $A'_{\text{peak}} = 4$ ; D,  $A'_{\text{peak}} = 5$  measured at infinitely high resolution (i.e.,  $\rho = 0$ ); (b) Corresponding spectra obtained when  $\rho = 1$ . (Reproduced from [2], by permission of the American Chemical Society; copyright © 1975.)

### 8.3. EFFECT OF APODIZATION

#### 8.3.1. Triangular Apodization

The effect of apodization on plots of  $\log A_{\text{peak}}^a$  versus  $\log A_{\text{peak}}^t$  can be quite dramatic. Figure 8.3 shows the effect of weighting the interferogram with a triangular apodization function. It can be seen that the slope of each of these curves is always less (and often much less) than unity at high values of  $A_{\text{peak}}^t$ , implying that a negative deviation from ideal Beer's law behavior is always observed. The reason why  $A_{\text{peak}}^a < A_{\text{peak}}^t$  is because the  $\text{sinc}^2$  ILS function (the FT of the triangular apodization function) is convolved with the true transmittance spectrum. The resulting spectrum is then converted to absorbance. The integrated area of an absorption band increases with concentration, but the increase in area is not only manifested as an increase in  $A_{\text{peak}}^a$  but also in an increase in the FWHH of the peak. The increased absorbance is also distributed to the sidelobes. Since all the sidelobes in the  $\text{sinc}^2$  ILS are positive, the value of  $A_{\text{peak}}^a$  increases with concentration at a less than linear rate.

The series of curves shown in Figure 8.3 is quite similar to the corresponding series of curves calculated by Ramsay for a monochromator with a triangular slit function. However, with the triangular apodization function, the slope of the plot of  $\log A_{\text{peak}}^a$  versus  $\log A_{\text{peak}}^t$  can be as small as  $\frac{1}{6}$ , indicating that  $A_{\text{peak}}^a$  can vary as  $(A_{\text{peak}}^t)^{1/6}$  when  $A_{\text{peak}}^t$  is very large.

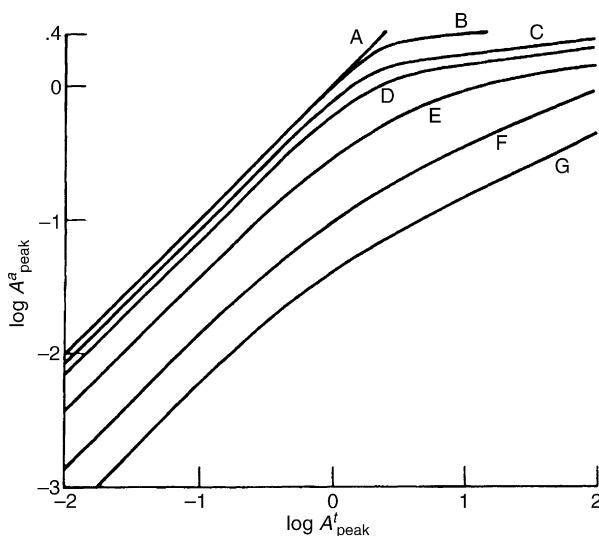


**Figure 8.3.** Variation of  $\log_{10} A_{\text{peak}}^a$  with  $\log_{10} A_{\text{peak}}^t$  for Lorentzian bands measured with triangular apodization. A,  $\rho = 0$ ; B,  $\rho = 0.1$ ; C,  $\rho = 0.5$ ; D,  $\rho = 1$ ; E,  $\rho = 3$ ; F,  $\rho = 10$ ; G,  $\rho = 25$ . (Reproduced from [2], by permission of the American Chemical Society; copyright © 1975.)

### 8.3.2. Norton–Beer Apodization Functions

The fact that positive deviations from Beer's law behavior are seen with boxcar truncation and negative deviations are observed with triangular apodization caused Zhu and Griffiths [3,4] to investigate the behavior of a number of other apodization functions to find if any function would minimize instrumentally induced deviations. They found that many of the common functions gave improved adherence to Beer's law, but that no function allowed linear Beer's law curves to be measured whenever  $\rho$  is much greater than 0.5 and  $A_{\text{peak}}^t$  exceeds about 2. Every function that they investigated gave superior performance to the triangular function, presumably because unlike the  $\text{sinc}^2$  function, the sidelobes oscillated between positive and negative values. The most important conclusions of this study were that (1) triangular apodization is to be avoided whenever quantitative measurements are being made with an FT-IR spectrometer, and (2) of the common apodization functions, the Norton–Beer medium function led to the best adherence to Beer's law for spectra measured at moderate resolution ( $\rho < 0.5$ ).

There are other apodization functions in use besides the Norton–Beer and the Happ–Genzel. These functions have not been tested as thoroughly; however, it has been noted by the authors that the Blackman–Harris and Blackman apodization functions (Section 2.4) are considerably broader than the Norton–Beer medium or Happ–Genzel apodization functions. It is expected that these functions will not adhere to Beer's law as well as the Norton–Beer medium function.

## 8.4. 100% LINES

### 8.4.1. Short-Term Performance

A 100% line is simply measured by ratioing two single-beam spectra acquired under identical conditions of resolution and measurement time. These spectra are often measured with no sample in the beam, with the second spectrum being acquired immediately after the first. A ratio of these two spectra indicates how the noise level varies across the spectrum (see Figure 8.4). For mid-infrared FT-IR spectrometry, it has become conventional to measure the noise level between 2000 and 2200  $\text{cm}^{-1}$ , as the amplitude of the single-beam spectrum is usually greatest in this region and there is minimal interference by the absorption of atmospheric water vapor and  $\text{CO}_2$ . For day-to-day checking of the performance of FT-IR spectrometers, however, it is often better to measure the noise level at shorter wavelengths e.g., between 4000 and 3800  $\text{cm}^{-1}$ , as the effect of interferometer misalignment is greatest in this region.

Noise is either measured as the *peak-to-peak* or *root-mean-square* (rms) value. Peak-to-peak noise is simply the difference between the maximum and minimum values of the 100% line in a given spectral region, whereas the rms noise is the standard deviation of *all* data points in this region. Because the peak-to-peak noise is determined by the noise excursion at only two wavenumbers, the rms noise is a statistically more valid measure of the noise level. For a 100% line

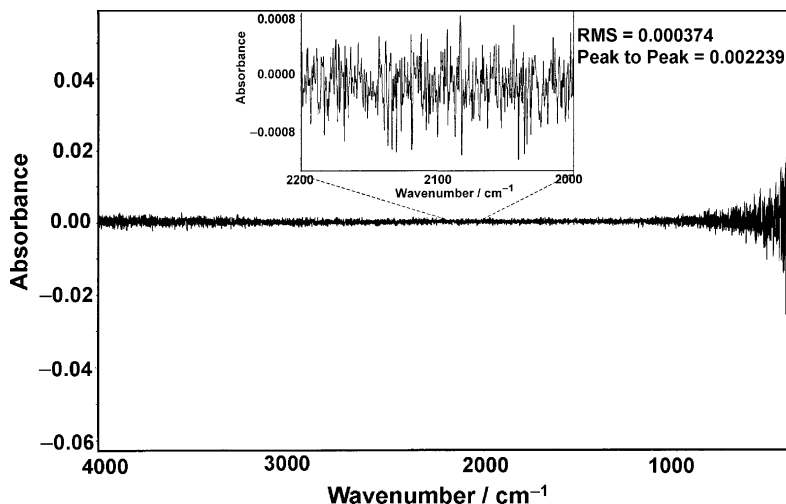


**Figure 8.4.** Typical 100% line. Note the increased noise at the low-wavenumber end of the spectrum because of the low energy in the single-beam spectrum. The region between 2200 and 2000  $\text{cm}^{-1}$  has been scaled expanded; the difference between the maximum and minimum datum in this region is the peak-to-peak noise. The root-mean-square noise is the standard deviation of all the data points in this region.

measured between 2200 and 2000  $\text{cm}^{-1}$  at a resolution of 2  $\text{cm}^{-1}$ , there are 100 independent data points (or resolution elements), in which case the peak-to-peak noise would be expected to be about five times larger than the rms noise since 99% of numbers with a Gaussian distribution are within 2.5 standard deviations of the mean. The greater the number of resolution elements in the spectral region being studied, the larger will be the ratio of the peak-to-peak and rms noise.

An analogous measurement with a reference cell in the beam can be used to determine the feasibility of any given experiment, as the noise on the spectral baseline can increase greatly in regions where the energy level of the background spectrum is low. Consider an example where the spectrum of a particular solute is to be measured. It is common to mount a cell containing the pure solvent in the infrared beam for measurement of the background spectrum. If the absorbance at the peak of a particular absorption band in the solvent spectrum is, say, 2.0 (percent transmission = 1.0%), the noise level near the absorption maximum will be 100 times higher than the noise level of the corresponding measurement made with no solvent in the beam. Detection limits are, of course, far lower in window regions of the solvent spectrum, where minimal absorption is evident in the background spectrum. Ideally, the solvent should be selected so that the key solute bands absorb in the windows of the solvent spectrum. Of course, this is not always possible. For example, the amide I band of proteins absorbs very near the H—O—H bending mode of water. If the amide I band of a protein in aqueous solution is of interest, it is important to know how the noise varies across the protein spectrum after compensation for the absorption spectrum of water.

Since signal-to-noise ratio (SNR) increases with the square root of the measurement time,  $t$ , the amplitude of the rms noise on the 100% line should always decrease with the square root of the number of scans,  $N$ . The SNR may be calculated from the rms noise on the 100% line as

$$\text{SNR} = \frac{100}{\text{rms noise}} \quad (8.1)$$

(assuming that the noise is measured as percent transmission). To determine whether a given instrument is signal-averaging correctly, the SNR should be plotted against  $N^{1/2}$ . (This is conveniently accomplished with  $N = 1, 4, 16, 64, 256, 1024, 4096$ , etc.) For many commercial FT-IR spectrometers, there is a limit to the number of scans for which such plots are linear, but most contemporary instruments will permit valid signal averaging for at least 4096 scans. On older FT-IR spectrometers, however, the SNR may stop increasing after only 100 scans have been averaged [5]. If long acquisition times are needed for a particular experiment, it is important to test how accurately the rms noise level decreases with the square root of the number of scans by plotting the reciprocal of the rms noise against  $\sqrt{N}$ .

The SNR of many FT-IR spectrometers designed for operation in the mid-infrared spectrum is usually worse between 600 and 400  $\text{cm}^{-1}$  than in any other spectral region. There is also a greater difference in the performance of commercial FT-IR spectrometers in this spectral region than in any other, as some manufacturers have taken more care to optimize the performance in this region than others. Three reasons account for the poor performance of mid-infrared spectrometers below 600  $\text{cm}^{-1}$ :

1. The mid-infrared energy emitted by any incandescent source is lowest at low wavenumber.
2. The efficiency of many mid-infrared beamsplitters is usually worse between 600 and 400  $\text{cm}^{-1}$  than at higher wavenumbers unless a CsI substrate has been specified.
3. For measurements made with low scan speeds, not only is the effect of  $1/f$  noise greatest at low wavenumber, but there is also a high probability of interference by harmonics of the electrical line frequency.

In the event that a spectroscopist is keenly interested in the region below 600  $\text{cm}^{-1}$ , we strongly recommend that 100% lines be measured in the region between 600 and 400  $\text{cm}^{-1}$  before deciding which instrument to purchase. If the performance of a spectrometer equipped with a KBr beamsplitter is inadequate, a beamsplitter with a CsI substrate should be used.

Similar arguments can be made for measurements made in the near-infrared region e.g., from 9000 to 4000  $\text{cm}^{-1}$ . In this case, the best performance is usually in the windows between the atmospheric water bands at about 5300 and 7200  $\text{cm}^{-1}$ . Good 200- $\text{cm}^{-1}$ -wide windows for measuring the optimum performance of FT-NIR spectrometers are 4600 to 4400 and 6200 to 6000  $\text{cm}^{-1}$ , while interferometer drift is best examined in the region above 8000  $\text{cm}^{-1}$ .



### 8.4.2. Glitches (Nonrandom Noise Sources)

The analysis above is valid if the noise is derived entirely from random noise on the interferogram. Occasionally, sinusoidal interferences contribute to the interferogram. Any sinusoidal interference at a frequency  $f$  hertz will be manifested as a “glitch” in the spectrum at a wavenumber of  $f/V \text{ cm}^{-1}$ , where  $V \text{ cm (retardation) s}^{-1}$  is the optical velocity of the interferometer mirror (see Eq. 2.11). A typical glitch is shown in Figure 8.5. Sources of sinusoidal interference may be electrical (e.g., harmonics of the electrical line frequency; see Section 6.2.1), optical (e.g., radiation from fluorescent light bulbs reaching the detector), or mechanical (e.g., a vibration of the optical bench or mirrors). Such glitches should be recognized in the 100% line and avoided in calculations of noise (especially peak-to-peak noise). If glitches appear at wavenumbers that are important to the particular experiment being performed, the velocity of the moving mirror of some interferometers can be changed to move the glitch to a less important spectral region. In any event, it is a good thing to trace down any source of interference at a specific frequency and attempt to eliminate it. The phase of sinusoidal interferences is rarely correlated with the phase of the infrared frequencies in the interferogram. Thus, like random noise, the amplitude of glitches in the spectrum of the type shown in Figure 8.5 will also decrease with the square root of the number of scans. Note, however, that if the amplitude of a glitch is greater than the detector noise level, it can never be reduced below the detector noise level by signal averaging.

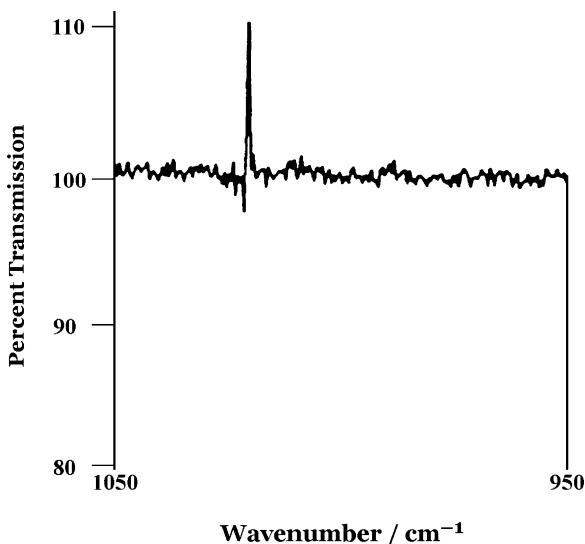


**Figure 8.5.** Typical glitch on the baseline of a transmission spectrum. In this case the glitch is at  $\sim 1020 \text{ cm}^{-1}$ . Since the spectrum was measured with a data acquisition frequency of 5 kHz using a HeNe laser interferogram to trigger data acquisition, the glitch was caused by interference by a sinusoid of frequency  $\sim 320 \text{ Hz}$ , possibly caused by a mirror vibrating at this frequency.

### 8.4.3. Long-Term Performance

If there is a significant time delay between the measurement of the two single-beam spectra used for calculation of the 100% line, the deviation of the resulting ratio-recorded spectrum from 100% gives an indication of the stability of the spectrometer with time. Typical time delays over which interferometer alignment must be maintained can be as short as 1 minute or as long as several days. If the first spectrum is measured when the interferometer is well aligned and the interferometer goes out of alignment before the measurement of the second spectrum, the resulting 100% line will lie below 100%. Because the effect of alignment errors depends on the ratio of the optical misalignment to the wavelength, the greatest deviation from 100%  $T$  is invariably seen in the short-wavelength region of the spectrum, as shown in Figure 2.17. The alignment of many interferometers varies with temperature. Thus, if an instrument is mounted in a room in which the temperature varies by more than 1 or 2°C, significant changes in the level of the 100% line can be expected in periods as short as a few minutes [6].

Many users save a single-beam spectrum of their instrument and use it as the background spectrum for the calculation of all transmittance spectra measured in a given day, and sometimes even longer. (The use of a particular background for more than a day is not recommended by these authors, however.) If it is common practice in a given laboratory to use one spectrum as the background for several sample spectra, the background spectrum should always be measured by co-adding at least four times the number of scans typically used for the sample spectra. In this way, the background spectrum contributes minimally to the noise in the transmittance spectrum.

It is worthwhile for users to test the alignment of their instruments over time periods ranging from a few minutes to several hours to check how well the performance of their interferometer is maintained. We also recommend that all users measure *and permanently save* a single-beam spectrum and a 100% line of all FT-IR spectrometers immediately after they have been installed or serviced (preferably in the presence of the service engineer). These spectra should be used as the benchmark for future instrument performance. By ratioing a single-beam spectrum measured on any given day to the saved benchmark single-beam spectrum, users can readily observe whether their interferometer has drifted out of alignment and realign their interferometer if necessary. It should be noted, however, that the spectrometer's control software may realign the interferometer periodically. In these cases deviation of the 100% line can be caused by a degradation of the source or misalignment of an optical element other than the beamsplitter.

In any laboratory where quality assurance is important, the performance of all instruments, including FT-IR spectrometers, should be tested on a regular basis. Measuring the rms noise on the 100% line between, say, 4000 and 3800  $\text{cm}^{-1}$  and 2200 and 2000  $\text{cm}^{-1}$  at least once a week gives users a good indication as to whether the performance of their instrument is still acceptable. The American Society for Testing and Materials (ASTM) has approved an additional series of

“level zero” tests that enable users to monitor the performance of their spectrometers [7]. Several manufacturers of contemporary FT-IR spectrometers include these tests as part of the operating software of their instruments. If tests of the type outlined above are scheduled to be run first thing on a Monday morning, it should be remembered that many interferometers take up to an hour to warm up to their equilibrium operating temperature. Since the typical lifetime of all components in a FT-IR spectrometer is at least one year, it is not good practice to switch off the instrument at night or even over the weekend.

#### 8.4.4. Effect of Sample Diameter and Thickness

Let us consider the effect of placing an aperture of diameter  $d_a$  at the beam focus in the sample compartment. Without this aperture present, the effective diameter of the beam at the sample focus,  $d_f$ , depends on whether the spectrometer is operating under the *constant throughput* or the *variable throughput* criterion (see Section 7.1). For instruments operating under the variable throughput criterion,  $d_f$  is governed by the effective diameter of the Jacquinot stop at the sample focus,  $d_j$ . The higher the resolution, the smaller is  $d_j$  and therefore the smaller is  $d_f$ . In this case, if  $d_a$  is reduced, the detector signal (as measured by the height of the interferogram at the centerburst) will not change significantly until  $d_a < d_f$ . At this point, the signal decreases as  $(d_a/d_f)^2$ . If, for example,  $d_a = 0.5d_f$ , the percent transmittance of the aperture relative to the unapertured beam should be equal to 25%, since the area of the aperture has been reduced by a factor of 4. However, since the response of many detectors is not absolutely uniform across their surface, it is common to find that the measured transmission of the aperture is not exactly 25% at all wavenumber values (i.e., the baseline will not be completely flat). Thus, when measuring the spectra of small samples, it is always a good idea to compensate for spatial inhomogeneity in the detector response by measuring the background spectrum with an aperture of the same diameter as the sample. Note also that the center of the sample should be at exactly the same position as that of the reference aperture; otherwise, a small shift in the wavenumber scale can result (see Section 2.6).

For most FT-IR spectrometers operating at low resolution and for all instruments that do not possess a Jacquinot stop, measurements are made under the constant throughput criterion. In this case,  $d_f$  is usually governed by the size of the detector, and a change in  $d_a$  will not lead to any change in  $d_f$  until the image of the beam at the detector is smaller than the detector element. Since most detectors are square and the beam is round, only a small change in the detector signal is first observed as  $d_a$  is reduced. When the beam diameter is less than the smallest dimension of the detector, the behavior becomes identical to the variable throughput case (i.e., the signal decreases as  $d_a^2$ ).

When a sample held between thick windows is inserted into the beam, the diameter of the beam at the detector focus can change because of refraction by the windows. In this case, variations in the height of the baseline may again result because of the spatial inhomogeneity of the detector response. If the beam

diameter at the detector becomes larger as a result of refraction by the sample, the signal will decrease and the baseline is shifted to lower transmittance. If the beam passing through the sample is refracted in such a manner that the diameter of the beam at the detector is reduced, the way the signal at the detector changes will depend on whether the spectrum is being measured under the constant or variable throughput criterion. When spectra are measured under the variable throughput criterion, the diameter of the beam at the detector is often less than or equal to the size of the detector element. In this case, a small increase in the beam diameter at the detector focus caused by refraction by the sample will not usually have an appreciable effect on the detector signal other than a degradation of the flatness of the baseline. When spectra are measured under the constant throughput criterion, the diameter of the beam at the detector usually exceeds the size of the detector element. If refraction by the sample causes the diameter of the beam at the detector to decrease, not only may the transmittance of the baseline rise above 100% but also the effect of response nonlinearity may increase with the higher photon flux if an MCT detector is being used (see Section 8.5.1).

Whether the transmittance of the baseline increases or decreases when a sample is inserted in the beam, it is often good practice to divide the transmittance spectrum by its maximum ordinate in a spectral region where the sample does not absorb before converting the spectrum to absorbance. (This operation is sometimes known as *single-point baseline correction*; see Section 10.1.)

## 8.5. ZERO ENERGY LEVEL

The measurement of 100% lines is a useful means of testing the noise level of FT-IR spectrometers but only indicates the repeatability of single-beam spectra. Trite as it may sound, 100% lines give no indication of the photometric accuracy of the instrument in the region near 0%*T*. Such measurements are not easy. Even though all FT-IR spectrometers report the transmission of a thick slab of a metal placed in the beam as exactly 0%, few FT-IR spectrometers give the transmittance at the peak of intense, sharp absorption bands as exactly 0% when the transmittance over most of the rest of the spectrum is high. Two factors account for this observation: the effect of a nonlinear response of the detector or its associated electronics, and the effect of changes in the modulation efficiency of the interferometer during the scan.

### 8.5.1. Detector Response Nonlinearity

For a FT-IR spectrometer to achieve perfect photometric accuracy, the response of the detector and its associated amplifiers and electronic filters must be independent of the photon flux on the detector. This condition is usually fulfilled with pyroelectric detectors but is particularly difficult to achieve in the mid-infrared with photoconductive MCT detectors. The photometric response of MCT detectors is usually linear at very low signal levels but may be easily forced into nonlinear behavior by

too large a bias current or photon flux [8]. Various mechanisms have been proposed to account for the observed nonlinearity of MCT detectors. For example, when the detector element is illuminated with photon fluxes in excess of  $10^{19}$  photons  $\cdot$  cm $^{-2}$   $\cdot$  s $^{-1}$ , the minority charge carrier lifetime is not linearly proportional to the photon flux,  $\Phi$ , but to  $\Phi^{-2/3}$ , producing an electrical conductivity proportional to the cube root of the photon flux [8].

When the response of a detector of a FT-IR spectrometer or its associated amplifier is nonlinear, the single-beam spectrum usually shows a nonzero value at wavenumbers below the detector cutoff [9], as shown in Figure 8.6. Although it is not immediately obvious by simply examining a single-beam spectrum, this nonzero baseline extends into the single-beam spectrum. The reason for this behavior may be visualized by recognizing that the effect of a nonlinear response is greatest when the signal at the detector is greatest (i.e., at the interferogram centerburst). The measured interferogram is the difference between the true interferogram (i.e., the interferogram that would have been measured had the response been linear) and the amount by which the true interferogram is reduced by the effect of nonlinearity, which we will call the *error interferogram*. Because the Fourier transform is a linear operation, the spectrum that is calculated from the FT of the measured interferogram is the true spectrum minus the FT of the error interferogram. Since the error interferogram has very little amplitude away from the centerburst,

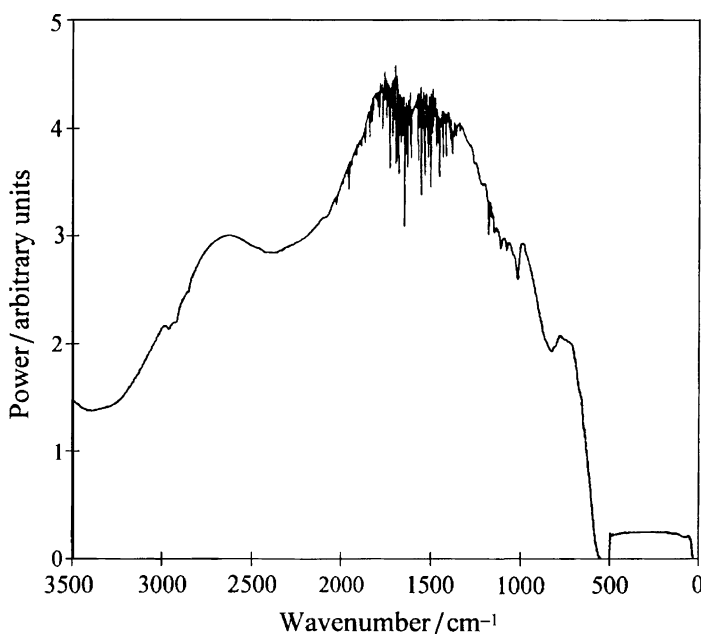


**Figure 8.6.** Single-beam spectrum measured with a midband MCT detector with a nonlinear response. The spectrum below the detector cutoff (from 0 to 600  $\text{cm}^{-1}$ ) should be at zero. In this case the spectrum in this region is negative but the phase correction software causes the spectrum to be flipped to the corresponding positive value. Power is in arbitrary units.

its transform will be a spectrum that varies slowly across the entire spectral range from  $0\text{ cm}^{-1}$  to the Nyquist frequency (see Chapter 3). (The error spectrum would be a constant had the error interferogram been a delta function at zero retardation.)

In practice, the usual effect of this error is to give a bias to the measured spectrum. This bias is most easily observed by examining the single-beam spectrum below the detector cut-on, where the energy should be exactly zero. Several phase correction algorithms flip any calculated negative value to a positive value below  $500\text{ cm}^{-1}$ , as shown in Figure 8.6. In this case, the true zero-energy level above  $500\text{ cm}^{-1}$  is probably still at a negative value, so the photometric accuracy across the entire spectrum is quite poor any time the single-beam spectrum below the detector cutoff is nonzero. (The Mertz phase correction algorithm often rectifies a negative number and calculation of the magnitude spectrum never gives a negative amplitude.)

The simplest way to reduce the effect of detector nonlinearity to an acceptable level is to insert a metallic (*not fiberglass*) screen into the beam to act as a neutral density filter. Many inexpensive screens that can be purchased at any hardware store have a transmission of  $\sim 50\%$ . The number of these screens in the beam should be increased until the level of the nonphysical energy below the detector cutoff becomes acceptable.

Several numerical methods have also been devised in an attempt to minimize the photometric error introduced to FT-IR spectra by a nonlinear response. By modeling nonlinear interferograms, calculating appropriate correction factors, and correcting the measured interferogram before computation of the phase angle, software correction algorithms offer improved response linearity without introducing additional noise or the need for additional electronic components. This approach has been used to minimize the dc signal present in solar occultation observations [10], and the manufacturer of at least one FT-IR spectrometer [11,12] currently offers a similar approach.

Electronics designed to minimize the effects of detector response nonlinearity are also becoming standard equipment on many FT-IR spectrometers. For example, signals from a two-output interferometer having the same amplitude but opposite phase have been combined such that the recorded interferogram is free of significant distortion caused by nonlinearity [13]. A patent has been issued for a constant voltage-biased photoconductive MCT detector–preamplifier–amplifier combination where the photometric response is linearized by a circuit that is calibrated for the relationship between the signal input to a given detector–preamplifier–amplifier combination with an accurate output signal [14]. (This patent also contains an excellent discussion of the factors involved in linearizing the response of MCT detectors used for FT-IR spectrometry.) The photometric linearity of MCT detectors may be greatly improved by changing from a constant-current to a constant-voltage bias [15], and a patent has also been issued for a preamplifier operating at a constant-voltage bias that incorporates a circuit that eliminates out-of-band energy [16]. However, even when operated under a constant-voltage bias the electronics involved in the signal train may introduce a nonlinear voltage response and phase errors [17]. Although all the approaches described above improve the photometric accuracy of FT-IR spectrometers equipped with MCT detectors, as of this writing

no approach has yet been reported that allows the effects of the type illustrated in Figure 8.6 to be eliminated completely.

If the zero-energy offset extends into the spectrum above the detector cut-on, the photometric accuracy of the spectrometer can be affected by as much as 10%*T* [18]. The effect can readily be observed above the detector cutoff simply by measuring the spectrum of a polymer film that is thin enough that its transmittance over most of the spectrum is high, but thick enough that several bands have an absorbance greater than 3.0. An example of such a film is 75- $\mu\text{m}$  (3-mil) polyethylene terephthalate (PET) (see Figure 8.7). The result is usually a repeatable offset in the 0%*T* line that is analogous to the effect of stray light in spectra measured with scanning monochromators.

This type of photometric error leads to strong deviations in Beer's law plots for strongly absorbing bands. Richardson et al. [19] showed that the nonlinearity of Beer's law plots measured under conditions of very low detector noise can be quantified by the plot's correlation coefficient,  $R^2$ . In this study, a simple method of correcting for the effect of a nonlinear detector response analogous to that used to correct for stray light was investigated. Although this technique worked well, it is not generally applicable to all spectra measured on a given instrument, as the zero-energy offset varies with the energy incident on the detector, and hence with the nature of the sample.

Pyroelectric detectors have a much more linear response than quantum detectors such as MCT. Thus, it is usually far preferable to use a DTGS detector rather than MCT for quantitative measurements by mid-infrared spectrometry. Even instruments incorporating DTGS detectors often measure low energies quite inaccurately. For example, Bowie and Griffiths measured the apparent spectrum in the region of the very strong bands in the spectrum of PET (see Figure 8.7) on three different instruments, each of which was equipped with a DTGS detector [5]. Although

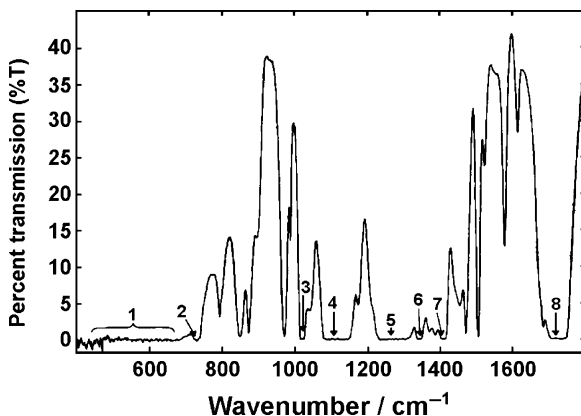


**Figure 8.7.** Transmittance spectrum of a 75- $\mu\text{m}$ -thick sheet of PET held between two  $\text{BaF}_2$  windows.  $\text{BaF}_2$  is opaque below  $650\text{ cm}^{-1}$  (marked region 1 on this spectrum). PET is opaque (transmission  $< 0.1\%$ ) in regions 2 through 8. (Reproduced from [5], by permission of the Society for Applied Spectroscopy; copyright © 2000.)

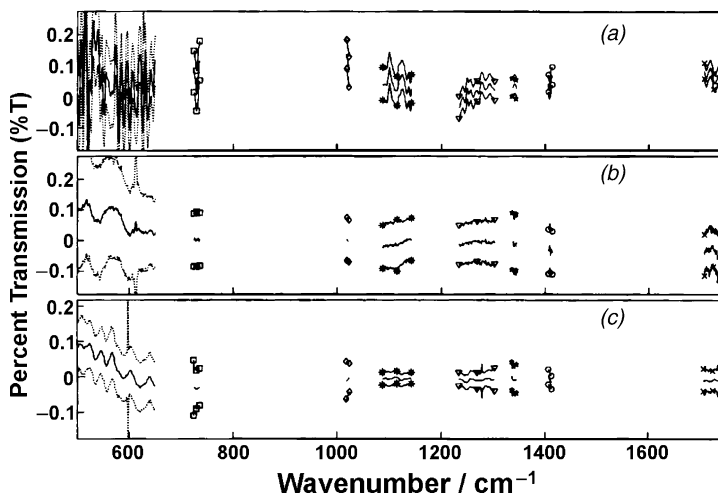


**Figure 8.8.** Percent transmission measured in regions 1 through 8 using three different FT-IR spectrometers. In each case, the middle curve was the result of adding the values of 512 different single-scan spectra, and the curves above and below this spectrum represent this line  $\pm\sigma$ , where  $\sigma$  is the standard deviation of the 512 data points. No instrument performs well in region 1. For the other regions, the spectra measured by instrument A showed repeatable spectral artifacts, while the spectra measured by instruments B and C were relatively flat, as they should be since the transmission of PET in these regions was less than 0.01%. The noise level of instrument C, as estimated by the standard deviation, was clearly lower than that of the other two instruments. (Reproduced from [5], by permission of the Society for Applied Spectroscopy; copyright © 2000.)

the true transmission of these bands was less than 0.01%, the absolute value of the measured transmission was often between 0.1 and 0.01%, as shown in Figure 8.8. In the case of one instrument (A in Figure 8.5), repeatable spectral structure can be seen. The cause of this photometric error is probably not detector response nonlinearity. Nonetheless, it is worthwhile remembering that these effects can adversely affect the measurement of very strong bands and that it is always wise to keep the peak absorbance well below 1 AU for accurate quantification.

### 8.5.2. Changes in Modulation Efficiency

Very small changes in the modulation efficiency of interferometers that occur during a scan can also affect the accuracy of the zero-energy level of spectra measured with a FT-IR spectrometer. These errors are manifested in a slightly different way to the effect of response nonlinearity. The most common way that the modulation efficiency changes from scan to scan is for the alignment of the moving optical element(s) of the interferometer to vary, as discussed in Chapter 5. The poorer the drive, the greater will be the effect on the modulation efficiency. Let us say that mirror jitter during the scan caused the modulation efficiency to vary between 100 and 98%, with an average value of 99%. Since the amplitude of the wings of the interferogram (i.e., the part of the interferogram that is displaced from the



centerburst) is very low, the effect of a small change of the modulation efficiency on the wings is going to be correspondingly small. On an absolute (*not* relative) basis, there will be a much larger change in the value of the interferogram near the centerburst. The effect of the change in modulation efficiency will therefore be a change in the zero-energy level of the spectrum, for the same reason given above for the effect of response nonlinearity. However, because the modulation efficiency can both increase *and* decrease, the effect on the spectrum will be to cause the zero-energy baseline to go either above *or below* the true zero. The end result is that if a series of spectra are measured sequentially, the transmittance at the center of a strong band will appear to vary. This effect is illustrated in Figure 8.9, which shows the spectrum of a 1-mm-thick layer of water in the region of the strong band at  $5150\text{ cm}^{-1}$ , which is opaque over a region of  $\sim 150\text{ cm}^{-1}$ . (Note that if the result of this effect was to drive the band to a negative value, the phase correction algorithm flips the spectrum to a positive value.) This effect was even seen on spectra measured using a dynamically aligned interferometer, suggesting that there must be a small error in the alignment, and hence the modulation efficiency, of the interferometer in order for the correction to be applied. It only needs a small alignment error to occur at one retardation near the centerburst for the photometric accuracy to be affected. Signal-averaging the interferogram will help ameliorate this situation,

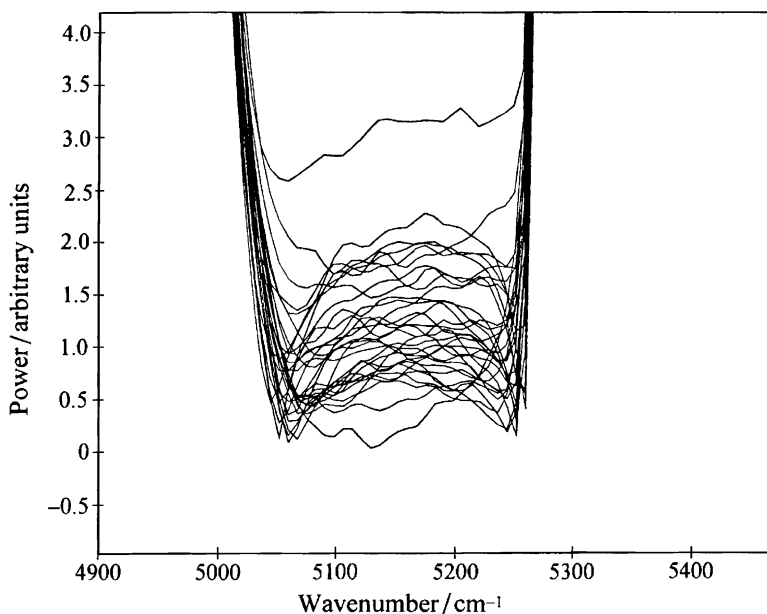


**Figure 8.9.** Highly expanded single-beam near-infrared spectra measured with a 1-mm pathlength containing water in the beam. The spectra should be reproducible, with the spectrum having an intensity of zero between  $5100$  and  $5200\text{ cm}^{-1}$ . These never reach zero, whereas many of the other spectra are negative in this region but have been flipped to the corresponding positive value during phase correction.

as the modulation efficiency at each point in the signal-averaged interferogram will approach an average value.

### 8.5.3. Sampling Effects

For mid-infrared spectrometry, the interferogram is sampled once per wavelength of the HeNe laser, so that the Nyquist wavenumber is  $\sim 7900 \text{ cm}^{-1}$ . By sampling the interferogram only once per wavelength, the sampling interval is exactly equal to  $\lambda_{\text{HeNe}}$ . On the other hand, for near-infrared measurements, the sampling interval must be shorter than  $\lambda_{\text{HeNe}}$ . If  $\lambda_{\text{min}} = 1000 \text{ nm}$  ( $10,000 \text{ cm}^{-1}$ ), the Nyquist wavenumber is at  $20,000 \text{ cm}^{-1}$  (500 nm). Thus, for instruments equipped with a HeNe laser, the interferogram must be sampled twice per laser wavelength. If the laser interferogram is slightly biased above or below zero and the ADC is triggered every zero crossing, the sampling interval will alternate between being slightly greater and slightly less than  $0.5\lambda_{\text{HeNe}}$ . This alternation will lead to a kind of aliasing that can readily be observed below the detector cutoff, but as for the case of a nonlinear detector response, will also affect the photometric accuracy of the spectrum in the spectral region of interest. An example of this effect is shown in Figures 8.10 and 8.11. The

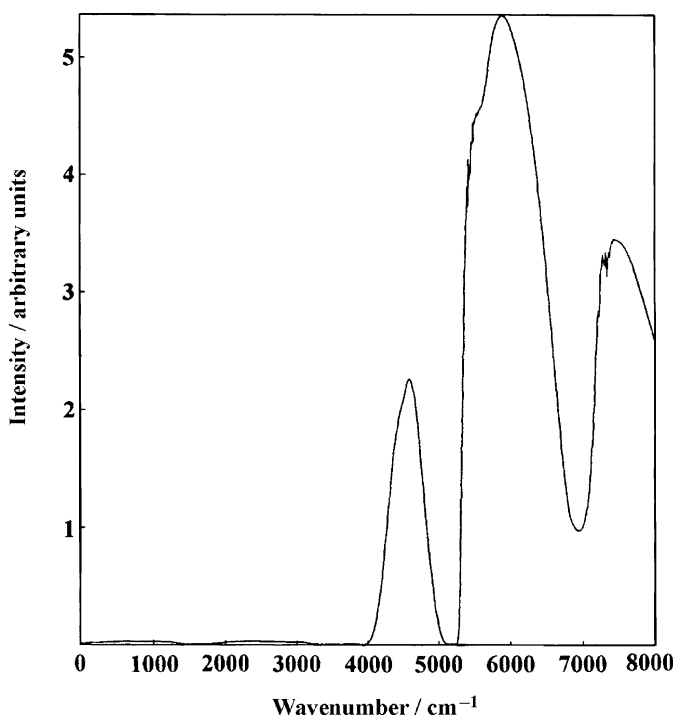


**Figure 8.10.** Ten full (unexpanded) NIR single-beam overlaid spectra showing that the absolute differences between the spectra are very small. Careful examination of the spectra below the cutoff of the InGaAs detector being used for this measurement ( $4000 \text{ cm}^{-1}$ ) shows that the spectrum is not zero in this region.

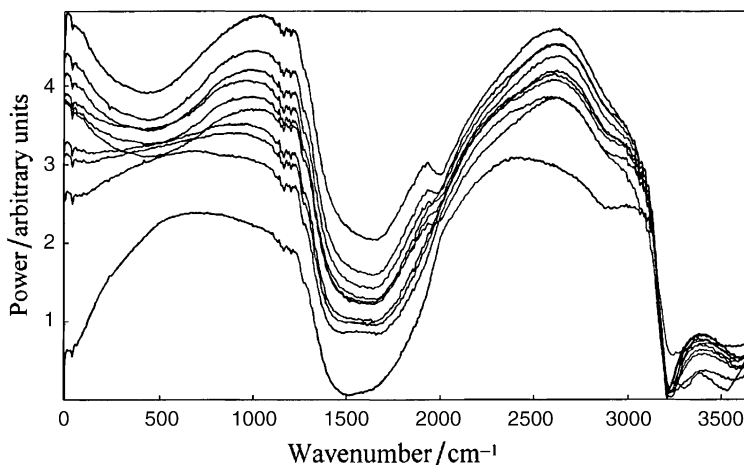


**Figure 8.11.** Expanded plot of the spectra shown in Figure 8.10, showing apparent spectral artifacts in the region where the spectral intensity should be zero. The artifact at about  $1500\text{ cm}^{-1}$  has a similar structure to the absorption band of water at  $\sim 7000\text{ cm}^{-1}$  and somehow results from folding, possibly because the interferogram was sampled at every zero crossing when the HeNe interferogram was not exactly centered at zero.

single-beam NIR spectrum of a 1-mm pathlength of liquid water is shown in Figure 8.10, from which it might be thought that the spectrum is quite reproducible. However, the expansion of the spectrum below the cutoff of the InGaAs detector used for this measurement in Figure 8.11 shows significant spectral structure that mimics the  $5150\text{-cm}^{-1}$  band of water. This is an unusual form of aliasing that has also been observed in FT-Raman spectrometry [20].

## 8.6. LINEARITY BETWEEN 100% AND 0% $T$

If errors in both the 100% and 0% lines are commonplace in FT-IR spectrometers, it is reasonable for users of these instruments to question the photometric accuracy between these extreme values. Fortunately, the situation here appears not to give cause for concern. Richardson et al. [18] have shown that the transmittance scale appears to be linear after correction for errors in the 0% line.

Most of the errors discussed in this chapter are relatively small. Provided that mid-infrared spectra are measured with an instrument that is equipped with a DTGS or DLATGS detector and care is taken to ensure that the peak absorbance of bands in the spectral region of interest is not excessive, the photometric accuracy of contemporary FT-IR spectrometers is remarkably high. The transmittance scale of these instruments should be accurate to better than  $\pm 0.001$  ( $\pm 0.1\%T$ ).

## REFERENCES

1. D. A. Ramsay, *J. Am. Chem. Soc.* **74**, 72 (1952).
2. R. J. Anderson and P. R. Griffiths, *Anal. Chem.* **47**, 2339 (1975).
3. C. Zhu and P. R. Griffiths, *Appl. Spectrosc.* **52**, 1403 (1998).
4. C. Zhu and P. R. Griffiths, *Appl. Spectrosc.* **52**, 1409 (1998).
5. B. T. Bowie and P. R. Griffiths, *Appl. Spectrosc.* **54**, 1192 (2000).
6. J. A. de Haseth, *Appl. Spectrosc.* **36**, 544 (1982).
7. *Standard Practice for Describing and Measuring Performance of Fourier Transform Infrared (FT-IR) Spectrometers: Level Zero and Level One Tests*, ASTM E 1421-91, American Society for Testing and Materials, Philadelphia, PA, 1991.
8. F. Bartoli, R. Allen, L. Esterowitz, and M. Kruer, *J. Appl. Phys.* **45**, 2150 (1974).
9. D. B. Chase, *Appl. Spectrosc.* **38**, 491 (1984).
10. M. C. Abrams, G. C. Toon, and R. A. Schindler, *Appl. Opt.* **33**, 6307 (1994).
11. A. Keens and A. Simon, Correction of the non-linear response of infrared detectors, in *Proceedings of the 9th International Conference on Fourier Transform Spectroscopy*, J. E. Bertie and H. Wieser, Eds., Society of Photo-Optical Instrumentation Engineers, Bellingham, WA, 1993, Vol. 2089, p. 222.
12. A. Keens and A. Simon, Correction of non-linearities in detectors in Fourier transform spectroscopy, U.S. patent 4,927,269 (assigned to Bruker Spectrospin Ltd., Milton, Ontario, Canada, May 22, 1990).
13. G. Guelachvili, *Appl. Opt.* **25**, 4644 (1986).
14. R. Curbelo, Techniques for correcting non-linearity in a photodetector using predefined calibration information, U.S. patent 5,262,635 (assigned to Bio-Rad Laboratories, Hercules, CA, November 16, 1993).
15. R. O. Carter III, N. E. Lindsay, and D. Beduhn, *Appl. Spectrosc.* **44**, 1147 (1990).
16. R. M. Carangelo, D. G. Hamblen, and C. R. Brouillette, Method and system for photo-conductive detector signal correction, U.S. patent 5,136,154.
17. K. Rahmelow, *Appl. Opt.* **36**, 2123 (1997).
18. R. L. Richardson, Jr., H. Yang, and P. R. Griffiths, *Appl. Spectrosc.* **52**, 572 (1998).
19. R. L. Richardson, Jr., H. Yang, and P. R. Griffiths, *Appl. Spectrosc.* **52**, 565 (1998).
20. B. T. Bowie, D. B. Chase, and P. R. Griffiths, *Appl. Spectrosc.* **54**, 164 (2000).



# QUANTITATIVE ANALYSIS

## 9.1. INTRODUCTION

One of the major advances in quantitative analysis has been an integration of spectrometry and multivariate, or *chemometric*, techniques. This integration has led to a number of ways that data can be extracted from spectra. Not all the information that is extracted is immediately recognized as quantitative information, but it is always related back to spectral properties that are quantitative responses. The relationship between absorbance and concentration is well known as Beer's law (see Chapter 1). When reliance is made upon Beer's law, precautions must be taken to assure that there is indeed a linear relationship between the absorbance that is measured by the spectrometer and concentration. Infrared spectrometry has been used for quantitative analysis since its early development, but it is only since the early 1980s that extensive use of infrared spectrometry for the analysis of multiple components has been made. The analysis of multiple components is the primary focus of this chapter.

## 9.2. BEER'S LAW

As shown in Chapter 1, Beer's law is

$$A_i(\tilde{\nu}) = a_i(\tilde{\nu})bc_i \quad (9.1)$$

where  $A_i(\tilde{\nu})$  is the absorbance of species  $i$  at wavenumber  $\tilde{\nu}$ ,  $a_i(\tilde{\nu})$  the absorptivity of the species at that wavenumber (in units of  $\text{concentration}^{-1} \cdot \text{distance}^{-1}$ ),  $b$  the path-length, and  $c_i$  the concentration of species  $i$ . Linear adherence to Beer's law is important, and aspects of this were discussed in Section 8.3.

If the peak absorbance of a band is too large, and the ratio of the numerical value of the resolution to the FWHH of the band (i.e., the resolution parameter,  $\rho$ ) is not sufficiently low, the relationship between the measured value of absorbance and  $c_i$  will become nonlinear. As shown in Section 8.3, some instrument lineshape

functions are better than others for linearity, and the best for quantitative analysis of condensed-phase samples is arguably that produced by the Norton–Beer medium apodization function. With this function, excellent linearity of absorbance versus concentration is maintained for  $A'_{\text{peak}} \leq 2$  absorbance units (AU) if the resolution parameter,  $\rho$ , is no greater than 0.5.

There is, not surprisingly, a difference between theory and practice. It must be remembered that an absorbance of 2.00 is equivalent to a transmittance of 0.010. In practice, spectra have noise, and the noise is present in all regions of the spectrum, including at the maxima of bands. For a spectrum with a root-mean-square (rms) signal-to-noise ratio ( $\text{SNR}_{\text{rms}}$ ) of 1000 : 1, the rms noise is  $\pm 0.001$  transmittance. If the rms noise is  $\pm 0.001$ , the peak-to-peak noise will be approximately five times greater, or  $\pm 0.005$  transmittance. This corresponds to an absorbance range of a peak ostensibly at 2.00 AU of 2.30 to 1.82 AU. At relatively high absorbance, even a small amount of noise has a dramatic effect on the absorbance. Even a  $\text{SNR}_{\text{rms}}$  of 1000 : 1 on the baseline can change the maximum absorbance from a peak value of 2.00 AU by as much as 0.30 AU. This problem becomes worse as the peak absorbance increases. If the peak absorbance were 3.00 AU, the same 1000 : 1  $\text{SNR}_{\text{rms}}$  could increase that absorbance to an infinite number, as the peak-to-peak noise of  $\pm 0.005$  transmittance is larger than the actual transmittance (0.001). That is, the measured transmittance at the band center,  $A'_{\text{peak}}$ , could range from +0.006 to  $-0.004$ .

A negative transmittance presents a problem, as the absorbance cannot be calculated. Zero transmittance is infinite absorbance, so negative transmittance must also be infinite. Infinity cannot be represented by a finite number, so instrument and software manufacturers deal with this problem by setting an arbitrary limit for maximum absorbance. This arbitrary number varies from manufacturer to manufacturer but is usually more than 7 AU, with the implicit assumption that no one will attempt quantitative analysis at such a high value. Clearly, at these values the absorbance varies nonlinearly with concentration. It should also be recalled that noise is not the only cause of negative transmittance; the use of boxcar truncation can also lead to negative transmittance values (see, e.g., Figure 8.2). Conversely, as the peak absorbance decreases, the effect of noise becomes less serious, but it cannot be ignored. With a high baseline  $\text{SNR}_{\text{rms}}$ , that is, greater than 10,000 : 1, maximum absorbances of 2.00 can often be tolerated if detector noise is the only source of error. Nevertheless, for optimal results, it is recommended that maximum absorbance in the spectral range being used for quantitative analysis not exceed 0.7 AU. This restriction cannot always be met, but many experiments can be designed so that this is the case.

Noise is rarely the only cause of error in the measurement of an intense absorption band. In Chapter 8, it was shown that the 0% line of many FT-IR spectrometers can be in error by as much as 0.1% (or more if an MCT detector is used for the measurement) [1]. Indeed, most manufacturers of FT-IR spectrometers rarely specify the ordinate scale accuracy as being better than  $\pm 0.1\%T$ . The limited photometric accuracy of FT-IR spectrometers in the region of 0% transmittance reinforces the recommendation made in the preceding paragraph that the peak absorbance of strong bands be held below 0.7 AU whenever possible.

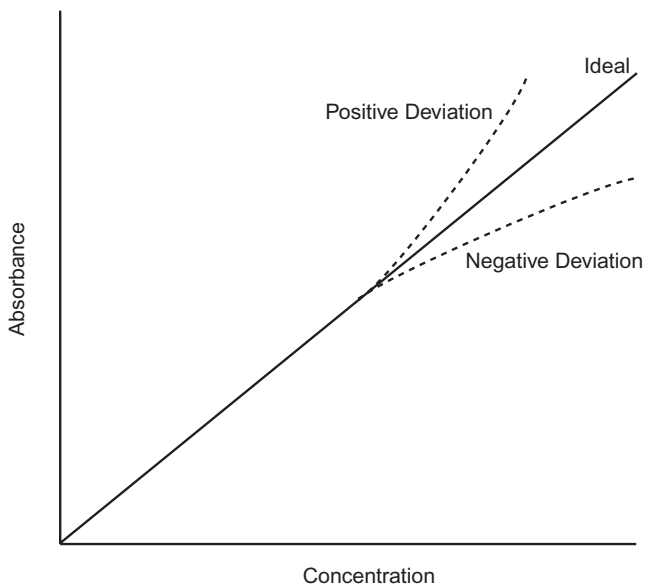


**Figure 9.1.** Beer's law plot that shows both positive and negative deviations.

Beer's law nonlinearity may be the result of instrumental or chemical effects. When a Beer's law plot is constructed, as shown schematically in Figure 9.1, the curve may be linear as anticipated, or it may show a positive or negative deviation. It is often desirable to determine whether nonlinearity is the result of an instrumental problem, or from chemical effects such as complexation, association, polymerization, dimerization, solvation, or dissociation. Fortunately, there is a method to distinguish these phenomena. Beer's law, as we know it, is more appropriately called the Bouguer–Lambert–Beer law [2]. Bouguer [3] was the first to realize (in 1729) that absorbance is proportional to pathlength, but it was not until the mid-1750s that Lambert [4] was able to express this in mathematical terms. (Almost a century passed before Beer published a paper that showed that absorbance was proportional to concentration [5].) If a Lambert plot is constructed (i.e., a plot of absorbance versus pathlength), the instrumental and chemical effects can be discriminated. If a chemical effect is the cause of a nonlinear response, Lambert plots are linear.

It is possible to purchase variable-pathlength liquid transmission cells, which commonly have a pathlength that can be varied between 5  $\mu\text{m}$  and 5 mm. A suitable sample must be chosen, preferably a neat solvent that has relatively wide peaks, the resolution of the spectrometer must be set so that the resolution parameter,  $\rho$ , is no greater than 0.5, and a Norton–Beer medium apodization function should be applied. A series of measurements at increasing pathlengths should yield a linear Lambert plot if the instrument is functioning correctly. Some instruments will exhibit linear Lambert plots up to 4 AU; however, this is unusual, and an acceptable



instrument will produce a linear plot to at least 2 AU. If the Lambert plot is linear, and a Beer's law plot (i.e., a plot of absorbance against concentration) is nonlinear, the problem is chemical in nature and the experiment should be redesigned. Unfortunately, there is no way to determine the cause of a nonlinear Lambert plot from the plot itself, since the cause of the problem may be optical or electronic, or may even arise from the data processing.

Other precautions must be taken when spectra are collected if high photometric precision (repeatability) is required. Photometric precision is not only restricted to quantitative analysis, but is also required for spectral subtraction (Section 9.3), and spectral search systems (Section 10.8). Repeatable sample preparation and placement is critical. If the aperture of the sample cell is small enough to become the limiting aperture in the spectrometer, any shift in the position of the sample from the center of the beam will cause a shift in wavenumber and possibly a change in the ILS function (Section 2.6). A small wavenumber shift will cause a peak maximum to be displaced, and the bandshape and peak absorbance may change due to the change in the ILS function [6] and the discrete sampling of the spectrum (Section 3.1).

Even if the sample itself is not the limiting aperture, a small wavenumber shift may be seen if the sample is not placed at a constant angle to the infrared beam. As the beam traverses the sample, it may be refracted at an angle that displaces the image on the detector. This has the effect of slightly changing the pathlength of the beam through the interferometer; hence, the relationship of the infrared interferogram to the HeNe laser interferogram is altered, resulting in a small wavenumber shift. In addition, when a sample is tilted with respect to the beam, the pathlength within the sample is altered, and this may change the measured absorbance slightly.

Some simple precautions can be taken to avoid sample placement errors. If an accessory such as an attenuated total reflection (ATR) accessory is used, it should be mounted in the spectrometer and not moved throughout the study. This criterion implies that the internal reflection element must be cleaned *in situ*, and samples must be placed on the internal reflection element when it is mounted in the spectrometer. For accessories that must repeatedly be placed into and removed from the sample compartment (e.g., a transmission cell), a simple procedure can be devised to reduce potential errors. Sample holders, although fastened in place, do have tolerances to allow insertion and removal of the sample accessory. Because of this, when a cell or accessory is placed into the sample compartment, it should be tapped gently on one corner; as a result, it will then settle into a reproducible position. It is suggested that the accessory be tapped with a cushioned object; the eraser on the end of a pencil is an ideal tool. The same number of taps should always be applied, and three is generally adequate.

Consistent sampling conditions are a necessity for careful quantitative work. In transmission spectrometry it is critical to fill the entire accessory aperture with the sample. If the actual sample area is smaller than the beam that passes through the aperture, stray light or excess radiation will reach the detector (Figure 9.2). The radiation that does not pass through the sample provides a spurious signal to the detector, and this excess radiation establishes a minimum transmittance. That is, no matter how strongly a sample absorbs, no band can have a transmittance below the minimum

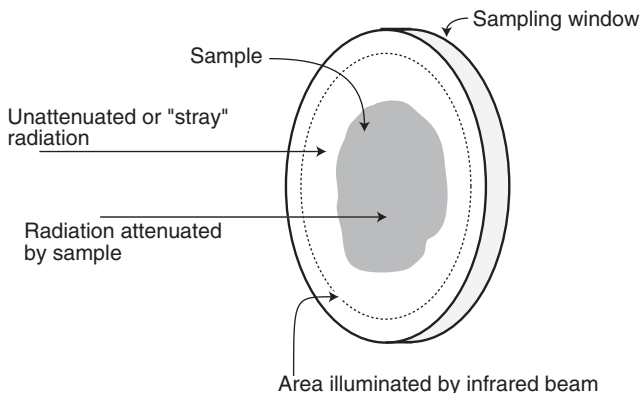


**Figure 9.2.** A transmission sample that does not completely cover the illuminated area of the infrared radiation will lead to stray light.

value set by the unattenuated radiation. Figure 9.3*a* shows the transmittance spectrum of the C—H stretching region of a strongly absorbing polyethylene film, and Figure 9.3*b* shows the same film when the sample covers only  $\sim 75\%$  of the beam aperture. The latter spectrum is considerably shifted in percent transmission to the first, with the true 100% line for the sample at  $\sim 25\%T$ . The phenomenon is clearly illustrated in Figure 9.3*c* and *d*, when the two spectra are plotted in absorbance where spectrum *c* corresponds to spectrum *a*. To avoid this type of problem, the sample should be masked, or a large enough sample should be used to fill the aperture of the accessory. Of course, care should be exercised when a sample is masked to avoid a wavenumber shift, as discussed above.

A special case of beam filling occurs with the measurement of ATR spectra. It is a common error to place a small sample on an internal reflection element (IRE) so that the sample does not cover the entire active surface of the element. A qualitative spectrum will result, but stray light may be present and quantitative precision will be lost. The sample does not have to cover the entire surface of the active portion of the IRE. As long as the sample covers the IRE uniformly in a direction perpendicular to the beam, no stray light will reach the detector, as shown in Figure 9.4.

### 9.3. SPECTRAL SUBTRACTION

If a spectrum is linear in absorbance, the spectrum can be scaled to represent the sample at a different concentration or pathlength, within certain limitations. If the factor by which the spectrum is scaled is too large, the absorbances will extend to unreasonable values. If a linear spectrum is scaled to very high absorbance values, the lineshapes will not match measured spectra as all subtractions fail at sufficiently high absorbances. Consequently, a spectrum scaled to very high absorbance is unrealistic. Nonetheless, if two spectra are of the same sample and are both linear

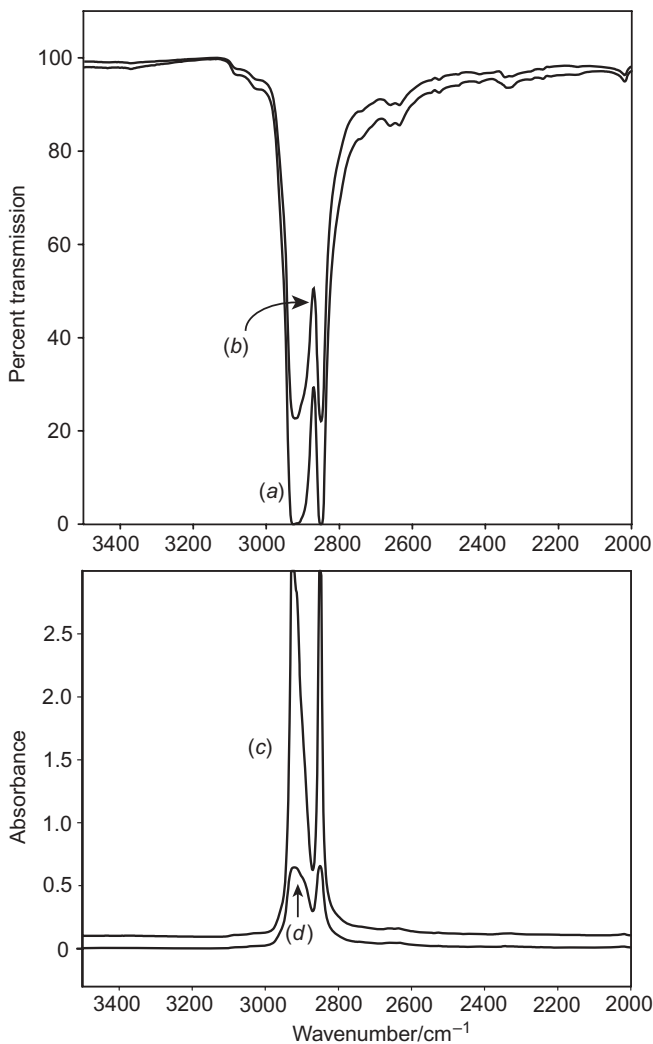


**Figure 9.3.** (a) Spectrum of a thick polyethylene film is seen to absorb totally in one region, but when the same film does not cover the illuminated area of the beam (b), the spectrum is displaced above a minimum transmittance. Spectra (c) and (d) are spectra (a) and (b), respectively, plotted in absorbance. The absorbance for (c) is infinite, whereas (d) has a maximum of  $\sim 0.7$  absorbance unit.

in absorbance, but of different concentration or pathlength, then

$$A_1(\tilde{\nu}) - kA_2(\tilde{\nu}) = 0 \quad (9.2)$$

where  $A_1(\tilde{\nu})$  and  $A_2(\tilde{\nu})$  are the two absorbance spectra and  $k$  is a scaling factor. Specifically,  $A_1(\tilde{\nu})$  is known as the *minuend* and  $kA_2(\tilde{\nu})$  is known as the *subtrahend*. The resultant should be zero except for any noise in the two spectra. If one

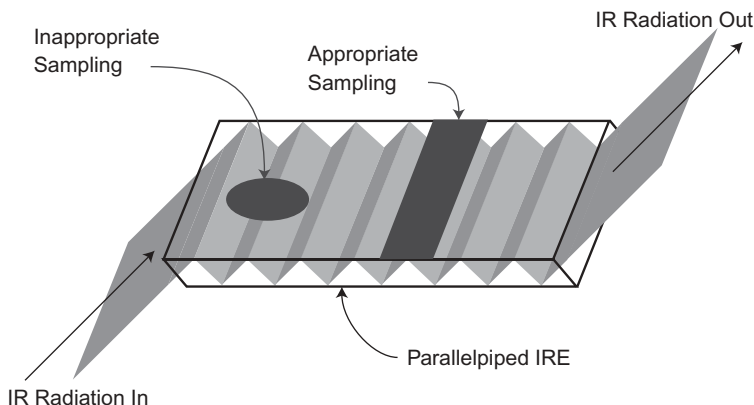


**Figure 9.4.** Inappropriate and appropriate sampling on a multireflection internal reflection element.

spectrum is a mixture of components,

$$M(\tilde{\nu}) = A_1(\tilde{\nu}) + A_2(\tilde{\nu}) + A_3(\tilde{\nu}) + \cdots$$

a common component can be removed to yield the spectrum free of the common component; that is,

$$M(\tilde{\nu}) - kA_2(\tilde{\nu}) = A_1(\tilde{\nu}) + A_3(\tilde{\nu}) + \cdots \quad (9.3)$$

where  $A_2(\tilde{\nu})$  is the spectrum of the common component, but may be a different concentration than initially found in the mixture.

This procedure is a powerful tool to elucidate the composition of a mixture or to verify the identity of a sample. The removal of a common component can simplify a mixture spectrum considerably. For a binary or ternary mixture, the difference spectrum may be more readily identifiable. Successive subtractions may yield the spectrum of a single component, but care must be taken when multiple subtractions are attempted. If a subtraction is performed and the difference spectrum shows no negative bands, it is usually assumed that the subtrahend was present in the mixture. There is often no verification of this, in that a nonnegative difference spectrum only indicates that all the sample absorbs radiation in the region of all the bands in the region being investigated, but these bands may be due to highly overlapped absorptions from multiple components. To verify that the subtraction is valid, the difference spectrum must be recognizable or interpretable.

Subtraction can be used to verify the identity of a sample. If a spectrum of a known compound is subtracted from a spectrum of what appears to be the same compound, and a zero residual results, the samples are identical. This is a useful tool for verification and should be used to validate identification after library searching (see Section 10.8).

Artifacts, or errors, are frequently observed in difference spectra. If the minuend and subtrahend spectra have shifted wavenumber scales with respect to each other,

for example because of sample misplacement or the effect of intermolecular interactions, the band centers will not match regardless of how carefully the scaling factor has been chosen. The difference spectrum will contain first-derivative-shaped bands. This phenomenon is most noticeable for sharp bands, and is commonly seen with water-vapor lines in spectra measured with poorly purged instruments. Note that even though the *effect* of the shift may be very obvious, the actual value of the shift is never more than one-fourth of the resolution (see Eq. 2.47).

It is not always the case that the minuend and the subtrahend will have the same lineshapes, in that the spectra may have been calculated with different apodization functions (something that should be avoided whenever possible), or the same lineshape may be distorted because of different concentrations. Differences in lineshape will often be exhibited as differences in bandwidth. If the minuend spectrum has bands that are broader than the subtrahend, even when the peak absorbances are matched, the difference spectrum will contain small doublets. The existence of these doublets is often taken as evidence of a minor component in the minuend, but in reality these are rarely more than subtraction artifacts. This phenomenon is generally more apparent when broad bands are subtracted.

Most commercial spectrometer and spectral data processing software include automated spectral subtraction routines. To perform automated subtraction, the manufacturer must implement an algorithm to perform the subtraction. The simplest of these is to scale the subtrahend so that the maximum peak absorbance for the largest band in a spectrum, or an appropriate band identified by the operator, matches the intensity of the same band in the minuend spectrum. After subtraction has been performed, the band center will be zero, but often there is a residual, either a small doublet, or a first-derivative-shaped residual, as discussed above. The result may be a mixture of the two. Another approach is to adjust the scaling factor so that the difference of the selected band has a zero integral. Thus, the shape of the residual may change so that some areas of the residual are positive and other areas are negative. Regardless, it should be realized that these features are consequences of the subtraction giving rise to artifacts in the spectra and are not true spectral bands. The spectroscopist always has the option to adjust the scaling factor to produce a more acceptable result. Hirschfeld has presented the sources of these artifacts in detail [7].

It is not always possible to perform a good spectral subtraction, as the minuend spectrum may be unavoidably nonlinear. (Generally, it is assumed that a reference spectrum, i.e., the subtrahend, will be linear if it is a good reference.) If the subtrahend can be remeasured under the same nonlinear conditions as the minuend, the nonlinearities should be sufficiently similar to effect a valid subtraction. In this case the scaling factor approaches unity, and reliable subtraction may be possible.

#### 9.4. LINEAR LEAST-SQUARES FITTING METHODS

In Section 9.1 we saw that Beer's law states that absorbance at any wavenumber is a linear function of concentration for a single component. Errors in the measurement

of Beer's law were discussed, but no mention was made as to how to deal with these errors mathematically so that the best answer is achieved. For a single component it is straightforward to measure the absorbances from a series of external concentration standards. Certainly, these data can be entered into a spreadsheet, or processed through spectrometer control software, to produce a curve of best fit for the data. For a single component that obeys Beer's law, a plot of absorbance versus concentration should be a straight line of the form

$$A(\tilde{\nu}) = mC - d \quad (9.4)$$

where  $A(\tilde{\nu})$  is absorbance,  $m$  the slope of the line,  $C$  the concentration, and  $d$  the intercept. In the ideal case,  $d$  should be zero, but this is rarely the case in practice (e.g., because of reflection loss at the cell windows). In any event, the absorbance of an unknown can be measured at some wavenumber,  $\tilde{\nu}$ , and its concentration can be simply calculated from Eq. 9.4.

Despite the fact that we can readily calculate concentration, it is instructive to understand the operations that take place to generate the final answer. These operations form the basis of the multivariate methods of analysis that are used to analyze multicomponent mixtures.

Least-squares analysis strives to minimize the errors in measured data. It is extremely unlikely that any set of concentration data will lie perfectly on a straight line. Undoubtedly, there will be errors in both the measured absorbances and the prepared concentrations. The most accurate approach is to measure the square of the distance from each point perpendicular to the line and to minimize the sum of the squares of all distances. Although the square of the distance from the point perpendicular to the line is the better measure, it is common practice to use the vertical distance from the point to the line. Figure 9.5 illustrates the difference between perpendicular and vertical distances. Vertical distances are chosen because (1) the principal source of error is the measurement of absorbance rather than concentration, (2) the difference in the result between perpendicular and vertical distances is rather small for real cases, and (3) the expressions for perpendicular distances are rather unwieldy. Furthermore, vertical distances can be extended rather easily from the linear to the nonlinear case, or more specifically, polynomial curves of best fit. Perpendicular distances cannot be extended to higher-order (nonlinear) cases and have to be derived for each form of the polynomial.

The basic mathematics for linear least-squares fitting can be found in most elementary texts on data handling, statistics, or quantitative analysis. The regression coefficient,  $m$ , or simply the slope of the line, can be calculated rather directly from the individual absorbance and concentration data. Once the regression coefficient is known, the intercept,  $d$ , can be calculated from the average absorbance and the average concentration values as well as the regression coefficient.

After the curve has been calculated, it is beneficial to know the goodness of the fit, which is usually measured, but not always correctly, as the correlation

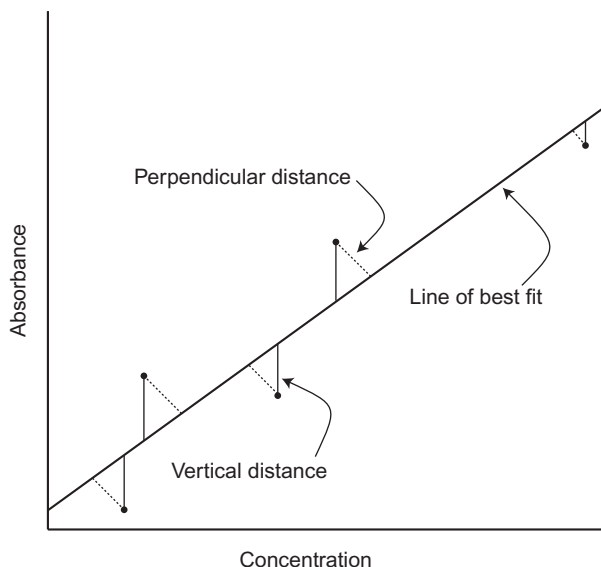


**Figure 9.5.** Perpendicular (dashed line) and vertical (solid line) distances for the computation of a least-squares line of best fit.

coefficient,  $R^2$ .  $R^2$  can be calculated directly from the raw absorbance and concentration values:

$$R^2 = \frac{\left( n \sum_{i=1}^n c_i a_i - \sum_{i=1}^n c_i \sum_{i=1}^n a_i \right)^2}{\left[ n \sum_{i=1}^n c_i^2 - \left( \sum_{i=1}^n c_i \right)^2 \right] \left[ n \sum_{i=1}^n a_i^2 - \left( \sum_{i=1}^n a_i \right)^2 \right]} \quad (9.5)$$

where  $c_i$  is each concentration,  $a_i$  the corresponding absorbance, and  $n$  the number of standards measured for the Beer's law plot of absorbance versus concentration.

A correlation coefficient of unity indicates that all the data fell exactly on the line.  $R^2$  values lower than unity indicate deviation from the line, and the lower the correlation coefficient, the greater the deviations of the point. Note that a value of  $R^2 < 1$  can arise either from noisy linear data or from nonlinear data. A correlation coefficient of zero indicates that the data were truly random and there is no correlation between the data and the curve of best fit. Of course,  $R^2$  values greater than 0.99 are desirable and indicate a good fit for the data. As  $R^2$  decreases the fit becomes worse and calculations based on the curve are likely to have larger errors.

As stated above, least-squares fitting can be extended to nonlinear curves. The major problem with this approach is that the form of the nonlinearity is frequently unknown. If a Beer's law curve does indeed deviate from linearity, it cannot be assumed that the curve will follow a simple quadratic or cubic expression. The nonlinearity may be logarithmic or some other functionality. Unless the form of

the curve is known, attempts to fit the data to a specific function may not yield improvement over the linear case. It is often simpler and more accurate to fit the curve to a succession of linear curves and iterate the process until the succession of linear fits converges to a minimum.

Linear least-squares regression is a univariate method; that is, all the variance is assumed to be attributable to a single component. Specifically, there are only two variables, a dependent variable (the spectral absorbance) and an independent variable (the concentration). These conditions impose some limitations on linear least-squares regression. First and foremost, the absorbance at the analytical wavelength(s) must be related to a single component, and no other component can contribute to the absorbance. Baseline errors, particularly errors that are either not constant or a direct function of concentration, will introduce uncertainty into the model. Finally, linear least-squares regression is restricted to very simple samples, such as solutions with a single component or the spectra of simple mixtures with nonoverlapping bands. On the other hand, least-squares regression is very simple to calculate and understand. For a well-behaved simple sample it will provide precise analyses.

## 9.5. CLASSICAL LEAST SQUARES

In the preceding section we showed that linear least-squares regression is limited to single components or simple mixtures where the bands are totally isolated from one another and there is no overlap in absorbance between the components. Under these conditions a separate linear least-squares regression can be completed for each of the components. This is the definition of a univariate system.

In practice, spectral components almost invariably do overlap, and hence the simple linear least squares regression approach is not feasible. It is, however, possible to construct a linear least squares regression model for more than one component if Beer's law is modified to recognize that measured absorbance is the sum of the absorbances of all the components in the mixture. Now the model becomes a *multivariate* system.

Let us assume that there are two components,  $x$  and  $y$ , in a mixture and that the bands for the components have some overlap. (We can ignore the case where all the bands from both spectra match completely, as this would signify that they are the same component.) Under these conditions there must be at least two wavenumbers where the concentrations of the components are seen to vary. Let these two wavenumbers be  $\tilde{\nu}_1$  and  $\tilde{\nu}_2$ . Then we can represent the absorbances at the two wavenumbers as

$$\begin{aligned} A_{\tilde{\nu}_1} &= a_{x,\tilde{\nu}_1} b C_x + a_{y,\tilde{\nu}_1} b C_y + E_{\tilde{\nu}_1} \\ A_{\tilde{\nu}_2} &= a_{x,\tilde{\nu}_2} b C_x + a_{y,\tilde{\nu}_2} b C_y + E_{\tilde{\nu}_2} \end{aligned} \quad (9.6)$$

where  $a_x, \tilde{\nu}_1$  is the absorptivity of component  $x$  at  $\tilde{\nu}_1$ ,  $a_y, \tilde{\nu}_1$  the absorptivity of component  $y$  at  $\tilde{\nu}_1$ , and so on. The pathlength is  $b$ , and  $C_x$  and  $C_y$  are the concentrations



of  $x$  and  $y$  in the mixture, respectively. The terms  $E_{\tilde{\nu}_1}$  and  $E_{\tilde{\nu}_2}$  refer to the residual errors from linear least-squares regression. Although the data have not as yet been fitted to a calibration curve, a calibration curve will be calculated and each set of data will have its own residual error.

Equation 9.6 is unnecessarily complex. The pathlength is a constant value, as in any quantitative analysis experiment it can readily be assumed that a single cell or accessory will be used for the analysis. Thus, the absorptivities can be combined with the pathlength to give a new parameter,  $k(k = ab)$ :

$$\begin{aligned} A_{\tilde{\nu}_1} &= k_{x,\tilde{\nu}_1} C_x + k_{y,\tilde{\nu}_1} C_y + E_{\tilde{\nu}_1} \\ A_{\tilde{\nu}_2} &= k_{x,\tilde{\nu}_2} C_x + k_{y,\tilde{\nu}_2} C_y + E_{\tilde{\nu}_2} \end{aligned} \quad (9.7)$$

where now  $k$  follows the same subscript convention as  $a$ ; that is,  $k_{x,\tilde{\nu}_1}$  is the absorption coefficient for component  $x$  at  $\tilde{\nu}_1$ .

Only one mixture is represented by Eqs. 9.7; it simply describes the absorbance of a single binary mixture at two different wavenumbers. This equation has only two known quantities, but four unknowns:  $k_{x,\tilde{\nu}_1}$ ,  $k_{y,\tilde{\nu}_1}$ ,  $k_{x,\tilde{\nu}_2}$ ,  $k_{y,\tilde{\nu}_2}$ . To be able to determine these four variables, another mixture of different concentrations of  $x$  and  $y$  must be prepared and the absorbances at  $\tilde{\nu}_1$  and  $\tilde{\nu}_2$  must be measured. The four equations (two from Eq. 9.7 and two from the new mixture) can be used to solve for the four unknown variables. Although this will give us a value for the absorptivities of the two components at  $\tilde{\nu}_1$  and  $\tilde{\nu}_2$  it is unwise (and for FT-IR spectrometry, unnecessary) to accept this as a good model. Essentially, we have only two data points, the two binary mixtures; consequently, we can fit a linear expression exactly to those data. Our residual errors will reduce to zero.

With linear least-squares regression, we chose many concentrations to calculate a good curve. The same should be done for the binary mixture, so that there are many mixtures of different concentrations, all measured at the two wavenumber positions. Rather than write a long series of equations to represent all the mixtures, we can employ a shorthand notation by which we represent all the terms in Eq. 9.7 in matrix notation; that is,

$$\mathbf{A} = \mathbf{K} \cdot \mathbf{C} + \mathbf{E} \quad (9.8)$$

where  $\mathbf{A}$  represents all the absorbance values at the two wavenumbers,  $\mathbf{K}$  is the representation of the absorption coefficients,  $\mathbf{C}$  represents the concentrations of the two components in each mixture, and  $\mathbf{E}$  is the set of residual errors for each measurement.

Upon closer examination of Eq. 9.8 there is no restriction on any of the matrices.  $\mathbf{A}$  is not restricted to just two wavenumbers and is valid even if we used more values. If we increase the number of wavenumbers where we record the absorbances, we have more redundancy in the model and are able to calculate a better model. That is, if we use more absorbances, we have more values to average; hence, our precision will improve. In fact,  $\mathbf{A}$  often represents the *entire* spectrum. Similarly, there is no restriction on  $\mathbf{C}$ . We are not confined to binary mixtures but

may look at more components. Our only restriction is that we must have no more concentrations than absorbances. This is rarely a problem, as in practice the number of components does not often exceed 10. An unusual case may have as many as 15 components. As  $\mathbf{A}$  and  $\mathbf{C}$  grow to include more absorbances and concentrations,  $\mathbf{K}$  and  $\mathbf{E}$  become larger to accommodate the changes.

When all the mixtures are prepared and all the spectra are measured, it is apparent that each component will have its own linear least-squares regression, and the errors,  $\mathbf{E}$ , represent the residuals to those linear regressions. For simplicity, the matrix  $\mathbf{E}$  will be eliminated from the equations, but it must be understood that it still exists. Then Eq. 9.8 becomes

$$\mathbf{A} = \mathbf{K} \cdot \mathbf{C} \quad (9.9)$$

Before the data can be used to determine the concentrations of components in an unknown mixture, the matrix  $\mathbf{K}$  must be evaluated.  $\mathbf{K}$  can be determined with the use of matrix inversion; that is,

$$\mathbf{K} = \mathbf{A} \cdot \mathbf{C}^{-1} \quad (9.10)$$

where  $\mathbf{C}^{-1}$  is the inverse of the concentration matrix  $\mathbf{C}$ . This operation will only be valid if  $\mathbf{C}$  is a square matrix; that is, it has the same number of rows as columns, and this will only be true if the number of samples is equal to the number of components.

When a Beer's law calibration curve is generated, the results are always better if the number of samples exceeds the number of components. A good rule of thumb for multicomponent mixtures is to have at least three times as many samples (mixtures) as components. When there are more components than samples,  $\mathbf{C}$  will not be a square matrix and its inverse cannot be calculated directly. Instead, its pseudoinverse can be calculated with the transpose of  $\mathbf{C}$ , that is,  $\mathbf{C}^T$ . The transpose of a matrix is obtained when the rows and columns of the matrix are switched. Thus,

$$\mathbf{K} = \mathbf{A} \cdot \mathbf{C}^T \cdot (\mathbf{C} \cdot \mathbf{C}^T)^{-1} \quad (9.11)$$

Once  $\mathbf{K}$  is known, the concentrations of the components of an unknown mixture can be calculated from the following equation:

$$\mathbf{C}_{\text{unk}} = (\mathbf{K} \cdot \mathbf{K}^T)^{-1} \cdot \mathbf{K}^T \cdot \mathbf{A}_{\text{unk}} \quad (9.12)$$

where  $\mathbf{C}_{\text{unk}}$  is the matrix that is calculated from the absorbances of the unknown mixture,  $\mathbf{A}_{\text{unk}}$ , and the absorptivity matrix  $\mathbf{K}$  calculated from Eq. 9.11. The concentrations of the components in the unknown mixture are contained in  $\mathbf{C}_{\text{unk}}$  as separate values.

The operations described in this section are known as *classical least-squares* (CLS) *regression*, or sometimes the  $\mathbf{K}$ -matrix method of quantitative analysis.

One interesting aspect of CLS is that if the entire spectrum is used in  $\mathbf{A}$ ,  $\mathbf{K}$  will be the absorptivities of each of the pure components, and each row of  $\mathbf{K}$  will represent a different component.

CLS has a number of advantages over linear least-squares regression. First, it is a multivariate technique, and the restriction of spectrally isolated components is removed. Second, the entire spectrum can be used and the use of a large number of wavenumber positions has an averaging effect on the data and errors are reduced. CLS can accommodate some baseline effects; that is, it can have nonzero intercepts for some components. (As noted above, at zero concentration the absorbance need not necessarily be zero because of spectral or instrumental anomalies.)

There is one serious shortcoming to CLS: The set of equations must be calibrated for *every* component in the mixture. This is a direct consequence of the relationship between absorbance and concentration. Absorbance is the sum of the concentrations of *all* the components in the mixture, and if one or more components are ignored, the equations are invalid. The corollary to this is that if an unknown or uncalibrated component appears in an unknown mixture, the model will be unable to predict *any* of the components correctly.

Other problems are a little more subtle. If any of the constituents interact chemically (including hydrogen bonding), the bands of the pure components in the calibration mixtures will distort as the concentration is changed. This is equivalent to having an unknown component that will cause the model to fail. The compositions of the calibration mixtures must be random and encompass the concentrations in the unknown mixtures. If the concentration of a component of an unknown mixture is lower or higher than all of the concentrations for that component in the calibration mixtures, the method will fail unless the system is completely linear. In this case the method may be able to extrapolate to those values outside the data set, but it is difficult to assure that the system is completely linear. Finally, the method will fail if any of the calibration mixtures are linearly related. A linear relation simply means that the concentrations of all the components in one mixture are a factor of all the component concentrations in another mixture. In this case, the method will fail because it will be mathematically impossible to invert the  $\mathbf{C}$  matrix;  $\mathbf{C}^{-1}$  will become indeterminate; that is, it is equivalent to dividing by zero.

Despite the shortcomings of CLS it is a valuable technique that can be used for quite complex mixtures. The shortcomings can be overcome in large part through rearrangement of Beer's law, as described in the following section.

## 9.6. INVERSE LEAST-SQUARES REGRESSION

The greatest shortcomings to CLS are that all the components of a mixture must be known and that no new components can be present in unknown mixtures. Only under very strictly controlled conditions will this be true, and such a situation is not applicable to many real-world problems. Furthermore, it is often the case that only a subset of the components is of interest; therefore, it is preferable that only those components are built into the model. This condition can be met if Beer's

law is rearranged so that concentration is the dependent variable and absorbance becomes the independent variable. That is,

$$C = \frac{A(\tilde{\nu})}{a(\tilde{\nu})b} \quad (9.13)$$

Again the pathlength will generally be held constant so that the pathlength and absorptivity can be combined. In Eq. 9.13 the combination term is the denominator; hence, the reciprocal can be replaced by a single variable,  $P$ :

$$C = PA + E_C \quad (9.14)$$

Note that an error value has been added in the same manner as with CLS.  $E_C$  is the residual error for the dependent variable, that is, concentration (whereas it was the residual error for absorbance in the CLS model).

If we have a binary mixture of components  $x$  and  $y$ , we can construct a set of equations to reflect the response at two wavenumber positions,  $\tilde{\nu}_1$  and  $\tilde{\nu}_2$ , in an analogous manner to the way we constructed Eq. 9.6. For the rearranged form of Beer's law (i.e., inverse Beer's law), we have

$$\begin{aligned} C_x &= P_{x,\tilde{\nu}_1}A_{\tilde{\nu}_1} + P_{x,\tilde{\nu}_2}A_{\tilde{\nu}_2} + E_x \\ C_y &= P_{y,\tilde{\nu}_1}A_{\tilde{\nu}_1} + P_{y,\tilde{\nu}_2}A_{\tilde{\nu}_2} + E_y \end{aligned} \quad (9.15)$$

where  $C_x$ ,  $C_y$ ,  $A_{\tilde{\nu}_1}$ , and  $A_{\tilde{\nu}_2}$  have been defined previously (Eq. 9.6),  $P_{x,\tilde{\nu}_1}$  is the linear reciprocal coefficient of absorptivity for component  $x$  at  $\tilde{\nu}_1$ , and  $E_x$  and  $E_y$  are the concentration errors for  $x$  and  $y$ , respectively.

Equations 9.15 are complete for the two concentrations of  $x$  and  $y$ . The concentrations are related to the absorbances at  $\tilde{\nu}_1$  and  $\tilde{\nu}_2$ , which accounts for the total concentration of each component. If other components are present in a mixture, their absorbances are not included in the equation. Thus, only components of interest need to be modeled and the model is theoretically immune to impurities.

As the number of components is increased and the number of absorbances included grows, it is more concise to represent the equation in matrix form:

$$\mathbf{C} = \mathbf{P} \cdot \mathbf{A} + \mathbf{E}_C \quad (9.16)$$

With classical least-squares regression we were able to increase the number of absorbances (dependent variable) essentially without limit, but here the absorbances are the independent variable and the number of absorbances cannot exceed the number of calibration spectra. Consequently, the wavenumbers at which the absorbance is measured should be picked with care to ensure that the absorbances at those wavenumber positions are reflective of the overall contribution of those components to the spectrum. An examination of Eqs. 9.15 shows that there must be at least one analytical wavenumber for each component. Equations 9.15 represent two components; consequently, there are two analytical wavenumbers,  $\tilde{\nu}_1$  and  $\tilde{\nu}_2$ .

Once a set of calibration samples has been made and their absorbance spectra measured, the reciprocals of the linear coefficients of absorptivities, or  $\mathbf{P}$  matrix, can be determined as

$$\mathbf{P} = \mathbf{C} \cdot \mathbf{A}^{-1} \quad (9.17)$$

More correctly, as  $\mathbf{A}$  is unlikely to be a square matrix,

$$\mathbf{P} = \mathbf{C} \cdot \mathbf{A}^T \cdot (\mathbf{A} \cdot \mathbf{A}^T)^{-1} \quad (9.18)$$

The concentrations of the components of interest in an unknown mixture can be determined by direct application of

$$\mathbf{C}_{\text{unk}} = \mathbf{P} \cdot \mathbf{A}_{\text{unk}} \quad (9.19)$$

The unknown concentrations are found simply by multiplication of the unknown spectrum absorbances ( $\mathbf{A}_{\text{unk}}$ ) by the  $\mathbf{P}$  matrix.

This method is commonly known as *inverse least-squares (ILS) regression*, but it is also referred to as the  $\mathbf{P}$ -matrix method or *multiple linear regression (MLR)* when the number of analytical wavenumbers is small. ILS is a multivariate technique that has some advantages over CLS, but ILS also has some shortcomings.

One shortcoming has already been discussed; the number of wavenumbers at which the absorbances are measured cannot be increased to improve the model, in fact, the number of wavenumbers cannot exceed the number of mixtures (i.e., spectra) in the training set. The number of components cannot be increased with impunity either. Although many components can be monitored (in practice up to about 10), an increase in the number of components can cause the method to become unstable. As the number of components is increased, more wavenumbers at which absorbances are measured are incorporated in the model. Component concentrations and absorbance values track each other, which is a condition known as *collinearity*. That is, all the absorbances tend to rise and fall in concert with the concentrations. When the matrices become collinear, the model becomes unstable and can fail.

The greatest difficulty in the application of the ILS method is the selection of the appropriate wavenumbers at which the absorbances should be measured. This operation is built into most commercial ILS algorithms, and typically, the model is iterated until an optimum set of wavenumber positions is found. This operation can be quite time consuming, but as computer speeds continue to increase, computation time is becoming less of a problem.

On the positive side, ILS is a robust method and it is not restricted by the requirement that the concentrations of all components be known. Thus, more complex mixtures can be analyzed than by CLS. ILS is not limited by component interactions; these interactions are treated as impurities and ignored. Baseline errors are also treated as impurities and the method is not seriously affected.

Both CLS and ILS have strengths and weaknesses, and it would be beneficial to combine their strengths and eliminate the weaknesses. A commonly accepted procedure to achieve this goal is to use spectral decomposition in the form of *principal component analysis* (PCA).

## 9.7. PRINCIPAL COMPONENT ANALYSIS

The advantages of CLS and ILS can be combined if we can reduce the number of wavenumbers at which absorbances are measured for ILS, yet retain the advantages of the use of the entire spectrum as in CLS regression. To do this we must consider what a collection of calibration spectra represents. First, we have the pure components. The calibration spectra are composed of different concentrations of the pure components, or for the spectra, different scalings. Unfortunately, there is more that we must consider. If the components interact, we have interaction spectra, and these will be present in different ratios in the individual calibration mixture spectra. Each instrument will bias the spectra, so we have instrument-induced artifacts that may vary with temperature, total absorbance, wavenumber, and so on. In all we have numerous contributions or factors that together comprise each of the individual calibration spectra. The only difference between all the individual calibration spectra is the proportion of the contributions.

If we had an ideal spectrometer and absolutely no interaction effects, we would be able to construct the individual calibration spectra from the spectra of the pure components alone. More important, we should be able to *decompose* the individual calibration spectra into the pure component spectra. Because we do not have ideal spectrometers and rarely have ideal calibration sets, this is not possible. Nonetheless, if it were possible, we could simply represent each spectrum in the calibration set as the proportions of the pure component spectra. For example, if there were three components, each calibration spectrum would be composed of the three components in different proportions. Three numbers would represent the proportions, one for each component.

The problem we have with ILS is that we cannot use as many wavenumbers as we can in CLS. In CLS, this was a distinct advantage, as the use of all the absorbances led to a more accurate prediction. If in the ILS model we use the proportions, or scores, in place of the absorbances, we have restricted the dependent variables to a small number as required in ILS; we also have a score for each component, also as required in ILS. On the other hand, the scores represent the *entire* absorbance spectrum and by default we have incorporated all the absorbance information and its associated advantage.

The problem lies in how we can extract pure components from a real data set. In reality such an operation is difficult, although several algorithms exist that can do precisely this. These algorithms are beyond the scope of this treatise, and recovery of the pure components' spectra is neither necessary nor often desirable. It is more important to decompose a set of calibration spectra into significant factors. These significant factors are also called *principal components*, *eigenvectors*, *loadings*,

*spectral loadings*, or *loading vectors*. For the sake of consistency, the term *principal components* will be used herein.

The principal components are not pure spectral components but contain portions of all the pure chemical components, the interactions between the chemical components, and the instrument artifacts. The principal components are determined by an iterative process whereby the most significant principal component is determined first and subsequent principal components have successively smaller contributions.

There are multiple algorithms to calculate principal components, and these include noniterative partial least squares (NIPALS), variance–covariance matrix decomposition, singular value decomposition (SVD), and successive average orthogonalization (SAO). Each algorithm has its own advantages and disadvantages, but they are all beyond the scope of this chapter. The first principal component is just the average of all the spectra in the calibration set. Each individual spectrum will vary about the average, so the average spectrum is the major component of all the individual spectra. In fact, this component is so large that it is often removed from the calibration spectra before any analysis is attempted. The removal of the average spectrum is known as *mean centering*.

Once the first principal component (PC) is determined, it is removed from all the calibration spectra. As each calibration spectrum is different, the contribution of the first PC to each spectrum is different as well. The calibration set now is comprised of the residuals after elimination of the first principal component.

The largest principal component of the residuals is calculated next and may be thought of as the average of all the residuals. This is a conceptual device only as the second PC is actually mathematically orthogonal to the first. The second principal component is removed from all the first residuals and the set then becomes the second residual. The process can be iterated until there are as many principal components as calibration spectra. This technique is known as *principal component analysis* (PCA).

Not all principal components are significant; consequently, only a subset of all the principal components is needed. While PCA is being performed, the contribution of each PC to the entire calibration data set is recorded. These contributions are known as the *eigenvalues*. Several test algorithms can be used to determine how many principal components are significant. The remaining principal components are simply noise and are neglected. After the significant number of principal components has been determined, those principal components and scores calculated from the principal components and the calibration set spectra are stored to represent the absorbance spectra. More specifically, this can be represented in vector notation; that is,

$$\mathbf{A} = \mathbf{S} \cdot \mathbf{F} + \mathbf{E}_A \quad (9.20)$$

where  $\mathbf{A}$  is the absorbance matrix (the calibration spectra),  $\mathbf{S}$  the scores matrix,  $\mathbf{F}$  the matrix of the principal components, and  $\mathbf{E}_A$  the error matrix, often referred to as the *matrix of residual spectra*.

PCA has given us a way whereby we can take a calibration set of full absorbance spectra and decompose them into a small number of principal components. The principal components are needed to find the scores of the principal components in unknown spectra, and the scores are used in place of the absorbance spectra in either a CLS or an ILS model. The next two sections present two methods that make use of the principal components and their scores.

## 9.8. PRINCIPAL COMPONENT REGRESSION

*Principal component regression* (PCR) is the algorithm by which PCA is used for quantitative analysis and involves a two-step process. The first is to decompose a calibration data set with PCA to calculate all the significant principal components, and the second step is to regress the concentrations against the scores to produce the component calibration coefficients. Generally, the ILS model is preferred, as it does not require knowledge of the complete composition of all the spectra. Therefore, if we use the ILS model from Eq. 9.16 but rewrite it for scores,  $\mathbf{S}$ , instead of absorbances,  $\mathbf{A}$ , we have

$$\mathbf{C} = \mathbf{X} \cdot \mathbf{S} + \mathbf{E}_C \quad (9.21)$$

where  $\mathbf{X}$  is the matrix of component calibration coefficients. As with ILS, we need to calculate  $\mathbf{X}$ , and this can be done simply from  $\mathbf{C}$  and  $\mathbf{S}$ .  $\mathbf{S}$  can be determined from the matrix of the principal components,  $\mathbf{F}$ , and the absorbance matrix,  $\mathbf{A}$ , from Eq. 9.20.

A characteristic of the principal component matrix is that it is an orthogonal matrix. When it is multiplied by its own transpose, the identity matrix,  $\mathbf{I}$ , is the result. An identity matrix when multiplied with any other matrix results in the other matrix.  $\mathbf{I}$  does not alter the other matrix in any way. Therefore, if we multiply Eq. 9.20 by the transpose of  $\mathbf{F}$ ,  $\mathbf{F}^T$ , we have

$$\mathbf{A} \cdot \mathbf{F}^T = \mathbf{S} \cdot \mathbf{F} \cdot \mathbf{F}^T = \mathbf{S} \cdot \mathbf{I} = \mathbf{S}$$

or

$$\mathbf{S} = \mathbf{A} \cdot \mathbf{F}^T \quad (9.22)$$

Now that we have  $\mathbf{S}$ , we can proceed with the calculation of  $\mathbf{X}$  from Eq. 9.21:

$$\mathbf{X} = \mathbf{C} \cdot \mathbf{S}^T \cdot (\mathbf{S} \cdot \mathbf{S}^T)^{-1} \quad (9.23)$$

To measure the concentrations of components in an unknown mixture, we must first calculate the scores for the unknown mixture spectrum. From Eq. 9.22,

$$\mathbf{S}_{\text{unk}} = \mathbf{A}_{\text{unk}} \cdot \mathbf{F}^T \quad (9.24)$$



Then we can calculate the concentrations directly (Eq. 9.21):

$$\mathbf{C}_{\text{unk}} = \mathbf{X} \cdot \mathbf{S}_{\text{unk}} \quad (9.25)$$

We have now accomplished what we set out to do: to find a method that can be used with complex mixtures for which we do not need to know all the components. In addition, we can use the full spectral data to improve the precision of the results. PCR incorporates the advantages of CLS and ILS but has few, if any, of the shortcomings.

Of course, there is one caveat. We have made the assumption that all the variance in the decomposition by PCA is related directly to the concentration change. This is not necessarily true, as the factors may be attributable to changes in constituents that we are not measuring. Ideally, we should try to correlate the principal components to the concentrations of the constituents. This, in general, is difficult to do, and most commercial PCR algorithms do not attempt the correlation. The end result is that PCR may use more principal components and scores than necessary, and the principal components may not relate directly to the constituents. Nonetheless, PCR is a powerful technique and can be a considerable improvement over ILS and CLS. One algorithm that does decompose both the absorbance and concentration matrices, and correlates the two, is *partial least-squares* (PLS) *regression*.

## 9.9. PARTIAL LEAST-SQUARES REGRESSION

Unlike PCR, PLS regression does not rely upon PCA to produce the spectral loadings. We use the term *spectral loadings* here because principal components are a direct result of PCA. In fact, the spectral loadings produced by PLS are not the same as the principal components calculated with PCA. PLS has its own spectral decomposition algorithm that simultaneously decomposes the constituent (or concentration) matrix. The result of the simultaneous decomposition is that the spectral loadings are ranked down from the constituent with the greatest contribution to the calibration spectra. This forces the relevant data into as few spectral loadings as possible and removes extraneous spectral loadings. The key element is that both the **A** and **C** matrices are decomposed together, which leads to a concise and robust model. The mathematical steps are considerably more complex than the other multivariate methods; hence, they are omitted from this section. The interested reader is directed to other references [8–10].

Prediction of concentrations of constituents in an unknown mixture generally follows the procedure of PCR, except that it is a more iterative procedure. The spectral loadings from the decomposition step are used to calculate the scores from the unknown absorbance spectrum. The scores are used with the loading vectors for the constituents to calculate the unknown concentrations. Since both **A** and **C** are decomposed, the concentrations of the constituents also have loading vectors. As with PCR, an ILS basis is used.

There are two general classes of PLS algorithms, usually designated as PLS-1 and PLS-2. The major difference between the two PLS algorithms is that PLS-2 calculates all the scores and loadings at one time, with just one set of loadings for all the components, whereas PLS-1 calculates them separately. PLS-2 is an iterative method and the loadings and scores are calculated by a convergence method in which all the convergences are done on all the spectral and concentration scores and loadings at once. This makes the calculation fairly rapid and the advantages of PLS are maintained. For each loading, scores are calculated for each component in parallel, and convergence is completed on the scores and loading before subsequent scores and loadings are calculated. PLS-1 is a potentially more accurate algorithm, but since each component is calibrated independently, can be slow if the number of components is large. For the first loading, each score is calculated from the full absorbance and concentration data set. For subsequent loadings, both the loadings and scores are calculated from successive residuals. PLS-1 spectral loadings retain a much better correlation to the constituent spectra than the other multivariate methods, but at the price of time. Prediction in PLS-1 and PLS-2 follow the procedures to determine the loadings and scores; PLS-1 calculates each unknown concentration individually, whereas PLS-2 calculates them in parallel.

The number of principal components that should be used for a PLS-1 or PLS-2 analysis is usually determined by first calculating the *root-mean-square error of cross validation* (RMSECV) using one principal component (PC.) The process is repeated using 2, 3, 4, and so on, PCs. The RMSECV, which is sometimes called the *prediction residual error sum of squares* (PRESS), is plotted against the number of PCs used for the calculation. (This graph is often called a PRESS plot.) The number of PCs that yield minimum PRESS value is the appropriate value to use for the experiment.

PLS has several strengths or advantages over the other multivariate methods, as it combines the strengths of CLS and ILS. CLS provides full spectral coverage and improves the precision of the data, and ILS allows modeling of a specific component. PLS tends to be extremely robust and can analyze very complex mixtures. The shortcomings are rather minor. The calculations tend to be rather slow, but this is becoming a moot point as computer speeds continue to increase. PLS does require a large number of mixture spectra to yield precise conditions but typically only three to five times as many mixtures as constituents.

## 9.10. VALIDATION

Knowing that a calibration is appropriate is of critical importance for chemometrics. Generally speaking, all multivariate analyses require that the algorithm being used should first be trained by measuring the spectrum of samples of known composition. The validity of the calibration for the type of samples measured must then be tested, ideally with an independent set of samples. Sometimes, the composition of samples in the *calibration set* is determined by mixing known weights or

volumes of the components. For other types of samples, this simple approach may be impossible. For example, it is not reasonable to mix pure samples of starch, protein, oil, and water, then expect the spectrum to match that of wheat! Instead, the concentrations of the components of interest in each sample of the calibration set must be determined by a *primary method* (i.e., a method that is known to yield the concentration of a given component accurately). For the case of wheat, the protein concentration of each sample in the calibration set is determined by a Kjeldahl titration or by combustion, the concentration of oil by hexane extraction, and the concentration of water by a Karl Fischer method. (The concentration of the carbohydrate is simply calculated by difference.) The spectrum of each wheat sample for which these calibration data have been found is then regressed against the analytical data to obtain the calibration matrix. Once the calibration matrix has been calculated, it is then used to calculate the concentrations of interest (e.g., protein, oil, and water) of each sample in the calibration set. The standard deviation of the difference between the measured and the calculated concentration of a given component is called the *root-mean-square error of calibration* (RMSEC) or simply the *standard error of calibration* (SEC).

The validity of the calibration should then be tested using an independent sample set (known as the *prediction set*) for which the concentrations of each component of interest have been measured by the primary analytical technique. The concentrations of each component are calculated using the calibration matrix determined above and the standard deviation of the difference between the measured and calculated concentration of a given component is called the *root-mean-square error of prediction* (RMSEP) or simply the *standard error of prediction* (SEP). The difference between the SEC and SEP is that the analytical data for the prediction set was not used for the calibration. Thus, the SEP is usually, but not always, a little larger than the SEC. If the SEP is much larger than the SEC, the calibration is generally invalid. A much more detailed discussion on the validity of data is beyond the scope of this book but is available in a number of excellent monographs on chemometrics [11–13].

It is often necessary to include at least 50 samples in the calibration and prediction sets. Sometimes, measurement of the primary analytical data of so many samples is excessively time consuming. The number of samples can be approximately halved, at the cost of computation time, by using only one calibration set and calculating the root-mean-square error of cross validation (RMSECV), as described in Section 9.9. In general, however, it is preferable to use an independent prediction set to investigate the validity of the calibration but the “leave-one-out method” significantly reduces the number of samples for which primary analytical data are required.

### 9.11. MULTIVARIATE CURVE RESOLUTION

A number of the techniques discussed above utilize decomposition of the data matrix to reduce the complexity of the techniques. It is common to consider the

data matrix, be it concentration or absorbance, symbolically as  $\mathbf{D}$ . If we take the simple Beer's law case of  $\mathbf{D}$  as absorbance, it is reasonable to assume that the absorbance matrix is a representation of the pure component spectra,  $\mathbf{S}$ , and their respective concentrations,  $\mathbf{C}$ . That is,

$$\mathbf{D} = \mathbf{C} \cdot \mathbf{S}^T + \mathbf{E} \quad (9.26)$$

where  $\mathbf{E}$  is the error matrix associated with the measurement. As we saw earlier, we do not decompose the data matrix into the pure component spectra, but rather, into principal components and scores. Both sets of matrices, principal components with scores and pure component spectra with concentrations, represent the data matrix equally well. The only difference between the two sets of matrices is that they are rotated with respect to one another in multidimensional space.

Decomposition of a matrix [14] is accomplished through the use of a transformation matrix,  $\mathbf{T}$ :

$$\mathbf{D} = \mathbf{C} \cdot (\mathbf{T} \cdot \mathbf{T}^{-1}) \cdot \mathbf{S}^T \quad (9.27)$$

$$\mathbf{D} = (\mathbf{C} \cdot \mathbf{T}) \cdot (\mathbf{T}^{-1} \cdot \mathbf{S}^T) \quad (9.28)$$

$$\mathbf{D} = \mathbf{C}' \cdot \mathbf{S}'^T \quad (9.29)$$

where  $\mathbf{C}' = \mathbf{C} \cdot \mathbf{T}$  and  $\mathbf{S}'^T = (\mathbf{T}^{-1} \cdot \mathbf{S}^T)$ . Unfortunately, there are as many solutions for  $\mathbf{C}'$  and  $\mathbf{S}'^T$  as there are matrices  $\mathbf{T}$ . Essentially, this number is infinite and there is only one solution that will yield the pure component spectra and their concentrations.

Methods to recover the pure components from decomposed data matrices have been the subject of investigation for a number of years. These initially were known as self-modeling strategies [15], from which other methods have been developed, such as automated spectral isolation (ASI) [16], iterative target transform factor analysis (ITTFA) [17], evolving factor analysis (EFA) [18], iterative key set factor analysis (IKS-FA) [19], fixed-size moving window evolving factor analysis (FSMW-EFA) [20], successive average orthogonalization iterative target transform factor analysis (SAO-ITTFA) [21], as well as non-factor analysis methods (e.g., SIMPLISMA [22]).

Multivariate curve resolution (MCR) [14] is the latest of the methods that seek to constrain the rotation of the matrices by forcing the  $\mathbf{C}$  and  $\mathbf{S}$  matrices to obey certain restrictions. One such restriction is that all absorbances in the spectra must be greater than or equal to zero. This restriction was also imposed in SAO-ITTFA [21]. In MCR it can be imposed that none of the concentrations will be less than zero. Other restrictions can result from chemical mass balance equations to determine composition in a dynamic system, or knowledge of some of the pure component spectra can be fed into the method algorithm to resolve other pure component spectra. One major advantage of MCR (and SAO-ITTFA) is to determine concentration profiles from kinetic systems as well as to determine the spectra of transient species.

### 9.12. GENERAL GUIDELINES FOR CALIBRATION DATA SETS

In the preceding sections of this chapter, several multivariate regression methods have been presented. All of these methods require standard mixture spectra. The construction of the mixtures will now be addressed in general, but more detailed discussion can be found elsewhere [23].

It is not a trivial task to make a good calibration set. The set should be designed so that each constituent spans the anticipated concentrations. As the number of constituents increases, this becomes progressively more difficult. The temptation is to omit constituents or use pure constituents, so that one “mixture” is 100% of a single constituent. This should be avoided unless it is possible that the constituent could indeed be pure in an unknown. It is more likely that a constituent could be missing from an unknown, in which case a mixture with a missing constituent is acceptable. The reason that pure samples should not be used is that none of the constituent interactions will be present in the spectra. Therefore, more than one parameter of the mixture will be missing, which can distort the model considerably.

A more subtle temptation is to generate the mixtures by successive dilution. Two or more mixtures that vary in concentration by only a factor will in reality produce the same spectral vectors. That is, the spectra are “identical” except that one has a different scale to the other. Mathematically, the two spectra represent the same ratios of components and they are not different. The two spectra force the absorbance matrix **A** to be collinear, but more important, the concentration ratios in the **C** matrix are also collinear. The **A** matrix will have noise associated with each spectrum, and as the noise is not the same in each spectrum, the **A** matrix will be only approximately collinear. **C** will be precisely collinear, and if **C** is inverted (even through pseudoinversion), the result will be indeterminate; that is, it is equivalent to division by zero. As soon as this happens, the regression fails and the model is invalid.

Another subtle problem is under- or overrepresentation of constituents. For example, if there is a three-constituent solution that contains constituents A, B, and C, A will be overrepresented if it is present in 12 out of 12 mixtures, and C will be underrepresented if it is only in 4 out of 12 mixtures. Ideally, A, B, and C should be in all 12 mixtures, but it could be anticipated that C will be absent in some unknowns. The model as constructed will predict A well but C rather poorly, as it has insufficient data to model C. If C is the only component anticipated to be missing from an unknown solution, A and B should be in all 12 calibration mixtures and C should be in nine or 10.

For ILS-based models, the solvent concentration can be omitted from the constituent matrix **C**. The solvent is a constituent, but it is generally not of interest. The constituent concentrations can be randomized and span the anticipated unknown concentrations, but care must be taken to ensure that the sum of all the constituents is not the same. That is, in any given mixture, the sum of all the concentrations should not be a constant. If the concentrations sum to a constant, the model only spans a plane in three or more dimensions (one dimension for each constituent). If the constituents are a binary mixture, the model will describe a line (a two-dimensional model). The model will have no “depth”, and any unknown mixture

where the constituent concentrations do not sum to the constant will be predicted incorrectly. The fundamental rule is to try to randomize the constituent concentrations as much as possible. This will help ensure that the model is robust and the predictions are reliable.

As a final note, it should be recognized that multivariate methods are not restricted to concentration. Any properties that vary linearly with absorbance can be modeled and predicted. Some of the earliest work with multivariate methods with infrared spectrometry was to predict important properties of coal to be used in the production of steel [24,25]. These properties included the number of British thermal units generated per ton of coal; although Btu do not have their own spectra, they are presumably related to the composition of the coal.

### 9.13. NEURAL NETWORKS

Although artificial neural networks (ANNs) are not widely used in vibrational spectrometry, we include a very brief description of this method of analysis, as it does have some important applications. Artificial neural networks are not a single algorithm but refer to a wide range of computational methods, or networks. The foundation of all ANNs is in biological systems, and ANNs try to mimic biological thought processes. ANNs have not approached the complexity of a human brain, but they can be designed for quite complex problem solving.

An artificial neural network consists of number of simple processing units. Each unit is called a *neuron*, and sets of neurons comprise a *layer*. The input to the first layer of neurons is a vector (known as the *input layer*), such as a spectrum or a series of concentrations of constituents in a single mixture. The output of the neuron is a scalar value. During training, the input to each neuron in subsequent (or *hidden*) layers is weighted; that is, it is given more or less significance based on the capability of the neuron to recognize patterns. When a neuron collects the input from a number of sources, it sums all the weighted vectors to produce the net input. The net input is fed into a transfer function that operates on the net input to produce the scalar output. The transfer function is designed into the neuron and is specific to the task of the neuron. A schematic diagram of the functionality of a neuron is shown in Figure 9.6.

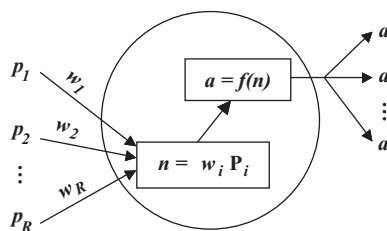


**Figure 9.6.** Artificial neuron or node.  $p$ ,  $a$ , and  $w$  represent the input, output, and weight, respectively.  $n$  is the net input and  $f$  is the transfer function. (Reproduced from [26], by permission of John Wiley & Sons, Ltd.; copyright © 2002.)

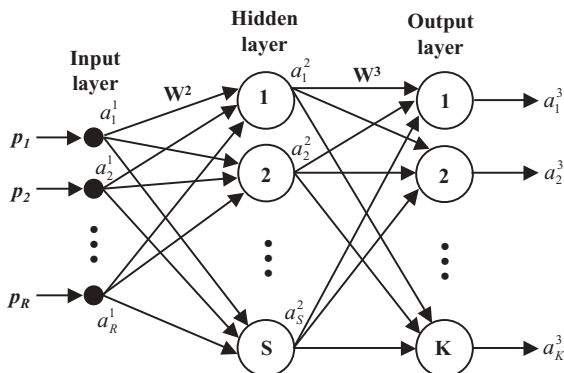


**Figure 9.7.** Architecture of a three-layer forward-feed neural network. The neurons in the input layer simply pass their inputs to the next layer without addition or transfer function. The conventions are the same as those used in Figure 9.6. (Reproduced from [26], by permission of John Wiley & Sons, Ltd.; copyright © 2002.)

Neurons generally operate in layers. The function of one layer may be to collect input from a process where each neuron receives a different input. Each input neuron processes the data according to its own transfer function and distributes the output to a second layer. If the second layer does not provide the final output, it is known as a *hidden layer*. Each neuron in the first layer passes its output to every neuron in the second layer. The second layer neurons each receive a series of data from each of the input neurons that constitutes a vector input. As the input to each neuron is different, the output will be different. The second layer processes the output from the first layer and distributes output to a third layer (usually, the *output layer*, but in principle it can be the second hidden layer).

Perhaps the simplest ANN design is a multilayer forward-feed neural network. A schematic diagram of a three-layer network is shown in Figure 9.7. Briefly, in this diagram the  $R$  vectors input to the first layer are labeled  $p_1 \cdots p_R$ , which go into the input neurons  $a_1^1 \cdots a_R^1$ . The outputs from the  $R$  input neurons are weighted with weights  $\mathbf{W}_2$ .  $\mathbf{W}_2$  is a matrix of weights to scale the inputs to the second, or hidden, layer. There need not be the same number of neurons in the second layer as the first, and the hidden layer has  $S$  neurons with outputs  $a_1^2 \cdots a_S^2$ . The output scalars are weighted with  $\mathbf{W}_3$  and fed into the  $K$  output neurons. The final output is the set of  $K$  scalar values  $a_1^3 \cdots a_K^3$ .

The neural network is first trained by inputting a series of data with known properties. A specific output from the network is desired or expected. During the training phase the weight matrices are modified until the desired output is achieved. For this to be successful, the network must be tested with known inputs, and validation of the ANN must result. Once the network is trained and validated, data to be processed are fed into the network with the expectation that the correct property will be recognized.

The majority of applications of artificial neural networks to mid-infrared spectroscopy have been directed to the classification of spectra into structural units; that

is, to identify functional groups in the molecule from the spectrum. This application is beyond the scope of quantitative analysis, but a review of these applications has been presented by Yang [26].

No quantitative applications of neural networks to quantitative analysis of linear systems have been reported where the results have been significantly better than those obtained by PLS, as would be expected since PLS (and indeed, the other multivariate methods described in this chapter) have been designed explicitly to handle linear systems. Analogous techniques, such as polynomial PLS or spline PLS, have been designed for nonlinear systems. It is interesting that with nonlinear data, neural networks have been shown to outperform any of the linear or nonlinear PLS techniques [27].

## REFERENCES

1. B. T. Bowie and P. R. Griffiths, *Appl. Spectrosc.* **54**, 1192 (2000).
2. D. W. Ball, *Spectroscopy* **14**(5), 16 (1999).
3. P. Bouguer, *Essai d'Optique sur la Gradation de la Lumière*, Paris, 1729.
4. J. H. Lambert, *Photometria*, Augsburg, 1760.
5. A. Beer, *Ann. Phys. Chem.* **86**, 78 (1852).
6. J. Genest and P. Tremblay, *Appl. Opt.* **38**, 5438 (1999).
7. T. Hirschfeld, Quantitative IR: a detailed look at the problems involved, in *Fourier Transform Infrared Spectroscopy*, J. R. Ferraro and L. J. Basile, Eds., Academic Press, New York, 1979, Vol. 2, p. 193.
8. P. Geladi and B. R. Kowalski, *Anal. Chim. Acta* **185**, 1 (1986).
9. A. Lorber, L. Wangen, and B. R. Kowalski, *J. Chemometr.* **1**, 19 (1987).
10. K. Beebe, R. J. Pell, and M. Seasholtz, *Chemometrics: A Practical Guide*, Wiley, New York, 1998.
11. M. A. Sharaf, D. L. Illman, and B. R. Kowalski, *Chemometrics*, Wiley, New York, 1986.
12. R. Kramer, *Chemometric Techniques for Quantitative Analysis*, Marcel Dekker, New York, 1998.
13. H. Mark and J. Workman, Jr., *Statistics in Spectroscopy*, Elsevier, San Diego, CA, 2003.
14. A. de Juan and R. Tauler, *Anal. Chim. Acta* **500**, 195 (2003).
15. W. H. Lawton and E. A. Sylvestre, *Technometrics* **13**, 617 (1971).
16. C.-H. Lin and S.-C. Liu, *J. Chin. Chem. Soc.* **25**, 167 (1978).
17. P. J. Gemperline, *J. Chem. Inf. Comput. Sci.* **24**, 206 (1984).
18. H. Gampp, M. Maeder, C. J. Meyer, and A. D. Zuberbühler, *Talanta* **32**, 1133 (1985).
19. K. J. Schostack and E. R. Malinowski, *Chemometr. Intell. Lab. Syst.* **6**, 21 (1989).
20. H. R. Keller and D. L. Massart, *Anal. Chim. Acta* **246**, 379 (1991).
21. X. Liang, J. E. Andrews, and J. A. de Haseth, *Anal. Chem.* **68**, 378 (1996).
22. W. Windig and J. Guilment, *Anal. Chem.* **63**, 1425 (1991).
23. S. J. Compton and D. A. C. Compton, Quantitative analysis: avoiding common pitfalls, in *Practical Sampling Techniques in Infrared Analysis*, P. B. Coleman, Ed., CRC Press, Boca Raton, FL, 1993, p. 217.



24. P. M. Fredericks, J. B. Lee, P. R. Osborn, and D. A. J. Swinkels, *Appl. Spectrosc.* **39**, 303 (1985).
25. P. M. Fredericks, J. B. Lee, P. R. Osborn, and D. A. J. Swinkels, *Appl. Spectrosc.* **39**, 311 (1985).
26. H. Yang, in *Handbook of Vibrational Spectroscopy*, J. C. Chalmers, P. R. Griffiths, Eds., Wiley, Chichester, West Sussex, England, 2002, Vol. 3, p. 2094.
27. H. Yang, P. R. Griffiths, and J. D. Tate, *Anal. Chim. Acta* **489**, 125 (2003).

# DATA PROCESSING

## 10.1. BASELINE CORRECTION

In an ideal infrared spectrum the baseline is flat, at either 100% in percent transmission or at zero in a spectrum plotted linear in absorbance.<sup>1</sup> In the absence of a sample, 100% lines (the ratio of two empty-cell or background spectra) often approach the ideal (see Figure 8.4). When a sample is introduced, it may alter the baseline from the ideal because of the effects of scattering, reflection, temperature, concentration, or instrument anomalies. Regardless, the baseline may deviate from either 100% transmission or zero absorbance, and either quantification or spectral searching may be compromised. It often falls to the spectroscopist to correct the baselines of spectra and remove these anomalies.

The simplest form of baseline error is an *offset*. For example, the sample may attenuate the spectrometer beam by the same amount at all wavelengths and consequently raise the absorbance of the sample with respect to the background. As all baseline corrections should be done with the spectrum linear in absorbance, so that the offset manifests itself as a baseline error above or below zero absorbance. To correct this offset, a constant (typically, the minimum value in the absorbance spectrum) is subtracted from all spectral data points. This results in a removal of the offset so that the baseline is reset to zero absorbance. Peak absorbance may then be read directly. This procedure is often known as *one-point baseline correction*.

A sloping baseline, one that has a linear slope from one end of the spectrum of the other, can simply be corrected by subtraction of a ramp function from the absorbance spectrum (*two-point baseline correction*). Most spectral software incorporates this correction, and the user simply picks a point on the baseline at one end of the spectrum and a second point at the other end. A linear interpolation is made through the two points, and resulting line is subtracted from the spectrum.

<sup>1</sup>From this point we use the terms *absorbance spectrum* to refer to a spectrum that is plotted linear in absorbance and *transmittance spectrum* to refer to a spectrum that is plotted linear in transmittance or percent transmission. Note that we use the term *transmission spectrum* to refer to a spectrum that is measured in the transmission mode.

Unfortunately, residual baseline anomalies are not often simple offsets or linear slopes, but are more complex functions.

An extension of two-point baseline correction is to correct a nonlinear baseline with a series of linear interpolations. If the slope of the baseline changes slowly, this method can give acceptable results. Several points can be picked along the baseline, and a linear interpolation is made between each pair of points. Each interpolated section is subtracted from the spectrum. If the baseline does not have a slope that changes slowly, a curved or undulating baseline may result. In addition, baseline discontinuities or abrupt changes in relative slope may result. Nonetheless, this is a useful correction if the original baseline only varies slowly.

Nonlinear baseline anomalies are better corrected by subtraction of a nonlinear correction function from the measured spectrum. The generation of this function can easily lead to further anomalies; hence, considerable care must be taken. The general procedure is to fit a polynomial or other higher-order function to the baseline of the original spectrum and subtract the fitted function. If the number of baseline points selected is greater than the order of the polynomial, the fitted functions are often calculated through a least-squares procedure. Polynomial or (more rarely) exponential functions are generally fit to operator-selected spectral data points where the sample is believed to have minimal absorption. Polynomials are usually limited to fifth- or sixth-order functions, as higher-order functions can have extraneous maxima and minima.

It is not unusual for a spectrum to have a large baseline anomaly in the fingerprint region, that is, below  $1500\text{ cm}^{-1}$ . If the sample is relatively highly concentrated, the weak overtone and combination bands that are not usually observable become stronger and overlap, which gives rise to an apparent baseline offset in the fingerprint region even though the baseline at a higher wavenumber may be reasonably flat. The application of a baseline correction procedure in this case is generally inappropriate. If quantitative precision of this region is required (e.g., for spectral subtraction, spectral searching, or quantitative analysis), baseline correction may not improve the spectrum and may even introduce additional errors. If at all possible, the spectrum should be measured with the sample at a lower concentration in an effort to avoid the problem. Regardless, if a high-order function is fit to the spectrum, great care is required so that the fitted function emulates the true baseline as closely as possible.

Manual baseline correction is usually dependent on the operator designating the correct wavelengths as baseline points. Occasionally, incorrect points may be selected, resulting in the loss of real spectral information. For example, if an analyte exhibits hydrogen bonding, broad features are seen in the O–H stretching region ( $3800$  to  $3000\text{ cm}^{-1}$ ) that can be misinterpreted by inexperienced users as a sloping baseline. Care must therefore be exercised for correct baseline correction of any spectrum.

Many automatic baseline correction routines that may be applied without operator intervention are available. These routines may be applied by default for operations such as spectral searching. Automatic baseline functions typically use linear or polynomial baseline fits in regions of the spectrum where no peaks are detected.

In those regions where there are peaks, either a correction function is extrapolated from an adjacent region, or a linear interpolation is made between surrounding baseline-corrected spectral regions. Among the more successful automated baseline correction routines that have been reported are iterative stripping [1], baseline standard deviation [2], ultralow-frequency filtering [3], binning [4], minima method [5], neighborhood comparison [6], derivatives [7], and the background method [8]. In the absence of any operator input, these methods all produce a correction that may be an improvement over the original spectrum, but it is very difficult for these routines to recognize anomalies in the baseline that may be readily recognized by an experienced spectroscopist. Thus, in general, any automatic baseline correction algorithm should be applied with care. This is not to say that reliable automated baseline routines will not be available in the future, and certainly this remains an active area of research [9].

## 10.2. INTERPOLATION

Spectra that have been measured on FT-IR spectrometers consist of a string of intensity values at equally spaced intervals. The discrete nature of the data has two results. First, it is highly unlikely that the maximum absorption of any band will correspond exactly with one of these data points. In addition, the slope of the spectrum can appear to change markedly from one point to the next (see Figure 10.1a). To eliminate these problems, some form of interpolation or alternative data processing is necessary. One of the most useful of these is *zero filling* [10].

Let us consider the complex Fourier transformation of an interferogram that consists of  $N$  data points. (See Section 4.1 for a discussion of complex Fourier transforms.) Current Fourier transform algorithms take the  $N$ -point interferogram as the real data and generate an empty (all zeros)  $N$ -point array for the imaginary data. After the FT has been completed, the real and imaginary spectra each contain  $N$  data points. Thus, each of these spectra contains one data point per resolution element. Although information theory indicates that these spectra contain all the information required to reconstruct the spectrum completely, a trained spectroscopist usually prefers to see at least two data points per resolution element so that adjacent features can be resolved visually. To obtain two data points per resolution element,  $N$  zeros are added to the end of the interferogram, and the empty imaginary data array is also doubled in length. The result of this simple operation is that two data points are computed per resolution element, and the  $N$  new calculated data points have the exact instrument line shape that corresponds to the maximum optical path difference of the interferogram and the apodization function that was applied. The original  $N$  data points are unchanged by this operation. All commercial FT-IR spectrometers perform the Fourier transform in this manner.

The addition of zeros to the end of an interferogram is a simple, accurate form of interpolation in any type of Fourier transform spectrometry. Further levels of interpolation may be achieved by the concatenation of additional zeros to the interferogram prior to the computation of the spectrum. To illustrate the effect of zero

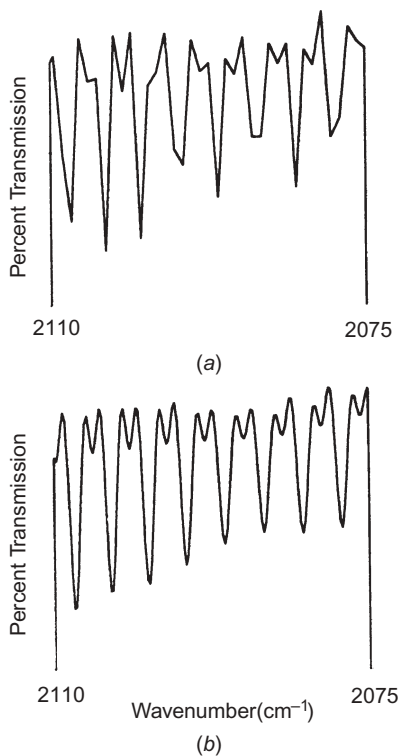


**Figure 10.1.** Unapodized spectra of carbon monoxide from 2110 to 2075  $\text{cm}^{-1}$ , showing the effect of zero filling; spectra were measured at an effective resolution of 2  $\text{cm}^{-1}$  with boxcar truncation: (a) one independent and one interpolated point per resolution element (i.e.,  $N$  zeros were added to the  $N$ -point interferogram); (b) one independent and seven interpolated points per resolution element, or  $3N$  zeros added to the  $N$ -point interferogram. (Reproduced from [10], by permission of the Society for Applied Spectroscopy; copyright © 1975.)

filling, the result of adding three times as many zeros to the end of the interferogram as there were original data points is shown in Figure 10.1b. The same effect could be achieved by computing the FT of the spectrum shown in Figure 10.1a, adding zeros to the end of this array and computing the reverse transform.

Other methods of interpolation are also applied in FT-IR spectrometers. The most common approach is the polynomial spline. For example, in a cubic spline, four neighboring data points are fit to a cubic equation of the form

$$y = ax^3 + bx^2 + cx + d \quad (10.1)$$

This curve is used to represent the spectrum between the two center points in this region. Cubic equations are computed for every four-point region of the spectrum, so that the entire range of interest is covered. This method is used by some manufacturers of FT-IR spectrometers to produce a smooth spectrum on a screen or on

hard copy, in contrast to the rather jagged appearance of the spectrum in Figure 10.1a, where the data are simply linked with a linear interpolation function.

### 10.3. PEAK PICKING

Since FT-IR spectra are often printed out on plain paper, it is very common to print out the wavenumber of each of the more intense peaks in a spectrum either in the form of a table or as values associated with each band. Automated peak picking involves two steps: (1) the recognition of peaks, and (2) the determination of the wavenumber values of maximum absorbance. A threshold absorbance value is usually set so that weak bands are not measured. In many programs, the first derivative of the spectrum is then calculated in those spectral regions where the absorbance exceeds the threshold. The peak location of band(s) in each region can readily be determined from the change of sign of the slope. A similar procedure is used to find the wavenumber values of bands in transmission spectra, except that in this case, the algorithm finds all the minima rather than the maxima. This algorithm is also quite successful at finding band shoulders.

The result that is reported as the peak wavenumber is frequently the wavenumber value of the maximum discrete point, which rarely corresponds to the exact center of the band. It is not uncommon for these values to be reported to four or five decimal places, as this is how well the wavenumber of each datum is recorded; however this number of digits is well beyond the realistic accuracy of most experiments. The use of the maximum data point for the wavenumber position of a band is suitable only for noncritical information. The actual band center may be considerably displaced from the maximum data point. For example, in a typical spectrum measured at  $4\text{-cm}^{-1}$  resolution, data points are typically computed at  $2\text{-cm}^{-1}$  intervals. Under these conditions simple peak-picking algorithms would not readily detect band shifts of about  $\pm 0.5\text{ cm}^{-1}$ . In practice, the wavenumber of the maxima of bands in the spectra of condensed-phase spectra measured at a resolution of 2 or  $4\text{ cm}^{-1}$  should only be reported to  $\pm 1\text{ cm}^{-1}$ .

Actual peak centers may be calculated efficiently by either a center-of-gravity or a least-squares method. In the center-of-gravity method [11], the spectrum in the region where the absorbance  $E(\tilde{\nu})$  of the peak exceeds a certain fraction  $f$  of the maximum peak height is used (see Figure 10.2). The center of gravity in this region,  $\tilde{\nu}_{\text{CG}}$ , is given for a continuous spectrum by

$$\tilde{\nu}_{\text{CG}} = \frac{\int_{\tilde{\nu}_j}^{\tilde{\nu}_k} \tilde{\nu} [E(\tilde{\nu}) - E_f] d\tilde{\nu}}{\int_{\tilde{\nu}_j}^{\tilde{\nu}_k} [E(\tilde{\nu}) - E_f] d\tilde{\nu}} \quad (10.2)$$

where  $\tilde{\nu}_j$  and  $\tilde{\nu}_k$  are wavenumber values at which  $E(\tilde{\nu}) = E_f$ .

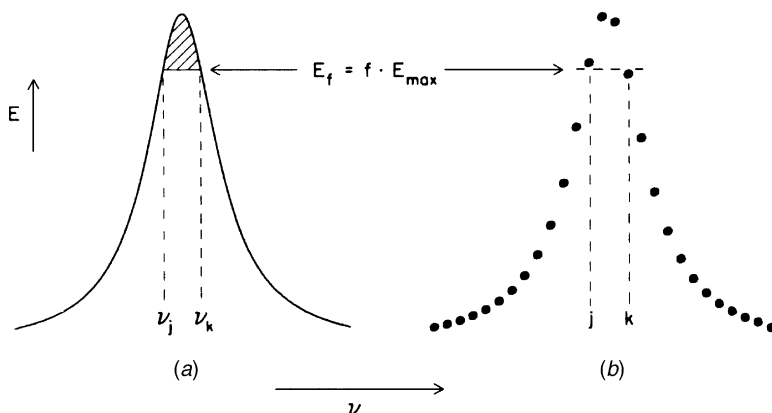


**Figure 10.2.** Center-of-gravity computation data. Fraction of the peak height,  $f$ , for (a) a continuous function, and (b) the same function as (a) digitized at constant-frequency intervals. (Reproduced from [11], by permission of the Society for Applied Spectroscopy; copyright © 1982.)

For a spectrum that is digitized at constant intervals,  $\tilde{\nu}_{\text{CG}}$  can be computed by the following summation:

$$\tilde{\nu}_{\text{CG}} = 0.5 \frac{\sum_{i=j}^k \tilde{\nu}_i (E_i - E_k)}{\sum_{i=j}^k (E_i - E_k)} + \frac{\sum_{i=j}^{k-1} \tilde{\nu}_i (E_i - E_j)}{\sum_{i=j}^{k-1} (E_i - E_j)} \quad (10.3)$$

where  $E_j \geq E_k$ , and  $E_k$  is the value of  $E(\tilde{\nu})$  closest to  $E_f$ . If the peak is symmetric,  $\tilde{\nu}_{\text{CG}}$  will be the wavenumber of the peak maximum. For asymmetric peaks,  $\tilde{\nu}_{\text{CG}}$  will differ from the true peak maximum by an amount that depends upon  $f$  and the degree of asymmetry. The choice of  $f$  is not very critical if the peak is fairly symmetrical. For a symmetrical peak with a full width at half-height (FWHH) value of  $10 \text{ cm}^{-1}$  measured with a SNR of 1000, the maximum uncertainty is less than  $0.01 \text{ cm}^{-1}$  for  $0.2 < f < 0.9$ , as shown in Figure 10.3.

An alternative approach is to fit a polynomial,  $y = f(x)$ , to the top of the peak and then to solve for  $dy/d\tilde{\nu} = 0$  (see Figure 10.4) [12]. Generally, cubic or quartic equations are used since higher-order polynomials rarely lead to increased precision. The first derivative of a cubic of the form

$$y = ax^3 + bx^2 + cx + d$$

is given by

$$\frac{dy}{dx} = 3ax^2 + 2bx + c$$

which is easily solved for  $dy/dx = 0$  (i.e., at the maximum of each band).

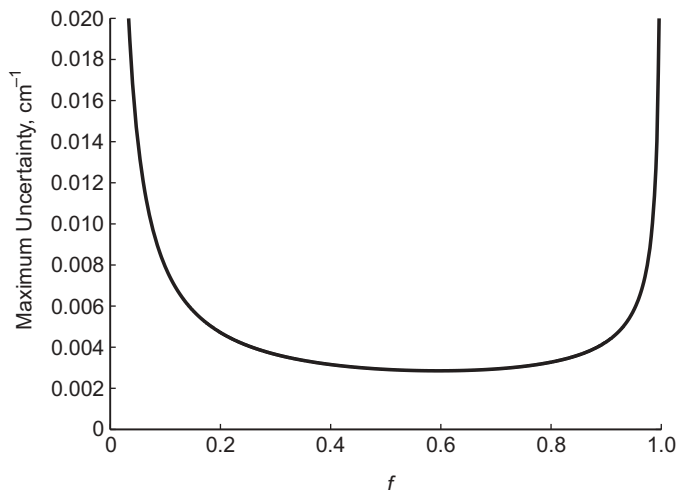


**Figure 10.3.** Maximum uncertainty in the band maximum using the center-of-gravity method versus  $f$  when the band has a FWHH of  $10\text{ cm}^{-1}$  and the SNR is 1000. (Recalculated from equation 17 in [11], by permission of the Society for Applied Spectroscopy; copyright © 1982. It should be noted that the original figure in [11] exhibited a slight error.)

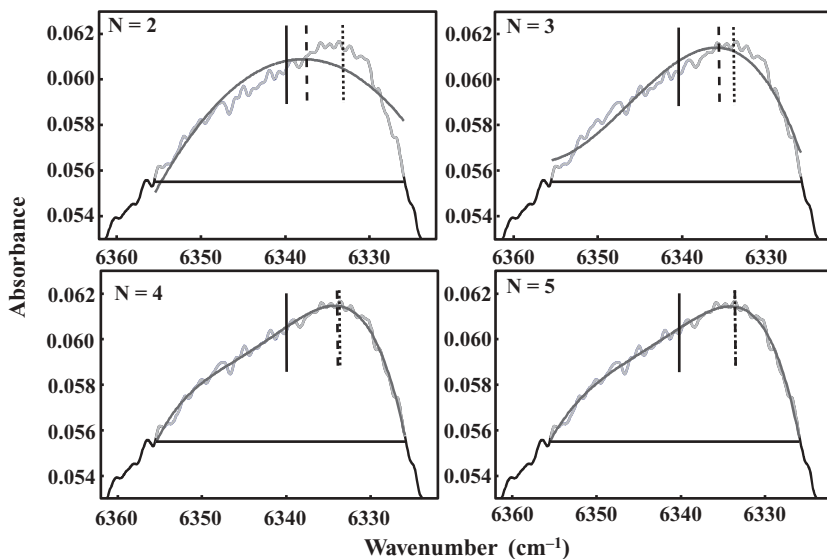


**Figure 10.4.** Result of fitting a broad asymmetric band with polynomials of different orders;  $N = 2$ ,  $N = 3$ ,  $N = 4$ , and  $N = 5$ . The noisy line is the spectrum measured, and the smooth curved line is the polynomial that best fits the data above the horizontal line, which represents 20% of the maximum value. The vertical lines represent the center of gravity (solid line), the maximum of the polynomial (dashed line), and the best estimate of the true band maximum based on the maximum of a fitted fifth order polynomial (dotted line). (Reproduced from [12], by permission of the Society for Applied Spectroscopy; copyright © 2003.)



It can be shown that the two approaches yield very similar values for the band center of symmetrical bands. The principal difference is that in the center-of-gravity approach, all points are weighted equally, whereas in the polynomial approach the weighting of a given point depends on its position relative to the band center. For asymmetrical bands, the two approaches yield slightly different values for the band center.

The accurate determination of bandwidths can also be very important: for example, in biochemical infrared spectrometry or in the study of polymorphs. Although bandwidths are often quoted at half-height, it may often be more informative to make the determination at some other fraction  $f$  of the peak height. The peak height may be defined as  $E_{\max} - E_{\text{ref}}$ , where  $E_{\text{ref}}$  is an arbitrarily selected zero point and  $\tilde{\nu}_{\max} = \tilde{\nu}_{\text{ref}}$ . The fractional width  $\Delta\tilde{\nu}_f$  may be calculated as

$$\Delta\tilde{\nu}_f = \left| \tilde{\nu}_{k-1} + \frac{\Delta\tilde{\nu}[f(E_{\max} - E_{\text{ref}}) - E_{k-1}]}{E_k - E_{k-1}} - \tilde{\nu}_j + \frac{\Delta\tilde{\nu}[f(E_{\max} - E_{\text{ref}}) - E_j]}{E_{j+1} - E_j} \right| \quad (10.4)$$

where  $E_j < f(E_{\max} - E_{\text{ref}}) < E_{j+1}$ , and  $E_k < f(E_{\max} - E_{\text{ref}}) < E_{k-1}$ .

Under carefully controlled conditions, wavenumber measurements may be *precise* to  $\pm 0.01 \text{ cm}^{-1}$  (discussed below), but usually only when a sample is left undisturbed in the sample compartment. Even if the sample is simply removed and reinserted between measurements, the repeatability is often worse than  $\pm 0.01 \text{ cm}^{-1}$ . Several reasons can be advanced to explain why band shifts occur. First, the temperature of the sample may change between measurements, which leads to small spectral shifts. Second, it was noted in Section 2.6 that changes in the effective solid angle of the beam through the interferometer can lead to small wavenumber shifts. Because the cell may represent a field (Jacquinot) stop, if a cell is not placed in exactly the same position for successive measurements, bands will appear to shift from one measurement to the next. Furthermore, if the cell is slightly tilted and the angle changes appreciably from one measurement to the next, the beam may be refracted to a different position on the detector, which also shifts the wavenumber scale. Loose or insecure sample mounts should be avoided if users require the wavenumbers of absorption band maxima to be repeatable to better than  $\pm 0.1 \text{ cm}^{-1}$ .

#### 10.4. SPECTRAL SMOOTHING

It is frequently found that the signal-to-noise ratio (SNR) of a spectrum is less than ideal. The optimal way to improve the SNR is to prepare a better sample or to use a better sampling technique. Alternatively, the spectrum may simply be remeasured by signal averaging a greater number of scans. It may be that these options are impossible or undesirable: for example, because of time constraints. There are data processing procedures that can improve the SNR, but these are applied at

the expense of spectral resolution. No matter how the smoothing routine is applied, the bands will become broader and features may be less resolved.

Many smoothing algorithms were first reported in the era of dispersive spectrometers. For these instruments, the operating parameters were often set so that the period of the noise was much less than the resolution of the spectrometer. Under these circumstances, smoothing could improve spectral quality significantly. This is not the case for FT-IR spectrometry, where the period of the noise is always exactly the same as the resolution. Since resolution is immediately lost on application of any smoothing algorithm in FT-IR spectrometry, it is far more effective to make the measurement at a lower noise level in the first place, even at the cost of decreased resolution or increased time, than to smooth the spectrum after the measurement. In this manner the signal-to-noise ratio may be improved, and no data-processing anomalies may be introduced. Nonetheless, since smoothing algorithms are incorporated in the software of many FT-IR spectrometers, we discuss them in this chapter.

One way to improve the signal-to-noise ratio is through convolution of the spectrum with an appropriate function such as a boxcar, Lorentzian, or Gaussian function. The operation of spectral convolution has been presented in Section 2.3. Such operations tend to distort the spectrum, as the lineshape function is altered. The broader the convolution function, the greater is the distortion of the spectrum. The most common such convolution is the Savitzky–Golay smoothing algorithm [13].

Another method by which spectral SNR improvement may be accomplished is by Fourier smoothing, which, in effect, is a form of apodization. Most condensed-phase infrared spectral bands have a bandshape that is very close to a Lorentzian function (see Section 1.4):

$$A(\tilde{\nu}) = A_{\text{peak}} \frac{\gamma^2}{\gamma^2 + 4(\tilde{\nu} - \tilde{\nu}_0)^2} \quad (10.5)$$

where  $A_{\text{peak}}$  is the maximum absorbance of the band,  $\gamma$  is the full width at half-height (FWHH) for the band, and  $\tilde{\nu}_0$  is the wavenumber of the center of the band. The Fourier transformation of  $A(\tilde{\nu})$  is given by

$$y(x) = \int_{-\infty}^{+\infty} A(\tilde{\nu}) \exp(+2\pi i x \tilde{\nu}) d\tilde{\nu} \quad (10.6)$$

$$= \frac{1}{4} (\gamma A_{\text{peak}}) \exp(-2\pi i \tilde{\nu}_0 |x|) \exp(-\pi \gamma |x|) \quad (10.7)$$

where  $x$  has units of reciprocal wavenumber. Effectively,  $x$  is the same as the optical path difference of an interferogram, but it is frequently referred to as the *spatial frequency* to indicate that its origin is not optical.

Equation 10.7 describes a sinusoidal curve,  $\exp(-2\pi i \tilde{\nu}_0 |x|)$ , that corresponds to a single band at a wavenumber,  $\tilde{\nu}_0$ , that has exponential decay of  $\exp(-\pi \gamma |x|)$ .

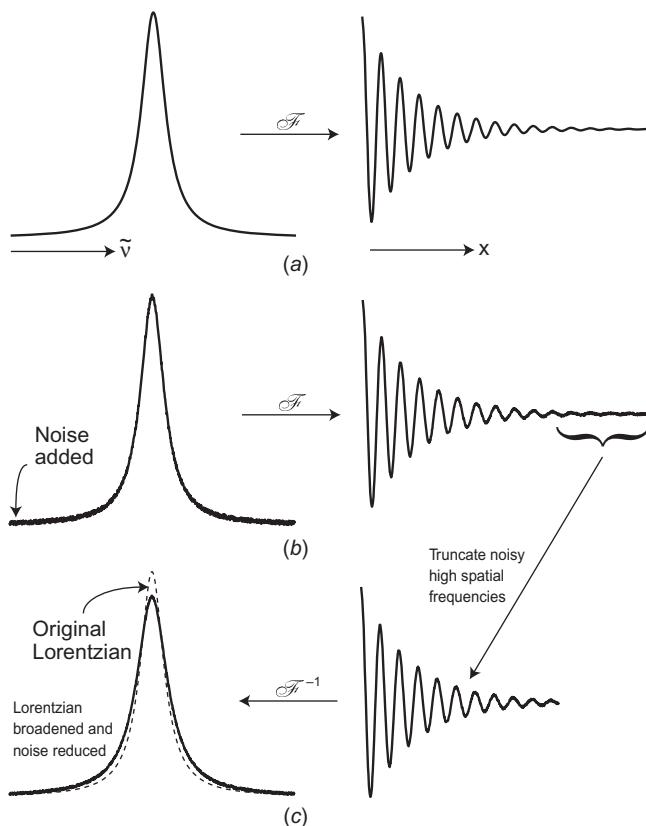


**Figure 10.5.** (a) Lorentzian band and its Fourier transform. (b) Same curves as in (a) but with a small amount of noise added; the noise is particularly recognizable in the region where the Fourier domain signal is low, that is, at the end of the decay function. (c) Result of truncation of the Fourier domain signal to remove the low-SNR region and its transformation back to the spectral domain; the noise on the Lorentzian band has been reduced at the expense of resolution.

A Lorentzian bandshape and its Fourier transform are shown in Figure 10.5a. It should be noticed that the signal decays to near zero as  $x$  increases. Noise, on the other hand, does not have a distinct waveform. Its Fourier transform is still noise. In an interferogram and a single-beam spectrum, the noise is approximately constant across the trace. In a transmittance or absorbance spectrum, the noise appears at all wavenumbers (i.e., on the baseline and on the tops of peaks), although the magnitude of the noise may vary with wavenumber because of the profile of the single-beam spectrum. The noise is most easily measured on the baseline, where the absorbance is zero, as a peak does not mask its effect. When the Fourier transform of a noisy spectrum is examined, the noise is most apparent where the signal is low i.e., at high spatial frequencies where the SNR decreases and noise is clearly discernible, although in fact the root-mean-square noise is constant across the entire array, which

we will call the *Fourier domain signal*. A noisy Lorentzian band and its Fourier transform are illustrated in Figure 10.5b.

Clearly, the SNR of the Fourier domain signal changes as a function of  $x$ . If the Fourier domain signal is truncated so that the low-SNR region is removed and the truncated Fourier domain signal is back-transformed to the spectral domain, the signal-to-noise ratio of the spectrum is better than it was originally, but the spectrum has lost resolution (see Figure 10.5c). This operation is equivalent to a reduction in the resolution at which the spectral data were collected (Section 2.3). Thus, the lineshape of the spectrum will be changed, as  $y(x)$  has simply been truncated, which will broaden the ILS function. The ILS function is modified when an apodization function is applied to the truncated Fourier domain signal, so that the lineshape of the spectrum will be altered further. Instead of simple truncation, the data in the Fourier domain signal can be replaced with zeros in the region where the data were eliminated. The resulting spectrum is still deresolved to the same degree, as if straight truncation were performed, but the data interval is the same as the original spectrum.

In summary, if spectral smoothing is applied to a spectrum, the resolution will suffer and the lineshape will change. The only manner in which these parameters will not be altered is to collect the spectrum and signal average for a larger number of scans, or to redesign the experiment so that the SNR is greater.

## 10.5. BAND FITTING

Spectral features in the infrared spectral region frequently result from the overlap of two or more bands. Thus, spectral features may have asymmetric shapes and possibly shoulders. It may be desirable to resolve all the overlapping features so that an accurate analysis of the spectrum can be completed. One temptation is to attempt to collect the spectrum at higher resolution. As noted in Section 1.4.2, each band in an infrared spectrum has an inherent width, and an increase in the spectrometer resolution does not resolve features once the spectrometer resolution is numerically less than the FWHH of the component bands. The effect of increased spectrometer resolution without a significant increase in measurement time is only to increase the noise in the spectrum.

One way to “resolve” the individual bands is to apply band fitting. This is a procedure whereby the spectroscopist attempts to create a set of bands that together give the same contour as the overlapped feature. To do this, the spectroscopist must make assumptions about the spectrum and the nature of the overlapped peaks [i.e., he or she must decide what shape the bands have, that is, whether they are Lorentzian, Gaussian, Voigt, or another bandshape (see Section 1.4)]. The number of bands must also be estimated. He or she must also provide some estimates for an initial model for the band-fitting procedure. The position, width, and height of each band must be estimated. Once the initial model is constructed, a band-fitting algorithm optimizes the model to best fit the original data. To determine if the model is converging to a best fit, a metric to determine the goodness of fit must be used. One

common procedure is to use the Levenberg–Marquardt method [14]. The  $\chi^2$  (*chi-squared*) metric developed for the Levenberg–Marquardt procedure is a useful measure of the goodness of fit:

$$\chi^2 = \frac{\sum_{i=j}^n [(A_{\text{meas}_i} - A_{\text{calc}_i})/\text{RMSnoise}]^2}{n - j + 1 - f} \quad (10.8)$$

where  $A_{\text{meas}_i}$  are the absorbances at the wavenumbers that correspond to the overlapped band in the measured spectrum,  $A_{\text{calc}_i}$  are the absorbances of the wavenumbers of the calculated sum of all the individual bands in the model, RMS noise is the root-mean-squared noise as estimated from the measured spectrum,  $f$  is the total number of variables from all the bands, and  $j$  and  $n$  are the beginning and ending wavenumber values for the overlapped band, respectively; thus,  $n - j + 1 - f$  corresponds to the number of degrees of freedom. The value  $\chi^2$  indicates whether the calculated model is coming into convergence with the actual spectrum. The value does not indicate the number of bands or whether the model is correct; it simply indicates how well the particular model matches the measured spectrum. A perfect convergence is when  $\chi^2$  is equal to zero.

Band fitting is fraught with problems. Undoubtedly, as the number of bands in the model is increased, the convergence between the measured spectrum and the calculated spectrum becomes better. The temptation is to increase the number of bands until nearly perfect convergence is achieved. In fact, all models may be improved simply by the addition of more bands, *whether or not these bands are real*. In practice, the number of bands present in the overlapped feature should be determined with some certainty before band fitting is used.

The true shape of the bands in the measured spectrum is probably not known, nor are their widths, heights, or center wavenumbers, and changes in the initial parameters may have a significant effect on the final outcome. Consequently, a change in the shapes of the bands in the initial model, or a different selection of starting parameters, may also improve the fit. The bandshape may sometimes be estimated from isolated bands in the spectrum, and bandwidth may also occasionally be estimated from other bands. (However, it should be realized that bandwidths in the infrared spectrum of any molecule may vary by much more than a factor of 2.) Convergence between the measured and calculated spectra does not in any way indicate that a correct model has been found. Therefore, band fitting should be applied only when additional information is present.

Once a model has been calculated from the information available, it should not be accepted at face value but should be validated by assignment of all the calculated bands in the overlapped band. This, of course, is not an easy task and must be undertaken with care to validate the model. Users of band-fitting software should also recognize that their own biases may well be incorporated in their selection of the initial parameters, the number of bands contained within the multiplet that is being modeled, and the assignment of all bands used to fit the multiplet.

**10.6. DERIVATIVES OF SPECTRA**

The resolution of overlapping bands is not limited to band fitting of the type described above. To resolve overlapped bands, mathematical derivatives of bands can be used to narrow their FWHH value. The derivatives of a Lorentzian band are shown in Figure 10.6. As can be seen from the sequence of derivatives, all

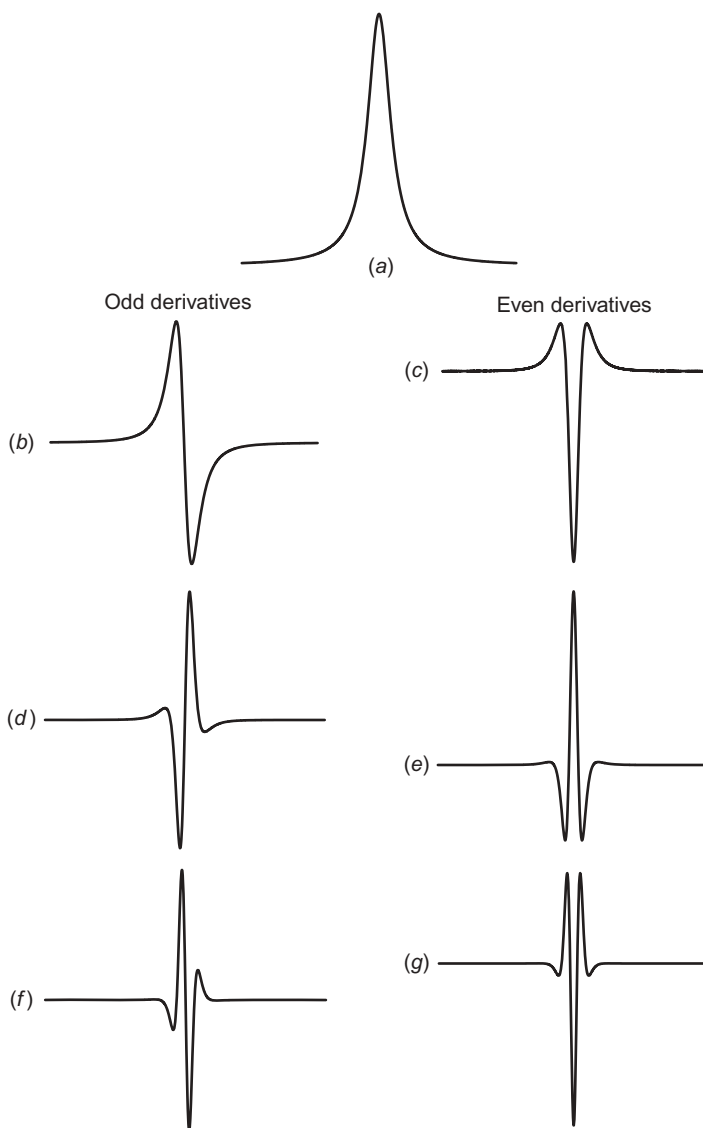


**Figure 10.6.** (a) Lorentzian band. Its odd derivatives (i.e., the first, third, and fifth derivatives) are illustrated in (b), (d), and (f), respectively. The even derivatives (the second, fourth, and sixth derivatives) are illustrated in (c), (e), and (g), respectively.

the odd derivatives have a dispersive character, whereas the even derivatives have a symmetrical bandshape that is more consistent with an absorption process. Some of the even derivatives are negative compared to the original Lorentzian band; this is not a serious problem, however, as the algorithm that computes the derivative can also invert it to make it appear positive. Differentiation is a means by which overlapped bands may be resolved. This may be considered a form of resolution enhancement, as the inherent lineshape for the spectral features is altered to a narrower lineshape, and the effect of band overlap may be less severe. It should be noted, however, that as the order of differentiation increases, the bandshape becomes more complex. Although the main bands have been narrowed, the sidebands may lead to an incorrect interpretation of the spectrum. The unfortunate superimposition of two sidebands from different bands may lead the spectroscopist to believe that a third band was present.

Derivatives of absorbance spectra can be calculated in a number of ways. The simplest manner in which a derivative can be calculated is via a simple successive-difference method. For a series of sequential data, such as a spectrum, the first derivative can be calculated by the subtraction of each datum from the preceding value,  $A_{i-1} - A_i$ . By increasing the gap between the two wavenumbers,  $\tilde{\nu}_{i-1}$  and  $\tilde{\nu}_i$ , and adding successive data points over a segment of the spectrum, the SNR can be increased at the cost of spectral resolution. Although this successive-difference method (sometimes known as the *gap-and-segment method*) is simple in concept, it does introduce some errors into the operation, as it does cause a shift in the peak center, which can be quite severe if the data interval is large. This shift is negated by the calculation of the second derivative by the operation  $2A_i - A_{i-1} - A_{i+1}$ . The Savitzky–Golay algorithm used for spectral smoothing [13] can also be used for differentiation.

Fourier differentiation is another method that is used less often but has the advantage of higher computational speed than the Savitzky–Golay algorithm and greater accuracy than the gap-and-segment method. In this approach the Fourier transform of an absorbance spectrum is multiplied by a function of the form  $ax^n$ ,

$$F(x) = ax^n \quad (10.9)$$

where  $a$  is a constant, typically  $\pi$ , and  $n$  is a positive integer. Forward computation of the product of Eq. 10.9 and the Fourier transform of an absorbance spectrum yields the  $n$ th derivative of the spectrum. Fourier transformation is a complex operation (Sections 4.1 and 4.3) and the odd-order derivatives will appear in the imaginary portion of the complex transformation array. Even-order derivatives will appear in the real portion of the array.

The functions from Eq. 10.9 increase in magnitude with spatial frequency; hence, the product of the differentiating function and the Fourier domain signal will cause the high-spatial-frequency regions to be emphasized. This will lead to degradation in the signal-to-noise ratio of the derivative spectrum (as do the techniques described above). Consequently, the noise in a spectrum will undergo differentiation along with the spectral features. As a result, the spectrum will decrease in

SNR as higher-order derivatives are calculated. A general rule of thumb is that for every successive even derivative, the signal-to-noise ratio decreases by an order of magnitude. Thus, if an original spectrum has a signal-to-noise ratio of 10,000 : 1, its sixth derivative spectrum will have a signal-to-noise ratio of only 10 : 1, unless some type of smoothing (apodization) is applied. Before derivatives are employed, therefore, the SNR of the spectrum must be high.

An illustration of the procedure to compute a second derivative of a spectrum is shown in Figure 10.7. A single Lorentzian band is transformed to the Fourier domain, where the signal is multiplied by a parabolic function. Upon transformation back to the spectral domain, the second derivative spectrum is shown. The FWHH of the second derivative band is approximately 2.5 times smaller than that of the original spectrum. Examples of second derivatives of protein spectra are shown in Figure 10.8.

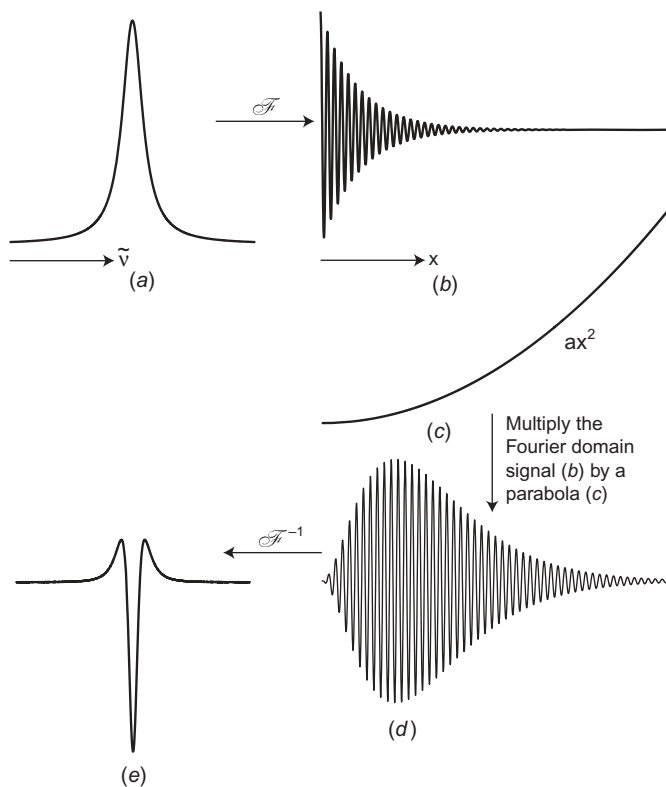


**Figure 10.7.** Fourier differentiation to produce a second derivative spectrum. A Lorentzian band (a) is transformed to the Fourier domain (b). The Fourier domain signal in (b) is multiplied by a parabolic function (c) to yield (d). Inverse Fourier transformation of (d) leads to the second derivative of the original Lorentzian band (e).



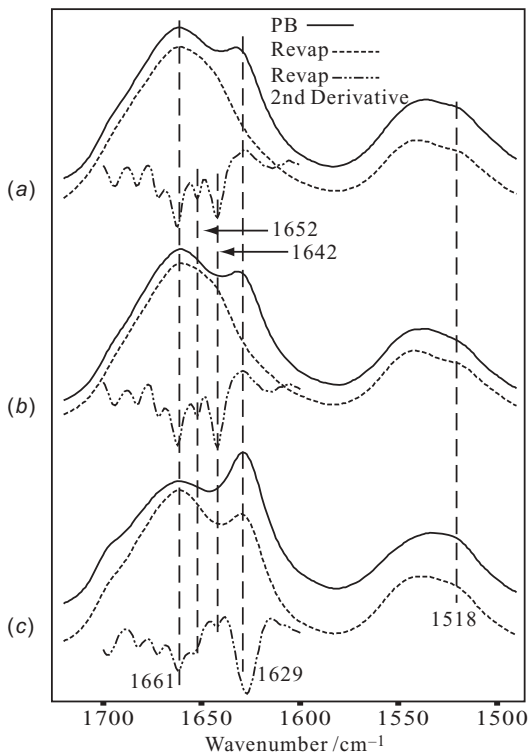


**Figure 10.8.** Second derivative spectra of Rnase A in different conformational states: (a) 0.1% TFA; (b) 8 M urea; (c) 8 M urea plus 2-mercaptoethanol. The spectra were produced with a particle beam (PB) interface, and the protein deposits were solvated and re-evaporated (Revap) to show conformational changes. (Reproduced from [15], by permission of the American Chemical Society; copyright © 1996.)

## 10.7. FOURIER SELF-DECONVOLUTION

The width of spectral bands may also be narrowed mathematically with a procedure known as *Fourier self-deconvolution* (FSD) [16–19]. This is considered a deconvolution method, as the inherent lineshape function of each band in the spectrum is altered and the peaks become narrower. The shape of a band in an absorbance spectrum may be considered to be the convolution of an infinitely narrow line (Dirac delta function) and the broadening function. The goal of FSD is to reduce the width of this broadening function without affecting the position or area of the band. To understand this procedure, one must review Eqs. 10.5 and 10.7 for a Lorentzian band and its Fourier transform. Equation 10.7 is composed of three parts: a magnitude part  $\frac{1}{4}\gamma A_{\text{peak}}$ , a sinusoidal component  $\exp(-2\pi i \tilde{\nu}_0 |x|)$ , and a decay function  $\exp(-\pi\gamma|x|)$ . The decay function contains  $\gamma$ , the FWHH. Therefore, in the Fourier domain, the rate of decay of function determines the FWHH of the band in the spectral domain. This is illustrated in Figure 10.9, which shows two Lorentzian functions, one with a large FWHH and the other with a narrow FWHH. As can be seen

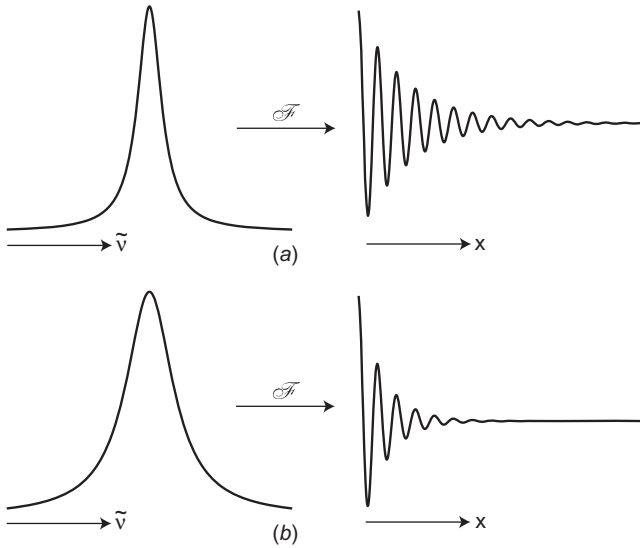


**Figure 10.9.** Difference in Fourier domain signals for a narrow Lorentzian band (a) and a broader Lorentzian band (b).

from their Fourier transforms, the curve with the larger FWHH has a faster decay than the narrower band. The only difference between the Fourier transforms of the two Lorentzian bands is the rate of decay of the sinusoids. It is mathematically possible to change one curve into the other simply by altering the decay function.

The simplest operation that can be undertaken is to remove the decay in its entirety. This is done by multiplying the Fourier domain signal by an exponential function that cancels the decay [i.e.,  $\exp(+\pi\gamma|x|)$ ], as

$$\exp(-\pi\gamma|x|)\exp(+\pi\gamma|x|) = e^0 = 1 \quad (10.10)$$

This will result in a cancellation of the decay, and the Fourier domain signal becomes a pure truncated cosine wave, as shown in Figure 10.10.<sup>2</sup> The Fourier transform of a pure truncated cosine wave is a sinc function, as shown in Section 2.3. The sinc function has a narrower FWHH than almost any other spectral waveform; however, it does have large sidelobes. Of course, these could be removed with apodization (Section 2.4), but it is usually easier to change the rate of decay in Eq. 10.7. If the Fourier domain array is multiplied by an exponential function with a different FWHH,  $\gamma'$  such that  $\gamma' < \gamma$ , that is,

$$f(x) = \exp(+\pi\gamma'|x|) \quad (10.11)$$

then the result of transformation back to the spectral domain will be a band with a reduced width. As  $\gamma'$  is less than  $\gamma$ , the decay on the sinusoidal signal is equivalent

<sup>2</sup>Implicit in the practice is the assumption that the FWHH of the band can be estimated accurately.

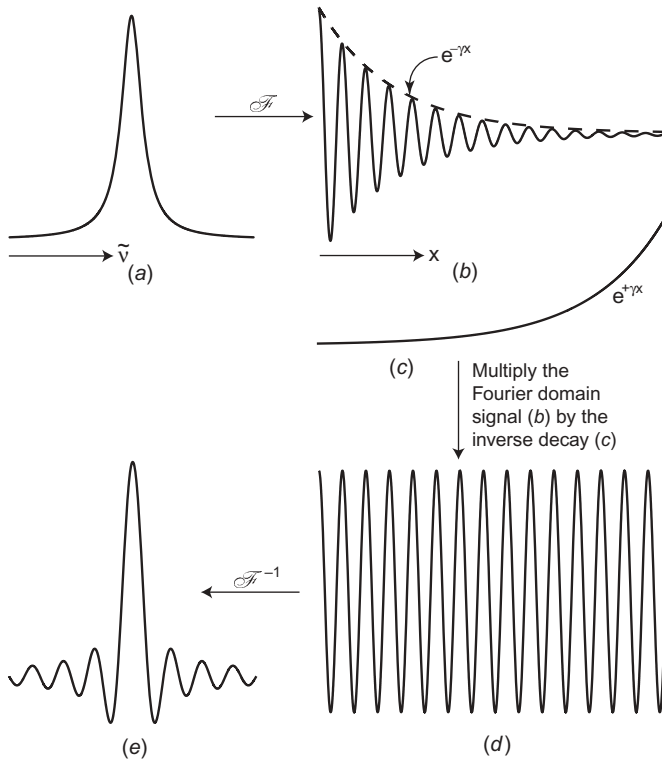


**Figure 10.10.** Full Fourier self-deconvolution of a Lorentzian band. The Lorentzian band (a) undergoes Fourier transformation to yield the Fourier domain signal (b), which has a decay,  $\exp(-\gamma x)$ . The signal in (b) is multiplied by the inverse exponential decay (c),  $\exp(+\gamma x)$ , to produce a truncated cosine wave (d). Upon inverse Fourier transformation of (d) a sinc waveform is produced (e). The sinc waveform has a narrower FWHH than that of the original Lorentzian band.

to an apodization function of the form

$$A(x) = \exp[-\pi(\gamma - \gamma')|x|] \quad (10.12)$$

This operation is illustrated in Figure 10.11. The FWHH of the band has been reduced to  $(\gamma - \gamma')$  and minimal sidelobes are seen. Furthermore, when the spectrum is recovered with an inverse Fourier transform, the bandshapes are still approximately Lorentzian, provided that  $(\gamma - \gamma') > \Delta\tilde{\nu}$ .

The functions used to change the decay functions in FSD increase the noise level faster than do the polynomial functions used for spectral derivatives because exponential functions tend to increase more rapidly at high spatial frequencies than polynomials. As a consequence, the effect on the data at high spatial frequencies in the Fourier domain signal (the region where the SNR is the lowest) is most severe. The general rule is that as the FWHH is narrowed by a factor of 2, the SNR of the spectrum decreases by an order of magnitude. In practice, the

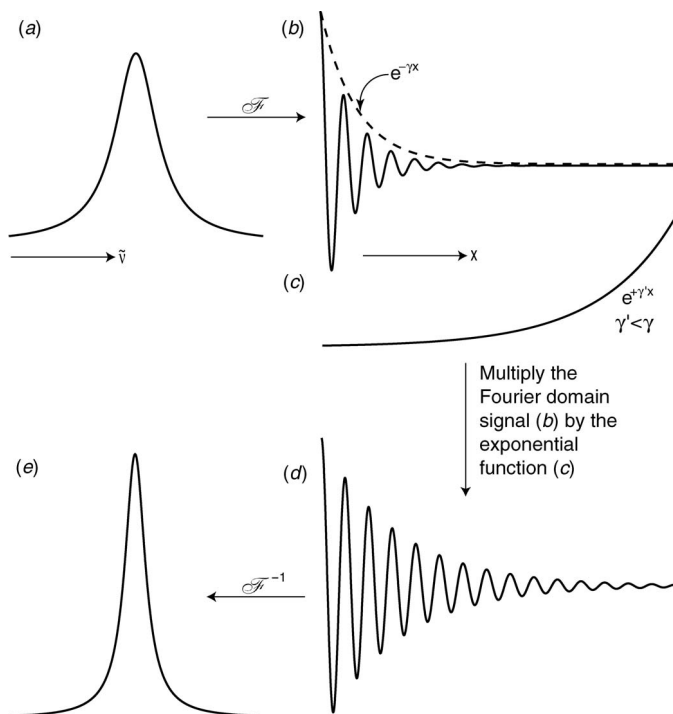


**Figure 10.11.** Fourier self-deconvolution can be applied simply to reduce the FWHH of a band and still largely retain the lineshape. A Lorentzian band (a) has a Fourier domain signal (b) with a decay,  $\exp(-\gamma x)$ . The signal in (b) can be multiplied by an exponential function (c),  $\exp(+\gamma' x)$ , where  $\gamma' < \gamma$ . The product, (d), still retains a decay function, but a weaker decay than in the original Fourier domain signal. The inverse Fourier transformation of (d) is a Lorentzian band (e) of smaller FWHH than that of the original band.

FWHH may often be reduced by as much as a factor of 2 without introducing excessive noise or sidelobes, although many software packages will lead the spectroscopist to believe that great reductions in FWHH are possible. An example of FSD for decreasing the widths in the spectrum of a high-rank coal is shown in Figure 10.12.

A problem that arises with this procedure is that the spectrum may easily be *over-deconvolved*, but the spectroscopist does not recognize this condition. Over-deconvolution occurs when the line has been narrowed to the point that the lineshape takes on distinct characteristics of a sinc lineshape; that is, it develops sidelobes. If sidelobes from two adjacent peaks are superimposed, a new “peak” appears in the spectrum. Thus, a simple doublet can easily be rendered into a multiplet. To prevent this, smoothing should be turned off and a section of the baseline around the band to be deconvolved should be monitored. FSD is an interactive operation on modern computing systems, so the bands can be seen to narrow in real time as  $\gamma'$

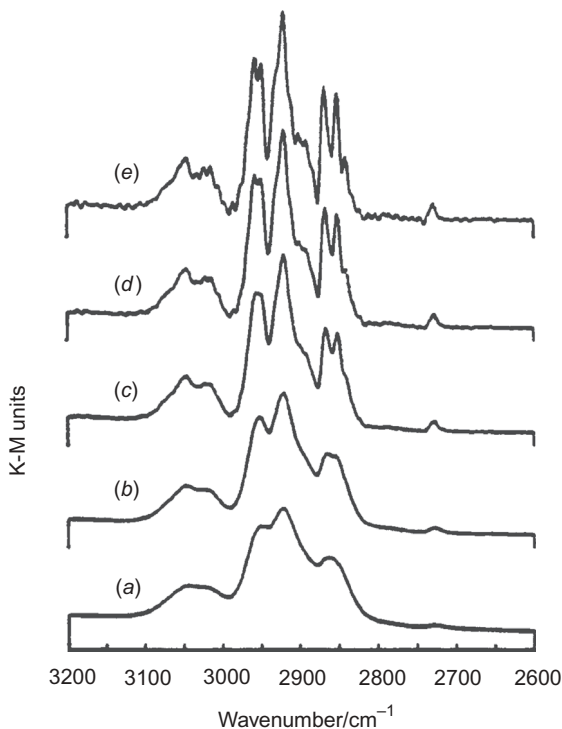


**Figure 10.12.** Series of progressively deconvolved diffuse reflection spectra of high-volatile bituminous coal: (a) original spectrum; (b)–(e) spectra calculated by multiplying the FT of (a) by  $\exp(+\gamma'x)$  and computing the inverse Fourier transformation. Values of  $\gamma'$  were (b) 5, (c) 7.5, (d) 11.5, and (e)  $12.5 \text{ cm}^{-1}$ . (Reproduced from [20], by permission of Elsevier Scientific Publishing; copyright © 1985.)

is changed. When the baseline begins to develop sidelobes, the operation should be halted and the deconvolution factor reduced so that the sidelobes disappear. At that point the band is optimally deconvolved.

Over-deconvolution has another insidious effect when the spectrum is being smoothed simultaneously. When spectra are over-deconvolved, the sidelobes that appear may be smoothed to the point that they are often manifested as apparent shoulders on real bands. The effect of over-deconvolution is that many bands seem to have been resolved. One way of checking for this occurrence is to measure the wavenumber difference between successive shoulders. If this difference is constant, it is more likely than not that the “shoulders” are due to sidelobes and the deconvolution has been performed incorrectly.

It is common practice in commercial software to incorporate more than one operation into FSD methods. As the SNR decreases so dramatically with a reduction in the FWHH, it is common to add Fourier smoothing (or what is sometimes called *filtering*) to the method. Here an additional apodization function is applied at

the same time as the decay function is being altered. A common smoothing function for this operation is a Bessel function,  $J(x)$ ,

$$J(x) = \left[ 1 - \left( \frac{x}{\Delta} \right)^2 \right]^2 \quad (10.13)$$

where  $\Delta$  is the maximum retardation. The FWHH is narrowed more by the exponential function than it is broadened by the smoothing function.

One shortcoming of FSD is that the altered FWHH affects all the component bands of an overlapped feature differently if their individual FWHHs are different. The value  $(\gamma - \gamma')$  from Eq. 10.12 will differ for each component peak if their respective widths are not identical. Thus, it is possible that narrow component bands will be over-deconvolved so that sidelobes are seen in the spectrum, whereas the widths of other bands will scarcely be altered. For this reason many workers prefer spectral derivatives, as the FWHH is adjusted individually; that is, there is no dependence on width with spectral derivatives. Although differentiation has this advantage over FSD, it should be noted that derivatives may be used to correct slowly varying baselines while FSD retains the baseline. Consequently, very broad bands may be eliminated when the derivative of the spectrum is calculated and will be narrowed minimally only with FSD.

Despite some of the problems associated with FSD and spectral derivatives, both techniques are powerful and useful tools if applied judiciously. With care, highly overlapped bands can be resolved into a reasonable number of component bands. The assignment of each new band should be validated through careful spectral interpretation. Even so, it may be an easy matter for a spectroscopist to carry out FSD under conditions that happen to yield the number of bands that he or she is looking for! In other words, as in the case for curve fitting, operator bias can have a significant effect on the results of FSD.

Provided that  $(\gamma - \gamma') > \Delta\tilde{\nu}$ , where  $\Delta\tilde{\nu}$  is the resolution at which the spectrum has been measured, the bandshape will still be Lorentzian and curve fitting can still be performed on the deconvolved spectrum. By narrowing each band in the spectrum that is being curve-fit, the number of peaks can be determined more reliably, and additional parameters, such as estimated peak position and relative intensity, can be supplied to the band-fitting model [21]. This will make band fitting more reliable.

Finally, it should be noted that the first term in the expression for the Fourier transform of a Lorentzian band (Eq. 10.7) is  $\frac{1}{4}\gamma A_{\text{peak}}$ , which is directly proportional to the area of the band. This term is unaffected by either multiplication of the Fourier domain array by an exponentially increasing function or by an apodization function. Thus, the area of each band in the spectrum is unaffected by FSD. Provided that  $(\gamma - \gamma') > \Delta\tilde{\nu}$  (i.e., provided that the bands are still Lorentzian), the peak height of each band is increased to  $A_{\text{peak}}\gamma/(\gamma - \gamma')$ , and their FWHH is reduced from  $\gamma$  to  $(\gamma - \gamma')$ .

There are many other mathematical methods that can be applied to spectra, such as algorithms that remove peaks (useful for the removal of CO<sub>2</sub> bands), algorithms that add bands to a spectrum, and other deconvolution algorithms. For example,

several workers have described ways in which the width of lines that are narrower than  $\Delta\tilde{\nu}$  may be narrowed still further; these have been reviewed by Kauppinen et al. [22]. An exhaustive list is beyond the scope of this book, but the spectroscopist should be aware that all these methods may easily be abused, as well as applied for great benefit. It is strongly suggested that these methods be applied carefully and the results verified.

## 10.8. SPECTRAL SEARCHING

One great advantage with digitized spectra is the capability to perform comparisons between the spectra of unknowns and reference spectra in a library. Infrared spectra are largely, but not completely, immune to collection conditions, that is, most spectral collection techniques (e.g., transmission, attenuated total reflection, diffuse reflection, photoacoustic spectrometry) will all produce *approximately* equivalent (but not identical) spectra if appropriate care is taken. Of course, some methods will be more successful than others for some samples or sample matrices, and those effects must be taken into account. Sample conditions are also important. Spectra can change with temperature, solvent, or crystallinity, for example, and as the samples change their physical states, the infrared spectra will reflect those changes.

Spectral searching did not begin in earnest until the late 1970s, when computing power was becoming available in the laboratory. At that time full spectral searches were initiated by compressing the entire spectrum into a small series of data points and performing a Euclidean distance comparison with the unknown and similarly compressed spectra in a library [23,24]. This was a radical departure from previous methods. The Euclidean distance method coded the entire spectrum into a vector and compared all the peak positions and their relative intensities simultaneously. This meant that only a single pass of the database had to be made, and the direct comparison method was a simple algorithm that required very little computational time.

The Euclidean distance,  $E_d$ , is simply calculated as

$$E_d = \sqrt{\sum (x_i - r_i)^2} \quad (10.14)$$

where  $x_i$  is the spectral intensity at the  $i$ th dimension (wavenumber) in the sample spectrum and  $r_i$  is the corresponding value from the library spectrum. Both spectra must be normalized before the Euclidean distance is calculated; otherwise, the results will be skewed by the relative concentrations of the samples. Normalization reduces a spectrum to unit vector length, that is, the length of the spectrum in multi-dimensional space is unity. One spectral search program gives a percent similarity value as the sum of the squares of the differences:

$$M_{SQ} = \left(1 - \frac{N}{D}\right) \times 100 \quad (10.15)$$

where  $N = \sum |x_i - r_i|^2$  and  $D = \sum (x_i)^2$ . Since the squared values often strongly weight differences in the intense bands relative to the smaller ones, the sum of the absolute differences,  $M_{AB}$ , may give better results.

$$M_{AB} = \left(1 - \frac{N}{D}\right) \times 100 \quad (10.16)$$

In this case,  $N = \sum |x_i - r_i|$  and  $D = \sum |x_i|$ .

All search algorithms have a goodness-of-fit or *hit quality index* metric to indicate which spectrum is the best match. In a true Euclidean distance metric, where the spectra are normalized to unity, the metric will report a value between zero and 1, where the value of zero represents a perfect match. Commercial software will often scale or adjust this number. For example, if the Euclidean distance is subtracted from 1 and the result multiplied by 1000, a perfect match gives rise to a hit quality index of 1000, and a complete mismatch gives a score of zero. Regardless, the algorithm to compare the spectra is virtually identical; only the way the results are reported varies.

In earlier versions of Euclidean distance searches, the spectra were compressed by normalizing to a constant maximum absorbance and setting the absorbance data to an 8-bit precision; that is, the absorbance was known to 1 part in 256. The entire spectrum was reduced in resolution to about  $16 \text{ cm}^{-1}$ . Finally, the region of the spectrum from about  $2800$  to  $1800 \text{ cm}^{-1}$  was also eliminated, as very few fundamental absorption bands occur in that region. All these modifications to the spectra meant that the spectra were greatly smoothed and less susceptible to noise than full-resolution spectra.

Since the 1980s, computers have improved remarkably, and some of the original constraints are no longer in place. The compression of spectra is no longer undertaken, as computer storage, memory, and speed have increased to the point that such savings are not necessary. Absorbances are now coded to 32-bit precision, and no region of the spectrum is removed; however, it is generally prudent to remove spectral features from atmospheric contaminants, most notably  $\text{CO}_2$ . The resolution of library spectra is higher than it was originally and is often  $4 \text{ cm}^{-1}$ . The signal-to-noise ratio of collected spectra has steadily increased and smoothing is no longer as necessary as before. The basic algorithms have not changed appreciably over the past 20 years, although several refinements have been incorporated.

The Euclidean distance algorithm relies on the total integrated intensity of the spectrum, and if band intensities in one region of the spectrum are much higher than in the rest of the spectrum, the results will be biased by reference spectra that have high absorbance values in that region. As search systems evolved, additional corrections and features were added. Tests were performed to determine if there were baseline offsets or tilt, and if so, automatic baseline correction was applied. These baseline corrections were not expected to produce good baseline correction, but rather consistent results were the goal.



When the baseline is not at zero, it may be better to use the first derivative spectrum rather than the absorbance spectrum as measured. An equation similar to Eq. 10.15 or 10.16 may again be used as the search metric, but in this case,  $N = \sum (y_i - s_i)^2$  and  $D = \sum (y_i)^2$ , where  $y_i = x_i - x_{i+1}$  and where  $s_i = r_i - r_{i+1}$ . The derivative algorithm essentially functions to correct baseline offset or tilt. An offset is reduced to zero, and a tilt is reduced to a constant when a first derivative of a spectrum is calculated. If the baseline is curved, the derivative algorithm tends not to perform as well as the standard Euclidean distance algorithm. In the case of mixtures, however, the derivative system is better than a direct Euclidean distance as a major component of the mixture can often be identified more frequently. If it is necessary to distinguish between very similar spectra, the derivative algorithm does not produce good results.

Another common modification of the original Euclidean distance algorithm is what is referred to as a *correlation algorithm*, a term that actually refers to several different methods of spectral comparison. The first algorithm involves mean centering; that is, both the unknown and library spectra are measured from their respective means; this algorithm is relatively insensitive to baseline offsets. The second correlation algorithm breaks the first derivative of the spectrum into several discrete regions and performs a separate Euclidean distance measure on each region of the unknown spectrum and corresponding regions of the library spectra. The results of all the regions are averaged to yield a final result. Another correlation algorithm has been used on derivative spectra of the type that are commonly used in near-infrared spectroscopy:

$$M_{CR} = \frac{N}{D} \times 100 \quad (10.17)$$

where  $N = \sum (y_i \times s_i) \times \sum (y_i \times s_i)$  and  $D = \sum (y_i \times y_i) \times \sum (s_i \times s_i)$ , where  $y_i = x_i - x_{i+1}$  and  $s_i = r_i - r_{i+1}$ . In the correlation algorithm developed by Galactic Industries (now part of Thermo Electron's Informatics Division) in their GRAMS/32 AI package, each spectrum is mean-centered before the vector dot product is calculated. The HQI is calculated as

$$HQI = 1 - \frac{(\text{Lib}_m \times \text{Unkn}_m)^2}{(\text{Lib}_m \times \text{Lib}_m)(\text{Unkn}_m \times \text{Unkn}_m)} \quad (10.18)$$

The vectors used in the correlation algorithm are defined as follows:

$$\begin{aligned} \text{Lib}_m &= \text{Lib} - \frac{\sum_{i=1}^n \text{Lib}_i}{n} \\ \text{Unkn}_m &= \text{Unkn} - \frac{\sum_{i=1}^n \text{Unkn}_i}{n} \end{aligned} \quad (10.19)$$

Hit quality indices calculated in this way are independent of the normalization of the spectra, preventing the baseline of a noisy spectrum from being shifted by negative spikes caused either by noise or (for Raman spectra) a cosmic ray event.

Search systems are powerful tools, but as for most algorithms described in this chapter, care must be taken when they are used. The “unknown” and the library spectra must both obey Beer’s law. Care must be taken that the wavenumber calibration of an instrument is correct as wavenumber shifts may occur between the unknown and the library spectra. The algorithms compensate for spectral shifts to some degree, but they cannot compensate for large shifts. In addition, the spectroscopist must remember two important caveats: (1) a library search cannot identify an unknown unless the unknown is in the library; and (2) a high value of the hit quality index is not necessarily an indication of a correct match. The judicious spectroscopist will visually compare the spectra of the unknown to the best matches to determine if they are indeed identical. In fact, the best test is to perform a spectral subtraction between the unknown and the library match to see if there is a nonzero residual. If the two spectra are not identical, a nonzero subtraction will result. Finally, *it should be recognized that spectral similarity does not indicate structural similarity*. Certainly, some of the functional groups in structurally similar molecules will be the same, but the overall structure of an unknown and the best matches that result from a search may be quite different.

## REFERENCES

1. J. Liu and J. L. Koenig, *Appl. Spectrosc.* **41**, 447 (1987).
2. G. A. Pearson, *J. Magn. Reson.* **27**, 265 (1977).
3. A. K. Atakan, W. Blass, and D. Jennings, *Appl. Spectrosc.* **34**, 369 (1980).
4. J. D. Jegla, R. L. Richardson, and P. R. Griffiths, An automated baseline correction algorithm for high- and low-resolution open-path FT-IR measurements, in *Optical Remote Sensing for Environmental and Process Monitoring*, Society of Photo-Optical Instrumentation Engineers, Bellingham, WA, 1996, Vol. 2883, p. 323.
5. I. Gornushkin, P. Eagan, A. Novikov, B. Smith, and J. Winefordner, *Appl. Spectrosc.* **57**, 197 (2003).
6. E. J. Sonneveld and J. W. Visser, *J. Appl. Crystallogr.* **8**, 1 (1975).
7. C. D. Brown, L. Vega-Montoto, and P. D. Wentzell, *Appl. Spectrosc.* **54**, 1055 (2000).
8. R. P. Goehner, *Anal. Chem.* **50**, 1223 (1978).
9. G. Schulze, A. Jirasek, M. M. L. Yu, A. Lim, R. F. B. Turner, and M. W. Blades, *Appl. Spectrosc.* **59**, 545 (2005).
10. P. R. Griffiths, *Appl. Spectrosc.* **29**, 11 (1975).
11. D. G. Cameron, J. K. Kauppinen, D. J. Moffatt, and H. H. Mantsch, *Appl. Spectrosc.* **36**, 245 (1982).
12. T. Isaksson, H. Yang, G. J. Kemeny, R. S. Jackson, Q. Wang, M. K. Alam, and P. R. Griffiths, *Appl. Spectrosc.* **57**, 176 (2003).
13. A. Savitsky and M. J. E. Golay, *Anal. Chem.* **36**, 1627 (1964).
14. D. W. Marquardt, *J. Soc. Ind. Appl. Math.* **11**, 431 (1963).

15. R. T. Bishop, V. E. Turula, and J. A. de Haseth, *Anal. Chem.* **68**, 4006 (1996).
16. H. Stone, *J. Opt. Soc. Am.* **52**, 998 (1962).
17. J. K. Kauppinen, D. Moffatt, D. G. Cameron, and H. H. Mantsch, *Appl. Opt.* **20**, 1866 (1981).
18. J. K. Kauppinen, D. Moffatt, H. H. Mantsch, and D. G. Cameron, *Anal. Chem.* **53**, 1454 (1981).
19. J. K. Kauppinen, D. J. Moffatt, D. G. Cameron, and H. H. Mantsch, *Appl. Opt.* **20**, 1866 (1981).
20. S. H. Wang and P. R. Griffiths, *Fuel* **64**, 229 (1985).
21. J. Pierce, R. Jackson, K. Van Every, P. R. Griffiths, and H. Gao, *Anal. Chem.* **62**, 477 (1990).
22. J. Kauppinen, D. Moffatt, H. Mantsch, and D. Cameron, *Appl. Spectrosc.* **35**, 271 (1981).
23. L. V. Azarraga and D. A. Hanna, *GIFTS: Athens ERL GC/FT-IR Software and Users' Guide*, Athens, GA.
24. A. Hanna, J. C. Marshall, and T. L. Isenhour, *J. Chromatogr. Sci.* **17**, 434 (1979).

## Chapter 11

# CONVENTIONAL TRANSMISSION SPECTROMETRY

### 11.1. CONDENSED-PHASE SAMPLES

#### 11.1.1. Window Materials

Most samples to be investigated by mid-infrared spectrometry, except polymer films and KBr pellets, must be held between two windows. Glass cannot be used as a window material in the mid-infrared, and salt plates are used instead. The two most important properties of the materials that are used for infrared spectrometry are the cutoff and the refractive index; these parameters are listed in Table 11.1.

#### 11.1.2. Band Intensities

The absorptivities of fundamental bands in the condensed-phase spectra of most samples vary by well over an order of magnitude, but the strongest band in the spectra of typical neat liquids or solids usually has an absorbance of between about 0.5 and 2 AU if the thickness of the sample is  $\sim 10\text{ }\mu\text{m}$ . This is only a rule of thumb, however. The absorptivity of strong bands in the spectra of polar analyte is almost invariably greater than that of the stronger bands in the spectra of nonpolar analytes. For example, the four strongest bands in the spectrum of a  $5\text{-}\mu\text{m}$  film of poly(ethylene terephthalate) are more intense than the strongest band in the spectrum of a  $20\text{-}\mu\text{m}$  film of polystyrene.

A convenient way of sampling viscous liquids is simply to place a drop on a salt plate and then place another salt plate on top of it. The film will spread between the windows into a film that is between 10 and  $20\text{ }\mu\text{m}$  in thickness and the windows will be held together by capillarity. Several vendors sell holders for samples of this type that fit in the sample mount of the spectrometer.

**Table 11.1. Optical, Mechanical, and Thermal Properties of Selected Infrared-Transparent Materials**

Material	Cutoff (cm <sup>-1</sup> )	Refractive Index <sup>a</sup>	Yield Strength (atm)	Highest Operating Temperature (°C)	Hardness (kg.mm <sup>-2</sup> )
Alkali halides					
NaCl	584	1.49 (10 μm)	0.05	400	18
KCl	439	1.45 (10 μm)	0.05	400	7
KBr	388	1.52 (10 μm)	0.02	300	7
CsI	172	1.73 (10 μm)	0.12	200	20
Fluorides					
LiF	1286	1.39 (5 μm)	0.23	400	105
CaF <sub>2</sub>	1025	1.40 (5 μm)	0.77	600	158
BaF <sub>2</sub>	782	1.45 (5 μm)	0.56	500	82
Heavy metal halides					
AgCl	404	1.90 (10 μm)	0.56	200	10
AgBr	292	2.22 (10 μm)	0.56	200	7
TlBr <sub>0.42</sub> I <sub>0.58</sub>	232	2.37 (10 μm)	0.56	200	40
Chalcogenides					
ZnS	722	2.25 (10 μm)	1.5	300	240
ZnSe	508	2.40 (10 μm)	1.2	300	120
CdTe	340	2.67 (10 μm)	0.12	300	45
AMTIR	625	2.50 (10 μm)	0.27	300	170
Miscellaneous					
Diamond	<2	2.41 (0.6 μm)	10.9	>700	5700
Si	969	3.41 (10 μm)	1.8	300	1150
Ge	574	4.00 (10 μm)	1.0	100	780
Sapphire	1834	1.76 (10 μm)	6.1	1700	1370
Quartz	2677	1.53 (1 μm)	4.2	>1200	460

Source: [1].

<sup>a</sup>The number in parentheses refers to the wavelength at which the refractive index was measured.

In Table 11.1, the cutoff is the wavenumber for which the percent transmission is 50% when the thickness of the window is 4 mm. The yield strength,  $P_e$ , is for a window 25 mm in diameter and 1 mm thick window with a safety factor of 4. To calculate the thickness,  $T$ , required for a given window diameter,  $D$ , subjected to a pressure,  $P$ , the following formula should be used:

$$\frac{T}{D} = 0.34 \sqrt{\frac{P}{P_e}} \quad (11.1)$$

The alkali halides listed are quite similar in many of their physical properties and differ primarily in the low-wavenumber cutoff. NaCl is the hardest and least hygroscopic and CsI the softest and most hygroscopic. Powdered KBr, KCl and CsI can each be compressed into transparent disks. When a small quantity of a very finely

ground sample is added to the powder before compression, a solid solution is formed when the mixture is subjected to high pressure. This is a common method of sampling solids but should be used only if there is no possibility of ion exchange between the sample and the alkali halide.

Of the fluorides listed in Table 11.1, all are harder and more resistant to water vapor than the alkali halides, but only  $\text{BaF}_2$  has good transmission below  $1000\text{ cm}^{-1}$ .  $\text{BaF}_2$  is a hard material suitable for high-pressure applications but is quite susceptible to thermal shock. All of the heavy metal halides are insoluble in water and have good transmission over a wide spectral range but are very soft. Mixed  $\text{AgCl}$  and  $\text{AgBr}$  form a glass that can be used for short optical fibers in the mid-infrared region.  $\text{TlBr}_{0.42}\text{I}_{0.58}$ , better known as KRS-5, was very commonly used as an internal reflection element (see Chapter 15). It is, however, both soft and extremely toxic (even by skin contact) and should only be handled with gloves. Practitioners of internal reflection spectroscopy are advised always to send KRS-5 crystals back to the manufacturer for repolishing.

The chalcogenides are all insoluble in water and other common solvents.  $\text{ZnSe}$  and  $\text{CdTe}$  have excellent transmission characteristics. The only problem with these materials is their high refractive index, which leads to high front-surface reflectance (see Section 13.2.2), so that transmission spectra of liquids held in cells fabricated from these materials often give rise to interference fringes (see Section 11.1.3). These materials all make excellent internal reflection elements. AMTIR (amorphous material that transmits infrared radiation) is a mixture of several chalcogenides. Many optical fibers used for mid-infrared spectrometry are made from this material (see Section 15.4).

Quartz ( $\text{SiO}_2$ ) and sapphire ( $\text{Al}_2\text{O}_3$ ) both have superb mechanical and thermal properties, but neither material transmits in the fingerprint region of the mid-infrared spectrum (below  $\sim 1500\text{ cm}^{-1}$ ), and hence these materials are only useful for the study of X—H stretching bands in the mid-infrared but are widely used for near-infrared (NIR) spectrometry. Optical fibers fabricated from  $\text{SiO}_2$  have good transmission in the NIR above about  $4500\text{ cm}^{-1}$ . Silicon and germanium have very high refractive indices and hence are used primarily for internal reflection spectrometry. Silicon has a strong band at about  $610\text{ cm}^{-1}$  and impurity bands in the region below  $1100\text{ cm}^{-1}$  that prevent it being used as a multiple internal reflection element (IRE). It is very useful, however, as a micro-IRE where the pathlength is only a couple of millimeters.

A few years ago, diamond was considered as an exotic, rather expensive material that was only used as a window material in high-pressure cells (see Section 14.3). Now synthetic diamonds are becoming more available, and diamond can also be used as a coating for less chemically resistant materials with and far lower cost and superior infrared transparency. Diamond has a characteristic doublet absorbing between about  $1900$  and  $2300\text{ cm}^{-1}$ , but fortunately, few functional groups absorb in this region.

### 11.1.3. Interference Fringes

Any time two surfaces of a cell or sample are parallel, a sinusoidal pattern (known as *interference fringes*) may be seen on the baseline of the spectrum. These fringes

are caused by interference between radiation that has been transmitted directly through the cell or sample with light that has been reflected internally. The higher the difference in refractive index of the materials at which the reflection occurs, the greater is the amplitude of the interference fringes that result from reflection between the two internal faces of the cell. When the surfaces are not perfectly parallel, the amplitude of the interference fringe decays with increasing wavenumber.

Interference fringes can be both a blessing and a curse. On the positive side, they allow the thickness of cells or self-supporting samples to be estimated. If  $m$  fringes are observed between wavenumbers  $\tilde{\nu}_1$  and  $\tilde{\nu}_2$ , the pathlength of the cell (or the thickness of the sample) may be calculated as

$$d = \frac{m}{2n(\tilde{\nu}_1 - \tilde{\nu}_2)} \quad (11.2)$$

where  $n$  is the refractive index of the material between the two surfaces that causes the fringes. On the down side, interference fringes can prevent quantitatively accurate spectra from being measured.

The complete elimination of interference fringes from spectra is extremely difficult because their spacing varies with the refractive index of the sample. Interference fringes have very low amplitude when the refractive index of the window,  $n_W$ , is approximately the same as that of the sample,  $n_S$ . Thus, if alkali halide windows are used to measure the spectrum of most organic liquids, the amplitude of the interference fringes is usually very low, since for both materials,  $n \sim 1.5$ . It should be remembered, however, that the refractive index of most materials changes significantly across an absorption band (see Figure 1.4). Interference fringes that are present only near strong absorption bands are easily missed because the amplitude of the spectrum is changing rapidly in these regions. Whether or not interference fringes are observed, their effect is to reduce the accuracy of quantitative analysis performed by infrared transmission spectrometry.

Several ways to eliminate interference fringes have been proposed. One of the more effective ways is to mount a polarizer in the beam and to mount the sample at Brewster's angle,  $\theta_B$ , calculated as

$$\theta_B = \tan^{-1} \frac{n_W}{n_S} \quad (11.3)$$

where  $n_W$  is the refractive index of the window and  $n_S$  is the refractive index of the sample. When the sample is a free-standing polymer film with  $n_S = 1.5$ , Brewster's angle is  $33.7^\circ$ .

Other methods have been proposed by which interference fringes can be minimized. All of them are based on the assumption that their spacing is constant across the spectrum. This assumption is valid only if the refractive index of the sample does not change with wavenumber, which we know not to be the case (see Figure 1.4). One method of fringe removal involves modeling the interference fringe as a decaying sinusoid.

Another approach involves measuring two spectra, one with the sample perpendicular ( $90^\circ$ ) to the beam and the other with the sample at an angle of  $\phi$ . When  $\phi = 90^\circ$ , the optical thickness of the sample is  $nd$ , whereas for the other measurement, the optical thickness is  $nd \cos \phi$ . Because the interference fringe is approximately sinusoidal and because the internally reflected beam travels a distance of  $2d$  farther than the beam that is transmitted directly through the sample, its effect is manifested as “spikes” at retardations of  $2nd$  and  $2nd \cos \phi$ , respectively, in the interferogram. Initially, the data points in the region of this spike were simply replaced by zeros. However, this procedure led to small distortions in the spectrum. A better procedure is to replace this region with the corresponding region of the interferogram that was measured with the sample held at an angle to the beam. If this region in the interferogram measured when the sample is perpendicular to the beam is replaced by the corresponding data in the other interferogram and the Fourier transform (FT) is computed, the amplitude of the interference fringe in the resulting spectrum will be very small and the spectrum is minimally distorted. This procedure has been called *grafting*. Since the same spikes can be seen in the FT of the transmittance or absorbance spectrum of samples giving rise to interference fringes, it is often convenient to perform the grafting operation on the FT of the spectrum rather than the interferogram, since the signal caused by atmospheric water and  $\text{CO}_2$  has been removed.

#### 11.1.4. Trace Analysis

First let us distinguish between trace analysis and microsampling. *Trace analysis* by FT-IR spectrometry is the measurement of the spectrum of a minor component of a sample. *Microsampling* is the measurement of the spectrum of a very small amount of a pure material or major component of a mixture. It is not too difficult to obtain the spectrum of 1 ng of a pure solid or liquid, but it can be exceedingly difficult to obtain the spectrum of the same amount of the same material when it is present at a level of 1 ppm in 1 mg of a strongly absorbing matrix. The measurement is almost impossible if the most characteristic bands in the spectrum of the matrix and the analyte absorb at similar wavelengths.

Let us recall the rule of thumb given at the start of this chapter (i.e., a strong band in a 10- $\mu\text{m}$  film of a pure material has a typical absorbance of about 1 AU). Furthermore, we will assume that the strongest band in the spectrum of the analyte must have an absorbance of at least 0.001 AU (1 mAU) for the analyte to be identified above the noise level, interference by atmospheric water vapor, and small variations of the baseline. These constraints imply that the thickness of a sample containing 1 ppm of the analyte must be 1 cm if a trace component is to yield a recognizable spectrum. However, the transmittance of most samples that are 1 cm thick is well below 0.1% in those spectral regions where chemically useful information is to be found (3100 to 2700 and 1800 to 400  $\text{cm}^{-1}$ ). Thus, windows in the spectrum of the matrix material must be found where at least one characteristic band of analyte absorbs. An example of just such a case is found in the determination of antioxidants in polyolefins. Many polyolefins have weak absorption between



3300 and 4000  $\text{cm}^{-1}$ , making it possible for the O—H stretching bands of hindered phenolic antioxidants present at the ppm level to be observed, even though the rest of their spectrum is masked completely.

These considerations should be borne in mind if the spectrum of a trace solute in a liquid solvent is to be obtained. In this case, the structure and polarity of the solvent must be considered. Most classical texts on infrared spectroscopy recommend that carbon tetrachloride or carbon disulfide be used as the solvent if the spectrum of a species in solution is to be measured.  $\text{CCl}_4$  and  $\text{CS}_2$  are both small, nonpolar molecules that have very simple infrared spectra containing wide window regions, and the transmittance of much of the spectrum of a 1-mm-thick film of both molecules is greater than 10%.

If, on the other hand, *n*-hexane is to be used as a solvent, the cell thickness must be reduced to about 100  $\mu\text{m}$ . Even though  $\text{CCl}_4$ ,  $\text{CS}_2$ , and *n*-hexane are all nonpolar, the increased structural complexity of *n*-hexane and the fact that it contains lighter atoms than  $\text{CCl}_4$  and  $\text{CS}_2$  mean that its fundamental absorption bands cover a greater region of the mid-infrared spectrum than those of  $\text{CCl}_4$  or  $\text{CS}_2$ . Thus, the window regions, where useful information on the solute can be found, are much shorter.

If the solvent is polar, this situation is exacerbated because the bands associated with vibrations of polar groups tend to be stronger than those associated with nonpolar groups since the dipole moment derivative,  $\partial\mu/\partial Q$  (see Section 1.2), is usually high. For example, a greater proportion of the spectrum of 2-hexanone held in a 100- $\mu\text{m}$  cell is lost by absorption than for *n*-hexane, even though these molecules both have approximately the same number of atoms. The worst case of all is when water is the solvent. For the study of aqueous solutions, the cell has to be no thicker than about 10  $\mu\text{m}$  if the transmittance at all wavenumbers below 2000  $\text{cm}^{-1}$  is to exceed 10%.

The optimum thickness for measuring the spectrum of any solute depends on the absorptivity of the solvent. It is well known from many textbooks on instrumental analysis that the optimum pathlength of a cell should be such that the transmittance of the solvent should be about  $1/e$ , where  $e$  is the base of Naperian logarithms. Thus, the optimum absorbance,  $A_{\text{opt}}$ , of the solvent should be  $\log_{10}e$ , or  $\sim 0.4$  [2]. If the cell thickness is increased beyond this optimum value, the transmittance of the solvent decreases faster than the absorbance of the solute increases. Vidrine [3] has published a useful compilation of spectral data for common solvents showing the thickness of the cell required to give an absorbance of  $\log_{10}e$ . The spectra of six representative solvents plotted in this format are reproduced in Figure 11.1.

## 11.2. GAS- AND VAPOR-PHASE SAMPLES

To measure the spectrum of a gas or vapor, the sample must be contained in a gas cell of an appropriate pathlength. The standard length of a cell for the measurement of the spectra at relatively high partial pressures (0.1 to 0.01 atm) is 10 cm. Cells of pathlengths between 1 and 10 cm fit easily in the sample compartments of all

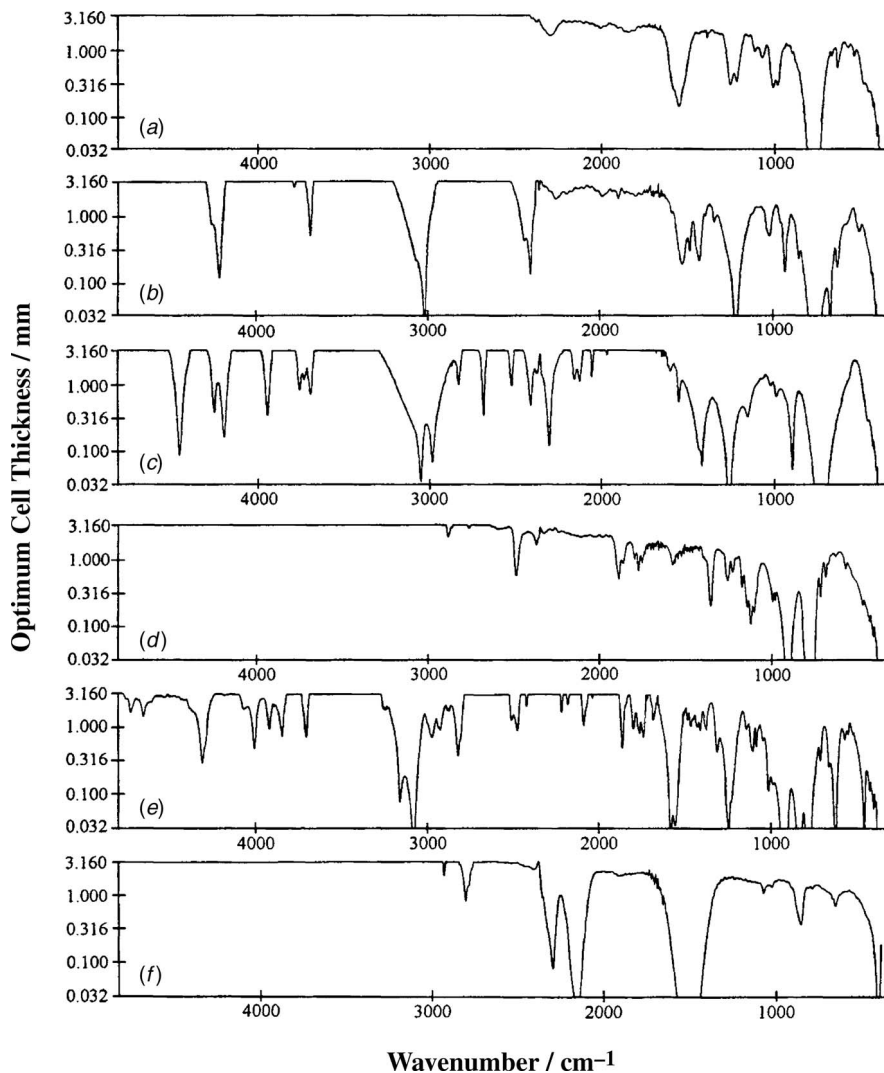


**Figure 11.1.** Spectra of six common halogenated solvents plotted in terms of the pathlength required to give the optimal transmittance  $1/e$  at any wavenumber: (a)  $\text{CCl}_4$ ; (b)  $\text{CHCl}_3$ ; (c)  $\text{CH}_2\text{Cl}_2$ ; (d)  $\text{Cl}_2\text{C}=\text{CCl}_2$ ; (e)  $\text{Cl}_2\text{C} + \text{CHCl}_3$ ; (f)  $\text{CS}_2$ . (Reproduced from [3], by permission of Academic Press; copyright © 1979.)

benchtop FT-IR spectrometers. If the analyte is present at a lower partial pressure or has a very low absorptivity (e.g.,  $\text{H}_2\text{S}$ ), a longer pathlength is needed. In this case, a cell in which the beam is multiply reflected should be used. This type of cell is commonly known as a *White cell*, after the designer of the original folded path cell, J. U. White [4], although several different variants of multipass gas cells have been reported.

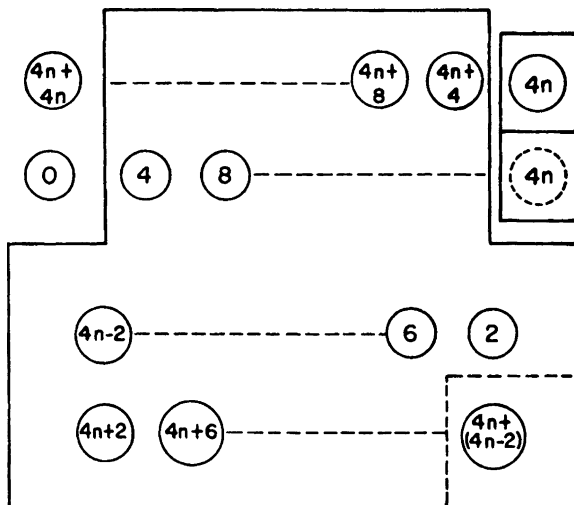


**Figure 11.2.** Position of the images on the field mirror of a multipass gas cell. (Reproduced from [6], by permission of Academic Press; copyright © 1979.)

In the cell design described by Hanst in 1971 [5], the beam from the interferometer is initially focused into an image at the entrance aperture of the cell (designated the 0 image in Figure 11.2). The beam diverges and is collected by a spherical mirror,  $M_1$ , located two focal lengths from the image. This mirror refocuses the beam (inverted) on the lower part of a second spherical mirror,  $M_2$ , of the same focal length as the first mirror. This mirror is known as the *field mirror*. The second mirror is adjusted so that the reflected beam falls entirely on a third mirror,  $M_3$ , located immediately below the first one.  $M_1$  and  $M_3$  have been called *nesting mirrors*.  $M_3$  is aligned to form another image, marked 4 in Figure 11.2, alongside the 0 image. The beam then alternates between  $M_1$  and  $M_3$ , with each on  $M_2$  located at a slightly different position, until after  $4n$  passes, it finally reaches the cutout on the field mirror and is passed to the detector.

In the design described by Hanst in 1971 [5], the images on the field mirror formed two lines. Hanst [6] later described a way of increasing the number of passes by splitting the images into two lines, in the manner shown in Figure 11.2. He went further and one of the cells sold by his company [7] has six lines of images, while his latest cell has 12 lines of images.

Another type of multipass cell, known as the *Herriott cell*, was described by Herriott and Schulte in 1965 [8]. Although the Herriott cell is most commonly used with lasers, it has also been used for long-path FT-IR measurements. This cell consists of two spherical mirrors with a separation that is about the same as the radius of curvature of the mirrors. If a laser beam is projected in just off the edge of one of the spherical mirrors, so that it hits the center of the other mirror, multiple passing ensues. Because the beam is off-axis and the mirrors are not quite confocal, the beams do not come back on themselves as they do in a White cell, but

instead, wander around the mirrors in Lissajous figures. Whether the images form a circle, an ellipse, or a figure eight depends on how far from confocal and how far off-axis the input beam is. This type of cell works very well for a laser beam, but with a convergent input beam, as is the case in FT-IR spectrometry, the beam spread makes the Herriott cell significantly less efficient than cells of the type designed by White or Hanst.

White cells with pathlengths between 1 and at least 200 m are commercially available from a variety of vendors. Concentrations of gases as low as 10 ppb (and even lower for compounds with bands of very high absorptivity) have been measured in such cells. By fabricating the cell body from quartz and surrounding the cell with banks of ultraviolet lamps, the mechanisms of gas-phase photochemical reactions can be studied. Some of the fundamental investigations into the formation of photochemical smog were performed by irradiating hydrocarbons present in air at a low parts-per-million level in a 400-m cell [9]. By measuring a series of spectra over a period of time, the mechanism and kinetics of the ensuing reactions could be followed, even though the products were present only at the low ppb level.

Most White cells are designed to monitor static samples and do not have good flow characteristics. The ideal cell in this respect has a high pathlength/volume ratio, so that the contents are readily flushed out. An example of such a cell is an internally gold-coated light-pipe of the type used to monitor the effluent from a capillary gas chromatograph by FT-IR spectrometry (GC/FT-IR). As described

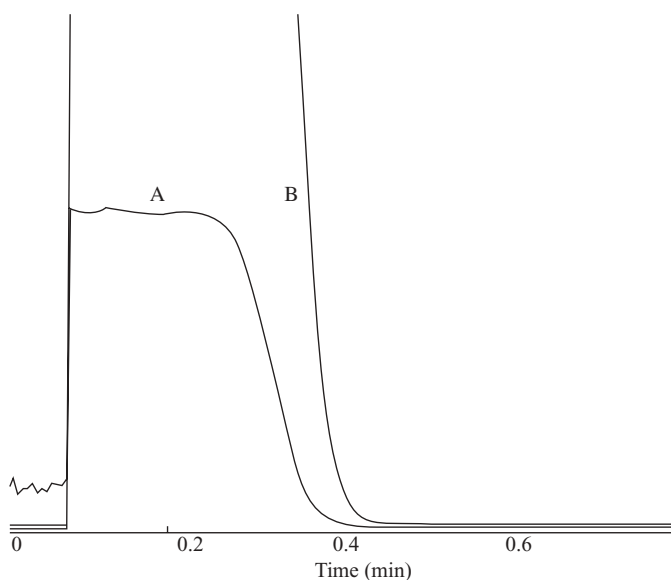


**Figure 11.3.** Variation of absorbance with time when a gas mixture of helium and acetone flowing through an Axiom gas cell was switched to pure helium. (Reproduced by permission of Axiom Analytical Corporation.)

in more detail in Chapter 23, a typical light-pipe designed for capillary GC/FT-IR is 10 cm in length and 1 mm in internal diameter (a volume of 80  $\mu\text{L}$ ). The reflection losses in such light-pipes are quite severe; a light-pipe with the dimensions given above has a transmission of less than 10%, so that a MCT detector is invariably used for GC/FT-IR measurements.  $\text{LN}_2$ -cooled detectors are not desirable for process monitoring and volumes of less than 1 mL are unnecessary. Thus, light-pipe gas cells are not appropriate for process monitoring.

Fortunately, other alternative designs are available. For example, a simple gas cell with a typical pathlength of 2 m (but which can be as long as 16 m) is available from Axiom Corporation [10]. This cell employs small-diameter, tubular, gold-coated brass light guides. Because of its high pathlength/volume ratio, this cell has excellent flow characteristics, as can be seen in Figure 11.3.

### REFERENCES

1. D. W. Vidrine, Optical materials, <http://www.vidrine.com/iropmat.htm>, 2002.
2. G. D. Christian, *Analytical Chemistry*, 5th ed., Wiley, New York, 1994, p. 439.
3. D. W. Vidrine, Liquid chromatography detection using FT-IR, in *Fourier Transform Infrared Spectroscopy: Applications to Chemical Systems*, J. R. Ferraro and L. J. Basile, Eds., Academic Press, New York, 1979, Vol. 2, p. 129.
4. J. U. White, *J. Opt. Soc. Am.* **32**, 285 (1942).
5. P. L. Hanst, *Adv. Environ. Sci. Technol.* **2**, 91 (1971).
6. P. L. Hanst, Pollution: trace gas analysis, in *Fourier Transform Infrared Spectroscopy: Applications to Chemical Systems*, J. R. Ferraro and L. J. Basile, Eds., Academic Press, New York, 1979, Vol. 2, p. 79.
7. Infrared Analysis, Inc., 1558-B South Anaheim Boulevard, Anaheim, CA 92805.
8. D. R. Herriott and H. J. Schulte, *Appl. Opt.* **4**, 883 (1965).
9. P. L. Hanst, A. S. Lefohn, and B. W. Gay, Jr., *Appl. Spectrosc.* **27**, 188 (1973).
10. Axiom Analytical, Inc., 17751 Sky Park Circle, suite ABC, Irvine, CA 92614.

# POLARIZATION

## 12.1. PLANE-POLARIZED RADIATION

The passage of photons through a vacuum or any medium generates an electromagnetic field that consists of two orthogonal components, one electric and the other magnetic, perpendicular to the direction of travel of the photon. The electric and magnetic fields have identical frequencies, but only the electric field vector interacts with the vibrational modes of the molecules in the beam path at any level of detectable strength. Consequently, we consider only the electric field vector. The electric field vector can lie in any plane perpendicular to the direction of travel, and when a large number of photons all travel in the same direction, it is expected that the electric fields are distributed in all possible planes. Such radiation is called *natural light* or *unpolarized radiation*.

If the electric fields from all the photons that travel in the same direction were forced into the same plane, the radiation is said to be *plane polarized* or *linearly polarized*. Radiation will retain the plane of polarization unless it is perturbed in specific ways. As discussed briefly in Section 1.6, plane-polarized radiation can be used to measure the orientation of functional groups in a sample. Oriented samples absorb radiation that is plane polarized in two perpendicular directions to different extents; such samples are said to exhibit *linear dichroism*. Linear dichroism is used to measure orientation in samples: in other words, the alignment of functional groups in different physical directions. This topic is discussed in more detail in Section 12.4.

Polarization is also important in reflection spectrometry, especially for the measurement of thin films on metallic and dielectric surfaces, as described in Chapter 13. For reflection measurements, radiation that is polarized such that its plane of polarization is parallel to the plane containing the incident and reflected rays (the plane of incidence) is said to be *p*-polarized. Radiation that is polarized such that its plane of polarization is perpendicular to the plane of incidence is said to be *s*-polarized (from the German word for “perpendicular,” *senkrecht*).

Plane-polarized radiation is produced with an optical element appropriately named a *polarizer*, or more correctly, a *linear polarizer*. Wire-grid polarizers are the most commonly used type of polarizer for mid-infrared FT-IR spectrometry. An array of very fine metal wires is deposited holographically on one face of an optically transparent window (usually, KRS-5 or ZnSe). Because an electric field oriented along the direction of the wires can induce electrical currents along the wires, the wire grid acts as a metal surface that reflects almost all the radiation polarized along the direction of the wires. Since the electric field perpendicular to the direction of wires is unable to induce electrical current in the wire grid, this radiation is transmitted through the polarizer, with the only loss being due to reflection from the substrate window. The efficiency of wire-grid polarizers is greatest for wavelengths that are much longer than the grid spacing, which makes wire-grid polarizers useful in the mid- and far-infrared spectral regions. Polarizers for far-infrared spectrometry are frequently made by embedding the wires in polyethylene.

When radiation is incident on the surface of a dielectric material (i.e., a material that refracts but does not absorb radiation), there is a certain angle at which all radiation with its plane of polarization identical to the plane of incidence is transmitted (i.e., the reflectance at this angle is zero; see Figure 13.1) and is equal to  $\tan^{-1} n$ , where  $n$  is the refractive index of the material. This angle is known as *Brewster's angle*. An alternative type of polarizer, known as a *Brewster's angle polarizer*, may be constructed by stacking transparent plates in the beam tilted so that the angle of incidence on the plates is Brewster's angle. Since at Brewster's angle, the reflectance of  $p$ -polarized light is zero, the  $p$ -polarized component passes through the plates without loss, while the intensity of the  $s$ -component is reduced by reflection losses at every surface. The intensity reduction of the  $s$ -component depends on the value of the reflectance as well as on the number of plates that are stacked together. In the mid-IR region, transparent materials of very high refractive index are available. For example, for germanium ( $n = 4.0$ ), Brewster's angle is  $76^\circ$ . At this angle, the front-surface reflectance of Ge to  $s$ -polarized radiation is  $\sim 0.80$ ; thus, the transmittance of  $s$ -polarized radiation through the front surface is 0.2. After internal reflection at the rear surface of the plate is taken into account, the transmittance of  $s$ -polarized radiation through a single Ge plate when radiation is incident at Brewster's angle is less than 0.1. It is therefore possible to construct an efficient polarizer by stacking only two Ge plates.

For the near-infrared region, the polarizer of choice is the Glan–Taylor polarizer. This type of polarizer is based on the birefringent property of some materials. These materials have different refractive indices for radiation of different polarizations. The light is brought onto an internally reflecting interface at an angle of incidence that is below the critical angle for total internal reflection (see Chapter 15) for one polarization and above the critical angle for the other polarization. Thus, radiation polarized in the unwanted direction is deflected out of the beam, while radiation with the desired polarization is transmitted, as shown in Figure 12.1. This process yields a polarizer with a very high efficiency that is essentially constant throughout the transparent spectral range of the crystal.

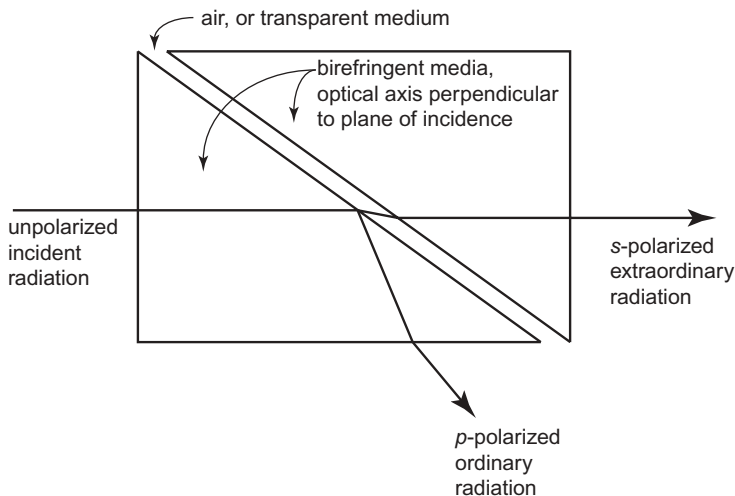


**Figure 12.1.** Principle of the Glan–Taylor polarizer.

## 12.2. CIRCULAR POLARIZATION

Polarization does not have to be restricted to a plane. It is possible to cause the electrical field to rotate as the wave propagates. If an observer could record the electric field vector of a wave as it was directed away from the observer, he would see a single line at a fixed angle for plane-polarized radiation. On the other hand, if the electric field vector rotated, the observer would see the angle sweep through  $360^\circ$ . This type of radiation is said to be *circularly polarized*, and the difference in absorption of radiation that is circularly polarized in opposite directions (clockwise and counterclockwise) by chiral compounds is known as *circular dichroism* (CD).

Let us consider the case when we have two plane-polarized light waves of identical frequency moving through the same region of space in the same direction. The amplitude and phase of the resultant depends on the amplitude and phase of the two superposing waves. If the electric field vectors of the two waves are aligned with each other, they will simply combine to give a resulting wave that is also linearly polarized. If the waves are of equal amplitude and orthogonal, superposition of the two waves can lead to plane-polarized, elliptically polarized, or circularly polarized radiation, depending on the phase difference between the two beams. If the two waves have a phase difference of zero or an integral multiple of  $2\pi$  radians, they are in phase and the resulting wave is linearly polarized. If the two waves are  $90^\circ$  out of phase, the resultant traces out a circle and the two waves are said to be circularly polarized. When the  $x$  component lags the  $y$  component by  $90^\circ$ , the resultant vector rotates clockwise (as seen approaching the observer and tracing out a right-hand helix in space), and the resulting wave is said to be *right circularly polarized*. If the  $x$  component precedes the  $y$  component by  $90^\circ$ , the resulting vector rotates



counterclockwise, and the resulting wave is said to be *left circularly polarized*. For any phase difference other than  $0^\circ$ ,  $90^\circ$ ,  $180^\circ$ ,  $270^\circ$ , and so on, the resulting beam is *elliptically polarized*.

Circularly polarized light is produced by retarding the phase of one polarization state. For example, if a birefringent crystal is cut so that its optic axis is parallel to the front and back surfaces, an incident monochromatic ray will propagate through the crystal as ordinary and extraordinary rays. Because of the difference in the refractive indices of the media through which these beams are passing, the velocity of the ordinary and extraordinary rays is different and a phase difference is introduced. The resulting wave is a superposition of the ordinary and extraordinary rays. If the thickness of the plate is such that a  $90^\circ$  phase difference results, the crystal is known as a quarter-wave plate. Circularly polarized radiation is usually produced by combining a linear polarizer and a quarter-wave plate. A half-wave plate can change right circularly polarized light to left, and vice versa.

### 12.3. POLARIZATION MODULATION

The difference between the absorption of radiation by two polarization states is often extremely small. This is particularly true for the absorption of *p*- and *s*-polarized radiation by very thin films on metallic surfaces (see Section 13.3). In this case the sensitivity of the measurement may be affected either by digitization noise or (more often) simply by the difference in the level of atmospheric water vapor between the single-beam spectra measured with *p*- and *s*-polarized radiation. The situation is even worse for *vibrational circular dichroism* (VCD) *spectrometry*: For most molecules exhibiting the VCD effect, the magnitude of the difference between the absorbance of right,  $A_R(\tilde{\nu})$ , and left,  $A_L(\tilde{\nu})$ , circularly polarized radiation,  $\Delta A_{CD}$ , is so small that subtracting a spectrum measured with left circularly polarized radiation from one measured with right circularly polarized radiation would require a signal-to-noise ratio well in excess of  $10^6$ . As we have seen in Chapter 7, such high sensitivity is quite difficult to achieve in FT-IR spectrometry, even with an MCT detector, because of the limited linearity of the detector and, sometimes, the limited dynamic range of the analog-to-digital converter. Thus, a huge number of scans would have to be signal-averaged for VCD spectra to be measured by subtracting two absorption spectra measured with right and left circularly polarized radiation.

A good way to avoid such problems is through the use of *differential spectrometry*, where the beam is rapidly modulated between the parent polarization states. For VCD spectrometry, modulation between right and left circularly polarized radiation would be imposed, so that the drawbacks involved with measuring  $A_R(\tilde{\nu})$  and  $A_L(\tilde{\nu})$  at times separated by several minutes is eliminated. Differential measurements make use of the well-known *ac advantage* (i.e., a small difference signal can be measured more accurately as the amplitude of a periodically varying ac signal than as the difference between two large time-independent signals). Measurement of the amplitude is usually achieved with a lock-in amplifier (LIA) tuned

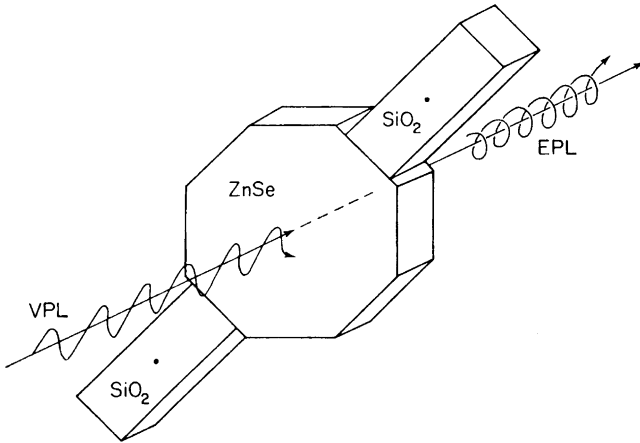


**Figure 12.2.** Photoelastic modulator in which an isotropic ZnSe plate is alternately stretched and compressed with SiO<sub>2</sub> piezoelectric transducers. In general, vertically polarized light (VPL) is converted to elliptically polarized light (EPL). At certain amplitudes, linearly or circularly polarized light may be formed. (Reproduced from [6], by permission of Academic Press; copyright © 1982.)

to the frequency of the modulation so that all contributions (random or coherent) at other frequencies are not detected.

For linear or circular dichroism measurements made in this way, phase retardation is usually achieved by passing plane-polarized radiation into a *photoelastic modulator* (PEM) [1,2]. This device is comprised of an isotropic crystal (commonly, ZnSe) that is alternately compressed and extended by piezoelectric transducers, as shown schematically in Figure 12.2, causing a synchronous variation in the difference in the refractive indices along two mutually perpendicular axes of the crystal. One of these two axes coincides with the axis along which the stress is applied. If a linear polarizer is set at 45° with respect to the orthogonal stress axes of the PEM, equal intensities of polarized radiation lie along these axes. When the ZnSe optical element is stretched and compressed by the PZTs, the indices of refraction of the ZnSe element along the stress axes vary in a sinusoidal manner. This extension and compression causes the components of polarized light along the axes to be phase advanced or retarded with respect to one another.

The behavior of the output beam depends on the amplitude of the PZTs, since this amplitude determines the change in refractive index along the stress axis. At a certain amplitude, the maximum phase retardation for a particular wavenumber ( $\tilde{\nu}_0$ ) is 90° and the beam emerging from the ZnSe plate becomes circularly polarized. The handedness of the circularly polarized radiation switches sinusoidally from left to right with a frequency equal to the frequency at which the ZnSe plate is being extended and compressed. (It is this property that is used for the measurement of VCD spectra.) For most other wavenumbers in the spectrum, the radiation is elliptically polarized, with the ellipticity increasing with the difference between

the wavenumber of interest and  $\tilde{\nu}_0$ . For radiation within a few hundred wavenumbers of  $\tilde{\nu}_0$ , the ellipticity of the radiation is small and the radiation can be considered to be circularly polarized to a good approximation at the maxima of the retardation cycles.

When the amplitude of the motion of the PZTs is doubled relative to the case discussed above, the phase retardation is  $180^\circ$  and the *plane* of polarization of the output beam from the PEM at  $\lambda_0$  changes by  $90^\circ$  at the extreme of the modulation cycle. When there is no tension on the ZnSe plate, the plane of polarization of the output beam is the same as that of the input beam. At the extremes of the extension and compression cycles, the plane of polarization is rotated by  $90^\circ$ . At this amplitude, therefore, the plane of polarization is modulated between *s* and *p* at a frequency of  $2f_M$ .

A common modulation frequency for ZnSe PEMs is 37 kHz; in this case, the modulation frequencies for circular and plane polarization modulation are 37 and 74 kHz, respectively. If the interferometer is scanned with an optical velocity of, say,  $0.3 \text{ cm} \cdot \text{s}^{-1}$ , the highest Fourier frequency (corresponding to a wavenumber of  $4000 \text{ cm}^{-1}$ ) is 1200 Hz (see Eq. 2.11). It is simple matter to filter out the signal generated by the interferometer with a high-pass electronic filter so that the only signal passed by this filter is caused by the polarization modulation. The output of the high-pass filter is input to a LIA. For circular dichroism measurements, the reference frequency of the LIA is the frequency of the PEM, whereas for linear dichroism measurements the reference frequency is the first harmonic of the PEM frequency. The LIA demodulates the signal at the polarization-modulation frequency to yield an interferogram that is due solely to the difference spectrum between the two polarization states. This interferogram is digitized every zero crossing of the laser interferogram in the customary manner, and the Fourier transform of this interferogram gives the appropriate dichroism spectrum.

To obtain the correct relative intensities of the bands in the dichroism spectrum, the spectrum as acquired above must be normalized against the conventional single-beam spectrum of the spectrometer. This spectrum is obtained simply by passing the detector signal through a low-pass filter to remove any information above about 5 kHz and measuring the conventional interferogram at the same time as the polarization-modulation interferogram. The process by which VCD spectra are measured is summarized in Figure 12.3.

## 12.4. APPLICATIONS OF LINEAR DICHROISM

The orientation of molecules in thin solid films, liquid crystals, and fibers can be studied by linear dichroism spectrometry. If the spectrum of an oriented film is measured with polarized radiation, its dipole moment derivative,  $(\partial\mu/\partial Q_i)$  (see Section 1.2) must have a component that is nonzero in the direction of the polarization if that band is to be seen in the infrared spectrum. As an example, let us consider the case of a film of poly(ethylene terephthalate) (PET) that has been drawn (stretched during the manufacturing process) such that the polymer chains

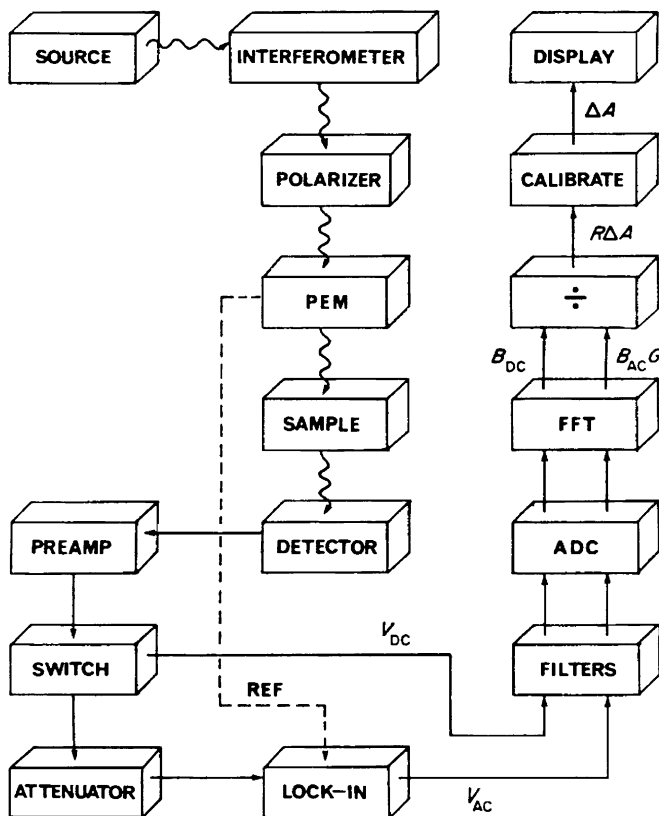
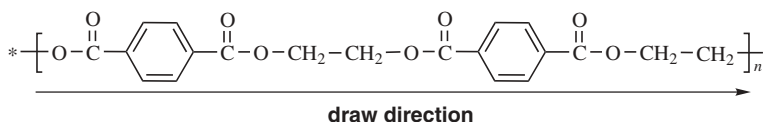


**Figure 12.3.** Typical IRRAS measurement using a photoelastic modulator. Radiation from the source and interferometer is passed through a linear polarizer and PEM and is reflected from the sample, after which it is measured at the detector. The preamplified detector signal may pass in one of two directions. To demodulate the high-frequency (ac) signal, it is first passed through a high-pass electronic filter and then into a lock-in amplifier referenced to the second harmonic of the modulation frequency of the PEM, from which it is sampled by the ADC. The FT of this signal gives the single-beam IRRAS spectrum. Alternatively, the detector signal is passed through a low-pass filter and this interferogram (here called the dc signal) is digitized directly to give the single-beam background spectrum. The ratio of the ac and dc spectra gives the IRRAS spectrum of the sample. (Reproduced from [6], by permission of Academic Press; copyright © 1982.)

become oriented in a certain direction. The C=O groups are oriented at  $\sim 90^\circ$  to the chain:



In this case, the C=O groups are predominantly oriented in a direction that is perpendicular to the draw direction. If we define *p*- and *s*-polarizations as being

parallel and perpendicular, respectively, to the draw direction, this argument leads to the conclusion that the C=O stretching band will be much more intense when the spectrum of a PET film is measured with *s*-polarized radiation than with *p*-polarization, which is in fact the case.

Absorbance spectra measured with *p*- and *s*-polarization are denoted as  $A_p(\tilde{\nu})$  and  $A_s(\tilde{\nu})$ , respectively.  $A_p(\tilde{\nu}) - A_s(\tilde{\nu})$  is known as the *dichroic difference*, and  $A_p(\tilde{\nu})/A_s(\tilde{\nu})$  is the *dichroic ratio*. Quantitative treatments of molecular orientation often require knowledge of the dichroic ratio. However, in regions where the sample absorption is very weak, calculation of the dichroic ratio involves taking the ratio of noise on the baseline of  $A_p(\tilde{\nu})$  and  $A_s(\tilde{\nu})$  when both parameters are approximately zero. Thus, if qualitative or semiquantitative information is all that is required, the dichroic difference spectrum is more useful than the dichroic ratio.

It is frequently found that polymer samples are too thick for the peak absorbance of the stronger fundamentals to be less than 2 AU. For example, the thickness of PET must be less than 3  $\mu\text{m}$  for this criterion to be fulfilled for the C=O and C—O stretching fundamentals. Pellerin et al. [3] showed that it is possible to measure the overtones of these bands and still obtain useful information. For example, they showed that it is possible to study the relaxation of a 300- $\mu\text{m}$  PET film by measuring the first overtone of the C=O stretching band at  $3433\text{ cm}^{-1}$ . Differences in orientation of samples that had been stretched and allowed to relax rapidly were observed over a period of 5 minutes through the use of a photoelastic modulator (see Figure 12.4). The strongest band in the dichroic difference spectrum (at  $3433\text{ cm}^{-1}$ ) shows a negative dichroism, which indicates that, as expected, the dipole moment derivative associated with the C=O stretch is largely perpendicular

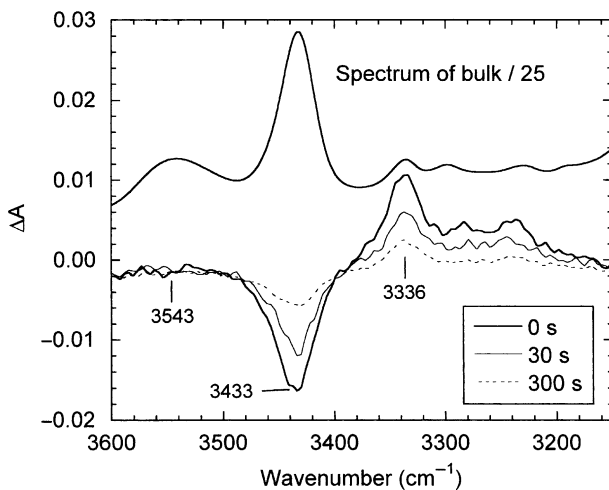


**Figure 12.4.** Spectrum of an undeformed 300- $\mu\text{m}$  PET film in the high-wavenumber region and the dichroic difference spectra recorded with a PEM at the end of the deformation and after 30 and 300 s of relaxation. (Reproduced from [3], by permission of the Society for Applied Spectroscopy; copyright © 2002.)

to the chain axis. Other bands in this spectral region, whose assignments are uncertain, show either a positive dichroism (which indicates that  $\partial\mu/\partial Q$  is largely parallel to the chain axis) or no detectable dichroism. The study of orientation by infrared (and Raman) spectrometry is not simply an academic exercise. For example, Pellerin et al. [3], describe how the orientation function of PET in plastic bottles can be calculated from dichroic difference spectra. A very detailed and important discussion of the way that orientation can be studied from infrared and Raman spectra has been published by Ikeda et al. [4].

The data shown in Figure 12.4 show that variations in orientation that take place in time scales on the order of a few seconds can be studied by conventional FT-IR spectrometers. Faster changes have been investigated using the ultrarapid scanning FT-IR spectrometer shown in Figure 5.23. This instrument was used to study the irreversible deformation of polymer films that were stretched to the point of fracture. For the first time this measurement was done with better than 10-ms time resolution [5]. The evolution of molecular orientation as a function of draw ratio and relaxation time was studied for films of amorphous PET stretched at temperatures above its glass transition temperature. Very good agreement was obtained between the results obtained by this instrument and slower measurements made by polarization modulation infrared linear dichroism spectrometry. Reversible *gauche*-to-*trans* conversions were observed, indicating that the PET chains assume the *trans* configuration when stretched, but revert to the amorphous form on relaxation.

## 12.5. VIBRATIONAL CIRCULAR DICHROISM

As noted above,  $\Delta A_{CD}$  for chiral molecules is generally rather small. For electronic transitions,  $\Delta A_{CD}$  is usually about 0.1% of the absorbance of the peak and is fairly easily measured. For example, ultraviolet-visible CD spectroscopy has been used for many years to study the conformation of biopolymers. For vibrational transitions,  $\Delta A_{CD}$  is rarely more than 0.01% of the peak absorbance and is often at least an order of magnitude smaller than this. Thus, the measurement of VCD spectra presents a real challenge from an instrumental viewpoint.

Originally, VCD spectra were measured on a scanning monochromator, but the measurements were slow and the spectral range that could be accessed was short. The combination of Fellgett's and Jacquinot's advantages has meant that far better results are obtained by FT-IR spectrometry. A block diagram of a typical Fourier transform VCD spectrometer was shown as Figure 12.3. Radiation from a standard broadband source is first modulated by the interferometer at Fourier frequencies between  $V\tilde{\nu}_{\max}$  and  $V\tilde{\nu}_{\min}$ , where  $V$  is the optical velocity and  $\tilde{\nu}_{\max}$  and  $\tilde{\nu}_{\min}$  are the maximum and minimum wavenumbers in the spectral range of interest. Thus, in a VCD measurement, the radiation is modulated at the Fourier frequencies *and* at the frequency of the PEM,  $f_M$ . To obtain the amplitude of the signal at  $f_M$ , there must be at least an order of magnitude between the highest Fourier frequency,  $V\tilde{\nu}_{\max}$ , and  $f_M$ , and it is preferable that they are separated by an even greater amount. Thus, the optical velocity of the interferometer should be as low as is consistent with a stable interferometer drive.

It should also be noted that the time constant for the LIA must be quite short (less than 1 ms) to ensure that the Nyquist sampling criterion is fulfilled.

The low-frequency interferogram that would be measured in the conventional FT-IR experiment, called  $V_{dc}(\delta)$  by Nafie [6], is given by (compare Eq. 2.30)

$$V_{dc}(\delta) = \int_0^{\infty} B(\tilde{\nu}) \frac{10^{-A_R(\tilde{\nu})} + 10^{-A_L(\tilde{\nu})}}{2} \exp(-2\pi i \tilde{\nu} \delta) d\tilde{\nu} \quad (12.1)$$

The PEM introduces a wavenumber- and time-dependent phase retardation angle,  $\alpha(\tilde{\nu}, t)$ , on the beam. The magnitude of the intensity variation generated by the PEM depends on the sine of  $\alpha(\tilde{\nu}, t)$ , given by

$$\sin \alpha(\tilde{\nu}, t) = \sin \alpha_0(\tilde{\nu}) \sin 2\pi f_M t \quad (12.2)$$

where  $\alpha_0(\tilde{\nu})$  is the polarization phase shift at wavenumber  $\tilde{\nu}$ . This equation can be expanded into a series of odd-order spherical Bessel functions:

$$\sin \alpha(\tilde{\nu}, t) = 2 \sum_{n, \text{odd}} J_n[\alpha_0(\tilde{\nu})] \sin 2\pi f_M t \quad (12.3)$$

The first term in the summation,  $2J_1[\alpha_0(\tilde{\nu})]$ , corresponds to the fundamental frequency of the PEM, so that the ac interferogram measured at the output of the LIA is given by

$$V_{ac}(f) = \int_0^{\infty} \frac{B(\tilde{\nu})}{2} [10^{-A_R(\tilde{\nu})} + 10^{-A_L(\tilde{\nu})}] 2J_1[\alpha_0(\tilde{\nu})] \exp(-V\tilde{\nu}\tau) \exp(-2\pi i \tilde{\nu} \delta) d\tilde{\nu} \quad (12.4)$$

where the function  $\exp(-V\tilde{\nu}\tau)$  represents the decrease in signal imposed by the time constant of the LIA,  $\tau$ .

The high-frequency signal, which is caused by the sample's dichroism, is demodulated by the LIA. Nafie [6] called the signal the ac interferogram,  $V_{ac}(\delta)$ .

Once the interferograms  $V_{ac}(\delta)$  and  $V_{dc}(\delta)$  have been transformed to yield the spectra  $B_{ac}(\tilde{\nu})$  and  $B_{dc}(\tilde{\nu})$ , respectively, these spectra are ratioed to give

$$\frac{B_{ac}(\tilde{\nu})}{B_{dc}(\tilde{\nu})} = 2J_1[\alpha_0(\tilde{\nu})] \exp(-V\tilde{\nu}\tau) \tanh\{0.5 \ln 10 [10^{-A_R(\tilde{\nu})} + 10^{-A_L(\tilde{\nu})}]\} \quad (12.5)$$

If  $\Delta A_{CD}$  is small, which it always is for VCD spectra, we have

$$\frac{B_{ac}(\tilde{\nu})}{B_{dc}(\tilde{\nu})} = 2J_1[\alpha_0(\tilde{\nu})] \Delta A_{cd} \quad (12.6)$$

The term  $2J_1[\alpha_0(\tilde{\nu})]$  accounts for the effectiveness of the PEM in producing circularly polarized radiation as a function of wavenumber. Its value can be determined experimentally by a calibration procedure based on the combined use of a birefringent waveplate followed by a polarizer at the sample position [6–8]. There are four possible settings for the waveplate and polarizer and the VCD intersection points of the curves that define a calibration plot given by

$$\left[ \frac{I_{ac}(\tilde{\nu})}{I_{dc}(\tilde{\nu})} \right]_{cal} = \pm 2J_1[\alpha_M^0(\tilde{\nu})] \exp(-V\tau) \quad (12.7)$$

Division of this curve into the ratio in Eq. 12.6 isolates the properly calibrated spectrum  $\Delta A_{CD}$ . The phase lag imposed by a lock-in amplifier can also be determined with the same equipment using the phase spectrum calculated from a monosignate VCD spectrum from a stressed optical plate. This procedure is necessary because the conventional Mertz phase correction leads to sign errors when the raw VCD spectrum changes sign. Alternatively, standard phase-correction algorithms can be altered to produce VCD spectra without the sign errors [9]. More detailed descriptions of the theory and instrumentation for VCD spectrometry can be found in a number of review articles by Nafie's group [6,10,11] and by Polavarapu [8]. Since 2002, Nafie's group has demonstrated a number of other instrumental advances not described above. These include the use of two PEMs, one for the VCD signal and the other to asynchronously scramble the polarization of the IR radiation to reduce baseline artifacts [12]. They have recently shown improvements for the measurement of VCD spectra when two sources are incorporated [13]. Finally, they have demonstrated the feasibility of extending the wavenumber range of VCD spectrometry to  $10,000\text{ cm}^{-1}$  [14]. An FT-IR spectrometer for the measurement of VCD spectra, the ChiralIR, is now commercially available from BioTools, Inc. [15].

VCD spectra of neat enantiomers can be measured in just a few minutes. For example, the VCD spectrum of (*S*)-(-)- $\alpha$ -pinene as a neat liquid in a  $73\text{-}\mu\text{m}$  cell is shown in Figure 12.5 along with the VCD noise measured as the half-difference between two spectral blocks (above) and the absorbance spectrum of (*S*)-(-)- $\alpha$ -pinene (below). The data acquisition for the VCD spectra of each enantiomer was 20 minutes.

Measurement of samples in solution, especially aqueous solution, is more challenging. Corresponding data to Figure 12.5 is shown for an acidified aqueous solution of L-valine at a concentration of  $250\text{ mg} \cdot \text{mL}^{-1}$  in a  $12\text{-}\mu\text{m}$  cell is shown in Figure 12.6. The acquisition time for this spectrum was 1 hour. Some chiral molecules give rise to a far stronger VCD spectrum than others. Whereas the peak absorbance of  $\alpha$ -pinene in the region shown in Figure 12.5 is only twice as large as that of (*S*)-methyl lactate in Figure 12.6, its VCD spectrum is a factor of 10 larger.

Just a few years ago, one could count the number of scientists making measurements of VCD spectra on the fingers of one hand, and all of these workers were located in academic laboratories. The state of the art of VCD spectrometry has now advanced to the point that it is being used routinely by a far greater number of biochemists and pharmaceutical chemists. VCD spectra of peptides and proteins



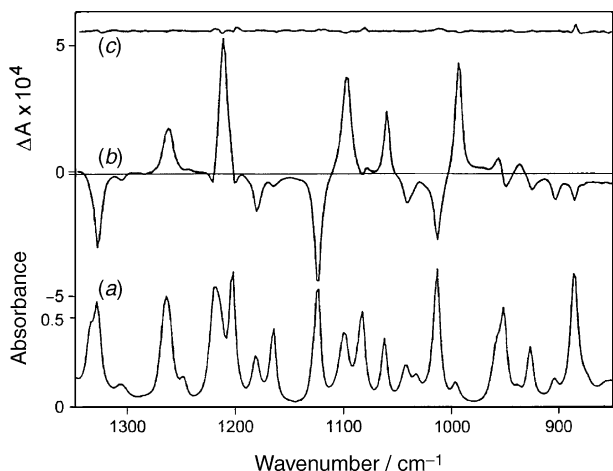


**Figure 12.5.** (a) Absorbance spectrum of (*S*)-(-)- $\alpha$ -pinene as a neat liquid in a 73- $\mu\text{m}$  cell; (b) VCD spectrum of the same compound measured in 20 min; (c) VCD noise spectrum measured with no sample in the beam. (Reproduced from [10], by permission of John Wiley & Sons; copyright © 2000.)

[16–18], nucleic acids [19,20], and carbohydrates [21,22] have all been reported. The calculation of VCD spectra has advanced to the point that the absolute configuration of molecules with fewer than 30 heavy atoms can now be determined with good certainty by matching measured spectra with spectra calculated for each

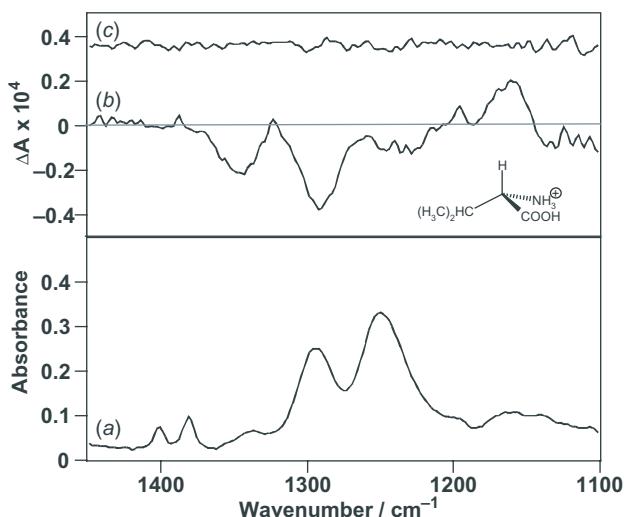


**Figure 12.6.** (a) Absorbance spectrum of acidified aqueous solution of L-valine at a concentration of 250  $\text{mg} \cdot \text{mL}^{-1}$  in a 12- $\mu\text{m}$  cell; (b) VCD spectrum of the same compound measured in 20 min; (c) VCD noise spectrum measured with no sample in the beam. (Reproduced from [10], by permission of John Wiley & Sons; copyright © 2000.)

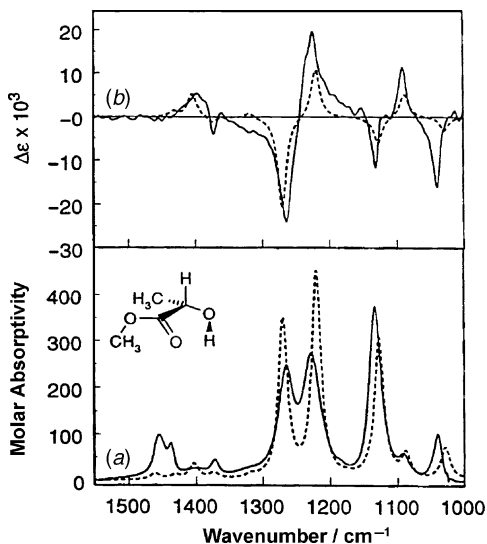


**Figure 12.7.** Calculated (dashed line) and measured (solid line) spectra of (*S*)-methyl lactate: (a) absorbance; (b) VCD spectra. (Reproduced from [26], by permission of Marcel Dekker, Inc.; copyright © 2001.)

configuration, as shown by the spectra in Figure 12.7. The corresponding calculations for quite complex pharmaceuticals have now advanced to the point that their absolute configuration at several chiral centers has been determined directly from their solution-phase VCD spectra [23–26]. Furthermore, the photometric precision of VCD spectrometry is now high enough that the relative concentration of two enantiomers (known as the enantiomeric excess, ee) can be determined with a standard deviation of about 2% [27–29]. For ee calculations, spectra must be very repeatable from scan to scan. To illustrate the repeatability of VCD at the state of the art in 2004, 12 spectra of (*S*)-(-)- $\alpha$ -pinene are superimposed in Figure 12.8.

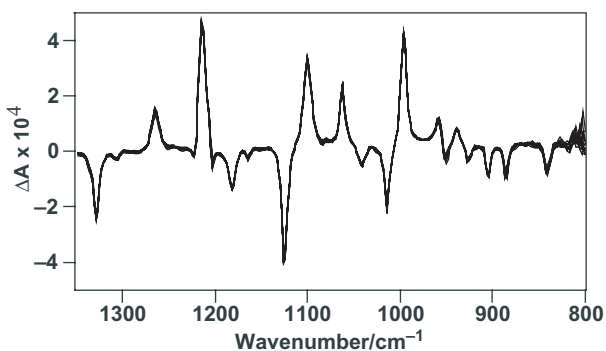


**Figure 12.8.** Superposition of 12 VCD spectra of (*S*)-(-)- $\alpha$ -pinene; the data acquisition time for each spectrum was 20 min of collection time per measurement. Three superimposed VCD spectra of (*S*)-(-)- $\alpha$ -pinene measured under the same conditions as in Figure 12.6. (Reproduced from [10], by permission of John Wiley & Sons; copyright © 2000.)

It is probably true to say that the efforts of four academic research groups (led by Philip Stephens, Larry Nafie, Tim Keiderling, and Prasad Polavarapu) have led to most of the seminal developments of VCD instrumentation. In particular, the work of Larry Nafie, along with his colleagues Teresa Freedman and Rina Dukor, has taken VCD from what 10 years ago may have seemed to others to be a rather arcane field of academic research to the point that it now can be forecast to play a vital role in pharmaceutical and biochemical analysis.

## REFERENCES

1. M. Billardon and J. Badoz, *Compt. Rend. Ser. A* **263B**, 139 (1966).
2. J. C. Kemp, *J. Opt. Soc. Am.* **59**, 950 (1969).
3. C. Pellerin, M.-E. Rousseau, R. E. Prud'homme, and M. Pézolet, *Appl. Spectrosc.* **56**, 17 (2002).
4. R. Ikeda, D. B. Chase, and N. J. Everall, Basics of orientation measurements in infrared and Raman spectroscopy, in *Handbook of Vibrational Spectroscopy*, J. M. Chalmers and P. R. Griffiths, Eds., Wiley, Chichester, West Sussex, England, 2002, Vol. 1, p. 716.
5. C. Pellerin, R. E. Prud'homme, M. Pezolet, B. A. Weinstock, and P. R. Griffiths, *Macromolecules* **36**, 4838 (2003).
6. L. A. Nafie and D. W. Vidrine, Double modulation Fourier transform spectroscopy, in *Fourier Transform Infrared Spectroscopy: Techniques Using Fourier Transform Interferometry*, J. R. Ferraro and L. J. Basile, Eds., Academic Press, Orlando, FL, 1982, Vol. 3, p. 83.
7. L. A. Nafie, M. Diem, and D. W. Vidrine, *J. Am. Chem. Soc.* **101**, 496 (1979).
8. P. L. Polavarapu, Fourier transform infrared vibrational circular dichroism, in *Fourier Transform Infrared Spectroscopy: Applications to Chemical Systems*, J. R. Ferraro and L. J. Basile, Eds., Academic Press, Orlando, FL, 1985, Vol. 4, p. 61.
9. C. A. McCoy and J. A. de Haseth, *Appl. Spectrosc.* **42**, 336 (1988).
10. R. K. Dukor and L. A. Nafie, Vibrational optical activity of pharmaceuticals and biomolecules, in *Encyclopedia of Analytical Chemistry: Instrumentation and Applications*, R. A. Myers, Ed., Wiley, Chichester, West Sussex, England, 2000, p. 662.
11. L. A. Nafie, R. K. Dukor, and T. B. Freedman, Vibrational circular dichroism, in *Handbook of Vibrational Spectroscopy*, J. M. Chalmers and P. R. Griffiths, Eds., Wiley, Chichester, West Sussex, England, 2002, Vol. 1, p. 731.
12. L. A. Nafie and R. K. Dukor, The use of dual polarization modulation in vibrational circular dichroism spectroscopy, in *Chirality: Physical Chemistry*, J. M. Hicks, Ed., American Chemical Society, Washington, DC, 2002, Vol. 810, p. 79.
13. L. A. Nafie, H. Buijs, A. Rilling, X. Cao, and R. K. Dukor, *Appl. Spectrosc.* **58**, 647 (2004).
14. X. Cao, R. D. Shah, R. K. Dukor, C. Guo, T. B. Freedman, and L. A. Nafie, *Appl. Spectrosc.* **58**, 1057 (2004).
15. BioTools, Inc., 17546 SR 710 (Bee Line Hwy), Jupiter, FL 33458.
16. C. Zhao, P. L. Polavarapu, C. Das, and P. Balaram, *J. Am. Chem. Soc.* **122**, 8228 (2000).

17. F. Eker, K. Griebenow, X. Cao, L. A. Nafie, and R. Schweitzer-Stenner, *Proc. Natl. Acad. Sci. USA* **101**, 10054 (2004); erratum: **101**, 12777 (2004).
18. R. Mahalakshmi, G. Shanmugam, P. L. Polavarapu, and P. Balaram, *ChemBioChem* **6**, 2152 (2005).
19. L. Wang, L. Yang, and T. A. Keiderling, *Biophys. J.* **67**, 2460 (1994).
20. B. D. Self and D. S. Moore, *Biophys. J.* **74**, 2249 (1998).
21. P. K. Bose and P. L. Polavarapu, *Carbohydr. Res.* **322**, 135 (1999).
22. P. K. Bose and P. L. Polavarapu, *Carbohydr. Res.* **319**, 172 (1999).
23. A. B. Dyatkin, T. B. Freedman, X. Cao, R. K. Dukor, B. E. Maryanoff, C. A. Maryanoff, J. M. Matthews, R. D. Shah, and L. A. Nafie, *Chirality* **14**, 215 (2002).
24. T. B. Freedman, X. Cao, R. K. Dukor, and L. A. Nafie, *Chirality* **15**, 743 (2003).
25. T. B. Freedman, X. Cao, R. V. Oliveira, Q. B. Cass, and L. A. Nafie, *Chirality* **15**, 196 (2003).
26. L. A. Nafie and T. B. Freedman, Biological and pharmaceutical applications of vibrational optical activity, in *Infrared and Raman Spectroscopy of Biological Materials*, H.-U. Gremlich and B. Yan, Eds., Marcel Dekker, New York, 2001, p. 15.
27. C. Guo, R. D. Shah, R. K. Dukor, X. Cao, T. B. Freedman, and L. A. Nafie, *Anal. Chem.* **76**, 6956 (2004).
28. C. Guo, R. D. Shah, R. K. Dukor, X. Cao, T. B. Freedman, and L. A. Nafie, *Appl. Spectrosc.* **59**, 1114 (2005).
29. D. Dunmire, T. B. Freedman, L. A. Nafie, C. Aeschlimann, J. G. Gerber, and J. Gal, *Chirality* **17**(Suppl.) (2005).



## Chapter 13

# SPECULAR REFLECTION

### 13.1. INTRODUCTION

Reflection from the surface of any flat material, where the angle of reflection is equal to the angle of incidence, is known as *specular reflection*. In infrared spectrometry, three cases of specular reflection may be distinguished. When the reflective surface is a bulk material, the reflection spectrum is governed by the Fresnel equations; as a result, this type of reflection has been called *Fresnel reflection*. When a layer of material is present on a flat reflective surface (usually, a metal), the reflection spectrum is no longer governed directly by the Fresnel equations. Instead, the nature of the reflection spectrum depends on the thickness of the layer,  $d$ . If  $d$  is much less than the wavelength of the radiation,  $\lambda$ , the measurement is usually called *infrared reflection–absorption spectrometry* (IRRAS). It has also been called *reflection–absorption infrared spectrometry* (RAIRS) and for reasons that we will see in this chapter, *grazing incidence reflection spectrometry*. When  $d \geq \lambda$ , the technique is called *transflection spectrometry*. Reflection spectrometry of bulk samples and thin and thick layers on metallic and other substrates are all covered in this chapter.

### 13.2. FRESNEL REFLECTION FROM BULK SAMPLES

#### 13.2.1. Fresnel Equations

Reflection occurs at any interface where the complex refractive index changes. We can define the medium with the lower refractive index as the *optically rare* medium and material with the higher refractive index as the *optically dense* medium. The optically dense medium will be designated by the subscript 2 and the optically rare medium will be designated by the subscript 1. We will just consider the case where the optically rare medium is a gas or a vacuum, so that the refractive index  $n_1 \sim 1$  and the absorption index  $k_1 \sim 0$ . In this case, the reflectance at the interface depends on the optical constants of the optically dense medium,  $n_2$  and  $k_2$ , the angle

of incidence,  $\theta$ , and the polarization of the radiation with respect to the plane of incidence (i.e., the plane that contains the incident and reflected beam).

The reflectance from the first surface of any flat material is governed by the Fresnel equations. The reflectance of radiation whose electric field is polarized parallel ( $R_p$ ) and perpendicular ( $R_s$ ) to the plane of incidence is given, respectively, by the following expressions:

$$R_p = \frac{\tan^2(\theta - \theta')}{\tan^2(\theta + \theta')} \quad (13.1)$$

$$R_s = \frac{\sin^2(\theta - \theta')}{\sin^2(\theta + \theta')} \quad (13.2)$$

where  $\theta'$  is the angle of refraction inside the material. It should be noted that because of reflections from the inside surface, the actual reflectance is greater than the reflectance calculated by Eqs. 3.1 and 2.3.

### 13.2.2. Nonabsorbing Materials

If the optically rare medium is a gas or a vacuum ( $n_1 \sim 1, k_1 \sim 0$ ), Snell's law gives  $\theta'$  as

$$\theta' = \sin^{-1} \frac{\sin \theta}{n_2} \quad (13.3)$$

When  $\theta \sim 0^\circ$  (normal incidence),  $\sin \theta \sim \tan \theta$  and a plane of polarization cannot be defined; thus,  $R_p = R_s$ . For nonabsorbing materials ( $k_2 \sim 0$ ), the reflectance for normal incidence is given simply as

$$R_p = R_s = \frac{(n_2 - 1)^2}{(n_2 + 1)^2} \quad (13.4)$$

The refractive index of many condensed-phase materials, including the alkali halides and most organic solids and liquids in regions of weak absorption, is approximately 1.5. In this case the reflectance at normal incidence is 0.04 (i.e., about 4%). As  $n_2$  is increased, the reflectance increases concomitantly. For germanium, for which  $n_2 = 4$ , the reflectance is much higher (36%). The variation of reflectance with  $\theta$  for these dielectric materials (materials for which  $n > 1$  and  $k = 0$ ) is significantly different for  $p$ - and  $s$ -polarized radiation, as shown in Figure 13.1. The reflectance for  $s$ -polarized radiation increases monotonically from  $\theta = 0^\circ$  (normal incidence) to  $\theta = 90^\circ$  (grazing incidence). On the other hand,  $R_p$  slowly decreases and has a value of zero at *Brewster's angle*,  $\theta_B$ , given by  $\theta_B = \tan^{-1} n$ .  $R_p$  then increases rapidly, until the material becomes totally reflective at  $\theta = 90^\circ$ .

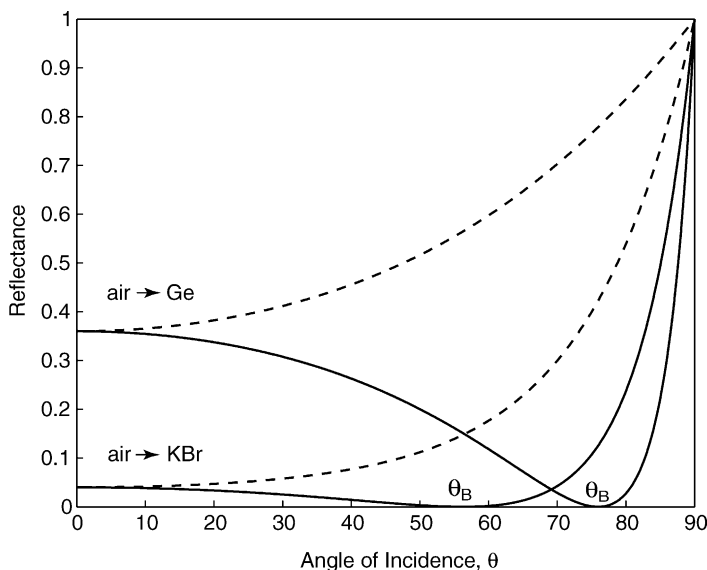


**Figure 13.1.** Variation of reflectance with incidence angle for two dielectric materials, potassium bromide ( $n = 1.5$ ) and germanium ( $n = 4.0$ ). Solid line is for  $p$ -polarized radiation and broken line is for  $s$ -polarization.

### 13.2.3. Absorbing Materials

When  $k \neq 0$ , the reflectance at normal incidence is given by the Fresnel equations as

$$R_p = R_s = \frac{(n_2 - 1)^2 + k_2^2}{(n_2 + 1)^2 + k_2^2} \quad (13.5)$$

It should be remembered that the refractive index varies with wavelength across an absorption band (see, e.g., Figure 1.4 and 13.19). When  $k_2$  is greater than 1, as it is near the maximum of strong bands in the spectrum of most inorganic salts containing oxyanions (nitrates, carbonates, sulfates, phosphates, etc.),  $k_2^2$  is usually much greater than either  $(n_2 - 1)^2$  or  $(n_2 + 1)^2$ . In such cases, the reflectance approaches unity. These very strong bands in reflection spectra are known as *reststrahlen* bands (German for residual rays).

On the other hand, the maximum absorption index of bands in the spectra of most *organic molecules* (including polymers) rarely exceeds 0.3 above  $\sim 1000 \text{ cm}^{-1}$ . In these cases,  $(n_2 - 1)^2 > k_2^2$ , and the reflection spectrum looks more like the  $n$  spectrum (see Figure 1.4b) than the  $k$  spectrum. The specular reflection spectrum of a polycarbonate polymer is shown in Figure 13.2. Few experienced spectroscopists would immediately recognize this spectrum as a polycarbonate. To convert this spectrum to the optical constant ( $n$  and  $k$ ) spectra, the *Kramers–Kronig*



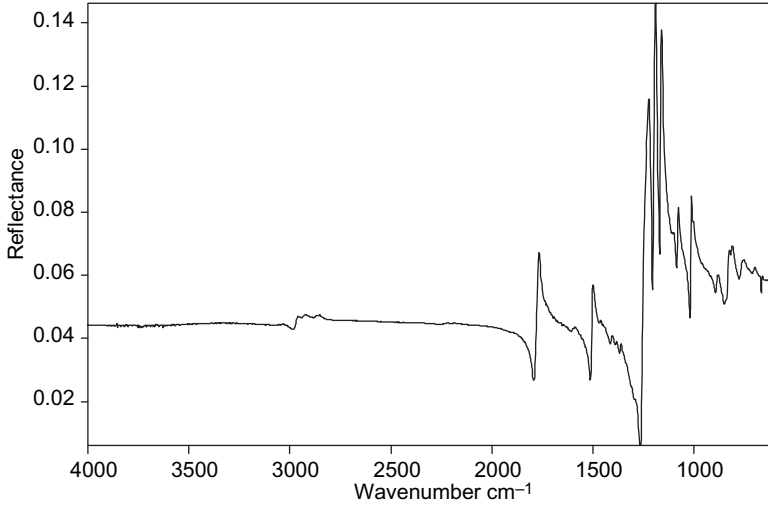


**Figure 13.2.** Specular reflection spectrum of a polycarbonate sheet.

*transform* must be carried out. Here, a model absorption spectrum is synthesized using the following antisymmetric linear combination of Lorentzian functions:

$$k_2 = \frac{k_{2,\max}\chi^2}{(\tilde{\nu} - \tilde{\nu}_0)^2 + \chi^2} - \frac{k_{2,\max}\chi^2}{(\tilde{\nu} + \tilde{\nu}_0)^2 + \chi^2} \quad (13.6)$$

where  $k_{2,\max}$  is the maximum value of  $k_2$ ,  $\tilde{\nu}_0$  is the wavenumber of maximum absorption, and  $\chi$  is the half-width at half-height ( $0.5\gamma$  in Eq. 1.13). For fundamental vibrations,  $k_2$  is dominated by the first term, and the second term is usually neglected. Nonetheless, the presence of the second term makes it possible to calculate the corresponding refractive index spectrum using the following equation:

$$n_2 = n_{2,\infty} - \frac{(\tilde{\nu} - \tilde{\nu}_0) k_{2,\max}\chi}{(\tilde{\nu} - \tilde{\nu}_0)^2 + \chi^2} + \frac{(\tilde{\nu} + \tilde{\nu}_0) k_{2,\max}\chi}{(\tilde{\nu} + \tilde{\nu}_0)^2 + \chi^2} \quad (13.7)$$

where  $n_{2,\infty}$  is the refractive index at infinite wavenumber. It can be shown that the optical constants generated by these equations satisfy the *Kramers–Kronig relations*:

$$n_2(\tilde{\nu}) = n_\infty + \frac{2}{\pi} P \int_0^\infty \frac{sk_2(s)}{s^2 - \tilde{\nu}^2} ds \quad (13.8)$$

$$k_2(\tilde{\nu}) = \frac{2\tilde{\nu}}{\pi} P \int_0^\infty \frac{n_2(s)^2}{s^2 - \tilde{\nu}^2} ds \quad (13.9)$$

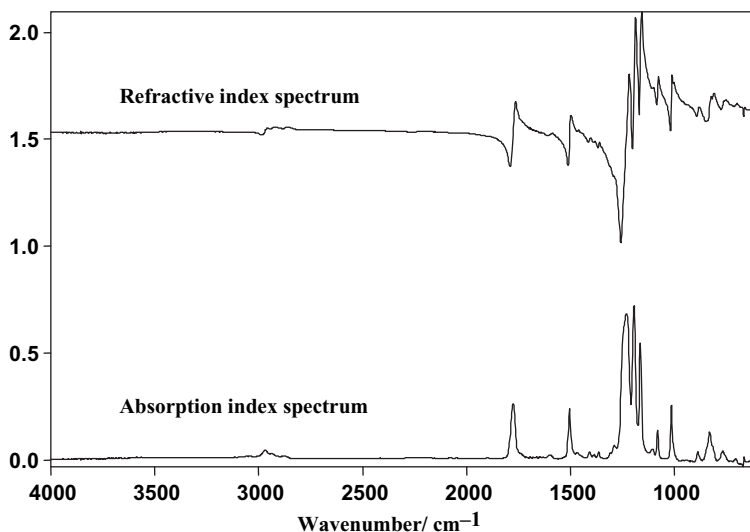


**Figure 13.3.** Refractive index and absorption index spectra calculated from the spectra shown in Figure 13.2.

where  $P$  is the principal value of the integral and  $s$  and  $\tilde{\nu}$  are wavenumbers. Programs to carry out these operations are installed in the software of most modern FT-IR spectrometers. The  $n$  and  $k$  spectra calculated from the specular reflection spectrum of the sheet of polycarbonate shown in Figure 13.2 are shown in Figure 13.3.

It should be remembered from Eq. 1.21 that  $k(\tilde{\nu}) = \alpha(\tilde{\nu})/4\pi\tilde{\nu}$ . Thus, to obtain the absorptivity spectrum or to match a measured absorbance spectrum measured by transmission, the  $k(\tilde{\nu})$  spectrum calculated from the Kramers–Kronig transform should be multiplied by the wavenumber at each point in the spectrum and then scaled appropriately.

Measurement of the Fresnel reflectance spectrum is a very useful way of obtaining the spectrum of solids with flat surfaces when sample preparation is not possible. For example, to measure the spectrum of an oriented polymer, the sample cannot be melted, dissolved, or finely ground. A microscopic sample of a hard polymer may be available that is too thick for transmission spectrometry. If the sample is so hard, rough, and/or thick that a good transmission or attenuated total reflection (see Chapter 15) spectrum cannot be measured, Fresnel reflection spectrometry presents a very useful means of obtaining the spectrum.

One note of caution should be sounded. If radiation is scattered from the interior of the sample, as might be the case because of the presence of a filler in the bulk of the sample, diffuse reflection (see Chapter 16) will take place along with the Fresnel reflection. In this case, the Kramers–Kronig transform will not yield an accurate estimate of the  $n$  and  $k$  spectra. One indication that diffuse reflection is contributing to the spectrum is that the bands in the  $k$  spectrum calculated from a given reflection spectrum are asymmetric.

### 13.3. INFRARED REFLECTION–ABSORPTION SPECTROMETRY WITH METAL SUBSTRATES

#### 13.3.1. Effect of Incidence Angle and Polarization

Consider the case of radiation being reflected at normal incidence from a metal surface with a monolayer film of an absorbing material on its surface. The beam passes through this film, is reflected from the metal, and passes back through the film. For a film of thickness  $x$  nanometers, we might expect the absorbance in the reflection–absorption spectrum measured at an incidence angle of  $\theta$  to be equal to  $2x/\cos \theta$ . If we assume that the thickness of a typical monolayer is  $\sim 0.5$  nm, and bearing in mind the rule of thumb given in Chapter 1 that strong bands in the spectrum of a  $10\text{-}\mu\text{m}$  film should have a peak absorbance of about 1 AU, we would expect strong bands in the reflection–absorption spectrum of a  $0.5\text{-nm}$ -thick film (i.e., a monolayer) to be about  $10^{-4}$  AU when measured at normal incidence. Although weak, the stronger bands in the spectrum of this film should still be measurable on a standard FT-IR spectrometer, where a baseline noise level of less than  $10^{-5}$  AU should be achievable by signal averaging a few hundred scans. In practice, however, the situation is far less favorable.

When electromagnetic radiation is reflected from a metal, the electric vector experiences a phase change  $\delta$  that depends on both the angle of incidence,  $\theta$ , and the state of polarization. Whereas the change in phase angle of  $s$ -polarized radiation (see Section 12.1) is approximately constant at  $180^\circ$ , this is not the case for  $p$ -polarized light. Several monographs [1,2] show that for  $s$ -polarized radiation,  $\delta$  varies with incidence angle in the manner shown in Figure 13.4a. This cannot be the

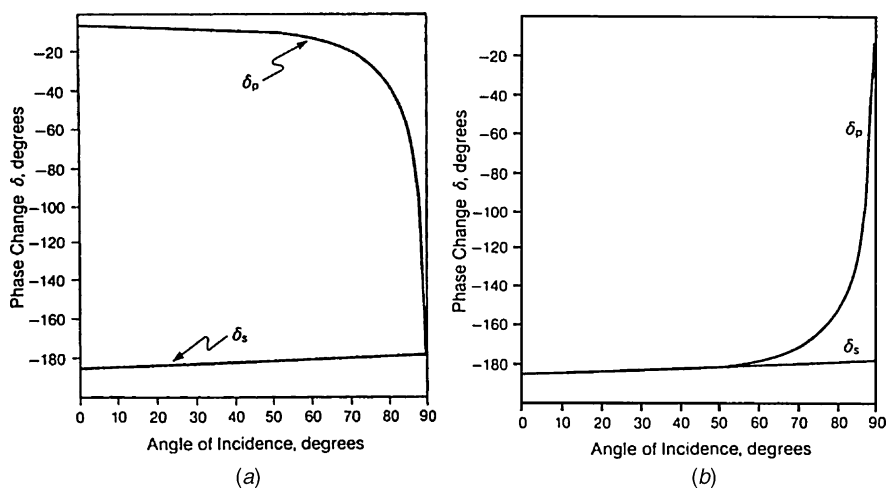


**Figure 13.4.** Variation of the phase change,  $\delta$ , of a beam reflected from a metal surface as a function of the angle of incidence,  $\theta$ , for  $p$ - and  $s$ -polarized radiation: (a) as shown in [1] and [2]; (b) as calculated using the appropriate formalism.

case, however, because a plane of polarization cannot be defined at normal incidence, so that  $\delta$  must change by the same amount for *s*- and *p*-polarized light. The solution to this problem was discovered by Milosevic [3], who found that change in sign of the amplitude reflectance used, for example, by Born and Wolf [4] or Jackson [5] led to the behavior shown in Figure 13.4*a* being calculated. When the formalism used by Feynman [6] was used, the behavior shown in Figure 13.4*b* is calculated. Since the value of  $\delta$  when  $\theta = 0^\circ$  must be the same for *s*- and *p*-polarized radiation, this behavior is obviously correct.

When the incident radiation undergoes a phase change of  $180^\circ$ , as it does when  $\theta = 0^\circ$ , there is destructive interference at the surface of the metal, and the intensity of the electric field due to the electromagnetic radiation is zero. Thus, a film of an absorbing material at the metal surface that is much thinner than the wavelength of the radiation cannot interact with the electric field of the incident radiation and will not absorb any light. As  $\theta$  is increased, the phase shifts for *s*- and *p*-polarized radiation behave in very different manners. For *s*-polarized light,  $\delta$  remains at  $\sim 180^\circ$  and the electric vectors of the incident and reflected rays interfere destructively. Thus, the resulting field next to the surface is approximately zero, as shown schematically in Figure 13.5*a*, and *s*-polarized radiation is never absorbed by a very thin film.

This is not the case for *p*-polarized radiation. As  $\theta$  is increased from  $0^\circ$  to  $90^\circ$ ,  $\delta$  changes by  $180^\circ$  (see Figure 13.4*b*). When the incidence angle is  $\sim 87^\circ$ , the phase shift between the incident and reflected beams is  $\sim 90^\circ$ . At this point, the sum of the electric vectors of the incident and reflected beams results in an electric field at the

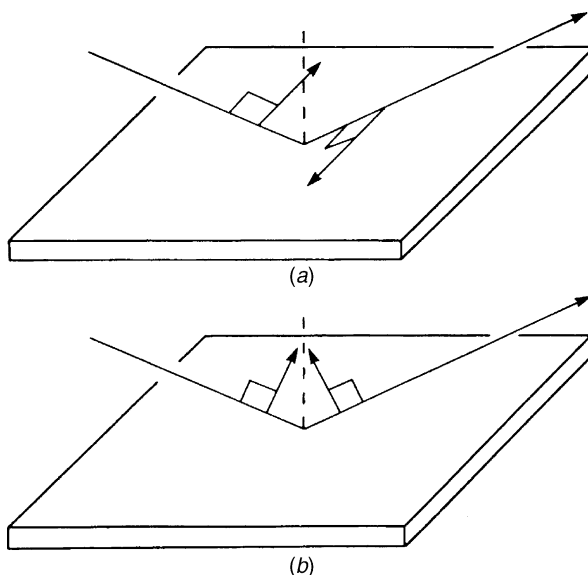


**Figure 13.5.** Vectorial addition of beams with (a)  $\delta = 180^\circ$  (b) and  $\delta = 90^\circ$ . (Reproduced from [7], by permission of the American Chemical Society; copyright © 1984.)

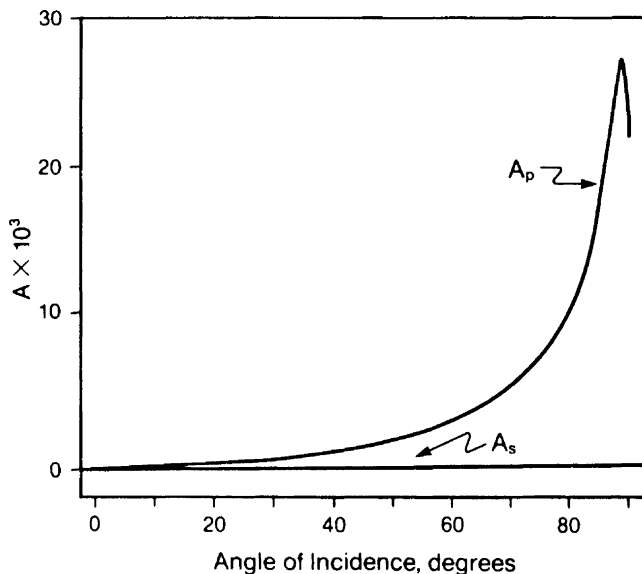


**Figure 13.6.** Variation of absorbance of a thin film as a function of incidence angle, measured with *p*- and *s*-polarized radiation. (Reproduced from [2], by permission of Academic Press; copyright © 1985.)

surface with a large component perpendicular to the surface normal (see Figure 13.5*b*). Because intensity is proportional to the square of the electric field amplitude, there is an enhancement of the field intensity near the surface of nearly four times the incident field intensity [8].

In summary, the absorbance of *p*-polarized light by surface species increases with the angle of incidence, reaching a maximum value at an angle of about 87° (see Figure 13.6). Spectra of a 1-nm-thick film of acetone on gold are shown as a function of the angle of incidence in Figure 13.7. The advantage of measuring the spectrum at close to grazing incidence is very obvious from these data. In principle at least, the spectra of thin films on metal surfaces should therefore always be measured with *p*-polarized radiation with the incidence angle approaching 87°.

In practice, it is rarely possible to measure IRRAS spectra with  $\theta$  much above 80°, even though several workers have claimed to use angles close to 87°. The beam in the sample compartment of a typical FT-IR spectrometer has a cone half-angle of about 6°, and the diameter of the focused beam is about 6 mm. Thus, even if the angle of incidence for this beam is 84°, the angles of incidence for the two extreme rays will be ~90° and 78°. The beam focus as projected on the sample under these conditions is elliptical, with the length being about  $6/\cos 84^\circ$  mm, or 5.7 cm. (The width is still 6 mm.) It is quite rare that samples this large are available, especially if one is interested in IRRAS spectrometry from defined crystal faces. Fortunately, even when the angle of incidence is only 75°, the absorbance of the analyte is not too far from its optimum value (see Figure 13.6), and the beam size is much smaller (2.3 cm for the example used above). By reducing the diameter of the J-stop, the beam size can be reduced further, albeit at the cost of the signal-to-noise ratio.

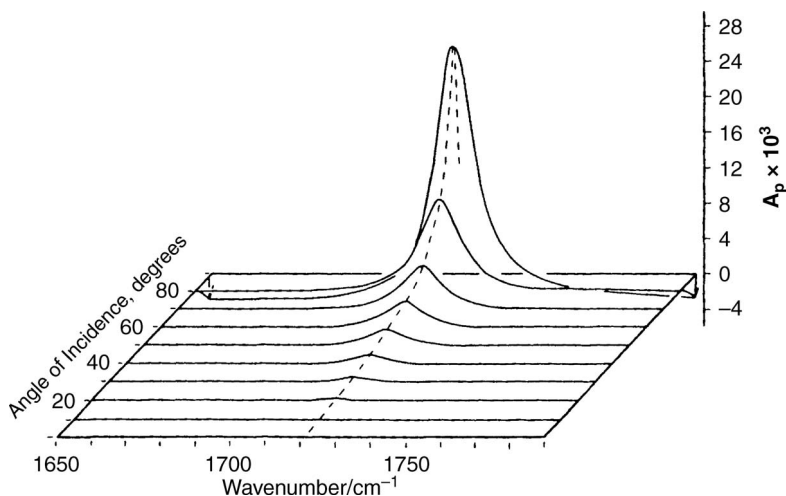


**Figure 13.7.** IRRAS spectra of a 1-nm-thick film of acetone on gold as a function of the angle of incidence. (Reproduced from [2], by permission of Academic Press; copyright © 1985.)

It is interesting to consider what would happen to the SNR of an IRRAS spectrum if the measurement were made with unpolarized light. When the beam of an FT-IR spectrometer is passed through a wire-grid polarizer oriented to transmit *p*- or *s*-polarized radiation, the ratio of a single-beam spectrum measured in this way to the single-beam spectrum measured without a polarizer is about 30%. The noise level on the baseline of a spectrum measured at a certain resolution with a certain number of scans with the polarizer in place would therefore be about three times higher than for the baseline of the corresponding spectrum measured without a polarizer. The absorbance of a thin film on the surface of a metal when measured at approximately grazing incidence with unpolarized radiation is one-half of the absorbance of the same film measured with *p*-polarized light. Thus, the SNR of an IRRAS spectrum measured without a polarizer should actually be higher than the corresponding spectrum measured with *p*-polarized radiation. It would, therefore, appear logical that IRRAS spectra are better measured with unpolarized radiation than with *p*-polarized light.

In practice, IRRAS spectra are almost invariably measured with *p*-polarized radiation. Because IRRAS spectra are usually so weak, the noise on the spectral baseline should be no greater than  $\sim 1 \times 10^{-5}$  AU (10  $\mu$ AU). To achieve this performance in a reasonable time, the measurement should be made with an MCT detector. However, so little radiation is lost in an IRRAS measurement that the power at the detector is very high. Under these conditions, the response of MCT detectors is usually highly nonlinear so that not only do photometrically inaccurate spectra result (see Section 8.6.1) but the SNR may be limited by digitization noise rather than detector noise (see Section 7.3). It is therefore necessary to attenuate the beam before making the measurement. It is far more efficient to attenuate the beam with a polarizer than with a screen or an iris because not only is the signal reduced

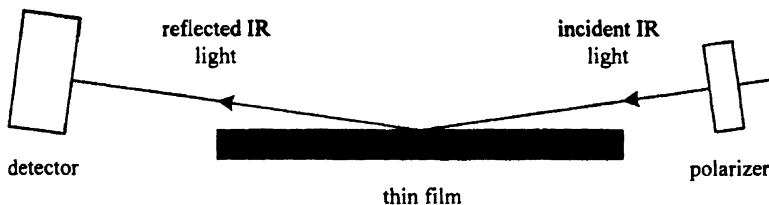


**Figure 13.8.** Typical optics for the measurement of IRRAS spectra at grazing incidence. (Reproduced from [9], by permission of Wiley-Interscience; copyright © 1998.)

by a factor of  $\sim 3$  (reducing the effect of detector/amplifier nonlinearity), but the intensity of the absorption bands of the thin film doubles with respect to the same measurement made with unpolarized light.

There are two types of specular reflection accessory suitable for measuring IRRAS spectra of thin films. The first is a simple device that has no focusing mirrors and affords a constant incidence angle of about  $80^\circ$ ; an optical schematic of a typical accessory of this type is shown in Figure 13.8. Alternatively, a variable angle accessory of the type shown in Figure 13.9 can be used. Such accessories usually have good efficiency to angles of  $70^\circ$  but lose efficiency at higher angles.

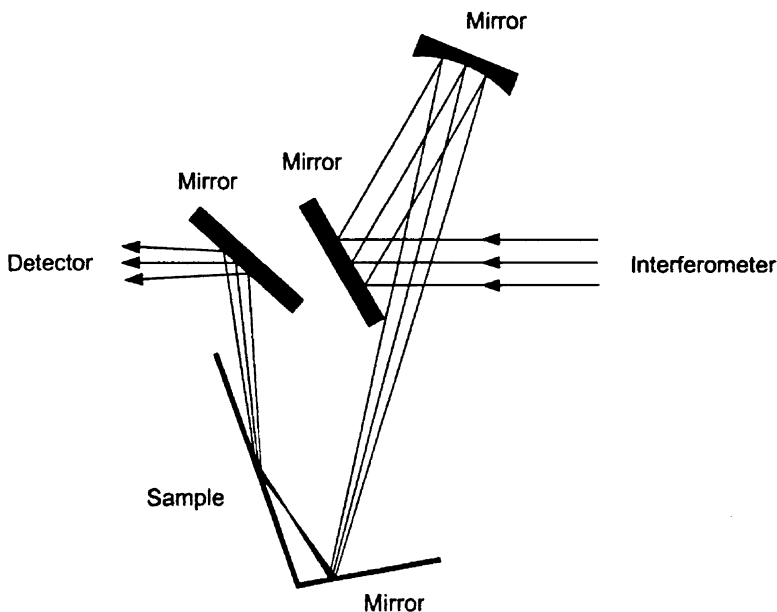


**Figure 13.9.** Optics for measuring specular reflection spectra with varying incidence angles. (Reproduced from [9], by permission of Wiley-Interscience; copyright © 1998.)

### 13.3.2. Polarization Modulation

The fact that only  $p$ -polarized radiation is absorbed by surface species has been applied by a number of workers to circumvent the problem of digitization noise. These workers have used a photoelastic modulator (PEM) configured to modulate the plane of polarization rapidly between  $s$  and  $p$ , as described in Chapter 12. The Fourier frequencies are removed with a high-pass electronic filter so that the only signal is caused by the difference between the absorption of  $p$ - and  $s$ -polarized radiation, which is caused solely by the surface species. A description of the signal processing and computation was given in Section 12.3.

In summary, the spectrum of a surface species can be measured by passing the beam from the interferometer first through a polarizer and then through a PEM. The beam is reflected from the sample at grazing incidence and then focused onto an MCT detector. The signal from the detector is processed by electronics of the type shown schematically in Figure 12.4.

The first report of the measurement of IRRAS spectra on an FT-IR spectrometer in this manner was by Dowrey and Marcott at Procter and Gamble [10], who used the simple optical configuration shown in Figure 13.10. They reported spectra of a 1-nm thick film of cellulose acetate on a copper slide measured both by the conventional approach and through the application of polarization modulation. These spectra are shown in Figure 13.11. At first glance, the spectrum measured by polarization modulation appears to have a significantly better SNR than the conventionally measured spectrum. However, most of the differences between these two spectra can be ascribed to the elimination of small interferences caused by uncompensated atmospheric water lines. Certainly, the use of a PEM reduces the effect of atmospheric interferences considerably and represents an important reason for using this technique. If one examines the spectra in Figure 13.11 in regions where water vapor does not absorb, however, the SNR of the two spectra is comparable. For polarization modulation to give a definite advantage in practice, the effect of digitization noise or atmospheric interference must be dominant. The polarizer and PEM cause the beam from the interferometer to be attenuated by a factor of

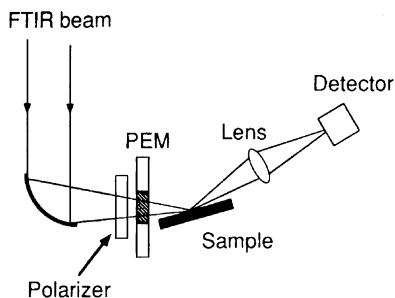


**Figure 13.10.** Optics for IRRAS using a photoelastic modulator reported by Dowrey and Marcott. (Reproduced from [10], by permission of the Society for Applied Spectroscopy; copyright © 1982.)



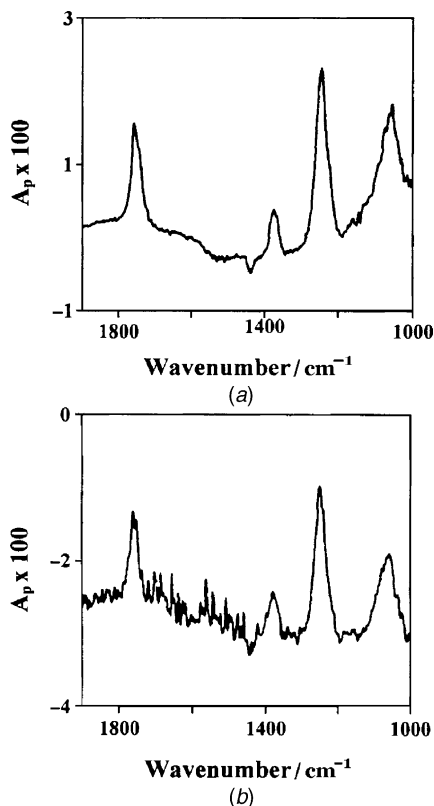


**Figure 13.11.** IRRAS spectra of a 1-nm-thick film of cellulose acetate reported by Dowrey and Marcott: (a) measured using a PEM; (b) measured in the conventional manner with *p*-polarized radiation but no PEM. (Reproduced from [10], by permission of the Society for Applied Spectroscopy; copyright © 1982.)

at least 4. Thus, in cases where the efficiency of the other optics is very high, the use of a PEM may well be beneficial since the SNR is still limited by digitization noise when an MCT detector is used for the measurement. When the optics cause further reduction of the signal by at least a factor of 2, there will probably be little advantage to using polarization modulation because, even with an MCT detector, the SNR should not be limited by the dynamic range of the ADC. In summary, when the optics are very efficient, the polarization-modulation technique can double the SNR that can be achieved for IRRAS measurements in a given time.

In the usual manifestation of this experiment, the velocity of the interferometer mirror must be low enough that the conventional interferogram can be filtered out before the signal is input to the lock-in amplifier. In addition, the amplitude of the PEM must be set at a certain value, so that for only one wavelength in the spectrum is the polarization of the output radiation at the extreme of the cycle rotated by exactly 90°. A method of performing polarization-modulation IRRAS

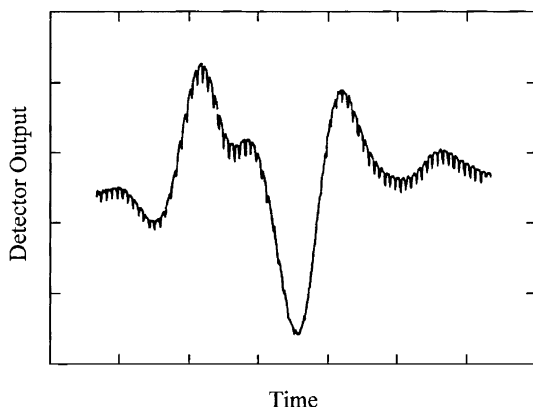


**Figure 13.12.** Region of a measured interferogram when linearly polarized was passed through a PEM and then reflected at grazing incidence from a 15-nm polyimide film on a metallic substrate. (Reproduced from [11], by permission of the American Chemical Society; copyright © 1991.)

measurements that circumvents these drawbacks has been described by Barner et al. [11]. Real-time sampling electronics were designed to measure the interferogram at  $0^\circ$  and  $90^\circ$  during each modulation cycle of the PEM with the optical velocity of the interferometer mirror set at  $\sim 2 \text{ cm}\cdot\text{s}^{-1}$ . A portion of the interferogram is shown in Figure 13.12.

The simultaneous measurement of  $I_p$  and  $I_s$  is performed by the quadratic approximation method depicted in Figure 13.13. When  $\gamma t = 90^\circ (\pi/2 \text{ radians})$ ,

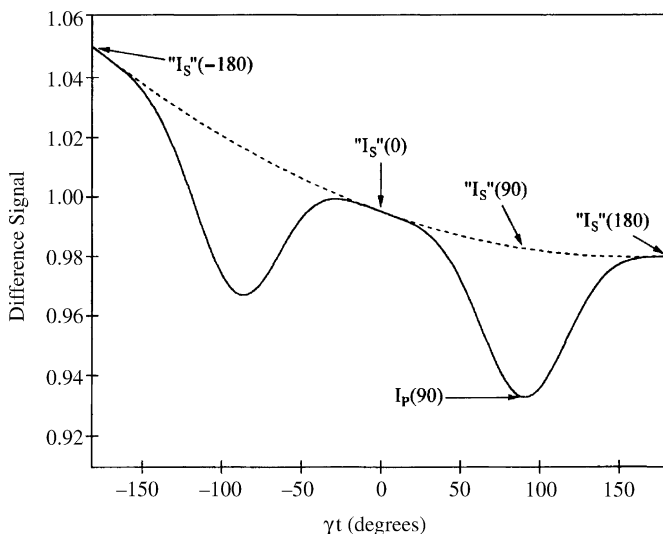


**Figure 13.13.** Expanded region of the interferogram shown in Figure 13.12 to demonstrate how the intensity is calculated at different phase retardations. (Reproduced from [11], by permission of the American Chemical Society; copyright © 1991.)

the interferogram is sampled to obtain one data point in the  $I_p$  interferogram. The  $I_s$  measurement at  $90^\circ$  is approximated by a Taylor series expansion about  $I_s$  at  $0^\circ$ :

$$I_s(\gamma t = 90^\circ) \approx I_s(0^\circ) + f' \Delta[\gamma t] + \frac{f'' \Delta[\gamma t]^2}{2} \quad (13.10)$$

where the first and second derivative terms  $f' \Delta[\gamma t]$  and  $f'' \Delta[\gamma t]^2/2$  are obtained from measurements of  $I_s$  at  $-180^\circ$  and  $+180^\circ$ . The real-time sampling electronics generate an average interferogram

$$I_A(\delta) = \frac{I_p(\delta) + I_s(\delta)}{2} \quad (13.11)$$

and a difference interferogram

$$I_D(\delta) = I_p(\delta) - I_s(\delta) \quad (13.12)$$

After appropriate amplification of  $I_D$ , these interferograms are digitized in alternating blocks of mirror scans and then Fourier transformed to yield the two spectra,  $I_A(\tilde{\nu})$  and  $I_D(\tilde{\nu})$ , respectively, as

$$I_A(\tilde{\nu}) = \frac{I_p(\tilde{\nu}) + I_s(\tilde{\nu})}{2} = \langle I(\tilde{\nu}) \rangle + \frac{\Delta I(\tilde{\nu})(1 + \cos \phi_0)}{4} \quad (13.13)$$

$$I_D = \frac{I_p(\tilde{\nu}) - I_s(\tilde{\nu})}{2} = \frac{\langle I(\tilde{\nu}) \rangle - \Delta I(\tilde{\nu})(1 + \cos \phi_0)}{4} \quad (13.14)$$

where  $\Delta I(\tilde{\nu}) \equiv I_p(\tilde{\nu}) - I_s(\tilde{\nu})$  and  $\langle I(\tilde{\nu}) \rangle \equiv [I_p(\tilde{\nu}) + I_s(\tilde{\nu})]/2$ . From these two spectra, the differential reflectance spectrum is calculated:

This equation demonstrates that the true reflectance spectrum  $\Delta I(\tilde{\nu})/\langle I(\tilde{\nu}) \rangle$ , which is equal to  $\Delta R/R$ , is obtained:

$$\frac{\Delta I(\tilde{\nu})}{\langle I(\tilde{\nu}) \rangle} = \frac{\Delta R}{R} = \frac{\{(1 - \cos \phi_0)/2 - [\Delta I(\tilde{\nu})/\langle I(\tilde{\nu}) \rangle] \times (\sin^2 \phi_0)/8\} \Delta I(\tilde{\nu})}{\langle I(\tilde{\nu}) \rangle} \quad (13.15)$$

multiplied by a term that looks like  $(1 - \cos \phi_0)/2$  if  $\Delta I(\tilde{\nu})/\langle I(\tilde{\nu}) \rangle$  is small. Because the phase shift varies linearly with wavenumber, IRRAS spectra measured with a PEM have a sinusoidal background, which must be subtracted from the measured spectrum in order to obtain the IRRAS spectrum of the surface species. Typical results are shown in Figures 13.14 and 13.15.

### 13.3.3. Surface Selection Rule

For a number of reasons the intensity of an IRRAS spectrum of a very thin film is rarely the same as would be calculated from the corresponding transmission spectrum of the bulk analyte. For example, any interaction between the analyte and the

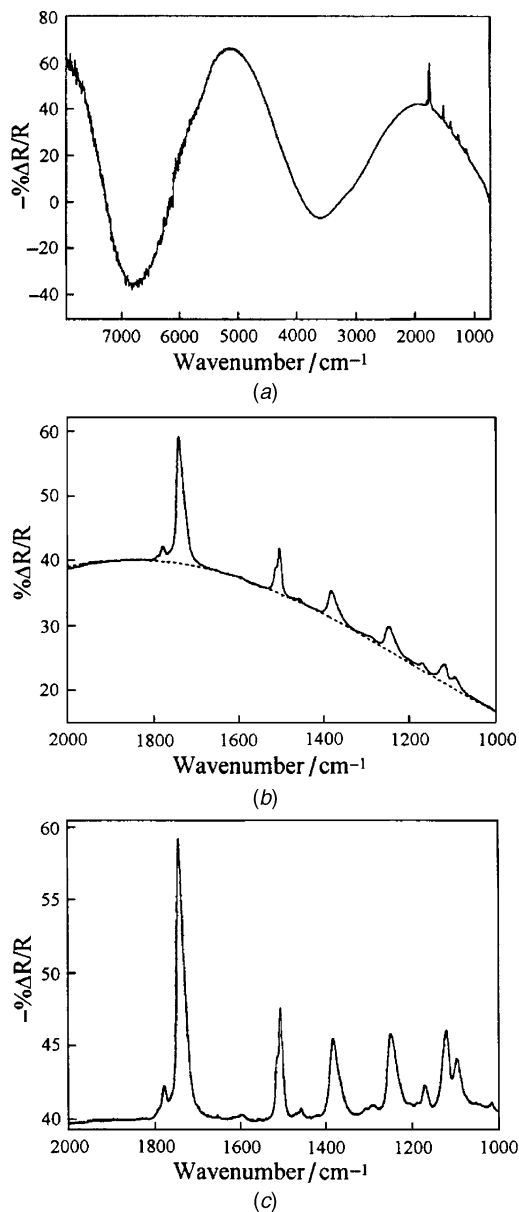


**Figure 13.14.** (a) Full-range IRRAS spectrum measured using the method of Barner et al. [11]; the large change in the amplitude of this spectrum is caused by the fact that *p*-polarized radiation is generated by the PEM only over a narrow range of wavelengths. (b) The region of this spectrum between 2000 and 1000  $\text{cm}^{-1}$ . (c) The same spectrum after baseline correction. (Reproduced from [11], by permission of the American Chemical Society; copyright © 1991.)

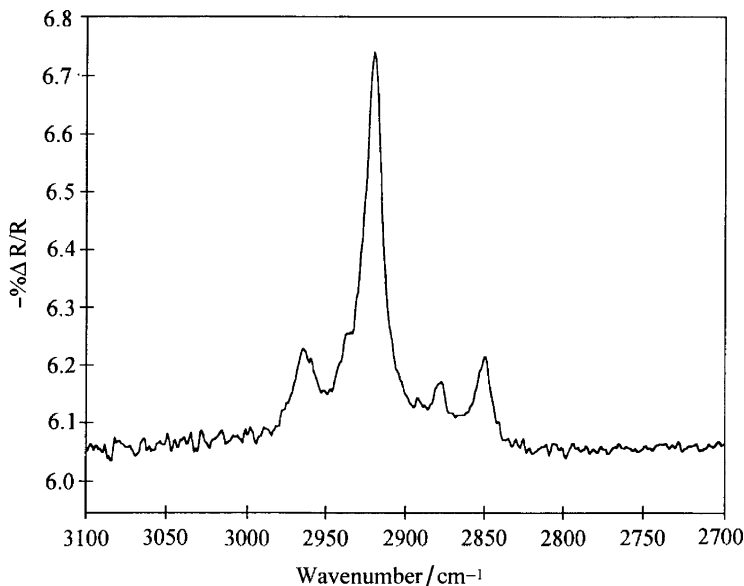


**Figure 13.15.** IRRAS spectrum of a self-assembled monolayer of octadecylthiol on gold measured by the method of Barner et al. (Reproduced from [11], by permission of the American Chemical Society; copyright © 1991.)

metal will change the strength of the bonds involved and hence lead to changes in the frequencies and absorptivities of vibrational modes of the adsorbate. For example, when carbon monoxide adsorbs on a transition metal, the carbonyl stretching mode is usually shifted to a wavenumber that is at least  $100\text{ cm}^{-1}$  below the fundamental frequency of gas-phase CO. In addition, the absorptivity of CO adsorbed on a metal surface is several times greater than the absorptivity of CO in the gas phase.

Besides the changes in wavenumber and absorptivity, which can be explained on chemical grounds, there is one other important difference between the spectra of surface and bulk species. For surface species, only those vibrational modes where the dipole moment derivative,  $\partial\mu/\partial Q$ , has a component in a direction perpendicular to the surface will be seen in an IRRAS spectrum. This phenomenon has been called the *surface selection rule*. It is caused by the fact that a dipole at the surface of a metal will have an image inside the metal at the same distance from the surface. The net dipole moment of the analyte *and its image* must change with the normal coordinate of the vibration for the mode to be seen in an IRRAS spectrum. Consider, for example, two possible orientations of CO chemisorbed to a metal substrate: perpendicular and parallel to the surface. If the adsorbate is parallel to the surface, a positive charge is induced in the metal at the negatively charged end of the molecule, and a negative charge is induced in the metal at the positively charged end of the molecule, as shown schematically in Figure 13.16. The result of these image dipoles is that the dipole moment is always zero and hence there is no change in the overall dipole moment of the molecule and the band is forbidden. On the

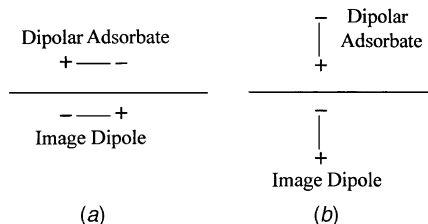


**Figure 13.16.** Origin of the surface selection rule. When a dipolar molecule is adsorbed on a metallic surface, an image of this dipole is formed below the metal surface. (a) If the dipole is oriented horizontally to the metal surface, the dipole of the molecule is exactly offset by the image dipole, so that when the dipole vibrates, the dipole moment remains at zero [i.e.,  $(\partial\mu/\partial Q) = 0$ ] and no absorption occurs. (b) If the dipole is oriented vertically to the metal surface, the dipole moment of the molecule is amplified by the dipole image [i.e.,  $(\partial\mu/\partial Q) \gg 0$ ] and the absorption can be quite large.

other hand, if the molecule is perpendicular to the metal surface, the image dipole is such that there is a large permanent dipole moment,  $\partial\mu/\partial Q$  is large, and a relatively strong band results.

### 13.4. IRRAS WITH DIELECTRIC SUBSTRATES

Dielectrics are commonly classified as a subgroup of nonmetallic materials with a vanishingly small absorption index and a refractive index between 1.3 and 4.0. Measurement of the infrared spectra of thin films on dielectric surfaces is more difficult than the corresponding measurement on a metal surface, for several reasons. First, the reflectance from dielectric surfaces is often very low (see Figure 13.1). Indeed, when the angle of incidence is close to Brewster's angle, the reflectance of *p*-polarized radiation is zero. Nonetheless, useful spectra of thin films on the surface of dielectrics can still be measured.

The intensity of a band of an adsorbate is commonly expressed as  $-\log(R_S/R_0)$ , where  $R_S$  is the reflectance of the sample (substrate + adsorbate) and  $R_0$  is the reflectance of the bare substrate at the wavenumber of maximum absorption. The SNR of an adsorbate band is proportional to both the background signal,  $R_0$ , and the difference between the background and sample signals ( $R_0 - R_S$ ). Both  $R_0$  and  $R_S$  depend strongly on the incidence angle, the polarization, and the optical constants of the substrate and adsorbate. Unlike the case for metallic substrates, where grazing incidence always leads to the most intense absorption bands, the optimum incidence angle for dielectric substrates varies strongly with the material and the information that is wanted from the spectrum.

Brunner et al. [12] have shown how  $R_S - R_0$  varies at  $3000\text{ cm}^{-1}$  for a hypothetical adsorbate with  $n = 1.5$  and  $k = 0.1$  adsorbed at a thickness of 1 nm on a typical low-index material (glass,  $n = 1.50$ ) and high-index material (silicon,  $n = 3.42$ ), with the corresponding data for gold ( $n = 3, k = 30$ ) shown for comparison (see Figure 13.17). One important effect to notice is that the sign of  $R_0 - R_S$  changes with the angle of incidence for *p*-polarized radiation. For low-index

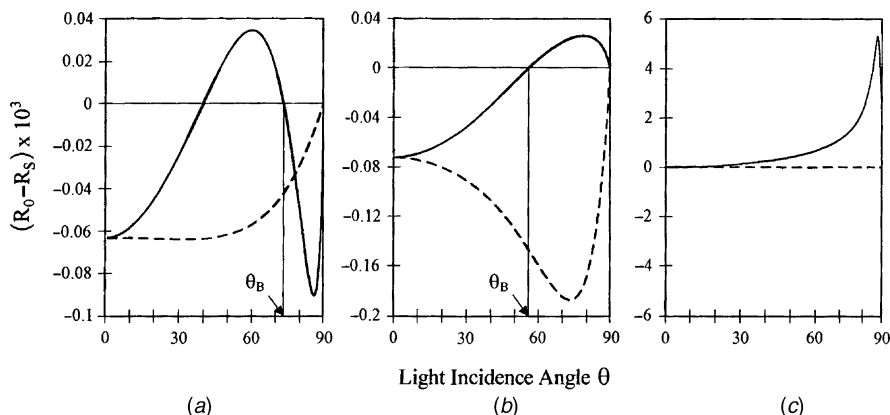


**Figure 13.17.** Calculated variation of the difference in reflectance at  $3000\text{ cm}^{-1}$  of a 1-nm-thick hydrocarbon film ( $n = 1.5$ ,  $k = 0.1$ ) on (a) silicon ( $n = 3.42$ ,  $k = 0$ ), (b) glass ( $n = 1.5$ ,  $k = 0$ ), and (c) gold ( $n = 3$ ,  $k = 30$ ),  $R_S$ , and the bare substrate,  $R_0$ , with incidence angle for  $p$ -polarized (solid line) and  $s$ -polarized (dashed line) radiation.  $\theta_B$  is Brewster's angle. (Reproduced from [12], by permission of the Society for Applied Spectroscopy; copyright © 1997.)

substrates,  $R_0 - R_S$  is negative below Brewster's angle and positive above it, whereas for  $s$ -polarized radiation,  $R_0 - R_S$  is always negative. (A negative value of  $R_0 - R_S$  implies that the reflectance of the sample *increases* when the adsorbate is present.) For a metallic substrate,  $R_0 - R_S$  is always positive as the sample always attenuates the beam. Note that the values of  $R_0 - R_S$  are almost two orders of magnitude smaller for dielectric substrates than metallic substrates.

By analogy to transmission spectrometry,  $-\log(R_S/R_0)$  for  $p$ - and  $s$ -polarized radiation are usually denoted as  $A_p$  and  $A_s$ , respectively. When  $-\log(R_S/R_0)$  is calculated for thin films on both dielectric and metallic substrates, the maximum absorbance is always on the order of 0.001 AU, but the signal measured from dielectric substrates is often very low because of the very low reflectance of the substrate,  $R_0$ . It is important to note that the sign of  $A_p$  is positive or negative depending on whether  $\theta$  is greater or less than  $\theta_B$ .

Brunner et al. [12] developed some very useful rules for IRRAS with dielectric substrates. Absorption of  $s$ -polarized light by the adsorbate leads to an increase in reflectance (i.e., inverted absorption bands in a reflection spectrum). Band intensities decrease with incidence angle and are substantially larger on low-index substrates than, say, silicon. This observation can be explained qualitatively by the corresponding changes in the surface electric field that result from the vectorial addition of the electric field vectors for the incident and reflected beams (analogous to Figure 13.5). For  $s$ -polarized radiation, the phase shift on reflection is always  $\sim 180^\circ$  for any substrate, regardless of the incidence angle. Thus, the surface electric field is negligible on totally reflecting substrates and increases with decreasing  $R_0$ . Since  $R_0$  increases with both  $\theta$  and  $n$ , the band intensities decrease with  $\theta$  and are always larger for substrates with lower refractive indices.

For  $p$ -polarized radiation, two regimes must be distinguished because of the discontinuity that occurs around Brewster's angle. At  $\theta_B$ , the reflectivity of the substrate,  $R_0$ , is zero and  $-\log(R_S/R_0)$  rises to infinity. Furthermore, there is a sudden phase change from  $0^\circ$  (for  $\theta < \theta_B$ ) to  $180^\circ$  (for  $\theta > \theta_B$ ), which leads to the inversion of the band at  $\theta_B$ . For  $\theta < \theta_B$ , perpendicular vibrational components give regular positive absorption bands, while parallel vibrational components give inverted negative bands, the intensities of which increase exponentially as  $\theta_B$  is approached. The reverse condition (positive bands for parallel components, negative bands for perpendicular components) holds for  $\theta > \theta_B$ .

IRRAS spectra of a monolayer of octadecylsiloxane (ODS) on a silicon substrate measured at several incidence angles are shown in Figure 13.18. Also shown in this figure are the spectra that are calculated by assuming that the ODS is present as an all-*trans* hydrocarbon chain tilted by  $10^\circ$ . Note that only when the spectrum is measured with  $p$ -polarized radiation above Brewster's angle is the absorbance positive, as it is for metallic substrates. Under all other conditions, the effect of the adsorbate is to cause the reflectance to increase above the value for the clean substrate. Thus, a knowledge of the optical constants of the substrate is vital if optimal IRRAS spectra of thin films on dielectric substrates are to be measured.

A detailed discussion of how to derive the orientation of adsorbates from reflection spectra of adsorbates on dielectric substrates is beyond the scope of this book, as the direction of the dipole moment derivative for each of the vibrational modes of the adsorbate must be known. To obtain the spectra on the right-hand column of Figure 13.19, Brunner et al. [12] calculated the spectra after varying the angles subtended by each functional group until the spectra calculated for  $p$ - and  $s$ -polarization matched the corresponding measured spectra at all incidence angles. Because the reflection spectra of thin films on dielectric surfaces may be measured with both  $p$ - and  $s$ -polarization, the orientation of adsorbates on dielectric substrates can be estimated more accurately in practice than on metallic substrates.

It has been thought that mode-selective measurements require polarizers and that the measurement of out-of-plane (OP) modes always requires a metallic surface to generate an electric field that is normal to the surface. Hasegawa has described a novel measurement technique for obtaining simultaneously the in-plane (IP) and OP vibrational modes of thin films deposited on dielectric substrates without the use of a polarizer [13]. These spectra correspond to the conventional transmission and IRRAS spectra, respectively, of the film. Hasegawa's technique overcomes the limitations of previous approaches by introducing the concept of virtual longitudinal-wave light that may be studied by a novel regression model. A beam of unpolarized radiation is transmitted through a film of the analyte on a high-index dielectric substrate that is held at several different angles to the incident beam. Two spectra that correspond to the conventional transmission and RA spectra result from the regression. Hasegawa has shown that this technique, which he called multiple-angle incidence resolution spectroscopy (MAIRS), can be used to evaluate molecular orientation of films on dielectric surfaces and has shown that band shifts caused by the splitting of transverse optical and longitudinal optical modes can be clearly observed. MAIRS is not strictly a form of reflection spectrometry; however,



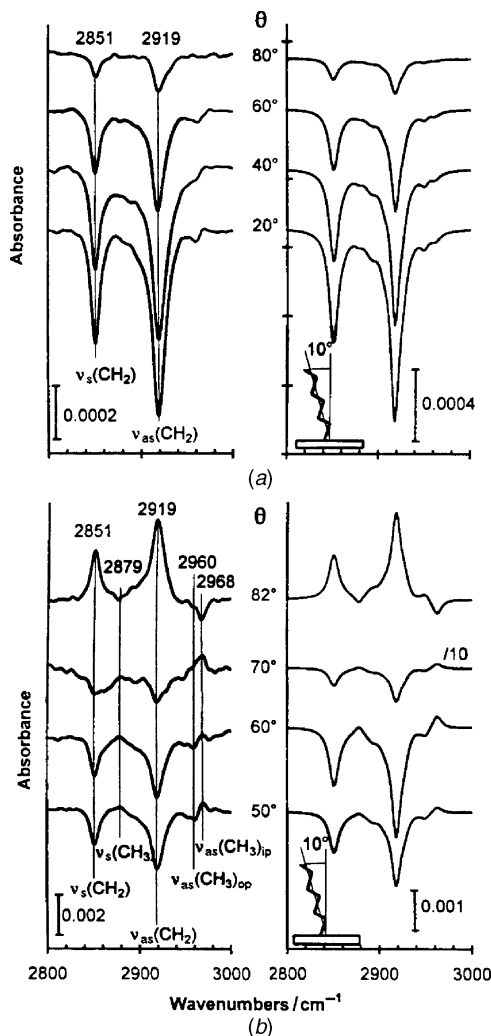


**Figure 13.18.** Experimental (left) and calculated (right) reflection spectra of an ODS monolayer on silicon for (a) *s*-polarized radiation, and (b) *p*-polarized radiation at different incidence angles. A uniform tilt angle of  $10^\circ$  of the alkane chain in the monolayer film was assumed for the simulated spectra. (Reproduced from [12], by permission of the Society for Applied Spectroscopy; copyright © 1997.)

the results are analogous to those that can be obtained by reflection spectrometry using polarized radiation, but are simpler to interpret.

Although dielectrics are usually defined as nonmetals for which  $k \sim 0$ , IRRAS spectra can be measured from absorbing substrates. One such substrate is glassy carbon, for which  $n = 2.9$  and  $k = 1.3$ . These spectra require an even better understanding of the physical processes that are taking place, as the absorption bands are often highly distorted with respect to the  $k$  spectrum. A good example of the IRRAS

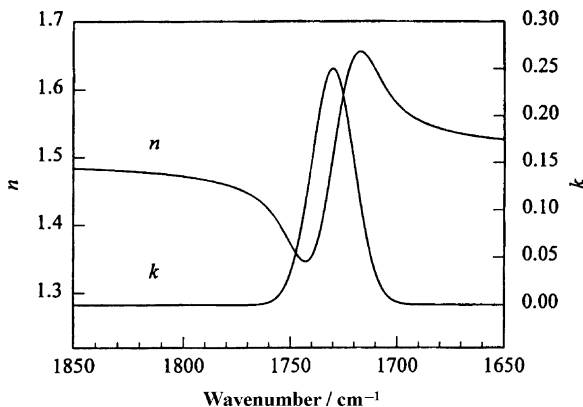


**Figure 13.19.** Optical constant spectra of a simulated infrared absorption band centered at  $1730\text{ cm}^{-1}$ . The values shown in these spectra are very similar to the  $n$  and  $k$  spectra of poly(methyl methacrylate) in the region of the C=O stretching band. (Reproduced from [9], by permission of Wiley-Interscience; copyright © 1998.)

spectra of a 100-nm-thick film of a model compound on glassy carbon has been reported by Lippert et al. [9]. The optical constants of this compound in the region of the C=O stretching mode are shown in Figure 13.19 and the calculated spectra at  $20^\circ$ ,  $59^\circ$ , and  $80^\circ$  are shown in Figure 13.20. Measured and simulated spectra of poly(methyl methacrylate) on glassy carbon at  $20^\circ$  incidence are shown in Figure 13.21, demonstrating excellent similarity.

### 13.5. TRANSFLECTION

#### 13.5.1. Thick Films on Metal Substrates

When the thickness of a surface film on a metallic substrate is on the same order as, or thicker than, the wavelength of the radiation, the reflection spectrum is usually quite similar to the transmission spectrum of the material. Since the beam has passed through the film twice, the absorbance of the bands measured by external reflection spectrometry is about twice as great as it is in the corresponding spectrum measured by transmission spectrometry. There is one major advantage in measuring the reflection spectrum of a film on a smooth metal substrate, however, and that is that interference fringes (Section 11.1.3) are not seen on the spectrum. For self-supported films, fringes are caused by interference of the beam that has been transmitted through the film with the beam that has been internally reflected and are always seen in reflection spectra of films of uniform thickness. These fringes have the same amplitude but are exactly out of phase with the fringes in the reflection spectrum of the same sample (provided that the incidence angle is the same). When the film is in contact with a highly reflective substrate, both the beam transmitted and the beam reflected are measured simultaneously by the detector and the

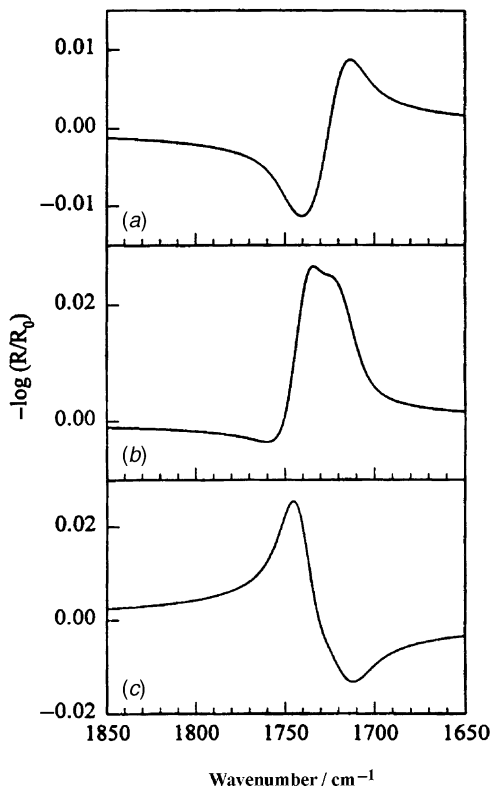


**Figure 13.20.** Simulations of the reflection-absorption band of a 0.1- $\mu\text{m}$ -thick film of the material whose optical constants are shown in Figure 13.21 on glassy carbon ( $n = 2.9$ ,  $k = 1.3$ ) at incident angles of (a)  $20^\circ$ , (b)  $59^\circ$ , and (c)  $80^\circ$ , measured with  $p$ -polarized radiation. (Reproduced from [9], by permission of Wiley-Interscience; copyright © 1998.)

fringes cancel out, leaving a flat baseline. Because the beam is transmitted through the film and reflected from the substrate, the measurement of the spectra of relatively thick films on metal substrates is usually known as *transflection spectrometry*. The film thickness,  $d$ , of samples studied by transflection must be on the order of one half-wavelength or more, so that the considerations that were discussed in Section 13.3 do not apply [which is why measurement of the spectra of very thin films ( $d \ll \lambda$ ) is known as IRRAS spectrometry, whereas for thicker films ( $d > 0.5\lambda$ ), the technique is known as transflection spectrometry].

We should note that interference fringes are sometimes seen in transflection spectra. When the film is smooth but the substrate is rough, the full intensity of the beam that has been reflected from the front surface of the film will be measured at the detector. However, only a fraction of the beam that has been diffusely reflected from the substrate will be focused on the detector element. In this case, the fringes are not completely canceled, and the baseline of the transfectance spectrum exhibits a sinusoidal modulation. This effect can often be seen in the transfectance spectrum

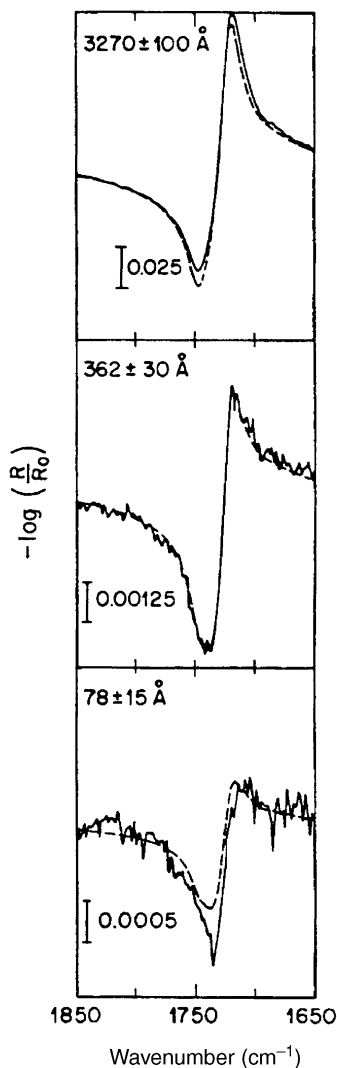


**Figure 13.21.** Experimental (solid line) and calculated (dashed line) reflection spectra of the C=O stretching band of poly(methyl methacrylate) of various thicknesses on glassy carbon for *p*-polarized radiation at an incident angle of  $20^\circ$ . (Reproduced from [9], by permission of Wiley-Interscience; copyright © 1998.)

of the polymer lining of aluminum beverage cans, where the metal has been passed through a mill so that its surface is not completely smooth.

Fresnel reflection from the front surface of the film is usually measured along with the radiation that is transmitted through the film. The distortion of the spectrum that is caused by the Fresnel reflection will lead to deviations from Beer's law,

making film thickness measurements and determination of the constituents inaccurate. Merklin and Griffiths [14] showed that Fresnel reflection can be eliminated through the use of polarized radiation. As can be seen from Figure 13.1, when the angle of incidence is equal to Brewster's angle, the reflectance of *p*-polarized radiation is zero. The refractive index of most polymers is about 1.5, so Brewster's angle is  $\sim 56^\circ$ . For incidence angles within  $\sim 4^\circ$  of Brewster's angle, Beer's law is accurately followed up to absorbances of 1 AU.

### 13.5.2. Liquid Sampling for Near-Infrared Spectrometry

Another type of transreflectance spectroscopy that is commonly used for measurements of near-infrared spectra falls somewhere between specular reflection and diffuse reflection spectroscopy (see Chapter 16). Because overtone and combination bands are weak, anomalous dispersion is usually negligibly small in the near infrared. It is quite common for the NIR spectra of liquids to be measured by transreflection using the same optical geometry used for diffuse reflection. In this case, the sample is loaded in a cell whose rear face is a ceramic disk. Radiation that has passed through the sample is scattered back through the sample, emerges from the window, and is focused onto the detector. This is a particularly useful way of measuring the spectrum of turbid samples, such as milk.

## 13.6. SUMMARY

In summary, the measurement of specular reflection spectra allows a very wide variety of samples, from partial monolayers on metallic and dielectric substrates to bulk liquids and polymer films, to be characterized.

## REFERENCES

1. F. M. Hoffman, *Surf. Sci. Rep.* **3**, 107 (1983).
2. W. G. Golden, Fourier transform infrared reflection-absorption spectroscopy, in *Fourier Transform Infrared Spectroscopy: Applications to Chemical Systems*, J. R. Ferraro and L. J. Basile, Eds., Academic Press, Orlando, FL, 1985, Vol. 4, p. 315.
3. M. Milosevic, Harrick Scientific Corporation, personal communication to P. R. Griffiths (2003).
4. M. Born and E. Wolf *Principles of Optics: Electromagnetic Theory of Propagation, Interference and Diffraction of Light*, 6th ed., Cambridge University Press, Cambridge, 1998.
5. J. D. Jackson, *Classical Electrodynamics*, Wiley, New York, 1980.
6. R. P. Feynman, *The Feynman Lectures in Physics*, Addison-Wesley, New York, 1963, Vol. 2.
7. W. G. Golden, D. D. Saperstein, M. W. Severson, and J. Overend, *J. Phys. Chem.* **88**, 574 (1984).
8. R. G. Greenler, *J. Chem. Phys.* **44**, 310 (1966).

9. R. J. Lipert, B. D. Lamp, and M. D. Porter, Specular reflection spectroscopy, in *Modern Techniques in Applied Molecular Spectroscopy*, F. M. Mirabella, Ed., Wiley, New York, 1998, p. 83.
10. A. E. Dowrey and C. Marcott, *Appl. Spectrosc.* **36**, 414 (1982).
11. B. J. Barner, M. J. Green, E. I. Sàez, and R. M. Corn, *Anal. Chem.* **63**, 55 (1991).
12. H. Brunner, U. Mayer, and H. Hoffman, *Appl. Spectrosc.* **51**, 209 (1997).
13. T. Hasegawa, *J. Chem. Phys. B* **106**, 4112 (2002).
14. G. T. Merklin and P. R. Griffiths, *J. Chem. Phys. B* **101**, 7408 (1997).



# MICROSPECTROSCOPY AND IMAGING

## 14.1. MICROSAMPLING WITH BEAM CONDENSERS

The linear dimension of the smallest sample that can be studied by infrared spectrometry is approximately equal to the wavelength of the incident radiation (see Section 14.2). Since the wavelength range of the mid-infrared is 2.5 to 25  $\mu\text{m}$ , the infrared spectra of samples as small as  $\sim 10 \mu\text{m}$  in diameter should be measurable provided that the signal-to-noise ratio (SNR) of the spectrum is high enough. If only the region above  $2000 \text{ cm}^{-1}$  is of interest, even smaller samples can be studied.

Until the late 1980s, the infrared spectra of microsamples were measured by mounting the sample behind an appropriate aperture. When samples mounted in this way are smaller than the infrared beam at its focus, much of the beam is blocked and the radiation from the source is said to be lost by *vignetting*. The diameter of the focused beam in the sample compartment of most contemporary FT-IR spectrometers is between 6 and 12 mm. Obviously, if a standard 13-mm KBr disk is mounted in the sample compartment of any FT-IR spectrometer, no light is lost by vignetting. On the other hand, if a 1-mm-diameter microdisk (area  $\sim 0.78 \text{ mm}^2$ ) is mounted in a beam with a diameter of 6 mm (area  $\sim 28 \text{ mm}^2$ ), about 97% of the radiation is lost by vignetting. If the beam diameter is 12 mm, more than 99% of the energy is lost when measuring a spectrum of this size.

To reduce this light loss, the diameter of the beam must be reduced without loss of étendue. The way that this was accomplished before about 1990 was to mount a *beam condenser* in the sample compartment. Typical optics for a  $6\times$  beam condenser are shown in Figure 14.1. In this device, the effective focal length (EFL) of the mirrors located immediately before and after the sample is about 5 cm, whereas the EFL of the mirror that focuses the beam in the sample compartment of the spectrometer is about 30 cm. The ratio of these two EFLs gives the factor by which the diameter of the beam is reduced at the focus of the beam condenser (see Figure 6.4). For this example, the beam diameter is reduced by a factor of 6, and the area is reduced by a factor of 36. Thus, if the diameter of the beam in the sample



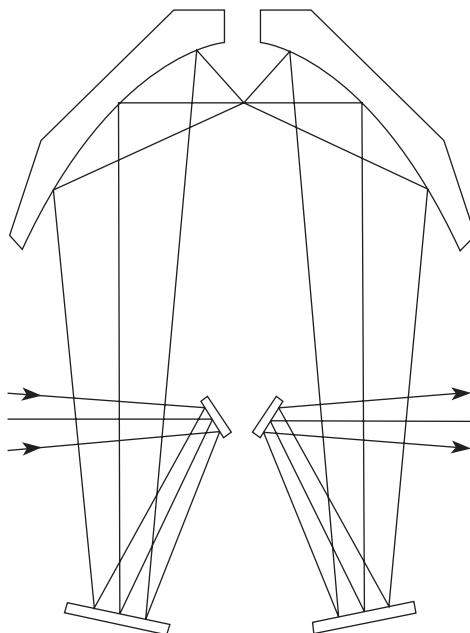


**Figure 14.1.** Typical 6× beam condenser. (Courtesy of Harrick Scientific Corporation.)

compartment is 6 mm, the corresponding size of the beam at the focus of the beam condenser is 1 mm. In this case, the spectrum of a 1-mm-diameter microdisk can be measured with minimal loss in optical efficiency.

Beam condensers have proven to be very useful when the sample can be prepared as a KBr disk, since devices are available for pressing disks as small as 0.5 mm in diameter. For the examination of very small regions of larger samples, however, beam condensers are less beneficial. Take, for example, the identification of an impurity in a polymer film. To examine samples of this type with a beam condenser, the impurity must be mounted immediately behind a pinhole aperture drilled in a metal plate. The smaller the region to be examined, the more difficult it is to mount the pinhole so that it is located exactly over the impurity. Because more and more samples of this type are being examined every day, beam condensers have fallen out of favor and a device with a remote aperture is used instead. This device is the *infrared microscope*.

## 14.2. MICROSCOPES

An optical schematic of a microscope that is fairly typical of many microscopes that were sold in the 1990s and are still commercially available is shown in Figure 14.2. Usually, the microscope is permanently mounted in the external beam of the spectrometer to leave the sample compartment free for other measurements. The

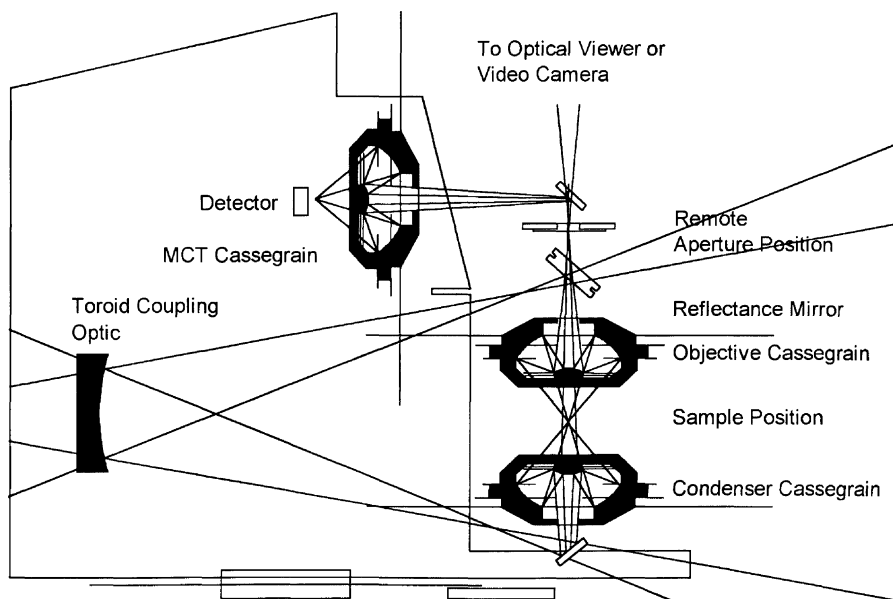


**Figure 14.2.** Optics of a typical microscope with a single aperture used for FT-IR microspectroscopy. (Courtesy of PerkinElmer Corporation.)

beam from the interferometer is focused onto the sample either with a fast off-axis paraboloidal or ellipsoidal mirror or with Cassegrain or Schwartzschild optics. For brevity, we shall just consider the case of a Cassegrain condenser like the one shown in Figure 14.2. In most microscopes, the entire beam that has passed through the interferometer is focused by the Cassegrain condenser onto the sample as a spot of 1 to 2 mm in diameter. The radiation that is transmitted by the sample is collected by another short-focal-length Cassegrain condenser that refocuses the beam at the remote aperture. A flip mirror is positioned such that the sample can be observed visually or with a video camera. The position of the sample is moved so that light from the region of interest is focused on the remote aperture, which is a key feature of all infrared microscopes. The jaws of this aperture are adjusted so that only light from this region is transmitted through the aperture. The flip mirror is then switched so that the infrared beam is focused by a third Cassegrain on a MCT detector at which the interferogram is measured.

The optics of many FT-IR microscopes are such that three identical Cassegrains are used, in which case the size of the sample image at the detector is identical to the size of the sample being observed. Since the SNR of the baseline of an FT-IR spectrum is proportional to  $A_D^{-1/2}$  (see Eq. 7.8), it is beneficial to use detectors that are as small as possible for microscopy. The linear dimension of most detectors that are installed in FT-IR microscopes is 250  $\mu\text{m}$ , which may be compared to a size of 1 or 2 mm for the detectors installed in the spectrometer. Had a 2-mm detector been installed in the microscope, the SNR of the spectrum would have been eight times worse.

The spatial resolution of the microscope is determined by the wavelength of the radiation,  $\lambda$ , and the numerical aperture (NA) of the Cassegrain. Less fundamentally, spatial resolution is also limited by the SNR that can be achieved when the size of the aperture is very small. The NA is the sine of the acceptance half-angle at the sample. At the beginning of this chapter it was stated that the diffraction-limited spatial resolution is approximately equal to the wavelength,  $\lambda$ . More accurately, it is given by

$$\text{spatial resolution} = \frac{0.61\lambda}{\text{NA}} \quad (14.1)$$

Since the largest NA that can be achieved on most microscopes is about 0.6, the spatial resolution can be approximated by the wavelength of the radiation. Fortunately, the SNR of spectra measured by most contemporary FT-IR microscopes is sufficiently high that acceptable spectra of samples as small as 10  $\mu\text{m}$  in diameter can be measured in less than 5 minutes.

Microscopes of the type shown in Figure 14.2 that are equipped with a single masking aperture have two fundamental drawbacks. First, because they may become misaligned, the spectrum obtained does not always correspond exactly to the area that is observed visually and defined by the remote aperture. This is especially true when the sample dimensions are very small. Second, any time that measurements are made when the size of the sample that is being observed is equal to, or slightly greater than, the diffraction limit, some radiation is transmitted to the detector from outside the region that was selected by the remote aperture. For example, the measured transmittance of the three strongest bands in the spectrum of a 10- $\mu\text{m}$ -diameter poly(ethylene terephthalate) (PET) fiber would usually be at least 10%, even though the true transmittance of these bands in the spectrum of a 10- $\mu\text{m}$  film of PET is much less than 1%.

To minimize this effect, *dual confocal aperturing*, in which the beam is focused at apertures located before and after the sample, may be applied. Each aperture is located at an image plane conjugate to the sample. If the beam of radiation is passed through apertures that are located before as well as after the sample, the amount of light detected from outside the masked area is reduced significantly. By illuminating the sample with an image that corresponds to its size, the intensity of diffracted light from the surrounding areas is reduced in contrast to the case where a single aperture is used, as shown in Figure 14.3. The improvement in spatial resolution that is achieved by dual confocal aperturing has been demonstrated nicely by Sommer and Katon [1].

The focusing optics are usually selected so that the diameter of the first aperture is the same as the aperture on the distal side of the sample. This optical configuration was called Redundant Aperturing by Spectra-Tech, the company that patented this arrangement for mid-infrared microspectrometry. This design had the disadvantage that users had some difficulty with precisely adjusting both masks, and the precise alignment of the two masks was difficult. A particularly elegant way of circumventing this problem was introduced by Spectra-Tech in 1998. In this microscope, a single aperture is used in the way shown in Figure 14.4.

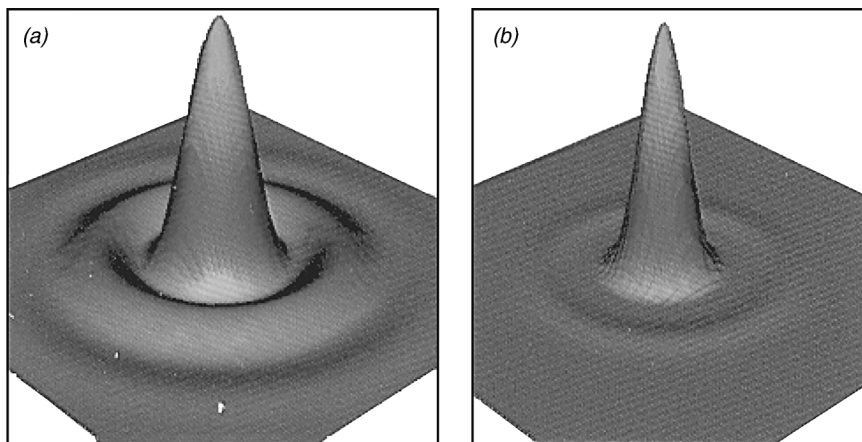


**Figure 14.3.** (a) Energy profile showing the diffracted radiation present outside the area defined by a single mask; (b) corresponding profile obtained with masks located before and after the sample. (Courtesy of ThermoElectron Corporation.)

To measure good spectra with the microscope, the same rules apply that hold for macroscopic measurements. The sample should be flat and no more than  $25\ \mu\text{m}$  in thickness (less for very polar samples). Because the samples are so small, it is quite easy to decrease their thickness with a small roller designed for this purpose

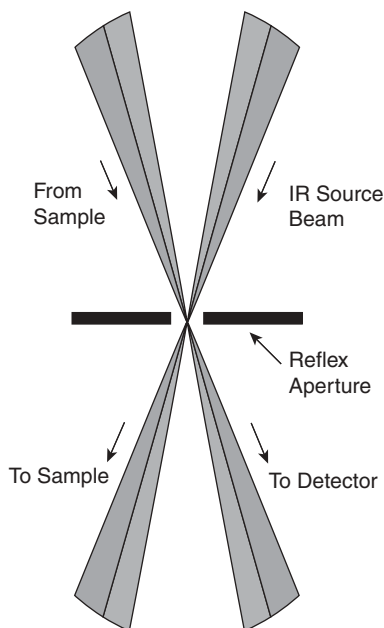


**Figure 14.4.** Dual confocal aperturing achieved with a single physical aperture. (Courtesy of ThermoElectron Corporation.)

or simply by squeezing them between two salt plates. Diamond anvil cells, which are described in the next section, are even better. Preparing a flat sample is particularly important when fibers are studied, as the fiber can act as a lens and distort both the image quality and the spectrum significantly.

The spectrum of each layer of a polymer laminate can be measured by microtoming the sample to a thickness between 10 and 25  $\mu\text{m}$ . The microtomed sample is then mounted vertically between two salt plates and located in the beam so that light passes through individual layers of the laminate and is transmitted through the remote aperture. For samples such as laminates, the aperture is usually rectangular, where one dimension is the thickness of the laminate layer and the other is the length of the laminate (typically determined by the straightness of the sample).

Before an infrared spectrum is measured, the sample must first be viewed by the operator to ensure that the correct part of the sample is interrogated. The jaws of the aperture are then adjusted so that only the area of interest is seen. Originally, this was done by means of a simple ocular, although in many later microscopes the ocular has been replaced with a video camera. The optics usually employ finite conjugate-image planes relative to the microscope objective. In this configuration the objective forms an image of the specimen at some distance, typically between 50 and 200 mm, from the objective pupil. An alternative approach is the infinity-corrected design, in which the light is collimated at the back pupil of the objective. A tele-lens forms an image of the specimen for relay to the viewing means. The infinity-corrected design allows the use of standard optical microscope viewers, objectives, and condensers. The implementation of ancillary optical modules is greatly simplified by mounting them in the collimated light path. These optical modules include image-contrasting optics such as polarizers, dichroic optics, or differential interference contrast prisms. The infinity-corrected design also allows the use of flat mirror relay optics in the IR beam path. The ease in alignment and stability of the system is improved through the use of flat mirror optics.

By mounting the sample on a computer-controlled  $x$ - $y$  stage, spectra of neighboring regions may be measured sequentially to yield an image of the sample, a procedure that is usually known as *mapping*. Because it often takes several minutes to measure each spectrum, mapping can be a time-consuming operation. If more than one or two samples per month need be characterized by mapping, users are advised to consider hyperspectral imaging, which is described in Section 14.5.

As noted above, most of the detectors installed in FT-IR microscopes are about  $250 \times 250 \mu\text{m}$  square. Remembering that the noise-equivalent power of infrared detectors is proportional to the square root of their area, the noise level of the signal generated by these detectors is about four times less than if a conventional  $1 \times 1 \text{ mm}$  detector were used. If one were only interested in measuring the spectra with a spatial resolution near the diffraction limit, it would seem logical to use even smaller detectors, and indeed  $50 \times 50 \mu\text{m}$  detectors have been installed on FT-IR microscopes. Nonetheless, the alignment of very small detectors is tricky and to our knowledge at least, detectors smaller than  $50 \mu\text{m}$  have not been installed on FT-IR microscopes. (Note that this is not the case with hyperspectral imaging

FT-IR spectrometers, for which the size of the pixels in focal plane array detectors is typically less than  $10\text{ }\mu\text{m}$ .)

In summary, measurement of the infrared spectra of samples as small as  $10\text{ }\mu\text{m}$  has now become a routine matter, and microscopes are installed on at least 10% of all FT-IR spectrometers in use today. The software is remarkably sophisticated. The visual image can be displayed along with the corresponding infrared map and the spectrum at one or more different points. Because spectra can be measured so quickly with most FT-IR microscopes, it is possible to map the composition of a sample by moving a motorized stage in increments as small as  $10\text{ }\mu\text{m}$ . Assuming that an acceptable spectrum of a  $10\text{-}\mu\text{m}$  spot can be obtained in 5 minutes, mapping a region that is  $100\text{ }\mu\text{m} \times 100\text{ }\mu\text{m}$  will take a little over 8 hours. This time may be reduced significantly through the use of an FT-IR imaging spectrometer.

### 14.3. DIAMOND ANVIL CELLS

One particularly effective way to reduce the thickness of microsamples is to squeeze them between two diamonds. Diamonds fall into two categories, Types 1 and 2, the spectra of which depend on the impurities that are present. Spectra of both types are shown in Figure 14.5*a* and *b*. Type 2 diamonds have a high transmittance throughout the mid-infrared spectrum except in the region of about  $2000\text{ cm}^{-1}$ . Fortunately, few materials have characteristic absorption bands in this region. If the region below  $2000\text{ cm}^{-1}$  is not of interest, sapphire windows may be used instead of diamonds, (see Figure 14.5*c*). The area of one face of a 0.5-karat diamond is about  $0.2\text{ mm}^2$  ( $0.5\text{ mm}$  in diameter), so that diamond anvil cells must be held either in a beam condenser or a microscope if good spectra are to be obtained.

In the 1960s, cells were developed for examining samples held between diamond windows under pressures of up to 100 kbar [2,3]. This type of pressure is unnecessary if one simply wishes to reduce the thickness of most samples. A force of only 1 kg applied to a 0.5-mm diamond will produce a pressure of about 500 bar, which is more than enough to reduce the thickness of polymers and most other samples. A much simpler diamond anvil cell is shown in Figure 14.6. The sample is simply mounted between two small diamonds, and three thumbscrews are tightened so that sufficient pressure is applied to reduce the thickness of the sample to any desired amount.

A very convenient way of measuring the spectra of polymer laminates is first to microtome them as described in Section 14.2 and then to mount the sample between the diamonds, with each layer perpendicular to the faces of the diamonds. When the sample is compressed, the layers often separate. In fortunate cases, the adhesive that is used to bond the layers may be squeezed out and formed into small droplets between the separated laminates and so may also be characterized. When present in the laminate, the thickness of the adhesive layers is generally less than the wavelength, so these layers are far too thin to measure without use of the diamond cell. By squeezing the adhesive out in this manner, the drops are larger than the wavelength and the spectrum of the adhesive can be acquired.

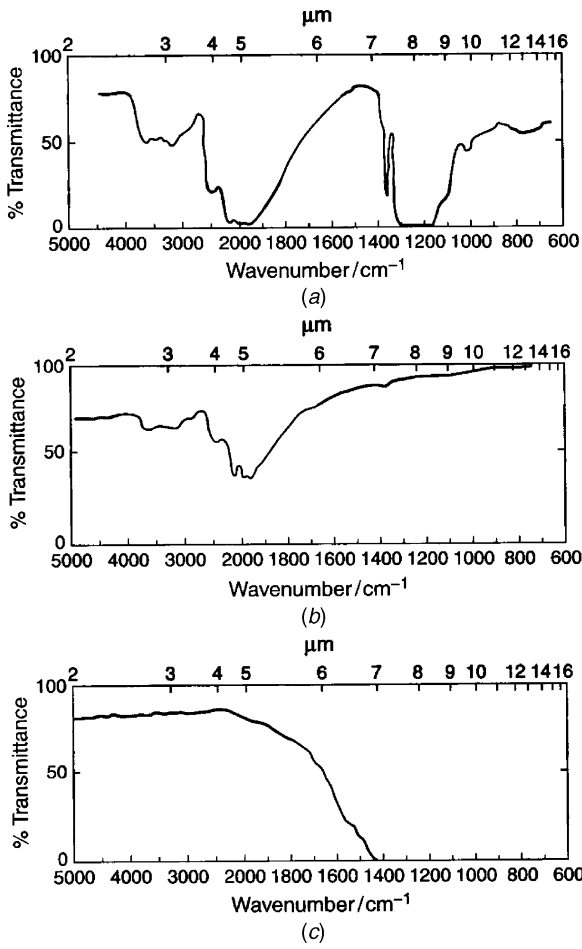


**Figure 14.5.** Transmission spectrum of (a) Type 1 diamond, (b) Type 2 diamond, and (c) sapphire. (Courtesy of High Pressure Diamond Optics Corporation.)

14.4. REFLECTION MICROSCOPY

Specular reflection spectra of microsamples can be measured by bringing the beam onto the sample from above. In the microscope shown in Figure 14.2, specular reflection spectra are measured by switching the toroidal coupling optic so that one-half of the beam that normally passes through the sample in the transmission mode is focused onto the sample from one-half of the Cassegrain located above the sample. (The lower Cassegrain is not employed for reflection measurements.) The reflected beam is picked up by the other half of the Cassegrain and focused on the remote aperture. Because of the way that the beam is input to the sample for reflection spectrometry, the efficiency of most microscopes used in their reflection mode is typically a little less than one-half of the efficiency in their transmission mode.

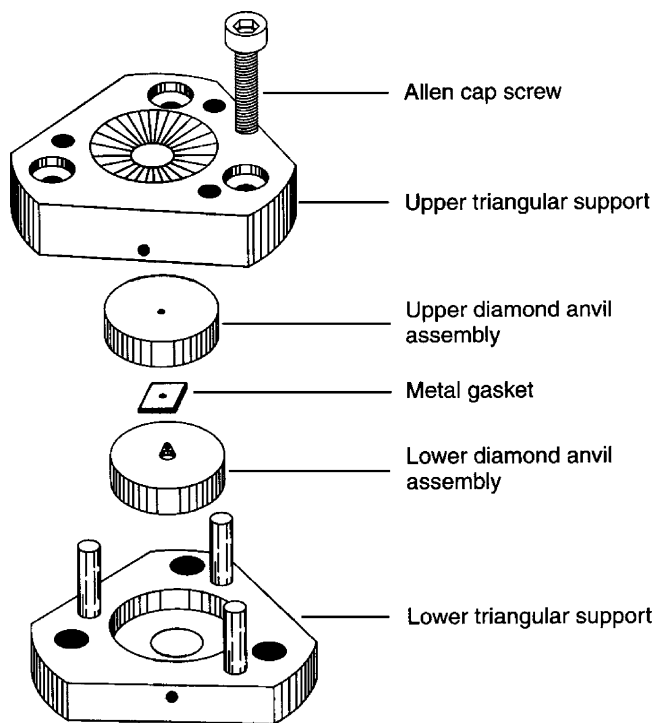


**Figure 14.6.** Simple hand-tightened diamond anvil cell. (Courtesy of High Pressure Diamond Optics Corporation.)

Fresnel reflection measurements are convenient for certain types of microsamples because essentially no sample preparation is required. Ideally, only radiation reflected from the front surface of the sample is measured at the detector in this type of measurement, so that the absorption spectrum may be calculated by the Kramers–Kronig transform, as described in Chapter 13. However, for scattering samples, diffusely reflected radiation (see Chapter 16) also contributes to the signal measured by the detector. When both mechanisms contribute significantly to the measured spectrum, no amount of data manipulation will allow an undistorted absorption spectrum to be calculated.

Vibrational microspectrometry will undoubtedly be applied to medical diagnosis in the near future. One particularly important application of microspectrometry is for the characterization of tissue samples. Tissue samples can be mounted on a water-insoluble infrared-transparent window such as ZnSe, but these windows are expensive and not conducive to visual examination (e.g., after staining of the tissue). A convenient alternative to transmission spectrometry is the measurement of the transmittance spectrum (see Section 13.5) of tissue samples mounted on low-emissivity glass slides [4]. These slides are transparent to visible light but highly reflective to mid-infrared radiation.



FT-IR microscopes have also been used occasionally for infrared reflection-absorption spectrometry (IRRAS) at near grazing incidence through the use of a specially designed objective. The image at the beam focus for a microscope used in its IRRAS configuration is elliptical, with the major axis typically 10 times longer than the minor axis. Thus, it is rarely possible to measure spots that are only 10  $\mu\text{m}$  in diameter by grazing incidence microscopy. To obtain useful results, the sample should be at least 50  $\mu\text{m}$  in the long dimension.

Attenuated total reflection (ATR) spectrometry is becoming an increasingly important sampling technique for infrared microspectrometry using both single-element and array detectors. This topic is covered in Chapter 15.

## 14.5. HYPERSPECTRAL FT-IR IMAGING

### 14.5.1. Hyperspectral Imaging with a Step-Scanning Interferometer

In Section 14.2 we described a way to map the composition of a sample by measuring a series of spectra sequentially, with the sample stage moved a small increment between each measurement. A more efficient (albeit more costly) way to obtain this information is to keep the sample stationary and to measure all the spectra simultaneously with an array detector. Simultaneous measurement of spectra from each point of an image is known as *hyperspectral imaging*, and the array of spectra obtained is often called a *hypercube*. The first hyperspectral imaging FT-IR microspectrometer, which was reported in 1995 [5], was the result of a joint effort between Levin's group at the National Institutes of Health and Marcott's group at Procter & Gamble. The first commercial instrument of this type (the Bio-Rad Stingray) was introduced a year later. An optical schematic of an FT-IR imaging spectrometer based on this principle is shown in Figure 14.7.

The first array detectors to be used for FT-IR hyperspectral imaging were focal-plane arrays (FPA) fabricated from InSb. MCT arrays were incorporated shortly thereafter, and these detectors are usually cold-shielded to improve their performance. The individual elements are "bump-bonded" onto small spheres of indium (a very soft metal). This method of fabrication sometimes led to poor reliability, but this problem has been largely overcome. Details of the construction of FPAs are given by the paper by Scribner et al. [6]. Most InSb and MCT arrays are square, with  $64 \times 64$ ,  $128 \times 128$ , or  $256 \times 256$  detector elements (pixels) that are  $6.25 \times 6.25 \mu\text{m}$  in size. Thus, the entire detector array is less than 0.5 mm on the side. Note also that when such small detectors are used, their NEP is concomitantly small (see Section 7.1).

At the state-of-the-art of digital electronics in 1995, when the first FT-IR imaging microspectrometer was reported [5], it was not feasible to sample every interferogram generated by a rapid-scanning interferometer from every pixel. Even if the moving mirror of the interferometer were moved at an optical velocity of  $3.16 \text{ mm} \cdot \text{s}^{-1}$ , such that the frequency of the He-Ne laser interferogram was only 5 kHz, the acquisition of all the data from a  $64 \times 64$  pixel FPA with a single

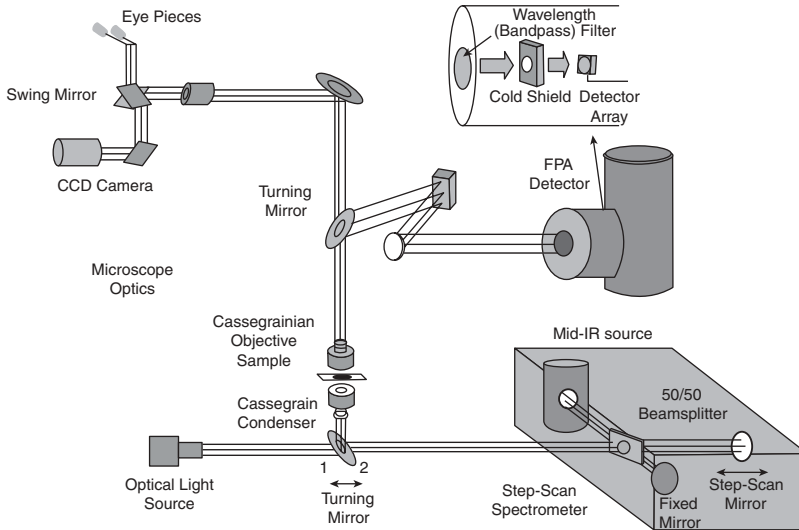


**Figure 14.7.** Typical FT-IR imaging spectrometer incorporating a step-scan interferometer and a focal plane array detector. (Reproduced from [21], by permission of CRC Press; copyright © 2003.)

ADC would have necessitated a data acquisition frequency of over 20 MHz; 20-MHz ADCs with the high dynamic range needed for FT-IR spectrometry are still not available. In the first imaging FT-IR spectrometers, the data acquisition frequency was reduced to a manageable level through the use of a step-scan interferometer (see Section 5.5).

For data acquisition, the mirror of the step-scan interferometer is held at a constant retardation while the signal from each of the 4K pixels (for a  $64 \times 64$  pixel detector) is integrated. The charge at each pixel is then read out and saved in separate files. Once the signal at the first sampling position has been acquired from each pixel, the interferometer mirror is stepped to the next position, and the signals from each pixel are acquired and saved in the appropriate file. This process is continued until enough interferogram points have been sampled to give the desired resolution. At this point, the 4K interferograms are then transformed into the same number of spectra. By 1999, imaging FT-IR spectrometers allowed hypercubes of 4K spectra to be measured at a resolution of  $8 \text{ cm}^{-1}$  in about 12 minutes. Of this time, about 75% was spent in readout, computer overhead, and stepping the interferometer to the next retardation, and less than 25% of the time was spent on data acquisition. Still better performance is now achieved routinely, to the point that continuous-scanning interferometers can now be used for hyperspectral imaging, as described in Section 14.5.2.

In the earlier software releases for hyperspectral imaging, the interferometer mirror was stepped to the next sampling position after reading out all the data from the array of pixels. An improvement in measurement efficiency was achieved by Levin's group [7], who showed that since about half the data acquisition time

was spent in reading out the charge from the pixels, the time required to obtain a complete hyperspectral image was approximately halved if the interferometer mirror was stepped forward and stabilized at the same time as the data from each pixel was being read out.

The MCT FPA detectors that were used in the first FT-IR imaging spectrometers led to three drawbacks. First, the MCT detectors operate in the photovoltaic (PV) mode; thus, the low-wavenumber cutoff is about  $900\text{ cm}^{-1}$  and the available spectral range is at least  $150\text{ cm}^{-1}$  shorter than that of rapid-scanning FT-IR spectrometers that are equipped with a photoconductive (PC) MCT detector. Second, MCT arrays were originally developed for military applications, and the data acquisition rate of the military hardware was relatively slow. Finally, many of the early FT-IR imaging spectrometers were equipped with FPAs that had been rejected by the military because of one or more “bad” pixels (i.e., detector elements that give no response). Even so, since over 99.9% of the pixels were “good,” and useful hyperspectral data could be obtained from the many operational pixels, the first users of these instruments usually believed that the loss of a small amount of information was an acceptable price to pay for the enormous number of spectra produced by FT-IR imaging spectrometers in such a short time.

Many of the problems associated with the manufacture of FPAs have now been overcome, and most contemporary instruments no longer suffer from the bad pixel problem. Instruments based on the combination of step-scanning interferometers and FPA detectors are now available from Varian (the Stingray), Thermo Electron (the Continuum XL), and Bruker Optics (the Hyperion 3000).

Hyperspectral images of large regions at lower spatial resolution than  $10\text{ }\mu\text{m}$  may be measured on several instruments by switching the objective of the microscope to one with a longer focal length. For the study of large samples at *high* spatial resolution, the sample is held on a computer-controlled stage that is moved to allow different regions of the sample to be investigated. The various hypercubes are then “stitched” together to allow images of the entire sample to be obtained.

#### **14.5.2. Hyperspectral Imaging with a Continuous-Scanning Interferometer**

As the speed of electronics increased, it became possible to use rapid-scanning interferometers at their lowest scan speed for hyperspectral imaging. The first report of this type of instrument was made by Snively et al. [8] at Purdue University in 1999. Several manufacturers of FT-IR spectrometers claim to have implemented continuous scan imaging for the first time, implying that they developed the idea. Perhaps they intended to say that they implemented it on their company’s interferometer for the first time, but Lauterbach’s group should be given credit for the original implementation.

A significant improvement in the performance of FT-IR imaging spectrometers that incorporate rapid-scanning interferometers *was* achieved by Digilab through the development of a fast, custom-built FPA (the Lancer) and its associated hardware, which includes a very fast readout. The fastest frame rate (i.e., the rate at which the signal can be read out) for a  $64 \times 64$  pixel array in 2004 was a little

over 6 kHz. For the optical velocity of  $3.16 \text{ mm} \cdot \text{s}^{-1}$  used by most benchtop FT-IR spectrometers, the frequency of the HeNe laser signal is 5 kHz (see Chapter 2). Since the fastest frame grabbers now operate at a little over 6 kHz, the signal from all the pixels of a  $64 \times 64$  array can be read out continuously at this scan speed. Because a step-scan interferometer is no longer required, the cost of instruments based on this type of hardware is somewhat lower than that of earlier imaging FT-IR spectrometers.

An alternative approach to hyperspectral imaging that is a hybrid of imaging and mapping was reported in 2001 by PerkinElmer (PE). PE designed an imaging FT-IR spectrometer (the Spectrum Spotlight) that incorporates a linear array of 16 photoconductive narrowband MCT detectors interfaced to a relatively inexpensive rapid-scanning interferometer. Since  $\tilde{\nu}_{\min}$  for the PC-MCT detectors used in the Spectrum Spotlight is about  $700 \text{ cm}^{-1}$ , the spectral range of this instrument is at least  $200 \text{ cm}^{-1}$  wider than that of the PV detectors used in MCT focal plane array detectors of the type that are incorporated in most other hyperspectral imaging FT-IR spectrometers. A representation of the operation of the PE Spectrum Spotlight is shown in Figure 14.8. The signals from each of the 16 detectors in the linear array are digitized simultaneously with separate ADCs. The sample is mounted on a computer-controlled stage that can be repositioned rapidly to allow the spectra from an adjacent region to be measured once the spectral data from a given stage position have been acquired. This process is repeated until the entire spatial region of interest has been covered. The maximum number of pixels per image can be as great as 260,000 and is limited only by the size of the data system. In addition to this linear detector array, a single  $100\text{-}\mu\text{m}$  medium-band MCT detector mounted in the same dewar allows individual spectra to be acquired over a wider range than the spectra

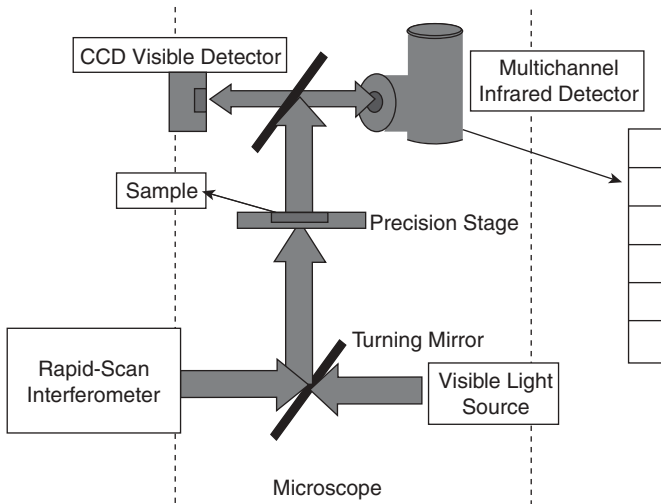


**Figure 14.8.** Hybrid imaging/mapping imaging spectrometer incorporating a rapid-scan interferometer and a linear array detector. (Reproduced from [21], by permission of CRC Press; copyright © 2003.)

measured with the array. Like the Digilab Stingray, the PE Spectrum Spotlight can be used in two modes, corresponding to high and low spatial resolution by switching the microscope objective. A similar instrument is now available from Thermo Electron.

### 14.5.3. Signal-to-Noise Ratio

By analogy with Eq. 7.8, Sniveley and Koenig [9] showed that the SNR on the baseline of a spectrum measured with an imaging FT-IR spectrometer is given by

$$\text{SNR} = \frac{0.12\pi A \left[ 1 - \sqrt{1 - (\text{NA})^2} \right] U_{\tilde{\nu}}(T) \Delta\tilde{\nu} D^* \sqrt{t}}{A_D^{1/2}} \quad (14.2)$$

where  $A$  is the area of the sample imaged onto the pixel and  $\text{NA}$  is the numerical aperture. All the other parameters have the same meaning as in Eq. 7.8. The factor of 0.12 is analogous to the efficiency term  $\xi$  in Eq. 7.8. Sniveley and Koenig used this equation to compare the performance of FT-IR imaging and single-detector microspectrometers and found that for measurements near the diffraction limit, the performance of imaging spectrometers should be higher than that of standard FT-IR microspectrometers if it is assumed that the  $D^*$  of the detectors and the area of the sample imaged onto the pixel are the same in both types of instruments. (In practice, the  $D^*$  of PV-MCT detectors is slightly higher than that of PC detectors for signals modulated at frequencies greater than 1 kHz, but the difference is small.) The biggest advantage of the imaging spectrometers is in the  $A_D$  term for array detectors in Eq. 14.2. Whereas most FT-IR microscopes are equipped with 250- $\mu\text{m}$  detectors, the pixel size in most FPAs is 6.25  $\mu\text{m}$ , which leads to a 40-fold advantage in  $\sqrt{A_D}$  for the imaging spectrometer.

To the best of our knowledge, the ramifications of the fact that the detector is operating effectively at dc when used to measure the interference record generated by a step-scan interferometer have not been discussed. Even though the low-frequency performance of PV-MCT detectors is better than that of PC-MCT detectors, the use of step-scan interferometers for hyperspectral imaging leads to some unique noise sources, several of which have been discussed extensively by both Levin's and Koenig's groups [7,9–13]. For example, very sharp spikes in the interferogram, which would usually be suppressed by the high-pass filter in the amplifier of conventional rapid-scanning FT-IR spectrometers, can present a real problem with step-scan FT-IR spectrometers. Bhargava and Levin [11] have demonstrated the effect of occasional occurrences of noise with a higher magnitude than would be expected to the usual Gaussian distribution of noise. This high-magnitude noise has a low probability of occurrence for a single measurement but almost certainly affects data collected in a multichannel, multiplexed modality such as hyperspectral imaging, so that SNR is not improved with  $t^{1/2}$  by signal averaging. To recover the time-averaging advantage, they proposed a general co-addition method that they call median filtered time averaging. In this approach, the mean and the median

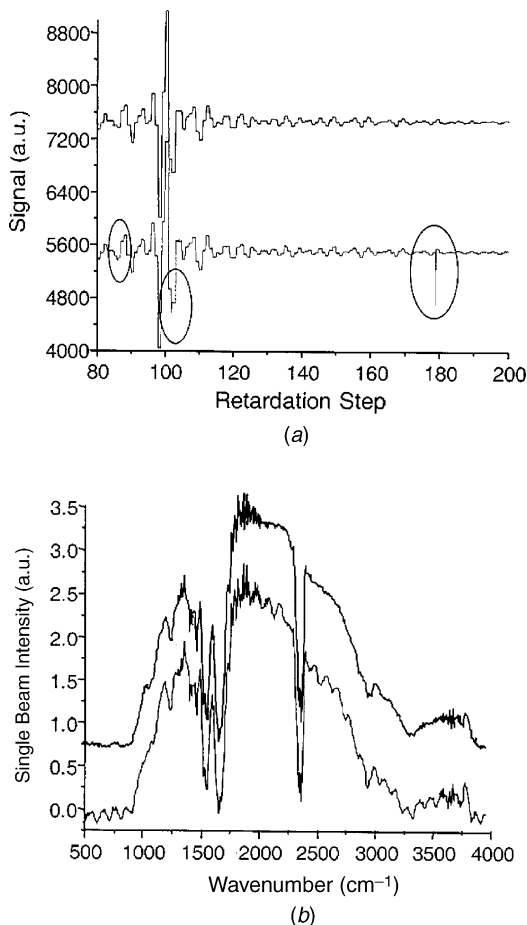


**Figure 14.9.** (a) Portions of interferogram measure at the same pixel before (lower trace) and after (upper trace) median filtering the data; noise spikes detected visually are circled in the lower trace. (b) Corresponding single-beam spectra obtained from these interferograms showing the improvement obtained by median filtering. (Reproduced from [11], by permission of the American Chemical Society; copyright © 2002.)

of the ensemble of the data are calculated to obtain an accurate estimate of the true signal. Examples of interferograms before and after median filtering are shown in Figure 14.9a, and the corresponding spectra are shown in Figure 14.9b.

It is perhaps worthy of note that the problems of the type discussed above are not encountered on a hybrid imaging/mapping instrument like the PerkinElmer Spectrum Spotlight, as interferograms are collected with this instrument in the conventional manner used for rapid-scanning interferometers. At the time of this writing, the SNR of spectra collected with this instrument appears to be significantly higher than for spectra measured using FPAs. It is certainly true that the performance of imaging FT-IR spectrometers in 2006 is significantly higher than it was seven years

ago, and it is probably true that the plateau of the learning curve has not yet been reached. Thus in the next decade, further significant improvements to the performance of all imaging FT-IR spectrometers can be forecast.

The intensity of the radiation emitted by a typical infrared source has a nonuniform distribution that is imaged onto the FPA. For a perfectly transparent isotropic sample, the same pattern appears in the sample and reference spectra of a given pixel and therefore can easily be corrected. When real samples are measured, however, this intensity nonuniformity produces image artifacts. Although these artifacts could in principle be eliminated by placing a diffusing element in the optical path, this is never done in practice, presumably because too much light would be lost. The sample itself can also cause a wide variety of image artifacts because of excessive absorption, diffraction, and scattering, the result of which has been described in detail by Snively and Koenig [9].

The unique method of fabricating the FPAs leads to additional sources of noise that are not found in single-element detectors. Each pixel has its own readout circuitry. The slight variations in the detectors that are introduced by the method of fabrication cause a type of noise called *spatial* or *fixed pattern noise*. This noise manifests itself as residual features in the resulting images. As long as the noise is mainly in the spatial domain and remains constant during the duration of the measurement, it is not a problem. If the noise changes during data acquisition, however, the effects cannot be removed.

To increase the SNR, signal averaging can be carried out either by holding the mirror at a constant retardation and co-adding frames (*frame co-addition*) or by acquiring a single frame for each step and repeating the scan several times (*image co-addition*). One would expect these two approaches to lead to the same result, but Sniveley and Koenig showed that image co-addition allowed the SNR to increase with the number of images that were averaged, but poorer performance was found for frame co-addition [9]. The reason for this behavior is that most frame grabbers were designed for real-time readout and were not designed to provide stable performance over a long period of time.

#### 14.5.4. Software

The software required to run and analyze the spectra measured by imaging spectrometers is quite sophisticated. Spectroscopists cannot be expected to examine the thousands of spectra measured by an imaging spectrometer individually, and so several methods of treating the spectra have been developed so that images rather than spectra are observed. Many different algorithms are supplied as part of the software packages that are integral parts of most FT-IR imaging spectrometers.

The simplest way to generate an image is to show the intensity at a certain wavenumber, or the area under the absorbance spectrum between two specified wavenumbers, as a false-color two-dimensional image. Because the thickness of microsamples often varies, a better way to view the data is to plot out the ratio or difference of band intensities at two different wavenumbers that correspond to absorption maxima of two known components of the sample. Even better is to

perform a principal component analysis of the spectra (see Chapter 9) and plot out the magnitude of certain eigenvectors. With so many spectra to deal with, the management of spectral libraries is of critical importance. Algorithms such as Euclidean distance, Mahalanobis distance, linear discriminant analysis, principal components analysis, fuzzy C-means clustering, and Kohonen mapping can all be used for multivariate classification and feature extraction.

Because the spatial resolution of FT-IR hyperspectral imaging is not as good as the corresponding image obtained with visible light, *image processing* can also be important. Morphological operators such as dilation, erosion, skeletonization, and edge detection have all been written into the ISys chemical imaging software supplied by Spectral Dimensions [15]. As the performance of the hardware continues to improve, we can expect similar improvements to the software to take place simultaneously.

#### 14.5.5. Applications of Hyperspectral Imaging

In light of the fact that the first FT-IR imaging microspectrometer was designed at the U.S. National Institutes of Health [5], it is not surprising that the application area in which FT-IR hyperspectral imaging is having its greatest effect is in the fields of biomedicine and medical diagnosis. For example, the NIH group has reported hyperspectral images of thin cerebellar sections from a rat brain that had been treated in several different ways [16,17]. The spatial variations of chemical components that represent the main structural ingredients in bone formation can be monitored [18]. By microtoming a number of thin sections of bone, Ou-Yang et al. [19] have even measured the three-dimensional structure of bone. In a related measurement, chemical composition data from FT-IR imaging and morphology were correlated for human iliac crest biopsies [20]. When imaging data from normal and osteoporotic human iliac crest biopsies were compared, the extent of mineral formation in the tissue could be quantified and it was shown that the average mineral levels in osteoporotic samples were reduced considerably and that crystal size and perfection were degraded substantially compared to normal bone. A useful review on biomedical FT-IR imaging was written by Bhargava and Levin [21].

Another area in which FT-IR imaging data have given significant information is in the field of polymers. Polymers often solidify in crystalline and amorphous domains that have different spectra and hence are studied readily by hyperspectral FT-IR imaging. Bhargava et al. [13] have followed the microscopic dissolution of polymers in a variety of solvents. The macroscopic properties of microscopically heterogeneous materials are often governed by specific molecular changes within the microdomains. One type of material in this category that has lent itself to study by FT-IR imaging is polymer-dispersed liquid crystals [22]. These materials can either transmit or reflect light, depending on the direction of an applied electric field. False-color images are invariably used to make the processes that are taking place clearer to the human eye. For cost containment, all the figures in this book are black and white; thus, no false-color images have been shown. Instead, the reader is



strongly recommended to go to the original references to get a better idea of the type of image that can be obtained.

## REFERENCES

1. A. J. Sommer and J. E. Katon, *Appl. Spectrosc.* **45**, 1633 (1991).
2. C. E. Weir, E. R. Lippincott, A. Van Valkenburg, and E. N. Bunting, *J. Res. Natl. Bur. Stand.* **63A**, 55 (1959).
3. C. H. Polsky and E. Van Valkenburg, The diamond anvil cell, in *Handbook of Vibrational Spectroscopy*, J. M. Chalmers and P. R. Griffiths, Eds., Wiley, Chichester, West Sussex, England, 2002, Vol. 2, p. 1353.
4. D. W. Rafferty and R. C. Virnelson, *Spectroscopy* **12**(5), 42 (1997).
5. E. N. Lewis, P. J. Treado, R. C. Reeder, G. M. Storey, A. E. Dowrey, C. Marcott, and I. W. Levin, *Anal. Chem.* **67**, 3377 (1995).
6. D. A. Scribner, M. R. Kruer, and J. M. Killiany, *Proc. IEEE* **79**, 66 (1991).
7. R. Bhargava, M. D. Schaeberle, D. C. Fernandez, and I. W. Levin, *Appl. Spectrosc.* **55**, 1079 (2001).
8. C. M. Snively, S. Katzenburger, G. Oskarsdottir, and J. Lauterbach, *Opt. Lett.* **24**, 1841 (1999).
9. C. M. Snively and J. L. Koenig, *Appl. Spectrosc.* **53**, 170 (1999).
10. R. Bhargava, D. C. Fernandez, M. D. Schaeberle, and I. W. Levin, *Appl. Spectrosc.* **55**, 1580 (2001).
11. R. Bhargava and I. W. Levin, *Anal. Chem.* **74**, 1429 (2002).
12. R. Bhargava, S.-Q. Wang, and J. L. Koenig, *Appl. Spectrosc.* **54**, 1690 (2000).
13. R. Bhargava, S.-Q. Wang, and J. L. Koenig, *Anal. Chem.* **73**, 360A (2001).
14. R. Bhargava, S.-Q. Wang, and J. L. Koenig, *Appl. Spectrosc.* **52**, 323 (1998).
15. ISys, 3.1, Spectral Dimensions, 3416 Olandwood Court, Suite 210, Olney, MD 20832.
16. D. S. Lester, L. H. Kidder, I. W. Levin, and E. N. Lewis, *Cell. Mol. Biol.* **44**, 29 (1998).
17. L. H. Kidder, P. Colarusso, S. A. Stewart, I. W. Levin, N. M. Apple, P. G. Pentchev, and E. N. Lewis, *J. Biomed. Opt.* **4**, 7 (1999).
18. C. Marcott, R. C. Reeder, E. P. Paschalis, A. L. Boskey, and R. Mendelsohn, *Phosphorus Sulfur* **146**, 417 (1999).
19. H. Ou-Yang, E. P. Paschalis, A. L. Boskey, and R. Mendelsohn, *Appl. Spectrosc.* **56**, 419 (2002).
20. R. Mendelsohn, E. P. Paschalis, and A. L. Boskey, *J. Biomed. Opt.* **4**, 14 (1999).
21. R. Bhargava and I. W. Levin, Recent developments in Fourier transform infrared (FTIR) microspectroscopic methods for biomedical analyses: from single-point detection to two-dimensional imaging, in *Biomedical Photonics Handbook*, T. Vo-Dinh, Ed., CRC Press, Boca Raton, FL, 2003, p. 1.
22. R. Bhargava, S.Q. Wang, and J. L. Koenig, *Macromolecules* **32**, 2748 (1999).

# ATTENUATED TOTAL REFLECTION

## 15.1. INTRODUCTION

Attenuated total reflection (ATR) has grown into the most widely practiced technique in infrared spectrometry. The reasons for this are fairly straightforward: the technique requires little or no sample preparation, and consistent results can be obtained with relatively little care or expertise. The technique is not foolproof, but it can be very forgiving. ATR spectrometry is known by a number of alternative names, for example, *multiple internal reflection* (MIR), which is not to be confused with “mid-infrared,” *frustrated multiple internal reflection* (FMIR), *evanescent wave spectrometry* (EWS), *frustrated total internal reflection* (FTIR), which is not the same as Fourier transform infrared (FT-IR) spectrometry, and *internal reflection spectrometry* (IRS), but IRS is better known, at least in the United States, as the Internal Revenue Service.

ATR is a technique whereby the sample is placed in contact with a sensing element, and a spectrum is recorded as a result of that contact. Unlike many other sampling techniques used in infrared spectrometry, radiation is not transmitted through the sample; consequently, the sample does not have to be thin enough to allow transmission of the incident radiation, with no band having an absorbance greater than 2.0 AU. Furthermore, samples can be measured in their neat state and do not require dilution to record the spectrum. The physical morphology of the sample is usually not a problem, as long as sufficient contact area between the sample and the sensing element can be maintained. Even highly irregular samples, such as powders and woven fabrics, will sometimes give good spectra, but sample contact area may be difficult to reproduce; hence, quantitative analysis may be difficult.

Because some samples may change their spectral characteristics upon grinding, melting, pressing, or other sample preparation techniques for transmission measurements that occur as a result of morphological changes, ATR spectrometry may provide an excellent alternative to the use of KBr disks, mineral oil mulls, or cast films.

As sample preparation is minimal or nonexistent, no changes in morphology are seen with ATR spectrometry.

## 15.2. THEORY

When radiation passes from one transparent medium to another and the two media have different refractive indices, the angle at which the radiation is refracted is described by Snell's law; that is,

$$n_1 \sin \theta_1 = n_2 \sin \theta_2 \quad (15.1)$$

where  $n_1$  and  $n_2$  are the refractive indices of the two transparent media, and  $\theta_1$  and  $\theta_2$  are, respectively, the angle of incidence and refraction with respect to the normal to the interface. If  $n_1 > n_2$ , medium 1 is known as the *optically dense* medium and medium 2 as the *optically rare* medium. If we assume that the radiation originates in the optically dense medium, the angle of incidence,  $\theta_1$ , will be smaller than the angle of refraction,  $\theta_2$ . This is illustrated in Figure 15.1.

Since  $\theta_2$  is always larger than  $\theta_1$ , if  $\theta_1$  is increased to a certain value, known as the critical angle,  $\theta_c$ , Snell's law suggests that the refracted angle can become equal to  $90^\circ$  [i.e., the beam will travel along the interface (see Figure 15.2)]. In reality, the refracted beam will approach  $90^\circ$  to the normal, but when the incident angle becomes greater than or equal to  $\theta_c$ , the beam reflects internally in the higher-refractive-index medium. The critical angle may be computed readily from the

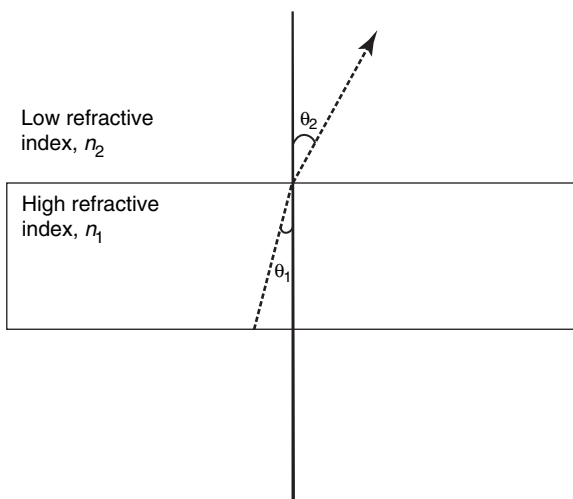


**Figure 15.1.** Snell's law where the beam originates in the optically dense medium of refractive index  $n_1$  and travels to the optically rare medium of refractive index  $n_2$ . The angles are measured with respect to the normal to the surface.

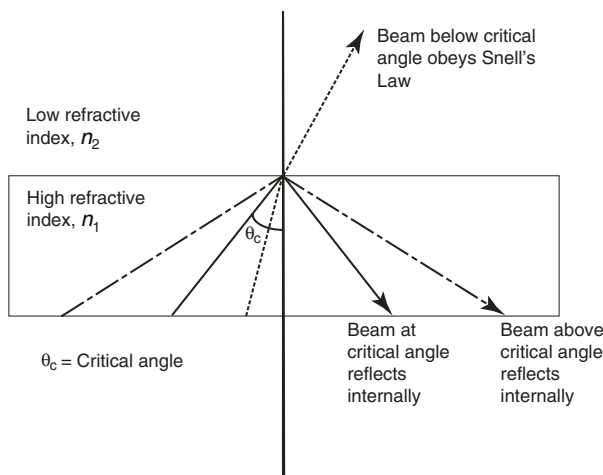


**Figure 15.2.** As the angle of incidence is increased from Figure 15.1, the radiation will internally reflect at angles greater than or equal to the critical angle,  $\theta_c$ .

refractive indices of the two media; that is,

$$\theta_c = \sin^{-1} \frac{n_2}{n_1} \quad (15.2)$$

At any angle of incidence greater than or equal to  $\theta_c$ , the beam will reflect internally with the angle of reflection equal to the angle of incidence. Unlike external reflection at a metal surface, for which the reflectance is always a little less than 1, internal reflectance is identically equal to 1 if the optically rare material does not exhibit any absorption. Any material or optic that exhibits internal reflection is known as an *internal reflection element* (IRE), although it is commonly, albeit incorrectly, called a “prism” or “crystal.” For practical purposes, IREs should have as high a critical angle as possible when in contact with the sample under investigation. Materials that

**Table 15.1. Common Materials Used as Mid-Infrared Internal Reflection Elements with Critical Angle when  $n_2 = 1.5$**

Material	Refractive Index, $n_1$	Critical Angle, $\theta_c$ (deg)
Silver chloride (AgCl)	1.90	49
KRS-5, (thallium bromide/ thallium iodide)	2.37	40
Zinc selenide (ZnSe)	2.40	40
Zinc sulfide (ZnS)	2.2	43
Germanium (Ge)	4.00	22
Silicon (Si)	3.41	26
Diamond	2.41	40

have been used for the fabrication of internal reflection elements are given in Table 15.1, along with their respective refractive indices ( $n_1$ ) and critical angles ( $\theta_c$ ). Since most organic compounds have a refractive index,  $n_2$ , of approximately 1.5, the critical angles are calculated when the refractive index of the optically rare medium has this value. Of the materials listed in Table 15.1, ZnSe and Ge are the most commonly used for ATR spectrometry. KRS-5 used to be the predominant material, but its softness and toxicity led to a great reduction in its use. As we will see later, the use of silicon and diamond for ATR spectrometry has also become important.

As implied by Eq. 15.2, all the materials in Table 15.1 must have higher refractive indices than the material with which they are in contact. Materials that are commonly used as windows in the mid-infrared [e.g., KBr ( $n_1 = 1.53$ ) and KCl ( $n_1 = 1.45$ )] are not included in this list, as their refractive indices are too low for use as IREs. Because the refractive indices of KBr and KCl are roughly equal to the refractive index of organic compounds, total internal reflection will not be observed. In this case, radiation passes directly through the IRE and sample without regard to the angle of incidence. In other words, these materials are better suited for use as infrared-transmitting windows than as internal reflection elements.

Although the beam is confined to the IRE, it must be remembered that a photon has an electromagnetic field perpendicular to its path. The field extends from the interface into the optically rare medium at the point of the contact. The electrical field of the photon extends perpendicular to the beam direction and decays exponentially with distance from the surface of the optically dense medium. At the interface the electrical field extends perpendicularly from the surface of the IRE into the optically rare medium. The strength,  $\mathbf{E}$ , of the electrical field is function of the distance,  $z$ , from the surface; that is,

$$\mathbf{E} = \mathbf{E}_0 e^{-\gamma z} \quad (15.3)$$

where  $\mathbf{E}_0$  is the field strength at the surface and  $\gamma$  is a constant. The field that extends from the surface into the optically rare medium is referred to as the *evanescent wave*.

The distance from the surface where the strength of the evanescent wave is a significant fraction of  $\mathbf{E}$  is small. The decay rate of the evanescent field depends directly on the wavelength of the radiation. The effective distance from the surface over which the evanescent wave can interact effectively with the optically rare medium can be approximated as the distance from the surface at which the strength of the field has decayed to  $1/e$  of its intensity at the surface. This distance, called the *depth of penetration*,  $d_p$ , is equal to  $1/\gamma$  in Eq. 15.3. It can be calculated from the wavelength of the incident radiation in a vacuum,  $\lambda$ , the refractive index of the IRE,  $n_1$ , the refractive index of the sample  $n_2$ , and the angle of incidence,  $\theta$ :

$$d_p = \frac{\lambda}{2\pi n_1 \sqrt{\sin^2 \theta - (n_2/n_1)^2}} \quad (15.4)$$

If we examine the two materials that are most commonly used as IREs, ZnSe and Ge, we can see how  $d_p$  is affected by the angle of incidence and the refractive index

**Table 15.2. Approximate Depths of Penetration ( $\mu\text{m}$ ) at  $1000\text{ cm}^{-1}$  for  $n_2 = 1.5$** 

IRE Material	Angle of Incidence		
	$30^\circ$	$45^\circ$	$60^\circ$
ZnSe	Below critical angle	2.0	1.1
Ge	1.2	0.66	0.51

of the IRE. Table 15.2 lists  $d_p$  for ZnSe and Ge at various angles of incidence at a wavenumber of  $1000\text{ cm}^{-1}$  (i.e., a wavelength of  $10\text{ }\mu\text{m}$  when  $n_2 = 1.5$ ). As can be seen from Table 15.2,  $d_p$  is considerably greater for a ZnSe IRE than for Ge. This is to be expected, as the refractive index of ZnSe is markedly lower than for Ge. The depth of penetration varies linearly with wavelength, hence at  $2000\text{ cm}^{-1}$  ( $\lambda = 5\text{ }\mu\text{m}$ ) all the values in Table 15.2 can be halved, at  $4000\text{ cm}^{-1}$  ( $\lambda = 2.5\text{ }\mu\text{m}$ ) they can be divided by 4, and at  $500\text{ cm}^{-1}$  ( $\lambda = 20\text{ }\mu\text{m}$ ) they can be doubled.

Clearly, the depth of penetration can be controlled with the refractive index of the IRE and the angle of incidence. Thus, if one wishes to restrict the examination of a sample to near the surface of the sample, a high-refractive-index material such as germanium is chosen as the IRE, and a high angle of incidence, say  $60^\circ$ , is used. On the other hand, if more of the bulk sample is to be investigated, a ZnSe IRE at  $45^\circ$  angle of incidence is more common.

Since the depth of penetration is directly dependent on the wavelength of the incident radiation, ATR spectra differ from transmission spectra of the same material, with the intensities at the high-wavenumber end of ATR spectra smaller than the intensities at the low-wavenumber end. Fortunately, the change in relative intensities is a linear function of wavelength, as indicated by Eq. 15.4. Hence, after conversion to absorbance, ATR spectra can simply be multiplied by wavenumber, or divided by  $\lambda$ , to yield a spectrum where the relative band intensities are, to a first approximation at least (see below), the same as those in an absorbance spectrum measured by transmission. An example of this correction is shown in Figure 15.3, with the original spectrum (a), the correction function (b), and the depth-of-penetration-corrected spectrum (c). Most manufacturers of FT-IR spectrometers incorporate the correction algorithm directly into the instrument control software. Thus, a user can tell the software program that an ATR accessory is being used, give the angle of incidence, and the material for the IRE. Even this level of interaction is not always necessary, as the user is often given choices of specific accessories, or the accessory is identified directly by the instrument by a bar-code or magnetic data strip on the accessory.

Although the relative band intensities of ATR spectra that have been subjected to the “ATR correction” are similar to those of the corresponding spectra measured in transmission, they are not the same because of the effect of anomalous dispersion (i.e., the variation of refractive index across an absorption band; see Section 1.5.2). Let the refractive index,  $n_2$ , of the optically rare material (the “sample”) in spectral regions where there is no absorption be  $n_{\text{ave}}$ . Because  $n_2$  is smaller than  $n_{\text{ave}}$  at higher wavenumbers than the band center,  $\tilde{\nu}_0$  (see, e.g., Figure 13.19), the depth of penetration will be less than the value calculated by Eq. 15.4 when  $n_{\text{ave}}$

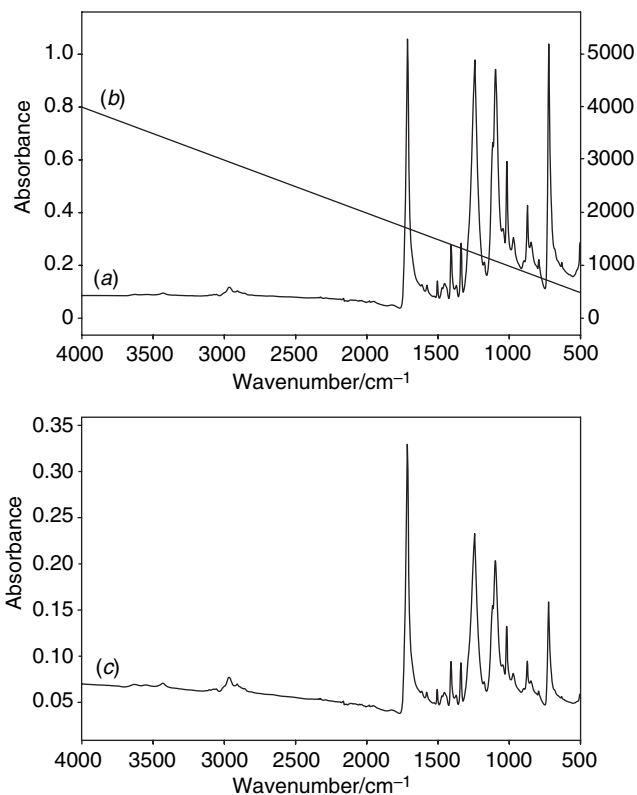


**Figure 15.3.** Depth of penetration correction for ATR spectra of PET: (a) spectrum as measured; (b) correction function by which the original spectrum is multiplied. The correction function is linear in wavenumber (the wavenumber scale is reproduced on the right-hand axis); and (c) the corrected spectrum. This spectrum has been scaled after multiplication.

is used as the value of  $n_2$ . Similarly,  $n_2$  is greater than  $n_{\text{ave}}$  at lower wavenumbers than  $\tilde{\nu}_0$ , so that the calculated value of  $d_p$  will be greater than the value calculated with  $n_{\text{ave}}$  as the value of  $n_2$ . Thus, the ATR spectrum measured in the region of an isolated symmetrical absorption will be asymmetrical. The closer the values of  $n_1$  and  $n_{\text{ave}}$ , the greater this effect will be. In fact, for very strong absorption bands,  $n_2/n_1$  can become greater than  $\sin \theta$ , and the critical angle is no longer exceeded. In this case the stronger bands will appear to have an infinitely large absorbance near their absorption maxima. Thus, if the goal of an ATR measurement is to identify a sample by spectral searching against a library of spectra that have been measured by transmission spectrometry, it is recommended that spectroscopists use an IRE with as high a refractive index as possible, even though  $d_p$  (and hence the intensity of the bands in the measured spectrum) is greater for IREs of lower refractive index.

Nunn and Nishikida [1] have taken a more in-depth approach to this problem. From the approach that the refractive index changes through an absorption band,

the absorbance measured in an ATR spectrum can be calculated as

$$A = (\log_{10} e) \frac{n_2}{n_1} \frac{E_0^2}{\cos \theta} \frac{d_p}{2} \alpha \quad (15.5)$$

where  $E_0$  and  $\alpha$  are the electric field strength of the evanescent wave at the interface and the linear absorption coefficient per unit thickness of the sample, respectively. This equation indicates that the absorbance actually depends on  $n_2 d_p \alpha$  instead of simply the linear absorption coefficient,  $\alpha$ . This effect will lead to a shift in the wavenumber of absorption bands to lower wavenumber. This argument is essentially the same as made above concerning the average refractive index,  $n_{\text{ave}}$ , but Eq. 15.5 characterizes the effect more fully. At the time of this writing (2006), a correction for wavenumber shift has been incorporated into proprietary software (Thermo Spectroscopy, Madison, Wisconsin), and it is anticipated that similar correction algorithms will be made by other vendors in the near future. An example of the ATR correction by Nishikida is shown in Figure 15.4. Figure 15.4a is the uncorrected ATR spectrum of silicone oil measured on a Ge IRE, and Figure 15.4b is the same spectrum after correction. Although the effects of anomalous dispersion should be less important for a high-refractive-index IRE (Ge in this case) the relative intensities of the strong bands in Figure 15.4a at 1125, 1084, and 1020  $\text{cm}^{-1}$  are considerably different from the relative intensities in Figure 15.4b. Furthermore, the band maxima have shifted to 1126, 1090, and 1028  $\text{cm}^{-1}$ . The spectrum in Figure 15.4b much more closely matches the transmission spectrum of the same compound. Spectra that have been corrected in this manner will match transmission spectra in computerized spectral searches (see Section 10.8) more accurately than will the uncorrected ATR spectra.

In summary, if we compare the use of ZnSe and Ge as IREs for FT-IR spectroscopy, ZnSe is preferable if the goal of the experiment is a “quick and dirty” identification of a bulk sample or one needs the highest possible sensitivity from a given measurement (e.g., when trace components in a bulk sample are investigated). Conversely, the use of Ge is preferable either if the measured spectrum is to be identified by spectral searching or if one attempts to examine materials that are less than 1  $\mu\text{m}$  from the surface of the sample.

### 15.3. PRACTICAL CONSIDERATIONS

Since ATR is a technique for studying the surface of a sample to a depth of about 1  $\mu\text{m}$ , any absorber that touches the surface will produce a spectrum. Often, bands due to impurities or contaminants in ATR spectra are simply the result of an unclean IRE or another compound that is accidentally in contact with the IRE. It is always a good idea to record spectra of common contaminants. For example, hand lotion or greasy fingerprints can easily be transferred to an IRE if it is handled with bare hands. Even if laboratory gloves are used to touch the IRE, talc, plasticizers, or slip agents may be transferred to the surface. Consequently, it is good idea



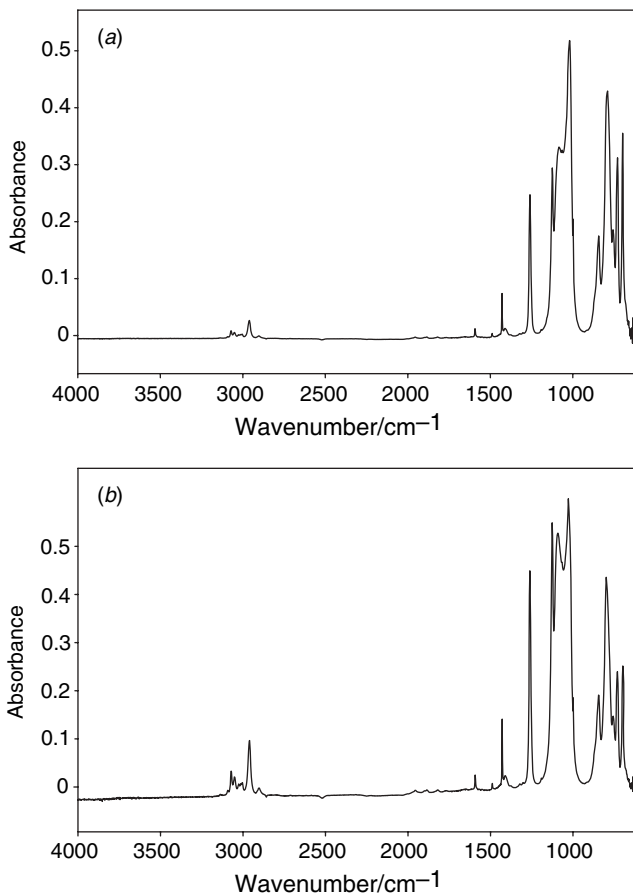


**Figure 15.4.** Silicon oil spectrum (a) collected on a Ge IRE, and (b) after application of the correction algorithm to account for anomalous dispersion.

to clean the outside of laboratory gloves before an IRE is handled. A very common contaminant in all laboratories is silicone oil or silicone grease, which does not even have to come in direct contact with the IRE, but will creep over surfaces and may eventually migrate to the surface of the IRE.

Many ATR accessories have a clamp to ensure good contact between the sample and the IRE. The clamps are often backed with a rubber or polymer pad. If the pad touches the IRE because the sample is too small to cover the entire area of the element, a spectrum of the pad will be collected in addition to that of the sample. O-ring seals constructed of rubber, Viton, or PTFE are frequently used with liquid ATR cells. Ideally, the absorption bands will be weak and will be eliminated when the ratio of the sample and reference spectra is calculated. Nonetheless, spectra of all these contaminants or potential interferents should be recorded and made available for future reference. If unexpected bands appear in a sample spectrum, the

spectra of common contaminant should be examined to see if one of them is the source of the problem. Once the source is known, the problem can easily be corrected.

As any compound in contact with the IRE produces a spectrum, clearly the only reasonable choice for a background or reference spectrum is the bare IRE. Under no circumstances should the clamp be closed on the IRE without the sample and used as a reference. Even with IREs that are used for liquid analysis, the single-beam spectrum of the clean IRE should be used for the background. For example, if the solution is aqueous and it is desirable to remove the water absorption, two separate background spectra should be recorded. One should be the absorbance spectrum of the aqueous solution referenced to an empty ATR cell, and the other should be the absorbance spectrum of water also ratioed to the spectrum of the empty ATR cell. A scaled subtraction of the water spectrum from the solution spectrum will generally produce better results than a ratio of the spectrum of the aqueous solution to that of pure water. This is because the solute displaces water from the solution, so that the amount of water that contributes to the solution and water spectra will not be identical, so they may not ratio correctly. Scaled subtraction, however, can correct for the difference provided that the solute does not cause a shift of the water band.

#### 15.4. ACCESSORIES FOR MULTIPLE INTERNAL REFLECTION

The traditional way to measure spectra by ATR spectrometry is to use a single- or double-sided IRE that is large enough to accommodate a fairly large sample and allow for multiple reflections within the IRE. To accomplish this, many early IREs were about 25 to 50 mm in length, 10 to 25 mm in height, and 2 or 3 mm in thickness. The geometry of the IREs was either a parallelepiped or a *vertical truncated triangular prism*. The latter IRE is often incorrectly called a *trapezoidal IRE*, yet this name is so pervasive that we will reluctantly use this nomenclature. Schematic diagrams of typical optical paths for a vertical parallelepiped and a trapezoidal prism are shown in Figure 15.5*a* and *b*, respectively. In both geometries the beam from the interferometer is directed at 90° to the narrow dimension (the entrance) of the IRE. At this angle, reflection losses as the beam enters and exits the IRE are minimized. As the IRE is relatively thin, the beam reflects multiple times before emerging from the IRE. The multiple reflections increase absorbance of bands in ATR spectra, but do not, of course, change the depth of penetration of the evanescent wave. Thus, the sensitivity of detection for minor components is improved. The number of reflections can be calculated rather simply with trigonometry, although the suppliers of IREs and ATR accessories generally provide the number of reflections on request.

In practice, the value of  $d_p$  calculated from Eq. 15.4 is only an approximation of the effective penetration depth,  $d_e$ , which is the thickness of a sample measured by transmission spectrometry that is required to match the corresponding absorbance in a single-reflection ATR spectrum [2]. The value of  $d_e$  depends on the polarization

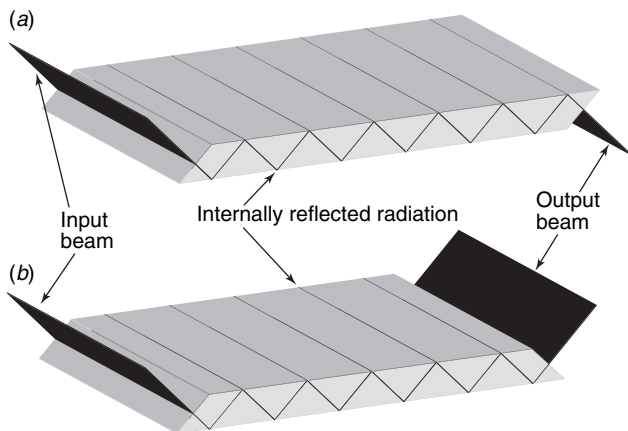


**Figure 15.5.** Two internal reflection element geometries: (a) parallelepiped; (b) trapezoidal IRE (or correctly, a vertical truncated triangular prism.)

of the beam. For a beam polarized so that the electric vector is polarized parallel to the plane of incidence at the surface of the IRE, the value of  $d_e$ ,  $d_{e,p}$ , is

$$d_{e,p} = \frac{n_{21}\lambda_0 \cos \theta (2 \sin^2 \theta - n_{21})}{n_2 \pi (1 - n_{21}^2) [(1 + n_{21}^2) \sin^2 \theta - n_{21}^2] (\sin^2 \theta - n_{21}^2)^{1/2}} \quad (15.6)$$

where  $n_{21} = n_2/n_1$ . For a beam polarized so that the electric vector is polarized perpendicular to the plane of incidence, the value of  $d_e$ ,  $d_{e,s}$ , is

$$d_{e,s} = \frac{n_{21}\lambda_0 \cos \theta}{n_2 \pi (1 - n_{21}^2) (\sin^2 \theta - n_{21}^2)^{1/2}} \quad (15.7)$$

The values of  $d_{e,p}$  and  $d_{e,s}$  for a sample with a refractive index of 1.5 are given for ZnSe and Ge in Table 15.3. As a first approximation for ATR spectra measured on a FT-IR spectrometer, the effective depth of penetration is simply the average of  $d_{e,p}$  and  $d_{e,s}$ . It should be recognized, however, that the beamsplitter efficiency is different for  $p$ - and  $s$ -polarized radiation, so again, this average is just an approximation of the true value of  $d_e$ . It should also be noted that Eqs. 15 and 16 are only accurate for weak absorption bands because of the effect of anomalous dispersion.

**Table 15.3. Effective Depths of Penetration ( $\mu\text{m}$ ) at  $1000\text{ cm}^{-1}$  for  $\theta = 45^\circ$  and  $n_1 = 1.5$**

IRE Material	$d_{e,p}$	$d_{e,s}$
ZnSe	5.82	2.91
Ge	0.41	0.82

To measure the ATR spectrum of a solid sample, it is simply clamped to one or both sides of the IRE. Care must be taken to assure that the cushioning pads on the clamps do not come in contact with the IRE; otherwise, a spectrum of the pads will be added to that of the sample. Care must also be taken such that the sample does not occlude the end of the IRE where the infrared radiation enters or leaves the IRE.

Vertical ATR accessories [i.e., accessories that orient the IRE sample surface(s) vertically] have the disadvantage that the sample must usually be solid, although cells for sampling liquids are available. In addition, the sample compartment must usually be opened to access or change the sample; hence, the dry-air purge is degraded. Vertical ATR accessories do have the advantage that it is relatively easy to change the angle of incidence in that the IRE can be rotated about a vertical axis, and the input and output mirrors can be adjusted to ensure that the beam is perpendicular to the end of the parallelepiped or trapezoidal element. To be absolutely aligned, an IRE with an appropriate angle on the parallelepiped or trapezoid should be used when the incidence angle is changed so that the reflection loss at the input and output edges of the IRE is minimized. Reflection losses will be minimized if the incident beam enters the IRE at a near normal angle. Nonetheless, most IREs can be used effectively over a range of approximately  $\pm 15^\circ$  from ideal without serious loss of performance. A diagram of a variable-angle ATR accessory is shown in Figure 15.6.

Horizontal attenuated total reflection (H-ATR) has become a sampling method of choice for a wide variety of sample morphologies and is not limited to solids, as is typical for vertical ATR accessories. To take advantage of all sample types, in many ATR accessories the IRE is mounted horizontally in the sample compartment. Although the angle of incidence can be varied, in this geometry most accessories use a fixed angle. A diagram of a typical fixed-angle horizontal ATR accessory is

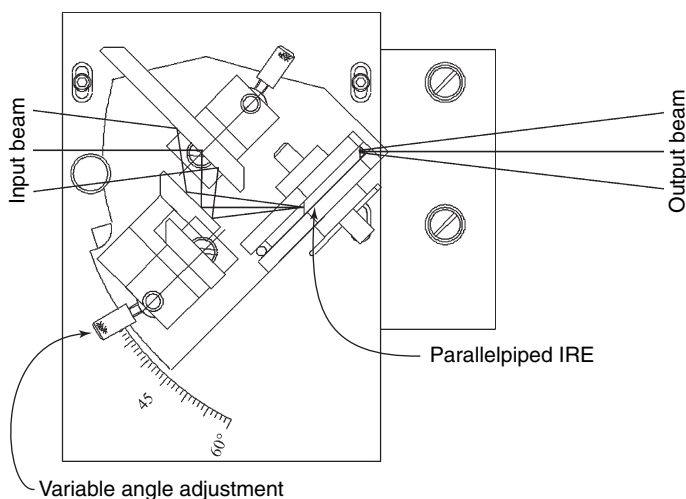


**Figure 15.6.** Vertical variable angle attenuated total reflection (VATR) accessory. (Courtesy of PIKE Technologies.)

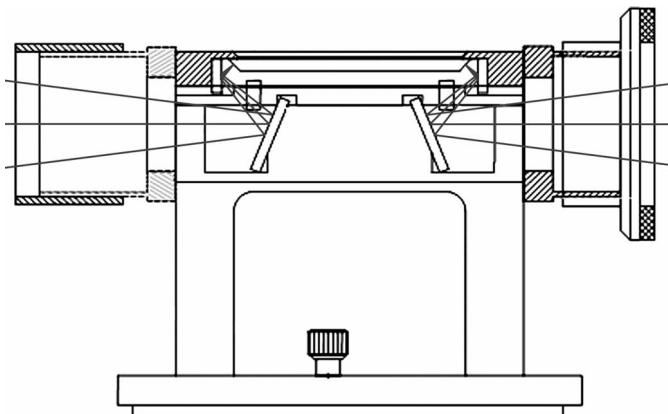


**Figure 15.7.** Horizontal attenuated total reflection (HATR) accessory with a trapezoidal internal reflection element. (Courtesy of PIKE Technologies.)

shown in Figure 15.7. It can be seen that the input beam is directed up so that it strikes the input of the IRE at normal incidence. The output beam exits the ATR in an analogous fashion. Since the input and output optics are generally identical, the IRE almost always has a trapezoidal geometry.

One distinct advantage of a horizontal ATR accessory is that the accessory can be mounted in the sample compartment so that the entire beam path is always purged. The accessory can be sealed to the walls of the sample compartment so that the atmosphere inside the ATR accessory is identical to that inside the spectrometer. If the spectrometer is simply desiccated rather than purged continuously, at least the concentration of water vapor and  $\text{CO}_2$  in the atmosphere will remain relatively constant, and interference due to these species will be minimal (Figure 15.8).

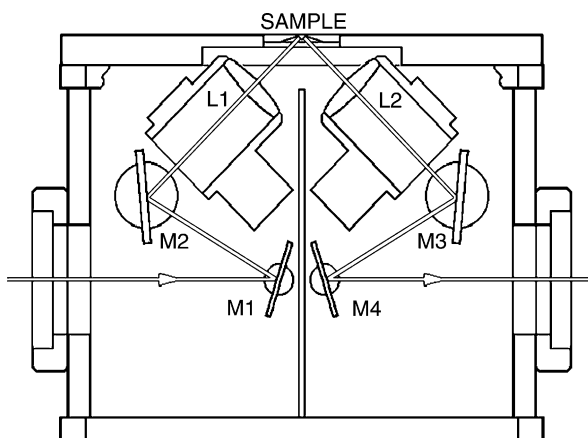


**Figure 15.8.** HATR accessory. This accessory, the Golden Gate, is unusual in that it uses lenses (L1 and L2) to focus the radiation onto a single-reflection diamond-coated IRE. (Courtesy of Specac, Inc.)

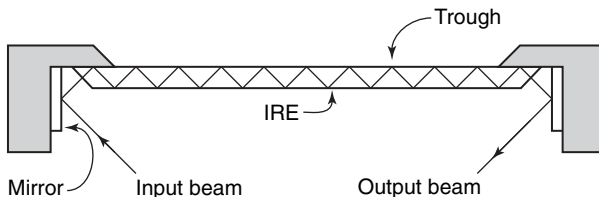


Figure 15.9. Trough IRE.

Horizontal ATR accessories can be constructed so that the IRE is mounted flush with the top of the accessory, which allows solid samples to be pressed against the IRE with a suitable weight. With the IRE flush to the surface, the sample can be considerably larger than the IRE itself. To facilitate the placement of very large samples, the IRE can be mounted parallel to the top of the instrument. Such a geometry, however, is not well suited to liquid or powdered samples.

To accommodate liquids and powders, the IRE is recessed below the surface of the accessory, so that the active surface of the IRE is in a depression or trough. A schematic diagram of a recessed IRE is shown in Figure 15.9. Liquids and fine powders may be placed directly into the recess. Liquids have an inherently good contact with the IRE; consequently, no cover needs to be placed over the recess unless the liquid is sufficiently volatile to evaporate or produce noxious fumes. Powders may have very large surface areas, but the contact area with the IRE may be low. Pressing the sample against the IRE can increase the contact area, but of course care must be taken not to damage the IRE, particularly if the sample has a greater hardness than the IRE. Although ZnSe and Ge are quite hard, they can be broken if enough pressure is applied.

Cleaning a recessed IRE can be accomplished simply by removing the mounting plate of the IRE and pouring out the contents. The IRE can be cleaned further with the use of a suitable solvent. Although the IRE mounting plates are removable and are often kinematically mounted, their removal may allow introduction of the external atmosphere into the beam path. If quantitative analysis is a concern, the IRE should not be moved, as this will introduce artifacts into quantitative models (Section 9.2). Consequently, IREs can be cleaned in situ with the use of suction to remove the sample and the use of an appropriate solvent to clean the IRE. (Acetone often contains trace solutes and generally is not a good choice, as a residue is frequently left on evaporation, whereas analytical-grade methyl ethyl ketone leaves little or no residue.)

ATR accessories for the measurement of liquids are not restricted to IREs with a trapezoidal or parallelepiped geometry. Alternatively, liquids can be measured with cylindrical IREs. A cylindrical internal reflection element is a rod that has a cone at each end, as shown in Figure 15.10. The cone typically has a  $45^\circ$  half-angle at the apex. The IRE is sealed into a liquid cell that exposes most of the rod to the liquid, and only the ends of the cell extend beyond the cell. Two geometries for cylindrical IREs are shown in Figure 15.11. The first (Figure 15.11a) is the CIRCLE cell (Thermo Spectroscopy Division, Madison, Wisconsin), where CIRCLE is an

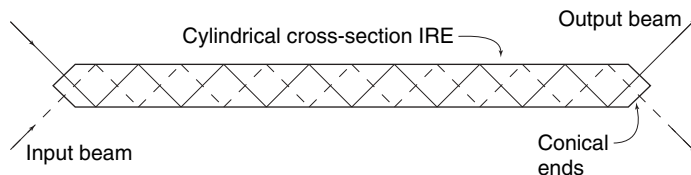


**Figure 15.10.** Cylindrical internal reflection element.

acronym for “cylindrical internal reflection cell for liquid evaluation”. As with many ATR accessories, the input and output optics are identical. The beam into the sample compartment strikes the conical mirror in front of the IRE and the radiation is reflected to an ellipsoidal mirror where the radiation is focused onto the conical end of the cylindrical IRE. It should be noted that the ellipsoidal and conical mirrors cover  $360^\circ$  to illuminate the IRE fully. The second geometry (Figure 15.11*b*) is the Tunnel cell (Axiom Analytical, Inc., Irvine, California). The optical geometry is considerably simpler than that of the CIRCLE cell in that the input and output optics are conical mirrors that serve to direct or collect the radiation to and from the cylindrical IRE.

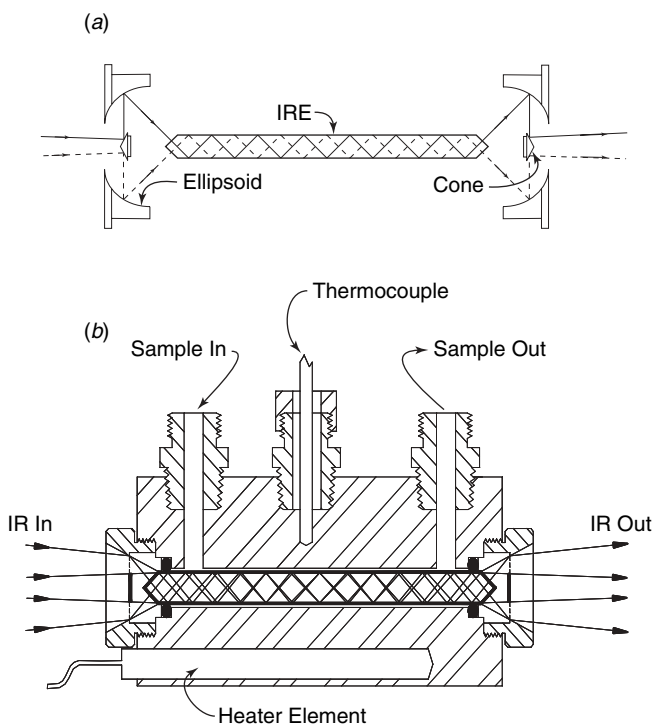


**Figure 15.11.** Optical diagrams for (a) a CIRCLE accessory, and (b) a Tunnel ATR accessory (courtesy of Axiom Analytical, Inc.). Both accessories use a cylindrical IRE.

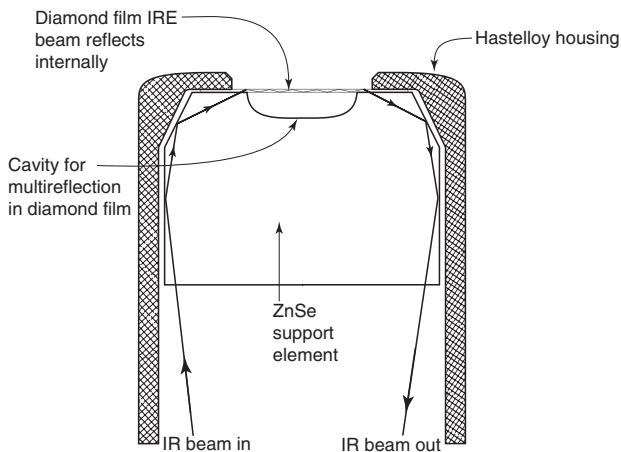


**Figure 15.12.** DiComp diamond film internal reflection element sensor. The radiation passes through the ZnSe support into the diamond film for internal reflection. The sensor housing acts as a waveguide to direct the radiation to and from the diamond IRE.

Both the CIRCLE and Tunnel cells can be filled and emptied remotely, and even be used for flow systems. Although these accessories are not sealed within the sample compartment, the sample compartment may be closed and only the flow lines need be accessible outside the spectrometer. The Tunnel cell also has the feature that the cell block can be temperature controlled with the use of either block electrical heaters or a coolant fluid.

ATR internal reflection elements can be used in high-pressure, high-temperature, or corrosive environments. Most IREs cannot withstand these conditions, so their design has been modified. An example of an adverse environment ATR sensor is the DiComp sensor shown in Figure 15.12. Rather than having the adverse environment located close to the spectrometer, a sensor is designed so that measurement can be made somewhat remotely. A hollow waveguide tube directs the radiation to a ZnSe element. The element is bevelled and on the top surface is a thin diamond film that is the actual IRE. Diamond and ZnSe have almost identical refractive indices; hence, the radiation passes from the ZnSe into the diamond with minimal reflection loss at the interface. A cavity is cut into the center of the ZnSe so that there is an air gap below most of the diamond IRE. Once the radiation is coupled into the film, it will reflect internally until the beam comes back in contact with the ZnSe element, at which point the radiation will travel back down the waveguide to the detector. The number of internal reflections inside the diamond film is no more than nine; otherwise, the diamond band at approximately  $2200\text{ cm}^{-1}$  reduces the transmission, and hence increases the noise, in that region of the spectrum (see Figure 14.5). Diamond ATR sensors can be encased in corrosion-resistant materials so that the entire sensor can be used under adverse chemical, temperature, and pressure conditions.



### 15.5. SINGLE-REFLECTION ACCESSORIES

Although sensitivity is enhanced in ATR infrared spectrometry through the use of multiple internal reflections, spectra measured on contemporary FT-IR spectrometers have sufficiently high signal-to-noise ratios that excellent spectra can be collected even if the beam interacts with the sample only one time. Accessory geometries that allow only one interaction with the sample are known as single-reflection or, more colloquially, single-bounce ATR accessories. As the beam interacts only one time with the sample, the active area of the IRE is usually considerably smaller than multiple-reflection accessories, and the spectra may be much weaker. Most of these single-reflection accessories have a circular entrance aperture compared to the rectangular entrance faces of many of the more conventional multiple-reflection geometries. This beam geometry can be more effective than multiple-reflection accessories, as the beam in an FT-IR spectrometer has a circular cross section. Conventional ATR geometries force the beam into a rectangular configuration that was appropriate for slit spectrometers but is less so for FT-IR spectrometers. Whereas conventional multiple-reflection accessories have sample areas up to  $50 \times 10$  mm, single-reflection IREs are typically 1 to 2 mm in diameter. They may, however, be as large as 15 mm or as small as  $250\text{ }\mu\text{m}$ .

In many single-reflection accessories, the beam is focused at the surface of the IRE so that its active area IRE is 2 mm or less in diameter, so that quite small samples may be measured efficiently. Recall that photometric problems are introduced when the sample area is underfilled (Section 9.2). These problems include *stray light*, so that strong bands cannot attain their true absorbance, and consequently, relative band heights are incorrect. The right way to measure the ATR spectrum of a small sample is to fill the beam area with the sample, as shown in Figure 9.3.

Single-reflection ATR accessories are almost invariably horizontal. In some accessories the typical vertical trapezoidal prism is replaced with a triangular prism as shown in Figure 15.13. All the focusing is accomplished by the optics before the IRE, yet the IRE maintains the diameter of the beam during internal reflection.

One of the reasons that ATR infrared spectrometry has become a method of choice for many applications is the minimal amount of sample preparation required. One shortcoming of ATR, however, has been the real possibility of damage to the

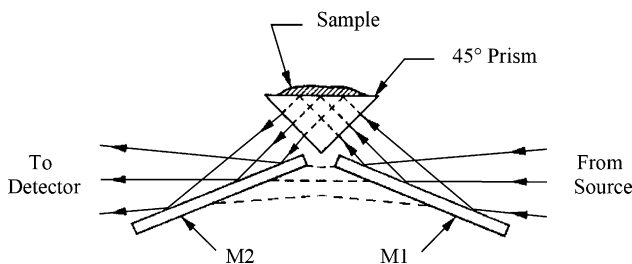


**Figure 15.13.** Single-reflection triangular prism IRE. (Courtesy of Harrick Scientific Corporation.)

internal reflection element. To overcome this limitation the active surface of some single-reflection internal reflection elements has been coated with diamond. As with the DiComp sensor discussed above, the diamond is coated on a ZnSe IRE, as ZnSe and diamond have almost identical indices of refraction. Unlike the DiComp probe, however, in single-reflection accessories there is no air gap under the diamond layer. Diamond-coated single-reflection IREs are extremely resistant to chemical attack and cannot be scratched except by any material with a hardness equivalent to diamond. Nonetheless, it must be remembered that they can still be broken if a sufficiently hard material is pressed against the surface with large force.

Further reduction in the active area of the IRE can be accomplished in the element itself or with the use of microscope optics. In ATR accessories that are mounted in the sample compartment, it is impractical to use full microscope optics, but the vertical triangular prism IRE can be replaced with a hemispherical IRE. In this case, the hemispherical IRE acts similar to a lens so that the beam is condensed when it strikes the hemispherical IRE. The degree of condensation is proportional to the refractive index of the IRE. For example, a 1-mm-diameter beam that strikes a hemispherical Ge IRE, which has a refractive index of 4, is contracted to a diameter of only 250  $\mu\text{m}$ . That is,

$$\text{contracted beam size} = \frac{\text{original beam size}}{\text{refractive index of the hemisphere}} \quad (15.8)$$

This design is used in the Split-Pea ATR accessory by Harrick Scientific (Pleasantville, NY). This entire hemispherical IRE is only about 3 mm in diameter, and can be made from a variety of materials, including ZnSe (with or without a diamond coating) and silicon. Silicon (for which  $n_1 = 3.4$ ) is rarely used as an internal reflection element, as it has a very strong absorption band at  $660\text{ cm}^{-1}$  and several weaker but still intense bands at higher wavenumbers. As hemispherical Si IREs are usually only a few millimeters in diameter, the pathlength through single-reflection IREs is short and sufficient radiation is transmitted below  $2000\text{ cm}^{-1}$  that the entire mid-infrared region can be measured even with a DTGS detector.

Hemispherical internal reflection elements have been mounted in infrared microscopes, typically at the focal point in the upper Cassegrain objective. As is done in specular reflection microspectrometry, the incident radiation fills one half of the Cassegrain and illuminates the IRE. The other half of the Cassegrain is used to collect the radiation emerging from the IRE and deliver it to the MCT detector, as shown in Figure 15.14. ZnSe internal reflection elements are sufficiently transparent to visible light that the sample can be seen through the microscope but only when the IRE is in contact with the sample. Thus, optimizing the sample location and isolation is generally an interactive process of raising and lowering the sample so that it makes and loses contact with the IRE and the sample position is adjusted until the desired location is aligned with the IRE. This is not as difficult as it may seem, as the ATR and transmission Cassegrain objectives can rapidly be switched in the microscope and their registration upon switching is very nearly

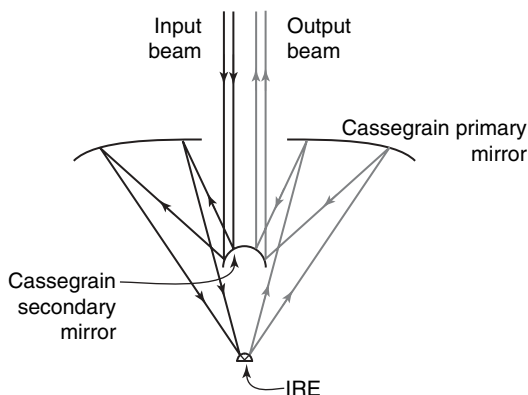


**Figure 15.14.** Cassegrain microscope objective with an IRE for surface analysis and mapping.

identical; hence once a sample is isolated with a transmission objective, switching to an ATR objective puts it in almost perfect optical alignment.

PerkinElmer has developed an ATR microscope objective, called the Multimode Objective, that permits both transmission and internal reflection measurements. The internal reflection element is mounted directly below the primary Cassegrain mirror and can be raised away from the focus of the objective for transmission studies and lowered for ATR measurements, as shown in Figure 15.15. This removes the problem of sample alignment. The IRE and sample are also protected from damage because if too much force is applied when the sample is pressed against the IRE, the IRE retracts automatically.

Although ZnSe can be used as a microscope IRE, most such IREs are fabricated from germanium or silicon. Silicon is rarely used in large IREs because of the strong absorption bands below  $2000\text{ cm}^{-1}$  that are caused by impurities. As noted above, when the pathlength through the IRE is short, as it is in microscopes, the use

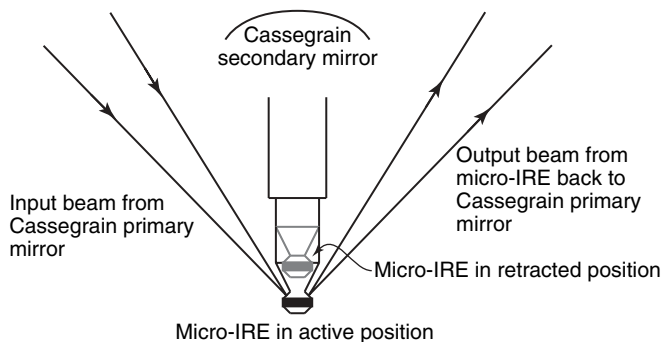


**Figure 15.15.** Microscope objective that can operate in both transmission and ATR modes. The IRE is raised for transmission measurements, and lowered for ATR measurements.

of silicon is no longer precluded. IREs used for microscopy are generally much smaller than the single-reflection IREs mounted in “macro-ATR” accessories, as the active area is usually only  $100\text{ }\mu\text{m}$  in diameter. It should be recalled that hemispherical IREs focus the beam due to their high refractive indices (see Eq. 15.8). If a transmission microscope has a diffraction limit of  $\sim 12\text{ }\mu\text{m}$  ( $\sim 800\text{ cm}^{-1}$ ) at the detector cutoff, that limit will drop to about  $3\text{ }\mu\text{m}$  with a Ge IRE.

Additional improvements have been made to single-reflection ATR accessories, even to the point where they have been made into stand-alone instruments. Smiths Detection (Danbury, Connecticut) markets stand-alone single-reflection ATR infrared spectrometers. One of these spectrometers, the IdentifyIR, is field-portable. It consists of a surface-mounted diamond-coated single-reflection ZnSe IRE that is interfaced to an interferometer. The spectrometer also includes a room-temperature detector. The active area of the IRE is slightly greater than 1 mm in diameter. To facilitate placement of the sample, a miniature video camera is placed below the IRE. Both ZnSe and diamond are sufficiently transparent in the visible region that samples in contact with the IRE can readily be seen. A small video screen is attached to the spectrometer so that the sample can be seen in real time. This is most useful for opaque samples where the area of interest is an isolated spot on one side of the sample. All data processing is provided by an external laptop computer. A schematic diagram of the IRE is shown in Figure 15.16. It should be noted that the geometry of the ZnSe/diamond IRE is similar to the DiComp (Figure 15.11) in that it is a truncated paraboloid. Harrick Scientific (Pleasantville, New York) also offers an FT-IR spectrometer accessory with a micro diamond ATR IRE ( $\sim 500\text{ }\mu\text{m}$  in diameter) that incorporates a video camera and display for sample examination and placement. This accessory is known as the Video Meridian ATR.

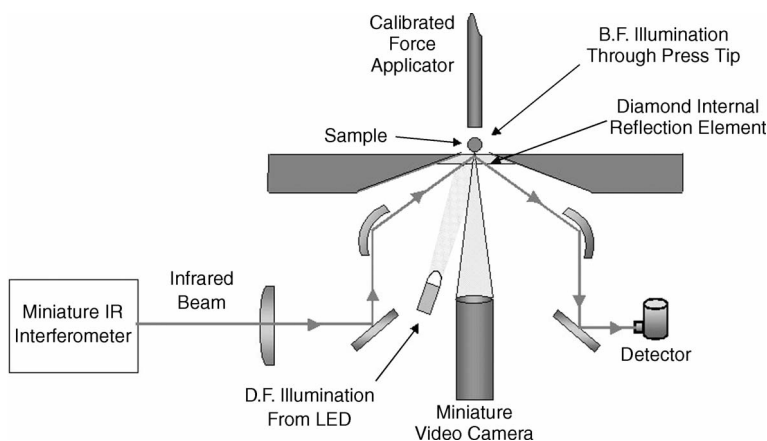


**Figure 15.16.** Stand-alone ATR accessory, the IdentifyIR, that incorporates a camera for visual inspection and alignment of a sample. (Courtesy of Smiths Detection.)

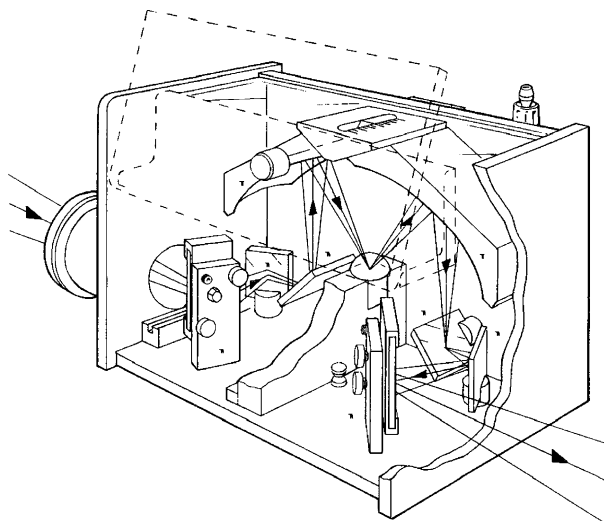


**Figure 15.17.** Seagull variable angle ATR accessory. (Courtesy of Harrick Scientific Corporation.)

Another stand-alone spectrometer from Smiths Detection is the IlluminatIR. This instrument is a miniature FT-IR spectrometer that can be interfaced to a commercial optical microscope. Although the primary use of the instrument is reflection microscopy, a diamond ATR infrared objective can be added to the optical microscope. The objective provides  $15\times$  magnification of the image and can be used to measure ATR spectra of samples as small as  $10\text{ }\mu\text{m}$ .

Although most single-reflection ATR accessories have a fixed angle of incidence, at least one accessory provides variable incidence angles. The Seagull by Harrick Scientific can accommodate a hemispherical IRE about 15 mm in diameter (see Figure 15.17). The hemisphere is placed with the plane side facing down so that the sample is mounted below the IRE. Two swing mirrors above the IRE can be adjusted so that the angle of incidence ranges from  $5^\circ$  to  $85^\circ$ . Of course, no IRE has a critical angle below  $22^\circ$  (Ge), but the same accessory can be used for specular and diffuse reflection.

One innovative design of a single-reflection IRE is a Fresnel design. In Chapter 13, Fresnel reflection was discussed with respect to specular reflection from a surface. In the current context, a Fresnel IRE refers to interaction of the radiation normal to the surface of the input of the IRE in an analogous manner to Fresnel lenses that were commonly installed in lighthouses to reduce the cost of lens fabrication. In a conventional IRE there is only one input and one output surface where the beam enters and exits the internal reflection element. A Fresnel IRE has multiple input and output surfaces for the beam. This is accomplished with five or six parallel bevels on the underside of a disk IRE as shown in Figure 15.18. An uncondensed beam at the focus of the sample compartment of an FT-IR spectrometer is usually between 6 and 12 mm in diameter. If the entire beam is directed to the beveled side of a Fresnel IRE, the whole beam interacts with the beveled surface

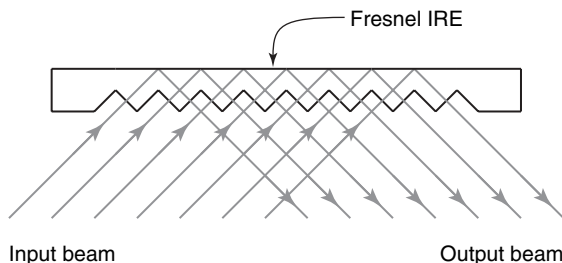


**Figure 15.18.** Cross section of a Fresnel IRE. The internal reflection elements are generally a disk to accommodate the circular beam from an FT-IR spectrometer.

and the beam will reflect only one time inside the element. Such elements are actually about 18 mm in diameter, but the active area is restricted to about 15 mm diameter because of beam obscuration by the mount around the IRE. Fresnel internal reflection elements are difficult to cut and polish compared to more conventional geometries, so the IREs are often made of extrudable or more malleable materials such as AMTIR I (a mixture of germanium, arsenic, and sulfur in the mole ratio  $\text{Ge}_{33}\text{As}_{12}\text{S}_{55}$ ) ( $n_1 = 2.50$ ) or  $\text{AgBr}$  ( $n_1 = 2.22$ ), although more conventional materials such as Ge can be cut to this geometry.

Some samples, such as thin films on substrates, are very difficult to measure by ATR infrared spectrometry. With much attention to semiconductor production and quality control, it has been found by Milosevic et al. [3] and Mulcahy et al. [4] that ATR can be used to measure monolayers on a silicon or metal substrate if the ATR measurement is made when the angle of incidence is near grazing. They showed that absorbance is actually enhanced for thin films on silicon at or near grazing-angle incidence when compared to thin films placed directly on the IRE. The spectrum of an organic monolayer on a silicon wafer is shown in Figure 15.19. An

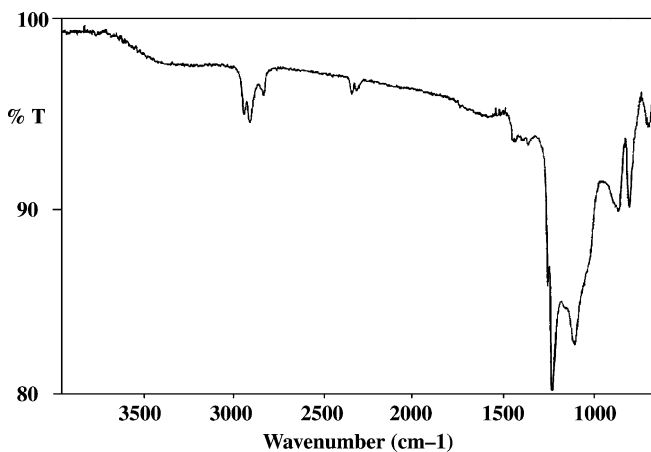


**Figure 15.19.** ATR spectrum of an organic monolayer on a silicon wafer. (Reproduced from [3], by permission of the Society for Applied Spectroscopy; copyright © 2003.)

absorbance of 0.1 AU (80% $T$ ) is much higher than is normally expected for a single monolayer.

## 15.6. INFRARED FIBERS

From previous sections it is obvious that IREs can be made into a variety of geometries. A cylindrical IRE can be extended to allow for more internal reflections. If the cylindrical IRE is extended far enough and its diameter is reduced, it becomes an infrared fiber. With a fiber the ends are planar and not conical, as was the case for the cylindrical IRE. In the ensuing discussion we define optical fibers as restricted to the visible and the short-wave near-infrared, whereas infrared fibers have transmission ranges from the near- though far-infrared.

A diagram of an infrared fiber is shown in Figure 15.20. Fibers are clad with a material of a lower index of refraction than the fiber itself. For example, chalcogenide fibers, which are fabricated from mixtures of Ge, As, Te, Sb, and S, have a refractive index of approximately 3.8 and are typically clad with a polyurethane or a polyamide coating (refractive index  $\sim 1.5$ ). Based on Eq. 15.2, this yields a critical angle of  $\sim 23^\circ$  inside the fiber as shown in Figure 15.20. For optical fibers the numerical aperture (NA) can be shown to be

$$\text{NA} = n_0 \sin \alpha = \sqrt{n_1^2 - n_2^2} \quad (15.9)$$

where  $n_0$  is refractive beyond the end of the fiber, which is usually air ( $n_0 \approx 1.0$ ),  $n_1$  is the refractive index of the fiber, and  $n_2$  is the refractive index of the cladding. Infrared fibers have much higher refractive indices than optical fibers and Eq. 15.9 fails when the angle  $\beta$  (Figure 15.20) is greater than the critical angle at the fiber–air interface. In reality, the numerical aperture of a high refractive index fiber is approximately unity [i.e., the acceptance angle ( $\alpha$ ) extends close to  $90^\circ$  from the normal]. Regardless, the input angle  $\beta$  cannot exceed the critical angle from the fiber side at the fiber–air interface. This means that the minimum angle of incidence is  $(90 - \beta)^\circ$ . For the example used above, where the refractive index of the fiber

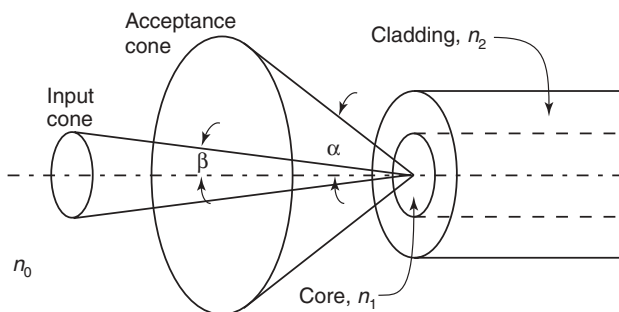


**Figure 15.20.** Infrared fiber showing the numerical aperture acceptance cone angle,  $\alpha$ .

core is 3.8, the internal input angle is approximately  $15^\circ$ , so that the minimum angle of incidence is  $\sim 75^\circ$ .

Infrared fibers can be used for the measurement of ATR spectra when the cladding is removed and the sample is in contact with the exposed fiber. At a minimum angle of incidence of  $75^\circ$ , the depth of penetration of the beam will be rather low. For a fiber of refractive index 3.8, a typical sample with a refractive index of 1.5 will have a depth of penetration of only  $0.066\lambda$ , or only  $0.66\text{ }\mu\text{m}$  at  $1000\text{ cm}^{-1}$ . Even though the fiber is rather narrow in diameter, the number of internal reflections per unit length will be fairly low. For a  $300\text{-}\mu\text{m}$ -diameter fiber with an angle of incidence of  $75^\circ$ , there will be an internal reflection approximately once every 1.1 mm, or only about nine reflections per centimeter. Thus, to achieve good sensitivity, an unclad fiber must be in contact with the sample over a length of several centimeters. In concept this is quite straightforward, but in practice there are several aspects that complicate the use of these fibers.

Materials that are commonly used for conventional and single-reflection IREs are often unsuitable as fiber materials. ZnSe, Ge, and other common materials are crystalline and they tend to form polycrystals when they are drawn into fibers. That is, they begin to crystallize into small particles, and even if they adhere to one another so that some fiber integrity is maintained, each crystal interface serves to scatter the radiation, and the fibers do not transmit sufficient radiation to be useful.

There are two classes of materials that have been fabricated successfully into infrared fibers, silver halides and chalcogenides. The silver halides are usually mixtures of AgCl and AgBr, that is,  $\text{AgCl}_x\text{Br}_{1-x}$ , where  $x \leq 1$ . Silver halide fibers are available with core diameters of about 1 mm, have fairly low losses, and have a transmission range from  $3300$  to  $50\text{ cm}^{-1}$ . These fibers have a minimum loss of approximately  $0.1\text{ dB/m}$ . ( $10\text{ dB}$  is equivalent to one absorbance unit.) Silver halide fibers are relatively soft and can be deformed under high pressure. In addition, like all silver halides, they are subject to photodegradation. Regardless, silver halide fibers have been used in a large number of ATR experiments.

Chalcogenide infrared fibers encompass a large class of compositions; in general, these are amorphous materials, that is, glasses composed of different combinations of elements Ge, Te, Se, Sb, As, and S. Chalcogenide glasses have different transmission ranges, but generally fall in the region  $7000$  to  $700\text{ cm}^{-1}$ . These fibers usually have diameters from about  $200$  to  $600\text{ }\mu\text{m}$  (i.e., they are significantly narrower than the silver halide fibers). Transmission losses tend to be higher than for the silver halides, most of which is attributed to absorption by the polymer cladding. Polymer-clad infrared chalcogenide fibers can have attenuation losses as high as  $1\text{ dB/m}$ , which makes them fibers useful only in lengths of a few meters.

Chalcogenide fibers have an extremely high tensile strength; that is, they can withstand considerable physical force if pulled along the axis of the fiber. Unfortunately, they are quite brittle and cannot withstand much shear (i.e., they will break easily if stressed perpendicular to the fiber axis). Regardless, they are quite flexible, and  $300\text{-}\mu\text{m}$ -diameter fibers can be bent to a radius of 1 to 2 cm without breaking.

Fibers are often used as ATR probes as opposed to sensors. A probe usually operates for a relatively short time and is not recovered. A good example of the



use of an infrared fiber is for polymer reaction monitoring. An infrared fiber can be optically coupled to an interferometer, often with the use of lenses rather than reflective optics. Lenses are used on-axis, and consequently have smaller foci than off-axis reflective focusing optics. The fiber can be placed in a reaction vessel and continue to the infrared detector element. MCT detectors are necessary as the radiative flux through a fiber is low and chalcogenide fibers cut off at about the same wavenumber as a midband MCT detector. Alternatively, the lens before the MCT detector can be eliminated and the fiber butted directly against the detector element, with the use of the appropriate vacuum coupling [5]. This is optically more efficient than a lens and can improve the SNR.

The fiber cladding is stripped where the fiber is inside the sample. A schematic diagram where a polymer reaction mechanism is investigated is shown in Figure 15.21. The reactants were poured into the sample container and the spectra were collected at the rate of a spectrum every 1 to 5 s. The data collected during the formation of a polyurethane foam reaction are shown in Figure 15.22.

Polyamide and polyurethane claddings can be difficult to remove from fibers. This problem is more often encountered with chalcogenide fiber as silver halide fibers are often unclad. Because it is very easy to break chalcogenide fibers, the cladding is best removed chemically. The cladding can be swollen with the use of dimethyl sulfoxide (DMSO) and then destroyed by dipping the swollen portion of the clad fiber into hot concentrated sulfuric acid. A short immersion will suffice and the degradation can be arrested by immersing the fiber back in DMSO. Any

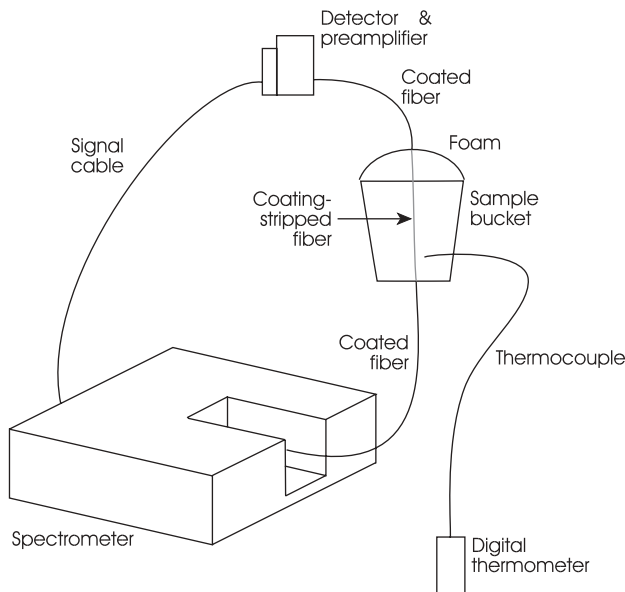


**Figure 15.21.** Experimental layout for a kinetic experiment with an infrared transmitting fiber. The spectrometer detector is remote to the instrument to reduce the length of the fiber. (Reproduced from [6], by permission of the Society for Applied Spectroscopy; copyright © 1993.)

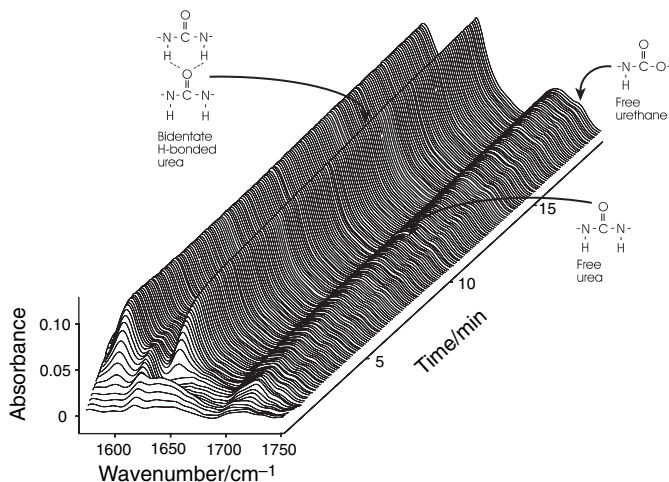


**Figure 15.22.** Absorbance spectra in the carbonyl region from the formation of a polyurethane foam. (Reproduced from [6], by permission of the Society for Applied Spectroscopy; copyright © 1993.)

residual cladding can be removed with the use of a piece of PTFE that has been shaped into a thin-edged knife or wedge. The fiber must be supported on a flat surface while it is scraped. It should be noted that chalcogenide fibers are resistant to dissolution at low pH, but they are certainly not impervious. Undue exposure to hot concentrated  $\text{H}_2\text{SO}_4$  will pit the fiber. The polymer coatings are very easily dissolved at high pH, but the chalcogenide glasses dissolve almost instantly at pH 11 or above. *Beware! The procedure above is dangerous and should only be undertaken in an appropriate fume hood and by a competent operator who has appropriate safety protection.*

To use single infrared fibers as ATR probes, the ends of the fiber must be perpendicular to the fiber axis and highly polished. This cannot be accomplished easily manually, and it is easier to polish the fiber ends with a commercial unit that is designed for polishing optical fibers. Such devices are sold for the telecommunications industry.

Single infrared fibers can be used as ATR probes and sensors in a wide variety of applications. Fibers are also used as waveguides to transfer radiation from the spectrometer to a remote location. Most often, chalcogenide fibers are used in bundles rather than single fibers. To reduce the attenuation found in polymer-clad fibers, the fibers are clad with another chalcogenide of lower refractive index than the core. As chalcogenide cladding has very low absorption, the attenuation can be reduced to as low as  $0.1 \text{ dB} \cdot \text{m}^{-1}$ .

Fiber bundles can be coupled to the ATR internal reflection elements. In Figure 15.23 it is shown how fibers are coupled to an internal reflection element that serves as a sensor. The radiation that emerges from about half the fibers couples directly into the IRE, but the radiation strikes the conical end of the IRE at an angle greater than the critical angle. The radiation does not emerge, but is directed back toward the fibers. The other half of the fibers in the bundle transmit the radiation to an IR detector.

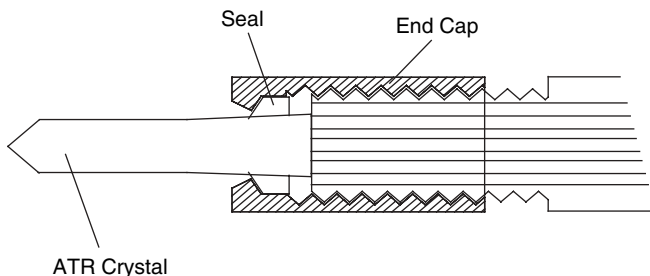


**Figure 15.23.** Infrared fiber bundle coupled to a frustrated total reflection IRE. The fiber bundle is bifurcated so that input and output radiation can be separated. (Courtesy of Remspec Corporation.)

Clearly, for this to happen, the bundle of cables must be bifurcated with one branch connected directly to the detector and the other coupled to the interferometer.

Fibers used solely as waveguides can be manufactured of other materials. Chalcogenide fibers can be clad with lower-refractive-index chalcogenides. These claddings cannot be removed, and the fibers cannot be used as internal reflection elements, but the claddings have lower attenuation losses than the polymer claddings. Therefore, the useful length of the infrared fibers as waveguides is considerably greater than the useful length for polymer-clad fibers. Another technology has been developed by Polymicro Technologies, LLC (Phoenix, Arizona), for infrared-transmitting hollow silica waveguides. The waveguides are constructed from a silica tube that is coated on the inside first with a silver film, then with a film of AgI. The exterior of the silica tube is clad with an acrylate coating. These waveguides have internal diameters of 300 to 1000  $\mu\text{m}$  and exhibit losses of 0.5 to 2.0  $\text{dB} \cdot \text{m}^{-1}$ , depending on the diameter and construction of the waveguide. They have a useful transmission range of approximately 3000 to 550  $\text{cm}^{-1}$ . A schematic diagram of hollow silica waveguide is shown in Figure 15.24.

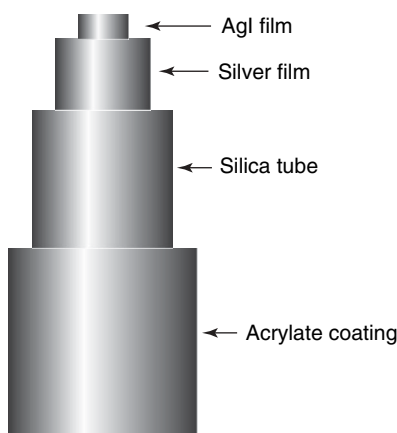


**Figure 15.24.** Hollow silica waveguide. The different layers have been separated to show the components that comprise the waveguide.

ATR sensors that employ fiber bundles have been constructed as “dip” sensors to sample drums or tanks of the solvents or solutions. Other accessory designs include small gas cells, diffuse reflection, and specular reflection accessories. Although fiber bundle accessories are available for benchtop FT-IR spectrometers, their greatest use is found when they are coupled to dedicated instruments for use in quality assurance/quality control applications.

## 15.7. SUMMARY

Attenuated total reflection is the most versatile of all the infrared sampling techniques. It requires very little sample preparation and can be used on samples of almost all morphologies. It is widely used for liquids and solid samples and the structural integrity of the sample can often be maintained. For solids, ATR spectra can be measured even for rough surfaces such as powders and woven textiles, as long as sufficient contact area between the sample and the IRE can be attained. Provided that a sample is not crushed, for example, between a diamond-coated IRE and a pressure ram, the chemical morphology will be retained. Sampling areas range from several square centimeters ( $10 \times 10$  mm trapezoidal or parallelepiped IREs) down to approximately  $300 \mu\text{m}^2$  (with a microscope ATR objective).

It should be remembered that ATR is in large part a surface technique. The actual interrogation of the sample is largely limited to the depth of penetration of the measurement, which is determined by the refractive indices of the IRE and the sample as well as the wavelength of the incident radiation and the angle of incidence within the IRE. The depth of penetration can be altered by the use of different IRE materials and changes in the angle of incidence. Nonetheless, the depth of penetration never exceeds  $\sim 60\%$  of the incident wavelength and is usually much smaller. In practical terms, the depth of penetration can be as large as  $12 \mu\text{m}$  for the longest wavelength and maximized depth of penetration, or as small as  $150 \text{ nm}$  at the shortest mid-infrared wavelength with minimal depth of penetration. If the sample is not homogeneous, ATR spectrometry will not measure the bulk properties or composition of a sample, but will record the spectrum of the near surface. Regardless, ATR spectrometry is an extremely powerful and versatile technique that can and should be applied to many samples.

## REFERENCES

1. S. Nunn and K. Nishikida, Advanced ATR Correction Algorithm, Application Note 01153, Thermo Electron Corporation.
2. N. J. Harrick, *Internal Reflection Spectroscopy*, Harrick Scientific Corporation, Pleasantville, NY, 1967.
3. M. Milosevic, S. L. Berets, and A. Y. Fadeev, *Appl. Spectrosc.* **57**, 724 (2003).

4. M. E. Mulcahy, S. L. Berets, M. Milosevic, and J. Michl, *J. Phys. Chem. B* **108**, 1519 (2004).
5. R. Krska, K. Taga, and R. Kellner, *Appl. Spectrosc.* **47**, 1484 (1993).
6. J. A. de Haseth, J. E. Andrews, J. V. McCluskey, R. D. Priester, Jr., M. A. Harthcock, and B. L. Davis, *Appl. Spectrosc.* **47**, 173 (1993).

# DIFFUSE REFLECTION

## 16.1. THEORY OF DIFFUSE REFLECTION

Diffuse reflection (DR) spectra result from the radiation incident on a powdered sample that is absorbed as it refracts through each particle and is scattered by the combined process of reflection, refraction, and diffraction. That fraction of the incident radiation that reemerges from the upper surface of the sample is said to be *diffusely reflected*. Because DR spectra result from an absorption process, they have the appearance of transmission spectra (i.e., bands appear in absorption), unlike the case for Fresnel reflection spectra of bulk samples (see Chapter 13). When DR spectra are acquired on Fourier transform spectrometers, the single-beam spectra of the sample and a nonabsorbing reference are measured separately and ratioed to produce the reflectance spectrum,  $R(\tilde{\nu})$ .

Like transmission spectra, DR spectra must be converted to a different form in order to convert  $R(\tilde{\nu})$  to a parameter that varies linearly with concentration. By analogy to transmission spectrometry, most practitioners of DR near-infrared (NIR) spectrometry convert  $R(\tilde{\nu})$  to  $\log_{10}[1/R(\tilde{\nu})]$ . Plots of  $\log_{10}[1/R(\tilde{\nu})]$  versus concentration are not linear over wide concentration ranges but are perfectly adequate for multicomponent quantitative analysis provided (a) that the concentration of each analyte does not vary by much more than a factor of 2, and (b) that the absorptivities of the analytical bands are fairly low. These criteria are often obeyed for the determination of the components of commodities by DR near-infrared spectrometry, but are not usually valid for mid-infrared spectra, where absorptivities are one or two orders of magnitude higher than in the near infrared.

The theories of diffuse reflection spectroscopy have been summarized by Griffiths and Dahm [1]. None of these theories allows  $R(\tilde{\nu})$  to be converted to a parameter that varies linearly with concentration over a wide range, but the Kubelka–Munk theory has provided the simplest and most useful parameter for practical measurements in the mid-infrared. Kubelka and Munk [2,3] derived a relationship between the reflectance of a sample at infinite depth,  $R_{\infty}(\tilde{\nu})$ , and its absorption coefficient,  $k(\tilde{\nu})$ , and scattering coefficient,  $s(\tilde{\nu})$ . (A sample whose DR spectrum does not change as it is made thicker is regarded as being at infinite

depth.) For pure materials,  $k(\tilde{\nu})$  is equal to twice the linear absorption coefficient,  $\alpha(\tilde{\nu})$  (see Eq. 1.17); for mixtures, the absorption coefficient is proportional to the concentration of each component present. The scattering coefficient used in the Kubelka–Munk equation,  $s(\tilde{\nu})$ , is twice the scattering coefficient for a nonabsorbing powdered sample measured by transmission, which is given by

$$T(\tilde{\nu}) = \frac{I(\tilde{\nu})}{I_0(\tilde{\nu})} = e^{-s(\tilde{\nu})b} \quad (16.1)$$

Kubelka and Munk derived a parameter,  $f(R_\infty)$ , that is simply the ratio of the absorption coefficient and the scattering coefficient. This parameter is given at any wavenumber,  $\tilde{\nu}$ , by

$$f[R_\infty(\tilde{\nu})] = \frac{[1 - R_\infty(\tilde{\nu})]^2}{2R_\infty(\tilde{\nu})} = \frac{k(\tilde{\nu})}{s(\tilde{\nu})} \quad (16.2)$$

$f(R_\infty)$  has one important drawback for quantitative work in that it is very sensitive to baseline errors relative to  $\log 1/R(\tilde{\nu})$  [4].

DR spectra plotted linear in the Kubelka–Munk function should be analogous to absorbance spectra of KBr disks. There is one difference, however. A well-prepared KBr disk is a solid solution of the analyte in KBr; thus, the crystal structure is often lost when the disk is being prepared. Fuller and Griffiths [5] showed that DR spectra are similar to poorly prepared KBr disks (see Figure 16.1). This means that the morphology of a crystalline sample is usually retained better when it is measured by DR spectrometry than when it is prepared as a KBr disk. In practice, the amount of grinding that a sample requires to prepare it for DR spectrometry (see Section 16.3) is similar to the grinding required for the preparation of a mineral oil mull, but without the loss of part of the spectrum by the mulling oil.

There is a problem with the nomenclature used in reflection spectroscopy. For example, diffusely reflected radiation can be measured from a rough metal surface, even though the beam has not penetrated the surface. Similarly, when the spectrum of a powder is measured, radiation that has been reflected from the front surface of a particle in the top layer according to the Fresnel equations (see Chapter 13) will be measured along with radiation that has penetrated into the sample, is refracted through several particles, is scattered at the interface between the particles, and ultimately emerges from the top surface of the sample. Brimmer et al. [6] proposed that the process of radiation reaching the detector in this way should be called *Kubelka–Munk reflection* and that radiation that is reflected from the front surface of a particle should be called *Fresnel reflection*. They use the terms *specular* and *diffuse* in a strictly geometrical sense [i.e., diffuse reflection refers to any radiation that is not reflected at a specular angle (when the angle of reflection  $\neq$  the angle of incidence)]. However, although logical, this proposal has not met with general acceptance by the spectroscopic community, in part because unless the absorptivity of the bands used for any analysis of powdered sample is quite low, the effect of Fresnel

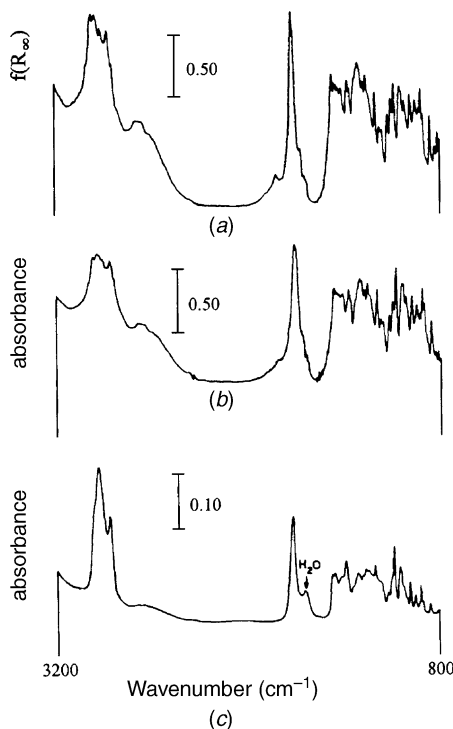


**Figure 16.1.** Spectra of cholic acid measured (a) by diffuse reflection and plotted linear in  $f(R_\infty)$ , (b) by transmission spectrometry as a poorly prepared KBr disk, and (c) by transmission spectrometry as a well-prepared KBr disk; (b) and (c) were plotted linear in absorbance.

reflection will be seen in the measured spectrum along with the (Kubelka–Munk) reflection. Front-surface reflection can be a major source of interference in mid-infrared DR spectra unless the sample is diluted by mixing it with between 10 and 100 times its weight of a powdered diluent, such as KBr or KCl.

The scattering coefficient is often believed to be constant across a DR spectrum, although in practice there may be a considerable variation [7]. The way that samples are prepared may have a large effect on the scattering coefficient. Many practitioners of mid-infrared DR spectrometry prepare their samples by loading the powder into the sample cup with a spatula and then running the spatula or a razor blade across the top of the cup to leave a flat surface. This approach is fine for preparing samples for qualitative or even semiquantitative analyses. However, the effect of running the blade across the surface is to make the scattering coefficient not only nonuniform across the surface but also different from the scattering coefficient of the sample just below the surface. A better way to prepare samples reproducibly is simply to load the cup so that it is slightly overfilled and to tap the cup on the bench until the top of the sample is exactly level with the top of the cup. A better but more time-consuming way of ensuring that the scattering coefficient is constant is to compress the sample lightly under a known force for a known length



of time. Band intensities of samples prepared in this way can be repeatable to better than  $\pm 1\%$  [8,9].

The sample cups used for mid-infrared DR spectrometry are usually 4 to 6 mm in diameter and 4 to 6 mm deep. Thus, between 50 and 200 mg of the sample is typically needed. Since the sample is diluted in a powdered alkali halide, a little less than 1 mg of the unknown is required. Cups for microsampling are typically 1 mm in diameter and 1 mm deep. In this case, only about 1 mg of sample, and less than  $10\text{ }\mu\text{g}$  of the unknown, is needed. In practice, mid-infrared DR spectroscopy is a remarkably good microsampling technique because when analytes are present at low concentration, the signal,  $1 - R(\tilde{\nu})$ , is proportional to the square root of the concentration [10]. For every other microsampling technique, the signal becomes linearly proportional to concentration when  $c$  is low.

For the measurement of good DR spectra, the particle size should be reduced to the point that passage of the beam through a single particle should not attenuate the beam by more than about 10%. It has been shown that in some DR measurements, the beam penetrates to a depth that is no greater than 10 particles below the surface [11]. Remembering that for mid-infrared spectroscopy, strong bands in a  $10\text{-}\mu\text{m}$ -thick sample of a typical organic have a peak absorbance of  $\sim 1$  AU (see Chapter 1), this implies that the average particle size should be reduced to about  $2\text{ }\mu\text{m}$ . Thus, to obtain the best spectra, samples require careful grinding, either by hand in a mortar or using a ball mill. Because of the low absorptivity of bands in near-infrared spectra, such careful grinding is not required, but the particle diameter should still be less than  $\sim 100\text{ }\mu\text{m}$  for optimal data.

Because of the simplicity of sample handling and the speed of the measurement, NIR DR spectrometry has been used for over 20 years for the quantitative analysis of a wide variety of powdered samples, including many cereal products and pharmaceuticals. A wide variety of instruments is available for these measurements, including fixed and tilting filter-based instruments, grating spectrometers with a single detector, or detector array and FT-NIR spectrometers. Measurements can be carried out in a couple of seconds, making NIR spectrometry an ideal technique for quality assurance and process monitoring.

Relatively few NIR DR spectra are measured on Fourier transform spectrometers, in part because the SNR of the interferogram in the region of the centerburst is often so high that the dynamic range of the analog-to-digital converter is exceeded. In addition, the effect of a nonlinear detector response at such high energy can reduce the photometric accuracy of the measurement (see Chapter 8). Because absorption bands in the NIR spectra of cereal grains and other agricultural products are generally quite broad ( $\text{FWHH} > 10\text{ nm}$ ), excellent NIR DR spectra can be measured by rapid-scanning grating spectrometers equipped with a PbS detector, and there is little need for the use of an FT-NIR spectrometer. This is not necessarily the case for pharmaceutical products, where bandwidths are usually far narrower. In this case FT-NIR spectrometers are being used extensively to obtain more useful DR spectra than can be measured with filter instruments, scanning monochromators, or polychromators.

For mid-infrared DR spectrometry, more sample preparation is needed than for NIR because of the increased band absorptivities, as described above. Furthermore,

the energy at the detector is usually about 10 times lower than it is for the corresponding measurement of a KBr disk. In the late 1970s, when mid-infrared DR spectroscopy first became popular, it was believed that an FT-IR spectrometer, ideally equipped with an MCT detector, was needed for the measurement of high-quality DR spectra, and the technique was dubbed diffuse reflection infrared Fourier transform, or DRIFT, spectrometry [5]. Even though it was later proved that similar measurements could be made on a grating spectrometer and DRIFT has all the wrong connotations for any spectroscopic measurement, this name has (unfortunately in our opinion) stuck to the present day. Regardless, we will persist in using *DR spectrometry*.

## 16.2. ACCESSORIES FOR DIFFUSE REFLECTION

Three types of devices have been described for the measurement of mid-infrared spectra: on-axis accessories, off-axis accessories that are mounted in the sample compartment of the spectrometer, and integrating spheres. On-axis accessories for diffuse reflection spectrometry are very much like highly efficient specular reflection accessories. They usually have a higher optical efficiency than either of the other two designs. A typical design of a DR accessory with on-axis geometry is shown in Figure 16.2.

Accessories of this type have one major drawback. The particles in the top layer of the sample are often aligned so that one of their planes is parallel to the macroscopic plane of the sample (especially when the top of the sample is flattened with a spatula or razor blade). In this case, much of the front-surface reflection is collected along with the diffusely reflected reflection that has penetrated into the sample before reemerging from its top surface. The result is that bands become distorted and plots of  $f(R_\infty)$  versus concentration become nonlinear at low concentration. Thus, DR accessories with an on-axis geometry are best used for qualitative measurements.

One way to eliminate radiation that has been reflected from the front surface of powdered samples is shown in Figure 16.3. All specularly reflected radiation (both

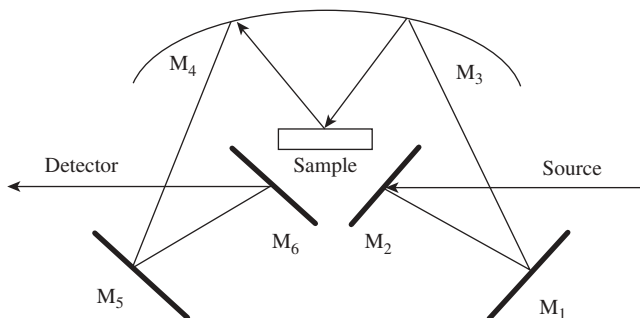


**Figure 16.2.** Spectra-Tech's Collector, a typical accessory with on-axis optical geometry for mid-infrared DR spectroscopy.  $M_1$ ,  $M_2$ ,  $M_5$ , and  $M_6$  are plane mirrors while  $M_3$  and  $M_4$  are opposed ellipsoids.

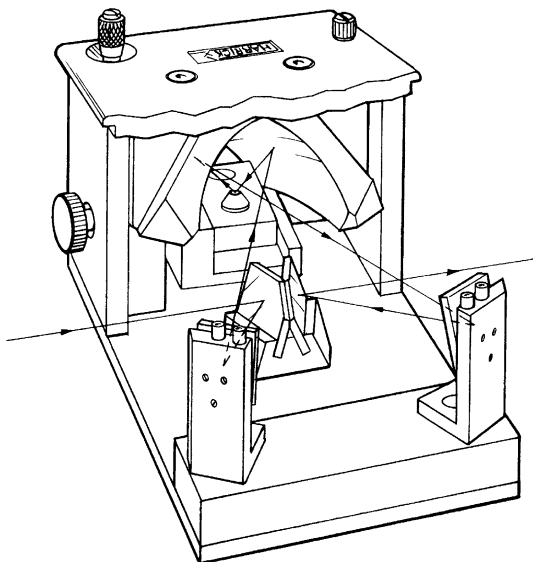


**Figure 16.3.** Harrick Scientific's Praying Mantis, a typical accessory with off-axis optical geometry for mid-infrared DR spectroscopy.

Fresnel and Kubelka–Munk) is eliminated by accessories with an off-axis geometry, such as the one shown in Figure 16.3. Although the optical efficiency of these devices, as measured by the signal at the detector from a nonabsorbing standard, is lower than that of on-axis accessories, the proportion of Fresnel reflection is decreased significantly. The result is that bandshapes are more symmetrical and the linearity of plots of  $f(R_\infty)$  versus concentration extend to higher concentration.

The best photometric accuracy of all is achieved by measuring DR spectra with an integrating sphere [12]. The integrating sphere is a hollow spherical cavity, the interior surface of which is coated with a high-reflectance diffuse coating. Finely powdered barium sulfate is commonly used for the visible region of the spectrum, but its strong absorption below  $1400\text{ cm}^{-1}$  precludes its use in the mid-infrared. For this spectral region, rough gold surfaces are the standard. Port openings are provided for the incident radiation, sample, and detector. To measure the reflectance of a sample, the ratio of the photon flux of the radiation reflected from the surface of the sample to that of the incident radiation must be measured. The measurement of a highly directional incident flux can be straightforward for flat samples. However, the flux reflected from a diffuse surface can be more difficult to quantify. In an integrating sphere, the ratio of the flux of the reflected radiation to that of the incident radiation is determined by comparing the signal from the sample to that of a standard of known reflectance. This ratio is known as the *reflectance factor*. Usually, the sample is mounted at an angle so that the radiation strikes it at an incidence angle of a little less than  $10^\circ$ . The port at which the sample is mounted should ideally be knife-edged to maximize the radiant exchange between the surface of the sample and the interior

of the sphere. If the beam penetrates well below the macroscopic surface of the sample, the port should be slightly larger than the illuminated area.

The measurement geometry that provides directional incident flux and hemispherical collection is shown in Figure 16.4*a*. A sample that is illuminated hemispherically and viewed at an angle that is near normal (as shown in Figure 16.4*b*) is called the *radiance factor*. The selection of the optical geometry depends on the particular application being studied.

A limitation imposed by the sample on the circumference of the sphere is the inability to vary the angle of incidence. In an alternative sphere design, the sample holder is projected onto the sphere center on an arm that is rotatable about an axis passing through the plane of the sample (see Figure 16.4*c*).

The signal-to-noise ratio of DR spectra measured with an integrating sphere is rarely as high as when the accessories shown in Figures 16.2 and 16.3 are used. However, if the accuracy at which the hemispherical reflectance must be known is high, the use of integrating spheres is recommended over the simple devices that are mounted in the sample compartment of the spectrometer.

### 16.3. APPLICATIONS OF MID-INFRARED DIFFUSE REFLECTION SPECTROMETRY

By far the greatest number of users of diffuse reflection accessories simply want to measure the spectrum of a powdered sample. Samples can be prepared for DR spectrometry much more quickly than KBr disks or mineral oil mulls. Organic samples are usually mixed with 10 to 100 times their weight of a powdered alkali halide (called a *diluent* in this chapter) and ground until their particle size is about 2  $\mu\text{m}$ . If a ball mill such as a Wig-L-Bug (Crescent Manufacturing Company, Chicago, Illinois) is used, this procedure takes only about 2 minutes. In this device, the sample is loaded into a stainless steel vial along with two ball bearings. The vial is rapidly moved in a figure-of-eight motion, allowing the balls to crush the sample very quickly. If inorganic materials are to be studied, the instantaneous pressure in the vial may lead to ion exchange between the sample and the diluent. This is particularly easy when KBr is used as the diluent. In such cases the sample should be ground separately from the diluent and the two powders mixed after the grinding step. When the sample is softer than the diluent, it may also adhere to the walls of the vial, so that the concentration of the mixture is less than would be expected from the amount of sample and diluent that were weighed into the vial. For quantitative DR measurements, it has been found to be quite difficult to prepare samples of accurately known concentration for calibration. Hamadeh et al. [13] have shown that shaking the sample and diluent together in a ball mill without loading the ball bearings in the vial gives very uniform dispersions.

Regardless, a better but more time-consuming method is to prepare the sample and diluent separately. The two are then mixed by hand by what is known as the pharmacist's method. With the sample in one dish, an equal amount of diluent is added to double the total volume. This is mixed carefully with a spatula. More

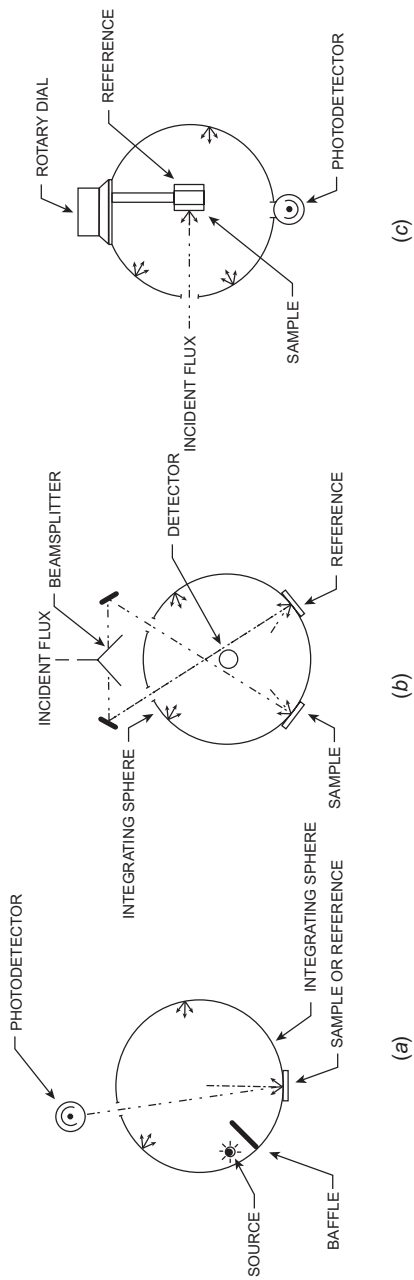


**Figure 16.4.** Geometries for an integrating sphere used in configurations for measuring (a) reflectance factor and (b) radiance factor; (c) center-mounted sample geometry.

diluent is added, so that the total volume doubles once again, and this is mixed with a spatula. The process is repeated until the desired composition is reached. This method will prevent ion exchange or the loss of material due to different hardnesses. If this procedure is done in a drybox, adsorbed water can be avoided. Clearly, this is more time consuming than the methods discussed above, yet it will provide better results.

A simple way of preparing very hard samples for DR spectrometry is to use fine silicon carbide paper (sometimes known as emery paper) to abrade some of the sample. The ratio of the single beam spectrum of the emery paper after and before abrading the sample is often very similar to the transmittance spectrum of the sample and allows a rapid identification to be made. This technique is particularly useful for thermosetting polymers. Another application is the characterization of samples that are too large to bring into the laboratory. For example, the spectrum of the paints of cars involved in an accident may be obtained by transferring the paint onto a disk of emery paper at the site of the accident and bringing the disk to the lab for measurement.

Another application of mid-infrared DR spectroscopy is the measurement of reacting samples in a controlled atmosphere. A number of cells has been designed to be compatible with commercially available DR accessories. A home-built accessory [14] is shown in Figure 16.5 and a typical commercially available accessory is shown in Figure 16.6. The efficiency of these accessories is quite low, so that they are generally used in conjunction with an MCT detector. When the cells are used at high temperature, a considerable amount of unmodulated thermal radiation is

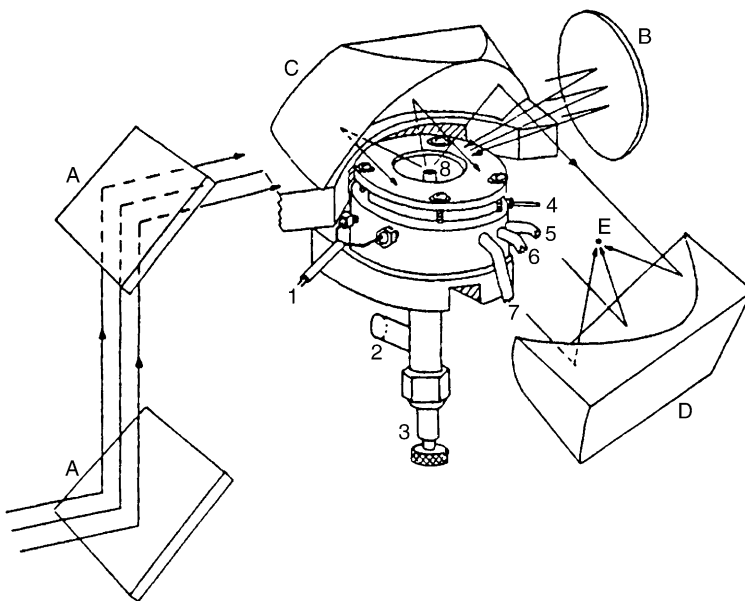


**Figure 16.5.** Accessory described by Hamadeh et al. [14] for the measurement of mid-infrared DR spectra of powdered samples at elevated temperature and in a controlled atmosphere.

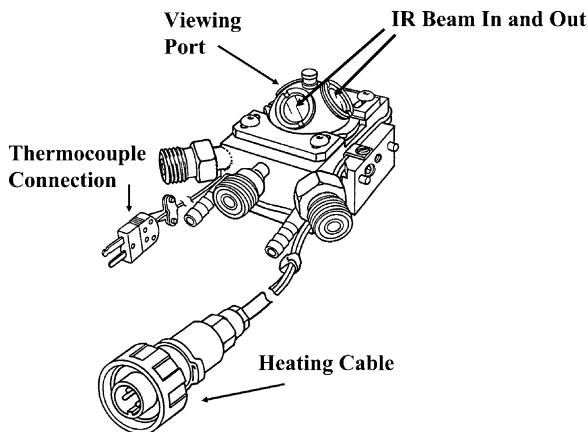


**Figure 16.6.** Accessory to Harrick Scientific's Praying Mantis accessory for DR spectroscopy for the measurement of mid-infrared DR spectra of powdered samples at elevated temperature and controlled atmosphere.

focused onto the detector element, promoting electrons from the valence band to the conduction band and reducing the response to modulated radiation (i.e., the interferogram) and hence the signal-to-noise ratio of the spectrum. This is the reason why the device shown in Figure 16.5 allows for water cooling.

These cells have proved useful for the measurement of a wide variety of applications, including the study of adsorption and catalytic and weathering reactions. In spectral regions where the absorptivity of the adsorbent is low, the sensitivity of DR spectrometry to small amounts of adsorbates is very high. For example, the spectrum that results when carbon monoxide is adsorbed on an alumina-supported rhodium catalyst, when the concentration of rhodium metal is 1% and 5%, is shown in Figure 16.7. It may be noted that good spectra of the same chemical system were measured on the accessory described by Hamadeh et al. [14] when the rhodium concentration is only 0.01%, the CO pressure is 1 millitorr, and spectra close to the detection limit were obtained at a rhodium concentration of 0.001% and a CO pressure of 2 millitorr [15]. Such good sensitivity can be found in spectral regions only where the absorbent has low absorption. If the band of the adsorbate is located in a spectral region where the adsorbent has a very high absorptivity, it is unlikely that any band due to the adsorbate will be seen, no matter how high its surface coverage.

#### 16.4. APPLICATIONS OF NEAR-INFRARED DIFFUSE REFLECTION SPECTROMETRY

Near-infrared (NIR) spectra are rarely used to identify materials, but NIR spectroscopy has nonetheless assumed a role of great importance for contemporary analytical chemists. Near-infrared (NIR) diffuse reflection spectroscopy became of great importance in the 1970s, when it was shown that the concentration of protein, oil, and water

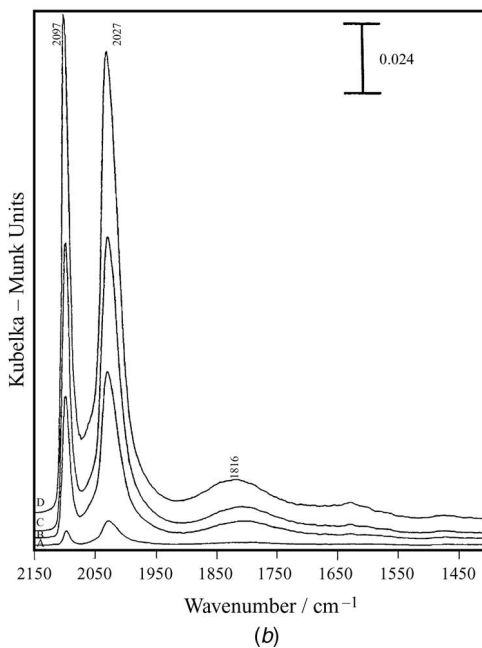
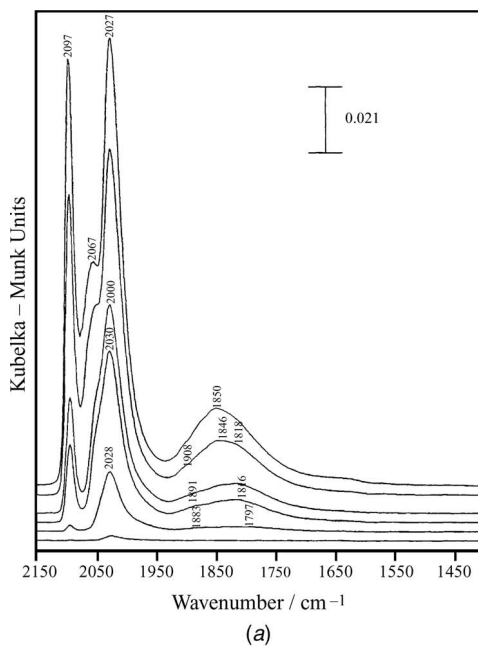


**Figure 16.7.** DR spectra of CO on (a) 1% and (b) 5% Rh-Al<sub>2</sub>O<sub>3</sub> under a pressure of 0.015 torr. (Reproduced from [14], by permission of Elsevier Publishing Co.; copyright © 1984.)



in cereals could be measured accurately from their DR spectra measured between 2500 and 1100 nm ( $4000$  to  $\sim 9000$   $\text{cm}^{-1}$ ). Today, many types of solids are analyzed by measuring their NIR DR spectrum. Unlike the case for mid-infrared spectra, NIR spectroscopy is almost never used for structural elucidation. Instead, spectra of samples of known composition are regressed against calibrations standards of known composition. In fact, it could be argued that much of the impetus toward the development of modern chemometrics is derived from the need to obtain accurate quantitative information from the NIR DR spectra of agricultural commodities.

The near-infrared region has several advantages for this type of measurement. First, NIR bands are either overtones of C–H, O–H, and N–H stretching modes or combinations of these modes with lower-frequency modes of the same functional groups. As a result, their absorptivities are at least an order of magnitude weaker than the absorptivities of the fundamentals from which they are derived. This gives rise to two fundamental advantages. First, there is no need to mix the sample with a non absorbing diluent. Because the samples can be measured neat, sample preparation is minimized. Second, anomalous dispersion is negligibly small, so that absorption bands in NIR DR spectra are not distorted by Fresnel reflection. There is, of course, some front-surface reflection, but this results in a small but constant displacement of the zero reflectance line, so that the bandshape is rarely distorted by the effect of Fresnel reflectance. The only effect is an increased non-linearity of plots of  $\log(1/R)$  against concentration. Since these curves are intrinsically nonlinear, an added nonlinearity has little effect on the data treatment.

NIR DR spectra are also used for assuring the identity of the reactants and products of industrial processes using a variety of algorithms for discriminant analysis. Gross errors in, for example, the identity of chemicals that have been shipped to a given plant are easily picked up by these algorithms. However, since the NIR spectra of organic materials are dominated by bands related to C–H, O–H, and N–H stretching vibrations, it may be thought that NIR spectra will be far less successful in distinguishing between structurally similar molecules. NIR spectrometry has a subtle advantage for this type of analysis. The in-plane  $\text{CH}_2$  bending mode absorbs at about one-half the frequency of the C–H stretching modes. The first overtone of the C–H bend can therefore interact with one of the C–H stretching fundamentals by Fermi resonance, borrowing intensity from the C–H stretch and slightly altering the wavenumber at which each mode absorbs in the region between  $2800$  and  $3000$   $\text{cm}^{-1}$  due to anisotropy. This effect is significantly larger in the region of the first overtone. As a result, small differences in the structure of chemically similar molecules can affect the extent of the interaction and alter their spectra to a degree that would not be expected by scientists who have only measured mid-infrared spectra.

As stated in Section 16.1, the measurement of NIR DR spectra for quantitative analysis of powdered products has been carried out by a number of different instruments, including filter spectrometers, scanning grating spectrometers, and acousto-optic tunable filters (AOTFs) with a single detector and grating polychromators with an array detector. It might be expected that the multichannel advantage of spectrometers equipped with array detectors and the multiplex advantage of

FT-NIR spectrometers would give these instruments a considerable advantage over single channel instruments, such as the scanning monochromator or AOTF. When fairly high resolution or a very precise wavenumber scale is needed (as it may be for the analysis of pharmaceuticals), FT-NIR spectrometers have a strong advantage over the other types of spectrometers. However, NIR bands are usually quite broad in the spectra of most agricultural commodities, and high resolution is rarely required. In this case, the problems associated with a nonlinear detector response when the energy being measured is very high (as it is near the interferogram centerburst) can degrade the photometric accuracy of FT-NIR spectrometers and measurements are better made using either a single- or multichannel spectrometer.

### 16.5. REFERENCE MATERIALS FOR DIFFUSE REFLECTION SPECTROMETRY

As noted above, diffuse reflectance spectra are measured by calculating the ratio of the single-beam spectrum of the sample and that of a suitable reference. For mid-infrared DR spectrometry measured using accessories of the type shown in Figures 16.2 and 16.3, the best reference is almost invariably the same material that was used as a diluent. KBr powder is frequently used for this purpose, but KBr is soft and not easily ground and quite hygroscopic. As a result of strong O–H stretching band of water, the baseline of mid-infrared DR spectra in the region between 3200 and 3800  $\text{cm}^{-1}$  is often degraded, making it difficult to decide whether broad bands are due to the analyte or water adsorbed on the surface of the KBr. NaCl can also be used but shows strong absorption below 700  $\text{cm}^{-1}$ . A good compromise is KCl, which is harder and less hygroscopic than KBr and allows spectra to be measured to about 550  $\text{cm}^{-1}$ . One final problem that may be noted with all alkali halides is that it is difficult to obtain them completely free of nitrate. As a result, even when the nitrate concentration is as low as 0.01%, a sharp band at 1380  $\text{cm}^{-1}$  is often seen in the spectrum. An alternative to alkali halides is diamond dust. Diamond powder is inexpensively available as an abrasive. Diamond does have a strong absorbance at  $\sim 2200 \text{ cm}^{-1}$ , but this is relatively broad and does not obscure the spectrum in this region. Diamond is very hard, but it is not hydroscopic.

An alternative reference material is a diffuse gold disk, sold commercially as InfraGold [12]. This is the recommended reference for all measurements made using an integrating sphere, as its reflectance properties are accurately known. Scattering from a gold surface is different from scattering from a powdered salt reference, so that the baseline of the reflectance spectrum measured using accessories such as those shown in Figures 16.2 and 16.3 is often well displaced from 100%. As noted above, if spectra are converted to the Kubelka–Munk function, baseline errors can lead to variations in the band intensity.

For measurements in the NIR, sintered ceramic disks or polytetrafluoroethylene (PTFE) are most commonly used. Neither type of reference is perfect, with ceramic disks having weak absorption bands caused by adsorbed water and PTFE disks having weak but reproducible bands caused by overtones of the C–F stretching modes. The

best compromise is the use of a roughened gold reference. Since most NIR DR spectra are converted to  $\log(1/R)$ , errors in the baseline are less important and easily corrected [4].

## REFERENCES

1. P. R. Griffiths and D. J. Dahm, Continuum and discontinuum theories of diffuse reflection, in *Handbook of Near Infrared Spectroscopy*, 3rd ed., D. Burns and E. Cziurczak Eds., Taylor & Francis, New York, 2007.
2. P. Kubelka and F. Munk, *Z. Tech. Phys.* **12**, 593 (1931).
3. P. Kubelka, *J. Opt. Soc. Am.* **38**, 338 (1948).
4. P. R. Griffiths, *J. Near Infrared Spectrosc.* **3**, 60 (1996).
5. M. P. Fuller and P. R. Griffiths, *Anal. Chem.* **50**, 1906 (1978).
6. P. J. Brimmer, P. R. Griffiths, and N. J. Harrick, *Appl. Spectrosc.* **40**, 258 (1986).
7. D. J. J. Fraser and P. R. Griffiths, *Appl. Spectrosc.* **44**, 193 (1990).
8. A. A. Christy, J. E. Tvedt, T. V. Karstang, and R. A. Velapoldi, *Rev. Sci. Instrum.* **59**, 423 (1988).
9. M. L. E. TeVrucht and P. R. Griffiths, *Appl. Spectrosc.* **43**, 1492 (1989).
10. M. P. Fuller and P. R. Griffiths, *Appl. Spectrosc.* **34**, 533 (1980).
11. J. M. Olinger and P. R. Griffiths, *Anal. Chem.* **60**, 2427 (1988).
12. K. F. Carr, *A Guide to FTIR Reflectance Spectroscopy*, Labsphere, P.O. Box 70, North Sutton, NH 03260.
13. I. M. Hamadeh, S. A. Yeboah, K. A. Trumbull, and P. R. Griffiths, *Appl. Spectrosc.* **38**, 486 (1984).
14. I. M. Hamadeh, D. King, and P. R. Griffiths, *J. Catal.* **88**, 264 (1984).
15. K. W. Van Every, Ph.D. dissertation, University of California, Riverside, CA (1987).

# EMISSION

## 17.1. INTRODUCTION

Compounds can be characterized by infrared transmission, reflection, photoacoustic, and emission spectroscopy. Of these techniques, infrared emission spectrometry is by far the least commonly used in most analytical chemistry laboratories. There is a number of reasons for this state of affairs:

- The sample must be above or below ambient temperature: The closer the temperature of the sample is to ambient, the lower the SNR of the spectrum.
- The radiation emitted by or reflected from the surroundings can be comparable to that of the sample.
- Obtaining accurate quantitative information can be extremely difficult because the sample temperature must be known.
- Temperature gradients across the sample distort the spectrum, making quantification even more inaccurate.

There are, however, several occasions when transmission, reflection, or photoacoustic spectra of remote samples simply cannot be measured and emission spectroscopy is the only possible way to obtain qualitative or quantitative information. In this chapter a brief outline of the theory and practice of infrared emission spectrometry is given.

## 17.2. INFRARED EMISSION SPECTRA OF GASES

The *emittance*, often called the *emissivity*, of a sample at any wavenumber,  $\epsilon(\tilde{\nu})$ , is defined as the ratio of the radiant power emitted by a sample at a given temperature and the corresponding radiant power that would have been emitted by a blackbody source with the same geometry at the same temperature. (Strictly speaking, the term *emissivity* refers to a fundamental physical quantity, whereas *emittance* refers to a

measurable quantity.) Kirchhoff's law states that for any sample, the sum of its transmittance,  $T(\tilde{\nu})$ , reflectance,  $R(\tilde{\nu})$ , and emittance at wavenumber,  $\tilde{\nu}$ , is equal to unity:

$$T(\tilde{\nu}) + R(\tilde{\nu}) + \varepsilon(\tilde{\nu}) = 1 \quad (17.1)$$

If the reflectance of a sample is low, as it is with gaseous samples,  $\varepsilon(\tilde{\nu})$ , is approximately equal to  $1 - T(\tilde{\nu})$ . Thus, for any sample for which a transmittance spectrum with discrete absorption bands can be measured, the emittance spectrum should yield equivalent information. As a result, qualitative analysis of the components of hot gases by infrared emission spectroscopy can be as easy as it is by transmission spectrometry. The problem of obtaining quantitative information by infrared emission spectroscopy is more difficult, since not only must the temperature of the sample be known if the radiant power from the blackbody is to be calculated, but the instrument response function must also be taken into account [1].

The instrument response function,  $F(\tilde{\nu})$ , is estimated by measuring the spectrum of a blackbody of known temperature and ratioing this spectrum against the spectral energy density of a blackbody at the same temperature (see Eq. 7.3) [2]. A typical result of applying this process is illustrated in Figure 17.1.

In many cases, the contribution of the surroundings,  $I_B(\tilde{\nu})$ , to the measured spectrum,  $I_S(\tilde{\nu})$ , must also be compensated [3]. The spectrum of the sample corrected

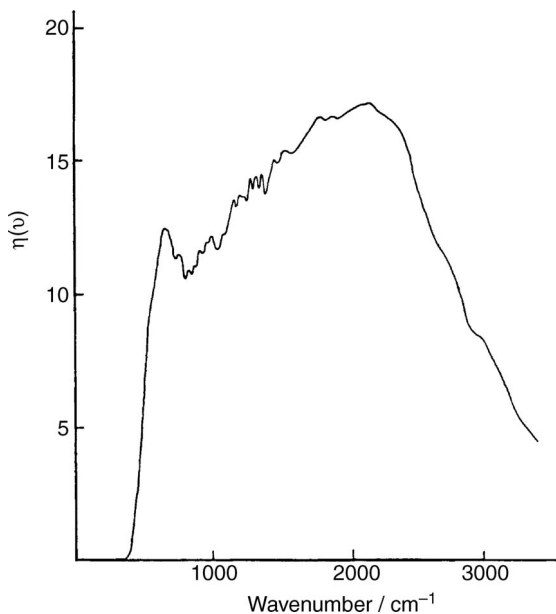


**Figure 17.1.** Instrument response function obtained by calculating the ratio of the spectrum of a blackbody at 200°C measured on a Digilab FTS-14 spectrometer with a Ge/KBr beamsplitter to the calculated spectral energy density of a blackbody at the same temperature.

for the instrument response function and the effect of background contributions,  $E_S(\tilde{\nu})$ , is then calculated as

$$E_S(\tilde{\nu}) = \frac{I_S(\tilde{\nu}) - I_B(\tilde{\nu})}{F(\tilde{\nu})} \quad (17.2)$$

For samples at a temperature close to ambient, a part of the background spectrum,  $I_B(\tilde{\nu})$ , comes from emission from the interferometer itself and may be out of phase with the radiation from the surroundings. In this case it is better to measure  $I_S(\tilde{\nu}) - I_B(\tilde{\nu})$  by subtracting the interferogram of the background from the sample interferogram, before calculating the Fourier transform to obtain the spectrum provided that the zero retardation position of the two interferograms is known [4]. The latter criterion was generally fulfilled by interferometers incorporating a separate white light channel (see, e.g., Figure 5.8) but may be less easily accomplished with contemporary fringe counting electronics.

Since the transmittance of any sample is (see Section 1.5)

$$T(\tilde{\nu}) = e^{-a(\tilde{\nu})bc} \quad (17.3)$$

by Kirchhoff's law, its emittance is

$$\varepsilon(\tilde{\nu}) = 1 - e^{-a(\tilde{\nu})bc} \quad (17.4)$$

The fact that  $1 - \varepsilon(\tilde{\nu})$  is identical to  $T(\tilde{\nu})$  in practice can be seen in Figure 17.2.

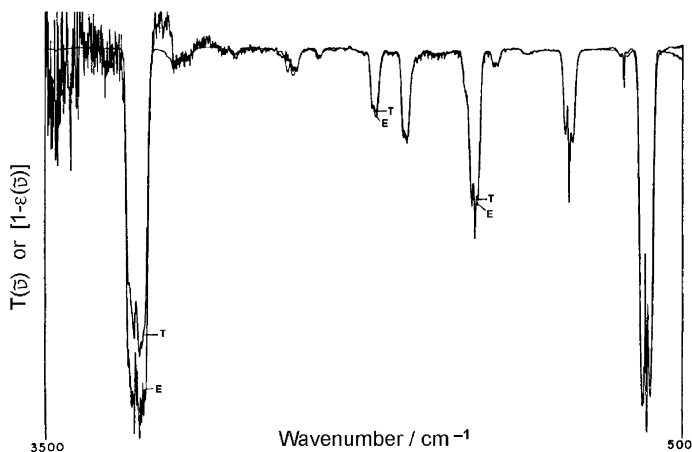


**Figure 17.2.** Emissivity (E) and transmittance (T) spectra of benzene vapor at 188°C. The difference between these two spectra at high wavenumbers is a result of the very low energy emitted by materials at 188°C above 2500  $\text{cm}^{-1}$ .

$E_S(\tilde{\nu})$  is linearly proportional to the product of  $\varepsilon(\tilde{\nu})$  and the spectral energy density of a blackbody at the temperature of the sample,  $U_{\tilde{\nu}}(T)$  (see Eq. 7.3). If  $K$  is the constant of proportionality, the absorbance at any wavenumber can be calculated as

$$A(\tilde{\nu}) = -\log_{10} \left[ 1 - \frac{E_S(\tilde{\nu})}{KU_{\tilde{\nu}}(T)} \right] \quad (17.5)$$

Once the absorbance is known, the concentration can be calculated by a simple application of Beer's law.

Obviously, the biggest problem with this approach is that the temperature must be known accurately for the spectral energy density to be calculated. Several spectral fitting approaches have been taken to find the temperature of the sample from  $E_S(\tilde{\nu})$ . One approach involves matching the intensities of as many bands as possible in the measured spectrum. Alternatively, the intensities of each line in one or more bands in the vibration-rotation spectrum can be fit. The latter method can give very accurate answers but is difficult to apply because of the effect of limited instrument resolution. The air-broadened width of most lines in a vibration-rotation spectrum is between 0.1 and 0.2  $\text{cm}^{-1}$ . To avoid nonlinear Beer's law behavior, the resolution parameter,  $\rho$ , should be no greater than 0.5 (see Section 8.2). However, to maintain a reasonably high signal-to-noise ratio, infrared emission spectra are rarely measured at a resolution of better than 1  $\text{cm}^{-1}$ . Although approaches have been described for quantitative analysis from emission spectra measured at moderate resolution ( $\rho > 1$ ), very detailed information about the effect of temperature and pressure on line widths is needed. Certainly, none of these approaches allows the concentrations to be predicted as accurately as in the corresponding measurement done by transmission spectrometry.

This having been said, it would be wrong not to mention some remarkable work that has been done by a number of workers who have measured emission spectra of the upper atmosphere and stratosphere. The pressure of the gases that contribute to these spectra (and hence the width of the rotational lines) can vary by over an order of magnitude. By fitting emission spectra measured at very high resolution, workers have been able to derive the concentration profiles of trace constituents in the stratosphere as a function of the distance from Earth's surface.

### 17.3. INFRARED EMISSION SPECTRA OF CONDENSED-PHASE SAMPLES

Emission spectra of solid and liquid samples are measured in a manner analogous to those of gases. As for gases, the ideal thickness of samples at thermal equilibrium should still be the same as the thickness required to yield a good transmission spectrum. When a thick sample is heated, each layer emits most strongly at those wavelengths where the absorptivity of the surface layer is greatest. Accordingly, the characteristic emission from layers well below the surface is absorbed by overlying layers. This process, called *self-absorption*, is especially noticeable when the upper layers are cooler than the layers well below the surface.

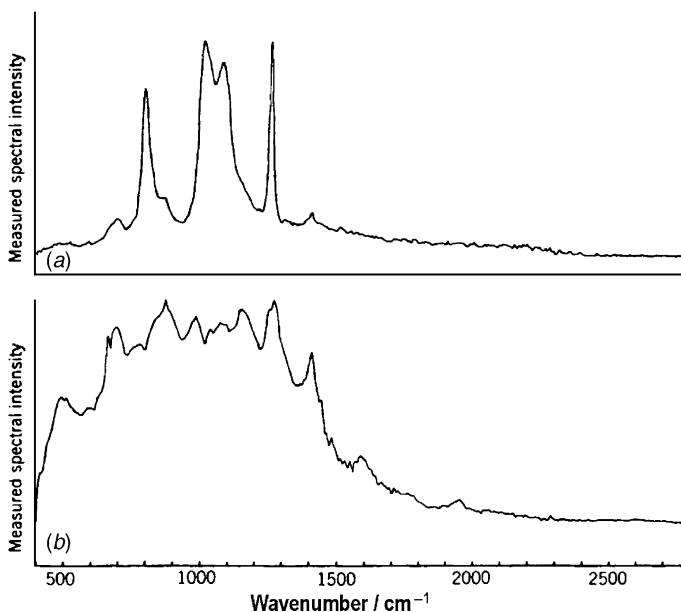


**Figure 17.3.** Single-beam emission spectra of (a) a thin ( $\sim 2\ \mu\text{m}$ ) layer of silicone grease, and (b) a much thicker ( $>50\ \mu\text{m}$ ) layer of silicone grease.

When deposited on substrates of low emissivity (e.g., metals or salt plates), very thin samples have minimal temperature gradients, so that self-absorption is also minimal. When the thickness is increased, the effects of self-absorption may lead to a dip at the band center. If the thickness of any sample is too great, its transmittance will be zero at all wavelengths. By Kirchhoff's law, therefore, the sample will have the same characteristics as a blackbody. Spectra of a thin and thick layer of silicone grease on a heated aluminum substrate are shown in Figure 17.3, showing how the spectrum of the thin layer has the appearance of a typical absorption spectrum of this material while the spectrum of the thick layer looks more like a blackbody [1]. This effect is particularly problematic for thick samples when their surface temperature is lower than the temperature of the bulk sample, as is often the case when hot samples are exposed to a cool atmosphere. However, it has cleverly been taken advantage of for transient infrared spectroscopy (see the next section). Because it is very difficult to make samples thin enough to avoid self-absorption, and useful analytical data can be obtained only when the temperature gradient of the sample is known accurately, infrared emission spectroscopy is rarely used for the analysis of samples at thermal equilibrium.

This is not to say that the measurement of emissivity is unimportant. For example, the spectral emissivity of materials is an important property for calculations of radiant heat transfer. Radiant heat transfer analysis is critical to designing the temperature-control systems of satellites and spacecraft, since convection and conduction are negligible in outer space. Radiant heat transfer analysis is also important



in the prediction of heat loss from boiler furnaces, air-conditioning equipment, and greenhouses, as well as the performance of passive solar heating devices. In many of these materials, the transmittance is zero, so Kirchhoff's law may be approximated as

$$\varepsilon(\tilde{\nu}) = 1 - R(\tilde{\nu}) \quad (17.6)$$

Thus, measurement of the hemispherical reflectance allows the emissivity of such samples to be calculated readily.

For most of the applications listed above, there is no need to measure the spectrum at high resolution, but high signal-to-noise ratio and radiometric accuracy are of paramount importance. It is interesting to note that even though integrating spheres are rarely used for chemical analysis, one of the principal applications of FT-IR diffuse reflection measurements using integrating spheres is for the accurate estimation of emittance for heat-transfer calculations (see Section 16.2).

#### 17.4. TRANSIENT INFRARED EMISSION SPECTROSCOPY

As noted above, it is difficult to account for the effect of temperature gradients across the sample, which makes quantification by infrared emission spectrometry rather inaccurate. A clever way of not merely getting around the problem of temperature gradients but actually benefiting from them has been described in a series of papers by Jones and McClelland [5–10]. The technique developed by these two workers is known as *transient infrared spectroscopy* (TIRS) and can be subclassified into two techniques, known as transient infrared emission spectroscopy (TIRES) [5,7] and transient infrared transmission spectroscopy (TIRTS) [8]. In both of these two techniques, the deleterious effect of self-absorption is minimized by avoiding the condition of thermal equilibrium that has been assumed for previous sections of this chapter.

In TIRES, a narrow jet of hot gas is passed onto the surface of a moving sample, so that only the region near the surface is heated. The intensity of radiation emitted from below the surface increases with time by thermal diffusion as heat is conducted into the bulk. Thus, the spectrum must be measured from a region of the sample very close to the point at which it is heated. The faster the sample is moved, the farther from the point of heating can the field of view of the spectrometer be located.

An approximate value of the emittance at wavenumber  $\tilde{\nu}$ ,  $\varepsilon'(\tilde{\nu})$ , may be obtained by calculating the ratio of the background-corrected emission from the sample at that wavenumber,  $E_s(\tilde{\nu})$ , and the emission at that wavenumber from a blackbody at the same temperature,  $E_{bb}(\tilde{\nu})$ :

$$\varepsilon'(\tilde{\nu}) = \frac{E_s(\tilde{\nu}) - E_{bg}(\tilde{\nu})}{E_{bb}(\tilde{\nu}) - E_{bg}(\tilde{\nu})} \quad (17.7)$$

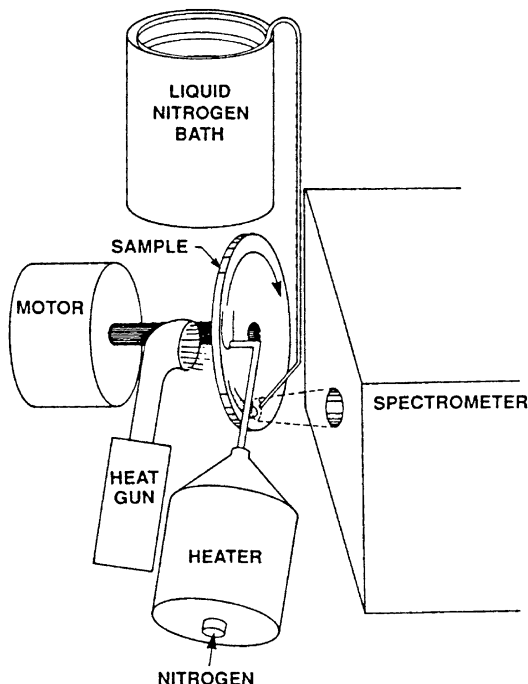


**Figure 17.4.** Experimental arrangement for TIRES. Samples are translated through the path of a jet of hot nitrogen within, or just before, the field of view (fov) of the spectrometer. A jet of chilled helium returns the sample surface to near ambient temperature. (Reproduced from [7], by permission of the American Chemical Society; copyright © 1990.)

where  $E_{bg}$  is the background signal from the spectrometer and sample. Since the thermal emission varies with depth, the temperature at different locations within the field of view of the spectrometer can vary greatly. The temperature of the blackbody used to calculate  $\varepsilon'(\tilde{\nu})$  must, therefore, be selected empirically. The blackbody temperature is usually chosen so that  $E_{bb}$  is slightly greater than  $E_s$  at all wavelengths. Jones and McClelland do not formally call the normalized TIRES spectra resulting from Eq. 17.7 *emittance spectra* because of the temperature spread across the sample, but  $\varepsilon'(\tilde{\nu})$  and  $\varepsilon(\tilde{\nu})$  are equivalent from a practical standpoint.

The experimental arrangement is shown schematically in Figure 17.4. A narrow jet of hot nitrogen is directed at the sample at a point within or just before the field of view of the spectrometer. A stream of helium that has been chilled by passing it through a liquid-nitrogen bath is often sprayed on the sample at a location after the field of view to return the sample temperature to near ambient. To achieve maximal sensitivity, spectra are typically measured with a MCT detector.

The alternative technique to TIRES is transient infrared *transmission* spectrometry (TIRTS). This technique is analogous to TIRES, but instead of the sample being at ambient temperature and being heated by the gas jet, the sample is above the ambient temperature and is cooled by a narrow jet of cold helium. Were the sample

to be uncooled, the spectrometer would measure a blackbody emission spectrum from all but the thinnest samples, as discussed in Section 17.3. By cooling the sample, the radiation emitted from hot layers below the surface is absorbed by the cooler layers near the surface. The resulting spectrum has the appearance of a typical single-beam spectrum measured using a Globar source, except that the energy at high wavenumbers is much lower because the temperature of the sample is much lower than the temperature of the Globar. For TIRTS,  $E_{bb}(\tilde{\nu})$  is an emission spectrum measured prior to switching on the flow of cold gas. As for TIRES, TIRTS spectra are usually measured with a wideband MCT detector. A typical experimental arrangement is shown in Figure 17.5.

Many experimental parameters affect TIRTS the same way that they do TIRES. For example, the extent of self-absorption depends on how long the emission is observed after the surface layer is heated, since the chilled layer starts to thicken immediately after being formed. Thus, the longer the chilled layer is observed after

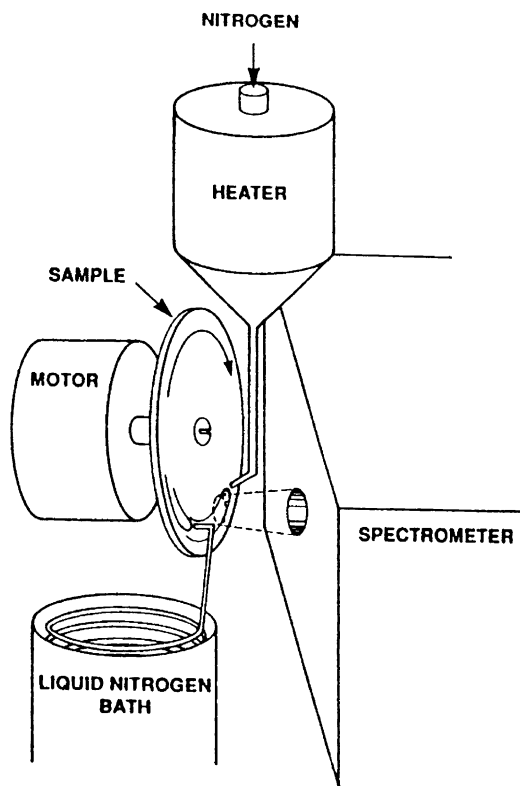


**Figure 17.5.** Laboratory apparatus for TIRTS. A jet of liquid-nitrogen-cooled helium is directed onto the sample disk within, or just before, the field of view of the spectrometer. A jet of heated nitrogen returns the sample surface to its original temperature. A heat gun warms the back of the sample disk for experiments with elevated sample temperatures. (Reproduced from [8], by permission of the American Chemical Society; copyright © 1990.)

being formed, the greater the average thickness of the layer and the higher the observed absorbance will be. The faster the sample is moved through the spectrometer's field of view (fov), either by reducing the diameter of the fov or by increasing the sample speed, less saturation will occur.

TIRES and TIRTS have many of the same properties as photoacoustic spectroscopy (see Chapter 20), in that they are largely insensitive to sample morphology and to the optical properties of the sample, such as scattering coefficient and front-surface reflection. Similarly, TIRES and TIRTS spectra are also largely unaffected by the sample backing (if any) and the surrounding atmosphere, although emission from hot water vapor and carbon dioxide must sometimes be subtracted from the spectrum after the measurement.

Typical TIRES spectra are shown in Figure 17.6. The lower two traces of Figure 17.6a are the spectrum of a 3-mm-thick sample of polycarbonate measured

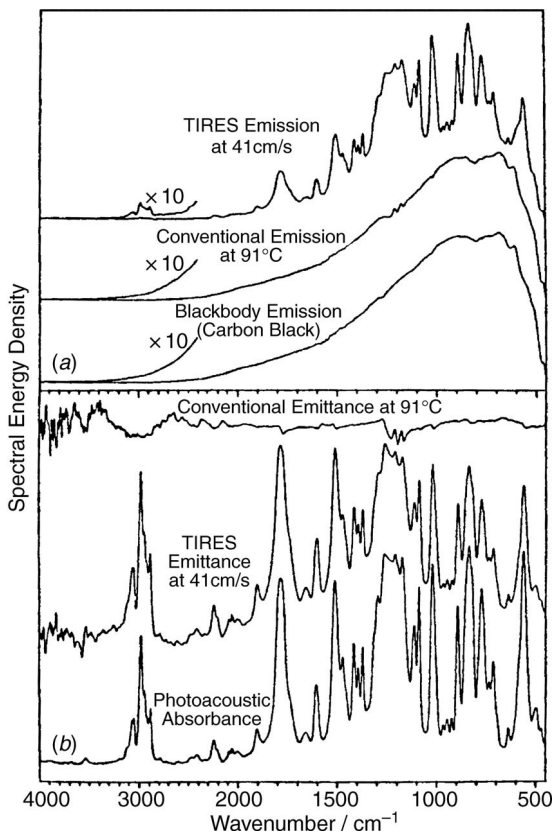


**Figure 17.6.** (a) Emission spectra of a 3-mm-thick polycarbonate sheet made by the TIRES technique and by uniformly heating the sample. A blackbody emission spectrum is shown below for comparison. (b) Emittance spectra of polycarbonate derived from the upper panel spectra compared to an absorption spectrum of polycarbonate recorded by photoacoustic spectrometry. (Reproduced from [7], by permission of the American Chemical Society; copyright © 1990.)

by uniformly heating the sample to 91°C (A) and the corresponding spectrum of carbon black at the same temperature (B). Both spectra are shown as measured (i.e., neither spectrum was corrected for the instrument response function). Since the polycarbonate sample was thick enough to act as a blackbody, both spectra are essentially identical. The top spectrum, which was measured by TIRES, obviously has more discrete spectral structure. The top spectrum of Figure 17.6*b* shows the emittance spectrum that was calculated by ratioing spectra A and B, again demonstrating the fact that a thick sample has an emittance very similar to that of a blackbody. The lower spectrum is the result of ratioing the TIRES spectrum shown in Figure 17.6*a* to the blackbody spectrum, B. Also shown is an absorption spectrum of the polycarbonate sample, which was actually measured by photoacoustic spectroscopy (PAS). Although PAS and TIRES yield spectra with equivalent information and the photoacoustic spectrum is less noisy, the sample does not have to be enclosed in a vibration-free enclosure isolated from all the sound in the room for TIRES measurements. Thus, TIRES is far more appropriate for process analysis than (PAS). The emission spectra of the same 3-mm-thick polycarbonate sample at 23 and 132°C measured with and without cooling by a jet of cold gas are shown in Figure 17.7.

Although the low sample temperature leads to significant noise at high wavenumbers in the ratioed TIRS spectra, the signal-to-noise ratio in both TIRES and TIRTS

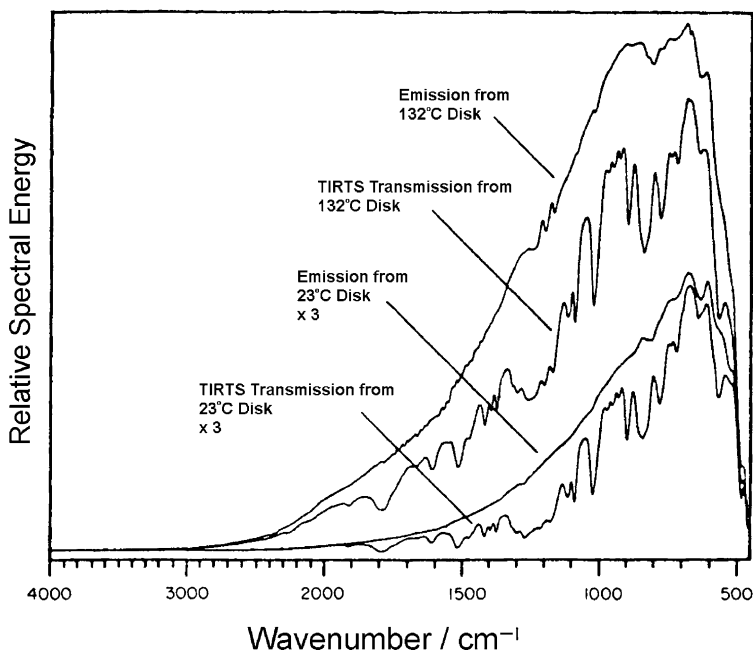


**Figure 17.7.** Emission spectra of the same polycarbonate sheet as that used for Figure 17.6, made with uniform sample temperature (emission) and with a chilled sample surface layer (TIRTS). (Reproduced from [8], by permission of the American Chemical Society; copyright © 1990.)

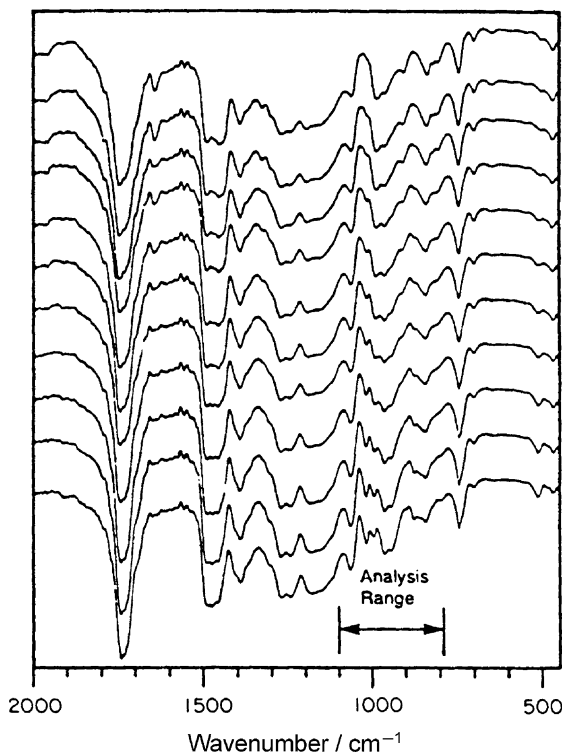


**Figure 17.8.** TIRTS spectra of 3-mm-thick poly[(methyl methacrylate-co(butyl methacrylate))] samples moving at  $40.8 \text{ cm} \cdot \text{s}^{-1}$ . The bulk temperature of these samples was  $23^\circ \text{C}$ . The percent methyl methacrylate was (top to bottom) 100.0, 93.1, 85.7, 77.8, 69.2, 60.0, 50.0, 39.1, 27.3, 14.3, and 0%. (Reproduced from [8], by permission of the American Chemical Society; copyright © 1990.)

spectra below  $2000 \text{ cm}^{-1}$  is remarkably high and allows accurate quantitative measurements to be achieved. For example, TIRTS spectra of a copolymer of methyl methacrylate (MMA) and butyl methacrylate (BMA) with compositions from 100% MMA to 100% BMA are shown in Figure 17.8. The standard error of prediction for the composition of the co-monomers obtained from these spectra in the region from  $1100$  to  $790 \text{ cm}^{-1}$  using principal component regression was 0.87%.

In summary, although infrared emission spectrometry is by no means as widely used as absorption, reflection, or even photoacoustic spectrometry, the capability of emission spectroscopy for remote, noncontact analysis of samples should not be overlooked.

## REFERENCES

1. P. R. Griffiths, *Appl. Spectrosc.* **26**, 73 (1972).
2. P. R. Griffiths, *Amer. Lab.* **7**, 39 (March 1975).

3. D. Kember, D. H. Chenery, N. Sheppard, and J. Fell, *Spectrochim. Acta* **35A**, 455 (1979).
4. D. B. Chase, *Appl. Spectrosc.* **35**, 77 (1981).
5. R. W. Jones and J. F. McClelland, *Anal. Chem.* **61**, 650 (1989).
6. R. W. Jones and J. F. McClelland, *Anal. Chem.* **61**, 1810 (1989).
7. R. W. Jones and J. F. McClelland, *Anal. Chem.* **62**, 2074 (1990).
8. R. W. Jones and J. F. McClelland, *Anal. Chem.* **62**, 2247 (1990).
9. R. W. Jones, S. Luo, and J. F. McClelland, Real-time infrared spectroscopy of moving solids for on-line analysis, in *Proceedings of the 8th International Conference on Fourier Transform Spectroscopy, 1991*, H. M. Heise, E. H. Korte, and H. W. Siesler, Eds., Society of Photo-Optical Instrumentation Engineers, Bellingham, WA, 1992, Vol. 1575, p. 220.
10. R. W. Jones and J. F. McClelland, *Spectroscopy* **7**(4), 54 (1992).

# FOURIER TRANSFORM RAMAN SPECTROMETRY

## 18.1. INTRODUCTION

Until 1986, when (coincidentally) the first edition of this book was introduced, it was generally believed that Fourier transform (FT) Raman spectrometry was not feasible because the huge signal due to Rayleigh scattering would swamp the very small signal caused by Raman scattering. Up to that date, Raman spectra were usually excited with a high-powered visible laser, such as the 488.0- or 514.5-nm line from an  $\text{Ar}^+$  laser. Spectra were measured by a scanning double or triple monochromator and a photomultiplier tube (PMT) detector. Double or triple monochromators were required to eliminate the stray light, and to minimize the resulting photon shot noise, from the intense Rayleigh line. When visible lasers are used for Raman spectrometry, the Stokes-shifted Raman bands are generally still in the visible region of the spectrum. For example, with 514.5-nm ( $19,436\text{-cm}^{-1}$ ) excitation, bands with Raman shifts of 100 to  $4000\text{-cm}^{-1}$  are found between 511.9 nm ( $19,536\text{-cm}^{-1}$ ) and 647.8 nm ( $15,436\text{-cm}^{-1}$ ) and hence are well within the range of many PMTs. Because these detectors can have quantum efficiencies approaching unity in the visible region of the spectrum, detection of Raman bands with a PMT is relatively straightforward.

Raman spectra of many pure colorless compounds can easily be measured with an instrument incorporating a visible laser, scanning double monochromator, and PMT. However, when spectroscopists attempted to measure the corresponding spectra of real-world samples with this type of instrument, good spectra were rarely obtained. The root cause of this difficulty was fluorescence by the sample, either because of its intrinsic electronic spectrum or, more likely, because of low levels of fluorescent impurities. Even for nonfluorescent samples, it often took at least 30 minutes to measure a reasonably noise-free Raman spectrum. Thus, with the exception of a few spectroscopists in industrial labs who could obtain their information in no other way, Raman spectrometry was considered to be largely



an academic pursuit—great for characterizing very pure white compounds but generally of little use for real-world samples.

To minimize the effect of fluorescence, the laser wavelength should be longer than the wavelength of electronic absorption bands that lead to fluorescence [i.e., it should be in the near infrared (NIR)]. The preferred laser is the 1064-nm (9398-cm<sup>-1</sup>) line of a neodymium-doped yttrium aluminum garnet (Nd : YAG) laser, since this laser is both powerful (>1 W) and readily commercially available. There are several drawbacks to the use of this laser, however. In Section 1.7 it was shown that the intensity of Raman bands is proportional to  $(\tilde{\nu}_0 - \tilde{\nu}_i)^4$ . Thus, a Raman band at 2950 cm<sup>-1</sup> would be 55 times weaker when measured with a 1064-nm Nd : YAG laser than the same band measured with the 488-nm line of an Ar<sup>+</sup> laser of the same power. It is apparent that extremely high laser powers are needed to offset the effect of the  $(\tilde{\nu}_0 - \tilde{\nu}_i)^4$  factor. High-powered Nd : YAG lasers fulfill this criterion but are invisible and thus very dangerous unless operated with great care. Furthermore, they can quite easily burn one's samples.

Another fundamental drawback of excitation at 1064 nm is the low sensitivity of the detectors that are needed. When excited by a Nd : YAG laser, Raman bands with shifts of 100 to 3400 cm<sup>-1</sup> are found between 1075 nm (~9300 cm<sup>-1</sup>) and 1670 nm (~6000 cm<sup>-1</sup>), which is well out of the range of a PMT. Although indium gallium arsenide (InGaAs) and germanium detectors can be used to measure spectra out to about 6000 cm<sup>-1</sup>, neither of these detectors is sensitive enough to allow the routine measurement of Raman spectra excited with a Nd : YAG laser using a monochromator. Nonetheless it should be noted that Fujiwara et al. [1] demonstrated the feasibility of such measurements using a pulsed Nd : YAG laser and boxcar averager. However, by comparison with spectra measured in the conventional manner with a dc Ar<sup>+</sup> laser of approximately the same power as the average power of the pulsed Nd : YAG laser and photomultiplier, their spectra were quite noisy and of low resolution (see Figure 18.1).

To improve this situation, either a multichannel or multiplex measurement was needed and the multiplex measurement came first. In fact, in the same issue of *Applied Spectroscopy* in which the paper of Fujiwara et al. [1] was published, Hirschfeld and Chase [2] demonstrated the feasibility of measuring Fourier transform Raman spectra with Nd : YAG laser excitation. A representative spectrum from their seminal paper is shown in Figure 18.2. The key to this work was the use of a notch filter that eliminated the Rayleigh line at 1064 nm while transmitting the Raman spectrum at longer wavelength. In their original work, Hirschfeld and Chase used a chevron filter that had a transmission of about 55% over most of the spectrum to a longer wavelength than 1064 nm but had a transmittance of  $4 \times 10^{-8}$  at 1064 nm. Even this performance was not good enough to eliminate the Rayleigh line completely, as can be seen at low wavenumber shift in Figure 18.2, but the quality of the spectra was still remarkably high.

The paper of Hirschfeld and Chase can be considered to herald the emergence of Raman spectroscopy as a truly important technique for analytical chemists. Within two years, at least five companies [Bio-Rad (now Varian), Bomem, Bruker, Nicolet (now Thermo), and Perkin-Elmer (now PerkinElmer)] had introduced commercial

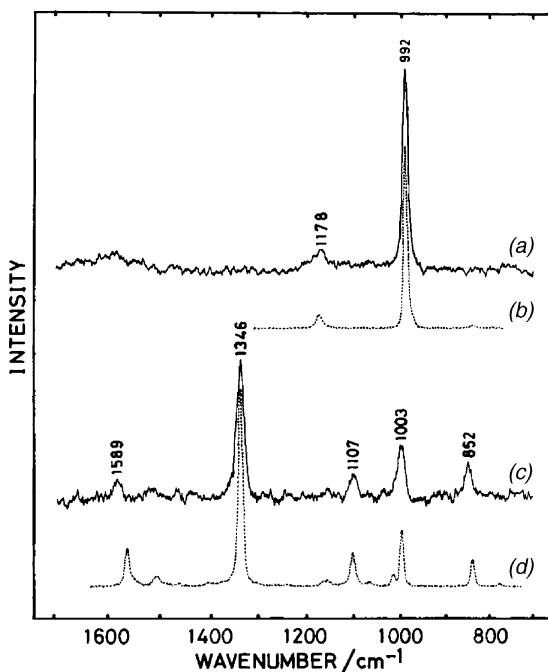


**Figure 18.1.** Spectra of neat (a) benzene and (c) nitrobenzene measured by Fujiwara et al. [1] using a pulsed Nd : YAG laser, monochromator, and boxcar averager; (b,d) corresponding spectra measured with a 514.5-nm Ar<sup>+</sup> laser. (Reproduced from [1], by permission of the Society for Applied Spectroscopy; copyright © 1986.)

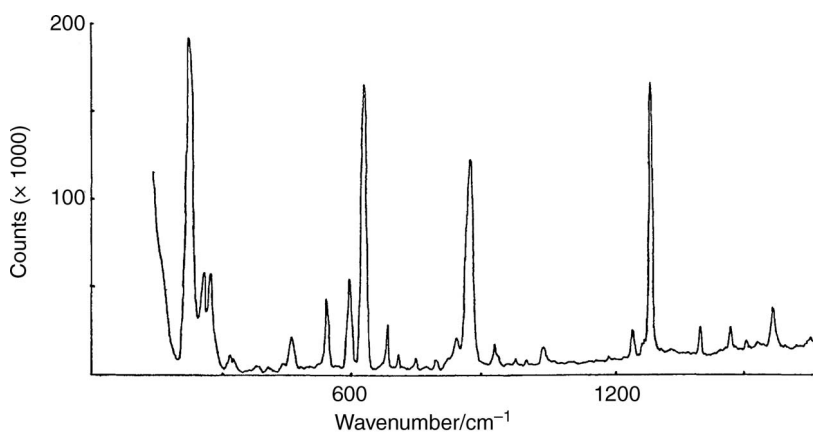


**Figure 18.2.** FT-Raman spectrum of pentaerythritol tetranitrate shown by Hirschfeld and Chase in the first report of FT-Raman spectrometry [2]. (Reproduced from [2], by permission of the Society for Applied Spectroscopy; copyright © 1986.)

FT-Raman spectrometers with performance significantly higher than that shown by Hirschfeld and Chase. Although the basic design of these instruments has not changed dramatically over the ensuing 20 years, improvements in the optical filters and detectors have dramatically improved the signal-to-noise ratio of FT-Raman spectra. These and other components are discussed in the next section.

## 18.2. INSTRUMENTATION

### 18.2.1. Nd : YAG Laser

The Nd : YAG laser involves the four-level system shown in Figure 18.3. Its upper-level lifetime is  $\sim 230 \mu\text{s}$ , which makes population inversion relatively easy to achieve. Absorption occurs from the ground state  $^4I_{9/2}$  to the upper states, and then the energy relaxes to the metastable state  $^4F_{3/2}$ . A large amount of heat is generated from the laser rod because of nonradiative decay to this state. The laser can be pumped either by a flashlamp or a diode, with flashlamp pumping generating up to 100 W of power at 1064 nm. Flashlamp-pumped Nd : YAG lasers require water cooling and (in the United States) usually operate at 220 V rather than the more standard 110 V. Diode pumping is a more efficient process than flashlamp pumping and a high-powered multimode diode emitting at 810 nm that matches the absorption band of the Nd : YAG well is the most common pump used today. The conversion efficiency of the pump light to the fundamental ( $\text{TEM}_{00}$ ) laser radiation can be

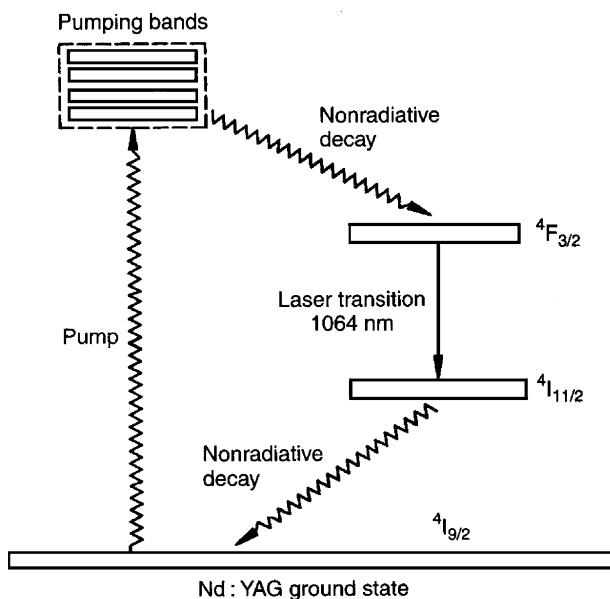


**Figure 18.3.** Energy-level diagram of the  $\text{Nd}^{3+}$  ion and its excitation process. (Reproduced from [3], by permission of John Wiley & Sons, Ltd.; copyright © 2002)

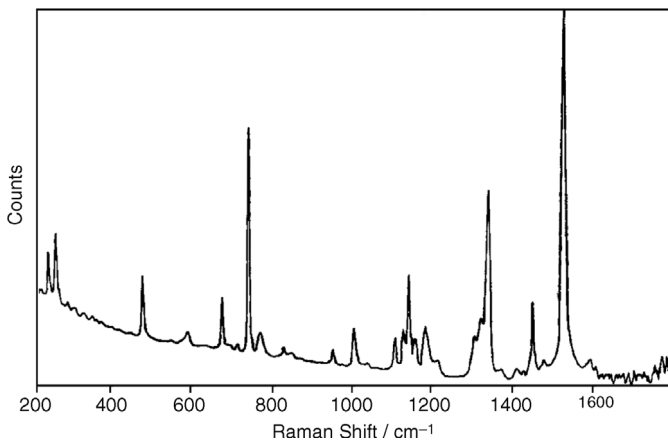


**Figure 18.4.** FT-Raman spectrum of copper phthalocyanine measured with the 1339-nm line of an  $\text{Nd}^{3+}$ : YAG laser. (Reproduced from [4], by permission of the Society for Applied Spectroscopy; copyright © 1994.)

higher than 50% and the power of the emitted radiation can exceed 10 W. However, such high powers are rarely used for Raman spectroscopy, as much more power than 1 W tends to burn up many samples. Today's diode-pumped Nd : YAG lasers offer 110-V operation, high efficiency, air cooling, small footprints, and better lifetimes than those of flashlamp-pumped lasers.

Well over 90% of all samples examined by FT-Raman spectroscopy with 1064-nm excitation yield an identifiable spectrum. For those samples that still fluoresce, longer-wavelength lines are available. For example, Asselin and Chase [4] have demonstrated that the spectrum of copper phthalocyanine can be measured with the 1339-nm line of Nd : YAG (see Figure 18.4), while the spectrum of this compound is swamped by fluorescence when the 1064-nm line of this laser is used, as shown in Figure 18.5. Because of the longer wavelength of this laser and the response characteristics of the germanium detector, however, the spectrum could only be measured to a Raman shift of  $1800\text{ cm}^{-1}$ .

Other solid-state lasers that have been used for NIR Raman spectrometry include neodymium-doped yttrium lithium fluoride (YLF) and yttrium vanadate ( $\text{YVO}_4$ ) [3]. Nd : YLF is preferred when high beam quality and high power are both necessary. Either of two wavelengths, 1047 and 1053 nm, may be selected for the Nd : YLF laser, depending on the polarization, with 1047 nm being the more common. It should be noted that every time a different laser line is used for FT-Raman spectroscopy, a different notch filter is also needed. Thus, titanium : sapphire lasers, which are broadly tunable in the NIR, are of little application for FT-Raman spectrometry. Nd :  $\text{YVO}_4$  lasers, which emit at 1064 nm, offer the advantage of having broader and stronger absorption bands than Nd : YAG, which is an advantage when frequency doubling is required and many suppliers have switched from Nd : YAG to Nd :  $\text{YVO}_4$ .

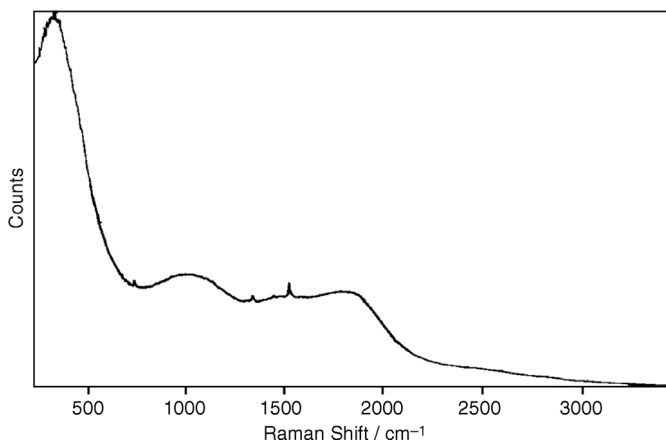


**Figure 18.5.** FT-Raman spectrum of copper phthalocyanine measured with the 1064-nm line of an  $\text{Nd}^{3+}$ :YAG laser. (Reproduced from [4], by permission of the Society for Applied Spectroscopy; copyright © 1994.)

### 18.2.2. Filters

Before the laser light reaches the sample, any atomic emission lines or continuous radiation leaving the laser must be filtered out. For a  $\text{Nd}$ :YAG laser, the most intense lines occur near  $7400\text{ cm}^{-1}$  ( $2000\text{-cm}^{-1}$  Stokes shift). These are easily filtered using either dielectric or holographic filters [5], with holographic filters being preferred due to their higher damage threshold. Users of FT-Raman spectrometers should look for leakage of these lines into their spectra as the filter degrades.

The second set of filters that is required for FT-Raman spectrometry is designed to take care of interference by the 632.8-nm line of the HeNe laser used for triggering data acquisition in all FT-Raman spectrometers used at the time of this writing. First, the beam passing to the photodiode being used to measure the HeNe interferogram should be passed through a notch filter to ensure that no light from the 1064-nm laser reaches the photodiode so that the reference interferogram is perfectly sinusoidal. Second, the radiation from the sample should be passed through a low-pass filter with a cut-on at about 800 nm, to ensure that no radiation from the HeNe detector is measured at the Raman detector.

Finally, and most important, the Rayleigh scattered light must be filtered out before reaching the detector. Because the power from the Rayleigh line can be up to 10 orders of magnitude more intense than the power from the Raman bands, a notch filter with a very high absorbance at the laser wavelength must be used. The transmission to longer wavelength must, however, be very high, preferably over 50% for Raman shifts between 100 and  $>3400\text{ cm}^{-1}$ . The good news is that since most spectroscopists are not interested in measuring the anti-Stokes spectrum, such high performance is not required on the short-wavelength side of the Rayleigh line.

Like the laser filters, these elements can be either dielectric or holographic. The optical power is much lower before than after the sample, so damage is far less

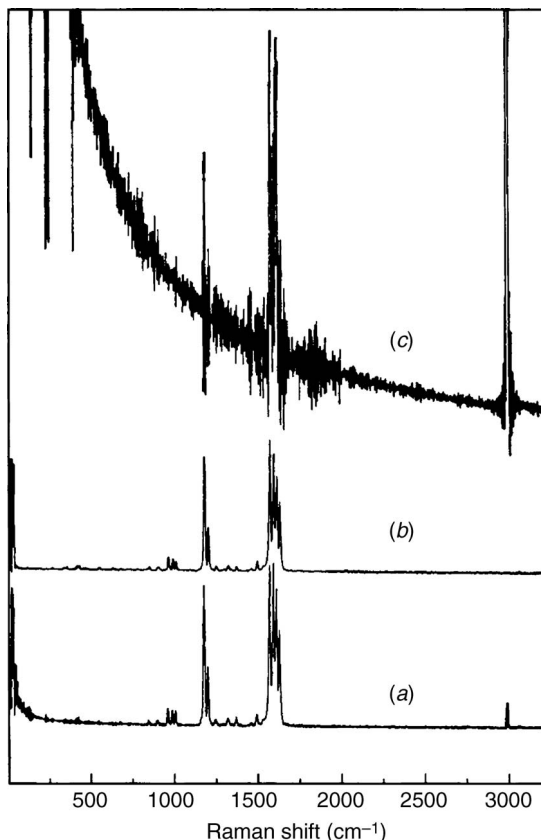


**Figure 18.6.** FT-Raman spectra of bis-methyl styryl benzene showing the shot noise introduced when the peak absorbance of the notch filter is decreased from (a) 10 to (b) 9 to (c) 8. (Reproduced from [6], by permission of the American Chemical Society; copyright © 1986.)

likely to occur. For optimum performance, it is critical to filter the Rayleigh line so that its intensity is less than that of the strongest band in the Raman spectrum. If this is not accomplished, the Raman spectrum will be severely degraded by shot noise [6], as shown in Figure 18.6. As the filtering is reduced, both the intensity of the Rayleigh line and the noise level in the spectrum increase significantly.

### 18.2.3. Collection Optics

In any Raman measurement, it is critically important to collect as many photons emitted from the sample as possible. It is a general rule of Raman spectrometry that the focal ratio of the collection optics should be as close to  $f/1$  as possible. For dispersive Raman spectrometry, the monochromator usually has  $f/4$  optics, so that the beam must be magnified by a factor of 4 at the entrance slit of the monochromator. Since this slit is typically  $\sim 100\ \mu\text{m}$  in width, the diameter of the sample that is being

measured is only about 25  $\mu\text{m}$ . For a typical two-beam interferometer, the equivalent entrance aperture has a diameter that is closer to 4 mm (Jacquinot's advantage). Thus, in this case, all the photons from a 1-mm-diameter spot can be collected. The power density of the laser at the sample can therefore be reduced significantly, concomitantly decreasing the probability of degradation of the sample. This subject is discussed in far greater detail in an excellent article by Schrader [7].

The Raman-scattered light can be collected with either a mirror or a lens. Some multielement lenses use optical cements that absorb in the infrared. In this case, air-gap lenses should be used.

#### 18.2.4. Interferometer

Any interferometer that is capable of at least  $2\text{-cm}^{-1}$  resolution at the excitation wavelength (1064 nm) can be used for FT-Raman measurements. Thus just about every interferometer that is sold today could be used for this purpose. Because the throughput should be optimized, however, it is better to use an interferometer with a 4- or 5-cm-diameter beamsplitter than a smaller size. Since NIR Raman measurements with a Nd : YAG laser are made between about 9300 and  $6000\text{ cm}^{-1}$ , the optimal beamsplitter should be one with a quartz substrate. While  $\text{CaF}_2$  and extended-range KBr beamsplitters have been used for FT-Raman spectrometry, it is usually advisable to purchase a beamsplitter that has been optimized for these measurements, as the higher the beamsplitter efficiency, the higher will be the signal-to-noise ratio of the spectrum.

#### 18.2.5. Detector

As we saw in Chapter 6, the lower the wavenumber at which a quantum detector cuts on, the higher is its sensitivity ( $D^*$ ). The sensitivity of detectors used for FT-Raman spectrometry is limited by the statistical fluctuations of the thermal background that is in their field of view (BLIP limit). As noted in the introduction, the low-wavenumber limit required for FT-Raman spectrometry with a Nd : YAG laser is about  $6000\text{ cm}^{-1}$ . Two detectors come closest to fulfilling this criterion: indium gallium arsenide and germanium. When cooled with liquid nitrogen ( $\text{LN}_2$ ), InGaAs cuts on at about  $6400\text{ cm}^{-1}$  (1560 nm), corresponding to a Raman shift of  $3000\text{ cm}^{-1}$ . This is not low enough to allow vibrational modes such as O—H, N—H, and aromatic or olefinic C—H stretching modes to be observed (see Figure 18.7c) [8]. When operated at 198 K (dry ice), InGaAs cuts on at about  $6100\text{ cm}^{-1}$  without losing much sensitivity, which is obviously far more useful for FT-Raman spectroscopy (see Figure 18.7b). Operation at ambient temperature moves the cutoff a further  $100\text{ cm}^{-1}$ , but at the cost of some sensitivity (see Figure 18.7a).

The preamplifier has a crucial role in determining the noise equivalent power of InGaAs detectors. Although it has been possible to achieve an NEP as low as  $10^{-15}\text{ W} \cdot \text{Hz}^{-1/2}$ , such detectors can by no means be purchased off the shelf. InGaAs detectors are operated with a very high feedback resistance, making their frequency response rather limited. Thus, when these detectors are used for FT-Raman

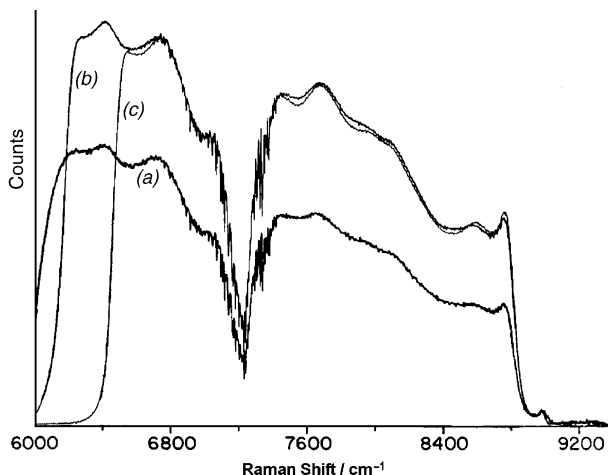


**Figure 18.7.** Spectra of white-light source measured with an InGaAs detector at (a) ambient temperature, (b) 198 K, and (c) 77 K. A filter to remove all radiation of shorter wavelength than 1064 nm is mounted in the optical path. (Reproduced from [8], by permission of Springer-Verlag, Vienna; copyright © 1987).

spectrometry, the optical velocity must be kept quite low ( $< 2 \text{ mm} \cdot \text{s}^{-1}$ , corresponding to a laser frequency of  $< 5 \text{ kHz}$ ). It is also worth noting that most the largest InGaAs detector element is usually about  $1 \text{ mm}^2$ , so this becomes the limiting aperture of the spectrometer.

Germanium detectors are almost always cooled to 77 K with  $\text{LN}_2$ . The first versions of these detectors were operated as low-bias diodes, and their noise performance was significantly worse than that of InGaAs detectors. The newer Ge detectors are fabricated from high-purity germanium elements and are biased near 100 V. These detectors cut on at about  $6000 \text{ cm}^{-1}$  ( $3400\text{-cm}^{-1}$  Stokes shift) and have excellent sensitivity, with an NEP that can be less than  $10^{-15} \text{ W} \cdot \text{Hz}^{-1/2}$ . Like the InGaAs detector, the frequency response of Ge detectors is limited and they require the interferometer to be operated with the same optical velocity as InGaAs. High-gain versions of the germanium detector are available with NEP values as low as  $10^{-16} \text{ W} \cdot \text{Hz}^{-1/2}$ , but these detectors have an even slower response. They do seem to be suitable for operation with a step-scan interferometer with phase modulation below 1 kHz.

In the early days of FT-Raman spectroscopy, it seemed that first the InGaAs detector would be the detector of choice, and then the next year the Ge detector would be favored, with the situation again being reversed the following year. At this point the situation seems to have stabilized in favor of the germanium detector. For example, Chase has reported the spectra of cyclohexane and anthracene measured on a Nicolet 910 FT-Raman spectrometer equipped with both a Ge and InGaAs detector under identical operating conditions [9]. He found that the SNR of bands in spectra measured with the Ge detector was up to five times greater than the corresponding band in a spectrum measured with InGaAs.



### 18.2.6. Spectrometer

Two types of FT-Raman spectrometer are commercially available. The first is an instrument that can be operated as a conventional FT-NIR spectrometer and modified to measure FT-Raman spectra; the second is a dedicated FT-Raman spectrometer. Examples of the two types of instruments are shown in Figures 18.8 and 18.9. Provided that all the considerations discussed above are accounted for properly, acceptable Raman spectra can be measured on both types of instruments. However, since the dedicated instrument has been designed explicitly for Raman spectrometry, the optical efficiency is usually superior. If an instrument is going to be used primarily for Raman spectrometry, we recommend that a dedicated instrument be purchased. If only a few Raman measurements are expected to be needed each week and NIR transmission and reflection measurements are also needed, it may well be financially advisable to purchase the more versatile instrument.

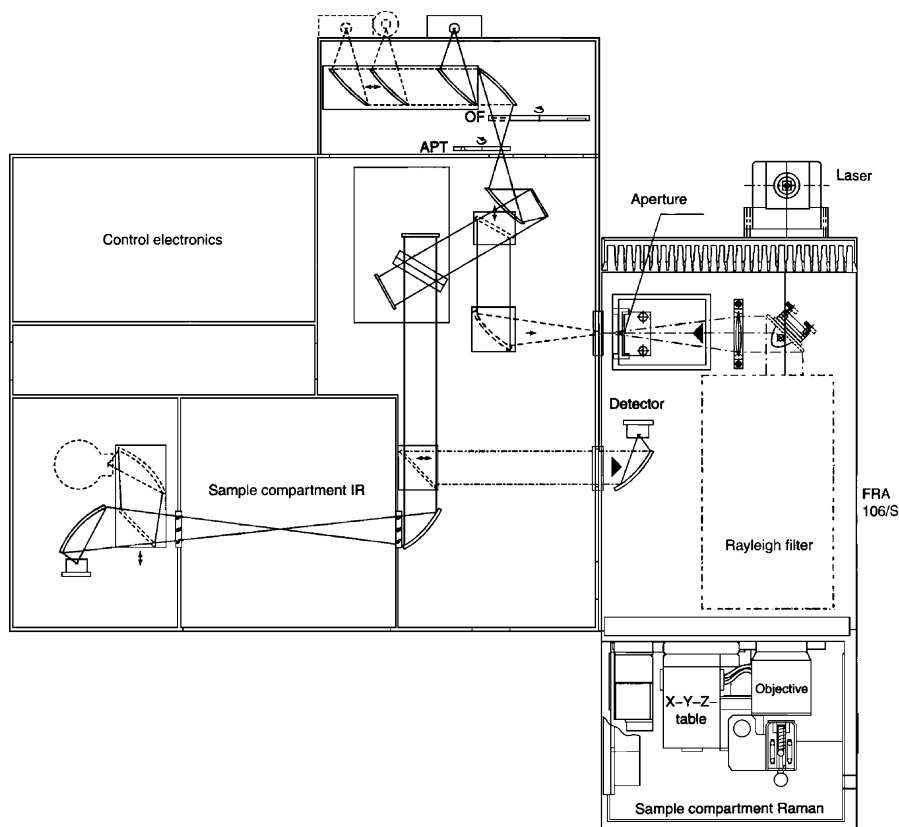


**Figure 18.8.** Optics of a typical instrument that allows both FT-IR and FT-Raman spectra to be measured (the Bruker Equinox). (Reproduced by permission of Bruker Optics).

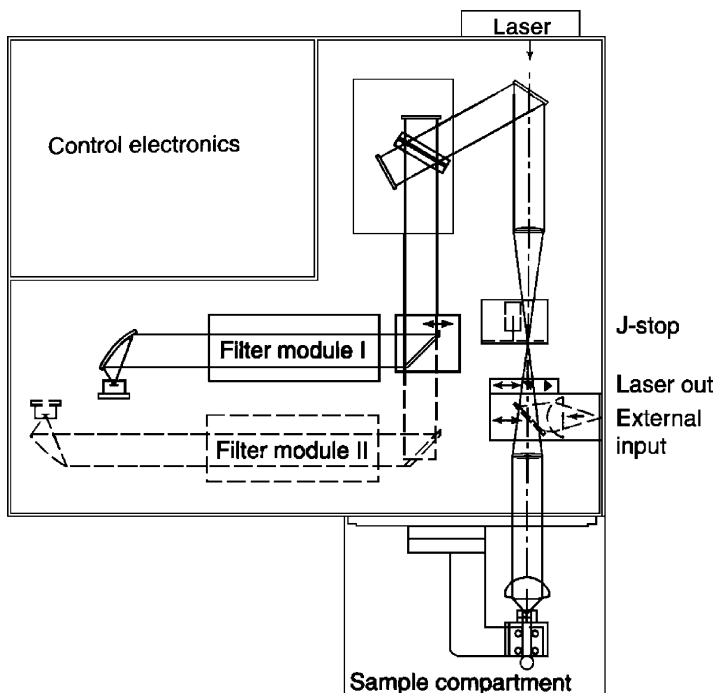


**Figure 18.9.** Optics of a dedicated FT-Raman spectrometer (Nicolet 910). (Reproduced by permission of Thermo Electron Corporation.)

### 18.3. FT RAMAN VERSUS CCD RAMAN SPECTROMETRY

In light of the fact that Fourier transform instrumentation was largely responsible for expanding Raman spectroscopy into the analytical laboratory, it is perhaps interesting to consider why Raman spectroscopy is so popular today but Fourier transform Raman does not play the dominant role. After a discussion of the poor sensitivity of NIR Raman spectrometry using a scanning monochromator with PMT detection in Section 18.1, it was stated: “To improve this situation, either a multichannel or multiplex measurement was needed and the multiplex measurement came first.” Multichannel measurements came very shortly afterward, however, and instruments based on polychromators with silicon-based charge-coupled-device (CCD) array detectors have become more popular than FT-Raman spectrometers. In this section we compare the performance of FT- and CCD-Raman spectrometers.

First, let us consider the effect of the  $(\tilde{\nu}_0 - \tilde{\nu}_i)^4$  factor in Eq. 1.23 on Raman spectra measured between a 100- and a 3400- $\text{cm}^{-1}$  Raman shift. The most common visible lasers used for contemporary Raman spectrometry are the frequency-doubled Nd : YAG laser (532 nm), the HeNe laser (632.8 nm). Radiation of longer wavelength is emitted by the 785-nm diode laser. The  $(\tilde{\nu}_0 - \tilde{\nu}_i)^4$  factor for these lasers in comparison to that of the Nd : YAG laser is shown in Table 18.1; the power

**Table 18.1. Comparative Values of  $(\tilde{\nu}_0 - \tilde{\nu}_i)^4$  for Various Raman Spectra<sup>a</sup>**

$\lambda_0$ (nm)	$\tilde{\nu}_0$ (cm <sup>-1</sup> )	$(\tilde{\nu}_0 - \tilde{\nu}_i)^4$ for:		Ratio for:	
		$\tilde{\nu}_i = 100$ cm <sup>-1</sup>	$\tilde{\nu}_i = 3400$ cm <sup>-1</sup>	$\tilde{\nu}_i = 100$ cm <sup>-1</sup>	$\tilde{\nu}_i = 3400$ cm <sup>-1</sup>
532	18,797	$12.22 \times 10^{16}$	$5.62 \times 10^{16}$	16.3	43.2
632.8	15,802	$6.07 \times 10^{16}$	$2.37 \times 10^{16}$	8.09	18.2
785	12,739	$2.55 \times 10^{16}$	$0.76 \times 10^{16}$	3.40	5.85
1064	9,398	$0.75 \times 10^{16}$	$0.13 \times 10^{16}$	1.00	1.00

<sup>a</sup>Measured with a doubled YAG (532 nm), HeNe (632.8 nm), and diode (785 nm) laser, and with a 1064-nm YAG laser, for vibrational bands at 100 and 3400 cm<sup>-1</sup>.

is assumed to be the same for each laser. Clearly, the use of visible lasers is indicated by the data in this table.

A further advantage of visible lasers is apparent when the type of detector needed for CCD- and FT-Raman spectrometry is considered. For measurements of Raman spectra excited with a Nd : YAG laser, the Stokes-shifted spectrum lies between 1075 nm (9298 cm<sup>-1</sup>) and 1667 nm (5998 cm<sup>-1</sup>), which mandates the use of an InGaAs or Ge detector. In the late 1980s and early 1990s, CCD array detectors with quantum efficiencies exceeding that of a single PMT were introduced. Not only are these CCDs far more sensitive than InGaAs or Ge, they are also slightly less expensive, since their development was driven by the consumer electronics industry, although the cost of a CCD that has a quantum efficiency as great as that of a PMT is usually at least \$10,000.

Silicon-based CCDs have a long-wavelength cutoff of about 1100 nm (9090 cm<sup>-1</sup>). Assuming that equivalent wavelength coverage to FT-Raman spectrometry is acceptable, this means that the excitation wavelength can be about 800 nm (i.e., 9090 + 3400 cm<sup>-1</sup>). Diode lasers emitting at 785 and 840 nm are commercially available with power of up to 100 mW and even more nowadays, so that these lasers can be used in conjunction with silicon-based CCD detectors. Although the power of these diode lasers is significantly less than that of the Nd : YAG laser, it is rare that the Nd : YAG laser can be used at its full power without burning up the sample. Thus, it is not uncommon to find the operating power levels of both types of lasers being about 100 mW.

With such an obvious advantage of sensitivity to CCD-Raman spectrometers, we must ask why FT-Raman spectrometers have found their place in the marketplace. The answer is found in one word—fluorescence! The shot noise introduced by fluorescence is so great that it offsets the sensitivity advantage of CCD-Raman spectrometers. Unlike the case for CCD-Raman spectrometry, fluorescence-free Raman spectra can usually be measured with a Fourier transform spectrometer in 5 or 10 minutes from almost any type of sample.

Both types of spectrometers have their own characteristic quirks. These have been covered in two articles by Bowie et al. [10,11], and in even more depth, in a review article in the *Handbook of Vibrational Spectroscopy* [12]. None of the spectral artifacts that are described in these articles usually affect measurement of the Raman spectra of routine samples, however. In fact, since sample preparation

is usually not required and measurement time is short, many labs equipped with both mid-infrared and Raman spectrometers will opt for a measurement of the Raman spectrum of a complete unknown first. Certainly, potential users of Raman spectrometry should not be put off by the very small artifacts that can be seen in both FT- and CCD-Raman spectra. The information in Raman spectra is so complementary to infrared spectra, and sample preparation is so simple, that many labs today are acquiring both types of instrument.

In summary, a typical multichannel Raman spectrometer comprising a visible laser, polychromator, and thermoelectrically cooled (TE-cooled) CCD array detector is almost an order of magnitude more sensitive than an FT-Raman spectrometer with an Nd : YAG laser and a germanium detector. The usefulness of CCD-Raman spectrometers is seriously restricted by the fact that so many samples fluoresce when illuminated by visible light. The longer the wavelength of the excitation, the less likely samples are to fluoresce. Diode lasers emitting at 785 nm are still compatible with silicon-based CCD detectors. Even though Nd : YAG lasers may be several times more powerful than diode lasers, Nd : YAG lasers may often not be used at their full power, as they can heat, and often ignite, the sample. If the sample does not fluoresce, CCD Raman spectrometers incorporating TE-cooled detector arrays are the instruments of choice. On the other hand, for fluorescent samples, the FT-Raman spectrometers will generally outperform CCD-Raman spectrometers.

Recently, a number of portable Raman spectrometers have been introduced for field measurements of drugs, explosives, and other hazardous materials. These instruments are usually equipped with inexpensive CCD cameras that operate at room temperature. The sensitivity of uncooled CCD arrays is over an order of magnitude less than that of detector arrays that have been thermoelectrically cooled to  $-40$  or  $-70^{\circ}\text{C}$ , so that the sensitivity of these instruments may actually be less than that of an FT-Raman spectrometer.

Another important advantage of FT-Raman spectrometers is their wavenumber stability (called the *Connes advantage*). This property of FT-Raman spectrometers is particularly important for process measurements where regular calibration may not be possible. Although the manufacturers of dispersive Raman spectrometers claim to have overcome the problem by incorporating neon lamps, variations in the wavelength scale are still evident when the temperature of the monochromator varies.

Good FT-Raman spectra can usually be measured in 5 or 10 min from almost any type of sample. Thus, if data acquisition time is not the limiting factor for a Raman measurement and a choice is to be made regarding purchase of a Raman spectrometer, the purchase of an FT-Raman instrument should be given serious consideration.

## 18.4. APPLICATIONS OF FT-RAMAN SPECTROMETRY

### 18.4.1. Standard Raman Spectroscopy

As noted above, Raman spectra of most solid or liquid samples can be measured with an FT-Raman spectrometer. Solid samples such as polymers can often be

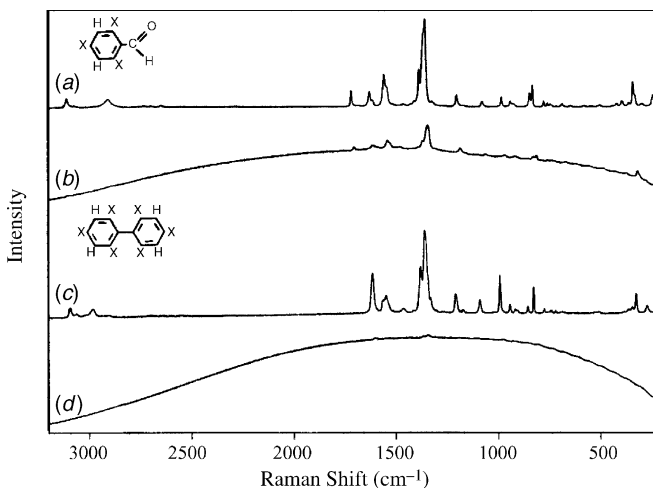


**Figure 18.10.** Raman spectra of trinitrobenzaldehyde measured with (a) a FT-Raman spectrometer and (b) a CCD-Raman spectrometer equipped with a 782-nm diode laser. Spectra of hexanitrobiphenyl measured in the same way are shown as (c) and (d), respectively (Reproduced from [13], by permission of Springer-Verlag, Vienna; copyright ©1995.)

measured as received, although it is common to mount powders in a glass or quartz capillary, such as a melting-point or NMR tube. Liquids are usually measured in the same type of tube, although special sampling tubes with a bulb at one end are sold by several suppliers.

Two examples will be given to demonstrate the advantage of FT-Raman spectroscopy with 1064-nm excitation over CCD-Raman spectroscopy for real-world samples. In the first, spectra of two explosives, trinitrobenzaldehyde and hexanitrobiphenyl, were measured with an FT-Raman spectrometer and a CCD-Raman spectrometer equipped with a 782-nm diode laser [13]. The spectra are shown in Figure 18.10. Although both of these explosives were colorless, fluorescent impurities were present at a high enough concentration to give rise to an intense sloping baseline in both spectra measured with 782-nm excitation. This baseline could be removed by standard baseline-correction software, but the signal-to-noise ratio of the resulting spectrum had been degraded by photon shot noise caused by the fluorescence.

In the second application, it was shown that softwoods and hardwoods could be distinguished through their FT-Raman spectra [14]. All the woods were colored to a greater or less extent, and useful spectra could not be obtained by CCD-Raman spectroscopy, even with 782-nm excitation. Representative spectra are shown in Figure 18.11. Even when 1064 nm was used, there was a relatively weak background caused by fluorescence and the spectra shown in Figure 18.11 were obtained after baseline correction.

One of the advantages of Raman spectroscopy that is listed in most textbooks on instrumental analysis is the fact that it is easier to measure the Raman spectra of solutes in aqueous solution than the infrared spectrum. This claim is based on the

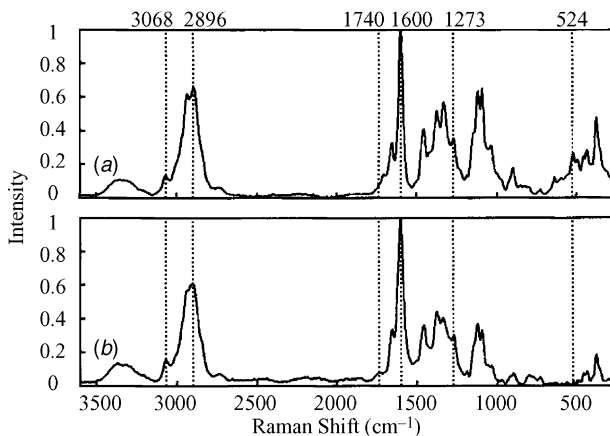


**Figure 18.11.** FT-Raman spectra of (a) a hardwood (cottonwood) and (b) a softwood (northern white cedar) after baseline correction. The vertical lines show some of the bands that proved to be important in distinguishing hardwoods and softwoods. (Reproduced from [14], by permission of Springer-Verlag, Vienna; copyright © 1994.)

fact that water absorbs infrared radiation very strongly whereas it is a very weak Raman scatterer, so that interference by the solvent is much less in Raman spectroscopy. In Section 11.1.4 we saw that the lowest concentration of aqueous solutes that may be detected by FT-IR spectrometry (either by transmission or ATR) is between 0.1 and 0.01%. The SNR of many FT-Raman spectra measured in reasonable data acquisition times is about 1000 : 1. It is therefore difficult to measure the Raman spectrum of a solute in any solvent at a much lower concentration than 0.1%. There are, however, two phenomena that allow the Raman spectrum of solutes to be obtained at significantly lower concentrations than 0.1%. The first, surface-enhanced Raman scattering (SERS), requires the solute to be adsorbed on roughened or nanoparticulate silver or gold; this technique will be described in the following section. The second, resonance Raman spectroscopy (RRS), requires the solute to have an electronic absorption band located at a wavelength that is close to the laser excitation. Since most analytes do not have electronic absorption bands in the near-infrared region, resonance Raman spectra are rarely, if ever, measured with FT-Raman spectrometers and RRS will not be described in this book. For those readers who wish to learn more on RRS, an article by McHale [15] is strongly recommended.

#### 18.4.2. Surface-Enhanced Raman Spectroscopy

More than 30 years ago, the phenomenon known as surface-enhanced Raman scattering (SERS) was predicted [16], discovered [17], and identified [18]. The literature on this subject is dominated by reports of research aimed at elucidating the details of the mechanism by which the Raman cross section of a molecule located next to the surface of a particle of gold or silver is increased as much as 1 million times [19–21]. Significantly fewer publications describe the investigation and

development of important applications. These applications include the detection of compounds as varied as organics and inorganics in groundwater at sub-part-per-million levels [22,23], chemical agents and their hydrolysis products [24,25], neurotransmitters in brain extract [26], anticancer drugs within biological targets [27], and even single molecules [28,29], including DNA [30].

The SERS effect can be described (albeit rather simplistically) as being caused by the incident laser photons coupling to free conducting electrons within a metal. When the electrons are confined by the particle surface, the photons collectively cause the electron cloud to resonate. These *surface plasmons* can interact with the electron orbitals of nearby molecules through two mechanisms that enhance Raman scattering: a classical interaction of the two electromagnetic fields and a charge transfer process [31,32]. As a result of the electromagnetic interaction, Raman cross sections may be enhanced by up to four orders of magnitude, while enhancement at two (or more) orders of magnitude is attributed to the chemical interaction. It has also been found that these interactions occur only if the particles (or surface imperfections) are much smaller than the wavelength of the incident radiation, the material has the appropriate optical properties to generate surface plasmons, and the molecule has matching optical properties (absorption) to interact with the plasmon field. These very specific conditions restrict SERS to the coinage metals: silver, gold, and copper with diameters between 5 and 200 nm.

Several methods have been developed to produce surfaces or solutions containing one of these metals with optimum roughness or diameter to promote SERS, including preparation of activated electrode surfaces, activated silver and gold colloids, and metal-coated substrates. Unfortunately, SERS has not become a routine analytical technique because these surfaces are not very reproducible and hence are unable to allow quantitative measurements. In an effort to overcome this limitation, Real-Time Analyzers (East Hartford, Connecticut) developed a sol-gel that allows silver or gold particles to be suspended in a porous glass. Processing conditions allow controlling particle and aggregate size, such that SERS activity can be, to a degree, tailored to the laser excitation wavelength. According to theory, the greatest enhancement for gold may be obtained using laser excitation beyond 1000 nm. Furthermore, the greater chemical inertness of gold compared to silver suggests that more stable SERS-active sample media could be prepared.

The SERS spectra of phenyl acetylene obtained from a silver and gold-doped tetraethyl orthosilicate (TEOS) sol-gel measured with 1064-nm excitation using an FT-Raman spectrometer are compared in Figure 18.12. Clearly, the silver-doped sol-gel yields greater enhancement, possibly because of the chemical component of the enhancement mechanism. The strong interaction between phenyl acetylene and silver is manifested by the shift of the  $\text{C}\equiv\text{C}$  stretching band from  $2112\text{ cm}^{-1}$  in the normal Raman spectrum to a doublet near  $2000\text{ cm}^{-1}$ . All the remaining bands appear in the standard Raman spectra and SERS spectra at about the same frequencies (near 1000, 1200, and  $1595\text{ cm}^{-1}$ ), indicating minimal interaction between the rest of the molecule and the metal surface. For the spectra shown in Figure 18.12, the enhancements have been calculated according to published procedures [19] to be approximately  $2.2 \times 10^5$  and  $2.8 \times 10^4$  for silver and gold, respectively.

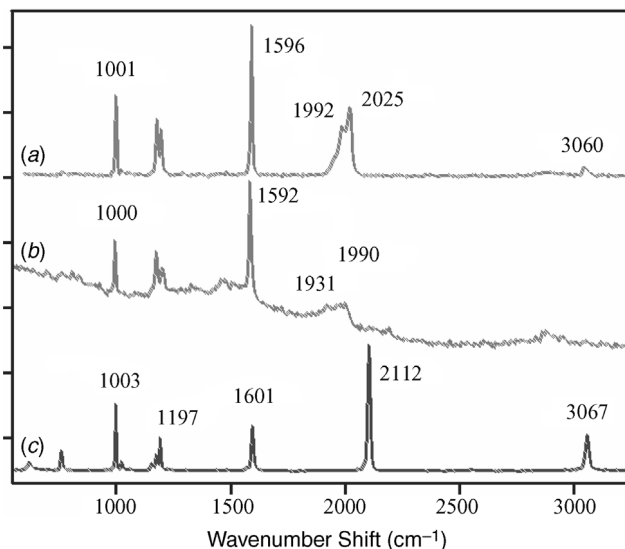


**Figure 18.12.** Surface-enhanced Raman spectra of phenylacetylene adsorbed from a 1% v/v solution in methanol onto (a) silver-doped and (b) gold-doped TEOS sol gel. (c) Standard Raman spectrum of the neat liquid. (Courtesy of Stuart Farquharson, Real-Time Analyzers, Inc.)

Real-Time Analyzers has developed a compact FT-Raman spectrometer weighing about 15 kg that allows this SERS technology to be applied to measurements of analytes such as methyl phosphonic acid (the hydrolysis product of the nerve agents), cyanide ion, pesticides, the DNA bases, cocaine, and several barbiturates all in water, while uric acid and creatinine have been measured in urine. The interferometer in this instrument is the same as the one shown in Figure 5.15 and is equipped with a quartz beamsplitter. The Nd:YVO<sub>4</sub> laser emits at 1064 nm and the detector is TE-cooled InGaAs.

## 18.5. SUMMARY

It is a little-known fact that Raman spectrometers first became commercially available in the 1930s, while the development of infrared spectrometers was triggered a decade later by World War II. The development of inexpensive double-beam infrared prism and grating spectrometers in the 1950s and 1960s heralded the great popularity of infrared spectroscopy for the structural elucidation of organic compounds. Raman spectrometers did not meet with the same approval from the analytical marketplace, in large part because of their instrumental complexity, relatively high cost, the long measurement time required to obtain a spectrum with a mercury arc source, the low signal-to-noise ratio of most Raman spectra once they had been measured, and the fact that so many samples fluoresced



when illuminated with visible radiation, completely masking the Raman spectrum. Even the commercial introduction of high-power gas lasers, such as HeNe, Ar<sup>+</sup>, and HeCd, in the early 1970s did not greatly change this state of affairs. The demonstration that Raman spectra could be measured with near-infrared excitation, either with 1064-nm excitation with an FT-Raman spectrometer or with 785- or 830-nm excitation with a CCD-Raman spectrometer, changed this situation radically. Although FT-Raman spectrometers are still significantly more expensive than benchtop FT-IR spectrometers, the complementary information afforded by infrared and Raman spectra have led to many labs acquiring both types of instruments.

## REFERENCES

1. M. Fujiwara, H. Hamaguchi, and M. Tasumi, *Appl. Spectrosc.* **40**, 137 (1986).
2. T. Hirschfeld and B. Chase, *Appl. Spectrosc.* **40**, 133 (1986).
3. M.-W. Pan, R. E. Benner, and L. Smith, Continuous lasers for Raman spectrometry, in *Handbook of Vibrational Spectroscopy*, J. C. Chalmers and P. R. Griffiths, Eds., Wiley, Chichester, West Sussex, England, 2002, Vol. 1, p. 490.
4. K. Asselin and B. Chase, *Appl. Spectrosc.* **48**, 699 (1994).
5. H. Owen, Volume phase holographic optical elements, in *Handbook of Vibrational Spectroscopy*, J. C. Chalmers and P. R. Griffiths, Eds., Wiley, Chichester, West Sussex, England, 2002, Vol. 1, p. 482.
6. B. Chase, *J. Am. Chem. Soc.* **108**, 7485 (1986).
7. B. Schrader, FT-Raman spectroscopy, in *Handbook of Vibrational Spectroscopy*, J. C. Chalmers and P. R. Griffiths, Eds., Wiley, Chichester, West Sussex, England, 2002, Vol. 2, p. 1289.
8. B. Chase, *Mikrochim. Acta* **III**(1), 81 (1987).
9. B. Chase, Fourier transform near-infrared Raman spectroscopy, in *Handbook of Vibrational Spectroscopy*, J. C. Chalmers and P. R. Griffiths, Eds., Wiley, Chichester, West Sussex, England, 2002, Vol. 1, p. 522.
10. B. T. Bowie, D. B. Chase, and P. R. Griffiths, *Appl. Spectrosc.* **54**, 164A (2000).
11. B. T. Bowie, D. B. Chase, and P. R. Griffiths, *Appl. Spectrosc.* **54**, 200A (2000).
12. B. T. Bowie, D. B. Chase, I. R. Lewis, and P. R. Griffiths, Anomalies and artifacts in Raman spectroscopy, in *Handbook of Vibrational Spectroscopy*, J. C. Chalmers and P. R. Griffiths, Eds., Wiley, Chichester, West Sussex, England, 2002, Vol. 3, p. 2355.
13. I. R. Lewis, N. W. Daniel, Jr., N. C. Chaffin, P. R. Griffiths, and M. W. Tungol, *Spectrochim. Acta A* **51**, 1985 (1995).
14. I. R. Lewis, N. W. Daniel, N. C. Chaffin, and P. R. Griffiths, *Spectrochim. Acta* **50A**, 1943 (1994).
15. J. L. McHale, Resonance Raman spectroscopy, in *Handbook of Vibrational Spectroscopy*, J. C. Chalmers and P. R. Griffiths, Eds., Wiley, Chichester, West Sussex, England, 2002, Vol. 1, p. 534.
16. M. R. Philpott, *J. Chem. Phys.* **62**, 1812 (1975).
17. M. Fleischmann, P. J. Hendra, and A. J. McQuillan, *Chem. Phys. Lett.* **26**, 163 (1974).

18. D. Jeanmaire and R. P. Van Duyne, *J. Electroanal. Chem.* **84**, 1 (1977).
19. M. J. Weaver, S. Farquharson, and M. A. Tadayyoni, *J. Chem. Phys.* **82**, 4867 (1985).
20. B. Pettinger, *J. Chem. Phys.* **85**, 7442 (1986).
21. C. L. Haynes, A. D. McFarland, and R. P. Van Duyne, *Anal. Chem.* **77**, 338A (2005).
22. J. M. E. Story, T. E Barber, R. D. Shelton, E. A. Wachter, K. T. Carron, and Y. Jiang, *Spectroscopy* **10**(3), 20 (1995).
23. S. Farquharson, W. W. Smith, and Y.-H. Lee, *J. Pure Appl. Chem.* **7**, 85 (2001).
24. A. M. Alak and T. VoDinh, *Anal. Chem.* **59**, 2149 (1987).
25. S. Farquharson, P. Maksymiuk, K. Ong, and S. D. Christesen, Chemical agent identification by surface-enhanced Raman spectroscopy, in *Vibrational Spectroscopy-Based Sensor Systems*, S. D. Christesen and A. J. Sedlacek III, Eds., Society of Photo-Optical Instrumentation Engineers, Bellingham, WA, 2002, Vol. 4577, p. 166.
26. N.-S. Lee, Y.-Z. Hsieh, R. F. Paisley, and M. D. Morris, *Anal. Chem.* **60**, 442 (1988).
27. A. Beljebbar, G. D. Sockalingum, J. F. Angiboust, and M. Manfait, *Appl. Spectrosc.* **50**, 148 (1996).
28. K. Kneipp, Y. Wang, R. Dasari, and M. S. Feld, *Appl. Spectrosc.* **49**, 780 (1995).
29. S. Nie and S. R. Emory, *Science* **275**, 1102 (1997).
30. D. Graham, W. E. Smith, A. M. T. Linacre, C. H. Munro, N. D. Watson, and P.C. White, *Anal. Chem.* **69**, 4703 (1997).
31. D.-S. Wang and M. Kerker, *Phys. Rev. B.* **24**, 1777 (1981).
32. G. C. Schatz and R. P. Van Dyne, Electromagnetic mechanism of surface-enhanced spectroscopy, in *Handbook of Vibrational Spectroscopy*, J. C. Chalmers and P. R. Griffiths, Eds., Wiley, Chichester, West Sussex, England, 2002, Vol. 1, p. 759.



# TIME-RESOLVED SPECTROMETRY

## 19.1. CONTINUOUS-SCANNING INTERFEROMETERS

### 19.1.1. Instrumental Considerations

The fact that conventional continuously scanning FT-IR spectrometers can measure an interferogram in a time of 1 second or less makes them excellent tools to follow transient or time-varying processes. Let us first examine some of the instrumental aspects of FT-IR spectrometers used for time-resolved spectrometry.

For standard instruments equipped with a DTGS detector, the data acquisition rate (i.e., the frequency of the HeNe laser interferogram) is rarely much greater than 5 kHz. For spectra measured at a resolution of  $8\text{ cm}^{-1}$ , there are 4000 data points per scan for symmetrically double-sided interferograms, so that the time per scan (the *active scan time*) is  $\sim 0.8\text{ s}$ . If 0.2 s is required to turn the mirror around and to reach the point at which data for the next scan are acquired, it can be seen that the time resolution for a series of spectra measured at a resolution of  $8\text{ cm}^{-1}$  is on the order of 1 s. To reduce this time, either the resolution at which the spectrum is measured must be degraded, the interferogram should be measured in the single-sided mode, or the speed of the moving optical element must be increased.

The effect of spectral resolution on the measurement is governed by the spectra of the chemical species being monitored. Even though spectra measured at low resolution may have a very different appearance from the corresponding spectra measured at higher resolution, it is often possible to obtain good quantitative information from low-resolution spectra, especially when the spectra are treated with some type of multivariate data-processing algorithm. Measuring the spectrum in the single-sided mode reduces the photometric accuracy slightly, as discussed in Section 4.3; for time-resolved measurements; however, this effect is usually of minor importance

In practice, whether or not the spectra can be measured beneficially at high scan speeds is often determined by the *duty-cycle efficiency* of the interferometer, which is defined as

$$\text{duty-cycle efficiency} = \frac{\text{active scanning time}}{\text{time between the start of successive scans}} \times 100\%$$

The time between the start of one scan and the start of the next is the sum of the active scan time and the *turnaround time*, the time that it takes to decelerate the moving mirror, turn it around, and accelerate it to the point at which data acquisition of the next scan starts. To reduce the time per scan for a conventional interferometer with a reciprocating mirror motion, the active scanning time is reduced by increasing the optical velocity. Ideally, this should be accomplished without an increase in the turnaround time. However, raising the optical velocity increases the momentum of the moving mirror assembly and makes it more difficult to slow it down, turn it around, and speed it up again. Thus, as the optical velocity is raised, the time required to turn the mirror around increases, and the duty-cycle efficiency almost invariably decreases. Note also that changing from double- to single-sided data acquisition also tends to decrease the duty-cycle efficiency.

This problem can be illustrated by the data given in a paper by Hinsmann et al. [1], who used a Bruker Equinox 55 interferometer (see Figure 5.17) for stopped-flow measurements (see Section 19.2). The mirror velocity on this instrument was set so that data were acquired with a HeNe laser frequency of 280 kHz. For a spectral resolution of  $32 \text{ cm}^{-1}$ , the time for each 1000-point interferogram was, therefore,  $1024 / (280 \times 10^3) \text{ s}$ , or 3.66 ms. The time between successive spectra was reported as 45 ms, so that the duty-cycle efficiency was 8.1%. Clearly, the time resolution for this measurement was limited by the turnaround time and not the active scanning time.

The response time of the detector should also be borne in mind when the time resolution is to be reduced well below 1 s. If the frequency of the HeNe interferogram is raised much above 10 kHz, the response of the DTGS detector is too slow and a faster detector must be used. In the mid-infrared, this is not a major problem, since MCT detectors operate optimally for modulation frequencies above 1 kHz. For near-infrared measurements, however, while InSb has a very fast response time, other quantum detectors, such as InGaAs, cannot be used at data acquisition speeds much above 5 kHz (see Section 18.2.5).

The long turnaround for conventional interferometers is caused by the time required to retard the moving mirror at the end of the scan, turn it around, and bring it back up to a constant velocity. This problem may be alleviated through the use of an interferometer with a rotating optical element, such as the Manning Mark 2 interferometer shown in Figure 5.23. For instruments of this type, the angular velocity is constant and the optical velocity varies sinusoidally with time. With this spectrometer, full mid-infrared spectra can be measured routinely at a spectral resolution of  $6 \text{ cm}^{-1}$  with a time resolution of 5 ms. For an interferometer in which the optical velocity varies sinusoidally, data are usually taken over about 70% of the

complete scan, in which case the optical velocity changes by about a factor of 2. Provided that the interferograms are processed correctly [2,3], the fact that the optical velocity is not constant throughout the scan does not degrade the signal-to-noise ratio.

It is interesting to speculate whether the time scale of dynamic measurements of complete infrared spectra by FT-IR spectrometry could be reduced further. It is unlikely that an interferometer in which the OPD is varied in a reciprocating manner could achieve submillisecond time resolution, but this is not the case for a rotating interferometer. The nutating mirror of the Manning interferometer has been tested at speeds as high as 500 Hz. Since two interferograms are generated per revolution, operation at this speed would correspond to a time resolution of 1 ms. The component that precludes operation of this instrument at such a high speed is the analog-to-digital converter. To acquire spectra with good signal-to-noise ratio and spectral resolution, a 20-MHz ADC with a dynamic range of at least 14 bits is needed. If the wedge angle of the mirror were reduced from its current value of  $\sim 1^\circ$  to a smaller angle, a slower ADC could be used, but spectra would be measured at lower resolution. Thus, it is not unreasonable to predict that some future instrumental developments will take place in this area.

Another potential way to improve the time resolution of FT-IR spectrometry is through the use of stationary interferometers of the type that were described in Section 5.6. Since these instruments do not require any moving parts, sampling the interferogram will again be the rate-limiting step, but the requirements of speed are not as severe for this type of interferometer as for one in which the optical path difference is generated by moving an optical element. However, no developments in this area have been reported recently, to the knowledge of these authors.

### 19.1.2. Applications

As noted at the start of this chapter, we saw that the time resolution of a typical benchtop FT-IR spectrometer equipped with a DTGS detector is on the order of 1 s (and longer if high resolution is called for). Thus, any process that is varying on a time scale of 10 to 100 s can readily be monitored by a standard benchtop FT-IR spectrometer. This property has been put to particularly good use by Mettler-Toledo AutoChem (formerly ASI Applied Systems, Columbia, Maryland), which has developed several instruments for monitoring chemical reactions both in the research and development laboratory and in chemical plants. In the ReactIR, for example, a horizontal internal reflection element (IRE) is mounted in the base of a reaction flask so that the spectrum of the contents of the flask can be measured as a function of time after the reaction has been initiated. Alternatively, an ATR sensor is attached to the instrument by infrared fibers or waveguides (Section 15.6). By making the IRE from such materials as diamond or zirconia, even reactions that involve highly corrosive reactants and products can be investigated over a very wide range of temperatures and pressures, providing a direct measurement of the reactants, intermediates, by-products, and products formed or consumed during a chemical reaction. Many of the applications undertaken have involved

pharmaceuticals where production efficiencies have been greatly improved by following the reaction mechanisms and understanding how to optimize conditions. Other applications include phosgenation reactions, nitrations in strong acidic solutions ( $\text{HNO}_3/\text{H}_2\text{SO}_4$ ) at temperatures that exceed  $120^\circ\text{C}$ , and urea formation under caustic conditions.

Reactions that take place over times of minutes or even hours can be studied with conventional rapid-scanning FT-IR spectrometers. The faster the reaction, however, the more specialized the instrumentation required for its study, and few processes that occur in time scales less than  $\sim 50$  ms have been studied with “conventional” FT-IR spectrometers. One investigation of a rapid reaction studied using an interferometer with a reciprocating mirror motion was a clever stopped-flow investigation that used micromachined parts reported by Hinsmann et al. [1]. The apparatus is shown in Figure 19.1. When the flow is on, the two solutions are mixed and passed through the inlet holes of the micromixing unit, where each is divided into 25 microchannels, with each stream being  $\sim 20\ \mu\text{m}$  in diameter. Immediately after the microchannels, the divided streams are reunited in the main channel,

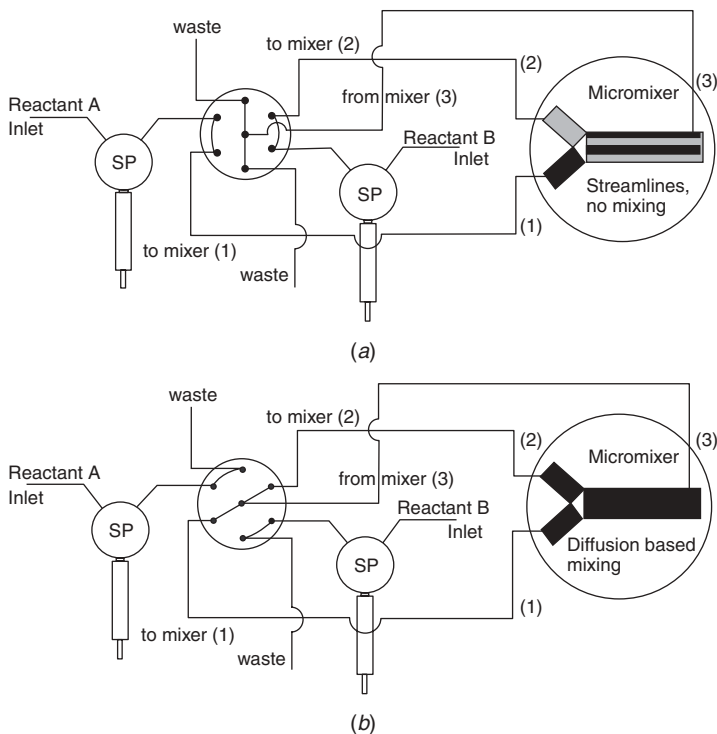


**Figure 19.1.** Liquid-handling system for stopped-flow measurements reported by Hinsmann et al. consisting of two syringe pumps (SP) and a custom valve; comparison between (a) the flow-on and (b) the stopped-flow positions. (Reproduced from [1], by permission of the Society for Applied Spectroscopy; copyright © 2001.)

forming 50 streams of alternating solutions. Since the flow rate is very high and the flow is approximately laminar, little mixing of the two components takes place. When the flow is stopped, the two solutions diffuse together rapidly and mix. Currently, the time resolution is limited by the diffusion of the components. For small molecules with a diffusivity of  $10^{-9} \text{ m}^2 \cdot \text{s}^{-1}$ , the mixing time is  $\sim 200 \text{ ms}$ , but faster speeds will be achievable if the diameter of the liquid streams is reduced. Several simple applications were described by Hinsmann et al., including the hydrolysis of methyl monochloroacetate by NaOH, for which each reactant was present in aqueous solution at a concentration of  $0.10 \text{ M}$ . A three-dimensional plot of their results is shown in Figure 19.2.

It was noted in Section 19.1.1 that the number of scans that can be acquired per second depends strongly on the duty cycle efficiency of the interferometer and that interferometers with rotating optical elements usually have significantly higher duty cycle efficiency than instruments with a reciprocating mirror. Several rapid processes have been measured with this type of spectrometer, including measurement of the adsorption rate of aldehydes onto granular adsorbents [4] and the change in order of polymers as they are stretched to the point of fracture [5,6], and we anticipate that more applications of this type of instrument to the study of reaction kinetics will be reported in the future.

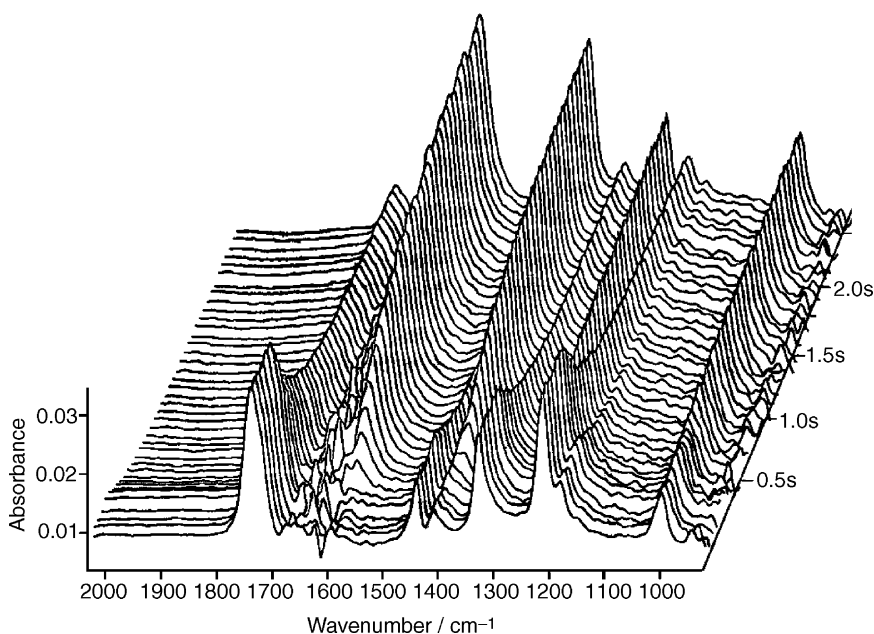


**Figure 19.2.** Three-dimensional plot of the spectra obtained from the basic hydrolysis of methyl monochloroacetate and NaOH ( $100 \text{ mM}$  each) using a rapid-scanning spectrometer. The time difference between subsequent spectra was  $65 \text{ s}$ . The first five spectra were measured during the flow-on period. (Reproduced from [1], by permission of the Society for Applied Spectroscopy; copyright © 2001.)



## 19.2. TIME-RESOLVED MEASUREMENTS USING STEP-SCAN INTERFEROMETERS

### 19.2.1. Instrumental Considerations

The only requirement on the reaction or process to be monitored in the manner described in Section 19.1 is that it takes place over a period of time that is longer than the time of a single scan. There is no requirement for the reaction to be repeatable. If, however, a reaction or sample perturbation is repeatable, much faster reactions can be monitored. The most common way to achieve this goal is through the use of a step-scan interferometer in which the optical path difference is held constant over the course of the reaction or perturbation. The OPD is then changed, typically by one wavelength of the HeNe laser, and the process is repeated. This procedure is reiterated at constant intervals of retardation until the OPD is sufficiently high that the desired spectroscopic resolution has been reached. The types of processes that have been studied in this way can be as varied as photolysis by irradiation of the sample with a pulsed laser [7,8], rapid mixing of two reagents by stopped-flow techniques [9], orientation dynamics of liquid crystals under the influence of an electric field [10,11] and rheological studies of polymer films when a rapid strain is applied [12]. In the following discussion, we use the term *reaction* to describe any chemical or physical process, but it should be recognized that many types of reactions and perturbations can be studied in this way.

Let the OPD corresponding to first point of the scan be denoted by the subscript  $\delta_1$ . When the mirror is stationary at this position, which is usually a zero crossing of the HeNe laser interferogram, the reaction is initiated. The detector signal is sampled at time  $t_0, t_1, t_2, \dots, t_T$ , after the reaction is initiated, where  $t = t_T$  is time corresponding to the end of the reaction. The signals sampled while the mirror is held stationary at retardation  $\delta_1$  at times  $t_0, t_1, t_2, \dots, t_T$  are denoted as  $I_{1,0}, I_{1,1}, I_{1,2}, \dots, I_{1,T}$ . After the reaction is complete, the interferometer mirror is advanced to the next zero crossing of the HeNe laser, at  $\text{OPD} = \delta_2$ , and the reaction is repeated. The signals are again sampled at times  $t_0, t_1, t_2, \dots, t_T$ , while the mirror is held stationary at  $\text{OPD} = \delta_2$ . In this case the sampled signals are  $I_{2,0}, I_{2,1}, I_{2,2}, \dots, I_{2,T}$ . The process is repeated  $N$  times, where  $N$  is the number of points in the interferogram needed for the desired resolution. The sampled data are summarized in Table 19.1.

**Table 19.1. Matrix of Data Taken During Time-Resolved Spectroscopic Measurements with a Step-Scan FT-IR Spectrometer**

OPD	$t = t_0$	$t = t_1$	$t = t_2$	$\dots$	$t = t_T$
$\delta_1$	$I_{1,0}$	$I_{1,1}$	$I_{1,2}$	$\dots$	$I_{1,T}$
$\delta_2$	$I_{2,0}$	$I_{2,1}$	$I_{2,2}$	$\dots$	$I_{2,T}$
$\vdots$	$\vdots$	$\vdots$	$\vdots$	$\dots$	$\vdots$
$\delta_N$	$I_{N,0}$	$I_{N,1}$	$I_{N,2}$	$\dots$	$I_{N,T}$

The data in the first column represent the interferogram measured at time  $t_0$ , the data in the second column represent the interferogram measured at time  $t_1$ , and so on. Spectra that correspond to each time,  $t_0, t_1, t_2, \dots, t_T$ , are obtained by performing the Fourier transforms of each of these interferograms. The signal-to-noise ratio of the spectrum measured at each time after initiation of the reaction may be increased by repeating the reaction several times while the OPD is still held constant and adding the new values of the signal added to those of the preceding reaction at that OPD.

The principal requirements for this type of measurement are as follows:

- The reaction must be precisely repeatable; any variations are manifested as spectral artifacts.
- The initiation of the reaction must be synchronized to the data acquisition.
- The response time of the detector and amplifier must be no longer than the time difference between successive samples [i.e., less than  $(t_0 - t_1)$ ].
- The optical path difference should be held very constant at each step; any variation in OPD will be manifested as noise.

The time resolution is limited primarily by the response time of the detector. For measurements in the mid-infrared, the response time of a conventional photoconductive MCT detector will limit the resolution to between 1  $\mu$ s and 100 ns. When a photovoltaic MCT detector is used, the resolution improves by about a factor of 10, and a time resolution of 10 ns has been claimed for most measurements with this detector.

At each step at which the optical path difference is held constant, data must be acquired at exactly equal times after the initiation of the reaction. Synchronization of the start of the reaction with data acquisition has been done in two ways. Usually, an external digital pulse generator serves as the master experimental clock. The pulse generator sends a trigger signal to the transient digitizer to mark the start of data acquisition before the reaction is initiated. The digitizer then initiates a stream of detector samples at constant time intervals. A second trigger signal shortly after the first then initiates the reaction or sample perturbation. The interferometer mirror remains stationary for a time that is governed by the time taken to complete the reaction. The mirror is then advanced to the next zero crossing of the HeNe laser interferogram, and the process is repeated.

The second way to perform these experiments is through the use of electronics that are supplied with the spectrometer itself. The interferometer is programmed to advance the interferometer mirror at a certain rate. At each step, the software starts data acquisition following a delay to allow the mirror to stabilize after it has advanced to the next point and then initiates the reaction a certain period of time after the mirror has stabilized. Using the stepping frequency of the master clock in this way precludes the initiation of multiple reactions at a single step, but signal averaging can be carried out by retracing the interferometer mirror and carrying out the reaction sequence again. In this case, spectra that correspond to a certain

time after the initiation of the reaction or perturbation, rather than the data points in the interferogram, must be signal averaged.

The choice of analog-to-digital converter is also critical. For measurements with a time resolution of 10 ns, the ADC samples at a rate of 100 MHz and the dynamic range of ADCs that operate at 100 MHz is usually restricted to 8 to 12 bits. If a conventional single-beam spectrum of a blackbody source were measured at a resolution of  $8\text{ cm}^{-1}$  with an 8-bit ADC, the SNR of the spectrum would not be much greater than 20 : 1, which is far too low to measure spectral features from weakly absorbing species. To circumvent this drawback, the amplifier is ac-coupled, so that only the *spectral differences* that occur on a nanosecond time scale are observed by the ADC, and the large signal at the centerburst due to the (constant) blackbody emission of the source does not contribute to the interferogram. Through the use of appropriate ac electronics, it is been possible to measure changes in absorbance of less than 1 mAU in time-resolved spectra measured with a step-scan interferometer.

The collection of an interferogram with ac electronics leads to a complication in data processing. Since the spectrum contains both positive and negative signals, the standard Mertz method of phase correction cannot be used. Therefore, an interferogram that has been amplified with standard dc electronics is collected simultaneously, and this interferogram is used to correct the phase of the ac interferograms. Although an interferogram could have been measured before the time-resolved measurement to yield the phase spectrum, concurrent collection of the ac and dc interferograms precludes any drift of the phase spectrum that might occur between the two measurements. More detailed descriptions of the hardware for time-resolved measurements made with a step-scan interferometer in the review articles by Smith and Palmer [13] and Rödiger and Siebert [14].

Most time-resolved measurements involve the investigation of reversible reactions such as stimulation of a compound to an excited state by a laser pulse followed by a relaxation to the ground state over a period of time. Alternatively, physical stress may be applied to a sample that reversibly changes a property of a sample (e.g., the rapid application of a strain to a polymer film by stretching it to an amplitude within the elastic limit). The concept of reversibility is important because the sample must be in the same state when the interferometer mirror is stepped to its next position and the reaction is reinitiated. A few workers have developed methods of recharging the cell at each step so that irreversible reactions can be studied. Examples of each of these processes are given in the following section.

### **19.2.2. Applications of Time-Resolved Spectroscopy with a Step-Scan Interferometer**

As noted above, there have been many reports of rapid time-resolved spectroscopy achieved using a step-scan interferometer, most of which involve the investigation of rapid photolysis reactions. We will give two examples of this type of measurement, one of a relatively ligand-exchange reaction and the second of a more complex biochemical system.

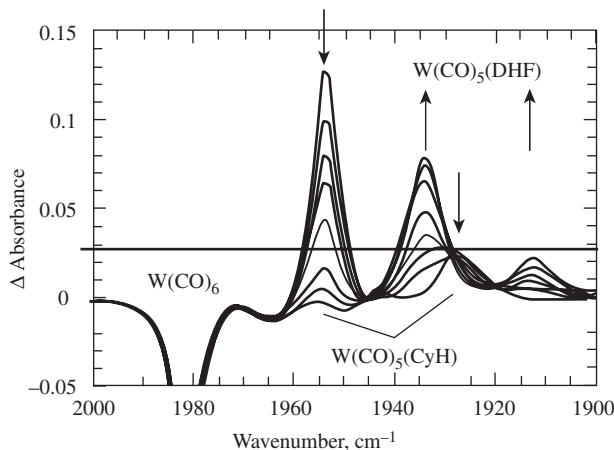
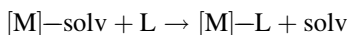


**Figure 19.3.** Time-resolved spectra for the reaction of  $\text{W(CO)}_5(\text{CyH})$  with 2,5-DHF. The spectra were acquired 0, 1, 2, 3, 5, 10, 15, and 25  $\mu\text{s}$  following the photolysis flash. The bands at 1954 and 1928  $\text{cm}^{-1}$  that disappear with time are assigned to  $\text{W(CO)}_5(\text{CyH})$ , and the bands at 1934 and 1913  $\text{cm}^{-1}$  that grow with time are due to  $\text{W(CO)}_5(2,5\text{-DHF})$ . (Reproduced from [15], by permission of the American Chemical Society; copyright © 2003.)

Lugovskoy et al. [15] investigated the mechanism and kinetics of the exchange of ligands, L, with an alkane solvent molecule, solv, that is weakly bound to a transition metal center, [M]:



In the reaction that we describe below,  $[\text{M}] = \text{W(CO)}_5$ , solv = cyclohexane (CyH), and L = 2,5-dihydrofuran (2,5-DHF). A solution of  $\text{W(CO)}_6$  in CyH was irradiated by pulses of a 308-nm XeCl excimer laser that was operated at the following conditions: pulse width  $\sim 20$  ns, power  $\sim 50$  mJ/pulse, and repetition rate  $\sim 4$  Hz. The time-resolved spectra that were measured are shown in Figure 19.3.

Within the 50-ns rise time of the detector, two strong bands at 1954 and 1928  $\text{cm}^{-1}$  and a weak band at 2087  $\text{cm}^{-1}$ , all of which are assigned to the solvated  $\text{W(CO)}_5(\text{CyH})$  intermediate, appear in the spectrum. This intermediate was shown previously to be formed within tens of picoseconds of the light pulse. These bands disappear in less than 100  $\mu\text{s}$ , with three new bands that correspond to the formation of  $\text{W(CO)}_5\text{L}$  appearing with the identical exponential time dependence (see Figure 19.4). By performing these measurements at temperatures between 20 and 60°C, Lugovskoy et al. were able to obtain the activation enthalpy,  $\Delta H^\ddagger$ , and entropy,  $\Delta S^\ddagger$ , of the reactions of several different furans and showed that as L becomes less strongly electron donating, as determined by the trans C—O stretching force constant of  $\text{W(CO)}_5\text{L}$ ,  $\Delta H^\ddagger$  rises and  $\Delta S^\ddagger$  become less negative and drew several significant conclusions on the reaction mechanism from their results.

Several workers have investigated the photochemistry and photophysics of proteins and other biomolecules by time-resolved FT-IR spectroscopy with a step-scan

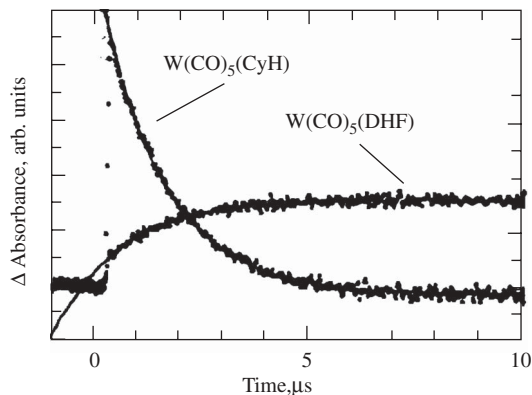


**Figure 19.4.** Variation of absorptions at  $1954\text{ cm}^{-1}$ , assigned to  $\text{W(CO)}_5(\text{CyH})$ , and at  $1934\text{ cm}^{-1}$ , assigned to  $\text{W(CO)}_5(2,5\text{-DHF})$ , following photolysis of a  $\text{W(CO)}_6$  solution containing 2,5-DHP. The solid lines are single-exponential fits to the data with  $k_{\text{obs}} = 6.58 \times 10^5\text{ s}^{-1}$ . (Reproduced from [15], by permission of the American Chemical Society; copyright © 2003.)

interferometer. The spectra associated with these reactions are far more complex and frequently much weaker than those shown in Figure 19.3. By far the most studied molecule is the light-driven proton-pump membrane protein, bacteriorhodopsin [16–18]. We describe one report, by Rammelsberg et al. [7], in which a step-scan FT-IR spectrometer was used to obtain information on this molecule with a time resolution of  $\sim 100\text{ ns}$ . The experimental setup is shown in Figure 19.5. Using this arrangement, difference spectra can be measured with time resolutions of  $5\text{ }\mu\text{s}$  to  $100\text{ ns}$ , the latter being the effective response time of the photovoltaic MCT detector. The dc spectrum that is measured simultaneously is used to normalize the difference spectra.

At every sampling point of the interferogram, the position of the movable mirror is checked to ensure that it is stable. An excimer laser then triggers the photoreaction. The output of this laser is monitored by a photodiode with a very fast (10-ns) response time, and data acquisition of the 200-MHz transient recorder is begun. Two actions were taken to cut down on the enormous amount of data that is generated at this sampling frequency. The acquisition rate is slowed down to 50 kHz at  $200\text{ }\mu\text{s}$  and the OPD difference between each step was increased to four wavelengths of the HeNe laser interferogram, making the Nyquist wavenumber equal to  $1975\text{ cm}^{-1}$ .

The procedure used to acquire the data was as follows. First a dc interferogram is measured with the 200-MHz transient recorder in the step-scan mode without sample excitation. The measured interferogram is used to calculate the phase spectrum,  $\Theta_{\tilde{\nu}}$ , and the single-beam background spectrum,  $S_R(\tilde{\nu})$ . The time-resolved measurement at a given OPD is then started by a laser flash at each step. The 200-MHz transient recorder measures the time-domain signal from  $100\text{ ns}$  to  $20\text{ }\mu\text{s}$  and the 200-kHz recorder monitors from  $5\text{ }\mu\text{s}$  until the end of the reaction. At every step, several photocycles are accumulated to improve the SNR. Because of the fact that

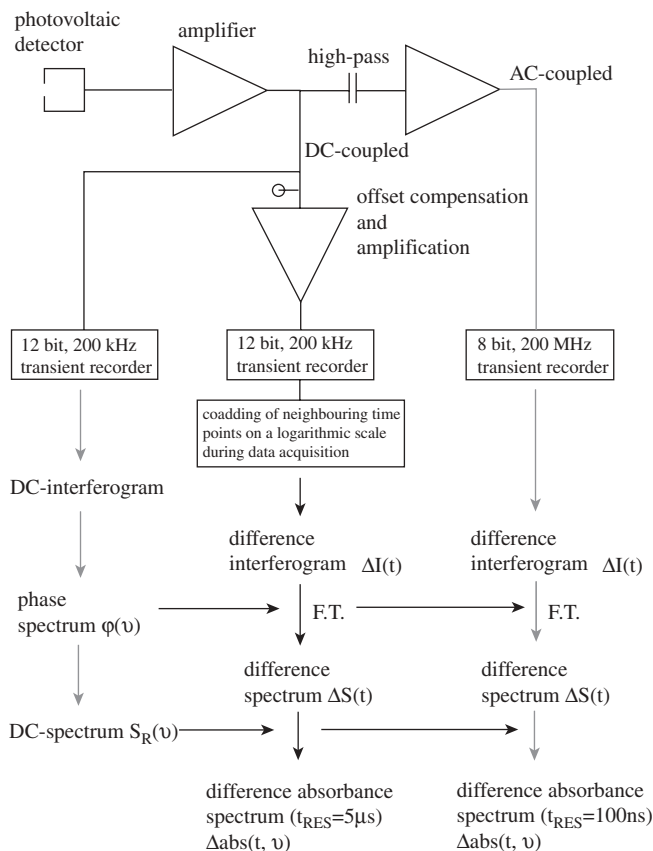


**Figure 19.5.** IR signal preamplification, data recording, and calculation of the difference spectra in the ac- and dc-coupled mode. (Reproduced from [7], by permission of the Society for Applied Spectroscopy; copyright © 1997.)

an ac-coupled amplifier is being used, the spectrum contains both positive and negative features, so that phase correction cannot be effected with the usual Mertz algorithm, and the stored phase spectrum  $\Theta_{\nu}$  is used.

Changes in absorbance of between  $10^{-3}$  and  $10^{-4}$  AU can be measured in spectra measured at a resolution of  $4 \text{ cm}^{-1}$ . A three-dimensional representation of the changes in the absorbance spectrum of bacteriorhodopsin between 1800 and  $100 \text{ cm}^{-1}$  is shown in Figure 19.6. The change in absorbance of a band at  $1188 \text{ cm}^{-1}$ , ascribed to a C—C stretching vibration of the 13-*cis* protonated Schiff base of the retinal moiety, is shown in Figure 19.7. The appearance of this band indicates that this moiety has changed from the original all-*trans* configuration to 13-*cis* on irradiation by the laser pulse. This configuration is known to be formed within 450 fs of the laser pulse and is therefore effectively instantaneous for these measurement. The disappearance of this band after  $200 \mu\text{s}$  is caused by the deprotonation of

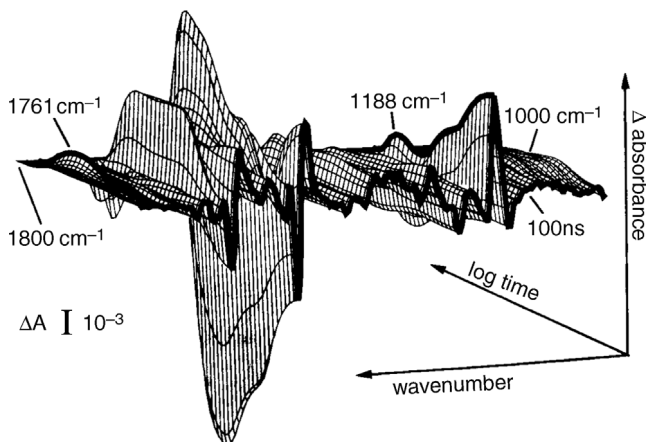


**Figure 19.6.** Three-dimensional plot of the changes in the absorbance spectra between 1800 and 1000  $\text{cm}^{-1}$  that accompany bacteriorhodopsin's photocycle measured with 100-ns resolution. The time axis has a logarithmic scale to show a complete bacteriorhodopsin photocycle in one representation. (Reproduced from [7], by permission of the Society for Applied Spectroscopy; copyright © 1997.)

the Schiff base. The deprotonation kinetics of the Schiff base agree with the reprotonation kinetics of the counterion Asp85, which can be followed at 1761  $\text{cm}^{-1}$ . The reappearance of the 1188- $\text{cm}^{-1}$  band in the millisecond time domain indicates the reprotonation of the Schiff base by a different aspartic acid moiety, Asp96, and its final disappearance shows the relaxation to the ground state of bacteriorhodopsin.

Measurements such as these show the remarkable capability of step-scan FT-IR for time-resolved measurements of extremely complex chemical systems. However,

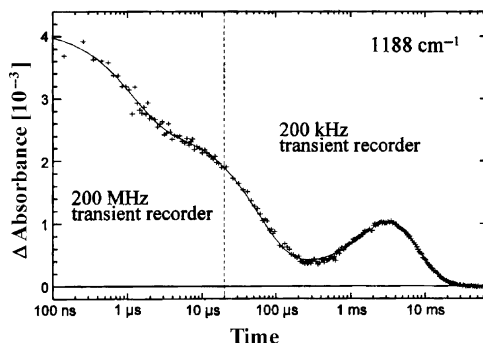


**Figure 19.7.** Example of a time course in the bacteriorhodopsin photocycle at a single wavenumber (1188  $\text{cm}^{-1}$ ). Data were recorded simultaneously with a 200-MHz and a 200-kHz transient recorder, so no inconsistency is seen in the overlap region near 20  $\mu\text{s}$ . The 1188- $\text{cm}^{-1}$  band is assigned to a C–C stretching vibration of the 13-*cis* protonated Schiff base retinal. (Reproduced from [7], by permission of the Society for Applied Spectroscopy; copyright © 1997.)

they rely on the photoreaction being completely reversible. When this is not the case, the sample must be completely regenerated between each laser pulse. When the reagents are expensive and the volume of the cell is large, such a procedure is often not feasible. In this case, several innovative approaches have been developed. For example, Rammelsberg et al. [19] mounted a solid sample at the focus of an IR microscope so that the laser beam and the IR beam were both about 200  $\mu\text{m}$  in diameter. The sample was then moved after each laser pulse. In this way, a photoreaction of a solid sample could be reinitiated about 2000 times on a 2-cm<sup>2</sup> sample. Rödiger and Siebert [20] used a sample-changing wheel with 10 cuvettes to allow the study of a slow reaction that took several seconds to return to the ground state.

### 19.3. STROBOSCOPIC SPECTROMETRY

At this point we mention briefly a technique known as *stroboscopic FT-IR spectrometry*, which has been used to obtain time-resolved spectra with a rapid-scanning spectrometer in the past but which is rarely used today because of the success of the measurements made with a step-scan FT-IR spectrometer. In this case, the reaction is initiated by a pulse that is generated at a laser zero crossing. For an interferometer operating at a scan speed that generates a HeNe reference interferogram with a frequency of 5 kHz, each zero crossing is separated by only 200  $\mu\text{s}$ . Since this time is so short, it is unlikely that the reaction will be complete at the next zero crossing, so the instruments were programmed so that the reaction was initiated every  $N$ th zero crossing of the laser interferogram.

Thus during the first scan, a pulse was generated to trigger the reaction at the first,  $(N + 1)$ st,  $(2N + 1)$ st, and so on, zero crossing. For each pulse, data were then acquired at times  $t_0, t_1, t_2, \dots, t_T$  after the pulse, where  $t = t_T$  is time corresponding to the end of the reaction. These data were stored in an analogous way to the way that data were stored in the measurement with the step-scan interferometer, except that the data for the 2nd, 3rd,  $\dots$ ,  $N$ th zero crossing were missing unless the acquisition times coincided with the zero crossings (see below). During the second scan, the reaction pulse was triggered at the 2nd,  $(N + 2)$ nd,  $(2N + 2)$ nd, and so on, zero crossing, and these data were added to the data acquired during the first scan. This process was repeated until the reaction had been sampled at every zero crossing and a matrix of data had been acquired. Note that if the frequency of the laser interferogram is  $f_L$ , the process must have relaxed back to its original condition after a time  $N/f_L$  records. Sorting the data to produce “constant-in-reaction-time” interferograms is a little more complex than for the step-scan experiment, nonetheless, a sorted data matrix similar to Table 19.1 is produced. The series of spectra is calculated in the manner described in Section 19.2.

In most early reports of time-resolved stroboscopic FT-IR spectrometry, data were not acquired with a clock. Instead, the ADC was triggered at each zero crossing after the one at which the reaction was initiated. In this case, the time resolution was equal to  $(f_L)^{-1}$  seconds. Thus, if the frequency of the laser interferogram was



5 kHz, the time resolution was 200  $\mu$ s. In some later experiments, the reaction was actuated by a pulse at the appropriate laser zero crossing and the detector signal was sampled using a clock of the type that is used for time-resolved measurements with a step-scan interferometer. In this case, there is no theoretical reason why time-resolved spectra produced in this manner should not be identical to the spectra measured with a step-scan interferometer. However, this experiment relies on the time between the zero crossings, and the time between initiation of reaction pulses must be held as short as possible; otherwise, the entire interferogram is collected before subsequent reaction pulses are initiated. Under these conditions the system being studied often has not fully relaxed back to its starting condition, and as a result, there is a greater probability of generating spectral artifacts [21]. Errors of this type are far less likely to be encountered when a step-scan interferometer is used, as the OPD can be held stationary for as long as it takes for the reaction to relax back to its original condition.

## 19.4. ASYNCHRONOUS TIME-RESOLVED FT-IR SPECTROMETRY

### 19.4.1. Instrumental Considerations

An alternative technique for time-resolved infrared measurements on a rapid-scanning FT-IR spectrometer that not only overcomes the limitations of stroboscopic spectroscopy described in Section 19.3 but under certain circumstances appears to have better time resolution than measurements made on a step-scan interferometer has been developed by Masutani et al. [22–25]. In this technique, the sample perturbation is not timed to coincide with the scanning and data acquisition of the spectrometer, (i.e., the two are asynchronous). The basic instrument used for asynchronous time-resolved FT-IR spectrometry is a standard rapid-scanning FT-IR spectrometer to which is added a boxcar integrator and some timing circuitry. The instrumental setup is shown in Figure 19.8.

The excitation, response of the sample, and output signals from each of the various units in this configuration are shown in Figure 19.9, where each trace shows the signal at the corresponding points shown in Figure 19.8. These signals are as follows: A standard interferogram (*a*) is generated by the interferometer. The sample is perturbed by a stimulus generator of the type that is used for time-resolved measurements with a step-scan or stroboscopic instrument. The stimuli (*b*) are applied at intervals of  $\tau$ . After each perturbation, the sample relaxes from its perturbed state to its original state (*c*). The excitation pulses also modulate the ordinary interferogram because of the change in the absorption spectrum of the sample (*d*). The modulated interferogram is passed to the gate circuit through the preamplifier and main amplifier. A trigger pulse (*e*) from each excitation pulse with a variable delay  $\Delta\tau$  is generated from the delay circuit. The signal arriving from the gate circuit is converted into a discrete signal (*f*), which constitutes a discrete interferogram that is time delayed with the stroboscopic process at the time delay  $\Delta\tau$  from the excitation set for each trigger pulse. A low-pass filter then converts the gate circuit

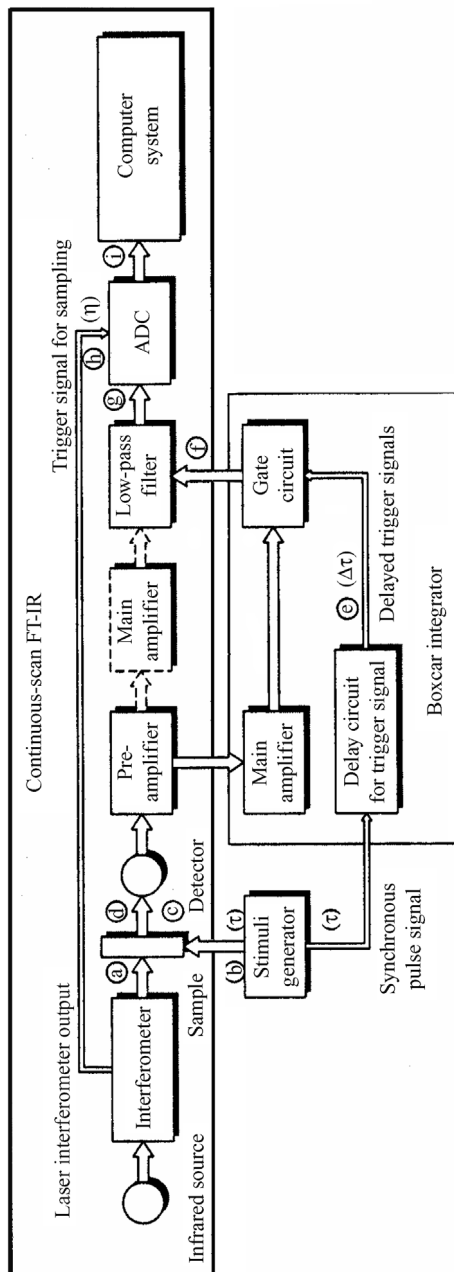


**Figure 19.8.** Typical setup for a single-channel asynchronous time-resolving FT-IR measurement. (Reproduced from [24], by permission of John Wiley & Sons, Ltd.; copyright © 2002.)

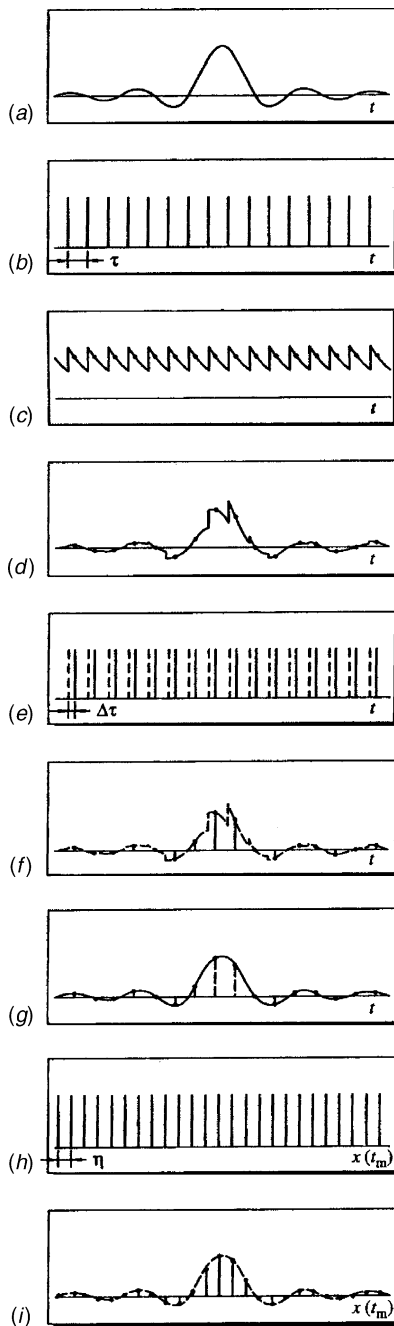


**Figure 19.9.** Signals in processes (a) through (i) in Figure 19.8: (a) ordinary interferogram before excitation; (b) excitation pulses; (c) response of sample; (d) modulated interferogram by excitation; (e) gate timing for time resolution; (f) time-resolved discrete interferogram; (g) time-resolved analog interferogram; (h) sampling timing of ADC; (i) sampled time-resolved interferogram. (Reproduced from [24], by permission of John Wiley & Sons, Ltd.; copyright © 2002.)

output back to a time-resolved analog interferogram ( $g$ ) for the time delay  $\Delta\tau$ . The HeNe laser interferogram sends the ADC the sampling timing ( $h$ ) at intervals  $\eta$  of the optical path difference ( $x$  in this figure). The output of the low-pass filter is sampled at the normal digitization rate (e.g., the frequency of the laser interferogram) and reconverted into a discrete interferogram ( $i$ ) at constant intervals  $\eta$  of OPD by the ADC and is sent to the computer. Fourier transformation of this interferogram gives a time-resolved spectrum for a time delay  $\Delta\tau$  from the perturbation.

A simplified description of this technique for time-resolved asynchronous FT-IR measurements is shown for a monochromatic source in Figure 19.10. The sinusoidal interferogram of the monochromatic light source shown in part (a) is further

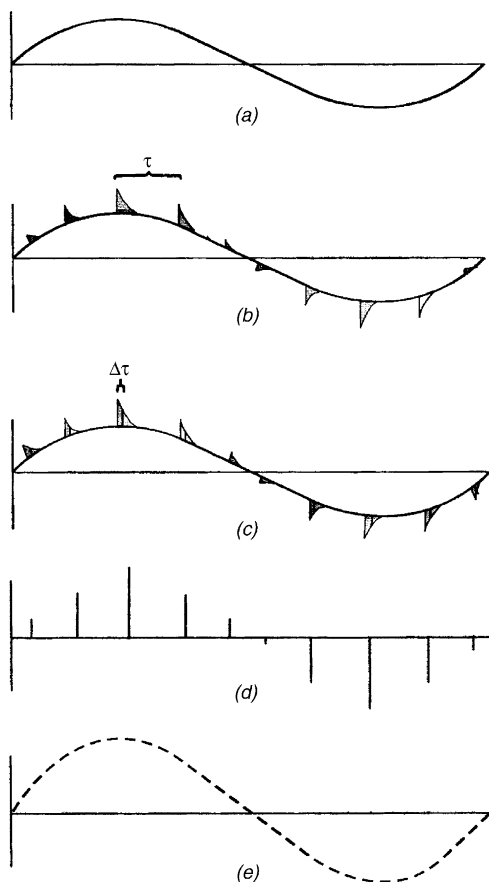


**Figure 19.10.** Data collection scheme for asynchronous sampling. (a) Fourier modulation of one wavelength. (b) This wavelength is further modulated by perturbation pulses at intervals of  $\tau$ . (c) Each perturbation is followed by a probe at  $\Delta\tau$  after the perturbation. (d) The detector gate or probe pulses generate a discrete interferogram. (e) The discrete interferogram is converted back to an analog interferogram for time  $\Delta\tau$  by the low-pass filter where the interferogram is sampled by the spectrometer's ADC at its normal rate. (Reproduced from [13], by permission of John Wiley & Sons, Ltd.; copyright © 2002.)

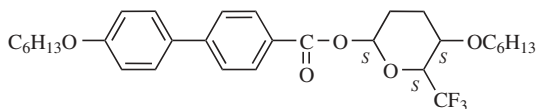
modulated by the perturbation pulses at intervals of  $\tau$  (*b*). Each perturbation is followed by a probe at a delay  $\Delta\tau$  after the perturbation (*c*). The detector gate generates a discrete interferogram (*d*) that is converted back to an analog interferogram for time delay  $\Delta\tau$  by the low-pass filter where the interferogram is sampled by the spectrometer's ADC at its normal rate (*e*). The Nyquist sampling theorem dictates that the repetition rate to create the transient event must be at least twice the highest Fourier frequency in the spectral range. In practice, a repetition rate that is 10 times that of the highest Fourier frequency is often used. A detailed formulation of time-resolved asynchronous FT-IR spectrometry has been given by Masutani [24].

One of the more interesting potential applications of asynchronous time-resolved FT-IR spectrometry is to be found in the area of laser photochemistry or photo-physics. If the gate is replaced by a probe pulse delayed by a time  $\tau$  from the pump pulse, the time resolution is no longer determined by the response time of the infrared detector but by the width of the pump and probe pulses and the time delay between them. In principle, a time resolution of less than  $10^{-12}$  s is achievable with this approach.

#### 19.4.2. Application to Liquid-Crystal Orientation Dynamics

One published application of time-resolved asynchronous FT-IR spectrometry involves the reorientation dynamics of ferroelectric liquid crystals induced by the reversal of the external electric field [26,27]. For the study to be described here, the liquid crystals were held in a 2- $\mu\text{m}$   $\text{CaF}_2$  cell whose windows had been coated with indium tin oxide, which served as the electrode, and with a polyimide film that had been oriented by stroking it in one direction. After the sample had been heated to 90°C to ensure that it was all in the isotropic liquid phase, it was injected into the cell, which had been heated to the same temperature. The cell was then allowed to cool to 40°C at a rate of 1°C min<sup>-1</sup> to obtain a homogeneously oriented liquid crystal. An IR polarizer was set at an angle of 45° to the orientation direction of the liquid crystal to obtain the maximum change in the absorption spectrum. Rectangular electric pulses with  $\pm 20$ -V peak voltages and a 20- $\mu\text{s}$  period were applied to the cell.

Two methods of acquiring the data were compared. In the first, a single boxcar integrator was used and 16 time-resolved spectra were measured sequentially by adjusting the time delay  $\Delta\tau$  of the gate. In the other, a multichannel device that allowed all 16 time delays to be measured simultaneously was installed. The total measurement time for the 16 spectra acquired with the single boxcar integrator was 90 min, where with the multichannel processor this time was reduced to 6 min. Only the latter data are shown in Figure 19.11. When the following chiral dopant, for which the three chiral carbon atoms are all in the *s* conformation:



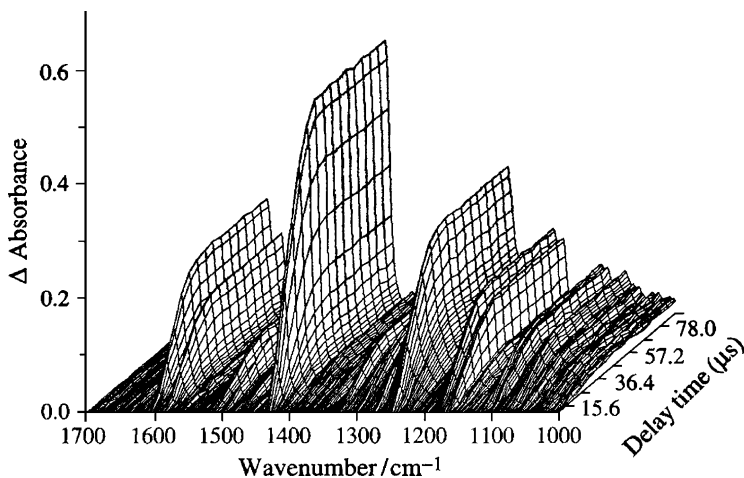
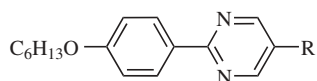


**Figure 19.11.** Time-resolved polarized spectra for the reorientation dynamics of a ferroelectric liquid crystal after reversal of the external electric field. (Reproduced from [25], by permission of the Society for Applied Spectroscopy; copyright © 1993.)

was added to base liquid crystals of the form



where  $R = C_9H_{19}$ ,  $C_8H_{17}$ , or  $C_7H_{15}$ , it was found that the  $C=O$  groups respond first to the applied electric field, and then the alkyl chains and other functional groups follow.

Similar experiments have also been carried out with a step-scan FT-IR spectrometer [28], and analogous results were obtained. Although this experiment was not performed with very short time resolution, it gives an idea of the quality of the data that can be obtained, and successful experiments with much shorter time resolution can be predicted.

## REFERENCES

1. P. Hinsmann, M. Haberkorn, J. Frank, P. Svasek, M. Harasek, and B. Lendl, *Appl. Spectrosc.* **55**, 241 (2001).
2. J. W. Brault, *Appl. Opt.* **35**, 2891 (1996).
3. H. Yang, P. R. Griffiths, and C. J. Manning, *Appl. Spectrosc.* **56**, 1281 (2002).
4. B. A. Weinstock, H. Yang, B. L. Hirsche II, and P. R. Griffiths, *Langmuir* **21**, 3915 (2005).
5. C. Pellerin, R. E. Prud'homme, M. Pézolet, B. A. Weinstock, and P. R. Griffiths, *Macromolecules* **36**, 4838 (2003).
6. C. Pellerin, M. Pézolet, and P. R. Griffiths, *Macromolecules*, **39**, 6546 (2006).

7. R. Rammelsberg, B. Hessling, H. Chorongiewski, and K. Gerwert, *Appl. Spectrosc.* **51**, 558 (1997).
8. R. Vogel and F. Siebert, *Curr. Opin. Chem. Biol.* **4**, 518 (2000).
9. P. Hinsmann, J. Frank, P. Svasek, M. Harasek, and B. Lendl, *Lab on a Chip* **1**, 16 (2001).
10. N. Katayama, T. Sato, Y. Ozaki, K. Murashiro, M. Kikuchi, S. Saaito, D. Demus, T. Yuzawa, and H. Hamaguchi, *Appl. Spectrosc.* **49**, 977 (1995).
11. N. Katayama, M. A. Czarnecki, M. Satoh, T. Watanabe, and Y. Ozaki, *Appl. Spectrosc.* **51**, 487 (1997).
12. H. Wang, R. A. Palmer, and C. J. Manning, *Appl. Spectrosc.* **51**, 1245 (1997).
13. G. D. Smith and R. A. Palmer, Fast time-resolved mid-infrared spectroscopy using an interferometer, in *Handbook of Vibrational Spectroscopy*, J. C. Chalmers and P. R. Griffiths, Eds., Wiley, Chichester, West Sussex, England, 2002, Vol. 1, p. 625.
14. C. Rödig and F. Siebert, Instrumental aspects of time-resolved spectra generated using step-scan interferometers, in *Handbook of Vibrational Spectroscopy*, J. C. Chalmers and P. R. Griffiths, Eds., Wiley, Chichester, West Sussex, England, 2002, Vol. 1, p. 641.
15. A. Lugovskoy, R. Paur-Afshari, and R. H. Schultz, *J. Phys. Chem. A* **104**, 10587 (2003).
16. M. S. Braiman and K. Rothschild, *Annu. Rev. Biophys. Chem.* **17**, 541 (1988).
17. K. Gerwert, *Biochim. Biophys. Acta* **1101**, 147 (1992).
18. F. Siebert, Infrared spectroscopic investigations of retinal proteins, in *Biomolecular Spectroscopy, Part A*, R. J. H. Clark and R. E. Hester, Eds., Wiley, Chichester, West Sussex, England, 1993, p. 1.
19. R. Rammelsberg, S. Boulas, H. Chorongiewski, and K. Gerwert, *Vib. Spectrosc.* **19**, 143 (1999).
20. C. Rödig and F. Siebert, *Vib. Spectrosc.* **19**, 271 (1999).
21. A. A. Garrison, R. A. Crocombe, G. Mamantov, and J. A. de Haseth, *Appl. Spectrosc.* **34**, 399 (1980).
22. K. Masutani, H. Sugisawa, A. Yokota, Y. Furukawa, and M. Tasumi, *Appl. Spectrosc.* **46**, 560 (1992).
23. K. Masutani, K. Numahata, K. Nishimura, S. Ochiai, Y. Nagasaki, N. Katayama, and Y. Ozaki, *Appl. Spectrosc.* **53**, 588 (1999).
24. K. Masutani, Fast time-resolved mid-infrared spectroscopy using an interferometer, in *Handbook of Vibrational Spectroscopy*, J. C. Chalmers and P. R. Griffiths, Eds., Wiley, Chichester, West Sussex, England, 2002, Vol. 1, p. 655.
25. K. Masutani, A. Yokota, Y. Furukawa, M. Tasumi, and A. Yoshizawa, *Appl. Spectrosc.* **47**, 1370 (1993).
26. M. A. Czarnecki, N. Katayama, M. Satoh, T. Watanabe, and Y. Ozaki, *J. Phys. Chem.* **99**, 14,101 (1995).
27. N. Katayama, M. A. Czarnecki, M. Satoh, T. Watanabe, and Y. Ozaki, *Appl. Spectrosc.* **51**, 487 (1997).
28. M. A. Czarnecki, Vibrational spectroscopy of liquid crystals, in *Handbook of Vibrational Spectroscopy*, J. C. Chalmers and P. R. Griffiths, Eds., Wiley, Chichester, West Sussex, England, 2002, Vol. 4, p. 3109.

# PHOTOACOUSTIC SPECTROMETRY

## 20.1. PHOTOACOUSTIC SPECTROMETRY OF GASES

The fundamental idea of photoacoustic (PA) spectrometry was discovered in 1880 by Alexander Graham Bell when he was investigating possible means of optical communication [1]. Bell found that if a beam of light is modulated at an audio frequency and focused on an absorbing sample, an audible sound may be produced. The more strongly the sample absorbs light, the louder is the sound. The photoacoustic effect can be encountered with both gaseous and solid samples. A simple explanation of the PA effect for gases is given in this section and the rest of the chapter is dedicated to PA/FT-IR spectrometry of solids.

Consider a gas that is contained in a closed cell fitted with an infrared-transmitting window and a pressure transducer (or microphone). Let the gas absorb light of wavenumber,  $\tilde{\nu}_0$ . If unmodulated (dc) monochromatic radiation at  $\tilde{\nu}_0$  is passed into the cell, some fraction will be absorbed by the gaseous molecules, which will be raised to an excited state. If these molecules return to their ground state through a radiationless transition (as is usually the case for infrared spectroscopy), the temperature of the gas increases. Since the volume of the vessel is constant, the pressure of the gas will increase (by Charles' law) until the rate of heat loss through the walls equals the rate at which the heat is generated. If the radiation is modulated in the audio-frequency range, the pressure changes are manifested as sound and can be measured by the microphone.

Now consider the case where the gaseous sample has a rich infrared spectrum and the radiation is emitted by a broadband infrared source, such as a Globar. If this radiation is passed through a rapid-scanning interferometer before entering the cell, each wavelength is modulated at its own characteristic Fourier frequency (see Eq. 2.11). The microphone will respond to each modulation frequency that corresponds to a wavelength at which the gas absorbs, and a photoacoustic interferogram will be measured at the microphone. The Fourier transform of this



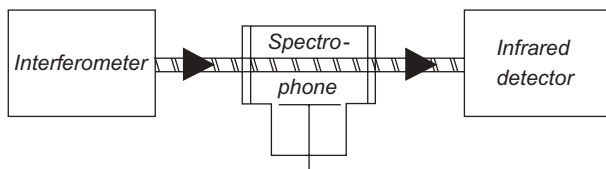


**Figure 20.1.** Optical configuration by which transmission and photoacoustic spectra of gaseous samples can be measured with the same cell. (Reproduced from [2], by permission of Elsevier Publishing Co.; copyright © 1978.)

interferogram will be the PA spectrum, which will have intensity only at those wavelengths where the sample has significant absorption.

The first experiment showing the feasibility of Fourier transform photoacoustic spectrometry was reported by Busse and Bullemer [2]. Their experimental layout is shown diagrammatically in Figure 20.1. The modulated beam from a rapid-scanning interferometer is passed through a short gas cell in which a microphone (or *spectro-phone*, as it was called by these authors) is mounted. With this configuration, both the PA and the conventional interferograms can be measured (see Figure 20.2).

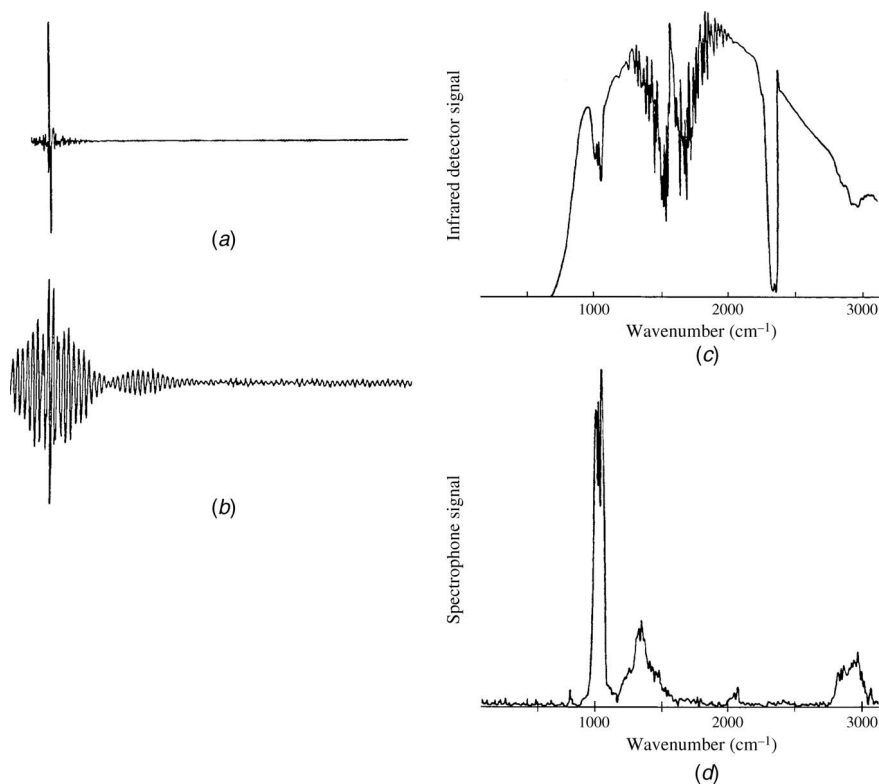


**Figure 20.2.** Interferograms of methanol vapor measured by (a) transmission spectrometry and (b) photoacoustic spectrometry; (c, d) corresponding spectra. (Reproduced from [2], by permission of Elsevier Publishing Co.; copyright © 1978.)

Note that the PA spectrum has significant intensity only at those wavelengths where the sample absorbs and the single-beam background is completely suppressed. The same concept was applied commercially by Brühl and Kjaer in Denmark, which developed a portable instrument for monitoring industrial atmospheres, the sensitivity of which was in the low parts-per-million range. However, this instrument no longer appears to be marketed.

## 20.2. PHOTOACOUSTIC SPECTROMETRY OF SOLIDS WITH A RAPID-SCANNING INTERFEROMETER

PA/FT-IR spectrometry is far more commonly used today for measuring the spectra of solids than gases. For the sake of simplicity, let us say that the sample is a homogeneous solid, such as a polymer, and the instrument is a standard rapid-scanning FT-IR spectrometer, so that each wavenumber  $\tilde{\nu}$  in the spectrum is modulated at a frequency of  $V\tilde{\nu}$  hertz, where  $V$  is the optical velocity of the interferometer (see Eq. 2.11). The sample is held in a closed cell that is filled with a nonabsorbing gas (usually, He because of its high thermal conductivity) and is illuminated with the beam from the interferometer. At wavelengths where the solid sample absorbs some fraction of the incident radiation, a modulated temperature fluctuation will be generated at the same modulation frequency (but not necessarily the same phase) as that of the incident radiation. The amplitude of the temperature variation in the sample decreases with the distance from its surface. Heat generated within the bulk of the sample is conducted to the surface so that the temperature of the layer of gas next to the surface varies at the same frequency as the incident radiation (but not with the same phase.) The resulting pressure modulation is detected microphonically.

McClelland et al. [3] have described the PA spectrometry of solids using a fairly simple model. The following discussion closely follows this model, the basis of which is shown schematically in Figure 20.3. Let the intensity of the beam from

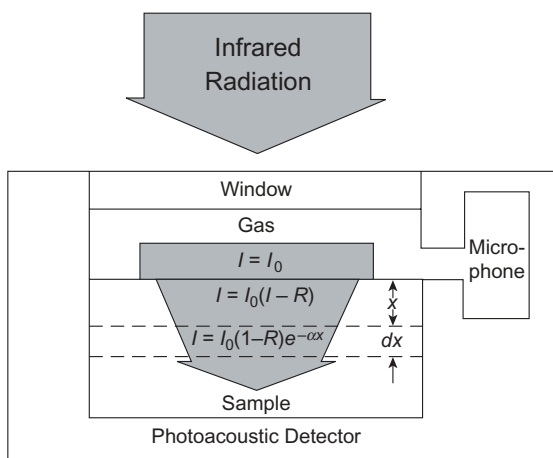


**Figure 20.3.** How an infrared beam is attenuated during measurement of a photoacoustic spectrum. (Reproduced from [3], by permission of CRC Press; copyright © 1993.)

the interferometer be  $I_0$ . When the beam has passed through the cell window and the infrared-transparent fill gas and is incident upon the sample, a fraction,  $R$ , is reflected from the sample's surface. Immediately below the surface, therefore, the intensity of the IR beam is given by  $I_0(1 - R)$ . Because of absorption of the beam by the sample, the intensity decays to a value  $I_0(1 - R)e^{-\alpha(\tilde{\nu})x}$  at depth  $x$ , where  $\alpha(\tilde{\nu})$  is the linear absorption coefficient (see Eq. 1.16).

Each layer  $dx$  of the sample that absorbs radiation experiences oscillatory heating at those Fourier frequencies that correspond to wavenumbers at which the sample has appreciable absorption. The amplitude of the temperature change is proportional to  $I_0(1 - R)\alpha(\tilde{\nu}) \exp[-\alpha(\tilde{\nu})x]dx$ . Each layer that oscillates in temperature is a source of thermal waves. In the one-dimensional energy flow schematic shown in Figure 20.4, thermal waves propagate from the bulk of the sample to the surface and thence to the surrounding gas. During propagation, thermal waves decay exponentially with a coefficient

$$a_s = \left( \frac{\pi f}{D} \right)^{1/2} \quad (20.1)$$

where  $f$  is the modulation frequency in hertz.  $D$  is the thermal diffusivity of the sample, equal to  $K_s/C_s\rho_s$  [3], where  $K_s$  is the thermal conductivity of the solid sample,  $C_s$  is its specific heat, and  $\rho_s$  is its density. (The subscripts  $s$  and  $g$  in this discussion refer to the solid sample and fill gas, respectively.) For a thermal wave generated at depth  $x$  just before it is conducted into the gas adjacent to the sample surface, the amplitude of the oscillating surface temperature,  $\Delta T_s$ , is given by

$$\Delta T_s = AI_0(1 - R)\alpha(\tilde{\nu}) e^{-\alpha(\tilde{\nu})x} e^{-a_s x} dx \quad (20.2)$$

where  $A$  is a constant of proportionality. A fraction,  $R_t$ , of the thermal wave is reflected back into the sample from its surface. Thus, the amplitude of the temperature oscillation in the gas,  $\Delta T_g$ , is proportional to  $I_0(1 - R)(1 - R_t)\alpha(\tilde{\nu}) \exp\{-[\alpha(\tilde{\nu}) + a_s]x\}dx$ .

The PA signal is generated by the thermal expansion of the gas caused by the sum of all the  $\Delta T_g$  contributions caused by each absorption band. Contributions originate from each of the sample layers in which the relevant wavelengths are absorbed and which are close enough to the surface that the thermal-wave amplitude has not decayed to a vanishingly small level after crossing the sample-gas interface.

The infrared absorption coefficient and thermal wave decay coefficients,  $\alpha(\tilde{\nu})$  and  $a_s$ , respectively, determine the magnitude of the photoacoustic signal. The term  $\alpha(\tilde{\nu}) \exp\{-[\alpha(\tilde{\nu}) + a_s]x\}$  in the expression for temperature oscillation leads to a linear PA signal dependence on infrared absorption when  $\alpha(\tilde{\nu}) \ll a_s$ . The reciprocal of  $a_s$  is correctly known as the *thermal wave decay length*,  $L$ , although it is sometimes referred to as the sampling depth, penetration depth, or thermal diffusion depth. The sample layer extending a distance  $L$  beneath the surface contributes



**Table 20.1. Approximate Thermal Wave Decay Lengths ( $\mu\text{m}$ ) for Various Thermal Diffusivities<sup>a</sup>**

$D(\text{cm}^2 \cdot \text{s}^{-1})$	Frequency (Hz)				
	1	10	100	1000	10,000
0.1	2000	600	200	60	20
0.01	600	200	60	20	6
<b>0.001</b>	<b>200</b>	<b>60</b>	<b>20</b>	<b>6</b>	<b>2</b>
0.0001	60	20	6	2	0.6

<sup>a</sup>A typical value of  $D$  for polymers is  $0.001 \text{ cm}^2 \cdot \text{s}^{-1}$ .

When the sample is optically opaque and thermally thin, ( $L > l$ ,  $L > \mu_\beta$ ), the PA signal is independent of  $\alpha(\tilde{\nu})$  and has a  $1/f$  dependence. When  $\mu_\beta$  is small (i.e., for very strong absorption bands) and  $L$  is large, most of the radiation has been absorbed within a length that is much shorter than  $L$ . This condition is invariably encountered for materials such as carbon black or heavily carbon-filled polymers; thus, these materials are often used as the reference for PA spectrometry.

Let us examine this situation in more detail for the situation where  $D = 0.001 \text{ cm}^2 \cdot \text{s}^{-1}$  (bold data in Table 20.1). When the modulation frequency is less than  $\sim 200$  Hz, the thermal wave decay length exceeds  $10 \mu\text{m}$ . However, the infrared beam cannot interrogate the sample much below the optical absorption depth, which for strong absorption bands is often less than  $5 \mu\text{m}$ . Since a thermal wave cannot be generated much deeper into the sample than  $\mu_\beta$  (since the infrared beam only has significant intensity this far into the sample), the strong bands in the PA spectrum cannot become any stronger even if  $\alpha(\tilde{\nu})$  were increased (photoacoustic saturation). Thus, at low enough modulation frequencies, most strong bands in the spectrum appear to have the same intensity.

The thermal wave decay depth, and hence the extent of saturation, may be reduced by increasing the modulation frequency, which is done by increasing the optical velocity of the interferometer. As the scan speed is increased, the situation changes from the condition where  $L > \mu_\beta$  to one where  $L < \mu_\beta$  and the relative intensities of the absorption bands becomes closer to their true values.

This effect can be observed in the three PA spectra shown in Figure 20.5, which shows how the spectrum of polyethylene (PE) changes as the optical velocity,  $V$  (given in terms of the HeNe laser frequency in this figure) is changed from 200 Hz to 20 kHz [5]. When the laser frequency is 200 Hz,<sup>1</sup> the modulation frequencies at 2900, 1460, and  $720 \text{ cm}^{-1}$  are about 37, 18, and 9 Hz, respectively. The actual thermal diffusivity of polyethylene varies with its source but is assumed

<sup>1</sup>When  $V$  is so small that the HeNe laser frequency is less than 1 kHz, many interferometers become unstable. For these measurements, the slowest scan was actually taken in the step-scan mode at 200 steps per second, with the spectrum being acquired just as one would in the rapid-scan mode.

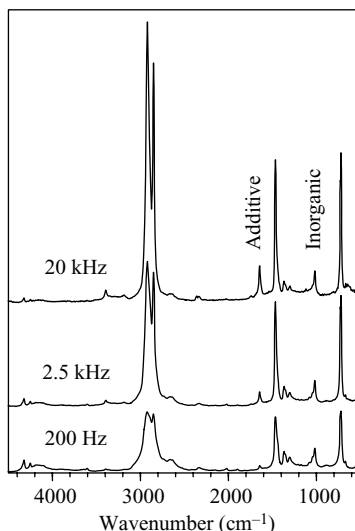


**Figure 20.5.** PA spectra of polyethylene pellets containing two additives: one distributed uniformly throughout the polymer and the other concentrated near the surface. The spectra were measured at three scan speeds, corresponding to HeNe laser frequencies of 200 Hz, 2.5 kHz, and 20 kHz. The spectra were scaled so that the weak band at  $1370\text{ cm}^{-1}$  was of constant height. (Reproduced from [5], by permission of the American Institute of Physics; copyright © 2003.)

to be  $0.0018\text{ cm}^2 \cdot \text{s}^{-1}$  here [6]. From the data in Table 20.1 and assuming that  $D = 0.0018\text{ cm}^2 \cdot \text{s}^{-1}$ , the calculated sampling depths corresponding to these modulation frequencies are shown in Table 20.2.

The values of the linear absorption coefficient  $\alpha(\tilde{\nu})$  and the optical absorption depth  $\mu_\beta$  at the peak of the strongest bands in three spectral regions are also given in Table 20.2. Clearly,  $\mu_s > \mu_\beta$  for each of these bands, which is the condition for photoacoustic saturation for spectra taken at the lowest optical velocity, so that these three bands in the PE spectrum all have about the same intensity.

When the scan speed is increased to 2.5 kHz ( $V \approx 0.16\text{ cm} \cdot \text{s}^{-1}$ ), the relative intensities of the  $1460\text{-}$  and  $720\text{-cm}^{-1}$  bands decrease slightly relative to that of the band at  $2920\text{ cm}^{-1}$ , but all bands still exhibit some level of saturation. Even when the scan speed is increased to 20 kHz ( $V \approx 1.3\text{ cm} \cdot \text{s}^{-1}$ ), the intensities of the

**Table 20.2.** Approximate Values for  $\alpha(\tilde{\nu})$ ,  $\mu_\beta$ , and  $\mu_s^a$

Band Center ( $\text{cm}^{-1}$ )	$\alpha(\tilde{\nu})$ ( $\text{cm}^{-1}$ )	$\mu_\beta$ ( $\mu\text{m}$ )	$\mu_s$ ( $\mu\text{m}$ )
2920	5750	1.7	39
1460	575	17	56
720	380	26	79

<sup>a</sup>Calculated for 200-Hz data acquisition for Three Bands in the Spectrum of Polyethylene. The values of  $\alpha(\tilde{\nu})$  were measured from a different sample of polyethylene than the one used for Figure 20.5. However, they are almost certainly good to  $\pm 20\%$ .

1460- and 720-cm<sup>-1</sup> bands are still approximately equal. This result suggests that an exceptionally high scan speed would be needed to eliminate the effect of photoacoustic saturation completely. It is for this reason that several workers have attempted to remove the effect of saturation numerically, as discussed later in this section.

The apparent increase in the relative intensity of certain bands in PA spectra as the optical velocity is increased has sometimes been assigned incorrectly to an increase in the concentration of a species near the surface, and great care must be taken in the interpretation of PA spectra measured with different scan speeds. In general, this conclusion can only be drawn for components at very low concentration or for bands with low absorptivities. For the spectra in Figure 20.5, for example, the band at 1650 cm<sup>-1</sup> has been assigned to an additive that is concentrated near the surface of the polymer, while the band at 1020 cm<sup>-1</sup> is due to an additive (probably an inorganic filler) whose concentration is uniform throughout the polymer. The fact that the intensity of the 1650-cm<sup>-1</sup> band increases relative to that of the neighboring band of polyethylene at 1460 cm<sup>-1</sup> as the scan speed is increased indicates that the additive does indeed have higher concentration at the surface than in the interior of the polymer. As the scan speed of the interferometer is increased, the intensity of the 1020-cm<sup>-1</sup> band drops slightly relative to the intensities of the bands at 1460 and 720 cm<sup>-1</sup>. However, because these two bands are saturated, this behavior would be expected because the strong bands become less saturated as the scan speed is increased. Since the concentration of the additives is low, the 1650- and 1020-cm<sup>-1</sup> bands are both weak and neither additive band is saturated. Thus, the fact that the intensity of the 1020-cm<sup>-1</sup> band stays approximately constant while the intensity of the surface additive band at 1650 cm<sup>-1</sup> increases with scan speed certainly indicates that the concentration of the surface additive is not uniform throughout the sample but rather, is indeed concentrated at the surface. The arguments made above are complex, but we hope they serve to show how important it is to account for the effect of saturation when interpreting photoacoustic spectra. The fact that the frequency at which the radiation is modulated by a rapid-scanning interferometer changes by a factor of 10 across the spectrum makes depth profiling by PA spectroscopy quite difficult. One way of reducing this problem is to use a step-scan interferometer, as described in the following section.

In the same way that variations in source intensity, beamsplitter efficiency, and detector response are compensated in transmission spectrometry by ratioing the single-beam spectra measured with and without the sample in the beam, in PA spectrometry the single-beam spectrum of the sample is ratioed against the spectrum of an optically opaque and thermally thick reference. As noted above, carbon black and heavily carbon-filled polymers make excellent reference materials for PA spectrometry.

McClelland et al. [3] have shown that PA spectra of polymers may be identified by comparing them to library spectra measured by transmission even when a modest amount of saturation has occurred. They recommend that after the ratio of the single-beam PA spectrum of a sample to a carbon-black reference has been calculated, the spectrum should be scaled so that its maximum value corresponds to 90%

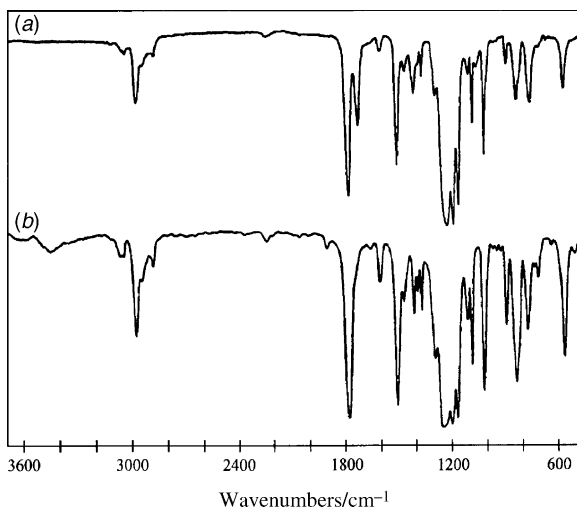


**Figure 20.6.** (a) Library spectrum of polycarbonate measured by transmission spectrometry; (b) photoacoustic spectrum of a polycarbonate sheet. (Reproduced from [3], by permission of CRC Press; copyright © 1993.)

and the minimum to 5%. By comparing only the wavenumbers of those peaks with a transmittance of less than 90% to the corresponding peaks in the spectral library, most polymers may readily be identified. A comparison of the PA spectrum of polycarbonate with a library spectrum is shown in Figure 20.6.

Photoacoustic spectrometry has the important advantage over other sampling techniques that the spectrum is largely independent of the morphology of the sample. This was first demonstrated by Vidrine [7], who published the spectra of a nitrile polymer with four different morphologies (see Figure 20.7). Even though the absolute intensities of the bands in the spectra varied by over a factor of 4, the relative intensities of the bands in each spectrum are constant. The main cause of variation of the absolute band intensities is the surface roughness. The rougher the sample, the greater is its surface area, and the more efficiently are the thermal waves conducted to the helium fill gas. The most intense PA spectra are therefore measured from fine powders.

PA spectrometry has several benefits over other sampling techniques. As noted in Chapters 13 and 16, Fresnel and diffuse reflection may contribute to the reflection spectra of solids; this problem is far less important in PA spectrometry. There is no need to prepare KBr disks or mineral mulls to acquire the spectra of powders. For polymers, PA spectrometry obviates the need to prepare films from the melt or from solution. Although PA spectra measured on some of the earlier accessories were often quite noisy, contemporary accessories allow remarkably good spectra to be measured in measurement times of 5 min or less.

McClelland et al. [3] have demonstrated that very small samples can be measured with a sensitivity approaching that of conventional microscopes of the type



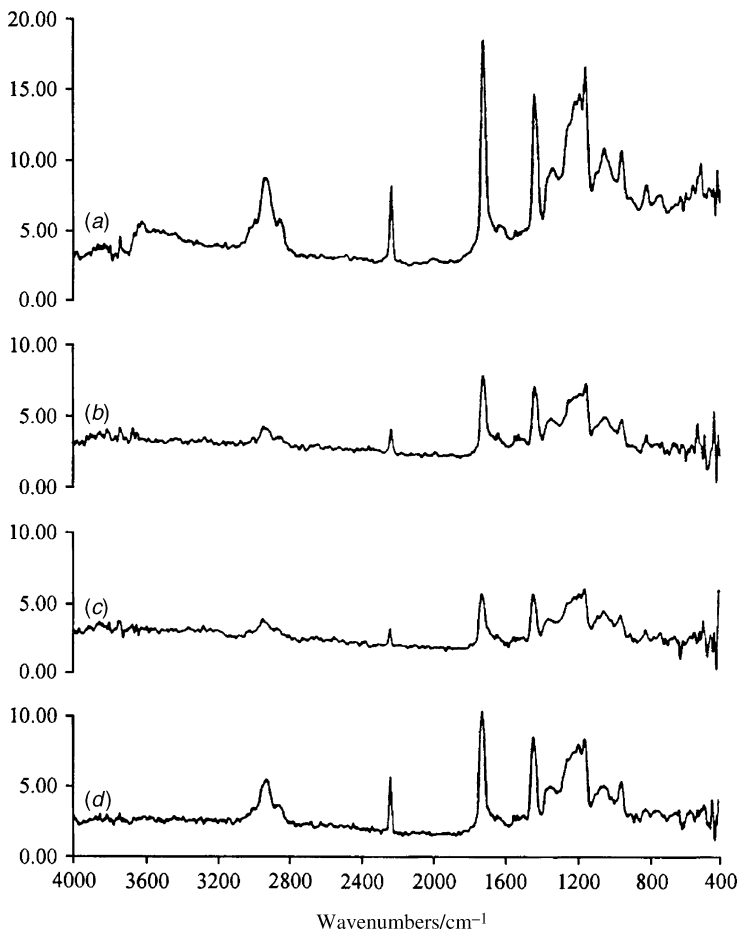


**Figure 20.7.** Photoacoustic spectra of acrylonitrile copolymer in the form of (a) a powder, (b) a sheet with a rough surface, (c) a sheet with a smooth surface, and (d) pellets. (Reproduced from [7], by permission of the Society for Applied Spectroscopy; copyright © 1980.)

described in Chapter 14. PA spectrometry is a particularly good way of obtaining the spectra of fibers, as illustrated in Figure 20.8. Many fibers are optically opaque and thermally thin ( $L > l$ ,  $L > \mu_B$ ). Thus, it is not uncommon for saturation effects to be observed. This can easily be seen by comparing the spectra of the top two nylons in Figure 20.8 with the bottom two. The amide I and II bands (at  $\sim 1650$  and  $1550\text{ cm}^{-1}$ , respectively) are usually the strongest bands in the spectra of nylons, but because of the effect of saturation, they are about the same intensity of all the other strong bands in the lower two spectra.

Water vapor is one of the biggest sources of interference in PA/FT-IR spectra. Very often, water vapor will be desorbed from the surface of the sample when the beam from the hot IR source is focused on it. Since the photoacoustic effect

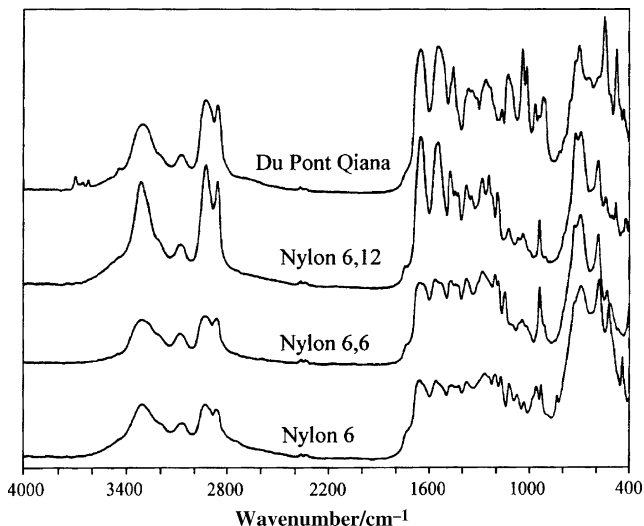


**Figure 20.8.** Photoacoustic spectra of single nylon fibers. (Reproduced from [3], by permission of CRC Press; copyright © 1993.)

is much stronger for gases than for solids, water vapor lines can be more intense than the PA spectrum of the solid sample. The best way to ameliorate this problem is to mount the sample on a desiccant and wait about 5 minutes, while the water vapor that has desorbed from the sample is adsorbed by the desiccant.

### 20.3. PHOTOACOUSTIC SPECTROMETRY OF SOLIDS WITH A STEP-SCAN INTERFEROMETER

#### 20.3.1. Phase Modulation

No matter what modulation frequency is used for PA/FT-IR spectrometry, the bands from the upper layers of the sample always dominate the spectrum. In addition, the fact that the thermal wave decay length varies as  $\tilde{\nu}^{-1/2}$  when the spectra are measured with a rapid-scanning interferometer has always led to suboptimal results. The variation of  $L$  with wavenumber may be circumvented through the use of a phase-modulated step-scan interferometer, and most contemporary PA/FT-IR spectra are now measured with this type of instrument.

As described in Section 5.5, phase modulation (PM) is achieved by rapidly modulating (or *dithering*) the position of one of the interferometer mirrors. The usual retardation amplitude for mid-infrared measurements is one or two laser fringes (633 or 1265 nm). An amplitude of two HeNe laser wavelengths is to be preferred because it gives a stronger signal within the mid-infrared, since the most efficient modulation occurs at  $3950\text{ cm}^{-1}$  and the node is out at  $7900\text{ cm}^{-1}$ . Larger amplitudes may be used if only the low-wavenumber end of the spectrum is of interest.

The PM frequency is determined by the sampling depth desired (see Table 20.1), which unlike the case of rapid-scanning interferometers, is the same for all wave-numbers in the spectrum. Provided that the amplitude of the mirror dither is typically one-fourth or one-half of the shortest wavelength of the spectrum of interest, the amplitude of the sinusoidal signal from the microphone depends on the *slope* of the interferogram. Thus, the signal from the microphone is the first derivative of the PA interferogram.

To measure the amplitude of the microphone signal, it must be demodulated at each sampling point. For many measurements of PA spectra made with a step-scan interferometer, demodulation has been accomplished with a lock-in amplifier (LIA) referenced to the PM waveform generator. Dual-phase LIAs allow both the interferograms that are in phase and  $90^\circ$  out of phase with the reference phase to be measured. The latter signal is usually known as the *quadrature interferogram*. The typical arrangement is shown in Figure 20.9. The reference phase of the LIA is usually set during measurement of the carbon-black or carbon-filled polymer reference, since this signal originates from the layers that are very close to the surface. When a sample is being measured, any signal that is delayed in phase from this signal originates from below the surface. Hence, compositional information can be obtained as a function of depth by examining both the in-phase (IP) and quadrature (Q) channels. After the IP and Q interferograms have been measured, the spectra are calculated using the stored phase spectrum calculated during the FT of the carbon-black reference spectrum. The ratio of the quadrature spectrum,

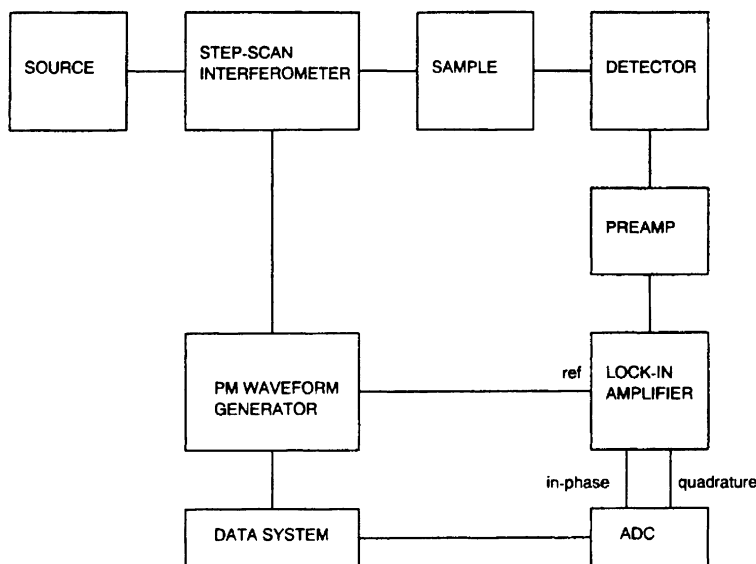


**Figure 20.9.** Typical electronics for photoacoustic spectrometry with a step-scan interferometer and a two-phase lock-in amplifier.

$Q(\tilde{\nu})$ , and the in-phase spectrum,  $IP(\tilde{\nu})$ , allows the phase spectrum,  $\phi(\tilde{\nu})$  to be calculated as

$$\phi(\tilde{\nu}) = \tan^{-1} \frac{Q(\tilde{\nu})}{IP(\tilde{\nu})} \quad (20.3)$$

Any spectral band originating from an inner layer will have a different phase than bands originating from the surface of the sample.

The bandshapes in the in-phase spectrum,  $IP(\tilde{\nu})$ , and quadrature spectrum,  $Q(\tilde{\nu})$ , are often asymmetrical because of the effect of phase. To calculate the spectrum independent of the effect of phase, the magnitude spectrum is calculated as

$$P(\tilde{\nu}) = [IP(\tilde{\nu})^2 + Q(\tilde{\nu})^2]^{1/2} \quad (20.4)$$

Although PA/FT-IR spectra measured with the use of a lock-in amplifier have proved to be very useful for depth profiling, LIAs have several disadvantages. One of the important parameters that must be set on a LIA is an electronic filter known as the *time constant*,  $\tau$ . The longer  $\tau$  is, the narrower the bandwidth and the lower the noise level of the demodulated signal. Thus, to minimize the noise, the longest possible time constant should be used. However, to allow the signal to equilibrate after the interferometer mirror has been stepped to each new retardation, it is necessary to wait five time constants, greatly reducing the efficiency of the measurement. For example, if  $\tau = 100$  ms, only two data points can be measured per second under this criterion and an interferogram with 8 K data points requires a measurement time of about an hour and a quarter, of which about 55 min is spent waiting for the output of the LIA to become stable after the mirror advances to each new retardation. LIAs have a further disadvantage for PA/FT-IR in that they are designed to recover a small signal at a certain frequency from high-amplitude broadband noise, whereas PA interferograms have a very high SNR, especially near the centerburst. Finally, LIAs are fairly expensive and increase the cost of the PA/FT-IR measurements by well over \$1000.

These three problems have been ameliorated by eliminating the LIA and digitizing the signal amplified from the microphone. After acquiring a certain number of points at a frequency of at least four times the modulation frequency (to avoid aliasing), the complex Fourier transform of the microphone signal is calculated at each sampling point. The real and imaginary spectra outputs at  $f_{PM}$  are equivalent to the in-phase and quadrature spectra calculated from the outputs of a dual-phase LIA. By demodulating the interferogram at each sampling point with a complex FT instead of using an LIA, the limited dynamic range of LIAs is no longer a factor because broadband amplifiers of the type used for conventional FT-IR measurements can be used. The FT can be calculated very quickly using digital signal processing (DSP) electronics; the time for a 1K FFT is as short as 1 ms on contemporary DSP chips, and even faster times can be predicted. Despite their high performance, DSP chips can cost less than \$10. It should come as no surprise,

therefore, to learn that many practitioners of PA/FT-IR with step-scan interferometers now use this mode of data processing.

Two approaches can be used to measure the depth profile of samples such as polymer laminates with a step-scan interferometer. The first makes use of the fact that the sampling depth varies as  $f_{PM}^{-1/2}$ , where  $f_{PM}$  is the PM frequency, as discussed above. In this case, several spectra must be measured with different PM frequencies. The second approach makes use of the fact that the phase of the photoacoustic signal varies with the distance from the surface from which the thermal wave originates.

20.3.2. Depth Profiling by Varying the Photoacoustic Phase

The use of phase shifts for PA/FT-IR depth profiling was first discussed by Dittmar et al. [8], who correlated the depth from which a spectral feature originated with its phase spectrum,  $\varphi$ , as calculated by Eq. 20.3. The photoacoustic phase shift,  $\theta_t$ , can be calculated for thermal wave propagation across a layer of thickness,  $t$ , from the velocity of the thermal wave [9,10]:

$$V' = (4\pi Df)^{1/2} \tag{20.5}$$

The distance that a thermal wave travels in one cycle is  $V'/f$ . Since  $L = (D/\pi f)^{1/2}$ , the phase shift of the PA signal emanating from a distance  $t$  below the surface,  $\theta_t$ , is  $t/L$  radians, or  $360t/2\pi L$  degrees. McClelland et al. [10] have listed the thermal wave propagation parameters with different modulation frequencies for a material with  $D = 0.001\text{ cm}^2 \cdot \text{s}^{-1}$ ; these parameters are listed in Table 20.3.

The phase shifts associated with different absorption bands are best observed by plotting the amplitudes of absorption peaks against the phase angle. If we denote the in-phase and quadrature interferograms as  $I_0(\delta)$  and  $I_{90}(\delta)$ , respectively, the interferogram at any phase angle,  $\varphi$ , can be calculated as

$$I_\varphi(\delta) = I_0(\delta) \cos \varphi + I_{90}(\delta) \sin \varphi \tag{20.6}$$

Table 20.3. Thermal Wave Propagation Parameters for Various Modulation Frequencies with  $D = 10^{-3}\text{ cm}^2 \cdot \text{s}^{-1}$

$f$ (Hz)	$L$ ( $\mu\text{m}$ )	$V/f$ ( $\mu\text{m}$ )	$t/\theta_t$ ( $\mu\text{m} \cdot \text{deg}^{-1}$ )
1	178	1,120	3.1
10	56.4	354	0.98
50	25.2	159	0.44
100	17.8	112	0.31
400	8.9	56.0	0.16
1,000	5.6	35.4	0.10
10,000	1.8	11.2	0.031

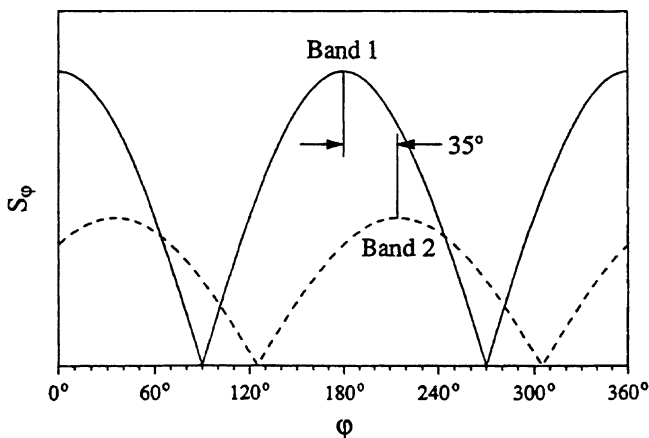


**Figure 20.10.** Variation of the magnitude spectrum with the phase of the photoacoustic signal for a weak band and a strong band. Because the IR beam penetrates more deeply into the sample when the band is weak, the phase lag is greater. (Reproduced from [10], by permission of Wiley-Interscience; copyright © 1998.)

$I_\phi(\delta)$  is Fourier transformed to obtain the spectrum,  $S_\phi(\tilde{\nu})$ , at a specific detection angle,  $\phi$ . Repeating this process for different angles of  $\phi$  allows a plot of  $S_\phi(\tilde{\nu})$  against  $\phi$  to be made. A plot of this type for typical weak and strong absorption bands is shown in Figure 20.10. This particular plot shows a phase shift of  $35^\circ$  between the strong band (band 1) and the weak band (band 2). As the absorptivity of the band increases, the phase shift decreases because the beam does not penetrate as deeply into the sample before it is completely absorbed. This figure may also be used to demonstrate the effect of a transparent coating on the phase of a band in the spectrum of the substrate.

The reduction in phase shift caused by absorption in the coating can be corrected for by a calculation based on the fact that the measured magnitude and phase are the vector sum of the signals generated in the coating and the substrate [10]. To determine the coating thickness, it is necessary to obtain the phase shift,  $\theta_s$ , for the substrate alone. This can be done trigonometrically using the following relationships:

$$S_S = [S_T^2 + S_C^2 - 2S_T S_C \cos(\theta_T - \theta_C)]^{1/2} \quad (20.7)$$

$$\theta_S = \theta_T + \cos^{-1} \frac{S_T^2 + S_S^2 - S_C^2}{2S_T S_S} \quad (20.8)$$

where  $S_S$ ,  $S_T$ , and  $S_C$  are the magnitudes of the substrate, total, and coating spectra, respectively, at the center of the substrate band used in the analysis.

Phase adjustment is usually necessary when a PA spectrum is measured using an LIA because the microphone and preamplifier add their own phase delay to

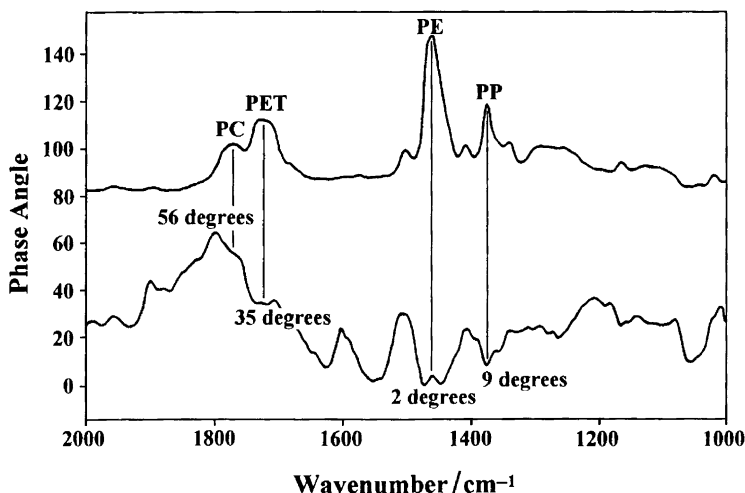


**Figure 20.11.** Photoacoustic phase spectrum of a polymer laminate consisting of a 10- $\mu\text{m}$  layer of polyethylene (PE) on 10  $\mu\text{m}$  of polypropylene (PP) and on 6  $\mu\text{m}$  of poly(ethylene terephthalate) (PET) on a thick polycarbonate (PC) substrate. (Reproduced from [14], by permission of the Society for Applied Spectroscopy; copyright © 1997.)

the signal originating from the sample. For measurements made at each phase modulation frequency, the phase setting of the LIA must be adjusted using a strongly absorbing reference material (usually, a heavily carbon-filled polymer). This topic has been covered in a series of papers by Jones and McClelland [5,10–13].

Drapcho et al. [14] demonstrated the feasibility of photoacoustic depth profiling with a sample consisting of 10  $\mu\text{m}$  of polyethylene (PE), on 10  $\mu\text{m}$  of polypropylene (PP), on 6  $\mu\text{m}$  of poly(ethylene terephthalate) (PET), and on a thick (0.25-mm) polycarbonate (PC) substrate. The phase and the magnitude spectra measured at a PM frequency of 100 Hz are shown in Figure 20.11. The phase spectrum shows a difference between the phase of the 1465- $\text{cm}^{-1}$  band of PE near the surface ( $2^\circ$ ), the 1373- $\text{cm}^{-1}$  band of the underlying PP layer ( $9^\circ$ ), the 1725- $\text{cm}^{-1}$  band of PET ( $35^\circ$ ), and the 1775- $\text{cm}^{-1}$  band due to the PC substrate ( $56^\circ$ ). Note that the phase of the stronger bands will lead the weaker bands of a given layer, as shown in Figure 20.10. Once each layer has been identified, its thermal-wave propagation parameters can be found from appropriate reference data and the phase delay converted to a depth as shown in Table 20.3. By this approach, depth profiling can be achieved from a PA spectrum measured with a single phase-modulation frequency.

It should be stressed that the type of information shown in Figure 20.11 can only be obtained when the layer nearest the surface is the most transparent, and the transparency decreases with depth into the sample. For example, had the upper layer of the sample been 10  $\mu\text{m}$  of PET, which is a very strong absorber ( $\mu_\beta \ll 10 \mu\text{m}$ ), the incident radiation over much of the spectrum below 1800  $\text{cm}^{-1}$  would have been absorbed well before it reached the second layer, and depth profiling would be impossible by any PA approach.

### 20.3.3. Multifrequency Measurements

In practice, photoacoustic depth profiling is best done *both* by measuring a phase spectrum of the type shown in Figure 20.11 *and* by measuring the magnitude spectrum at several different PM frequencies. The most common way of measuring PA spectra at several frequencies is to measure each spectrum with a given PM frequency, changing the PM frequency after each measurement. This approach can be quite time consuming, however. To get around this problem, a number of ways of making PA measurements at several different frequencies simultaneously have been described.

The first of these was reported by Manning et al. [15,16], who drove the PZTs that control the phase-modulated mirror with a multifrequency waveform that was synthesized in the spectrometer's computer and passed into a digital-to-analog converter (DAC) and hence to the power amplifier of the PZTs. A schematic representation of the detector signal measured with a single-frequency PM waveform and a waveform composed of three frequencies is shown in Figure 20.12. The actual waveform used by Manning et al. was the sum of three cosine waves corresponding to frequencies of 10, 60, and 360 Hz. Data acquisition was synchronized to the first point in this waveform, where all the waves were in phase, which in this case occurred at intervals of 100 ms. In this way, phase coherence was preserved and the complex FT yields the real and imaginary spectra at each data point. One spectrum reported by this group [15] was that of a 5- $\mu\text{m}$  layer of a silicone on a polycarbonate substrate (see Figure 20.13). Even for the 360-Hz measurement, the intense silicone bands were saturated, but at lower PM frequencies, the bands from the polycarbonate substrate (marked by the arrows) intensify. These authors showed that spectra measured in this way were identical to each spectrum measured with a single PM frequency.

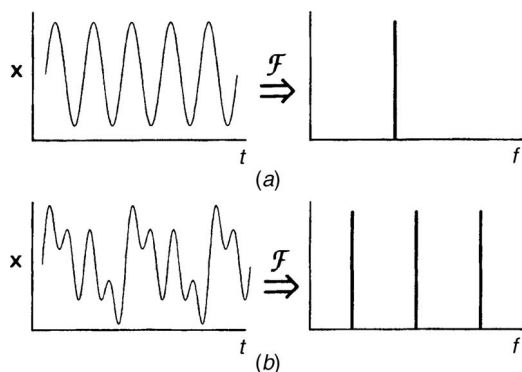


**Figure 20.12.** (Left) Detector signal measured with (a) a single-frequency PM waveform and (b) a waveform composed of three frequencies. (Right) Result of performing the Fourier transform of these signals.



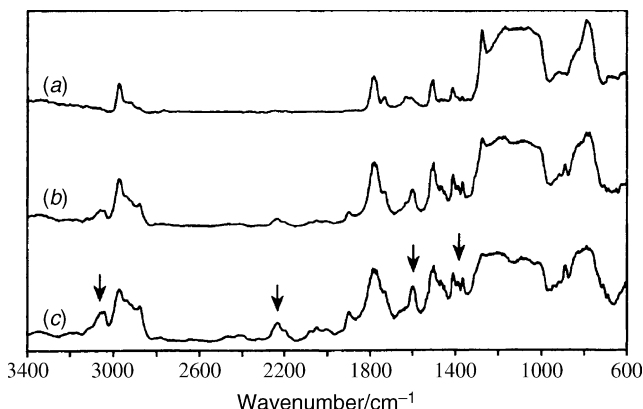


**Figure 20.13.** PA spectra of a sample consisting of a 5- $\mu\text{m}$  layer of a silicone on a polycarbonate substrate measured with three superimposed phase modulation frequencies: (a), 360 Hz; (b), 60 Hz; (c), 10 Hz. Many bands in the spectra of silicones have very high absorptivity, so that the strong silicone bands exhibit photoacoustic saturation even for such a thin layer. The bands of the polycarbonate (marked with arrows) can be seen to increase in intensity as the phase modulation frequency gets lower.

Drapcho et al. [14] demonstrated a very elegant way of performing multifrequency PA measurements. Rather than using a PM waveform composed of the sum of several sinusoidal waves, they drove the phase-modulation mirrors with a square wave, as shown schematically in Figure 20.14. A square wave with frequency  $f$  hertz is composed of the odd harmonics of  $f$ :

$$\sin 2\pi ft + \frac{1}{3} \sin 6\pi ft + \frac{1}{5} \sin 10\pi ft + \frac{1}{7} \sin 14\pi ft + \dots$$

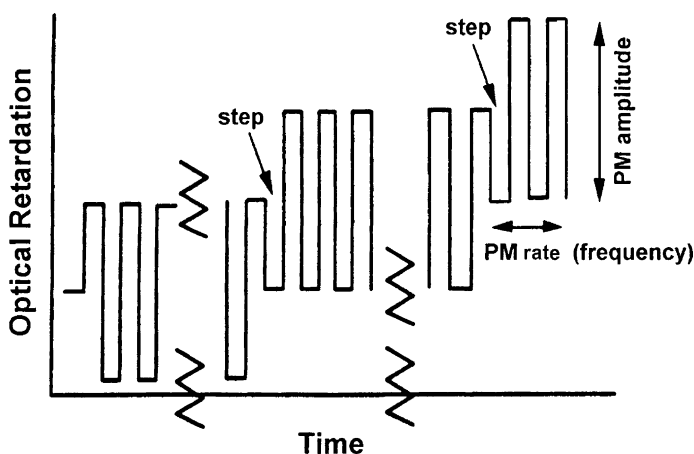


**Figure 20.14.** Square-wave phase modulation waveform used by Drapcho et al. (Reproduced from [14], by permission of the Society for Applied Spectroscopy; copyright © 1997.)

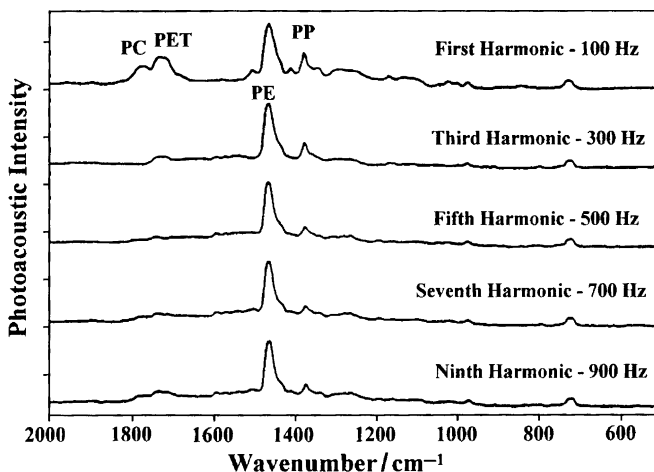


**Figure 20.15.** PA spectra of the same sample used for Figure 20.11 when measured with a 100-Hz square-wave. The spectra are shown at the odd harmonics of the 100-Hz square-wave frequency. (Reproduced from [14], by permission of the Society for Applied Spectroscopy; copyright © 1997.)

Thus, the complex FT of the signal at each data point yields the real and imaginary spectra at the odd harmonics,  $f$ ,  $3f$ ,  $5f$ ,  $7f$ , and so on. For square-wave phase modulation with  $f = 100$  Hz, Drapcho et al. were able to measure PA spectra at 100, 300, 500, 700, and 900 Hz. It is difficult to drive the phase-modulated mirror with a perfect square wave because the mass of the mirror will lead to the waveform being rounded out to a certain extent. In practice, it is very unlikely that harmonic PM frequencies much higher than 2 kHz will be able to be achieved in this way. Magnitude spectra of the same sample described in Figure 20.13, measured using square-wave phase modulation with  $f = 100$  Hz, are shown in Figure 20.15. At 900 Hz,  $L < 10 \mu\text{m}$ ; thus, only the upper layer (PE) can be seen in the spectrum. At 100 Hz, on the other hand, bands assignable to PE, PP, PET, and PC can be seen in the spectrum.

In summary, photoacoustic spectrometry is a versatile technique for studying solid samples, especially when a step-scan interferometer is available for the measurement.

## REFERENCES

1. A. G. Bell, *Am. J. Sci.* **20**, 305 (1880).
2. G. Busse and B. Bullemer, *Infrared Phys.* **18**, 631 (1978).
3. J. F. McClelland, R. W. Jones, S. Luo, and L. M. Seaverson, in *Practical Sampling Techniques for Infrared Analysis*, P. B. Coleman, Ed., CRC Press, Boca Raton, FL, 1993, Chap. 5.
4. A. Rosencwaig and A. Gersho, *J. Appl. Phys.* **47**, 64 (1976).

5. J. F. McClelland, R. W. Jones, and S. Luo, *Rev. Sci. Instrum.* **74**, 285 (2003).
6. J. F. McClelland, personal communication to P. R. Griffiths (2006).
7. D. W. Vidrine, *Appl. Spectrosc.* **34**, 314 (1980).
8. R. M. Dittmar, J. L. Chao, and R. A. Palmer, *Appl. Spectrosc.* **45**, 1104 (1991).
9. H. S. Carslaw and J. C. Jaeger, *Conduction of Heat in Solids*, Clarendon Press, Oxford, 1959.
10. J. F. McClelland, S. J. Bajic, R. W. Jones, and L. M. Seaverson, Photoacoustic Spectroscopy, in *Modern Techniques in Applied Molecular Spectroscopy*, F. M. Mirabella, Ed., Wiley, New York, 1998, p. 221.
11. R. W. Jones and J. F. McClelland, *Appl. Spectrosc.* **50**, 1258 (1996).
12. R. W. Jones and J. F. McClelland, *Appl. Spectrosc.* **55**, 1360 (2001).
13. R. W. Jones and J. F. McClelland, *Appl. Spectrosc.* **56**, 409 (2002).
14. D. L. Drapcho, R. Curbelo, E. Y. Jiang, R. A. Crocombe, and W. J. McCarthy, *Appl. Spectrosc.* **51**, 453 (1997).
15. C. J. Manning and P. R. Griffiths, *Appl. Spectrosc.* **47**, 1345 (1993).
16. C. J. Manning, G. L. Pariente, B. D. Lerner, J. H. Perkins, R. S. Jackson, and P. R. Griffiths, Multiple modulation step-scanning Fourier transform infrared spectroscopy, in *Computer Assisted Analytical Spectroscopy*, S. D. Brown, Ed., Wiley, New York, 1996, Chap. 1.

# SAMPLE MODULATION SPECTROMETRY WITH A STEP-SCAN INTERFEROMETER

## 21.1. DYNAMIC INFRARED LINEAR DICHROISM MEASURED WITH A MONOCHROMATOR

In Chapter 19 we saw that kinetic processes cannot be studied with a conventional rapid-scanning interferometer when the reaction rate is so fast that the reaction is essentially complete by the time just one or two interferograms have been measured. Instead, very fast reactions must be repeated at each retardation step of a step-scan interferometer. A different but related approach to the measurement of reversible dynamic systems can also be made with step-scan interferometers. In this case, however, very small changes in the state of the sample are introduced by subjecting it to a *modulated perturbation* of some type. Dynamic information can be obtained when the phase of the induced signal lags behind the phase of the perturbation by several degrees. An example of a reversible modulated process is when a polymer film is subjected to a modulated uniaxial strain, and this measurement is discussed in some detail in the first four sections of this chapter.

The viscoelastic or rheological properties of bulk polymers are often studied by a *dynamic-mechanical analyzer*. This instrument measures the phase lag  $\delta$  (or its tangent) of the strain to a modulated applied stress that is varied sinusoidally at a frequency of 10 to 50 Hz. If there is no phase lag ( $\delta = 0$ ), the polymer is said to respond to the applied strain *elastically*, whereas if the stress lags the strain by  $90^\circ$ , the polymer is completely *viscous*. Although dynamic mechanical analyzers measure  $\tan \delta$  for the bulk polymer, it is quite possible, or even likely, that different parts of a polymer chain respond to the applied strain at different rates. For example, a functional group associated with the polymer backbone might be expected to follow the applied strain with a very small phase delay, whereas the phase delay for groups on a pendant substituent may be significantly longer. A spectroscopic probe that could determine the value of  $\tan \delta$  for each part of a polymer chain would be

tremendously useful in explaining the physical properties of polymers on the basis of the viscoelastic behavior of each functional group.

A variety of phenomena could lead to changes in a spectrum when a strain is applied. If the polymer chains become more oriented under the applied strain, the dichroic ratio or dichroic difference of certain bands may change; thus, polarized radiation should be used for this experiment (see Chapter 12). An increase or decrease in the bond length or angle of a certain functional group when a strain is applied may result in a small shift in the frequency or intensity of bands associated with that group. If the polymer becomes more ordered when the polymer is stretched, the width and position of bands may change. Difference spectra, where the minuend spectrum is measured with the sample relaxed and the subtrahend is measured with the sample extended, reflect the change in the spectrum between the extended and relaxed states of the polymer at equilibrium, enabling these small spectral changes to be visualized clearly. Bisignate bands (bands shaped like the first derivative of an absorption band) often indicate that the dipole moments of the components associated with the band reorient in different directions with respect to the static polarization axis under strain. Bisignate bands can also arise from stress-induced frequency shifts. A change in bandwidth will be manifested as a feature with the shape of the second derivative of the static spectrum. If the orientation of a given functional group aligns with the plane of polarization of the incident radiation, the band will be seen as a positive-going feature in the difference spectrum. Such difference spectra are relatively easy to measure when a static strain is applied. To obtain the analogous information in a dynamic manner is clearly more difficult, as the goal of these measurements is to measure all the spectral changes as the polymer is being subjected to a dynamic strain.

This goal was first achieved by Noda et al. at Procter & Gamble Corporation (P&G) with a monochromator [1–3] by a technique that they called *dynamic infrared linear dichroism* (DIRLD). The approach that they developed is shown schematically in Figure 21.1. In their original work, a polymer film was mounted between the jaws of a mechanical device that subjected the film to a low-amplitude strain at a frequency of 23 Hz. In order that the elastic limit of the polymer not be exceeded, its length was never extended by more than about 0.1%. Thus, all spectroscopic changes will have a magnitude that is no larger (and usually much smaller) than 0.1%; detection of such small spectral changes can prove to be a real test even for the most modern FT-IR spectrometer.

The radiation from the source was first chopped at a frequency of  $\sim 1$  kHz and then passed into a monochromator with a fairly wide ( $9\text{ cm}^{-1}$ ) spectral slit width. The resolution element that was passed by the exit slit was polarized by a wire-grid polarizer and then passed through a photoelastic modulator (PEM) (see Section 12.3). The fundamental frequency,  $\omega_m$ , of most PEMs is between 30 and 70 kHz. Since the plane of polarization changes at a frequency of  $2\omega_m$ , the polarization-modulation frequency is well over an order of magnitude greater than the chopper frequency. The beam is then transmitted through the polymer film, which is subjected to a modulated strain at a frequency of 23 Hz, well over an order of magnitude lower than the chopping frequency. The reason for the separation of the

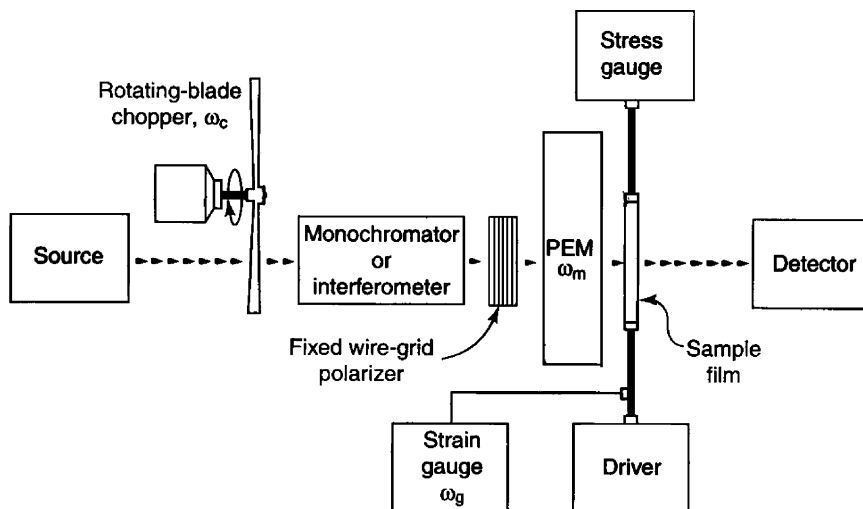


**Figure 21.1.** DIRLD experiment. The infrared beam is modulated by the chopper; the wavelengths passed by the monochromator are modulated by PEM and sample. (Reproduced from [3], by permission of the Society for Applied Spectroscopy; copyright © 1988.)

frequency of the stretcher, the chopper, and the PEM is to allow each of the signals being modulated at these frequencies to be demodulated separately with a train of lock-in amplifiers (LIAs). The monochromatic light that reaches the detector is now modulated at three independent frequencies: the mechanical light-chopper frequency,  $\omega_c$ , the polarization modulation frequency,  $\omega_m$ , and the dynamic strain frequency,  $\omega_s$ . To demodulate each of these sinusoidal components, the signal from the detector is processed by five lock-in amplifiers, as shown in Figure 21.2. The signal from the MCT detector is preamplified and then input to LIAs **A** and **D**. Let us consider these two paths separately.

The signal that passes to LIA **A** contains the information in terms of the static, or total, dichroic spectrum as well as the dynamic dichroic spectra. A high-pass electrical filter blocks the very large signal due to the chopper from being input to LIA **A**. LIA **A** demodulates the component that is generated by the PEM at a frequency of  $2\omega_m$ . The output of this LIA is proportional to the total optical anisotropy of the system, including the sample. A very short output time constant (0.1 ms) is used with this LIA so that the dichroic information may be demodulated. The output from LIA **A** is input to LIA **B**, which is referenced to the chopper frequency. The phase of both LIAs is tuned by inserting a second polarizer in the beam after the PEM and adjusting the phase control to maximize the outputs. The output from LIA **B** gives the static dichroism spectrum. The output from LIA **B** is then input to a dual-phase LIA, **C**, which is referenced to the stretcher frequency. The reference phase of this LIA is set prior to the experiment by installing a piece of cardboard between the jaws of the stretcher so that it blocks a small fraction of the beam. The phase control of the LIA is then adjusted so that the entire output signal falls in the

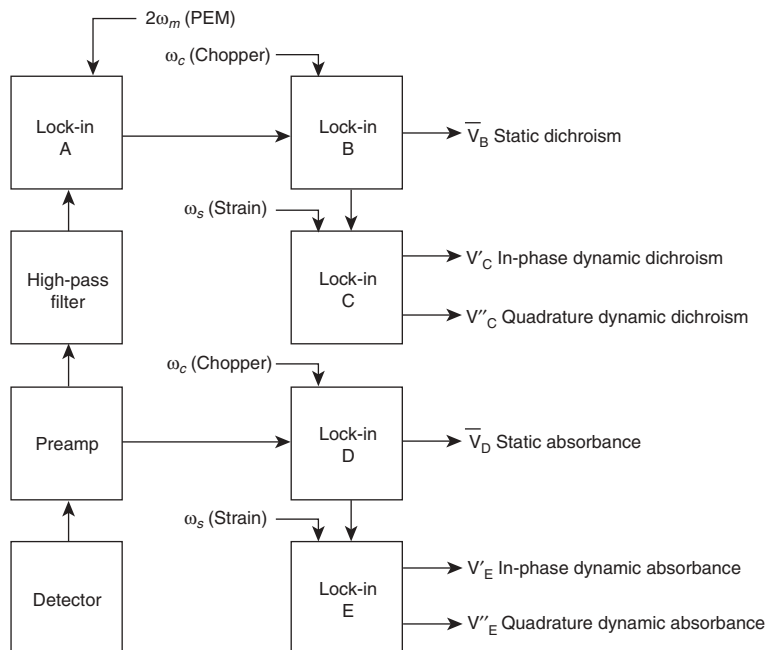


**Figure 21.2.** Configuration of the lock-in amplifier train for the DIRLD spectrometer. (Reproduced from [3], by permission of the Society for Applied Spectroscopy; copyright © 1988.)

in-phase channel and the output from the quadrature channel is zero. The two outputs from LIA **C** are the in-phase and quadrature dynamic dichroism spectra.

The output from the detector preamplifier is also passed into a fourth LIA, **D**, referenced to the chopper, the output of which is the static absorption spectrum: in other words, the conventional single-beam spectrum. Finally, the output of this LIA is input to another dual-phase LIA, **E**, referenced to the chopper frequency. The phase control of LIA **E** had been set prior to the experiment in the same way as LIA **C**. The outputs of LIA **E** are the in-phase and quadrature absorbance spectra.

The complete theory of how the output signals from the five lock-in amplifiers are treated in order to obtain static and dynamic spectra was originally given by Noda et al. [3] and Noda [4,5]. The inclusion of the full theory is beyond the scope of this book. Suffice it to say that the end result is calculation of the average static absorbance spectrum, the in-phase and quadrature components of the parallel and perpendicular absorbances, and the static and dynamic dichroic difference spectra. Of these, the in-phase and quadrature DIRLD spectra give the most important information about the rheological behavior of the polymer on a submolecular level.

The first spectra reported from the P&G group were measured with an InSb detector, and only the C—H stretching region of the spectrum was covered. The PEM was fabricated from CaF<sub>2</sub> and operated at a frequency of 56.7 kHz

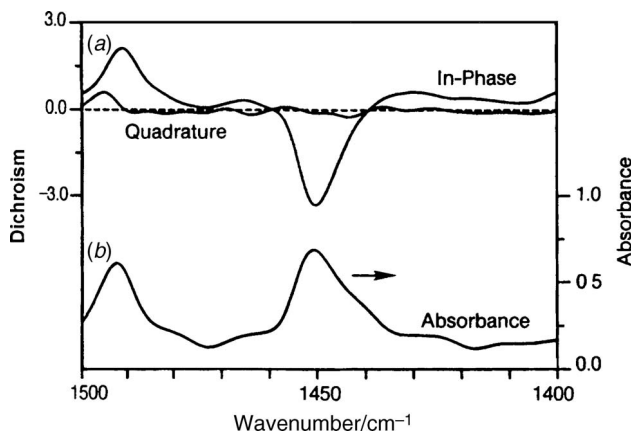


**Figure 21.3.** (a) In-phase and quadrature DLRD spectra of atactic polystyrene under a 23-Hz oscillatory strain; (b) absorbance spectrum of the same sample. (Reproduced from [3], by permission of the Society for Applied Spectroscopy; copyright © 1988.)

( $2\omega_m = 113.4$  kHz); the PEM was set so that optimum performance was exactly in the middle of the spectral range ( $3000\text{ cm}^{-1}$ ). To minimize optical anisotropy,  $\text{CaF}_2$  lenses were used instead of mirrors in the optical train. The slowest time constant of any of the LIAs (C) was 12.5 s, and the total time to collect and process the spectral data was 167 minutes. The most intense band in the in-phase DLRD spectrum was about  $10^{-4}$  AU, and the peak-to-peak noise level in the spectrum was about  $1 \times 10^{-5}$  AU.

Acquiring corresponding data in the region below  $2000\text{ cm}^{-1}$  requires the use of an MCT detector, the  $D^*$  value of which is about an order of magnitude lower than the  $D^*$  value of InSb. The static and in-phase and quadrature DLRD spectra of a sample of atactic polystyrene in the  $100\text{-cm}^{-1}$  region between  $1500$  and  $1400\text{ cm}^{-1}$  are shown in Figure 21.3. Other than the need to replace the InSb detector by MCT, the principal hardware differences between the measurement of spectra above and below  $2000\text{ cm}^{-1}$  by the P&G group were the fact that a ZnSe PEM with  $2\omega_m = 74$  kHz was used, all lenses were ZnSe, and the spectral resolution was  $4\text{ cm}^{-1}$ . The monochromator was set to step 96 times for each resolution element, and data were acquired four times at each step. The spectrum was measured by scanning 24 times, 12 times in each direction. The data were condensed to 301 points and an eight-point Savitsky-Golay filter function was applied before the dynamic dichroic difference spectra were plotted. These conditions were required to yield a peak-to-peak noise level of  $1 \times 10^{-5}$  AU. The total time needed to obtain the spectrum shown in Figure 21.3 was a little over 14 hours.

Time-resolved dichroic difference spectra of atactic polystyrene generated from the spectra shown in Figure 21.3 over a little more than one cycle of the stretcher are shown in Figure 21.4, along with the variation of the applied strain over the same period. From this curve, the variation in intensity and phase of each of the bands in the spectrum can be visualized. Under the same scan conditions, it would



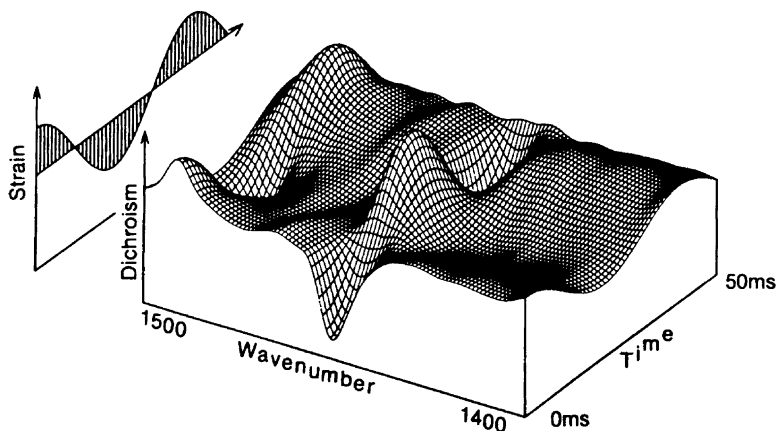


**Figure 21.4.** Time-resolved variation of the IR dichroic difference spectrum of atactic polystyrene. (Reproduced from [3], by permission of the Society for Applied Spectroscopy; copyright © 1988.)

take about a week to obtain the full mid-infrared spectrum. Obviously, the experiment should be accomplished more efficiently with a Fourier transform spectrometer. How this can be achieved is described in the following section.

## 21.2. DIRLD SPECTROMETRY WITH A STEP-SCAN FOURIER TRANSFORM SPECTROMETER

Because the modulation frequency of a conventional rapid-scanning spectrometer varies with wavenumber, these instruments cannot be used in a fashion analogous to the monochromator setup shown in Figure 21.1, but a step-scan interferometer could be. If a step-scan interferometer were to be used in conjunction with a light chopper, the dynamic range of the signal throughout the measurement would be enormous, since all resolution elements would be modulated by the chopper throughout the measurement. In this case, the dynamic range of the signal would be far too great for a conventional LIA to demodulate without a large loss in information. As it was for photoacoustic spectrometry (Chapter 20), the way to make this measurement by FT-IR is to eliminate the chopper and to apply phase modulation (PM).

The first report of DIRLD using a step-scan interferometer was by Palmer et al. [6]. In their early work they did not use a photoelastic modulator, so the signal-processing scheme was considerably simpler than the one shown in Figure 21.2 since only two lock-in amplifiers were needed, one to demodulate the phase modulation, the other to demodulate the signal caused by the modulated strain. The first spectra reported by this group [6] were of a sample of poly( $\gamma$ -benzyl-L-glutamate) deposited on the surface of a film of isotactic polypropylene. The spectra were measured at  $8\text{-cm}^{-1}$  resolution with a wideband MCT detector on a commercial

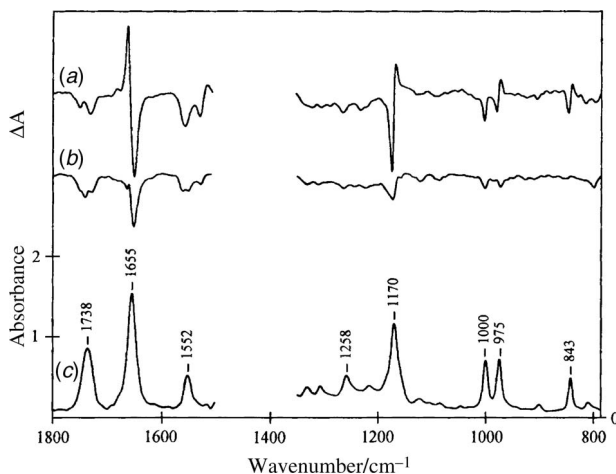


**Figure 21.5.** (a) In-phase and (b) quadrature spectra of the DIRLD spectra of a composite sample of poly( $\gamma$ -benzyl-L-glutamate) and polypropylene; (c) static absorbance spectrum of the sample. (Reproduced from [6], by permission of the Society for Applied Spectroscopy; copyright © 1991.)

rapid-scanning FT-IR spectrometer that had been modified for step-scan operation [7] (see Figure 21.5). The PM amplitude was  $2\lambda_{\text{HeNe}}$  ( $1.26\ \mu\text{m}$ ), giving a maximum in the PM efficiency curve at  $2300\ \text{cm}^{-1}$ , so that the efficiency was reasonably high across the entire spectral range being investigated; the PM frequency was 400 Hz [6]. An optical filter was installed to reduce the spectral range to  $1800$  to  $700\ \text{cm}^{-1}$  in order not to overload the detector or amplifiers and to allow data to be acquired with a sampling interval of four HeNe laser wavelengths (Nyquist wavenumber =  $1975\ \text{cm}^{-1}$ ). The same stretcher used for the spectra shown in Figure 21.3 was employed for this work. The signal from the detector preamplifier was input to a LIA with a time constant of 30 ms, which was long enough to demodulate the 400-Hz phase modulation and short enough to pass the spectroscopic information caused by the modulated stretching. For this work, the instrument's computer was programmed to co-add 670 analog-to-digital conversions from each of the three channels (the first LIA and the in-phase and quadrature signals from the second LIA) over a period of 25 s. A total of 720 data points was sampled, for a total acquisition time of 5 hours. When the difference in resolution between the spectra in Figures 21.3 and 21.5 is taken into account, the performance of the two measurements was comparable in terms of sensitivity, although the spectral range of the spectrum in Figure 21.5 is 10 times wider.

In later experiments, a PEM was added and the electronics were optimized so that the measurement time was much shorter. Performance equivalent to that demonstrated in Figure 21.5 can now be obtained in a few minutes. High-quality DIRLD spectra of nylon-11 subjected to a modulated deformation with an amplitude of  $50\ \mu\text{m}$  at a frequency of 11 Hz have even been measured with a DTGS

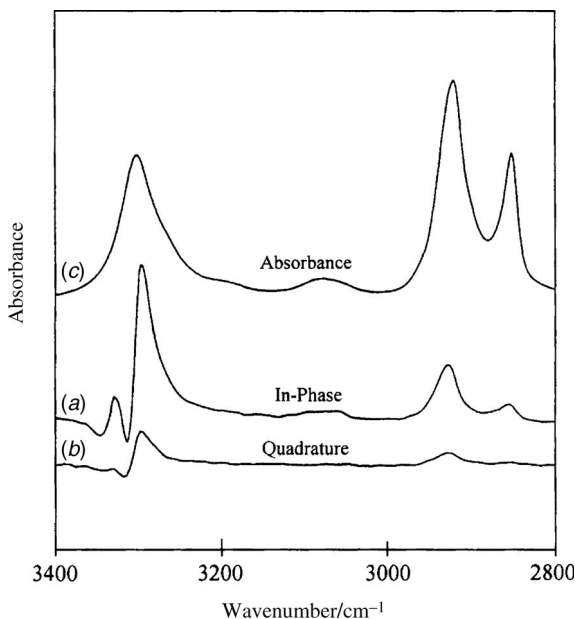


**Figure 21.6.** (a) In-phase and (b) quadrature spectra of the DIRLD spectra of nylon 11 measured using a DTGS detector; (c) static absorbance spectrum of the sample. (Reproduced from [8], by permission of the Society for Applied Spectroscopy; copyright © 1995.)

detector [8] (see Figure 21.6). For this measurement, a PEM could not be used because of the poor high-frequency response of pyroelectric detectors.

To illustrate the type of information that can be obtained in experiments of this type, let us examine the DIRLD spectroscopy of poly(*p*-phenylene vinylene) (PPV) that was reported by Shah et al. [9]. This paper showed both static and dynamic dichroism spectra, with the dynamic data either in the form of in-phase,  $IP(\tilde{\nu})$ , and quadrature,  $Q(\tilde{\nu})$ , spectra or as magnitude,  $S(\tilde{\nu})$ , and phase,  $\Phi(\tilde{\nu})$ , spectra. As noted by Budevskas et al. [10], the two outputs are simply different ways of displaying the same data, since

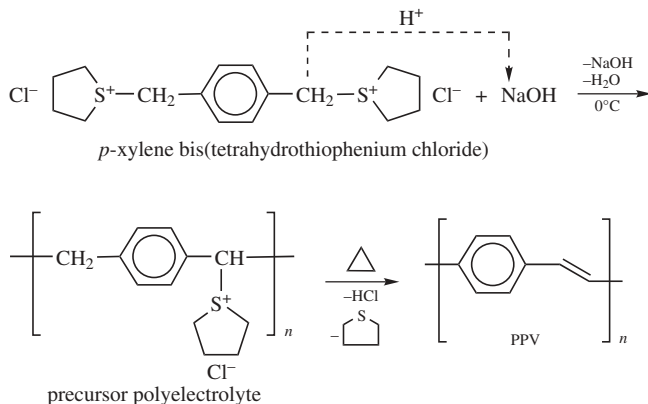
$$S(\tilde{\nu}) = [IP(\tilde{\nu})^2 + Q(\tilde{\nu})^2]^{1/2} \quad (21.1)$$

and

$$\Phi(\tilde{\nu}) = \tan^{-1} \frac{Q(\tilde{\nu})}{IP(\tilde{\nu})} \quad (21.2)$$

The spectra from the paper by Shah et al. illustrate many of the concepts introduced earlier in the chapter. PPV is of interest because of its high electrical conductivity upon doping. Because of the extensive conjugation, PPV is insoluble and intractable. It is made by casting a film of a high-molecular-weight precursor and converting this precursor into a film of PPV by a thermal elimination reaction in the

manner shown below. Before the measurement, the surfaces of all films were abraded with fine sandpaper to eliminate interference fringes.



PPV undergoes an anisotropic enhancement in conductivity upon uniaxial orientation; for example, a draw ratio of 7 : 1 leads to an increase in conductivity by two orders of magnitude for the doped polymer. Another interesting feature of this polymer system is the striking difference between the mechanical properties of the precursor polymer and PPV itself. Because of its flexible backbone and weak intermolecular forces, the precursor is highly elastic in nature, like common thermoplastics. On conversion to PPV, however, the material becomes viscous and rigid. These changes in the viscoelastic properties can be monitored at the submolecular level with DIRLD, and the molecular changes can then be related to the bulk macroscopic properties of the polymer. The results not only provide an insight into the reorientation dynamics of different functional groups but also reflect the changes in the viscoelastic behavior of the polymer as it is converted from the precursor form to conjugated PPV.

All spectra of the undoped PPV and its precursor were measured on a Bio-Rad FTS-6000 spectrometer equipped with a wideband MCT detector and a Polymer Modulator from Manning Applied Technology (hereafter called the *stretcher*) operating at a frequency of 16 Hz with an amplitude of 75  $\mu\text{m}$ . The IR beam was passed through a 3950- $\text{cm}^{-1}$  low-pass optical filter and a wire grid polarizer, to plane-polarize the beam along the stretching direction, before reaching the sample. The stress and strain outputs of the modulator were recorded and the phase difference  $\delta$  determined. Results were confirmed by separate measurements on a dynamic mechanical analyzer.

Figure 21.7 shows the absorbance spectra of the precursor and PPV obtained during a step-scan experiment. It should be noted that the precursor is partially converted into PPV during synthesis, so that the precursor may be visualized as a random copolymer consisting of precursor and PPV repeat units. Hence, the precursor shows spectral features of PPV such as vinylene stretching and bending modes, as well as those due to the presence of tetrahydrothiophenium (THT) pendant groups and aliphatic units on the backbone characteristic of the precursor polymer.

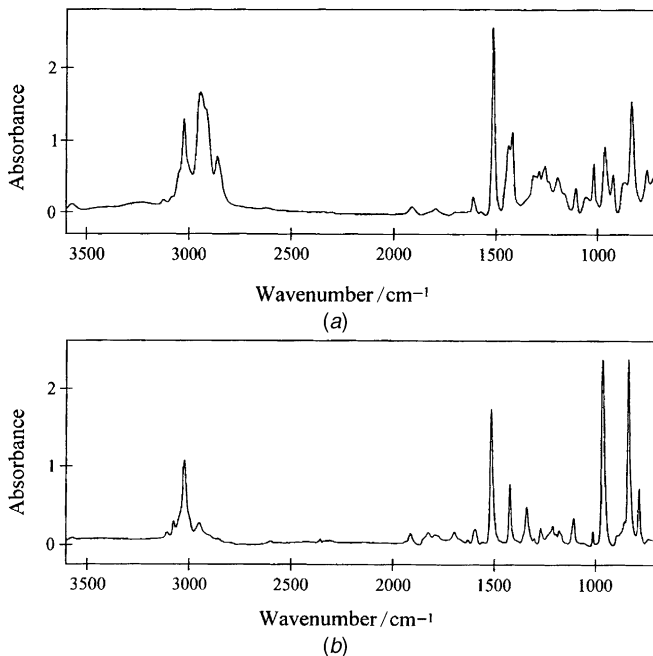
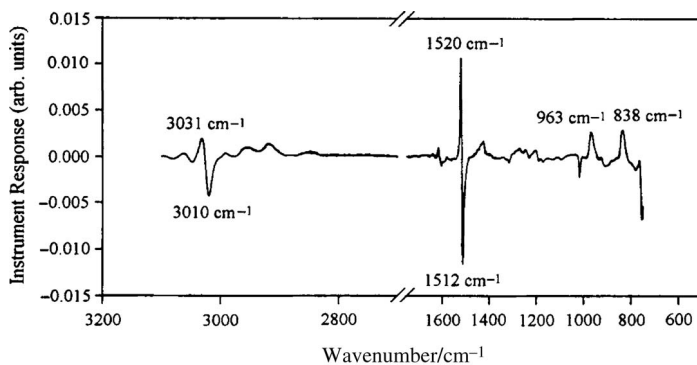


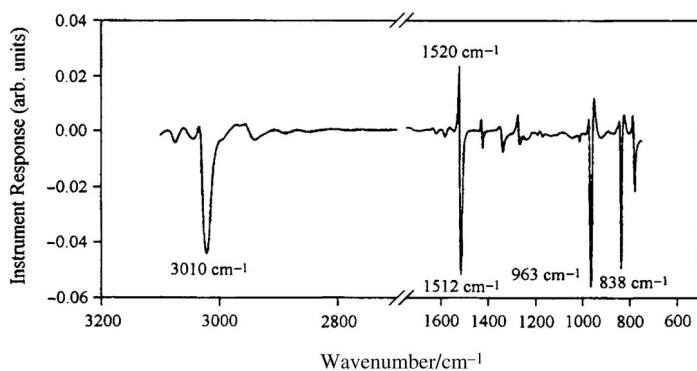
**Figure 21.7.** Absorbance spectra of (a) the precursor and (b) the PPV obtained during DIRLD measurement. (Reproduced from [9], by permission of the Society for Applied Spectroscopy; copyright © 1999.)

The static stretching difference spectrum of the PPV precursor is shown in Figure 21.8a. Measurement of the static difference spectrum is a quick and convenient way to determine the spectral features and peak shapes that can be expected to appear in the dynamic spectra. The spectral features observed in this difference spectrum are labeled. The most noticeable features are the two bisignate bands in the C—H region (at 3010 and 3031  $\text{cm}^{-1}$ ) and the fingerprint region (peaks at 1520 and 1512  $\text{cm}^{-1}$ ), which correspond to the vinylene C—H stretch and C—C ring stretch, respectively. The static stretching difference spectrum of PPV is shown in Figure 21.8b. The relative intensity of the vinylene C—H stretch to the C—C ring stretch is much higher for PPV than for its precursor because of a higher concentration of vinylene C—H units than in the precursor. A similar observation can also be made for the vinylene C—H out-of-plane bend at 963  $\text{cm}^{-1}$ .

Typical dynamic in-phase and quadrature spectra of the PPV precursor are shown in Figure 21.9. The in-phase spectrum looks quite similar to the static difference spectrum shown in Figure 21.8a. The intensity of all the features in the quadrature spectrum is smaller than the corresponding features in the inphase spectrum, from which it may be concluded that the PPV precursor is highly elastic in nature. The fact that the polymer stress and strain are nearly in phase indicates that the molecules are reorienting freely under these conditions.



(a)



(b)

**Figure 21.8.** Static difference spectra of (a) the precursor and (b) the PPV.

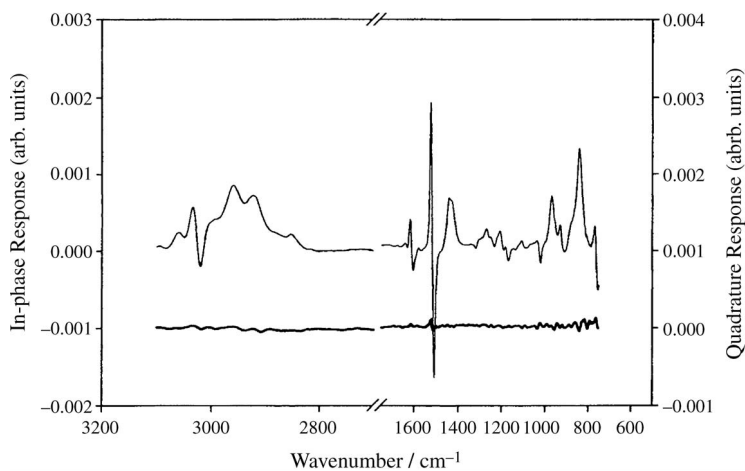


**Figure 21.9.** Dynamic in-phase (thin line) and quadrature (thick line) spectra of the precursor. (Reproduced from [9], by permission of the Society for Applied Spectroscopy; copyright © 1999.)

The magnitude and phase spectra of the precursor in the region of the C—H stretching bands are shown in Figure 21.10. The phase is flat across the aliphatic C—H stretching region (3000 to 2820  $\text{cm}^{-1}$ ) shown in Figure 21.10*b*, which indicates that these molecular motions are completely in phase. However, in the region of C—H stretching modes of the vinylene groups (3015 to 3050  $\text{cm}^{-1}$ ) seen in Figure 21.10*a*, the phase changes across part of the band, indicating that there are at least two different microstructural environments surrounding the vinylene CH units. These environments apparently have different responses to the applied perturbation.

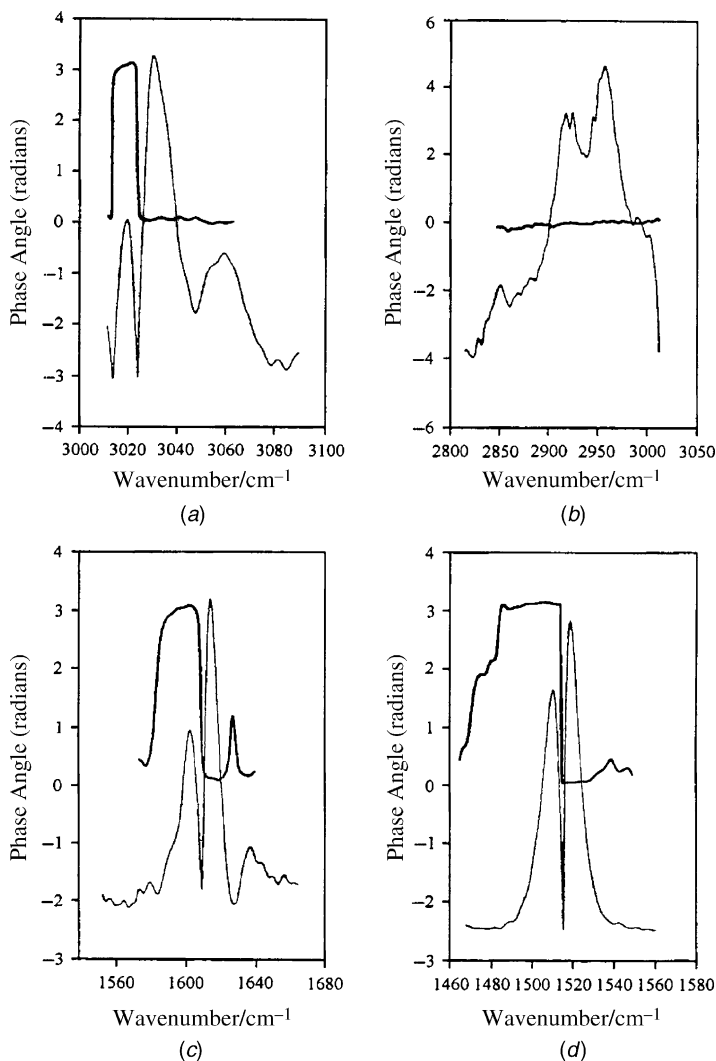


**Figure 21.10.** Phase (thick line) and magnitude (thin line) spectra of the precursor in four spectral regions: (a) 3000 to 3100  $\text{cm}^{-1}$ ; (b) 2800 to 3000  $\text{cm}^{-1}$ ; (c) 1550 to 1670  $\text{cm}^{-1}$ ; (d) 1470 to 1560  $\text{cm}^{-1}$ . (Reproduced from [9], by permission of the Society for Applied Spectroscopy; copyright © 1999.)

The C—C ring stretch in the precursor gives rise to several peaks in the region 1600 to 1400  $\text{cm}^{-1}$ . A weak bisignate band with peaks at 1614 and 1602  $\text{cm}^{-1}$  has a phase response similar to the vinylic CH region, as shown in Figure 21.10c. The bisignate band also indicates the presence of two or more microstructural environments. The strong bisignate ring stretch with peaks at 1519 and 1510  $\text{cm}^{-1}$  exhibits a similar phase response (see Figure 21.10d), but the sharp change in phase angle is due to crossing a quadrant boundary. Not shown in this figure is the fact that the semicircle aromatic ring stretching mode, with dual peaks at 1438 and 1426  $\text{cm}^{-1}$ , shows a very flat phase response across the entire band, indicating that these molecular motions are synchronous with the aliphatic C—H stretches.

The in-phase and quadrature spectra in the region between 1050 and 900  $\text{cm}^{-1}$  are shown in Figure 12.11. The peak at 1018  $\text{cm}^{-1}$  in the quadrature spectrum has been assigned to a vibration of the THT pendant group. The phase of the pendant group vibrations is different from that of the C—C ring stretches and the vinylic C—H stretch indicating that these vibrations are independent of the backbone vibrations.

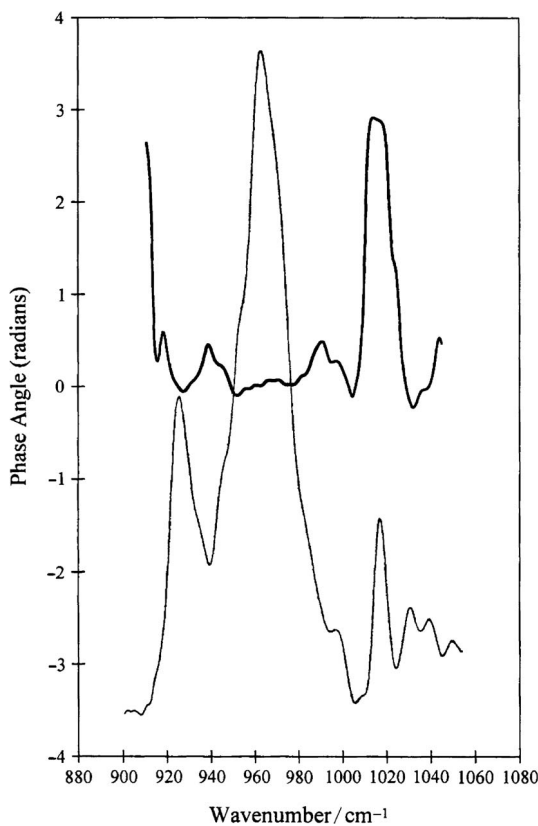


**Figure 21.11.** Phase (thick line) and magnitude (thin line) spectra of precursor in the region between 1060 and 900  $\text{cm}^{-1}$ . (Reproduced from [9], by permission of the Society for Applied Spectroscopy; copyright © 1999.)



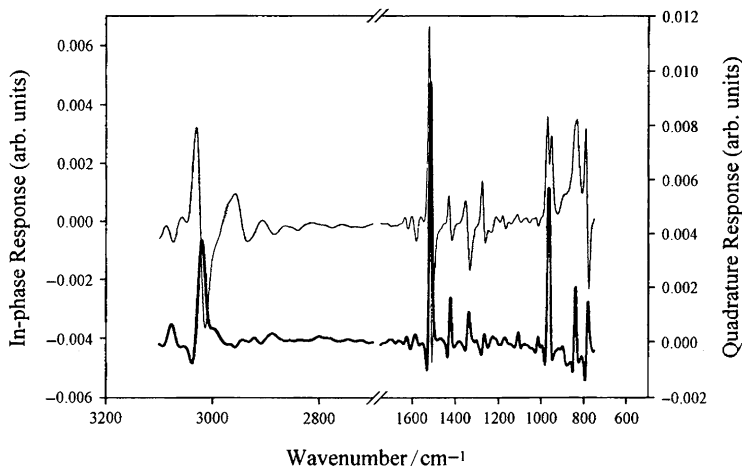


**Figure 21.12.** Dynamic in-phase (above) and quadrature (below) spectra of PPV. (Reproduced from [9], by permission of the Society for Applied Spectroscopy; copyright © 1999.)

The dynamic spectra of PPV, on the other hand, show a completely different phase response to the applied strain. The material is more viscous with a strong quadrature response as shown in Figure 21.12. This behavior is in marked contrast with the quadrature response of the precursor shown in Figure 21.9. PPV has a significant out-of-phase component (phase lag). The phase and the magnitude spectra for the vinylene C—H stretch at  $3024\text{ cm}^{-1}$ , the C—C ring stretch at  $1517\text{ cm}^{-1}$  and  $1424\text{ cm}^{-1}$  and *p*-phenylene C—H in-plane bend at  $1270\text{ cm}^{-1}$  are as shown in Figure 21.13. These figures show that the phase across the entire width of each band varies rapidly. The range of phase probably indicates a range of microstructural environments.

### 21.3. TWO-DIMENSIONAL CORRELATION PLOTS

Visualizing the detailed dynamics of polymers subjected to a modulated strain from plots such as the one shown in Figures 21.8 to 21.13 can be quite difficult. The fact that the bands in the in-phase and quadrature spectra have such different shapes indicates that the time dependence of the dichroism for each band in the spectrum is quite different, since the rate of reorientation of each functional group in the molecule when subjected to the effect of a modulated strain may well be determined by their local environment. The fact that these rates vary can be used to differentiate between highly overlapped bands, as can be seen in the N—H stretching region of the in-phase and quadrature spectra of nylon-11 shown in Figure 21.6.

Noda has described an alternative approach that simplifies the comprehension of DIRLD spectra [4] and has subsequently generalized this approach [11] so that it

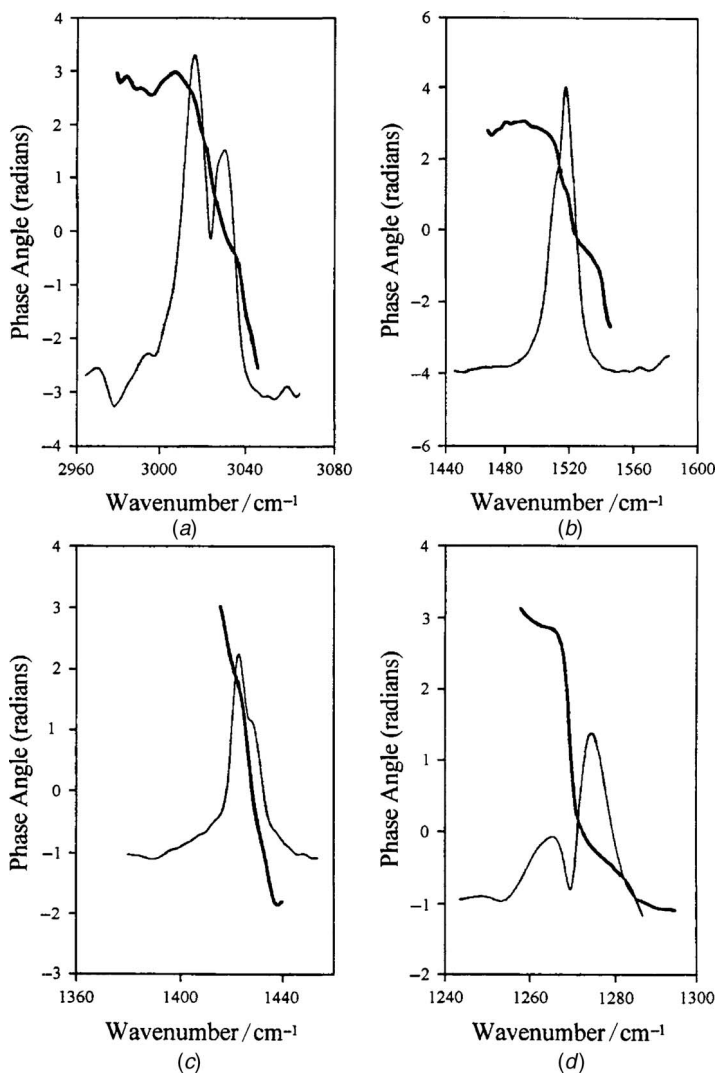


**Figure 21.13.** Phase (thick line) and magnitude (thin line) spectra of precursor in four spectral regions: (a) 2960 to 3070  $\text{cm}^{-1}$ ; (b) 1440 to 1600  $\text{cm}^{-1}$ ; (c) 1380 to 1460  $\text{cm}^{-1}$ ; (d) 1240 to 1300  $\text{cm}^{-1}$ . (Reproduced from [9], by permission of the Society for Applied Spectroscopy; copyright © 1999.)

can be applied to a number of other types of spectroscopic data, including photo-acoustic spectra [12] and the correlation of near- and mid-infrared spectra [13]. Noda called any transient fluctuations in spectra, such as the ones seen for DIRLD spectra, *dynamic spectra*. The type of information in a dynamic spectrum is determined by the manner in which the specific type of perturbation interacts with the sample. Here we shall simply discuss how the dynamic tensile strain leads to dynamic spectra, but it should be stressed that this is a general phenomenon.

Noda showed that the wavenumber-dependent variations of the dynamic dichroism may be analyzed by a correlation technique. For a pair of DIRLD signals measured at two different wavenumbers,  $\Delta\hat{A}(\tilde{\nu}_1, t)$  and  $\Delta\hat{A}(\tilde{\nu}_2, t)$ , the dynamic infrared cross-correlation function  $X(\tau)$  is defined as

$$X(\tau) = \lim_{T \rightarrow \infty} \frac{1}{T} \int_{-T/2}^{T/2} \Delta\hat{A}(\tilde{\nu}_1, t) \Delta\hat{A}(\tilde{\nu}_2, t + \tau) dt \quad (21.3)$$

The correlation period  $T$  for the integration is taken to be very long (i.e.,  $T \rightarrow \infty$ ). The correlation time  $\tau$  may be regarded as an arbitrary time interval between the measurement of two dynamic dichroism signals. For a fixed correlation time,  $X(\tau)$  is determined by a pair of independent wavenumbers  $\tilde{\nu}_1$  and  $\tilde{\nu}_2$ , which allows the dimensionality of the analysis to be reduced from three (as in Figure 21.4) to two.

The dynamic dichroic difference signal takes the form

$$\Delta\hat{A}(\tilde{\nu}, t) = \Delta\hat{A}(\tilde{\nu}) \sin[\omega t + \beta(\tilde{\nu})] \quad (21.4)$$

where  $\Delta\hat{A}$  is the amplitude and  $\beta(\tilde{\nu})$  is the phase delay of the dichroic difference signal at wavenumber  $\tilde{\nu}$ . For two periodic signals with an identical angular frequency  $\omega$ , the cross-correlation function reduces to the form

$$X(\tau) = \Phi(\tilde{\nu}_1, \tilde{\nu}_2) \cos \omega\tau + \Psi(\tilde{\nu}_1, \tilde{\nu}_2) \sin \omega\tau \quad (21.5)$$

The *synchronous* and *asynchronous* (i.e. quadrature) *correlation intensities*,  $\Phi(\tilde{\nu}_1, \tilde{\nu}_2)$  and  $\Psi(\tilde{\nu}_1, \tilde{\nu}_2)$ , of the dynamic spectrum are given by

$$\begin{aligned} \Phi(\tilde{\nu}_1, \tilde{\nu}_2) &= 0.5 \Delta\hat{A}(\tilde{\nu}_1) \Delta\hat{A}(\tilde{\nu}_2) \cos[\beta(\tilde{\nu}_1) - \beta(\tilde{\nu}_2)] \\ &= 0.5 [\Delta A'(\tilde{\nu}_1) \Delta A'(\tilde{\nu}_2) + \Delta A''(\tilde{\nu}_1) \Delta A''(\tilde{\nu}_2)] \end{aligned} \quad (21.6)$$

$$\begin{aligned} \Psi(\tilde{\nu}_1, \tilde{\nu}_2) &= 0.5 \Delta\hat{A}(\tilde{\nu}_1) \Delta\hat{A}(\tilde{\nu}_2) \sin[\beta(\tilde{\nu}_1) - \beta(\tilde{\nu}_2)] \\ &= 0.5 [\Delta A''(\tilde{\nu}_1) \Delta A'(\tilde{\nu}_2) - \Delta A'(\tilde{\nu}_1) \Delta A''(\tilde{\nu}_2)] \end{aligned} \quad (21.7)$$

where  $\Delta A'(\tilde{\nu}) = \Delta\hat{A}(\tilde{\nu}) \cos \beta$  and  $\Delta A''(\tilde{\nu}) = \Delta\hat{A}(\tilde{\nu}) \sin \beta$ . These two terms represent the real and imaginary components of the dynamic infrared cross-correlation function  $X(\tau)$ .

The synchronous correlation intensity,  $\Phi(\tilde{\nu}_1, \tilde{\nu}_2)$ , characterizes the degree of coherence between two signals that are measured simultaneously and is maximized when the variations of the two dynamic infrared dichroism signals are totally in phase with each other and minimized when the two signals are out of phase. Conversely, the asynchronous correlation intensity  $\Psi(\tilde{\nu}_1, \tilde{\nu}_2)$  characterizes the degree of coherence between two signals that are measured at two different instants that are separated in time by a correlation time  $\tau/2\omega$ . Thus, the maximum value of

$\Psi(\tilde{\nu}_1, \tilde{\nu}_2)$  is found when the dynamic signals are orthogonal to each other, and  $\Psi(\tilde{\nu}_1, \tilde{\nu}_2)$  is zero for a pair of signals that are either in phase or  $180^\circ$  out of phase with each other. Two-dimensional spectra are obtained by plotting these correlation intensities as functions of two independent wavenumbers,  $\tilde{\nu}_1$  and  $\tilde{\nu}_2$ .

In principle, there is no difference in the information content of a pair of synchronous and asynchronous correlation spectra and the corresponding power and phase spectra. Some spectroscopists find it easier to interpret the former pair of spectra and some the latter. However, the use of two-dimensional correlation maps to assist in the interpretation of spectral data is becoming extremely common.

The synchronous map of the precursor in the C—H stretching region is shown in Figure 21.14. The aliphatic C—H stretches at  $2913$  and  $2944\text{ cm}^{-1}$  show autopeaks (diagonal) as well as cross-peaks (off-diagonal), indicating that these bands are in phase with each other, which is also clearly evident from the spectral phase shown in Figure 21.10*b*. The vinyne CH stretch at  $3024\text{ cm}^{-1}$  appears as a bisignate band and has a negative peak at  $3010\text{ cm}^{-1}$  and positive peak at  $3031\text{ cm}^{-1}$ , as shown in Figure 21.12. From the spectral phase response in Figure 21.10*a*, it can be observed that the band at  $3010\text{ cm}^{-1}$  has a different phase than that of the aliphatic bands, whereas the  $3031\text{-cm}^{-1}$  band and the aliphatic bands have a similar phase. Accordingly, in Figure 21.14, a strong synchronous correlation is observed between the vinyne C—H stretch at  $3031\text{ cm}^{-1}$  and the two aliphatic bands at  $2913$  and  $2944\text{ cm}^{-1}$ . From the two-dimensional plot, it may also be seen that the vinyne

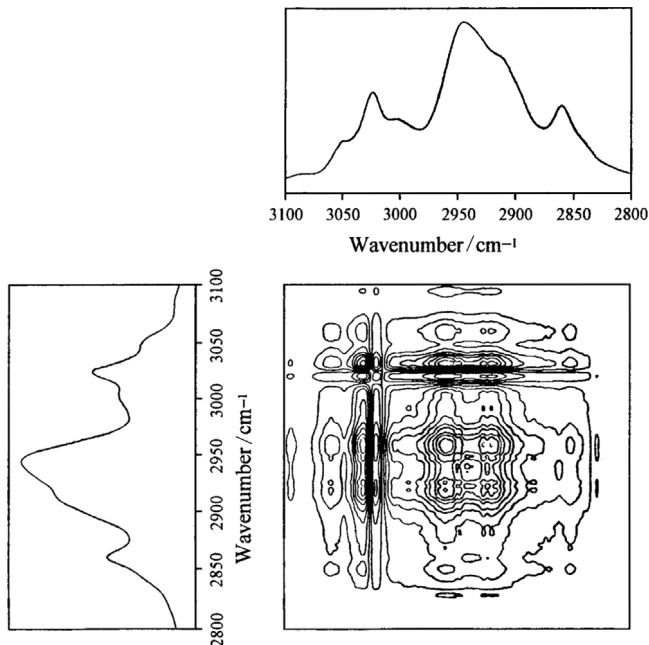


**Figure 21.14.** Synchronous two-dimensional map for the precursor in the region  $3100$  to  $2800\text{ cm}^{-1}$ . (Reproduced from [9], by permission of the Society for Applied Spectroscopy; copyright © 1999.)

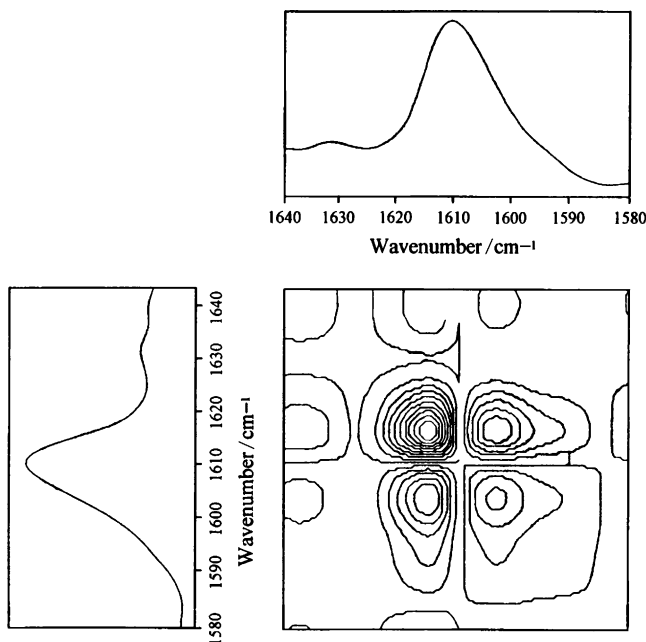


**Figure 21.15.** Synchronous map for the precursor in the region 1580 to 1640  $\text{cm}^{-1}$ . (Reproduced from [9], by permission of the Society for Applied Spectroscopy; copyright © 1999.)

C—H stretch is composed of at least two components at 3010 and 3031  $\text{cm}^{-1}$ , in accordance with the bisignate feature observed in Figure 21.12. Two-dimensional maps can often be used to separate overlapping peaks such as these and thereby improve the effective spectral resolution.

Figure 21.15 shows the synchronous map for the precursor in the region between 1580 and 1640  $\text{cm}^{-1}$ . The 1610- $\text{cm}^{-1}$  C—C ring stretch appears as a bisignate feature on the dynamic spectra with a positive peak at 1602  $\text{cm}^{-1}$  and a negative peak at 1614  $\text{cm}^{-1}$ , as shown in Figure 21.9. As evident in Figure 21.10c, there is a substantial phase difference between the two peaks of the bisignate band. Accordingly, the synchronous plot in Figure 21.15 shows autopeaks at 1602 and 1614  $\text{cm}^{-1}$ , and the asynchronous plot in Figure 21.16 shows cross-peaks at these two wavenumbers. This behavior again clearly distinguishes the two components associated with this vibration, indicating more than one microstructural environment.

The synchronous and asynchronous plots of PPV in the CH region are as shown in Figures 21.17 and 21.18. The rapid change in phase across the vinyne C—H bend as shown in Figure 21.13a would imply the presence of several microstructural environments. The synchronous plot shows that the vinyne CH stretch can easily be resolved into two peaks at 3015 and 3030  $\text{cm}^{-1}$ . The presence of peaks in the asynchronous plot at these two wavenumbers indicates that these two components are reorienting at different rates.

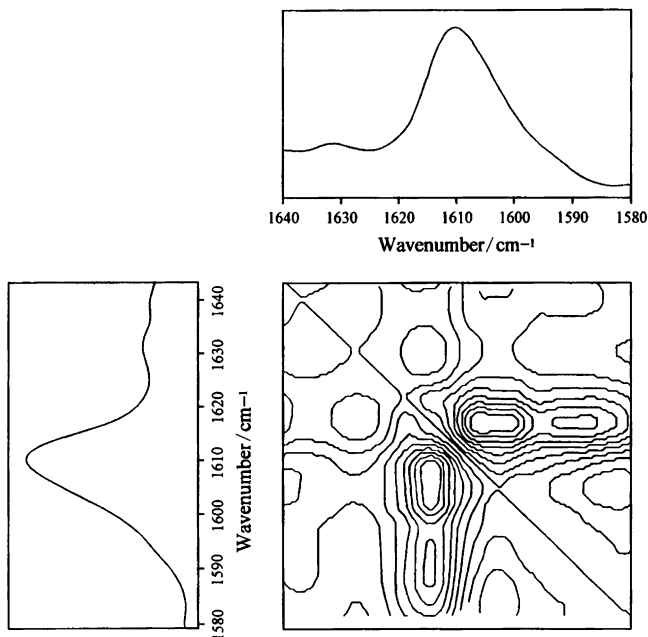


**Figure 21.16.** Asynchronous map for the precursor in the 1580 to 1640  $\text{cm}^{-1}$  region. (Reproduced from [9], by permission of the Society for Applied Spectroscopy; copyright © 1999.)

The more viscous behavior of PPV relative to its precursor can also be noticed at a macroscopic level by measuring the phase difference,  $\delta$ , between the dynamic strain applied and the resulting stress using the built-in stress and strain transducers in the stretcher. Figure 21.19 shows a sample output of the phases of dynamic stress and strain extracted from the data for PPV precursor. The thin solid lines is the dynamic stress, which shows a peak at the applied frequency. The dashed and the thick solid lines are the phase of the dynamic stress and strain, respectively. These were calculated as the arctangent of the ratio of the imaginary and real components of the Fourier transforms of the respective signals. The phase difference is then obtained by simple subtraction at the desired frequency (16 Hz in this case). Thus, a sinusoidal strain amplitude of 68  $\mu\text{m}$  resulted in a dynamic sinusoidal stress with an amplitude of 4.2 N and a  $\tan \delta$  of 0.18 for the PPV precursor.

On the other hand, for PPV, a dynamic sinusoidal stress with an amplitude of 4.2 N resulted in a sinusoidal strain amplitude of 64  $\mu\text{m}$  with a  $\tan \delta$  of 0.21. These values were verified by performing dynamic mechanical analysis (DMA) on the precursor and PPV samples over a range of temperature.  $\tan \delta$  values for PPV and its precursor at a modulation frequency of 16 Hz were measured in the temperature range  $-30$  to  $50^\circ\text{C}$  over which both the materials are stable; the value of  $\tan \delta$  was found to be constant. The phase difference in PPV measured both using the stretcher and using the DMA was found to be significantly higher than that observed in its precursor. Thus, the phase difference between dynamic stress and strain in

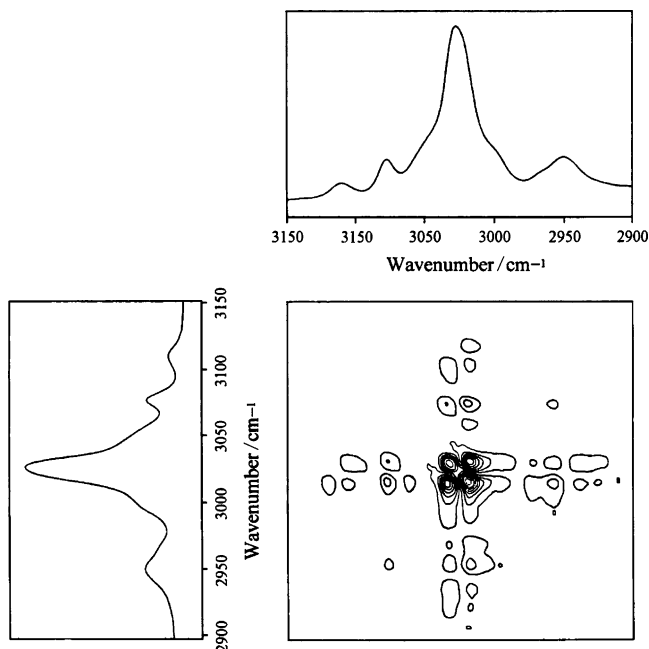


**Figure 21.17.** Synchronous two-dimensional map for PPV in the region 3150 to 2900  $\text{cm}^{-1}$ . (Reproduced from [9], by permission of the Society for Applied Spectroscopy; copyright © 1999.)

PPV and its precursor measured by two different types of instrumentation show the same trends and also support the viscoelastic behavior observed at microscopic levels as shown by DIRLD.

With this rather lengthy example, we have tried to show not only how much information is contained in DIRLD spectra but how this information can be interpreted from static dichroism and dynamic spectra using not only magnitude and phase spectra, but also two-dimensional correlation diagrams.

#### 21.4. DIRLD SPECTROMETRY WITH A FT-IR SPECTROMETER AND DIGITAL SIGNAL PROCESSING

In Chapter 20 we saw how photoacoustic (PA) spectra could be measured with a step-scan interferometer no matter whether the PA signal was demodulated with a lock-in amplifier or by digital signal processing (DSP). For DSP, a Fourier transform (FT) has the same function as the lock-in amplifier. Manning et al. [14] showed that the same approach is feasible in DIRLD spectrometry with a step-scan FT-IR spectrometer but without a PEM. Consider the case where the detector signal contains components caused by simultaneous sinusoidal phase modulation at frequency  $f_{\text{PM}}$ , and sample modulation at frequency  $f_s$ . The phase- and sample-modulated components of the signal can be demodulated either with a

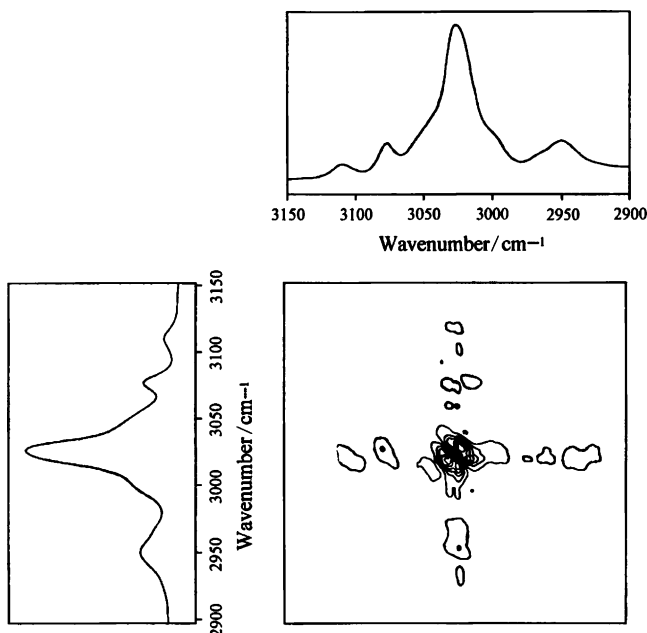


**Figure 21.18.** Asynchronous two-dimensional map for PPV in the region 3150 to 2900  $\text{cm}^{-1}$ . (Reproduced from [9], by permission of the Society for Applied Spectroscopy; copyright © 1999.)

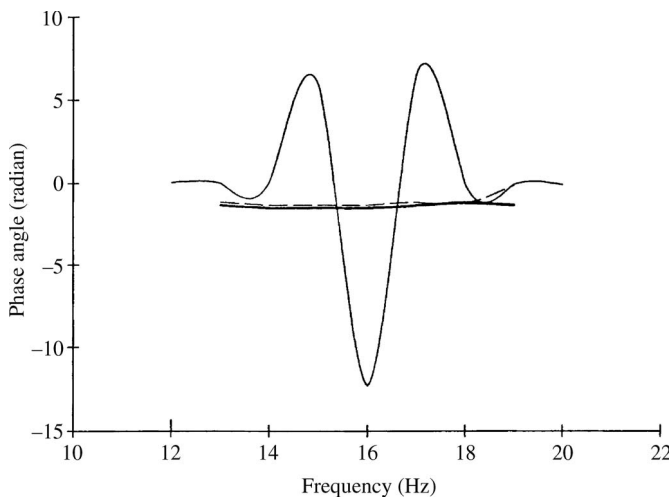


**Figure 21.19.** Fourier transform of the dynamic stress (solid line), phase of the dynamic stress (dashed line), and phase of the dynamic strain (thick line) with respect to the stretching frequency for the PPV precursor. (Reproduced from [9], by permission of the Society for Applied Spectroscopy; copyright © 1999.)



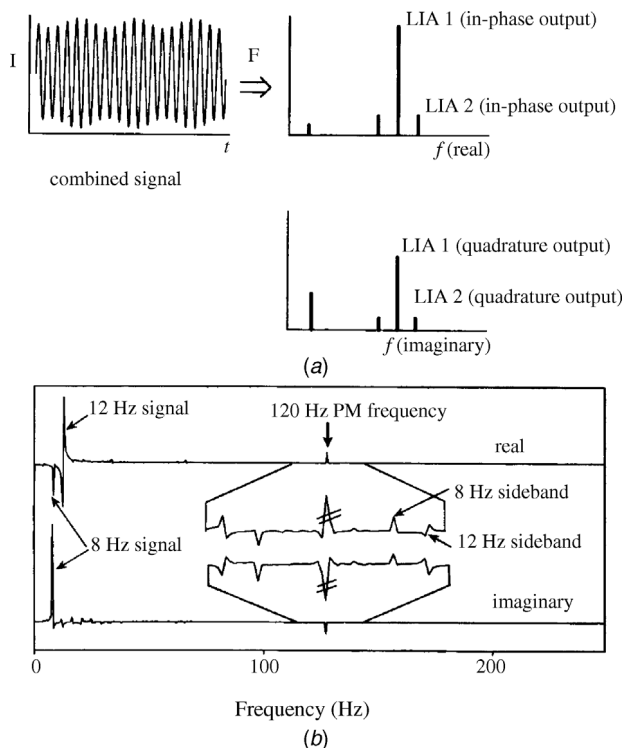


**Figure 21.20.** (a) (Left) Sinusoidal signal produced by a combination of phase modulation (large amplitude) and modulated strain (small amplitude); (right) real (above) and imaginary (below) Fourier transforms of this signal. (b) Fourier transform of the actual detector signal; the large amplitude signal from the phase modulation has been clipped. (Reproduced from [14], by permission of Wiley-Interscience; copyright © 1996.)

lock-in amplifier or by performing the complex FFT of the time-domain signal, as shown schematically in Figure 21.20a. The amplitude of the real part of the frequency spectrum at  $f_{PM}$  corresponds to the in-phase output of a dual-phase LIA, while the imaginary spectrum corresponds to the output of the quadrature channel of the first LIA in Figure 21.2. Picking the amplitude at the phase-modulation frequency,  $f_{PM}$ , at each sampling point yields an interferogram that, on Fourier transformation, gives the single-beam spectrum. If the sample modulation frequency is  $f_S$ , the corresponding sample-modulation interferogram points are found at  $f_S$  and  $f_{PM} \pm f_S$ .  $f_S$  is usually sufficiently low that  $1/f$  noise dominates the spectrum; the signal at this frequency is, therefore, rarely sampled. (This is the reason for using the phase-modulation waveform as a carrier.) Instead, the sample-modulation interferogram points are read off at  $f_{PM} + f_S$  or  $f_{PM} - f_S$ , or both. This information corresponds to the output signal of the second lock-in amplifier in Figure 21.2.

We saw in Chapter 20 that phase modulation could be achieved by dithering the interferometer mirror with a waveform that was the sum of several sinusoids.

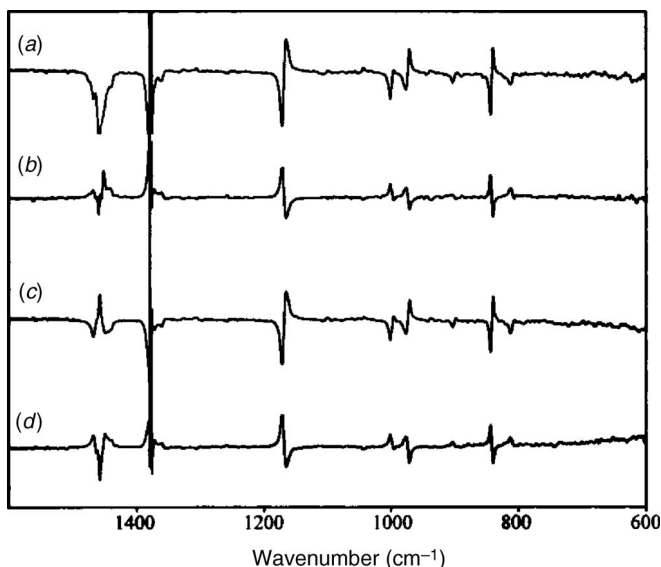


**Figure 21.21.** Spectra of polypropylene film stretched at 8 and 12 Hz simultaneously: (a) in-phase and (b) quadrature response to 8 Hz; (c) in-phase and (d) quadrature response to 12 Hz. (Reproduced from [14], by permission of Wiley-Interscience; copyright © 1996.)

In sample-modulation spectrometry, the same type of effect can be achieved by using a single phase-modulation frequency but driving the stretcher with a waveform comprised of more than one frequency. The result of using 120-Hz phase modulation and a stretching waveform comprising both 8- and 12-Hz waveforms is shown schematically in Figure 21.20*b*. The in-phase and quadrature spectra of isotactic polypropylene modulated in this way are shown in Figure 21.21.

When a PEM is incorporated in the DIRLD experiment, demodulation of the polarization-modulation signal by DSP is far more difficult. To demodulate the PEM-generated signal with a DSP process, we need to know not only the exact frequency of the PEM drive at the time the data were collected, but also its phase relative to the sampling clock. One solution would be to collect the sinusoidal reference signal from the PEM drive with a second digitizer channel in the spectrometer so that the frequency and phase information can be extracted in the DSP process. This choice involves more hardware capability than is required to collect only the signal of interest and is another DSP task. Another solution would be to lock the PEM frequency to the system master clock. This is not practical, however, as it would require substantial modification of the PEM to obtain a stable output. An efficient solution is to measure the frequency and phase of the PEM drive from the data collected for the actual experiment. In most cases, the PEM carrier is present in the signal because of residual polarization in the optical train. For the case when the residual polarization has been substantially eliminated, a small amount of the

PEM drive can be added to the signal, as a pilot carrier, to be used to recover the frequency and phase of the PEM drive.

In the DIRLD experiments, the polarization signal of interest is present in the sidebands around  $2f_M$ , where  $f_M$  is the PEM drive frequency. In this case, the signals generated, although widely spread in the frequency domain, have a rather small bandwidth, on the order of the phase modulation frequency. At first sight, it might be thought that the infrared signal should be sampled at a frequency of  $4f_M$  or greater in order to characterize the PEM frequency and phase properly. Nonetheless, we can take advantage of the sparse spectral distribution to avoid sampling at that rate. A fairly simple antialiasing filter can be built that allows sampling at a lower rate and also prevents folding of noise over the signal bandwidth. For a DIRLD experiment with a  $f_M = 37$  kHz and this filter, the signals can be sampled at 20 kHz, and signals near 74 kHz will be translated down to 6 kHz.

A new method to determine the PEM carrier frequency is to measure the phase of the signal at different times during a step with respect to the system master clock [15]. Assuming that the PEM frequency varies slowly during each interferometer step, the average frequency can then be calculated, as described by Curbelo [16]. Thereafter, the DSP for the each step in the interferogram can proceed because all the modulation frequencies and phases are known.

## 21.5. OTHER SAMPLE MODULATION MEASUREMENTS WITH STEP-SCAN INTERFEROMETERS

### 21.5.1. Liquid-Crystal Electroreorientation

Rapid reversible processes can be studied by FT-IR spectrometry in at least four ways, two using rapid-scan interferometers and two using step-scan interferometers. Three of these approaches, asynchronous sampling and stroboscopic measurements with a rapid-scan interferometer and time-resolved spectroscopy with a step-scan interferometer, were described in Sections 19.2 and 19.3. The fourth approach involves the use of a step-scan interferometer and some type of sample modulation. We have seen one application in the earlier part of this chapter, and two other applications will now be described. The reorientation of liquid crystals induced by rapid switching of the electric field to which they are being subjected has been studied by at least three of these approaches. Results have been summarized in an excellent article by Czarnecki [17]. In this section we discuss the application of sample-modulation FT-IR spectrometry to this problem.

The first measurements of this type were reported by Palmer et al. [18], who noted the similarity of the experimental setup for dynamic polymer rheo-optical measurements and liquid-crystal electroreorientation. However, because the changes in the polarized spectrum on switching the electric field can be very large, the measurement of liquid-crystal electroreorientation tends to be much easier than the DIRLD measurements described in Section 21.2. Two-dimensional correlation analysis is frequently used to aid in interpreting the results.

The first investigators to work in this area investigated the behavior of model liquid crystals such as 4-pentyl-4'-cyanobiphenyl (5CB) and 1-(4cyanophenyl)-4-*n*-pentylcyclohexane (5PCH). (Results obtained from many other liquid crystals are proprietary in view of their important application in digital displays.) The synchronous and asynchronous two-dimensional correlation maps of 5PCH reported by Palmer et al. [18] are shown in Figure 21.22*a* and *b*, respectively. The presence of cross-peaks in the synchronous correlation between the  $\text{C}\equiv\text{N}$  stretching band at  $2226\text{ cm}^{-1}$  (not shown) and the biphenyl ring bands at  $1606$  and  $1496\text{ cm}^{-1}$  and the absence of such cross peaks in the asynchronous map confirms that the rigid

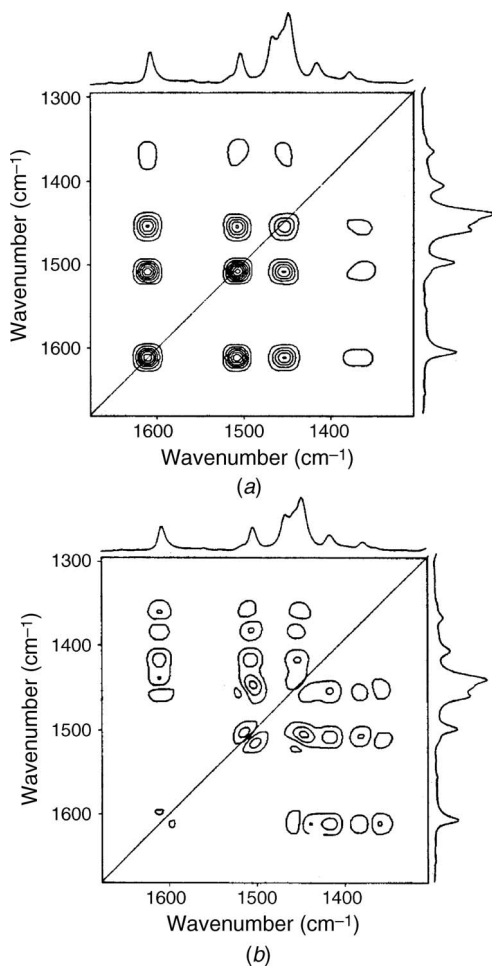


**Figure 21.22.** (a) Synchronous and (b) asynchronous two-dimensional correlation maps of ac-field induced homogeneous/homeotropic transition in the nematic liquid crystal 5PCH. (Reproduced from [18], by permission of the Society for Applied Spectroscopy; copyright © 1993.)

part of the molecule reorients as a unit. Surprisingly, the cross-peaks in the asynchronous map between the rigid-core modes at 2226, 1606, and 1496  $\text{cm}^{-1}$  and the pentyl  $\text{CH}_3$  mode at 1397  $\text{cm}^{-1}$  indicate that the pendant pentyl tail reorients before the rigid core.

### 21.5.2. Infrared Spectroelectrochemistry

Several workers have investigated the mechanism of electrochemical processes that occur at the surface of electrodes by infrared spectrometry by external or internal reflection spectrometry. A useful review of measurements of this type has been given by Korzeniewski [19]. A typical setup for external reflection measurements is shown schematically in Figure 21.23. A very thin ( $\sim 10\text{-}\mu\text{m}$ ) film of the electrolyte is held between the surface of the electrode and an appropriate window (often  $\text{CaF}_2$ ). The electrode can usually be moved back from the window to prepare it for the experiment, and then pressed against the window for infrared measurements. Thus, the IR beam can probe either species that are adsorbed on the surface of the electrode or are present in the bulk of the electrolyte. When the potential of the working electrode is increased above a certain value, the reduced form of an electroactive molecule will be oxidized. In a sample modulation experiment, the potential applied to the electrode is modulated between values above and below the potential at which the electrochemical reaction is initiated. By using a technique analogous to the one described for DIRLD or the electroreorientation of liquid crystals described earlier in this chapter, spectra that are in phase and  $90^\circ$  out of phase to the applied potential can be measured. It is found that the signal due to the reduced and oxidized form of an electroactive species in solution are  $180^\circ$  out of phase. The phase of the signal from an adsorbed molecule and that of the corresponding solution-phase species are slightly different. Thus, by rotating the phase of the spectra measured, it is possible to distinguish between the spectra of species in solution and on the surface of the electrode.

Pharr and Griffiths [20] studied the electrolytic oxidation of ferrocyanide ion on a platinum electrode by modulating the potential of the electrode around the standard

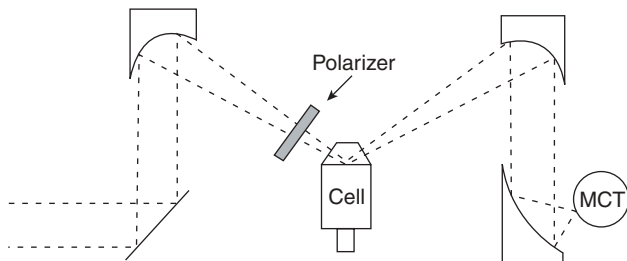


**Figure 21.23.** Typical arrangement for IR spectroelectrochemical measurement by external reflection spectrometry. In this case, a trapezoidal  $\text{CaF}_2$  window was used to optimize the amount of radiation passed through the cell. (Reproduced from [19], by permission of John Wiley & Sons, Ltd.; copyright © 2002.)

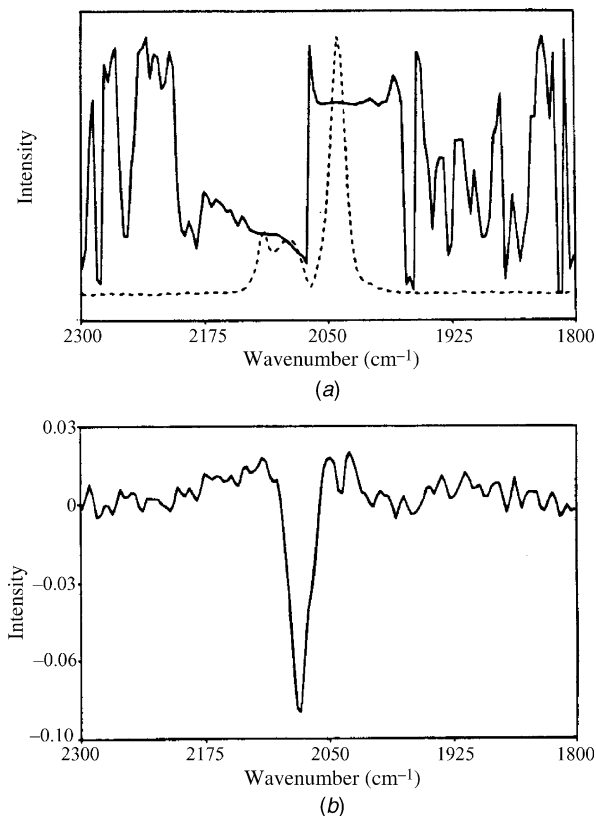


**Figure 21.24.** (a) Magnitude (dashed line) and phase (solid line) spectra of ferricyanide and ferrocyanide with hexacyanoferrate adsorbed on the electrode surface; (b) in-phase spectrum after phase rotation of solution-phase ferricyanide and ferrocyanide bands into the quadrature channel. 10 mM ferrocyanide; 1 Hz modulation frequency; potential modulation limits, 0.02 to 0.42 V versus SCE. (Reproduced from [20], by permission of the American Chemical Society; copyright © 1997.)

potential for this reaction. Figure 21.24 shows the magnitude and phase spectra of ferricyanide ( $2115\text{ cm}^{-1}$ ) and ferrocyanide ( $2040\text{ cm}^{-1}$ ) along with a band at  $2092\text{ cm}^{-1}$  that they assigned to a hexacyanoferrate complex formed on the surface electrode. By rotating the solution-phase ferricyanide and ferrocyanide bands into the quadrature channel, only the spectrum of the adsorbed hexacyanoferrate complex remains in the in-phase channel.

In summary, we have described in this chapter how the dynamics of three of the types of reversible chemical and physical changes can be investigated using a step-scan interferometer by modulating some property of the sample. It can be expected that several more reports of analogous processes will be reported in the future.

## REFERENCES

1. I. Noda, A. E. Dowrey, and C. Marcott, *J. Polym. Sci. Lett. Ed.* **21**, 99 (1983).
2. I. Noda, A. E. Dowrey, and C. Marcott, Characterization of polymers using polarization-modulation infrared techniques: dynamic infrared linear dichroism (DIRLD) spectroscopy, in *Fourier-Transform Infrared Characterization of Polymers*, H. Ishida, Ed., Plenum Press, New York, 1987, p. 33.
3. I. Noda, A. E. Dowrey, and C. Marcott, *Appl. Spectrosc.* **42**, 203 (1988).
4. I. Noda, *Appl. Spectrosc.* **44**, 550 (1990).
5. I. Noda, *J. Am. Chem. Soc.* **111**, 8116 (1989).
6. R. A. Palmer, C. J. Manning, J. L. Chao, I. Noda, A. E. Dowrey, and C. Marcott, *Appl. Spectrosc.* **45**, 12 (1991).
7. M. J. Smith, C. J. Manning, R. A. Palmer, and J. L. Chao, *Appl. Spectrosc.* **42**, 546 (1988).
8. A. Singhal and L. J. Fina, *Appl. Spectrosc.* **49**, 1073 (1995).
9. H. V. Shah, C. J. Manning, and G. A. Arbuckle, *Appl. Spectrosc.* **53**, 1542 (1999).
10. B. O. Budevskas, C. J. Manning, and P. R. Griffiths, *Appl. Spectrosc.* **48**, 1556 (1995).
11. I. Noda, *Appl. Spectrosc.* **47**, 1329 (1993).
12. E. Jiang, W. J. McCarthy, D. L. Drapcho, and R. A. Crocombe, *Appl. Spectrosc.* **51**, 1736 (1997).
13. F. E. Barton II, D. S. Himmelsbach, J. H. Duckworth, and M. J. Smith, *Appl. Spectrosc.* **46**, 420 (1992).
14. C. J. Manning, G. L. Pariente, B. D. Lerner, J. H. Perkins, R. S. Jackson, and P. R. Griffiths, Multiple modulation step-scanning Fourier transform infrared spectroscopy, in *Computer Assisted Analytical Spectroscopy*, S. D. Brown, Ed., Wiley, New York, 1996, Chap. 1.
15. R. Curbelo, Digital signal processing (DSP) techniques for FT-IR multiple modulation measurements using a photoelastic modulator, U.S. patent 6,025,913 (assigned to Bio-Rad Laboratories, Hercules, CA, February 15, 2000).
16. R. Curbelo, Digital signal processing (DSP) applications in FT-IR: implementation examples for rapid and step scan systems, in *Fourier Transform Spectroscopy: 11th International Conference, 1997*, J. A. de Haseth, Ed., American Institute of Physics, Woodbury, NY, 1998, Vol. 430, p. 74.
17. M. A. Czarniecki, Vibrational spectroscopy of liquid crystals, in *Handbook of Vibrational Spectroscopy*, J. C. Chalmers and P. R. Griffiths, Eds., (Wiley, Chichester, West Sussex, England, 2002), Vol. 4, p. 3109.
18. R. A. Palmer, J. L. Chao, R. M. Dittmar, V. G. Gregoriou, and S. E. Plunkett, *Appl. Spectrosc.* **47**, 1297 (1993).
19. C. Korzeniewski, Infrared spectroelectrochemistry, in *Handbook of Vibrational Spectroscopy*, J. C. Chalmers and P. R. Griffiths, Eds., Wiley, Chichester, West Sussex, England, 2002, Vol. 4, p. 2699.
20. C. M. Pharr and P. R. Griffiths, *Anal. Chem.* **69**, 4665 (1997).

# ATMOSPHERIC MONITORING

## 22.1. EXTRACTIVE ATMOSPHERIC MONITORING

There are two ways to monitor the concentrations of trace gases in the atmosphere by FT-IR spectrometry. The first is to draw the atmosphere in the region of interest into a long-path gas cell, and the second is to measure the spectrum of the atmosphere in situ. The first approach, which is known as *extractive monitoring* [1], is covered in this section, and the second, known as *open-path FT-IR spectrometry* (OP/FT-IR) [2], is covered in Section 22.2.

Extractive monitoring techniques have both advantages and disadvantages with respect to OP/FT-IR spectrometry. First, the background spectrum is usually a single-beam spectrum measured through the evacuated cell, so that the baseline of an absorbance spectrum is generally at exactly 0 AU. It is sometimes possible to dry the atmospheric sample to remove all spectral lines caused by atmospheric water vapor. In addition, if the background spectrum does contain atmospheric H<sub>2</sub>O vapor and CO<sub>2</sub>, some clever ways to exactly match the level of water vapor in the sample and background spectra have been described. These are discussed later in this section. Finally, the cell can be thermostated, so that the Boltzmann population of each rotational state is the same for all measurements, and in principle at least, spectral subtraction of the lines in the vibration–rotation spectrum of CO<sub>2</sub> and water vapor is possible. Provided that the reference spectra used for calibration are measured at the same temperature as the cell, the concentration of each component can be determined very accurately.

In practice, there are one or two drawbacks to extractive monitoring. Most important, the sample is usually collected only from a specific location (i.e., extractive monitoring is a point sampling technique). Thus, unless the atmosphere that is being monitored is homogeneous, meteorological conditions may determine whether or not a representative sample has been collected. Also, some care must be taken in the choice of material from which the long-path gas cell is constructed, since some analytes may adsorb on the walls of the cell or react with other species inside the cell before or during the measurement.



Most extractive measurements are made with the use of multipass gas cells with a pathlength of 20 or 40 m. The construction of these cells was described in Section 11.2. Some of these cells are reasonably small and may be mounted in the sample compartment of the spectrometer. Typical detection limits are on the order of 100 parts per billion by volume (ppbv).

Several transportable instruments based on extractive monitoring have been reported, such as the one designed at Radian Corporation [3–6] that is described in some detail in this section. The Radian instrument incorporates two 120-m-pathlength multipass gas cells. For each cell, the base pathlength is  $\sim 1.5$  m, and the beam undergoes about 80 passes through the cell. Spectra are typically measured at  $0.5\text{-cm}^{-1}$  resolution using a Stirling-engine-cooled MCT detector. The entire unit is mounted in a 4-m-long towable trailer, so that it can be brought close to the site of interest. One of the cells is evacuated and then filled with an atmospheric sample while the contents of the other are being measured. Each cell takes about 5 minutes to evacuate and refill and the spectral measurement also takes 5 minutes, so that the composition of the atmosphere being sampled may be monitored at 5-min intervals. Operation of the entire system has been automated so that it can run unattended for as long as two weeks. Stirling-cycle coolers add some low-frequency noise to the interferogram. Provided that the optical velocity of the interferometer is sufficiently high, this noise usually falls below the Fourier frequencies of the infrared radiation and does not change the signal-to-noise ratio of the spectrum.

Two enhancements of the basic instrument have been described. In one, the gas is first passed through a dryer to remove all water vapor and then through a channel containing soda-lime to remove the  $\text{CO}_2$ . By eliminating the primary atmospheric interferents in this way, the spectral range is greatly enhanced and the number of analytes that can be measured is increased. For example, the  $\text{C}=\text{O}$  stretching band of formaldehyde is completely masked by water-vapor absorption, yet when  $\text{H}_2\text{O}$  is removed, the detection limit for formaldehyde is 7 ppbv. Similarly, the strongest band in the spectrum of benzene absorbs within  $2\text{ cm}^{-1}$  of the Q branch of  $\text{CO}_2$  at  $668\text{ cm}^{-1}$ . When  $\text{CO}_2$  is removed prior to the measurement, the detection limit for benzene is 26 ppbv. Equal or lower detection limits were achieved for the toluene and the three xylene isomers.

A major problem occurs during the extractive monitoring of acid stack gases. When the temperature of the gas drops below a certain level, water vapor condenses into a fine mist into which the acid components of the stack gas are dissolved. To maintain the analytes in the vapor phase, both the transfer line and the long-path cell must be heated above  $100^\circ\text{C}$ . To accomplish this, the input gas to the Radian instrument is passed through a stainless steel line heated to  $140^\circ\text{C}$ . (Surprisingly, Teflon did not stand up to high concentrations of  $\text{H}_2\text{SO}_4$  as well as did stainless steel.) A flow rate of  $5\text{ L}\cdot\text{min}^{-1}$  was required to keep adsorption losses in the line below 10%. One of the cells could be heated to a temperature of up to  $186^\circ\text{C}$  to maintain all analytes in the vapor phase, and detection limits for  $\text{H}_2\text{SO}_4$  and  $\text{HCl}$  were 18 and 20 ppbv, respectively [4].

Data may be output in a number of ways [1]. The measured concentrations of one or more species may simply be plotted as a function of the time of day. The

95% confidence interval may be added to these plots. Alternatively, for a given time of day, the concentration of all species of interest may be shown as a fraction of the maximum allowed concentration on a bar chart.

By measuring spectra at 5-minute intervals, transient emission of one or more molecules may be detected, whereas transient species would not be observed with conventional time-averaging point-monitoring techniques. As noted by Bashour and Spellicy [5], one of the major strengths of this approach is its capability to detect such transients and correlate unforeseen emissions with batch activities inside a plant.

As stated above, the biggest problem of analyzing for trace atmospheric gases by mid-infrared spectrometry is interference by water vapor and  $\text{CO}_2$ . One way to circumvent this problem is to remove these interferents before they are admitted to the cell, as described previously. Another way around this problem of absorption by atmospheric  $\text{H}_2\text{O}$  and  $\text{CO}_2$  is to ensure that the concentrations of these gases are exactly the same in the sample and reference spectra, so that all lines are removed when the ratio of these two spectra is calculated. Usually, it is extremely difficult to achieve this goal in practice, but Hanst has described a very clever way of accomplishing it for gases that can be photolyzed by ultraviolet (UV) radiation [7]. He calls this approach photolysis-assisted pollution analysis (PAPA). In PAPA, three spectra are recorded. The first two are the same as would be measured in any extractive monitoring measurement. The first (spectrum A) is acquired through an evacuated long-path cell, and the second (spectrum B) is measured after the cell has been filled with the sample of interest. After measurement of the second spectrum, the contents of the cell are irradiated with ultraviolet radiation from a quartz-mercury lamp which converts some of the oxygen into ozone and oxygen atoms, which leads to the formation of hydroxyl radicals after reactions with other molecules. These species react with many types of molecules, including nitrogen oxides; oxygenated organic molecules, including acids, ethers, esters, and ketones; reactive hydrocarbons such as the isoprenes; aromatic molecules, including halogenated species; and mercaptans and other sulfur-containing compounds, including  $\text{H}_2\text{S}$  and  $\text{CS}_2$ . The third spectrum (spectrum C) is measured after photolysis is complete. Since the concentration of  $\text{H}_2\text{O}$  and  $\text{CO}_2$  formed by these photolysis reactions increases only slightly, a scaled subtraction of the absorbance spectrum obtained by ratioing spectra B and A from the spectrum obtained by ratioing spectra C and A will leave the absorption bands of the analytes that have been removed by photolysis.

Another way of compensating for absorption by rotational lines in the spectra of small molecules such as water involves accurately calculating their spectrum and subtracting them. Perhaps the most successful analysis of atmospheric spectra has been made using a program developed by Griffith [8,9]. This program, called MALT (multiple atmospheric layer transmission), allows very accurate representations of the spectra of over 30 small molecules to be calculated under a wide range of environmental and instrumental conditions. Starting from a compilation of line parameters known as HITRAN [10], the effect of pressure and temperature on simulated spectra measured at a given pathlength is calculated to give the spectrum

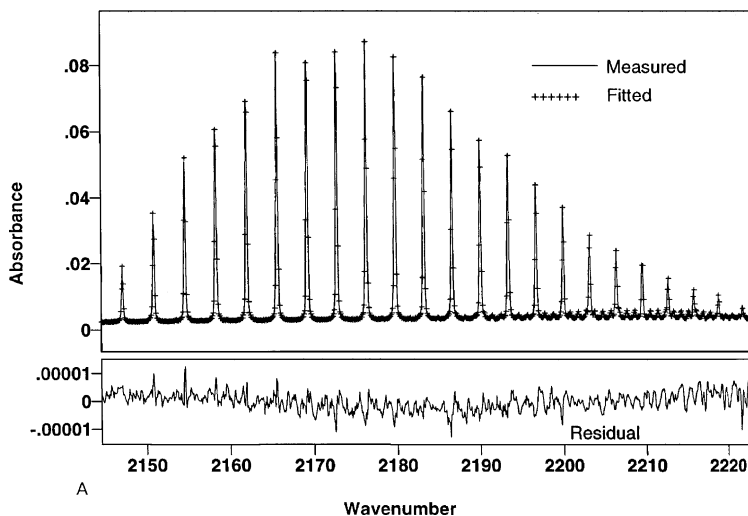


**Figure 22.1.** (a) Measured absorbance spectrum of CO and the fitted absorbance spectrum calculated by MALT; (b) (highly expanded) difference spectrum.

as it would appear if measured at very high resolution. The effect of the measurement is then calculated.

We saw in Chapter 2 that measuring the spectrum of an infinitesimally narrow line with a finite retardation leads to changes in the width and shape of the line and also leads to a small shift in wavenumber. Thus, the spectra that are calculated in the first step must be convolved with the appropriate instrument lineshape and spectral shifting functions. Using MALT, an atmospheric spectrum measured at any resolution and calculated with any common apodization function can be accurately simulated. As an example of the accuracy of this program, the measured spectrum of the R branch of 161.9 ppmv of carbon monoxide at 500 torr pressure at temperature 296 K in a 5.6-m White cell, measured at a resolution of  $0.2\text{ cm}^{-1}$ , is shown in Figure 22.1. Also shown in this figure are the values that were calculated using MALT and the difference between these values and the measured spectrum.

One of the most important uses of MALT is calculation of the lines in the spectrum of water vapor. By subtracting the calculated spectrum of water vapor from a measured spectrum measured by extractive monitoring or OP/FT-IR spectrometry, the spectrum of the remaining molecules in the beam may be seen more clearly, and multivariate analytical protocols such as CLS and PLS regression work even better.

## 22.2. OPEN-PATH ATMOSPHERIC MONITORING

The alternative technique to extractive monitoring is open-path FT-IR spectrometry. In this approach, no gas cell is used to contain the air sample. Instead, the beam is passed through a path (typically, between 100 and 400 m in length) that crosses the

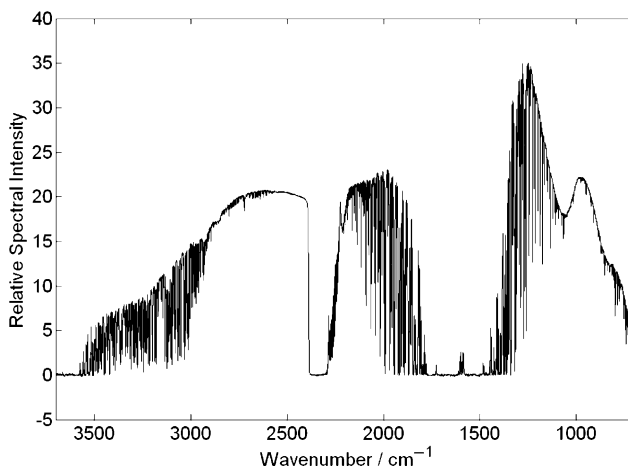


**Figure 22.2.** Single-beam OP/FT-IR spectrum measured at a resolution of  $1\text{ cm}^{-1}$  over a total pathlength of 218 m. The spectrum was measured when the relative humidity was approximately 30% and the temperature was  $13.6^{\circ}\text{C}$ ; the intensity of the water lines will be even greater than shown in this spectrum if the pathlength is longer or the humidity is higher.

location of interest. Because atmospheric water vapor and  $\text{CO}_2$  cannot be removed from OP/FT-IR spectra, absorption by these molecules severely limits the available spectral range; a typical atmospheric spectrum is shown in Figure 22.2. A detailed description of OP/FT-IR spectrometry is to be found in two documents sponsored by the U.S. Environmental Protection Agency (EPA) [11,12], and a good review has been written by Russwurm and Childers [2]. The primary difference between OP/FT-IR spectrometry and extractive atmospheric monitoring is that the *path-integrated concentration* of each component is measured by OP/FT-IR, not the concentration at a single point. Thus, the possibility of missing the presence of any component by point sampling at a location where that analyte is absent is eliminated. In addition, there is no possibility of trace or reactive components being lost in the container used for point sampling. The main disadvantage of OP/FT-IR measurements compared with extractive monitoring is the difficulty of obtaining a suitable background spectrum and the fact that it is almost impossible to achieve a baseline at 0 AU without some type of baseline correction.

There are two ways by which OP/FT-IR spectra can be measured: *bistatic* and *monostatic*. For bistatic OP/FT-IR measurements, the source is located at one end of the optical path and the detector is located at the other end. Two types of bistatic systems can be distinguished. In the first (shown in Figure 22.3a), the radiation from the source is modulated by the interferometer before being expanded by a telescope and passed over the path of interest. The beam is collected by a second telescope and focused onto the detector. This design has the advantage that the electronics only sense the signal that has been modulated by the interferometer; any stray radiation reaching the detector is unmodulated and hence is not sensed (see below). This very real benefit is offset in practice by the fact that the detector

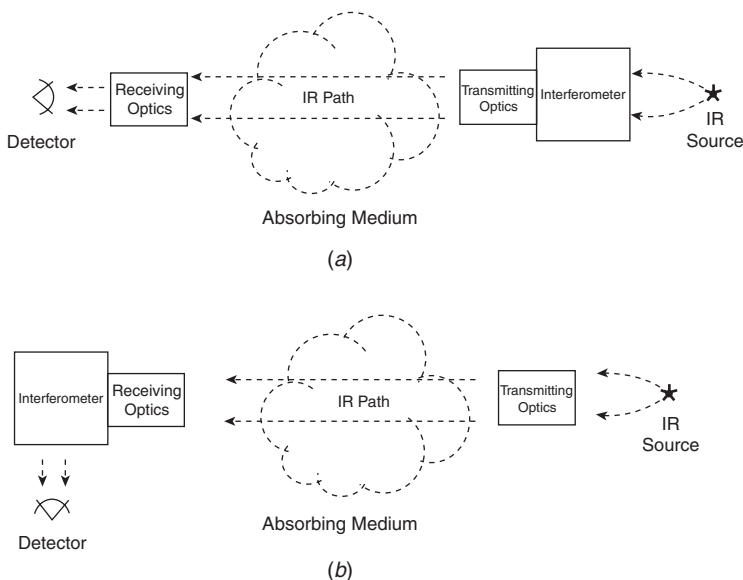


**Figure 22.3.** Bistatic OP/FT-IR instruments with (a) transmitting optics and (b) receiving optics at the distal end of the system.

must often be mounted over 100 m from the interferometer, and a very long cable is needed if this signal is to be measured by the instrument's electronics. In the alternative configuration (shown in Figure 22.3b), a stand-alone source, often powered by an automobile battery, is needed. Such batteries are heavy and awkward to deploy. The mid-infrared radiation emitted by the source is collected by a large-diameter paraboloidal mirror to produce an approximately collimated beam that is passed through the analytical path to a receiving telescope. The diameter of the telescope must be at least as large as that of the source paraboloid. The receiving telescope reduces the beam diameter to 5 cm or less, and this beam is passed to the interferometer. The beam that emerges from the interferometer is then focused on a narrowband MCT detector. For field measurements, the detector is usually held at 77 K with a Stirling-engine cooler. OP/FT-IR spectrometers operated in the bistatic mode have the disadvantage of requiring electrical power at both the source and the interferometer and detector, and most OP/FT-IR measurements today are made in the monostatic mode.

The reason for expanding the beam with the large paraboloidal mirror is to increase its collimation and hence to allow the beam to be transmitted over long pathlengths with minimal light loss. The divergence angle of the beam passing through a typical interferometer in a benchtop FT-IR spectrometer operating at a resolution of  $1\text{ cm}^{-1}$  is  $(1/4000)^{1/2}$ , or about 0.016, rad (see Section 7.1). By the time this beam has traveled a distance of 100 m, its diameter will be greater than 200 cm; obviously, most of this beam will not be collected by the telescope. By expanding the beam diameter to 25 cm and operating with the same étendue as

the typical benchtop spectrometer, the beam diameter is only  $\sim 44$  cm after 100 m. About 30% of this beam enters a 10-inch (25-cm) receiving telescope and is focused on the detector. This is enough energy that many narrowband MCT detectors have a nonlinear response. Thus, bistatic OP/FT-IR spectrometers are often operated at pathlengths of at least 200 m to keep the signal below the level needed to saturate the detector. For shorter pathlengths, the beam must usually be attenuated by inserting a screen in the beam to avoid detector saturation.

In monostatic instruments, all components that require power are mounted at the same location. The beam from the interferometer is then expanded by a telescope. Schematic representations of two possible monostatic systems are shown in Figure 22.4. In the first (shown in Figure 22.4a), radiation from the source is first modulated by the interferometer and then expanded by the transmitting telescope. After passing through the path of interest, the beam is laterally translated by two 45° plane mirrors so that it returns along a path that is parallel to the outbound path to a second (receiving) telescope from which it is focused onto the detector. This system is difficult to align and rarely has high optical efficiency because of the distortion of the lateral transfer mirrors.

The second type of optics for monostatic OP/FT-IR spectrometry (shown in Figure 22.4b) is the basis of most commercial OP/FT-IR spectrometers. Here, a single telescope is used in conjunction with the optical arrangement such as the

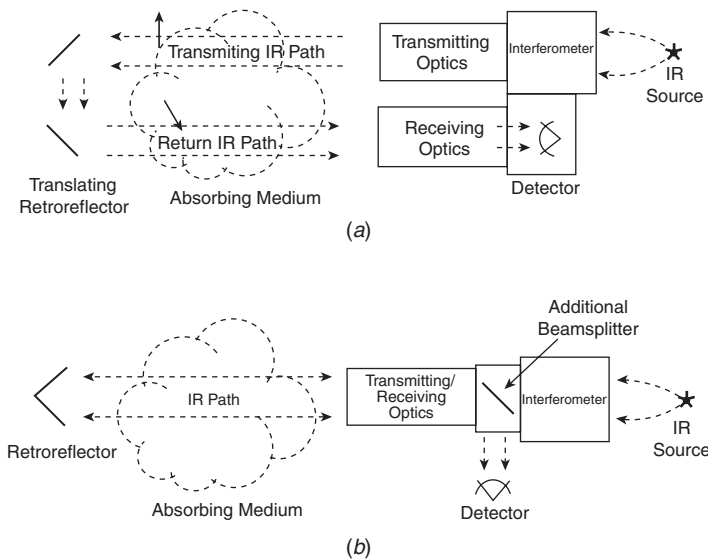


**Figure 22.4.** Monostatic OP/FT-IR instruments with (a) separate telescopes for transmitting and receiving the beam and a lateral transfer retroreflector, and (b) with a single telescope for transmitting and receiving the beam and optics similar to those shown in Figure 22.5 to distinguish between the transmitted and reflected beams.

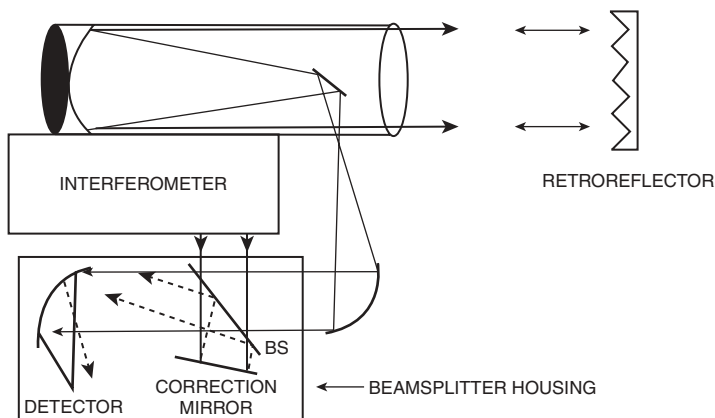


**Figure 22.5.** Optics required for monostatic OP/FT-IR instruments with a single telescope. The modulated radiation from the interferometer is passed onto a beamsplitter where one-half of the beam is passed to the telescope, where it is expanded and passed to the retroreflector. The return beam from the retroreflector is passed back to the beamsplitter, where half of it is passed to the detector. Tilting of the collection mirror ensures that only radiation that has been received from the collection mirror is measured at the detector. (Reproduced from [13], by permission of the Society for Applied Spectroscopy; copyright © 1997.)

one shown in Figure 22.5. Radiation from a Global-type source is collimated by same type of optics that are used in benchtop spectrometers and passed directly into the interferometer. The modulated beam emerging from the interferometer is passed to a beamsplitter that reflects  $\sim 50\%$  of the beam to a telescope similar to the transmitting telescope shown in Figure 22.3a. The expanded beam is directed into the path of interest to a *retroreflector* that is located at the end of the path. The function of the retroreflector is to direct the beam back to the telescope from which the beam was transmitted. The return beam is passed to the same beamsplitter that was used to direct the beam from the interferometer into the telescope, and  $\sim 50\%$  of this beam is transmitted to the detector. In the optics shown in Figure 22.5 [13], stray light that is collected by the telescope that did not pass through the path of interest is directed away from the detector by a plane “correction mirror.”

It may be noted that even with a perfect beamsplitter, only one-fourth of the beam that emerged from the interferometer is passed to the detector, so that even narrowband MCT detectors are rarely saturated. In addition, this optical configuration is easier to align than any of the other designs shown in Figures 22.3 and 22.4 and less susceptible to the effect of wind than the design in Figure 22.4a (although we recommend that both ends of the system be protected from the wind and rain). The pathlength of the measurement is twice the distance between the telescope and the retroreflector, giving OP/FT-IR spectrometers operated in the monostatic mode another advantage over bistatic instruments because of this increased pathlength.

The retroreflector for monostatic measurements could—in principle at least—be a plane mirror. However, plane mirrors are very difficult to align, and slight misalignment (due, e.g., to a gust of wind) causes the reflected beam to miss the

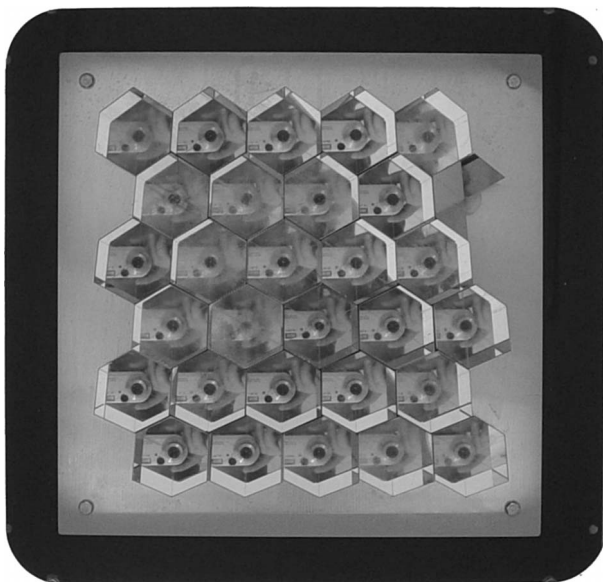


**Figure 22.6.** Typical cube-corner array retroreflector. An image of the camera can be seen at the center of each element.

telescope completely. A plane mirror would have to be very large and tends to distort under its own weight. Furthermore, as noted above, the expanded beam diverges with a half-angle of about 0.003 rad. Were a plane mirror to be used as the retroreflector when the distance between the telescope and the retroreflector is 100 m, the beam diameter would be about 90 cm by the time it returned to the telescope.

It is much more effective to use an array of small cube-corner mirrors as the retroreflector, as shown in Figure 22.6. In this device, each individual cube corner reflects the beam back exactly in the direction from which it entered. Thus, a cube-corners array acts like a spherical mirror whose focal length is always optimized for any pathlength. Furthermore, monostatic OP/FT-IR systems equipped with cube-corner array retroreflectors are far more easily aligned than the corresponding instruments with a plane mirror used as the retroreflector and maintain most of their efficiency even when the alignment is affected by a gust of wind.

The monostatic OP/FT-IR spectrometer designs shown in Figure 22.4 have the great advantage that the beam from the source is modulated before it is expanded and passed into the path being analyzed. Thus, only the radiation emitted by the source contributes to the measured spectrum. In bistatic measurements such as the one shown schematically in Figure 22.3*b*, radiation emitted from other ambient sources (hills, clouds, trees, etc.) that is collected by the telescope is passed to the interferometer along with the source radiation. The end result is that monostatic OP/FT-IR spectra have higher photometric accuracy than that of the corresponding bistatic spectra.



One of the major experimental difficulties with OP/FT-IR measurements is the need to minimize the effect of water vapor and carbon dioxide on the spectra. With pathlengths of over 100 m, essentially all radiation between about 4000 and 3500  $\text{cm}^{-1}$  and 2000 and 1300  $\text{cm}^{-1}$  is totally absorbed by atmospheric water vapor, and the radiation between 2150 and 2500  $\text{cm}^{-1}$  and between 700  $\text{cm}^{-1}$  and the cutoff of the MCT detector is lost because of absorption by  $\text{CO}_2$ . Thus, useful analytical information can be obtained from OP/FT-IR spectra only in the three *atmospheric windows* (700 to 1300, 2000 to 2150, and 2500 to 3000  $\text{cm}^{-1}$ ). Even in these atmospheric windows, however, water lines can still be observed in the spectrum.

The acquisition of any spectrum by FT-IR spectrometry requires the measurement of both a sample and a background single-beam spectrum. The EPA-recommended protocol for measuring OP/FT-IR spectra is to calculate the ratio of a single-beam spectrum measured over the optical path of interest and a background spectrum measured over an identical path but without the analytes present [11,12]. This is much more easily said than done, however. In OP/FT-IR, three types of background spectra may be used: synthetic, equidistant, and short-path. For a synthetic single-beam background spectrum, the features due to the analyte of interest are replaced by a curve that resembles the instrument baseline as closely as possible. Sometimes this is achieved by using a set of polynomial functions to match the instrument response function. Other workers have simply drawn a baseline across regions where water lines absorb appreciably. In any event, the use of a synthetic background spectrum generally requires a knowledge of which analytes are present in the sample spectrum and is normally applied after the sample spectrum was measured. Thus, the real-time benefit of OP/FT-IR is eliminated and the spectroscopist is limited to the analysis of compounds whose presence is known a priori. Furthermore, absorption lines due to water vapor at atmospheric pressure have a Lorentzian profile where there is significant absorption by the wings of the lines. As a result, the baseline is often drawn incorrectly and the line is compensated incompletely.

The second type of background spectrum is one taken over the same pathlength as the sample spectrum; this is called an *equidistant background*. This background spectrum should ideally be acquired under conditions of equal temperature and humidity as the sample spectrum. (If the temperature changes, the relative intensity of the lines in a vibration-rotation spectrum also changes.) An absorbance spectrum acquired under such conditions, referred to as an *EQ- $I_0$  spectrum*, is typified by a level baseline centered at 0 AU and the absence of strong absorption features due to atmospheric constituents in the atmospheric windows. EQ- $I_0$  spectra are well suited for use with any of the multivariate analysis techniques used in OP/FT-IR, of which classical least-squares (CLS) regression is the most common and the one that is recommended by the U.S. Environmental Protection Agency (EPA) [11,12]. However, the acquisition of an appropriate equidistant single-beam background spectrum is difficult at best and impossible in many situations, as the analyte should be completely absent in the background spectrum, and the humidity and temperature must be closely matched between the background and sample single-beam spectra. The latter requirement necessitates that a new background spectrum be

acquired at regular intervals. In a field deployment, this means locating the retro-reflector in such a manner that an analyte-free column of atmosphere with the same length as the sample column should be sampled.

Two approaches have been suggested for measuring the background spectrum if the composition of the plume from a suspected pollution source is to be acquired [2,11,12]. One is to locate the entire OP/FT-IR system upwind of the source. The other is to rotate the interferometer unit through  $90^\circ$  and to relocate the retroreflector so that the path is parallel to, but to one side of, the direction of the plume. Both procedures are time consuming and reduce the time that the sample plume may be analyzed. Furthermore, they require the wind direction to be constant and the wind speed to be high enough that the plume does not disperse appreciably. In the case where a very diffuse plume is being measured, it may be impossible to set up the spectrometer and retroreflector in an area free of contaminant. In such cases, a *short-path background* spectrum must be used.

Short-path background spectra for OP/FT-IR measurements are acquired by placing the retroreflector a distance of 1 to 5 m from the transmitting-receiving telescope of a monostatic OP/FT-IR spectrometer. Because the true absorbance is directly proportional to pathlength and the typical distance between the spectrometer and retroreflector is 100 to 200 m, the absorbance due to analytes and interferents in the sample beam is 20 to 200 times larger than the corresponding absorbances in the background spectrum. An absorbance spectrum acquired under such conditions is referred to as a *SP- $I_0$  spectrum*, in which the instrument response function is compensated but all absorption features of atmospheric water and carbon dioxide remain in the spectra. The measurement of SP- $I_0$  OP/FT-IR spectra allows for rapid deployment of the equipment for field measurements. The acquisition of a single reference spectrum during installation is usually sufficient for use throughout the sampling period. However, OP/FT-IR spectra obtained with short-path single-beam spectra are not as well behaved as EQ- $I_0$  spectra. SP- $I_0$  spectra are often characterized by sloping nonzero baselines and always show lines caused by weak transitions of water vapor in the atmospheric windows. Multivariate quantification methods with a high sensitivity to noise and baseline drift, such as CLS regression, perform poorly when operating on SP- $I_0$  spectra. For spectra measured in this way, CLS regression can no longer be used to quantify the analytes with overlapping absorption bands unless very short spectral regions are examined (in which case only one analyte can be quantified at a time) [12]. Hong and Cho [14] measured OP/FT-IR spectra in downtown Seoul, where a dozen different hydrocarbons are found in the atmosphere at high-enough concentration to give rise to absorption bands with a peak absorbance above the noise level. They confirmed that when several compounds of the same chemical class are present in the beam, the results obtained by CLS regression are often greatly in error. To get around this problem, they developed an approach that they call constrained classical least-squares regression, in which all the concentrations of all species that absorb in a given spectral range are constrained to fall within reasonable values. Results obtained when the measured spectra were treated by constrained CLS regression were far better than when the original CLS algorithm was applied to their spectra.

Instead of using CLS or one of its modifications, Hart et al. [15] showed that partial least-squares (PLS) regression could be used to obtain accurate quantitative data over wide spectral regions even when OP/FT-IR spectra were measured with a short-path background. Their calibration set was obtained by measuring a large number of background spectra measured under pristine conditions (i.e., only water and CO<sub>2</sub> contributed to the spectrum) over widely varying pathlengths, optical alignments, temperatures, and humidities. Random (but known) amounts of the spectra of the analytes were added to these spectra to generate the calibration set. To accommodate all the sources of variance in the background spectra, nine factors were needed, along with one factor for each component known to be present in the atmosphere. This approach was applied for the data shown at the end of this chapter, where the concentrations of three ketones present in the atmosphere were measured (see Figure 22.8).

There have been extensive discussions between practitioners of OP/FT-IR spectrometry as to the optimum resolution at which to measure the spectra [15–20]. By measuring the spectrum at relatively high resolution ( $\Delta\tilde{\nu} = 0.5$  or  $1\text{ cm}^{-1}$ ), the absorption lines of water can appear like a picket fence, and the absorption spectrum of analytes can sometimes be seen in the regions where the water lines do not totally absorb. It is for this reason that the EPA recommend that OP/FT-IR spectra be measured with relatively high resolution (e.g.,  $\Delta\tilde{\nu} = 1\text{ cm}^{-1}$ ).

On the other hand, for spectra measured in equal times and with equal optical throughput, the noise on the baseline is inversely proportional to  $\Delta\tilde{\nu}$  (see Section 7.1). Because the separation of lines in the spectra of molecules with a molecular weight greater than  $\sim 100\text{ g}\cdot\text{mol}^{-1}$  is usually less than the collision-broadened width of these lines, they can rarely be resolved at any resolution setting of the spectrometer. As a result, the peak absorbance of bands in the spectra of many volatile organic compounds (VOCs) is only minimally affected by resolution until  $\Delta\tilde{\nu}$  exceeds the FWHH of the band (see Figure 22.7). Thus, if OP/FT-IR spectra of VOCs were to be measured at relatively low resolution (e.g.,  $\Delta\tilde{\nu} = 4$  or  $8\text{ cm}^{-1}$ ), the noise level of the spectrum is decreased and the minimum detectable quantity of analytes with broad bands is decreased concomitantly.

In summary, there is a real benefit in measuring the spectra of VOCs with unresolvable rotational fine structure by measuring the spectrum at lower resolution than  $2\text{ cm}^{-1}$ . When  $\Delta\tilde{\nu}$  is much greater than  $8\text{ cm}^{-1}$ , however, the bands are broadened to the point that they can overlap neighboring bands from other analytes, and the prediction errors increase. For small molecules with resolvable rotational fine structure, the effect of resolution on analytical accuracy depends on the presence of other analytes with nearby absorption bands and the presence of water lines in the same spectral region.

Other more subtle factors also have an impact on the optimal resolution for OP/FT-IR spectrometry. For example, for CLS regression to operate optimally, Beer's law should be obeyed by all bands in the spectrum [i.e., the *measured* absorbance,  $A_{\text{peak}}^a$ , at each wavelength should vary linearly with the partial pressure of each analyte (see Section 8.2)]. Even in the analytical windows, the *true* peak absorbance,  $A_{\text{peak}}^t$ , of several water-vapor lines in the background spectra of humid atmospheres

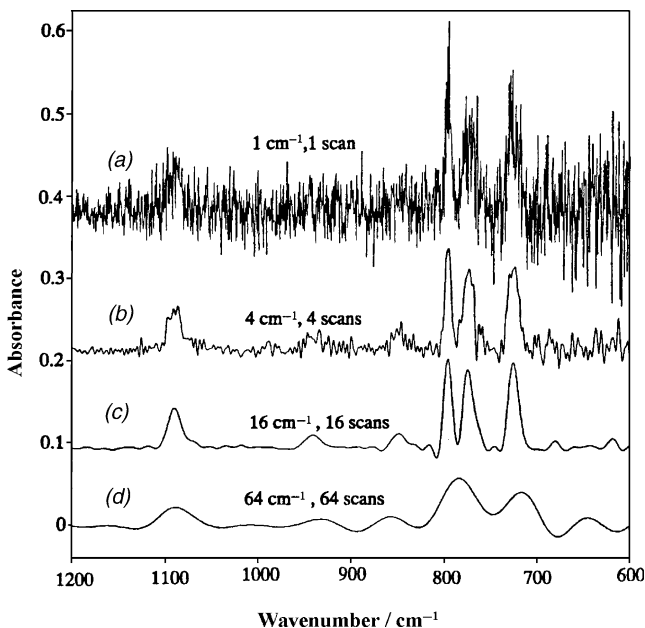


**Figure 22.7.** Spectra of a mixture of chlorinated hydrocarbons measured with active data equal acquisition times at resolutions of (a)  $1\text{ cm}^{-1}$ , (b)  $4\text{ cm}^{-1}$ , (c)  $16\text{ cm}^{-1}$ , and (d)  $64\text{ cm}^{-1}$ .

can be much greater than 1 AU when the pathlength exceeds 100 m. This may not be obvious from low-resolution spectra at first glance because  $A_{\text{peak}}^a$  is usually less than 1 AU. Since the FWHH of the lines in the spectrum of water vapor in 1 atm of air is about  $0.2\text{ cm}^{-1}$ , the resolution parameter for spectra measured with  $\Delta\tilde{\nu} = 1\text{ cm}^{-1}$  is  $\sim 5$ . Under these circumstances, Beer's law is not obeyed by strong lines and  $A_{\text{peak}}^a$  varies in a nonlinear manner with the partial pressure of water vapor (see Section 8.2). Thus, unless the background spectra for EQ- $I_0$  spectra are measured so that the pathlength, temperature, and humidity match the corresponding parameters for the sample spectrum exactly, standard CLS regression will not yield quantitatively accurate results unless there are no lines due to atmospheric  $\text{H}_2\text{O}$  or  $\text{CO}_2$  in the region selected for the analysis. Most pollutants are present at such low concentration that it is quite rare that the true peak absorbance,  $A_{\text{peak}}^t$ , of all bands in their spectra is greater than 1 AU. In this case, accurate data can be achieved from EQ- $I_0$  spectra by CLS regression provided that the effects of  $\text{H}_2\text{O}$  and  $\text{CO}_2$  can be compensated exactly. It is interesting to note that OP/FT-IR spectra measured with a short-path background yield accurate results when quantification is effected by PLS regression [15], but the standard error of prediction is higher than when the water lines are compensated.

There is one other problem with EQ- $I_0$  OP/FT-IR spectra. We have seen in Chapter 2 that a spectral shift will be caused when the effective beam path through the interferometer is different for the sample and background spectra. As a result, a small difference in the alignment of the retroreflector for the measurement of the

sample and reference spectra can lead to residuals that are shaped like the first derivative of the lines in the water-vapor spectrum. These artifacts again lead to a reduction of the quantitative accuracy obtainable from EQ- $I_0$  spectra.

Despite all the potential problems of OP/FT-IR spectrometry, remarkably good results have been found. Typical detection limits for the path-integrated concentration are less than 10 ppm-meter. Thus, for a pathlength of 100 m, the detection limits for most pollutants is less than 100 ppbv. Detection limits are greater than are obtained by extractive monitoring, but the problems introduced by point sampling are eliminated.

OP/FT-IR has three advantages for monitoring of toxic air pollutants over point sampling techniques such as GC/MS or extractive FT-IR monitoring: versatility, time, and safety. OP/FT-IR is capable of measuring any compound that exists at high enough concentration and has an IR signature (i.e., it is not a monatomic or homonuclear diatomic molecule). Of the 189 hazardous air pollutants listed in the U.S. Clean Air Act and its amendments, 135 pollutants and an even larger number of compounds for which environmental or health concerns have been raised can be monitored. Libraries of the air-broadened reference spectra of over 1000 vapor-phase compounds are available. OP/FT-IR provides the ability to examine all these compounds without modification of the analysis conditions. In addition, one can go back to a spectrum acquired at an earlier point in time and check for the presence of a compound that may not have been a concern at the time of the measurement. To determine the concentration of a compound that was not quantified in the original sampling protocol, one merely needs to apply a few new spectra to the calibration set acquired previously.

OP/FT-IR instruments may be used indoors or outside and can sample areas where it would be impractical to place other sampling devices (e.g., by locating the retroreflector on one side of an active waste disposal site and the rest of the instrument on the other). Pathlengths anywhere from 1 m to >1 km in length can be sampled, although the typical distance from retroreflector to spectrometer is between 100 and 200 m.

The time in which a particular compound may be quantified is usually less than 5 min when the spectrum is measured at a resolution of  $1\text{ cm}^{-1}$  and even less for measurements made at lower resolution or when the analyte is present at high concentration. Because quantification is usually achieved rapidly once the absorbance spectrum has been measured, the time resolution is determined largely by the spectral acquisition time. The acquisition time can be reduced significantly if OP/FT-IR spectra are measured at low resolution. The need for a short response time is of primary importance for spills of toxic or hazardous materials, since for such compounds a decision to order an evacuation of the area must be made as quickly as possible after the spill. The short response time of OP/FT-IR measurements contrasts with many point-source analysis techniques where the atmosphere is sampled over a period of time by adsorption onto charcoal filters followed by extraction and analysis by GC/MS in the analytical laboratory. In these types of analysis it may be several hours or even days before the analyst has an idea which, if any, pollutants are present. For many systems where an air sample is taken and analyzed at a later

time, the number of compounds analyzed is very limited in scope, and the sample is destroyed in the analysis process. With OP/FT-IR, all the sample information for over 130 compounds is contained in the sample spectrum.

Finally, there is the safety factor. In OP/FT-IR spectrometry, path-integrated spectra are measured, whereas for point-sampling approaches, the analytes are collected over a period of time at a single location. Thus, the plume of pollutants may be located anywhere along the beam path and the pollutants will still be detected. OP/FT-IR allows the analyst to sample the plume while remaining at a relatively safe distance and to receive the results in minutes. The ability to detect catastrophic releases of toxic gases rapidly could prevent the loss of hundreds of lives. However, it should be recognized that if an analyte concentration of less than  $\sim 10$  ppb must be monitored, as is the case near plants for the storage or incineration of chemical warfare agents, the detection limits of OP/FT-IR spectrometry are not low enough to allow useful measurements to be made.

Surprisingly, given all of its capabilities and benefits, OP/FT-IR still plays a minor role in the detection and monitoring of hazardous air pollutants. The two main reasons for this state of affairs (in 2006) are the cost of the instrument and the need for highly trained operators. The initial purchase price of an OP/FT-IR instrument often exceeds \$100,000. In addition, with current analytical protocols, it is virtually a necessity that a highly trained (and, therefore, highly paid) spectroscopist operates the instrument. This requirement for a skilled operator is mainly because of the need to identify all pollutants before the multivariate regression algorithms that are used to examine the spectra and produce the quantitative data required by the analysis protocol can be applied.

The need for the automated identification of trace analytes from OP/FT-IR is slowly being realized, although at the time of this writing, no infallible approach to compound identification has been incorporated in the software of contemporary OP/FT-IR spectrometers. Two promising approaches involving artificial neural networks have been described [21,22]. In the first [21], a conventional back-propagation algorithm was trained to recognize the presence of low-level analytes in OP/FT-IR spectra measured with equal-path and short-path backgrounds. Components with peak absorbances as low as 0.05 AU could be recognized in SP- $I_0$  spectra in the presence of up to 10 other interferents in addition to atmospheric  $H_2O$  and  $CO_2$ , provided that the network had been trained to recognize these interferents. Even better performance was achieved using a Hopfield network, since compounds could be recognized in the presence of interferents that the network had not been trained to recognize [22].

One of us (P.R.G.) has incorporated neural network software into a low-resolution OP/FT-IR spectrometer. Once the components had been identified, an online PLS calibration and prediction was carried out. Preliminary results are promising. As an example, a mixture of acetone, methyl ethyl ketone (MEK), and diisobutyl ketone was allowed to evaporate close to the beam of an OP/FT-IR instrument. The software recognized the presence of these three compounds and allowed their quantification. The data obtained in this way are shown in Figure 22.8. Acetone and MEK are seen at relatively high concentrations at the start

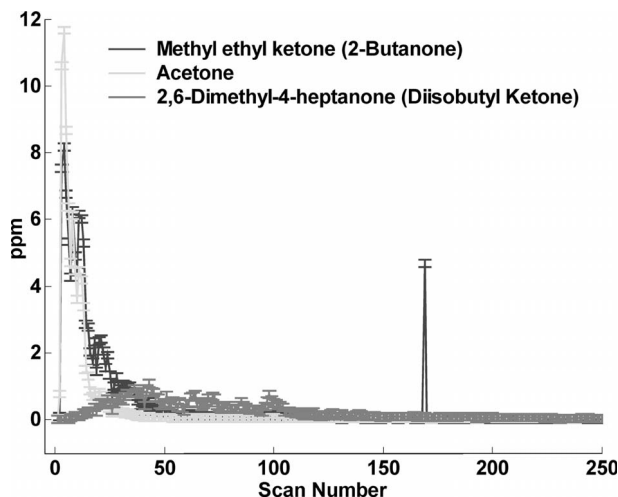


**Figure 22.8.** Automatically generated atmospheric concentration profiles of acetone, methyl ethyl ketone, and diisobutyl ketone as they evaporated from a liquid mixture of these compounds. A neural network was used to detect when each component was present, and the concentration of each molecule was calculated by PLS regression. (One bad point can be seen for MEK.)

of the run but are quickly lost from the liquid sample by evaporation. Diisobutyl ketone is always present at low concentrations but evaporates more slowly than acetone and MEK. Even though these compounds are all ketones, the software recognized the presence of all three and their concentrations varied in a logical manner. Thus, it would seem that a completely automated OP/FT-IR spectrometer could be commercially available within a very few years.

## REFERENCES

1. R. L. Spellicy and J. D. Webb, Atmospheric monitoring using extractive techniques, in *Handbook of Vibrational Spectroscopy*, J. M. Chalmers and P. R. Griffiths, Eds., Wiley, Chichester, West Sussex, England, 2002, Vol. 2, p. 1721.
2. G. M. Russwurm and J. W. Childers, Open-path Fourier transform infrared spectroscopy, in *Handbook of Vibrational Spectroscopy*, J. M. Chalmers and P. R. Griffiths, Eds., Wiley, Chichester, West Sussex, England, 2002, Vol. 2, p. 1750.
3. R. L. Spellicy, D. M. Hull, W. F. Herget, and G. J. Krametbauer, Development and testing of a dual-cell ambient-air FTIR monitoring system, in *Optical Remote Sensing for Environmental and Process Monitoring*, R. R. Romano, Ed., Society of Photo-Optical Instrumentation Engineers, Bellingham, WA, 1996, Vol. 2883, p. 37.
4. R. L. Spellicy, R. J. Brewer, J. R. Morphew, and H. R. Woodard, Development and evaluation of a modular FT-IR monitor for industrial use, in *Electro-Optic, Integrated Optic, and Electronic Technologies for Online Chemical Process Monitoring*, M. Fallahi,

- R. J. Nordstrom, and T. R. Todd, Eds., Society of Photo-Optical Instrumentation Engineers, Bellingham, WA, 1999, Vol. 3537, p. 42.
5. K. Bashour and R. L. Spellicy, *TI Tech. J.* (July–August 1994), p. 58.
  6. A. Cantu, G. Pophal, S. Hall, and C. T. Lausch, *Appl. Phys. B* **67**, 493 (1998).
  7. P. L. Hanst, Infrared Analysis, Inc., 1558-B South Anaheim Boulevard, Anaheim, CA 92805.
  8. D. W. T. Griffith, *Appl. Spectrosc.* **50**, 59 (1996).
  9. M. B. Esler, D. W. T. Griffith, S. R. Wilson, L. P. Steele, and L. Paul, *Anal. Chem.* **72**, 206 (2000).
  10. <http://cfa-www.harvard.edu/hitran>.
  11. G. M. Russwurm and J. W. Childers, *FT-IR Open-Path Monitoring Guidance Document*, ManTech Environmental Technology, Inc., Research Triangle Park, NC, 1995.
  12. U.S. Environmental Protection Agency, *Compendium Method TO-16: Long-Path Open-Path Fourier Transform Infrared Spectroscopy of Atmospheric Gases*, EPA 625R-96/010b, NTIS PB99-172355, Center for Environmental Research Information, Office of Research and Development, Cincinnati, OH, 1999.
  13. R. L. Richardson and P. R. Griffiths, *Appl. Spectrosc.* **51**, 1254 (1997).
  14. D. Hong and S. Cho, *Appl. Spectrosc.* **57**, 299 (2003).
  15. B. K. Hart, R. J. Berry, and P. R. Griffiths, *Environ. Sci. Technol.* **34**, 1337 (2000).
  16. P. R. Griffiths and R. L. Richardson, in *Optical Remote Sensing for Environmental and Process Monitoring*, R. R. Romano, Ed., Society of Photo-Optical Instrumentation Engineers, Bellingham, WA, 1996, Vol. 2883, p. 323.
  17. J. W. Childers and E. L. Thompson, in *SP-89 Optical Sensing for Environmental Monitoring*, Air and Waste Management Association, Pittsburgh, PA, 1994, p. 38.
  18. T. L. Marshall, C. T. Chaffin, V. D. Makepeace, R. M. Hammaker, W. G. Fateley, P. Saarinen, and J. Kauppinen, *J. Mol. Struct.* **324**, 19 (1994).
  19. P. Jaakola, J. D. Tate, M. Paakkunainen, J. Kauppinen, and P. Saarinen, *Appl. Spectrosc.* **51**, 1159 (1997).
  20. P. R. Griffiths, R. L. Richardson, D. Qin, and C. Zhu, Open-path atmospheric monitoring with a low-resolution FT-IR spectrometer, in *Optical Sensing for Environmental and Process Monitoring*, O. A. Simpson, Ed., Society of Photo-Optical Instrumentation Engineers, Bellingham, WA, 1995, Vol. 2365, p. 274.
  21. H. Yang and P. R. Griffiths, *Anal. Chem.* **71**, 751 (1999).
  22. H. Yang and P. R. Griffiths, *Anal. Chem.* **71**, 3356 (1999).





# COUPLED TECHNIQUES

## 23.1. INTRODUCTION

In Chapter 19 we saw that chemical or physical systems that vary with time scales in the second or hundred-millisecond range can be investigated with standard rapid-scan FT-IR spectrometers. Perhaps the most common examples of instruments in the analytical chemistry laboratory that yield data that vary on such time scales are gas and liquid chromatographs and thermogravimetric analyzers. For example, the components separated by a typical capillary gas chromatography (GC) column elute with a full width at half-height (FWHH) of between 1 and 5 s. The fact that FT-IR spectra can be measured in less than a second with good SNR means that the spectrum of each “peak” should be measurable in real time (i.e., a time somewhat less than the FWHH of the peak). In this case, each component could be identified by its infrared spectrum in a manner analogous to the way in which mass spectrometry (MS) is used so extensively today.

Some chemists have argued that infrared spectra are not needed because GC/MS has very low detection limits, and identifiable electron ionization (EI) mass spectra measured over the full mass range can be obtained from compounds injected into the chromatograph at levels of a few nanograms, and often less. Indeed, for many compounds this is a valid argument. However, mass spectrometry is not such a useful technique for distinguishing between substitutional isomers, whereas the infrared spectra of these isomers are readily distinguished. The classic example of isomers that yield very similar EI mass spectra but have very different infrared spectra are *o*-, *m*-, and *p*-xylene [1,2], but larger isomers such as 1,2,3,5-, 1, 2, 3, 4-, and 1, 2, 4, 5-tetrachlorobenzene have the same molecular weight and fragment in a similar way when bombarded with high-energy electrons; thus, their mass spectra are also essentially identical [3,4]. For example, a by-product of chlorine dioxide disinfection of drinking water could not be identified by GC/MS but was readily classified as a mono-substituted maleic anhydride by GC/FT-IR. The compound 2-*tert*-butyl maleic anhydride was finally identified by synthesis of the compound followed by MS and IR spectral matching of the unknown and the synthesized compound, as well as by GC retention time [5]. In this case, an instrumental technique

is needed that provides complementary structural information to mass spectrometry and distinguishes between substitutional isomers. Infrared spectrometry is just such a technique. Indeed, one of the long-standing goals of environmental analysts has been the development of a GC/FT-IR/MS interface [1–4, 6–8].

Any technique that is to be used as a complement to MS should have similar detection limits. Despite the enormous *potential* benefits of the GC/FT-IR interface for distinguishing between isomers, instruments of this type have not found great popularity, however, largely because the detection limits of MS are so much lower than those of FT-IR spectrometry. Although the detection limits of GC/FT-IR have been reduced significantly since the early 1980s, developments in GC/FT-IR that have been made over the past 20 years have always been offset by concomitant increases in sensitivity of GC/MS systems. Thus, GC/FT-IR has never attained the same level of acceptance by analytical chemists as GC/MS, even though some recent developments (mentioned later in this chapter) suggest that the detection limits of the two techniques are becoming more similar.

In this chapter we show how the design of the GC/FT-IR interface has led to improvements in sensitivity. We will then examine how various other instrumental techniques that produce an output stream where the composition is changing with time have been interfaced to FT-IR spectrometers. These include high-performance liquid chromatography (HPLC), supercritical fluid chromatography (SFC), and thermogravimetric analysis (TGA).

## 23.2. LIGHT-PIPE-BASED GC/FT-IR INTERFACES

### 23.2.1. Instrumental Considerations

The most obvious way in which the infrared spectra of the components eluting from a GC column can be measured is to pass the gas stream through a heated gas cell and to measure a continuous series of spectra at intervals of  $\sim 1$  s. The gas cell should fulfill several criteria:

- The pathlength should be long enough that the absorbance of compounds present at very low concentration is sufficiently high to be measurable above the baseline noise.
- The volume must be small enough that two components that have been resolved by the GC column are not present in the cell at the same time. For separations made on typical capillary GC columns (0.25 or 0.32 mm i.d.), this criterion means that the volume of the cell should be less than 100  $\mu\text{L}$ .
- The transmission of the cell should be great enough that the noise on the baseline of the measured spectrum is as low as possible, but not so high that the ADC is overfilled (i.e., the largest data point in any interferogram measured with an MCT detector is greater than the largest voltage that can be sampled with the ADC).

- The temperature of the cell must be sufficiently high that semivolatile compounds do not condense, even temporarily, as they pass through the cell. For many separations, this criterion means that the cell should be held at a temperature between 250 and 300°C.

The type of cell that meets all these criteria is the *light-pipe*. The most popular light-pipe design was first described by Azarraga [9], who showed how a highly reflective gold film can be deposited on the inside surface of borosilicate glass tubes. For most contemporary GC/FT-IR interfaces, the internal diameter (i.d.) of the tube is  $\sim 1$  mm. The length of 1-mm-i.d. light-pipes is usually about 10 cm, so that the cell volume is  $\sim 80 \mu\text{L}$ . The infrared beam is multiply reflected from the gold walls as it passes through the cell, leading to an effective pathlength that is slightly longer than the length of the tube.

The effluent from the GC column is passed via a heated transfer line into the light-pipe through either an appropriate fitting or through a small hole drilled near one end of the tube and passes out through a similar fitting or hole at the other end. KBr windows are usually mounted on both ends of the light-pipe, and the entire device is mounted in an oven to ensure that no component condenses as it passes through the light-pipe. Two light-pipe designs are shown in Figure 23.1.

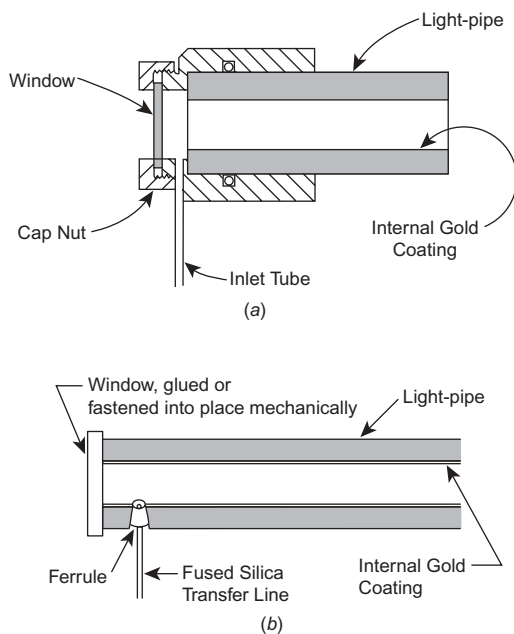


**Figure 23.1.** Two types of light-pipe used in the GC/FT-IR interface: (a) with effluent from the GC column passing through a fitting; (b) with GC effluent passing through a laser-drilled hole in the borosilicate tube from which the light-pipe is constructed.

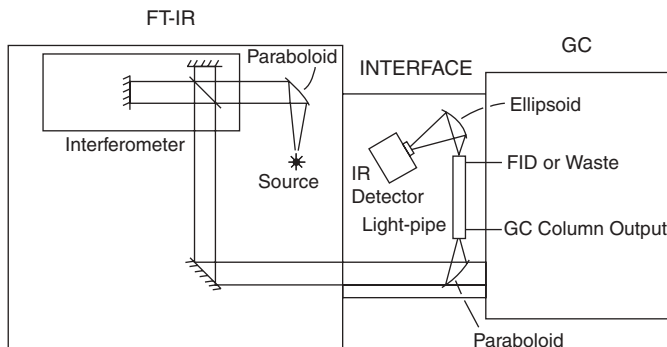


**Figure 23.2.** Typical GC/FT-IR interface.

Because the gas flow through the tube is approximately laminar, the resolution of the chromatogram is not degraded and the output from the light-pipe can be passed into another detector for further characterization. Most commonly, a flame ionization detector (FID) is used, so that accurate quantitative information can be obtained. Alternatively, the effluent can be passed to a mass spectrometer, since the combined information from a mass and infrared spectrum will usually lead to an unequivocal identification of each component [1–8].

In most GC/FT-IR interfaces, the beam from the interferometer is simply focused onto the front window of the light-pipe and the beam that emerges from the other end is focused directly onto a narrowband MCT detector, as shown schematically in Figure 23.2. There is one disadvantage associated with this approach. Because the light-pipe is fabricated from glass tubing, the annular glass end acts as a blackbody emitter. The higher the temperature at which the light-pipe is held, the greater the amount of unmodulated radiation that is focused on the detector. As the light-pipe is heated, the intensity of this unmodulated radiation increases; thus, the conduction bands in the MCT detector become filled and its responsivity to both unmodulated and modulated radiation (i.e., the interferogram) decreases, and the SNR of the measured spectra is reduced concomitantly. In some GC/FT-IR systems, the SNR may be reduced by as much as a factor of 10 on increasing the temperature of the light-pipe from ambient to 300°C.

One way around this problem is through the use of optics that focus the beam emerging from the light-pipe at a point where an aperture can be located. The beam is then refocused at the detector. The infrared image of the unmodulated radiation at the intermediate focus is an annulus that corresponds to the glass end of the light-pipe. At the center of this annulus is the image of the inner diameter of the light-pipe. By placing an aperture at the intermediate focus that has the appropriate diameter to block the annular image of the glass light-pipe, only radiation that has passed through the light-pipe will reach the detector, and all unmodulated radiation that has been emitted by the hot glass will be blocked. Henry et al. found that the temperature of the light-pipe could be raised from ambient to 250°C with a loss in signal of only a few percent when the optical arrangement shown in Figure 23.3 is used [10].

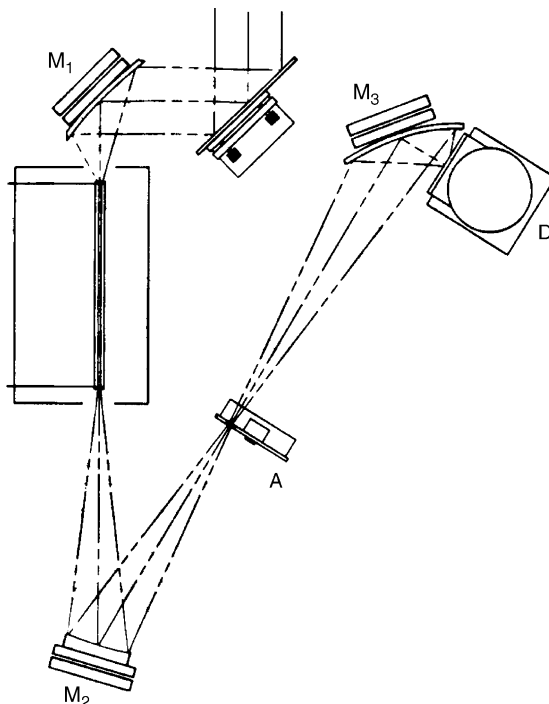


**Figure 23.3.** Layout of the optics for GC/FT-IR designed to minimize the amount of unmodulated infrared radiation emitted from the glass ends of the light-pipe that reaches the MCT detector. (Reproduced from [10], by permission of the American Chemical Society; copyright © 1987.)

### 23.2.2. Spectroscopic Considerations

Because the composition of gas passing through a light-pipe is identical to that of gas that has emerged from the column a short time before, each component is (1) at relatively low concentration, and (2) in the vapor phase. These two criteria have important spectroscopic ramifications.

Since the concentration is low, the absorbance is also low. For many GC/FT-IR measurements where detection is effected with an 80- $\mu\text{L}$  light-pipe, a 0.32-mm-i.d. capillary GC column with a stationary-phase thickness of 0.4  $\mu\text{m}$  gives the optimal combination of sample capacity and chromatographic resolution. The typical flow rate of the helium mobile phase is 2  $\text{mL min}^{-1}$ , and a typical FWHH of the peak is 3 s (0.05 min). For a Gaussian GC peak, the average volume of gas between the half-height points of the peak is  $\sim 100 \mu\text{L}$ . For an optimal GC/FT-IR measurement, the GC temperature program should be set so that the volume between the half-height points of a typical peak should be slightly greater than the volume of the light-pipe.

Consider an analyte of molecular weight  $\sim 200 \text{ Da}$  that is injected onto the column at a level of 1 ng. The average concentration of the peak as it passes through

the light-pipe is  $\sim 1$  ppm. Were the volume not limited, the vapor-phase infrared spectra of species at such low concentrations would usually be measured with a long-path (multipass) gas cell in order to bring the pathlength–concentration product up to the point that the absorbance of the analyte is easily measurable (see Section 11.2). However, for GC/FT-IR, the volume of the gas cell must be held below 100  $\mu\text{L}$  and the use of a multipass gas cell is precluded. The “bottom line” is that even with a light-pipe with a 10 cm pathlength, the peak absorbance of the strongest band of a polar analyte is usually significantly less than 1 mAU. In this case, the analyte would be present in the light-pipe at a concentration that is below the detection limit when the measurement time is restricted to 1 s. In practice, the detection limit for GC/FT-IR measurements of polar compounds is between 5 and 10 ng, and this quantity must be increased by at least a factor of 4 if an unknown compound is to be identified from its infrared spectrum. Note also that the measurement time for any chromatography/FT-IR spectrum acquired using a flow-through cell is determined by the FWHH of the peak and cannot be increased by extended signal averaging. As a result, the sensitivity of conventional GC/FT-IR measurements is at least an order of magnitude lower than the corresponding GC/MS measurement made with a benchtop quadrupole mass spectrometer. This difference in sensitivity is, we believe, the main reason why GC/FT-IR has not been accepted by analytical chemists with the same alacrity as GC/MS. Nonetheless, this technique has been used for the solution of many problems, and light-pipe-based GC/FT-IR interfaces have been produced by at least six manufacturers.

For most libraries of infrared reference spectra, the sample is in the liquid or solid state. For GC/FT-IR measurements made using light-pipes, the fact that the analytes are in the vapor phase causes their spectra to be very different from standard condensed-phase reference spectra, especially for compounds that are strongly hydrogen-bonded in the liquid or solid state. As a result, a database of vapor-phase infrared reference spectra measured at a temperature of  $\sim 250^\circ\text{C}$  is needed if components being characterized by GC/FT-IR are to be identified. About 12,000 vapor-phase infrared reference spectra are now available from such sources as Nicolet-Aldrich and the Informatics Division of Bio-Rad (formerly Sadtler Research). Although this is a fairly large number, it is not nearly as large as the number of reference mass spectra that are available in, say, the database compiled by the U.S. Environmental Protection Agency and National Institutes of Health.

### 23.2.3. Chromatogram Construction

Several techniques are available to construct chromatograms from the series of interferograms that are acquired in a GC/FT-IR measurement. For those chemists with experience in GC/MS, it may be helpful to summarize the ways in which chromatograms are reconstructed by GC/MS and to compare these techniques to the ones used for GC/FT-IR.

Two principal methods for the construction of chromatograms from GC/MS data are available. The first involves measurement of the total ion current. Since molecules of all types produce an ion current on being bombarded with electrons, this

method can be considered as a *universal* detection technique. In the second, only the current from ions with one or more selected values of  $m/z$  is measured; in this approach, only those molecules that yield ions with this  $m/z$  ratio on fragmentation are observed. This approach is, therefore, a *selective* detection technique. Two analogous methods for the construction of chromatograms from GC/FT-IR measurements were described in papers given back to back at the 1977 International Conference of Fourier Transform Spectroscopy by Coffey and Mattson [11] and de Haseth and Isenhour [12]. One is a universal technique and the other is more selective. Both methods have been refined in subsequent years, but the principle of each approach remains the same.

The universal technique is the more challenging to understand from a mathematical standpoint and is based on the algorithm known as *Gram-Schmidt vector orthogonalization* [13]. For this application, the vector is simply the consecutive values of a discrete interferogram. The Gram-Schmidt method relies on the fact that each datum in the interferogram contains information about every datum in the spectrum. Hence, a small region of the interferogram should contain ample information to determine not only whether a compound is present in the light-pipe at any given time, but also how much is present. An interferogram  $I$  with  $n$  data points may be represented as an  $n$ -dimensional vector in hyperspace as

$$\mathbf{I} = (i_1, i_2, i_3, \dots, i_n) \quad (23.1)$$

where  $\mathbf{I}$  is the vector notation for interferogram  $I$  and  $i_1, i_2, i_3, \dots, i_n$  are  $n$  consecutive values of the interferogram. The Gram-Schmidt algorithm is really a normalized subtraction routine. In this procedure, two vectors are examined and any component found in one that is common to the other is removed. Thus, if two interferograms are recorded when the light-pipe is empty, theoretically there is no difference between them. The orthogonalization would show that there is no uncommon element, and the resultant is therefore zero. If one of the interferograms were measured when an analyte was present in the light-pipe above the detection limit and the other were background, the orthogonalization would yield a nonzero difference. The magnitude of the difference depends on the concentration of the analyte in the light-pipe.

Gram-Schmidt orthogonalization is general and is performed as follows. The first step is to form a unit vector  $\mathbf{U}_1$  from an interferogram vector  $\mathbf{I}_1$ . Vector  $\mathbf{I}_1$  is an interferogram that was recorded when no compound is present in the light-pipe.

$$\mathbf{U}_1 = \frac{\mathbf{I}_1}{\sqrt{\mathbf{I}_1^T \mathbf{I}_1}} \quad (23.2)$$

where  $\mathbf{I}_1^T$  is the transpose of  $\mathbf{I}_1$  and is simply a mathematical formality to denote the dot product of two vectors. For two vectors  $\mathbf{J}$  and  $\mathbf{K}$ , the dot product is a scalar equal to  $\sum_{m=1}^n j_m k_m$ . Thus, the term  $\sqrt{\mathbf{I}_1^T \mathbf{I}_1}$  is the scalar length of  $\mathbf{I}_1$ .  $\mathbf{I}_1$  may be



recorded before the sample is injected into the chromatograph but may also be recorded at different times throughout the chromatogram: for example, to account for the effect of column bleed.

If  $\mathbf{I}_1$  were noise-free,  $\mathbf{U}_1$  would be a good representation of the interferogram measured through an empty light-pipe. In the presence of noise, however, more than one interferogram is needed to characterize the signal through the empty light-pipe. In this case, a second background interferogram  $\mathbf{I}_2$  is chosen, and all components common to the first interferogram are removed:

$$\mathbf{V}_2 = \mathbf{I}_2 - c_1 \mathbf{U}_1 \quad (23.3)$$

where  $\mathbf{V}_2$  is the vector that remains after the common components are removed and  $c_1$  is a scalar that causes  $\mathbf{V}_2$  to be orthogonal to  $\mathbf{U}_1$ . If two vectors are orthogonal, their dot product is zero; hence,

$$\mathbf{U}_1^T \mathbf{V}_2 = \mathbf{U}_1^T (\mathbf{I}_2 - c_1 \mathbf{U}_1) = 0 \quad (23.4)$$

Because  $\mathbf{U}_1^T$  and  $\mathbf{U}_1$  are unit vectors,  $\mathbf{U}_1^T \mathbf{U}_1 = 1$ ; therefore,

$$c_1 = \mathbf{U}_1^T \mathbf{I}_2 \quad (23.5)$$

and

$$\mathbf{V}_2 = \mathbf{I}_2 - (\mathbf{U}_1^T \mathbf{I}_2) \mathbf{U}_1 \quad (23.6)$$

Both  $\mathbf{U}_1$  and  $\mathbf{V}_2$  are background interferograms, but the unit vector form is more useful; thus,

$$\mathbf{U}_2 = \frac{\mathbf{V}_2}{\sqrt{\mathbf{V}_2^T \mathbf{V}_2}} \quad (23.7)$$

The combination of  $\mathbf{U}_1$  and  $\mathbf{U}_2$  describes the background signal in an interferogram more accurately than  $\mathbf{U}_1$  alone. The combination is called a *basis*. In some instances, two interferograms may be insufficient to characterize the background signal and more interferograms must be added to the basis set. This is a sequential operation (one added at a time) and can be expressed as:

$$\mathbf{V}_k = \mathbf{I}_k - \sum_{j=1}^{k-1} (\mathbf{U}_j^T \mathbf{I}_k) \mathbf{U}_j \quad (23.8)$$

and the appropriate unit vector is

$$\mathbf{U}_k = \frac{\mathbf{V}_k}{\sqrt{\mathbf{V}_k^T \mathbf{V}_k}} \quad (23.9)$$

Once the background has been characterized by the basis, interferograms can be compared to the basis by an operation similar to that described in Eq. 23.8:

$$\mathbf{V}_p = \mathbf{I}_p - \sum_{j=1}^k (\mathbf{U}_j^T \mathbf{I}_p) \mathbf{U}_j \quad (23.10)$$

where  $\mathbf{I}_p$  is not in the set 1 through  $k$ . The magnitude of the vector  $\mathbf{V}_p \left( \sqrt{\mathbf{V}_p^T \mathbf{V}_p} \right)$  is the deviation of the interferogram under study from the basis, or background characterization. Each single-scan interferogram in a GC/FT-IR run can be compared to a basis, and the resulting scalar from each interferogram is a measure of the quantity of the analyte in the light-pipe. Most chromatograms require fewer than 10 interferograms for the basis set.

It was stated above that the orthogonalization procedure applies because of the multiplex nature of the interferogram. This means that it is not necessary to use the entire interferogram to construct the chromatogram. It was found [13] that the optimum signal is produced if 100 data points in the region starting ~50 points from the centerburst (assuming that the interferogram is sampled once per wavelength of the HeNe laser). The reason for this finding was discussed by Brissey et al. [14], who showed that the centerburst should be excluded because the largest variations in interferogram intensity from scan to scan are found in this region. Similarly, the envelope of the FT of Lorentzian bands decays exponentially from zero retardation. Therefore, the amplitude of the signal from any absorption band of finite width is greatest near the centerburst: The wider the band, the more rapidly its interferogram decays. Sampling the interferogram between about 50 and 150 points from the centerburst allows even the widest bands to give an acceptable signal in interferograms constructed in this way. Because all compounds give rise to infrared absorption bands, the FT-IR spectrometer may be classified as a universal detector when chromatograms are constructed by the Gram-Schmidt algorithm. Since only 100 interferogram points are used for this calculation, Gram-Schmidt chromatograms can readily be calculated in real time and the progress of the chromatography can be followed in the same way as it with a conventional detector such as an FID.

The alternative way in which chromatograms are constructed involves computation of the spectrum immediately after each interferogram is measured, calculation of the ratio of this spectrum to a background spectrum measured when only the mobile phase is present in the beam, and converting this transmittance spectrum to absorbance [15]. The absorbance spectrum is then integrated between wavenumber limits that are chosen to represent the range over which a particular functional group absorbs. When operated in this fashion, the GC/FT-IR interface may be classified as a selective detector. When this technique was first implemented, computers were slow and spectra were calculated at a resolution of  $32 \text{ cm}^{-1}$  in order to be able to output a chromatogram in real time (i.e., while the next interferogram was being acquired.) With contemporary computing power, spectra can now be measured at much higher resolution so that more selective chromatograms can be output in real

time. This approach goes under several names. The first company to implement it (Nicolet) called chromatograms constructed in this way Chemigrams. Other implementations of the same algorithm went under a variety of names, so we will use the more generic term *functional group chromatogram* when describing results obtained using this approach.

Several variations on the basic technique described above have been reported. For example, the absorbance values between  $4000\text{ cm}^{-1}$  and the detector cutoff can be integrated. Since all compounds give rise to a signal when this approach is used, the GC/FT-IR system switches from being a selective detector to being a universal detector. In an alternative approach, the chromatogram is simply constructed from the value of the largest absorbance measured in each spectrum. GC/FT-IR interfaces used in this manner would also be considered universal detectors.

Since the bands that are measured in GC/FT-IR experiments are almost invariably very weak, their integrated absorbance varies linearly with the quantity of each analyte injected. On the other hand, when chromatograms are constructed using the Gram-Schmidt algorithm, the signal that is measured is proportional to the absorptance,  $1 - T(\tilde{\nu})$ , of each band. Since transmittance and absorbance are related as

$$T(\tilde{\nu}) = 10^{-A(\tilde{\nu})} = \frac{e^{-A(\tilde{\nu})}}{\ln 10} \quad (23.11)$$

and

$$e^{-x} = 1 - x + \frac{x^2}{2!} - \frac{x^3}{3!} + \frac{x^4}{4!} \cdots \quad (23.12)$$

therefore

$$\ln 10[1 - T(\tilde{\nu})] \approx A(\tilde{\nu}) \quad (23.13)$$

when the absorbance is low and absorptance becomes linearly proportional to absorbance and hence to the quantity of sample injected. The intensity of bands in Gram-Schmidt chromatograms varies linearly with concentration only when the transmittance of the strongest band is greater than about 0.9 [i.e.,  $A(\tilde{\nu}) < 0.05$  AU], while functional group chromatograms are linear over at least an order-of-magnitude greater range in concentration. This having been said, it should be recognized that only rarely is the peak absorbance of bands in GC/FT-IR spectra greater than 0.05 AU.

#### 23.2.4. Example of GC/FT-IR

There are many examples of components of mixtures that have identified by GC/FT-IR, so just one example will be given here. Norton and Griffiths [16] separated a mixture of eight barbiturates by capillary GC and measured their GC/FT-IR spectra using a light-pipe-based interface. Barbiturates are very polar molecules, and the absorptivity of several of their bands is atypically high (and much higher than the absorptivities of most bands in the spectra of most compounds of lower polarity.) As a result, the amount of each component required to yield an

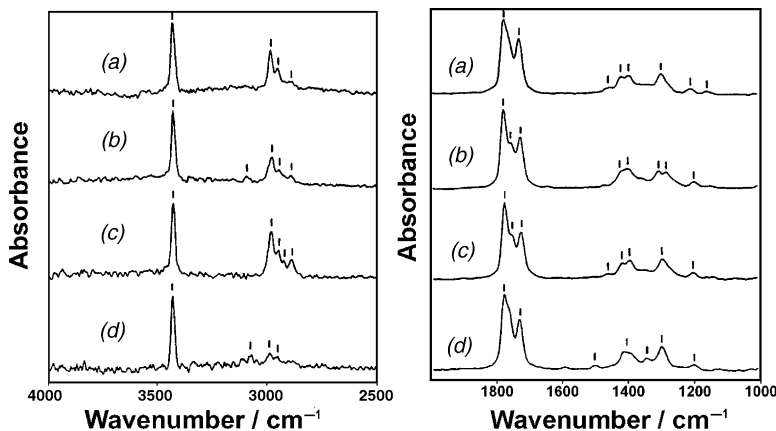


**Figure 23.4.** Vapor-phase GC/FT-IR spectra of 12.5-ng each of barbital, aprobarbital, butabarbital, and phenobarbital separated on a 30-m-long 0.32-mm-i.d. column measured as the output from the GC column flows through a light-pipe. (Reproduced from [16], by permission of Elsevier Publishing Co.; copyright © 1995.)

identifiable spectrum was sometimes less than 10 ng, an unusually low detection limit for this technique. Representative spectra are shown in Figure 23.4.

### 23.3. MOBILE-PHASE ELIMINATION APPROACHES FOR GC/FT-IR

#### 23.3.1. Introduction

GC/FT-IR measurements based on light-pipes have two fundamental disadvantages: They lack sensitivity and require libraries of vapor-phase reference spectra. In principle, the absorbance of spectra measured on a light-pipe-based GC/FT-IR interface could be increased by a factor of 10 if the light-pipe were made 10 times longer and the diameter were reduced by a factor of  $\sqrt{10}$ . However, in this case, 90% of the incident radiation is lost by vignetting. Furthermore, the beam would undergo  $\sim 30$  times more reflections as it passes through the light-pipe than for the shorter, wider light-pipe. The transmittance of typical 10-cm light-pipes is about 0.1. The transmittance of a 0.1-mm-i.d. 10-m-long light-pipe would be less than  $10^{-6}$ , which is far too small to allow a detectable signal to be measured. Obviously, another way to reduce the effective diameter of the beam must be found.

#### 23.3.2. Matrix Isolation GC/FT-IR

The first approach in which the sample was concentrated into a spot that was smaller than 1 mm in diameter was made by Reedy et al. [17], who mixed a small amount of argon with the helium mobile phase and sprayed the effluent of the column onto a rotating gold disk that was cooled to about 12 K. This temperature is

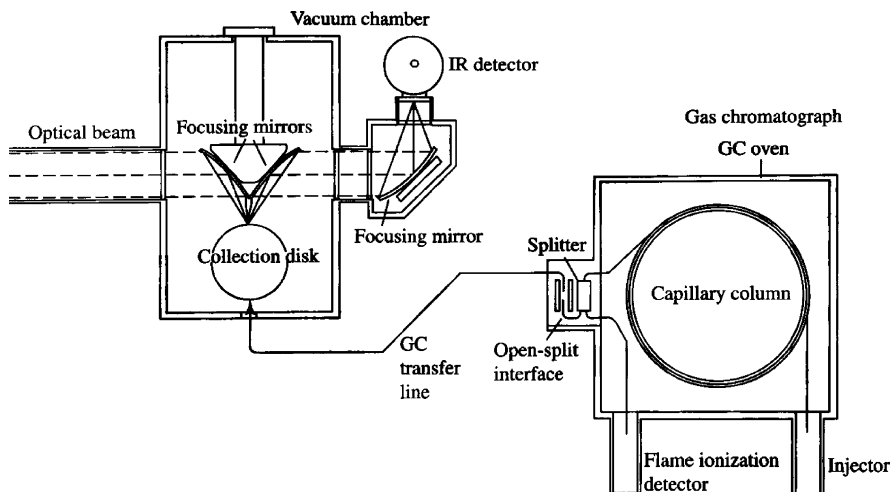


**Figure 23.5.** Cryolect matrix-isolation GC/IR interface. (Reproduced from [17], by permission of the American Chemical Society; copyright © 1985.)

low enough to condense the argon, along with each separated component of the sample, but high enough that helium does not condense and can be pumped away. To measure the spectrum, the infrared beam is passed through the argon matrix, reflected from the gold surface so that it passes again through the argon layer, and is then focused onto an MCT detector, as shown in Figure 23.5.

Each trapped component is surrounded by argon atoms and thus is fairly isolated from other analyte molecules. As a result of this *matrix isolation*, the width of bands in the spectra of light molecules is reduced significantly. Since the integrated absorbance of a given band when the spectrum of a molecule either in an argon matrix or in the vapor phase is about the same, the band intensities in the GC/FT-IR spectra of a given amount measured by this matrix isolation approach are considerably greater than if the same amount of material had been measured with a light-pipe-based interface, even if the area over which the sample had been deposited was about the same as the cross-sectional area of the light-pipe. In reality, the width of each GC peak that is trapped in an argon matrix is about three times smaller than the i.d. of a light-pipe. As a result, the detection limits obtained using a matrix isolation interface are at least an order of magnitude less than those obtained using a light-pipe interface. The smaller the molecule, the greater the factor by which the widths of the bands in its spectrum are reduced and the greater the advantage of the matrix-isolation system over a light-pipe-based interface.

In practice, however, the matrix-isolation GC/FT-IR interface has three main drawbacks:

- It is mechanically complex.
- Matrix-isolation spectra cannot be compared to spectra found in libraries of either conventional condensed- or vapor-phase reference spectra.

- Because the IR beam is reflected from the opposite side of the gold cylinder from the point at which the sample was deposited, measurements are not made in real time.

As a result, while instruments based on this principle are still available commercially [18], relatively few units have been sold in the past decade.

### 23.3.3. Direct Deposition GC/FT-IR

At first glance it may be thought that the disadvantage caused by the difference between matrix isolation spectra and conventional condensed-phase spectra could be overcome simply by eliminating the argon from the mobile phase and depositing each component directly on the gold cylinder. The problem with this approach is that the thickness of the layer of the analyte would be much less than the wavelength of mid-infrared radiation. If, for example, 1 ng of a molecule is deposited uniformly over a 0.3-mm-diameter circle, the thickness of the layer is  $\sim 10$  nm. For such a thin layer, reflection-absorption measurements must be made at grazing incidence (see Section 13.3). Since the beam required for reflection-absorption measurements at an incidence angle of, say,  $75^\circ$  is highly elliptical, the sensitivity would be reduced significantly by comparison with a putative measurement made with a circular beam with a diameter of 0.3 mm. In practice, if compounds that elute from a gas chromatograph are to be condensed in the absence of a thick argon matrix, deposition on an infrared-transparent material and measurement of the transmission spectrum is more appropriate.

The latter approach was first reported by Griffiths' group [19] and first developed by Bio-Rad into a commercial instrument called the Tracer [20]. An instrument based on the same principle was subsequently developed by Bourne Scientific as the IRC [21]. All these instruments operate on the same basic principle. The effluent from the GC is sprayed onto a liquid-nitrogen ( $\text{LN}_2$ )-cooled ZnSe plate via a heated 50- $\mu\text{m}$ -diameter tube, the end of which is held  $\sim 100$   $\mu\text{m}$  from the surface of the plate. With this arrangement, each component can be deposited as a spot of diameter of  $\sim 100$   $\mu\text{m}$  if the substrate is stationary and a trace with a width of  $\sim 100$   $\mu\text{m}$  if the substrate is moving (as is the case in practice). Transmission spectra of this trace are measured with optics that are similar to those of a rudimentary infrared microscope. Since the diameter of the deposited analyte is about three times less than the one formed during the matrix-isolation deposition, the integrated intensity of the bands from a given amount of material injected into the chromatograph is almost an order of magnitude higher. In fact, measurable spectra of considerably less than 1 ng of polar compounds deposited in this manner can be measured in less than 1 second (see Figure 23.6).

Comparison of Figures 23.4 and 23.6 shows the enormous difference between the spectra of barbiturates in the vapor and condensed phases. For these two sets of spectra, the amount of each barbiturate injected for the light-pipe measurement was  $\sim 30$  times higher than the amount measured by direct deposition. The difference between vapor- and condensed-phase spectra is, of course, greatest for

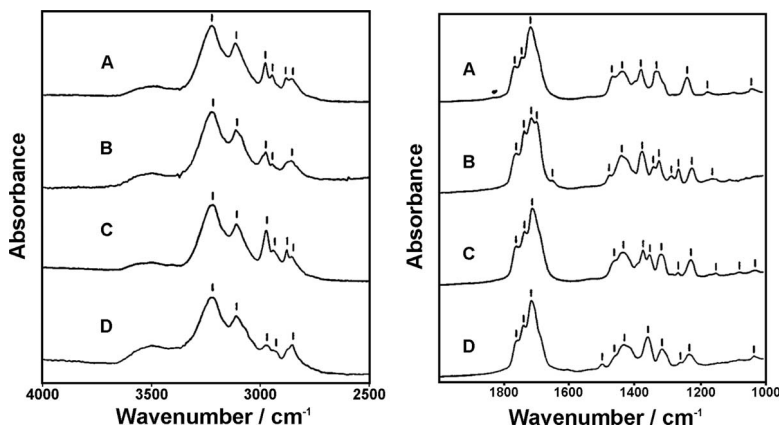


**Figure 23.6.** Direct-deposition GC/FT-IR spectra of 375 pg each of barbital, aprobarbital, butabarbital, and phenobarbital; see Figure 23.5 for details of the separation. (Reproduced from [16], by permission of Elsevier Publishing Co.; copyright © 1995.)

compounds exhibiting strong hydrogen bonding. Surprisingly, perhaps, the spectra of materials deposited onto a cooled ZnSe substrate in this way are little different from standard reference spectra of materials prepared as KBr disks. For example, Norton and Griffiths have shown that several barbiturates with very similar spectra can be identified by searching direct-deposition (DD) GC/FT-IR spectra against the Georgia State Crime Laboratory library of infrared spectra of commonly abused substances in which all the barbiturates were prepared as KBr disks [16].

The detection limits of DD-GC/FT-IR measurements have not yet reached their ultimate detection limits. Heaps and Griffiths have demonstrated that a further sensitivity increase in these measurements can be achieved by coating the ZnSe substrate with a very thin layer of silver or gold nanoparticles [22]. When thin ( $\sim 5$  nm) films of metal particles are deposited on dielectric substrates, typically by physical vapor deposition, the absorbance of thin organic films on the surface of the nanoparticles is increased significantly. This phenomenon has been dubbed surface-enhanced infrared absorption (SEIRA) spectroscopy and has been studied extensively by Osawa's group in Japan. Osawa showed that the spectra of molecules within about 5 nm of the metal surface are enhanced by between one and two orders of magnitude [23]. When the DD-GC/FT-IR experiment is carried out using a silver-coated ZnSe substrate cooled with  $\text{LN}_2$ , *n*-, *sec*-, *iso*-, and *tert*-butylbenzene was each recognized as the first "hit" when that molecule was injected at a level that yielded nothing but noise when deposited on an uncoated substrate [22]. This performance was achieved even though the reference library spectra were measured with the analytes in the liquid state at room temperature. Although this technique is not commercially available at the time of this writing (2006), this paper indicates that further reductions in the detection limits achievable by DD-GC/FT-IR are still feasible.

Even without the application of SEIRA, the sensitivity of the DD-GC/FT-IR interface has now reached the point that it rivals, and sometimes exceeds, that of quadrupole GC/MS instruments. Indeed, one user of a DD-GC/FT-IR interface had to purchase an ion-trap GC/MS interface because her quadrupole GC/MS system had lower sensitivity than the Bio-Rad Tracer [24]! However, the popularity of GC/FT-IR has, in anything, waned since 1990. Although this is partly a matter of expense it is also a matter of education. Regrettably, many GC/MS users are unaware that the first “hit” obtained by a spectral search routine is often not the correct answer and hence do not understand the need for a complementary technique.<sup>1</sup> Finally, the DD-GC/FT-IR interface is mechanically complex and more prone to down-time than GC/MS. The DD-GC/FT-IR interface must be simpler and more robust than the versions that are commercially available at the time of this writing if this technique is to gain more widespread popularity. For more details of GC/FT-IR interfaces of all types, the review article by Visser is strongly recommended [25].

### 23.4. HPLC/FT-IR INTERFACE

#### 23.4.1. Measurements Made with Flow Cells

In general, the interface between chromatographs and FT-IR spectrometers can be divided into two types: those based on flow cells (such as the light-pipe GC/FT-IR interface) and those based on elimination of the mobile phase (such as the DD-GC/FT-IR interface). Although not without its limitations, as outlined earlier in this chapter, the flow-cell (light-pipe) approach for GC/FT-IR has proved to be a useful tool for the solution of a number of important problems of chemical analysis. Unfortunately, the same cannot be said for HPLC/FT-IR measurements, in which the column effluent is simply passed continuously through a flow cell. Let us examine the reason for this situation.

We saw in Section 11.1.4 that the pathlength of a solution that contains 1 ppm of a trace component must be 1 cm if the solute is to yield a recognizable spectrum. In practice, it is very rare to encounter a solvent with such good transmission characteristics, and a maximum pathlength of 1 mm (with a concomitant increase in the detection limit) is more realistic. Let us now look at the case for HPLC/FT-IR measurements made using a flow cell. Consider first the case for a solute that has characteristic absorption bands in a spectral region in which the solvent is quite transparent when the pathlength of the cell is 1 mm. In this case, the concentration of the solute must be at least 10 ppm if these bands are to be observable at a SNR of at least 10.

The diameter of a flow-through cell needs to be no greater than 3 mm to avoid losses by vignetting, provided that the cell is mounted in appropriate beam-condensing

<sup>1</sup>In a personal communication to one of us (PRG), Fred McLafferty, one of the leading mass spectro-metrists in the country, estimated that at least 50% of the first “hits” of all GC/MS searches are incorrect.



optics. Thus, the volume of liquid present in the cell at any time is  $\pi \times (1.5)^2 \times 1 \mu\text{L}$ , or  $\sim 7 \mu\text{L}$ . For a typical HPLC separation made using a column with an i.d. of 0.46 mm, the flow rate is  $\sim 1 \text{ mL} \cdot \text{min}^{-1}$  and the FWHH of a typical peak is about 15 s, or 250  $\mu\text{L}$ . Thus, on the average, no more than  $(7/250) \times 100\%$ , or  $\sim 3\%$ , of a given component is present in the flow cell at any given time as the peak passes through the cell. In this case, more than 2.5  $\mu\text{g}$  of a given component must be injected onto the column if the strongest band is to be detectable. The fraction of a given peak that can be present in a 7- $\mu\text{L}$  flow cell is increased if the i.d. of the column is reduced. However, the capacity of microbore HPLC columns decreases with their cross-sectional area, so that a smaller sample volume must be injected if the column is not to be saturated.

Unfortunately, the example above represents the ideal case, where absorption by the solvent in a cell with a pathlength of 1 mm is negligible. Even for a relatively weakly absorbing solvent such as *n*-hexane, the pathlength must be restricted to 0.1 mm if absorption is not to be excessive (see Section 11.1). In this case, the limit of detection for HPLC/FT-IR measurements made using a 1-mm-diameter flow cell is increased to 25  $\mu\text{g}$ . With a very strongly absorbing solvent such as water, the pathlength of the cell must be reduced by at least another order of magnitude, so that the limit of detection is now 250  $\mu\text{g}$ . Over 90% of all HPLC separations today are carried out by reverse-phase (RP) chromatography, with water as one component of the mobile phase. Needless to say, very few successful RP-HPLC/FT-IR measurements have been made using flow cells.

The situation is made even more difficult when the separation is effected by gradient elution, since accurate compensation for absorption by the solvent when its composition is changing throughout the measurement is exceptionally difficult. In fact, the only chromatographic technique for which the use of a flow cell does not completely preclude the use of flow-cell HPLC/FT-IR is size-exclusion chromatography (SEC) with a mobile phase that is highly transparent throughout most of the mid-infrared spectrum. A noble effort involving the use of deuterated chloroform as the mobile phase in conjunction with a microbore HPLC column was reported [26], but it is unlikely that many chromatographers would use pure  $\text{CHCl}_3$ , let alone  $\text{CDCl}_3$ , as the mobile phase for any HPLC separation.

### 23.4.2. Mobile-Phase Elimination Techniques for HPLC/FT-IR

Since most of the problems associated with flow-cell HPLC/FT-IR interfaces are caused by the presence of the mobile phase, the obvious solution is to eliminate the solvent prior to measurement of the infrared spectrum of the solute. A number of techniques for mobile-phase elimination have been reported in the past, with varying degrees of success. For conventional HPLC separations performed with 4.6-mm-i.d. columns, the biggest difficulty is complete evaporation of the solvent, for which the flow rate is typically  $1 \text{ mL min}^{-1}$ , while the solute is deposited simultaneously in a small area on a suitable substrate.

One early approach to reducing the volume occupied by an HPLC peak was to use microbore columns. In this case, the volume flow rate of the mobile phase could

be reduced without changing its linear velocity and hence the chromatographic efficiency. (It should be noted, however, that the capacity of microbore columns is much less than that of conventional 4.6-mm-i.d. columns, so that the volume of the sample that can be injected is proportionately less.) Jinno was the first to demonstrate the success of this approach with microbore columns of less than 1 mm i.d. Solutes were deposited on a moving window, and the spectrum of each component was measured after the chromatography was complete [27,28]. In several ways, Jinno's work can be seen to presage the contemporary practice of HPLC/FT-IR described later in this chapter. Griffiths et al. [29,30] and Kalasinsky et al. [31,32] investigated the use of powdered substrates to facilitate solvent evaporation. In this case, diffuse reflection rather than transmission spectra were measured, but none of the DR interfaces was particularly user friendly, and real-time operation was difficult.

More recent efforts became geared toward the development of a device that is analogous to the DD-GC/FT-IR interface (i.e., one in which the mobile phase is eliminated while depositing the analytes in as small an area as possible), so that ideally at least, the spectrum of each eluate can be measured in real time. Many different techniques for solvent elimination have been applied to the DD-HPLC/FT-IR interface, including thermospray [33], concentric flow nebulizer [34], particle beam (sometimes called a monodisperse aerosol generator) [35], ultrasonic nebulizer [36], and pneumatic nebulizer [37,38]. A comparison of many of these techniques has been made by Somsen et al. [39], but at the time of this writing, the "book is still out" as to the identity of the optimum approach. An excellent summary of HPLC/FT-IR interfaces is to be found in a review article by Kalasinsky and Kalasinsky [40].

The first commercially successful off-line DD-HPLC/FT-IR interface was the LC Transform, made by Lab Connections [41]. With this device, nebulization is initiated ultrasonically and the solvent is evaporated with either a thermospray or a concentric flow nebulizer. The solutes are first deposited on a rotating germanium disk on the underside of which a thick layer of aluminum has been deposited. After the deposition step, the disk is then moved to a specular reflection accessory that is mounted in the sample compartment of a standard FT-IR spectrometer. The developers of the LC Transform recognized that it is more convenient to measure the spectra of the components that had been deposited on the disk by reflection spectrometry than by transmission. However, the deposition of a very thin film of each eluate on a metal substrate would not allow its reflection-absorption spectrum to be measured with adequate efficiency without resorting to grazing incidence measurements, for which the disadvantages were discussed in Section 23.3.3.

To measure the spectrum at each point of the deposit, the infrared beam is passed through the sample deposited on the Ge plate and reflected from the aluminum backing and again passes through the Ge plate and the sample, as shown in Figure 23.7. The high refractive index of Ge causes the beam to be refracted on entering the plate so that it hits the aluminum film at an incidence angle of  $\sim 10^\circ$ . The result is that on the second pass through the analyte, the beam is displaced relative to the first pass by less than 2 mm. Since the diameter of the eluates deposited is typically

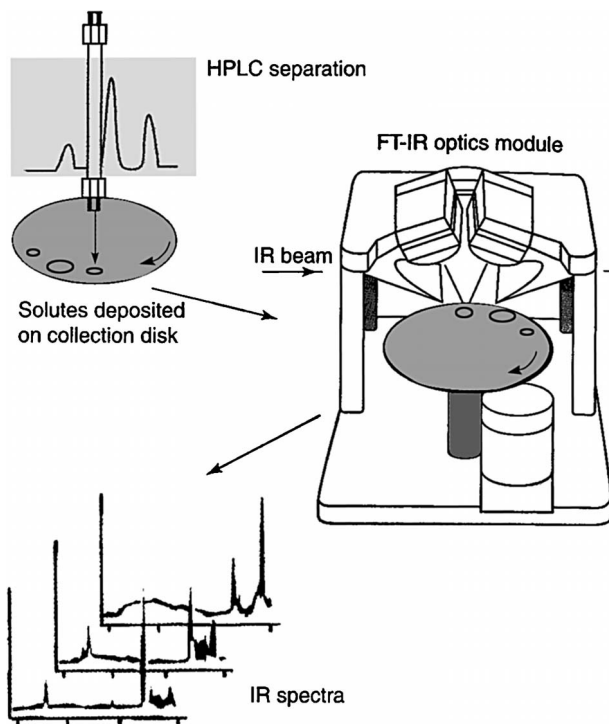


**Figure 23.7.** Mode of operation of the LC Transform. Components that have eluted from the HPLC column are deposited on the rotating substrate (top left). After deposition, the disk is moved into the beam of a specular reflection accessory mounted in the sample compartment of the FT-IR spectrometer (right) where the spectra are measured (bottom left.) (Courtesy of Lab Connections, a wholly owned subsidiary of Mocon, Inc.)

2 to 4 mm, the chromatographic resolution is not degraded significantly. Because the spot size is much larger than can be achieved, for example, in the DD-GC/FT-IR interface, the sensitivity of the early versions of the LC Transform was not very high. Thus, the principal application was for size-exclusion chromatography, for which a large volume of the sample could be injected onto the column without greatly degrading the resolution. More recent modifications have allowed the spot size to be reduced, so that this device can now be used successfully with normal- and reverse-phase HPLC.

The LC Transform has one fundamental drawback: It cannot be used to identify the components of mixtures in real time since the process takes place in two steps, deposition and spectral measurement. For real-time HPLC/FT-IR measurements, the spectrum must be acquired very shortly after the deposition. Just how long after the deposition the spectrum should be measured for the technique to be classified as taking place in real time is an interesting philosophical question. With few exceptions, all HPLC detectors are separated from the end of the column by a length of tubing, so that there is always a short time delay between the elution

of a given component and its detection. With online direct-deposition HPLC/FT-IR interfaces, this delay is usually a few seconds rather than a few milliseconds. In the opinion of these authors, the distinction is trivial and the devices to be described in the next two paragraphs will be classified as operating in an online manner.

The first online DD-HPLC/FT-IR interface was reported by Lange et al. [42], who interfaced a concentric flow nebulizer to the Bio-Rad Tracer. Solutes were deposited on a continuously moving ZnSe substrate as a trace that was  $\sim 150\text{ }\mu\text{m}$  in width. In a manner analogous to DD-GC/FT-IR measurements, the solute spots were transported into the beam of a rudimentary microscope, and transmission spectra were measured at intervals of 1 to 2 s. It was not possible to eliminate aqueous solvents at a rate of more than about  $50\text{ }\mu\text{L min}^{-1}$  with the concentric flow nebulizer, so the separations either had to be carried out on a 1-mm-i.d. column or to use a wider-bore column with an output stream splitter. Although Robertson et al. reported the elimination of aqueous mobile phases at flow rates up to  $1\text{ mL} \cdot \text{min}^{-1}$  using a monodisperse aerosol generator and achieved spot diameters of between 300 and  $50\text{ }\mu\text{m}$  [35], it was not possible to direct the IR beam inside the vacuum chamber, and this device was never used online.

The only online DD-HPLC/FT-IR interface that has been introduced commercially is the Bourne Scientific IRC. The IRC is a real-time direct-deposition interface that can be used for identifying the components of mixtures separated by GC, HPLC, and SFC. In its HPLC/FT-IR manifestation, an ultrasonic nebulizer, desolvation tube, and vacuum chamber are used to evaporate the solvent from the HPLC stream. The last of the solvent evaporates as the droplets drift through the desolvation chamber, the temperature of which can be varied from 25 to  $150^{\circ}\text{C}$ . The sample residue then condenses onto a moving ZnSe window, the temperature of which can be varied between 25 and  $100^{\circ}\text{C}$ . The data station collects a continuous array of spectra as the dry sample track on the window moves through the focused beam of the spectrometer. Chromatograms may be plotted with either the Gram-Schmidt or functional group algorithms, and spectra are displayed simply by clicking on the appropriate region of the chromatogram. The software finds the chromatographic peaks automatically, and produces a spectrum for each one. For most compounds, identifiable spectra are obtained from 20 ng of material injected onto the column, although the limit of detection is, of course, affected by the volatility of the solute. (More volatile components are separated faster and with greater efficiency by capillary GC, and the detection limits of the DD-GC/FT-IR interface are lower than those of the DD-HPLC/FT-IR by well over an order of magnitude.)

HPLC/FT-IR measurements have considerable potential utility both because the infrared reference spectra of well over 150,000 solid samples prepared as KBr disks are available and because the spectrum of a given compound measured by DD-HPLC/FT-IR is very similar to the corresponding KBr disk spectrum, so the number of compounds that can potentially be identified by DD-HPLC/FT-IR is very large. However, efforts to fabricate a rugged, sensitive, online HPLC/FT-IR interface have been taking place for over 20 years, and a suitable instrument has not yet been introduced commercially, even for normal-phase separations, where the mobile phase is usually quite volatile. The prognosis for reverse-phase separations, where

water is almost invariably a component of the mobile phase, is even less positive, especially when the mobile phase contains nonvolatile salts such as phosphates and citrates.

### 23.5. SFC/FT-IR INTERFACE

Supercritical fluid chromatography (SFC) is a hybrid of GC and HPLC in which the mobile phase is a compound that is held above its critical temperature ( $T_c$ ) and critical pressure ( $P_c$ ). By far the most common compound that is used as an SFC mobile phase is  $\text{CO}_2$ , for which  $T_c \approx 31^\circ\text{C}$  and  $P_c \approx 73$  atm. The diffusivities of many compounds in supercritical  $\text{CO}_2$  are high enough that either packed-column or open-tubular columns may be used. The solvent strength of supercritical  $\text{CO}_2$  is roughly intermediate between those of *n*-hexane and benzene; thus, many compounds that are too nonvolatile to be separable by GC can be separated by SFC. Detection of solutes separated by SFC is also easy, since GC detectors such as the FID and HPLC detectors such as UV absorption detectors can both be used.

Detection by infrared spectrometry should also be relatively easy with a flow cell.  $\text{CO}_2$  is a small, symmetrical, nonpolar molecule; thus, it has a very sparse infrared spectrum. Of the two infrared-active fundamental modes, the bend at  $\sim 667\text{ cm}^{-1}$  is below the cutoff of narrowband MCT detectors, and the antisymmetric stretch at  $\sim 2348\text{ cm}^{-1}$  is in a spectral region where few compounds have fundamental absorption bands. Thus, it may be thought that supercritical  $\text{CO}_2$  would be the ideal solvent for infrared spectrometry and that the sensitivity of SFC/FT-IR interfaces based on the use of flow cells would be close to that of light-pipe-based GC/FT-IR interfaces. Furthermore, since supercritical  $\text{CO}_2$  vaporizes as soon as the pressure is released, the DD-SFC/FT-IR interface should be far simpler than the corresponding DD-HPLC/FT-IR interface. In practice, however, several factors mitigate against the SFC/FT-IR interface.

First, supercritical fluid chromatography has not been readily accepted by analytical chemists. The biggest drawback to SFC is the need for a suitable restrictor, which is a device mounted at the end of the column that restricts the flow to the point that the pressure can be maintained well above  $P_c$  and yet allows the appropriate flow rate. These restrictors must withstand pressures that can sometimes reach above 500 atm. They are also very easily clogged, so that maintaining a constant pressure and flow rate is not trivial. The solvent strength of supercritical fluids depends strongly on their density, and the maintenance of a constant pressure throughout the length of a column is not an easy matter, especially when packed columns are used for the separation.

From a spectroscopic viewpoint, although the two fundamental absorption bands of  $\text{CO}_2$  do not present a major problem for flow-cell-based SFC/FT-IR measurements, a broad doublet in the region near  $1400\text{ cm}^{-1}$  does. These bands are assigned to the first overtone of the bend and the (infrared forbidden) symmetric stretch, which exhibit second-order coupling, or Fermi resonance (see Section 1.2). In the supercritical state, this doublet becomes weakly allowed (see Figure 23.8).

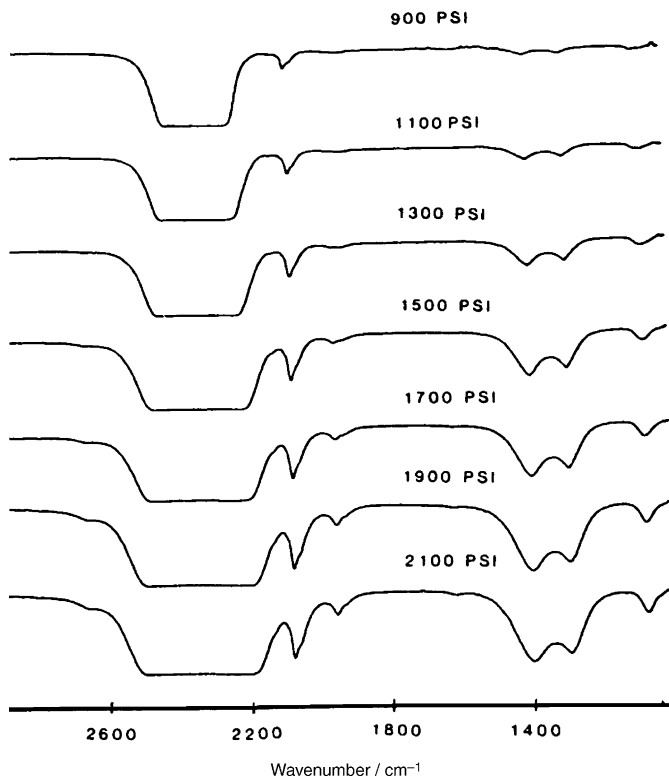


**Figure 23.8.** Transmittance spectra of supercritical CO<sub>2</sub> in a 1-cm-pathlength flow cell at 40°C and pressures between 900 psi (61 atm) and 2100 psi (142 atm). The intensification of the Fermi doublet near 1400 cm<sup>-1</sup> with increasing pressure should be noted. (Reproduced from [43], by permission of the American Chemical Society; copyright © 1986.)

As the pressure is increased, the doublet becomes disproportionately strong [43]. Since SFC separations are usually performed using a pressure program (analogous to temperature programming in GC and gradient elution in HPLC), the intensity of this band usually increases throughout the chromatogram, and it is difficult to compensate for changes that occur in order to observe the spectrum of trace solutes at high levels of ordinate expansion. Nonetheless, several SFC/FT-IR measurements made using flow cells have been reported, as have several examples of spectra measured with flow cells [44–47].

The problem of absorption by the mobile phase should disappear if the mobile phase is eliminated prior to measurement of the infrared spectrum. (This is particularly important when polar modifiers such as methanol are added to the CO<sub>2</sub> for separations made with packed columns.) Not surprisingly, therefore, several reports of DD-SFC/FT-IR measurements have appeared in the literature. A review article by Bartle summarizes many of these results [47]. Detection limits are in the low-nanogram range, as shown by the spectra in Figure 23.9, and measurements may be

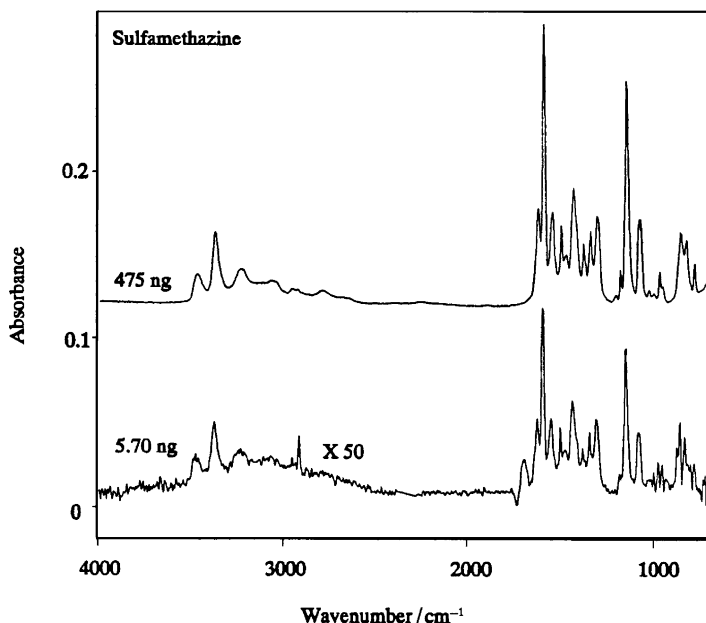


**Figure 23.9.** On-line DD-SFC/FT-IR spectra of sulfamethazine for injected quantities of 475 and 5.7 ng. (Reproduced from [48], by permission of Elsevier Publishing Co.; copyright © 1997.)

made even when the pressure in the column is over 500 atm, as shown in Figure 23.10 [48]. It may be noted that no flow cell for SFC/FT-IR has been reported that can withstand pressure this high. Even though DD-SFC/FT-IR measurements initially appeared to be quite promising, and the Bourne Scientific IRC can be modified for DD-SFC/FT-IR measurements fairly simply, this interface has not proved to be very popular, for the reasons given earlier in this section.

### 23.6. TGA/FT-IR

The term *hyphenated technique* was first used by Tomas Hirschfeld [49] to describe the coupling of two instruments with complementary functions, so that the output gives significantly more analytical information than either instrument used individually. So far we have discussed the case where one of these instruments is a chromatograph, which separates but does not identify each component, and the other is an FT-IR spectrometer that performs the identification of each of these components. The first instrument does not have to be a chromatograph, however. For example, during operation of a thermogravimetric analyzer, gases are evolved during the controlled pyrolysis of a sample as it is heated. The output of a simple TGA is the percentage weight loss of the sample as the temperature is ramped up. An FT-IR spectrometer can be used to identify and quantify each component of the gas that is being evolved (with the exception of homonuclear diatomics) in real time.

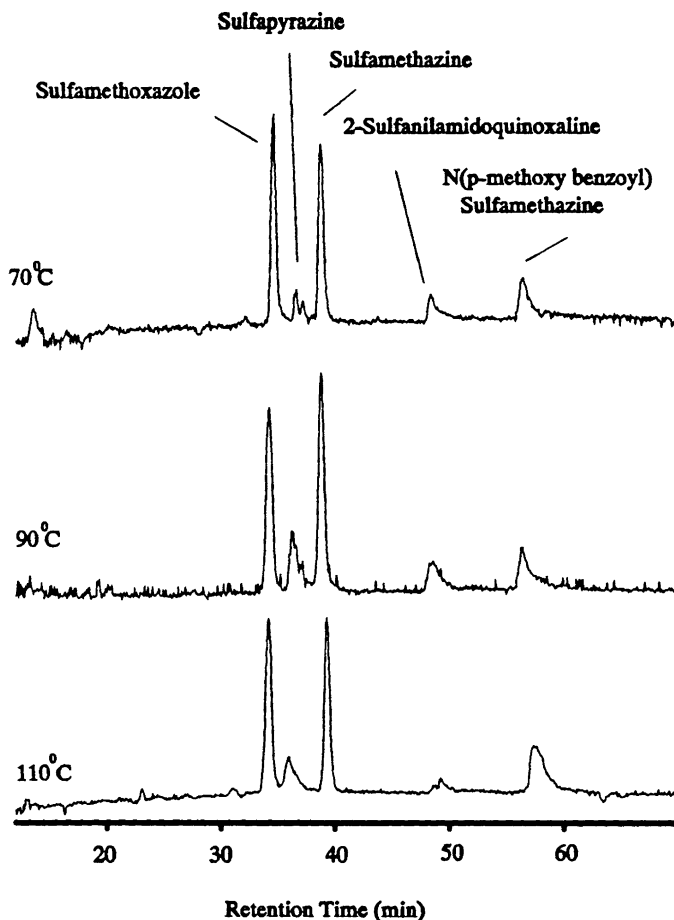


**Figure 23.10.** DD-SFC/FT-IR chromatogram of the separation of five sulfa drugs (sulfamethoxazole, sulfapyrazine, sulfamethazine, sulfanilamidoquinoxaline, and *N*-(*p*-methoxybenzoyl)sulfamethazine constructed from the integrated absorbance between 1800 and 1640  $\text{cm}^{-1}$  for column temperatures of 70, 90, and 110°C. For each chromatogram, the pressure was held at 3000 psi ( $\sim 200$  atm) for 10 min and then ramped at 200 psi per minute to a final pressure of 7500 psi. (Reproduced from [48], by permission of Elsevier Publishing Co.; copyright © 1997.)

This interface is analogous to a light-pipe-based GC/FT-IR system but is somewhat simpler because the flow rate of the gas required for TGA is larger than that for GC, and the volume of the gas cell can be much larger than 80  $\mu\text{L}$ .

The first measurements of molecules that were involved during thermogravimetric analysis were reported by Lephardt and Fenner [50,51], who showed the time evolution of several gases that are evolved when tobacco or other thermally labile samples are heated. Despite the obvious information that this experiment yielded and the simplicity of the apparatus, it took several years for instrument companies to introduce a commercial TGA/FT-IR interface. The gas cell installed in these systems is much



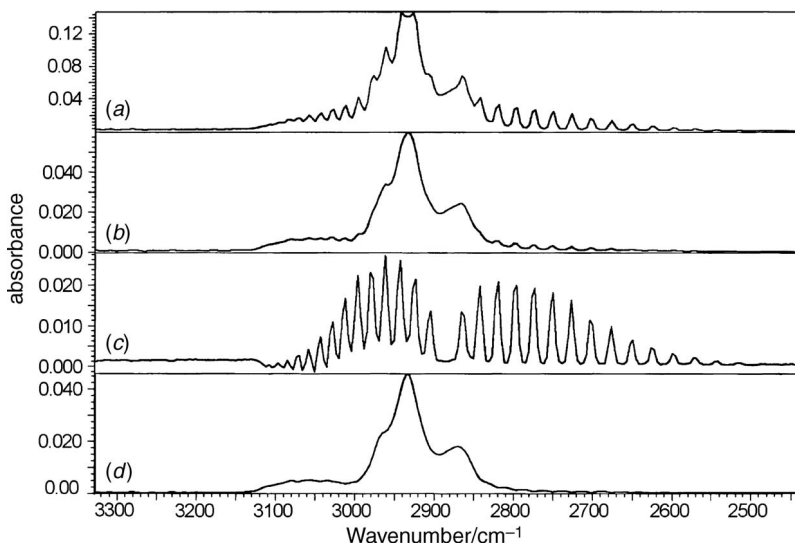


**Figure 23.11.** TGA/FT-IR spectra obtained during the thermogravimetric analysis of PVC (a) after 13.61 min (trailing edge) and (b) 13.15 min (leading edge). (c) Result of spectral subtraction of (b) from (a), giving the spectrum of HCl. (d) Result of spectral subtraction of (a) from (b), giving the spectrum of the phthalate plasticizer. (Reproduced from [52], by permission of John Wiley & Sons; copyright © 2002.)

larger than GC/FT-IR light-pipes. As a result, its transmission is far higher and MCT detectors are rarely needed. With the exception of the detector that is needed, operation of the TGA/FT-IR and light-pipe GC/FT-IR interfaces is quite similar. Interferograms are recorded throughout the thermal decomposition, and either Gram-Schmidt or functional group thermograms can be constructed. Results obtained during a typical TGA/FT-IR analysis are shown in Figure 23.11. In this example, a sample of poly(vinyl chloride) was subjected to a linear temperature ramp, and spectra of the evolved gases were measured at intervals of 2 s. Unlike the case for GC/FT-IR measurements, it is rare that a single compound is present in the cell at a given time, and different molecules elute at different rates. In this example, spectra measured from the trailing and leading edges of a particular peak in the thermogram are shown in Figure 23.11a and b, respectively. Subtraction of these spectra with appropriate scaling factors enables the spectra of the two components to be obtained. The spectrum shown in Figure 23.11c is clearly that of HCl. The spectrum in Figure 23.11d is that of a phthalate plasticizer. For more details on the TGA/FT-IR interface, the review article by Hellgeth is strongly recommended [52].

### 23.7. OTHER COUPLED TECHNIQUES

FT-IR spectrometry has also been used to identify components separated by thin-layer chromatography (TLC) and capillary electrophoresis (CE). Many reports of

the identification of the components of mixtures that have been separated by TLC have been reported. Since most of these do not describe instrumental developments, they are not discussed in this chapter. A comprehensive review of TLC/FT-IR has been written by Chalmers [53], and interested readers are encouraged to read this article for more details.

The development of the CE/FT-IR interface is still in its infancy at the time of this writing, and a discussion of the strengths and weakness of this technique is premature at this point. Suffice it to say that the major problem with CE/FT-IR is that the mobile phase is an aqueous buffer solution. Since most buffers are nonvolatile, they co-deposit with the analytes. For buffers such as phosphates, absorption by the anion is much greater than absorption by the analytes, and careful spectral subtraction is needed to obtain identifiable spectra of the separated molecules. (Of course, the same problem is found with buffered mobile phases in DD-HPLC/FT-IR measurements.) Furthermore, CE columns have a very limited capacity, so that the sample quantity required to yield an identifiable spectrum is usually so great that the column capacity is exceeded. Despite this rather unpromising prognostication, some interesting developments are taking place and we can look forward to some more encouraging results in the future.

In many respects the development of coupled techniques mirrors the development of FT-IR spectrometry. Even though new results have been reported for over 30 years, reports of exciting new instruments, accessories, and applications are still appearing every year, and there seems to be little indication that this situation will change in the next decade. As noted in Chapter 1, FT-IR spectrometry has passed through its second childhood. However, it is nowhere near its seventh age.

## REFERENCES

1. C. L. Wilkins, G. N. Giss, G. M. Brissey, and S. Steiner, *Anal. Chem.* **53**, 113 (1981).
2. R. W. Crawford, T. Hirschfeld, R. H. Sanborn, and C. M. Wong, *Anal. Chem.* **54**, 817 (1982).
3. D. F. Gurka and L. D. Betowski, *Anal. Chem.* **54**, 1819 (1982).
4. D. F. Gurka, S. Billets, J. W. Brasch, and C. J. Riggle, *Anal. Chem.* **57**, 1975 (1985).
5. S. D. Richardson, A. D. Thurston, Jr., T. W. Collette, K. S. Patterson, B. W. Lykins, Jr., G. Majetich, and Y. Zhang, *Environ. Sci. Technol.* **28**, 592 (1994).
6. C. L. Wilkins, G. N. Giss, R. L. White, G. M. Brissey, and E. Onyiriuka, *Anal. Chem.* **54**, 2260 (1982).
7. C. L. Wilkins, *Anal. Chem.*, **66**, A295 (1994).
8. C. L. Wilkins, Directly-linked gas chromatography-infrared-mass spectrometry, in *Handbook of Vibrational Spectroscopy*, J. M. Chalmers and P. R. Griffiths, Eds., Wiley, Chichester, West Sussex, England, 2002, Vol. 2, p. 1627.
9. L. V. Azarraga, presented at the 27th Pittsburgh Conference on Analytical Chemistry and Applied Spectroscopy, Cleveland, OH, March 1976, Paper 374; *Appl. Spectrosc.* **34**, 224 (1980).
10. D. E. Henry, A. Giorgetti, A. M. Haefner, P. R. Griffiths, and D. F. Gurka, *Anal. Chem.* **59**, 2356 (1987).

11. P. Coffey and D. R. Mattson, A programmable specific GC detector–GC-FTIR system capable of on-the-fly functional group differentiation, presented at the 1977 International Conference on Fourier Transform Infrared Spectroscopy, Columbia, SC, June 1977, Paper MB6.
12. J. A. de Haseth and T. L. Isenhour, The direct reconstruction of chromatograms from interferometric GC-IR data, presented at the 1977 International Conference on Fourier Transform Infrared Spectroscopy, Columbia, SC, June 1977, Paper MB7.
13. J. A. de Haseth and T. L. Isenhour, *Anal. Chem.* **49**, 1977 (1977).
14. G. M. Brissey, D. E. Henry, G. N. Giss, P. W. Yang, P. R. Griffiths, and C. L. Wilkins, *Anal. Chem.* **56**, 2002 (1984).
15. P. Coffey, D. R. Mattson, and J. C. Wright, *Amer. Lab.* **10**(5), 126 (1978).
16. K. L. Norton and P. R. Griffiths, *J. Chromatogr. A* **703**, 383 (1995).
17. G. T. Reedy, D. G. Ettinger, J. F. Schneider, and S. Bourne, *Anal. Chem.* **57** 1602–1609 (1985).
18. Reedy Scientific Instruments, Inc., 197 West Harrison Street, Bourbonnais, IL 60914.
19. A. M. Haefner, K. L. Norton, P. R. Griffiths, S. Bourne, and R. Curbelo, *Anal. Chem.* **60**, 2441 (1988).
20. S. Bourne, A. M. Haefner, K. L. Norton, and P. R. Griffiths, *Anal. Chem.* **62**, 2448 (1990).
21. S. Bourne, *Amer. Lab.* **30**(16), 17F (1998).
22. D. A. Heaps and P. R. Griffiths, *Anal. Chem.* **77**, 5965 (2005).
23. M. Osawa, *Bull. Chem. Soc. Jpn.* **70**, 2861 (1997).
24. K. S. Kalasinsky, personal communication to P. R. Griffiths (1997).
25. T. Visser, Gas chromatography/Fourier transform infrared spectroscopy, in *Handbook of Vibrational Spectroscopy*, J. M. Chalmers and P. R. Griffiths, Eds., Wiley, Chichester, West Sussex, England, 2002, Vol. 2, p. 1605.
26. R. S. Brown and L. T. Taylor, *Anal. Chem.* **55**, 723 (1983).
27. K. Jinno, C. Fujimoto, and Y. Hirata, *Appl. Spectrosc.* **36**, 67 (1982).
28. K. Jinno, C. Fujimoto, and D. Ishii, *J. Chromatogr.* **239**, 625 (1982).
29. D. T. Kuehl and P. R. Griffiths, *Anal. Chem.* **52**, 1394 (1980).
30. C. M. Conroy, P. R. Griffiths, P. J. Duff, and L. V. Azarraga, *Anal. Chem.* **56**, 2636 (1984).
31. K. S. Kalasinsky, J. A. S. Smith, and V. F. Kalsinsky, *Anal. Chem.* **57**, 1969 (1985).
32. V. F. Kalasinsky, K. G. Whitehead, R. C. Kenton, J. A. S. Smith, and K. S. Kalsinsky, *J. Chromatogr. Sci.* **25**, 273 (1987).
33. A. M. Robertson, L. Wylie, D. Littlejohn, R. J. Watling, and C. J. Dowle, *J. Chromatogr. A* **588**, 15 (1991).
34. P. R. Griffiths and A. J. Lange, *J. Chromatogr. Sci.* **30**, 93 (1992).
35. R. M. Robertson, J. A. de Haseth, J. D. Kirk, and R. F. Browner, *Appl. Spectrosc.* **42**, 1365 (1988).
36. G. W. Somsen, E. W. J. Hooijschuur, C. Gooijer, U. A. Th. Brinkman, N. H. Velthorst, and T. Visser, *Anal. Chem.* **68**, 746 (1996).
37. M. A. Castles, L. V. Azarraga, and L. A. Carreira, *Appl. Spectrosc.* **40**, 673 (1986).
38. A. H. Dekmezian and T. Morioka, *Anal. Chem.* **61**, 458 (1989).

39. G. W. Somsen, C. Gooijer, and U. A. Th. Brinkman, *J. Chromatogr. A* **856**, 213 (1999).
40. K. F. Kalasinsky and V. F. Kalasinsky, High performance liquid chromatography/Fourier transform infrared spectroscopy, in *Handbook of Vibrational Spectroscopy*, J. M. Chalmers and P. R. Griffiths, Eds., Wiley, Chichester, West Sussex, England, 2002, Vol. 2, p. 1641.
41. Lab Connections, a wholly owned subsidiary of Mocon, Inc., 10 Bearfoot Road, Northborough, MA 01532.
42. A. J. Lange, D. J. J. Fraser, and P. R. Griffiths, *Anal. Chem.* **63**, 782 (1991).
43. K. H. Shafer, S. L. Pentoney, and P. R. Griffiths, *Anal. Chem.* **58**, 58 (1986).
44. R. C. Wieboldt, K. D. Kempfert, and D. L. Dalrymple, *Appl. Spectrosc.* **44**, 1028 (1990).
45. R. C. Wieboldt, G. E. Adams, and D. W. Later, *Anal. Chem.* **60**, 2422 (1988).
46. R. C. Wieboldt, K. D. Kempfert, D. W. Later, and E. R. Campbell, *J. High Resolut. Chromatogr.* **12**, 106 (1989).
47. K. D. Bartle, SFC/FT-IR (flow cell and direct deposition), in *Handbook of Vibrational Spectroscopy*, J. M. Chalmers and P. R. Griffiths, Eds., Wiley, Chichester, West Sussex, England, 2002, Vol. 2, p. 1634.
48. J. Yang and P. R. Griffiths, *J. Chromatogr. A* **785**, 111 (1997).
49. T. Hirschfeld, *Anal. Chem.* **52**, 299A (1980).
50. J. O. Lephardt and R. A. Fenner, *Appl. Spectrosc.* **34**, 174 (1980).
51. J. O. Lephardt and R. A. Fenner, *Appl. Spectrosc.* **35**, 95 (1981).
52. J. W. Hellgeth, Thermal analysis-IR methods, in *Handbook of Vibrational Spectroscopy*, J. M. Chalmers and P. R. Griffiths, Eds., Wiley, Chichester, West Sussex, England, 2002, Vol. 2, p. 1699.
53. J. M. Chalmers, Thin-layer chromatography and vibrational spectroscopy, in *Handbook of Vibrational Spectroscopy*, J. M. Chalmers and P. R. Griffiths, Eds., Wiley, Chichester, West Sussex, England, 2002, Vol. 2, p. 1683.



## INDEX

- Abscissa scale, 46  
Absorbance(s), 13, 197, 205, 210, 211, 219, 255, 259  
Absorbance matrix, 214, 220  
Absorbance spectrum, 110, 212–216, 225, 255  
Absorption, 33  
  band(s), 33, 46, 198, 254  
  coefficient, 208  
  index, 14  
  index spectra, 14, 281  
  spectra, 35  
  spectrometry, 373  
Absorptivity, 13, 211, 251, 256, 257, 259  
Absorptivity matrix, 209  
ac advantage, 264  
Acceptance angle, 129  
Accessory aperture, 200  
ac-coupled mode, 405  
Acetone, 259, 333, 478  
Acoustooptic tunable filters (AOTFs), 360  
Acquisition, 476  
  time, 51, 63  
Active scanning time, 396  
Actual signals, 65  
AgBr, 253  
AgCl, 253  
Air bearing, 98  
Air-conditioning equipment, 368  
Aliasing, 59, 62  
  conceptual discussion of, 58  
  mathematical discussion of, 60  
Alkali halide(s), 252–254  
Alkane solvent molecule, 403  
All-*trans* hydrocarbon, 295  
Alumina-supported rhodium catalyst, 358  
American Chemical Society, 179, 317  
American Society for Testing and Materials (ASTM), 185  
Amorphous material that transmits infrared radiation (AMTIR), 253  
Amplification(s), 23  
Amplifier(s), 23, 62  
  characteristics, 23  
  circuitry, 52  
Amplitude(s), 23–25, 29, 30, 33, 34, 58, 64, 108, 126, 133, 254, 255  
  of high-intensity signals, 64  
  of the white-light interferogram, 107  
Analog interferogram, 61, 412  
Analog-to-digital converter(s) (ADC), 58, 64, 67, 71, 104, 143, 166, 352, 397, 402  
  conventional, 163  
  specifications, 64  
Analyte, 255  
Angle of incidence, 284  
Angle of refraction, 133  
Angular acceptance, 125  
Angular velocity, 121, 122  
Anharmonicity constant, 4  
Anharmonic potential function, 4  
Anomalous dispersion, 15  
Anti-Stokes scattering, 16  
Anti-Stokes spectrum, 380  
Aperture, 118, 124  
  stop, 98  
Apodization, 30, 32, 33, 35, 44, 69  
Apodization functions, 32, 34, 36, 181, 235  
  Blackman–Harris, 34  
  boxcar, 28–32, 198  
  Happ–Genzel, 33–35  
  Norton–Beer, 34, 88, 165, 181, 198  
  triangular, 32, 165, 180

- Apparent mirror position, 123
- Archival-quality spectra, 2
- Array detector(s), 131
- Artificial neural network(s) (ANN), 221
  - applications of, 222
  - design, 222
- Artificial neuron or node, 221
- Atmospheric monitoring, 463
- Atmospheric windows, 472
- Atomic emission spectrometry (AES), 171
- Atomic emission spectrum, 105
- Attenuated total reflection (ATR), 200, 312, 321
  - correction, 325
  - internal reflection, 345
  - spectra, 201
  - spectrometry, 322
- Audio-frequency range, 415
- Automated peak picking, 229
- Automated spectral isolation, 219
- Automated subtraction, 204
- Automatic baseline functions, 226
- Avatar spectrometer, 103
- Axiom gas cell, 259
  
- Background limit for infrared photons (BLIP), 152
- Bacteriorhodopsin, 404, 406
- BaF<sub>2</sub>, 253
- Balmer line, 26
- Band fitting, 235
- Band intensity, 66, 251
- Band-fitting procedure, 235
- Band-fitting software, 236
- Bandpass, 59
- Bandshape, 200
- Bandwidth(s), 35, 59, 61, 62, 204
- Barbiturates, 490
- Baseline-corrected spectral regions, 227
- Baseline correction, 225
- Baseline discontinuities, 226
- Baseline noise, 483
- Beam(s), 20, 22, 116, 119, 159, 255
  - aperture, 201
  - condenser, 303
  - diameter, 303
  - divergence, 45, 49
- Beamsplitter(s), 22, 132
  - efficiency, 23, 132, 133, 137
  - efficiency curve, 137
  - stop, 98
- Bearings, 98
- Beat frequency, 27
- Beat signal, 25, 27
- Beer's law, 12, 197, 204, 206, 209, 210, 219, 249, 299, 300
- Bench-top instruments, 100
- Bending mode, 8, 9
- Benzene vapor, emissivity (E) and transmittance (T) spectra of, 365
- Bessel functions, 270
- Biased cosine wave, 128
- Binary chop approximation, 71
- Binary mixture(s), 208, 220
- Biochemical system, complex, 402
- Biological and biomedical spectroscopy, 1
- Biological systems, 221
- Birefringent prisms, 127
- Birefringent waveplate, 271
- Bisignate bands, 436
- Bit path, 73
- Blackbody emission spectrum, 370
- Blackbody-type source, 40
- Blackman function, 35
- Blackman–Harris function, 34
- Block engineering model, 100
- Boiler furnaces, 368
- Boltzmann population, 16, 463
- Bomem interferometer, 116
- Bomem MB-100 spectrometer, 116
- Bouguer–Lambert–Beer law, 199
- Boxcar function, 28, 29
- Boxcar integrator, 408
- Boxcar truncation, 32, 198
  - function, 28, 30
- Brewster's angle, 254, 262, 278, 293, 300
  - polarizer, 262
- Brick-wall, 168
  - filters, 106
- British thermal units, 221
- Broadband continuous source, 32
- Broadband spectral sources, 26
- Bruker 120 HR spectrometer, performance of a, 105

- Bühler interferometer, 127  
Built-in stress and strain transducers, 453  
2-Butanone, 478  
2-*tert*-Butyl maleic anhydride, 481  
Butyl methacrylate (BMA), 373
- C=O stretching, 268, 464  
C $\equiv$ C stretching band, 390  
CaF<sub>2</sub> lenses, 439  
Calcium fluoride, 137  
Calibration, 220  
    matrix, 218  
    set, 217  
    spectra, 211, 213, 214, 216  
Calibration data sets, general guidelines  
    for, 220  
Capillarity, 251  
Capillary electrophoresis (CE), 504  
Capillary gas chromatograph, 259  
Capillary GC/FT-IR, 260  
Carbohydrate, 218  
Carbon-black reference, 422  
Carbon disulfide, 256  
Carbon-filled polymer(s), 420,  
    422, 426, 430  
Carbon tetrachloride, 256  
Cassegrain condenser, 305  
Cassegrain objective, 337  
Cat's eye(s), 118  
    interferometer, 110, 118  
    retroreflectors, 118  
Cavity effect, 138  
CCD-Raman spectrometry, 388  
C–C ring stretches, 447  
C–C stretching vibration, 405  
CdTe, 253  
CE/FT-IR interface, 505  
Cell windows, 205  
Centerburst, 40, 108, 110, 131  
Center-of-gravity approach, 232  
Center-of-gravity method, 229  
Central fringe, 42  
Central light fringe, 41  
Central lobe, 33  
Central ray, 42, 45  
Centrifugal distortion, 7  
Cesium iodide (CsI), 137, 252  
C–H stretches, aliphatic, 451  
C–H stretching region, aliphatic, 446  
Chalcogenides, 252, 253, 343  
Charge-coupled device (CCD), 385  
    array detector, 171, 387  
Chebyshev recursion formula, 77  
Chemical component(s), 214  
Chemical mass balance equation(s), 219  
Chemometrics, 217, 218  
Chemometric techniques, 197  
Chiral compounds, 263  
Chirped interferogram, 70  
Chirping, 69, 134  
Circle accessory, 334  
Circular dichroism (CD), 263  
Circular interference fringes, 41  
Circularly polarized radiation, 263  
Circular piston, 112  
Circular polarization, 263  
Classical least-squares (CLS), 207,  
    210–212, 216, 472  
    regression, 209, 211, 213  
CO<sub>2</sub>, 255  
Coal, 221  
Coating thickness, 429  
Cold gas, jet of, 372  
Collimated beam, 19, 47, 49, 126  
Collimated radiation, 138  
Collinearity, 212  
Colthup charts, 5  
Coma, 156  
Commercial Fourier transform  
    spectrometers, 66  
Commercial FT-IR spectrometers,  
    69, 109  
Commercial interferometers, 105  
Comparator, 72  
    circuit, 108  
Compensator, 124  
    plate, 136  
Complex Fourier transform(s), 38, 227  
    of the microphone signal, 427  
Component(s)  
    ac, 133  
    calibration coefficients, 215  
    chemical, 214  
    cosinusoidal, 38  
    dc, 133  
    modulated (ac), 23  
    orthogonal, 261  
    out-of-phase, 448



- Component(s) (*continued*)
  - phase- and sample-modulated, 454
  - p*-polarized, 262
- Compressor, 100
- Computation time, 218
- Concentration matrix, 209
- Concentration profiles, 219
- Concentric rings, 46
- Condensed-phase infrared
  - spectral bands, 233
- Condensed-phase sample(s), 121, 251
  - quantitative analysis of, 198
- Condensed-phase spectra, 164, 251
- Condensed- or vapor-phase
  - reference spectra, 492
- Connes advantage, 73
- Connes-type interferometers, 127
- Constant-frequency intervals, 230
- Constant throughput criterion, 164
- Constituent matrix, 220
- Constructive interference, 22, 42
- Continuous-scanning
  - interferometer, 314, 395
- Continuous-wave NMR spectrometry, 171
- Conventional interferogram, 288
- Conversion(s), *gauche*-to-*trans*, 269
- Convex spherical mirror, 118
- Convolution, 28, 29, 30, 177, 179, 180, 250
- Cooley–Tukey algorithm, 79
- Corner reflector, 125
- Corner retroreflector, 113
- Corrector plate, 115
- Correlation algorithm, 248
- Correlation coefficient, 190, 206
- Cosine Fourier transform, 23, 26, 39
- Cosine function, 43
- Cosine wave(s), 24, 26, 27, 38, 57, 128
  - interferogram, 30, 38
- Coupled techniques, 481
- Cross-correlation function, 450
- Cross-peaks (off-diagonal), 451
- Cryoclect matrix-isolation
  - GC/IR interface, 492
- Cube corner, 113–115, 118, 122, 124
  - array, 471
  - disadvantages of the, 116
  - interferometers, 110, 112
  - retroreflector(s), 112, 116, 118, 121, 122
- Curve-fitting, 235, 245
- Cutoff frequency, 106
- 1-(4-Cyanophenyl)-4-*n*-pentylcyclohexane (5PCH), 459
- Cycle efficiency, 399
- Data collection, 50
- Data processing, 225
- dc and ac signals, 129
- dc component, 133
- dc-coupled mode, 405
- dc intensity, 132
- dc interferogram, 404
- DD-HPLC/FT-IR measurements, 505
- DD-SFC/FT-IR chromatogram, 503
- DD-SFC/FT-IR spectra, 502
- Decay, 33
- Decimation
  - in frequency, 84
  - in time, 84
- Depth of penetration, 324
- Depth profiling, 419
- Derivatives of a Lorentzian band, 237
- Destructive interference, 22
- Detectors 19–23, 41, 42, 46, 48, 57, 58, 99–111, 122, 200, 201, 258
  - bolometer, 146
  - charge-coupled device (CCD), 171, 387
  - diode array, 129
  - deuterated L-alanine-doped triglycine sulfate (DLATGS), 147, 195
  - deuterated triglycine sulfate (DTGS), 72, 144, 173, 397
  - electronics, 74
  - element, 128
  - focal-plane array, 63, 309, 312–313
  - germanium, 376, 379, 382, 383, 387
  - doped, 149
  - indium antimonide (InSb), 114
  - indium gallium arsenide (InGaAs), 383
  - lead sulfide (PbS), 352
  - lithium tantalate, 147
  - MCT, *see* Mercury cadmium telluride
  - response nonlinearity, 187
  - responsivity, 131
  - signal, 128
- Detector–preamplifier–amplifier
  - combination, 189
- Deuterated L-alanine-doped
  - triglycine sulfate (DLATGS), 147
- detector, 194

- Deuterated triglycine sulfate (DTGS), 147
  - detector, 72, 144, 173, 397
  - pyroelectric detector, 53
- Diamond, 252, 253
  - anvil cells, 308, 309
- Dichroic difference, 268, 436
  - spectra, 268
- Dichroic ratio, 268, 436
- Difference spectrum, 46, 203, 204, 436
- Differential spectrometer, 264
- Diffraction-limited grating
  - monochromator, 31, 32
- Diffraction-limited grating spectrometer, 30
- Diffraction-limited spatial resolution, 306
- Diffuse reflection (DR), 349, 353
  - spectra, 361
  - theory of, 349
- Digilab Stingray, 316
- Digital filter, 72
- Digital filtering, 106
- Digital signal processing (DSP),
  - 74, 94, 454
  - electronics, 427
- Digital-to-analog converter(s) (DAC), 71, 72, 431
- Digitization, 65
  - noise, 66, 166
  - rate, 71
- Digitizer, 69
- Diisobutyl ketone, 478
- Diluent, 355
- Dimerization, 199
- 2,6-Dimethyl-4-heptanone (diisobutyl ketone), 478
- Dimethyl sulfoxide (DMSO), 344
- Diode array, 129
- Dirac delta comb, 60, 61
- Dirac delta function, 60
- Direct-deposition (DD) GC/FT-IR spectra, 494
- Direction-dependent phase error, 52
- Discrete Fourier transform (DFT), 79
- Dispersion, 125, 131
- Dispersive spectrometers, 233
- Dispersive spectrometry, 170
- Dissociation, 199
- Divergence angle, 109, 123
- Diverging beam, 42
- Doping, 149
- Doppler effect, 10
- Double-beam grating spectrometer, 159
- Double-pendulum design(s), 116, 118
- Double-pendulum interferometer, 116, 117
- Double-sided complex transform, 78
- Double-sided interferograms, 40, 50, 86, 395
- Double-sided mirror, 115, 116
- Double-sided phase correction, 131
- Drive mechanism, 49
- Dry-air purge, 331
- Dual confocal aperturing, 306, 307
- Dual-bearing interferometers, 100
- Dual-phase LIA(s), 426, 437, 438, 456
- Duty-cycle efficiency, 51, 98, 108, 110, 121, 166, 396
- Dynamic alignment, 110, 111
  - approach, 110
  - process, 112
- Dynamically aligned interferometer, 112, 192
- Dynamic balance, 116
- Dynamic dichroism spectra, 438
- Dynamic friction, 104
- Dynamic infrared linear dichroism (DIRLD), 435, 436
  - spectra, high-quality, 441
  - spectrometer, 438, 440
- Dynamic mechanical analysis (DMA), 453
- Dynamic-mechanical analyzer, 435
- Dynamic range, 64–67, 69
  - of the ADC, 104
  - of the interferogram, 65
- Dynamic spectra, 449
- Dynamic strain frequency, 437
- Effect
  - of apodization, 165, 180
  - of beam divergence, 41
  - of changing mirror velocity, 165
  - of finite resolution, 26
  - of the J-stop diameter, 155
  - of mirror misalignment, 46
  - of a poor mirror drive, 49
  - of resolution and throughput on SNR, 164
  - of sample diameter and thickness, 186
  - of spectral resolution, 177
- Effective focal length (EFL), 153, 303

- Eigenvalues, 214
- Eigenvectors, 213
- Eight-point Savitsky–Golay filter
  - function, 439
- Electrical frequencies, 62
- Electric field, 133
  - vector(s), 261, 294
- Electric vector, 138
- Electrical line frequency, harmonics of
  - the, 184
- Electrochemical process(es), mechanism
  - of, 460
- Electromagnetic actuators, 110, 111
- Electromagnetic field, 261
- Electromagnetic radiative noise, 74
- Electromagnetic transducer, 97
- Electromagnetic waves, 21
- Electronic(s), 36, 109
  - filter(s), 38, 52, 62, 63
- Electronic and software designs, 105
- Electron ionization (EI), 481
- Elementary concepts, 75
- Ellipsoids, toroids, and other aspherical
  - mirrors, 155
- Elliptically polarized light (EPL), 265
- Emery paper, 357
- Emissivity, 363
- Emittance, 363
  - spectra, 369
- Empirical boundary relation, 33
- Enantiomeric excess (ee), 273
- Entrance aperture, 124, 258
- Entrance pupil, 98
- Entrance slit, 131
- Equidistant background, 472
- Error interferogram, 189
- Error matrix, 214, 219
- Euclidean distance method, 246
- Evanescent wave, 324, 327
- Evanescent wave spectrometry
  - (EWS), 321
- Even function, 26
- Evolving factor analysis (EFA), 219
- External beam, 158
- External chopper, 52
- External forces, 118
- External reflection spectrometry, 297
- Extractive monitoring, 463
- Extreme ray(s), 43, 45
- Fair alignment, 47
- False-color images, 319
- False-color two-dimensional image, 318
- Far-infrared beamsplitter, 136
- Far-infrared FT-IR spectrometers, 136
- Far-infrared measurements, 134
- Far-infrared sources, 146
- Far-infrared spectra, 127
- Far-infrared spectral regions, 262
- Far-infrared spectrometry, 48, 126, 127
- Fast Fourier transform (FFT), 78
- Fellgett's advantage, 69, 169, 171
- Fermi resonance, 500
- Ferrocyanide bands, 461
- Fiber–air interface, critical angle at
  - the, 342
- Field mirror, 258
- Field plane, 99
- Field stop, 98
- Field widening, 123, 129
- Field-widened interferometer, 124
- Field-widening approach, 123
- Fifth-order comparators, 72
- Film thickness, 136
- Fingerprint bands, 5
- Fingerprint region, 226
- Finite conjugate-image planes, 308
- First-derivative-shaped bands, 204
- Fixed arm, 121
- Fixed mirror, 19, 22, 46, 47, 69,
  - 103, 108, 110, 116
- Fixed plane mirror, 97, 119
- Fixed-size moving window evolving
  - factor analysis (FSMW-EFA), 219
- Flame ionization detector (FID), 454
- Flat folding mirror, 116
- Flat mirror(s), 115, 118, 119
- Flex pivot(s), 101, 117, 118
  - bearings, 101
- Flexing parallelogram, 116
- Flexure diaphragm, 103
- Flexure pivots, 116
- Flexure ring, 103, 110
- Flip mirror, 158
- Flow characteristics, 260
- Fluctuation noise, 169
- Fluorescence, 386
- Fluorescent light bulbs, 184
- Fluoride(s), 252, 253

- Focal length, 258  
Focal-length mirrors, 154  
Focal plane array(s) (FPA), 312  
  detector(s), 63, 309, 313  
Folded Jamin interferometer, 125  
Folded path cell, 257  
Folding frequency, 67  
Folding mirror(s), 115, 116  
Forward-feed neural network, 222  
Forward and reverse interferograms, 52  
Forward and reverse scans, 108  
Fourier domain, 240  
  signal, 235, 242  
Fourier frequency, 24, 58, 67, 111, 287, 412  
Fourier self-deconvolution (FSD), 240  
Fourier transform, 24–26, 28, 29,  
  31, 57, 62, 105, 128, 266  
  classical, conventional, or discrete, 75  
  lens, 130  
  mathematics, 58, 60  
  pictorial essay, 88  
  spectrometer, 19, 23, 24, 29,  
    41, 46, 49, 386  
  VCD spectrometer, 269  
Fourier transformation, 28  
Fourier transform photoacoustic  
  spectrometry, 416  
Four-point region, 228  
Fractional instability, 109  
Frame co-addition, 318  
Free-standing polymer, 254  
Fresnel design, 340  
Fresnel equations, 133, 134, 277  
Fresnel reflectance spectrum, 281  
Fresnel reflection, 277, 281, 299, 340, 350  
  measurements, 311  
  spectra, 349  
Frictional drag, 98  
Fringe(s), 69  
  contrast, 44, 46  
  counting, 108  
  pattern, 41  
  referencing, 104, 109  
Front-surface reflectance, 253  
Front-surface reflection, 360  
Frustrated multiple internal reflection  
  (FMIR), 321  
Frustrated total internal  
  reflection (FTIR), 321  
FT-IR microspectrometry, 145  
FT-IR spectrometer(s), 2, 30, 68, 71, 99, 118,  
  119, 132, 161, 198, 257, 271,  
  303, 330, 392  
  bench-top, 109  
  optics of an, 98  
  optics and electronics of, 100  
  optics of low-resolution, 155  
  performance of, 104  
FT-IR spectrometry  
  asynchronous time-resolved, 408  
  photometric accuracy in, 177  
  trading rules in, 164  
FT-Raman spectrometer(s), 387, 392  
FT-Raman spectrometry, 18, 377, 387  
Full width at half-height (FWHH),  
  32–34, 177, 481  
  criterion, 30  
Functional group chromatogram, 490  
Fundamental frequency, 4  
  
Gain curve, 109  
Gain ranging, 68, 73, 104  
  amplifier(s), 68, 167  
  radius, 69  
Gap-and-segment method, 238  
Gas cell, 260  
Gas chromatography interfaces, 158  
Gas-phase photochemical reactions, 259  
Gas-phase samples, 256  
Gaussian apodization, 34  
Gaussian bands, 11  
Gaussian function, 33  
GC/FT-IR, 490  
  mobile-phase elimination  
    approaches for, 491  
GC/FT-IR interfaces, light-pipe-based,  
  483, 486  
GC/FT-IR/MS interface, 483  
Ge/KBr beamsplitters, 138  
Ge plate, 262  
Germanium, 134, 253, 278, 279  
  film, 136  
  plate, 136  
Glan–Taylor polarizer, 262  
Glass plate, 103  
Glass tube, 103  
Globar, 104, 143  
Goodness-of-fit index, 247

- Grafting, 255
- Gram–Schmidt algorithm, 489
- Gram–Schmidt chromatograms, 489
- Gram–Schmidt thermograms, 504
- Gram–Schmidt vector
  - orthogonalization, 487
- Granite, 123
- Graphite, 103
  - composite bushings, 103
- Grating instruments, 29
- Grating monochromator(s), 178
  - for far-infrared spectrometry, 138
- Grating spectrometer, 173
- Grazing incidence reflection
  - spectrometry, 277
- Greenhouses, 368
- Ground-glass surfaces, 112
  
- Hädingen fringes, 41
- Half-angle, 45, 99
- Halides, 252
- Halogenated solvents, 257
- Halogen source, 127
- Happ–Genzel function(s), 33–35
- Hardness, 252
- Harmonic oscillator, 3
- Heavy metal halides, 253
- Helium, 259
- Helium–neon (HeNe) laser(s), 53,
  - 63, 74, 104, 105,
  - 108–110, 127, 489
- frequency, 419
- interferogram, 200, 411
- HeNe detector, 73
- HeNe frequency, 53
- HeNe interferogram, 64, 194, 380
- HeNe signal amplifier, 73
- HeNe wavelength, 63
- Herriott cell, 258, 259
- Hexacyanoferrate complex, 461
- n*-Hexane, 256
- Hexane extraction, 218
- Hexanitrobiphenyl, 388
- 2-Hexanone, 256
- Hidden layer, 222
- High-amplitude broadband
  - noise, 427
- Higher-order derivatives, 239
- Highest operating temperature, 252
  
- High-frequency signal, 270
- High-molecular-weight precursor, 442
- High optical velocity, 51
- High-pass filter, 316
- High-performance liquid chromatography (HPLC), 483
  - normal- and reverse-phase, 498
- High-precision roller bearings, 112
- High-pressure cells, 253
- High-reflectance diffuse coating, 354
- High-refractive-index material, 325
- High-resolution FT-IR spectrometers,
  - 110, 118
- High-resolution interferometers, 118
- High-resolution scans, 113
- High-resolution spectra, 62
- High-resolution spectrometry, 62, 111
- High-resolution step-scan
  - interferometers, 127
- High-resolution ultraviolet spectrum, 104
- High-spatial-frequency noise, 165
- High-speed time-resolved
  - spectrometry, 127
- High-wavenumber region, 268
- H–O–H bending mode, 10
  - of water, 182
- Horizontal attenuated total reflection (H-ATR), 331
- HPLC/FT-IR
  - interface, 495
  - mobile-phase elimination
    - techniques for, 496
- H-shaped swing arms, 102
- Hybrid imaging/mapping imaging
  - spectrometer, 315
- Hybrid imaging/mapping instrument, 317
- Hydrocarbons, 259
- Hydrogen bonding, 210
- Hydrogen spectrum, 25
- Hypercube, 312
- Hyperspectral FT-IR imaging, 312, 319
- Hyperspectral imaging, 53, 127, 308
  
- Ideal Beer's law behavior, deviation
  - from, 179
- Ideal phase-modulated interferometer, 128
- Identity matrix, 215
- Image co-addition, 318
- Image-contrasting optics, 308

- Imaginary part, 39
- Imaging measurements, 128
- Impulse function, 60
- Incidence, 120
- Incident angle, 22, 112, 121, 123
- Incident radiation, 133
- Indium gallium arsenide (InGaAs), 376
- Infinity corrected design, 308
- Information-rich infrared spectra, 3
- Infrared absorption coefficient, 418
- Infrared beam, 104, 106, 200
  - divergence angle of the, 108
- Infrared detector(s), 23, 52,
  - 73, 104, 107
- Infrared emission spectra
  - of condensed-phase samples, 366
  - of gases, 363
- Infrared emission spectrometry, 363
- Infrared grating spectrometer(s), 112
- Infrared interferogram(s), 106,
  - 107, 108, 123
- Infrared microscope(s), 63, 158, 304
- Infrared radiation, 106, 201
  - sources for transmission and reflection spectrometry, 143
- Infrared reflection–absorption spectrometry (IRRAS),
  - 277, 282, 312
  - measurement, 267
  - spectrometry, 298
  - spectrum, 291
- Infrared signal, 105, 111
  - amplifier, 73
- Infrared spectrum, 5, 19, 111, 303, 308
- Infrared spectroelectrochemistry, 460
- Infrared (IR) spectrometry, 1, 30,
  - 19, 197, 221
- Infrared spectroscopy, 256
- Infrared transmission spectrometry, 254
- Infrared-transmitting windows, 324
- Infrared-transparent
  - material(s), 252, 493
- InGaAs detector, 383
- In-phase (IP) channel(s), 426, 438
- In-phase interferograms, 428
- In-phase output, 456
- In-phase spectrum, 427, 444
- Input beam, 20, 259
- Input channels, 73
- Input layer, 221, 222
- Input neurons, 222
- Input voltage, 72
- InSb detector, 114
- Instrument artifacts, 214
- Instrument line shape (ILS)
  - algorithms, 212
- Instrument line shape (ILS)
  - function(s), 29, 33, 34,
    - 200, 212, 216
- Instrument line shape (ILS) method,
  - 212
- Instrument line shape (ILS) model, 215
- Instrument response function, 364
- Instrumental considerations, 400
- Intensity, of diffracted light, 306
- Interaction spectra, 213
- Interfacial phenomena, 1
- Interfacial species, 2
- Interference, 19, 127
  - effects, 132
  - fringe(s), 134, 253–255
  - record, 22
- Interferogram(s), 23–27, 32, 33,
  - 36, 38, 48, 50, 57, 65, 110, 255
  - amplitudes, 73
  - centerburst, 189
  - clipped, 64
  - coherent signal-averaging
    - (co-adding), 106
  - constant-in-reaction-time, 407
  - distribution of, 69
  - envelope of the, 26
  - generation of an, 20
  - measurement of, 108
  - sampling the, 57
  - voltage of the, 71
- Interferometer(s), 19, 20, 23, 26, 28, 41,
  - 46–48, 97, 99, 114, 119–121, 123,
    - 129, 131, 258, 419
  - bidirectional rapid-scanning, 52
  - block, 102
  - construction of an, 116
  - continuous scan, 20
  - designs of, 97
  - drift, 183
  - mirror(s), 49, 111
  - versus grating spectrometers, 171
- Interferometry, 19, 64

- Interleaved mirrors, 138  
Intermolecular interactions, 204  
Internal reflectance, 135  
Internal reflection element (IRE),  
200, 201, 203, 253, 323, 397  
Internal reflection spectrometry  
(IRS), 253, 321  
Internal reflection spectroscopy, 253  
Invar, 123  
Inverse Fourier transformation, 243  
Inverse least-squares (ILS)  
regression, 210, 212  
Isotactic polypropylene, 440, 457  
Iterative key set factor analysis  
(IKS-FA), 219  
Iterative process, 214  
Iterative target transform factor analysis  
(ITTFA), 219  
  
Jacquinot's advantage, 2, 171, 172  
Jacquinot stop (J-stop), 42, 44,  
46, 99, 155  
Jamin interferometer, 126  
  
Karl Fischer method, 218  
KBr, 252  
optics, 68  
pellets, 251  
KCl, 252  
Kinetic systems, 219  
Kirchhoff's law, 365, 368  
Kjeldahl titration, 218  
K-matrix method, 209  
Kramers–Kronig relations, 280  
Kramers–Kronig transform,  
279, 281, 311  
KRS-5 crystals, 253  
Kubelka–Munk equation, 350  
Kubelka–Munk reflection, 350  
Kubelka–Munk theory, 349  
  
Lambert plots, 199  
Lamellar grating interferometer(s),  
138–140  
Laser beam(s), 106, 108, 110, 125, 258, 259  
Laser detector(s), 104, 107, 125  
Laser-drilled hole, 483  
Laser fringe, 108  
zero crossings, 74  
  
Laser interferogram(s), 71, 72, 105–108,  
123, 127  
frequency of the, 72, 108  
zero crossing of the, 106  
Laser-referenced interferometers, 106  
Laser signal, 73, 109  
Laser wavenumber, 46  
Lateral displacements, 113  
Lateral separation, 100  
LC Transform, 498  
Least-squares analysis, 205  
Least-squares fitting, 206  
Least-squares method, 229  
Least-squares regression, 208–210  
Leave-one-out method, 218  
Level zero tests, 186  
Levenberg–Marquardt method, 236  
Lever-arm system, 110  
Ligand-exchange reaction, 402  
Light-chopper frequency, 437  
Light-driven proton-pump membrane  
protein, 404  
Light-emitting diode, 129  
Light-pipe design, 483  
Light-pipe gas cells, 260  
Light-pipe-based interface, 490  
Limiting aperture, 42, 156  
Linear absorption coefficient, 13, 327,  
419, 421  
Linear array detector, 128  
Linear dichroism, 261  
applications of, 266  
Linear least-squares fitting, 205  
methods, 204  
Linear least-squares regression, 207, 208  
model, 207  
Linear molecule, 8  
Linear PLS techniques, 223  
Linear reciprocal coefficient, 211  
Linear systems, 223  
Liquid chromatographs, 481  
Liquid-crystal electroreorientation, 458  
Liquid-handling system, 398  
Liquid-nitrogen bath, 369  
Liquid-nitrogen-cooled helium, 370  
Liquid-nitrogen (LN<sub>2</sub>)-cooled ZnSe, 493  
Lissajous figures, 259  
Lithium tantalate, 147  
LN<sub>2</sub>-cooled detectors, 260

- Loading vectors, 214, 216  
Lock-in amplifier(s) (LIA), 128, 264, 426,  
    437, 456  
    train, 438  
Longitudinal separation, 100  
Long-path FT-IR measurements, 258  
Long-path (multipass) gas cell, 486  
Lorentzian band(s), 11, 25, 243  
Lorentzian functions, 280  
Lorentzian profile(s), 26, 472  
Loudspeakers, 98  
Low-amplitude phase modulation, 128  
Low-amplitude strain, 436  
Low-emissivity glass slides, 311  
Low-expansion coefficient, 123  
Low-frequency interferogram, 270  
Low-frequency noise, 166, 464  
Low-friction bearing interface, 103  
Low-index material, 293  
Low-pass electronic filter, 59, 105  
Low-pass filter, 266, 408, 411  
Low-pressure mercury lamp, 129  
Low-resolution FT-IR spectrometer(s),  
    42, 157  
Low-resolution measurements, 162  
Low-resolution scans, 51  
Low-resolution spectra, 395  
Low-resolution spectrometers, 110  
Low-resolution stationary  
    interferometers, 131  
Low-spatial-frequency noise, 165  
Lubricant, 98  
  
Macroscopic measurements, 307  
Magnetic field, 98  
Manual baseline correction, 226  
Mapping imaging spectrometer, 315  
Mapping instrument, 317  
Mass spectrometry (MS), 1, 481  
Matrix isolation approach, 492  
Matrix isolation GC/FT-IR, 491  
Matrix-isolation spectra, 492  
Mattson interferometers, 112  
Maximum-allowed divergence, 163  
Maximum amplitude, 24  
Measured digitized value, 72  
Mechanical design, 105  
Mechanical velocity, 105  
Median ray, 19  
  
Medium-resolution FT-IR spectrometers, 110  
Melinex, 134  
2-Mercaptoethanol, 240  
Mercury cadmium telluride (MCT), 53, 150,  
    187, 198, 260, 264, 314, 344, 401, 443,  
    464  
    bolometers, 71  
    PbS, *see* Lead sulfide  
    photomultiplier tube (PMT), 170, 375  
    pneumatic detector, 146  
    pyroelectric, 66, 69, 146, 174  
    thermistor bolometer, 146  
    thermocouple, 146  
Mertz method, 86  
Mertz phase, 271  
    correction algorithm, 108, 189  
Metal mesh beamsplitter, 139  
*N*-(*p*-Methoxybenzoyl)sulfamethazine, 503  
Methyl ethyl ketone (MEK), 477, 478  
    analytical-grade, 333  
(*S*)-Methyl lactate, 273  
Methyl methacrylate (MMA), 373  
Methyl monochloroacetate, 399  
Methyl phosphonic acid, 391  
bis-Methyl styryl benzene, 381  
Michelson interferometer, 19, 20, 22, 24, 41,  
    42, 46, 97, 98, 101, 110–112, 121, 124,  
    129, 138, 139  
    ray diagram of a, 132  
Michelson interferometer with rotating  
    retroreflector (MIROR), 121  
Michelson-type interferometers, 97  
Microsamples and trace analytes, 2  
Microsampling, 255  
    with beam condensers, 303  
Microscopic dissolution, 319  
Microspectroscopy and hyperspectral  
    imaging, 1  
Microspectroscopy and imaging, 303  
Midac interferometer, 102  
Mid-infrared beamsplitters, 183  
Mid-infrared energy, 183  
Mid-infrared Fourier transform  
    spectrometry, 174  
Mid-infrared FT-IR spectrometer(s), 62, 63,  
    138, 262  
Mid-infrared interferograms, 104  
Mid-infrared measurements, 138, 425  
Mid-infrared microspectrometry, 306



- Mid-infrared pyroelectric bolometer, 64
- Mid-infrared region, 111
- Mid-infrared spectra, 9, 65, 106, 109, 253, 256, 353, 440
- Mid-infrared spectrometry, 62, 128, 161, 251, 253
- Mid-infrared spectroscopy, 136, 222
- Minuend spectrum, 204
- Mirror carriage, 102
- Mirror drive, 100, 115
- Mirror motion, 121
- Mirror scans, 109
- Mirror shear effects, 118
- Mirror tilt, 118
- Mirror velocity, 57, 68, 108, 121
  - variations in the, 168
- Mode hopping, 109
- Modulated interferogram, 410
- Modulated perturbation, 435
- Modulated strain, 448
- Modulation efficiency, 121
  - changes in, 191
- Modulation frequency, 23, 105, 418, 428
- Molecular vibrations, 3
- Monochromatic beam, 41, 104
- Monochromatic light, 42
  - source, 411
- Monochromatic line, 29
- Monochromatic radiation, 20, 22, 24, 44, 132
- Monochromatic source, 23, 126
- Monochromator(s), 30, 99, 129, 435
- Monolithic common-path interferometer, 130
- Monolithic designs, 129
- Movable cube corner, 113
- Movable facets, 139
- Movable wedge, 124
- Moving double-sided mirror, 116
- Moving mirror, 22, 26, 47–50, 53, 54, 98, 102, 103, 105, 108–110, 127
  - assembly, 100
  - velocity of the, 51
- Moving optical element(s), 116, 121
- Moving plane mirror, 97
- Multichannel spectrometer, 361
- Multidimensional space, 219
- Multifrequency waveform, 431
- Multilayer beamsplitters, 138
- Multipass gas cell, 258
- Multiple-angle incidence resolution spectroscopy (MAIRS), 295
- Multiple atmospheric layer transmission (MALT), 465
- Multiple internal reflection (MIR), 321
- Multiple linear regression (MLR), 212
- Multiple-reflection accessories, 336
- Multiplex advantage, 171
- Multiplicative noise, 131
- Multivariate curve resolution (MCR), 218, 219
- Multivariate methods, 217, 223
- Multivariate regression methods, 220
- Multivariate system, 207
- Multivariate technique(s), 197, 210
- Mylar, 134
  - beamsplitter, 138
  - film, 135
- Nafie's group, 271
- Naperian logarithms, 256
- Narrowband MCT detectors, 150
- National Institutes of Health, 312, 486
- Natural light, 261
- Near-infrared analysis, 112
- Near-infrared (NIR) diffuse reflection spectroscopy, 358
- Near-infrared (NIR) DR spectra, 352
- Near-infrared (NIR) interferograms, 104
- Near-infrared measurements, 136, 138, 396
- Near-infrared (NIR) spectrometry, 98, 127, 128, 248, 253
- Near-infrared (NIR) spectrum, 6, 63, 104, 114, 300, 352, 358
- Negative bands, 203
- Negative transmittance, 198
- Nernst glower, 144
- Nesting mirrors, 258
- Neural networks, 221, 223
- Neuron, 221
- Nitric oxide, 7
- Noise band, 68
- Noise equivalent power (NEP), 161
- Noise-free signal, 67
- Noise injection, 67
- Noise power, 161
- Noise-shaping filters, 72
- Nominal resolution, 32, 114
  - of the spectrometer, 178

- Nonabsorbing gas, 417  
Nonabsorbing materials, 278  
Noncollimated beam, 42  
Nonfactor analysis methods, 219  
Noniterative partial least squares (NIPALS), 214  
Nonlinear Beer's law, 366  
Nonlinear PLS techniques, 223  
Nonlinear systems, 223  
Nonpolar analytes, 251  
Nonpolar molecules, 256  
Normal coordinate, 4  
Normal-phase separations, 499  
Norton–Beer apodization functions, 37, 181  
Norton–Beer medium, 35, 199  
    apodization, 198  
    function, 88  
Norton–Beer strong apodization function, 34, 165  
N-point interferogram, 227, 228  
Nuclear magnetic resonance (NMR), two-dimensional, 1  
Numerical aperture (NA), 306  
Nyquist criterion, 50, 57, 58, 74  
Nyquist frequency, 57, 58, 62, 68, 72, 189  
Nyquist sampling criterion, 59, 270  
Nyquist sampling theorem, 412  
Nyquist wavenumber, 104–106, 168, 441  
  
5 o'clock effect, 170  
Octadecylsiloxane, 295  
Off-axis accessories, 353  
Off-axis ellipsoid, 156  
Off-axis geometry, 354  
Off-axis paraboloid(s), 125, 153  
Off-axis ray, 42  
O–H stretching bands, 256  
O–H stretching region, 226  
One-point baseline correction, 225  
Open-path atmospheric monitoring, 466  
Open-path FT-IR spectrometry, 463  
Operator-selected spectral data points, 226  
Optical absorption depth, 419, 421  
Optical anisotropy, 439  
Optical bench, 119, 136  
Optical center, 131  
Optical constants, 14, 15  
Optical element(s), 69, 121, 128  
Optical filters, 63  
Optically opaque fibers, 424  
Optical path, 119, 124  
Optical path difference (OPD), 21, 24, 49, 98, 99, 110, 121, 127, 411  
    velocity, 24  
Optical retardation, 21, 27  
    of the interferometer, 63  
Optical Society of America, 34  
Optical thickness, 255  
Optical throughput, 98, 162  
Optical train, 131  
Optical velocity, 24, 53, 57, 105, 121  
Optics, 109  
    Cassegrain or Schwartzschild, 305  
Optimum absorbance, 256  
Optimum pathlength, 256  
Organic liquids, 254  
Orthogonal components, 261  
Orthogonal matrix, 215  
Out-of-band energy, 189  
Output beam(s), 20, 113, 117, 125  
Output layer, 222  
Output scalars, 222  
Overlapped bands, 238  
Oxyanions, 279  
  
PA/FT-IR depth profiling, 428  
PA/FT-IR spectrometry, 417  
Paraboloidal mirrors, 152, 157  
Parallel input beams, 21  
Partial least squares (PLS), 223, 474  
    algorithms, 217  
    model, 112  
    regression, 112, 216  
Partial pressure(s), 256, 257  
PA spectrometry, 422  
PA spectrum, of polycarbonate, 423  
Passive solar heating devices, 368  
Path difference, 19, 21, 24, 42, 43, 45, 48, 118, 119, 121, 138  
Path-integrated concentration, 467  
Pathlength(s), 22, 207, 208, 211, 253, 254, 257, 259, 260  
Pathlength–concentration product, 486  
PbS detector, 352  
PC-MCT detectors, 315  
Peak absorbance(s), 198, 200, 204  
Peak picking, 229  
Peak-to-peak detector noise, 65

- Peak-to-peak noise, 181, 198  
  level, 67, 163
- Pendant group vibrations, 447
- Pendant pentyl tail, 460
- Pendulum, 116, 118  
  axis, 116, 118
- Penetration depth, 54
- 4-Pentyl-4'-cyanobiphenyl (5CB),  
  459
- Percent transmission, 252
- Periscope interferometer, 119
- Permanent magnet, 98, 103
- Pharmacist's method, 355
- Phase angle, 36, 38
- Phase-angle bandpass, 87
- Phase-angle spectrum, 87
- Phase change, 22
- Phase-corrected interferogram, 87
- Phase-corrected spectrum, 70
- Phase-corrected transmittance spectrum,  
  92
- Phase correction, 39, 85, 110
- Phase difference, 111
- Phase errors, 76
- Phase-modulated mirror, 431
- Phase-modulated step-scan  
  interferometer, 425
- Phase modulation (PM), 52,  
  128, 440  
  frequency, 432, 456, 457  
  measurements, 128  
  waveform, 456
- Phase shift  
  plate, 125  
  reduction in, 429
- Phase spectrum, 40
- Phenolic antioxidants, 256
- Photoacoustic (PA), 415, 454  
  effect, 415  
  phase shift, 428  
  phase spectrum, 430  
  saturation, 419, 432  
  spectroscopy, 127, 372  
  spectrum, 417
- Photoacoustic spectrometry, 53, 371, 373  
  of gases, 415
- Photochemical smog, 259
- Photoconductive (PC) MCT detector, 314  
  conventional, 401
- Photoelastic modulator (PEM), 265, 436  
  generated signal, 457
- Photolysis-assisted pollution analysis  
  (PAPA), 465
- Photometric accuracy, 32, 41
- Photometric precision, 200
- Photomultiplier tube (PMT), 170, 375
- Photons, 22
- Photovoltaic (PV) mode, 314
- Phthalate plasticizer, 504
- Physical constraints, of the optics, 162
- Physical properties, 252
- Physical scan, 53
- Piezoelectric transducer(s), 110, 111, 128
- $\alpha$ -Pinene, 271
- (S)-(-)- $\alpha$ -Pinene, 271–273
- Piston, 98, 103  
  tolerances of the, 103
- Pixel response, 129
- Plan view, 115
- Planar reflectors, 120
- Plane of incidence, 261
- Plane mirror(s), 19, 112–115, 119–122, 155
- Plane-mirror Michelson interferometer,  
  112, 113
- Plane-polarized radiation, 261, 262
- P matrix, 212
- Polar analyte, 251
- Polarizability, 16
- Polarization, 261  
  effects, 118  
  interferometers, 125, 127  
  modulation, 264  
  modulation frequency, 266, 436  
  modulation signal, 457  
  plane of, 266
- p*-Polarization, 133
- s*-Polarization, 133
- p*-Polarized component, 262
- p*-Polarized light, 262, 284
- Polarized radiation, 15, 125, 135,  
  136, 296, 436
- p*-Polarized radiation, 134, 283, 284
- s*-Polarized radiation, 134, 278, 283
- Polarizer, 15, 254
- Poly( $\gamma$ -benzyl-L-glutamate), 440
- Polycarbonate sheet, photoacoustic  
  spectrum of a, 423
- Polycarbonate (PC) substrate, 372, 430

- Polyethylene (PE), 262, 430
  - film, 201, 202
  - thermal diffusivity of, 420
- Poly(ethylene terephthalate) (PET), 134,
  - 190, 251, 266, 306, 430
  - beamsplitter(s), 136, 138, 139,
  - film(s), 135, 136
- Polymer-clad fibers, 346
- Polymer-dispersed liquid crystals, 319
- Polymer films, 251
- Polymerization, 199
- Polymer modulator, 443
- Poly(methyl methacrylate), 297, 299
- Poly[(methyl methacrylate-co(butyl methacrylate)] samples, 373
- Polynomial curves, 205
- Polynomial PLS, 223
- Polyolefins, 255
- Poly(*p*-phenylene vinylene) (PPV), 442
- Polypropylene (PP), 430
- Polystyrene, 66, 251
  - atactic, 439, 440
- Polytetrafluoroethylene (PTFE), 100, 361
- Poor digitization accuracy, 65
- Poor mirror drive, 49
- Porch swing design, 101
- Porch-swing drive, 101
- Positive-going feature, 436
- Potassium bromide, 137, 279
- Potential function, 4
- Powdered barium sulfate, 354
- Precision-ground piston, 103
- Prediction residual error sum of squares (PRESS), 217
  - plot, 217
  - value, 217
- Prediction set, 218
- Primary method, 218
- Principal component(s) (PC),
  - 213–215, 217
- Principal component analysis (PCA),
  - 213, 214, 216
- Principal component regression (PCR),
  - 215, 216
  - algorithms, 216
- Protein, 218
  - concentration, 218
- Pseudoinversion, 220
- Pure component spectra, 213, 219
- Pyroelectric bolometer(s), 66, 146
- Pyroelectric detector(s), 69, 174
- Q branch, 9
- Quadrant detector, 103, 110
- Quadrature (Q) channel(s), 426, 438
- Quadrature interferograms, 428
- Qualitative spectrum, 201
- Quantitative analysis, 197, 223
  - of complex mixtures, 1
- Quantitative considerations, 12
- Quantitative information, 197
- Quantization, 65
  - levels, 71
- Quantum detectors, 129, 148
- Quarter-wave plate, 264
- Quarter-wave retardation plate, 108
- Quartz (SiO<sub>2</sub>), 137, 252, 253, 259
- Quartz prisms, 123
- Quartz–tungsten–halogen (QTH) lamp, 145
- Radiant heat transfer analysis, 367
- Radiation, 19, 24, 116, 203, 261
- Raman bands, 375
- Raman shifts, 375
- Raman spectrometry, 16, 375, 379, 388
  - analytical, 18
- Raman spectrum, 138, 171, 249, 381, 392
- Rapid photolysis reactions, 402
- Rapid-scan FT-IR spectrometers, 481
- Rapid-scan interferometer(s), 20, 50, 53, 54,
  - 62, 104, 458
- Rapid-scanning FT-IR spectrometers, 314
- Rapid-scanning grating spectrometers, 352
- Rapid-scanning interferometer(s), 40, 48, 64,
  - 66, 68, 100, 127, 131, 317, 416,
  - 417, 435
- Rapid-scanning Michelson
  - interferometers, 23
- Rapid-scanning mode, 127
- Rapid-scan systems, 54
- Ratio spectrum, 48
- Rayleigh criterion, 30, 32
- Rayleigh line, 381
- Rayleigh scattered light, 380
- Rayleigh scattering, 16, 375
- Ray tracing, 125
- Real part, 39
- Real-time direct-deposition interface, 499

- Real-time sampling, 290
- Rear-silvered mirror, 124
- Reciprocating motion, 121, 122
- Recombination, 22, 126
- Rectangular mirror, 122
- Redundant aperturing, 306
- Reference interferometer, 107
- Reflectance, 21, 132, 133
  - factor, 354
  - of radiation, 278
- Reflected beam, 112
- Reflection–absorption infrared spectrometry (RAIRS), 277
- Reflection–absorption measurements, 493
- Reflection–absorption spectrum, 282
- Reflection loss, at the windows of the cell, 13
- Reflection spectrometry, 261, 296, 310, 373
  - external or internal, 460
- Reflector, 121
- Refractive element, 121
- Refractive index, 14, 69, 109, 124, 133, 134, 136, 137, 251, 253, 254, 262, 281, 294
  - of germanium, 136
  - spectrum, 14
- Refractively scanned interferometers, 123, 125
- Refractive optical element, 124
- Regression coefficient, 205
- Relative beamsplitter efficiency, 135
- Relative magnitude, 33
- Repolishing, 253
- Residual error
  - for absorbance, 211
  - for the dependent, 211
- Residual spectra, matrix of, 214
- Resistance, 121
- Resolution, 26, 28, 32, 35, 40, 49, 121, 123, 129
  - parameter, 177, 197–199
  - spectra, 123
- Resonance modes, 109
- Resonance Raman spectroscopy (RRS), 389
- Responsivity, 23
- Reststrahlen bands, 279
- Retardation(s), 21, 22, 24, 26, 27, 33, 41, 51–53, 105, 109, 110, 131
- Retardation and computation time, 62
- Retroreflectors, 112, 118
- Reverse-phase (RP) chromatography, 496
- Reverse scans, 52
- Rheo-optical measurements, 458
- Rocking mirror, 126
- Roll axis, 100
- Roll motion, 100
- Roof retroreflector, 112, 113
- Root-mean-square (rms), 181
  - noise, 64, 234
  - positional uncertainty, 128
  - signal-to-noise ratio ( $\text{SNR}_{\text{rms}}$ ), 198
- Root-mean-square error of calibration (RMSEC), 218
- Root-mean-square error of cross validation (RMSECV), 217, 218
- Root-mean-square error of prediction (RMSEP), 218
- Rotating interferometer, 122
- Rotating mirror, 121, 122
- Rotation(s), 121
  - angle, 121
- Rotational axis, 118
- Rotational energy, 6
- Rotational energy states, 7
- Rotational motion, 101, 120
- Rotational quantum number, 6
- Rotational transition, 114
- Sagnac interferometer, 128
- Salt plates, 251
- Sample-and-hold ADC(s), 65, 71, 74
- Sample-and-hold technology, 72
- Sample-changing wheel, 407
- Sample compartment, 200
- Sampled signals, 65
- Sample holders, 200
- Sample modulation, 54
  - FT-IR spectrometry, 458
  - interferogram points, 456
  - measurements, 128
  - spectrometry, 457
  - spectroscopy, 127, 435
- Sampling, 110
  - accessory, 46
  - amplitudes, 58
  - detector noise, 65
  - effects, 36
  - error, 167

- frequency, 57, 59, 61, 62, 64, 68, 71, 105
- interval, 64, 131
- point(s), 63, 128
- rate, 71
- timing of ADC, 410
- Sande–Tukey algorithm, 84
- Sapphire ( $\text{Al}_2\text{O}_3$ ), 252, 253
- Satellite-borne interferometers, 69
- Savitzky–Golay algorithm, 238
- Savitzky–Golay smoothing algorithm, 233
- Scalar output, 221
- Scalar value, 221
- Scaling factor, 202, 204
- Scan cycle, 110
- Scanning interferometers, 128, 129
- Scanning monochromators, 73, 190
- Scanning time, 121
- Scanning two-beam interferometers, 19
- Scanning wedge, 125
- Scan speed, 53
- Scan velocity, 53
- Second-order coupling, 500
- Self-absorption, 366
- Self-apodization, 44
- Self-compensation, 115
- Self-modeling strategies, 219
- Self-supporting thin-film (pellicle), 134
- Shaft, 98
  - encoder, 127
- Shah function, 60
- Shear offset, 121
- Shift, 99
- Short optical fibers, 253
- Short-focal-length Cassegrain condenser, 305
- Short-path background, 473
- Short-term performance, 181
- Short-term variations, 131
- Shot noise, 170
- Sigma–delta ( $\Sigma-\Delta$ ) ADC(s), 71, 74, 167
- Signal averaging, 50, 104, 108
- Signal-averaging systems, 67
- Signal-averaging techniques, 67
- Signal interferogram, 104
- Signal-processing scheme, 440
- Signal-to-noise ratio(s) (SNR), 41, 54, 64, 67, 104, 128, 129, 143, 161, 242, 247, 284, 303, 336, 378, 391, 464
  - of a commercial FT-IR spectrometer, 175
  - of reflection–absorption spectra, 145
  - of spectra, 127
- Silicon, 134, 253
  - film, 137
  - wafer, 341
- Silicone bands, 432
- Silicone grease, 367
- Simple peak-picking algorithms, 229
- Simple spectra, 24, 25
- Sinc function(s), 30–32, 36, 37
- Sinc ILS function, 179
- Sine transform, 39
- Sine wave, 58
  - frequency of the, 58
  - interferogram, 39
- Single-beam background, 417
  - spectrum, 404
- Single-beam IRRAS spectrum, 267
- Single-beam PA spectrum, 422
- Single-beam spectral intensity, 23
- Single-beam spectrum, 47, 48, 110, 159, 181, 187, 285, 438, 472
- Single boxcar integrator, 412
- Single-channel dispersive spectrometer, 169
- Single-channel spectrometer, 361
- Single-frequency PM waveform, 431
- Single off-axis segment, 156
- Single-point baseline correction, 187
- Single phase-modulation frequency, 430
- Single physical aperture, 307
- Single-reflection accessories, 336
- Single-sided interferograms, 40, 87
- Single-sided measurements, 41
- Single-sided mode, 106
- Single-sided spectrum, 78
- Single-surface reflectance, 136
- Singular value decomposition (SVD), 214
- Sinusoidal function, 57
- Sinusoidal interferogram(s), 24, 26, 111, 411
- Sinusoidal phase modulation, 454
- Sinusoidal wave, 67, 108
- $\text{SiO}_2$  piezoelectric transducers, 265
- Size-exclusion chromatography (SEC), 496
- Skeletal modes, 5
- Slow-scanning interferometers, 48

- Small spectral shifts, 159  
Snell's law, 278, 322  
Society for Applied Spectroscopy, 190, 191, 398  
Sol-gel, 390  
Solid angle, 123  
    maximum allowed, 162  
Solution-phase ferricyanide, 461  
Solution-phase species, 460  
Solvation, 199  
Source(s), 19, 21, 22, 32, 41, 48, 99, 122, 125, 129, 130  
    intensity, 131  
    of phase error, 85  
Spatial or fixed pattern noise, 318  
Spatial frequency, 233  
Spatial resolution, of the microscope, 306  
Spatial and spectral resolution, 131  
Special quality, 35  
Specific detectivity, 149, 161  
Spectral absorbance, 207  
Spectral band, 26  
Spectral brightness, 161  
Spectral convolution, operation of, 233  
Spectral coverage, 138, 217  
Spectral differences, 402  
Spectral dynamic range, 65, 66  
Spectral emissivity, 367  
Spectral energy density, 145  
Spectral information, 19  
Spectral lines, 35  
Spectral loadings, 214, 216  
Spectral noise, 65  
Spectral range, 133, 134, 136, 138, 253  
Spectral resolution, 27, 108  
Spectral smoothing, 232  
Spectral smoothing, 235  
Spectral vectors, 220  
Spectrometer(s), 30, 113  
    design, 156  
Spectrometric measurements, 23  
Spectrometric technique, 23  
Spectrometry, 20, 197, 415  
Spectrophone, 416  
Spectroradiometer, conventional, 129  
Spectroscopic ramifications, 485  
Spectroscopic trading rules, 164  
Spectrum, 24, 28, 32, 61, 62, 66, 113, 121, 131, 253–255  
    of barbiturates in the vapor and condensed phases, 493  
    of condensed-phase samples, 11  
    at higher resolution, 157  
Specular reflection, 277  
    spectra, 310  
Spherical mirror, 258  
Spike, 255  
Spinning retroreflectors, 121  
Spring-loaded plastic element, 103  
Square matrix, 212  
Square-wave frequency, 433  
Square-wave phase modulation, 433  
    waveform, 432  
Stainless steel, 123  
Standard condensed-phase reference spectra, 486  
Standard deviation, 218  
Standard error of calibration (SEC), 218  
Standard error of prediction (SEP), 218  
Standard Raman spectroscopy, 387  
Starch, 218  
Static and dynamic dichroism spectra, 442  
Static friction, 104  
Stationary cube corners, 125  
Stationary interferometer(s), 24, 128, 131  
    sensitivity and instability of, 129  
Stationary mirror, 116  
Stationary plane mirrors, 113  
Stationary (shaded) facets, 139  
Steel design, 121  
Step-scan interferometer(s), 20, 53, 54, 62, 63, 104, 127, 128, 313, 402, 422, 435  
Step-scan mode, 404  
Step-scanning interferometer(s), 54, 170, 312  
Step-scanning mode, 111  
Stingray, 314  
Stokes Raman scattering, 16  
Stokes-shifted Raman bands, 375  
Stokes-shifted spectrum, 386  
Stopped-flow investigation, 398  
Stopped-flow techniques, 400  
Stray light, 201  
Stress-induced frequency shifts, 436

- Stretching modes, O–H, N–H, and aromatic or olefinic C–H, 382
- Stroboscopic spectrometry, 407
- Strong apodization, 37
- Substrate, 124, 137
  - and compensator plates, 69
- Successive average orthogonalization (SAO), 214
- Successive average orthogonalization iterative target transform factor analysis (SAO-ITTFA), 219
- Sulfamethazine, 503
- Sulfamethoxazole, 503
- Sulfanilamidoquinoxaline, 503
- Sulfapyrazine, 503
- Supercritical fluid chromatography (SFC), 483
- Superior infrared transparency, 253
- Surface-enhanced infrared absorption (SEIRA) spectroscopy, 494
- Surface-enhanced Raman scattering (SERS), 389
- Surface plasmons, 390
- Surface selection rule, 290, 291
- Symmetric stretch, infrared forbidden, 500
- Taylor series, 290
- Temperature, 121
  - oscillation, 418
- Terahertz spectrometers, 140
- Ternary mixture, 203
- Test voltage, 71
- Tetraethyl orthosilicate (TEOS), 390
- Tetrahydrothiophenium (THT) pendant groups, 443
- TGA/FT-IR, 502
  - spectra, 504
- Theoretical efficiency, 138, 139
- Thermal conductivity, 418
- Thermal detectors, 146
- Thermal effects, 109
- Thermal expansion, 119
- Thermal properties, 253
- Thermal shock, 253
- Thermal stability, 121
- Thermal wave, 419
  - amplitude, 418
  - decay, 418
  - decay coefficients, 418
  - decay depth, 420
  - decay lengths, 420
  - propagation, 430
  - propagation parameters, 428
- Thermogravimetric analysis (TGA), 483
- Thermogravimetric analyzer(s), 481, 502
- Thin films, 261
- Thin layer chromatography (TLC), 504
- Three-layer forward-feed neural network, 222
- Three-layer network, 222
- Threshold voltage, 106, 107
- Tilt, 99, 100, 110, 112, 113, 121, 125
  - angle, 101
  - table, 119
- Tilt-compensated interferometers, 112, 118, 121
- Tilting, 110, 119
- Tilt and shear compensation, 121
- Tilt and shear immunity, 115
- Time-domain signal, 404
- Time-resolved analog interferogram, 410
- Time-resolved discrete interferogram, 410
- Time-resolved dichroic difference spectra, 439
- Time-resolved measurement, 402
- Time-resolved polarized spectra, 413
- Time-resolved spectra, 412
- Time-resolved spectrometry, 53, 395
- Time-resolved stroboscopic FT-IR spectrometry, 407
- Top-of-the-line FT-IR spectrometers, 111
- Toroidal (doughnut-shaped) mirrors, 156
- Torque, 116, 118
- Total internal reflection, 324
- Total pathlength, 467
- Trace analysis, 255
- Trace solute, 256
- Traditional air-bearing interferometers, 103
- Transept or Doyle interferometer, 124
- Transfer function, 221, 222
- Transflectance spectrum, 311
- Transflection, 297
  - spectrometry, 277, 298
- Transformations in Optics*, 125
- Transformation matrix, 219
- Transient infrared emission spectroscopy (TIRES), 368



- Transient infrared spectroscopy (TIRS), 368
- Transient infrared transmission spectroscopy (TIRTS), 368
- Transient species, 219
- Translational motion, 101
- Transmission, 23, 136, 260
  - cell, 200
  - spectrum, 110
- Transmission spectrometry, 200, 294, 311, 364, 422
  - conventional, 251
- Transmittance, 12, 21, 132, 198, 202, 255, 256
  - spectrum, 225
- Transmitting–receiving telescope, 473
- Transmitting telescope, 469
- Transparent disks, 252
- Transparent spectral range, 262
- Trapezoidal IRE, 329
- Triangular apodization, 165, 180
  - function, 32, 180
- Triangular functions, 61
- Triangular slit function, 29, 30
- Triangular squared function, 33
- Triglycine sulfate, 147
- Trigonometric functions, 33
- Trinitrobenzaldehyde, 388
- True analog value, 72
- True peak absorbance, 178
- True spectrum, 29
- Truncated Fourier domain signal, 235
- Truncated sine wave, 39
- Truncation function, 28
- Tungsten-filament light bulb, 145
- Tunnel ATR accessory, 334
- Tunnel cell(s), 334, 335
- Turnaround point, 108
- Turnaround time, 121, 396
- Two-beam interferometer(s), 19, 24, 97, 132, 171
- Two-dimensional array detector, 131
- Two-dimensional correlation plots, 448
- Two-dimensional hyperspectral imaging spectrometry, 63
- Two-dimensional imaging, 131
- Two-dimensional model, 220
- Two-dimensional roof retroreflector, 112
- Two-point baseline correction, 225
- Typical atmospheric spectrum, 467
- Typical cube-corner array retroreflector, 471
- Typical glitch, 184
- Typical optical arrangement, 157
- Ultrarapid scanning FT-IR spectrometer, 269
- Ultraviolet lamps, 259
- Unapodized spectrum, 114, 228
- Unchirped interferogram, 70
- Undersampling ratio, 63
- Unidirectional interferometers, 108
- Unidirectional rapid-scanning interferometer, 51
- U.S. Environmental Protection Agency, 486
- Unmodulated infrared radiation, 485
- Unpolarized radiation, 261
- Unweighted sinusoidal interferogram, 29
- UV–visible spectra, 171
- L-Valine, 271
- Vapor-phase infrared reference spectra, 486
- Vapor-phase infrared spectra, 486, 491
- Vapor-phase samples, 256
- Variable-pathlength liquid transmission cells, 199
- Variable throughput criterion, 164
- Variance–covariance matrix decomposition, 214
- Vector input, 222
- Velocity errors, 112
- Vertically polarized light (VPL), 265
- Vertical truncated triangular prism, 329
- Vertical variable angle attenuated total reflection (VATR), 331
- Vibration, of the optical bench or mirrors, 184
- Vibrational circular dichroism (VCD), 269
  - spectra, 265
  - spectrometry, 264
- Vibrational microspectrometry, 311
- Vibrational modes, 3
- Vibrational spectrometry, 221
- Vibration-free enclosure, 372
- Vibration-rotation spectroscopy, 6
- Vibration-rotation spectrum, 6, 165, 463, 472
  - bands in the, 366
  - of gases, 10

- Video and audio industries, 71  
Vignetting, 109  
Vinylene C–H bend, 452  
Vinylene C–H stretch, 447  
Vinylene C–H units, 444  
Vinylene groups, 446  
Virtual state, 16  
Viscoelastic behavior, 436  
Visible light, 106  
Visible spectrum, 111  
Voice coil, 102, 103, 113  
    voltage to the, 108  
Voice-coil transducer, 97  
Voigt profile, 11  
Volatile organic compounds (VOCs), 474
- Water-insoluble infrared-transparent  
    window, 311  
Waveform, 58, 64  
Wavefront, 138  
Wavelength(s), 24, 42, 53, 106, 109,  
    123, 255  
Wavenumber(s), 23–25, 27–30, 39, 53, 57,  
    73, 208, 254, 256, 281  
Wavenumber accuracy, 125  
    of FT-IR spectra, 108  
Wavenumber-dependent phase lag, 38  
Wavenumber-dependent variations, 450  
Wavenumber instability, 109  
Wavenumber precision, 109  
Wavenumber scale, 46  
Wavenumber shift, 159, 200, 201  
Weak narrow bands, 69  
Weak and strong absorption bands,  
    429  
Wedge angle, 124  
Weight matrices, 222  
White cell(s), 257–259  
White light detector, 107, 125  
White-light interferogram(s), 106–108  
Wide-range beamsplitters, 138  
Window diameter, 252  
Window materials, 251  
Wire grid, 126  
    polarizer(s), 126, 262, 436
- X–H stretching bands, 253  
X-ray diffraction, 1
- Yield strength, 252
- Zachor–Aaronson noise, 168  
Zero crossing(s), 104, 108  
    positive- and/or negative-going, 106  
Zero energy level, 187  
    accuracy of the, of spectra, 191  
Zero filling, 227  
Zero path difference (ZPD), 21, 22,  
    48, 50, 70  
Zero-phase difference point, 48, 69  
Zero retardation, 21, 22, 24, 28, 32, 41, 42,  
    64, 69, 118  
    decrease, 48  
    point, 36, 40  
Zero transmittance, 198  
ZnSe, 253, 262



# **CHEMICAL ANALYSIS**

A SERIES OF MONOGRAPHS ON ANALYTICAL CHEMISTRY  
AND ITS APPLICATIONS

*Series Editor*  
**J. D. WINEFORDNER**

VOLUME 171

# CHEMICAL ANALYSIS

A SERIES OF MONOGRAPHS ON ANALYTICAL CHEMISTRY  
AND ITS APPLICATIONS

*Series Editor*  
**J. D. WINEFORDNER**

- Vol. 1 **The Analytical Chemistry of Industrial Poisons, Hazards, and Solvents.** *Second Edition.*  
By the late Morris B. Jacobs
- Vol. 2 **Chromatographic Adsorption Analysis.** By Harold H. Strain (*out of print*)
- Vol. 3 **Photometric Determination of Traces of Metals.** *Fourth Edition*  
Part I: General Aspects. By E. B. Sandell and Hiroshi Onishi  
Part IIA: Individual Metals, Aluminum to Lithium. By Hiroshi Onishi  
Part IIB: Individual Metals, Magnesium to Zirconium. By Hiroshi Onishi
- Vol. 4 **Organic Reagents Used in Gravimetric and Volumetric Analysis.** By John F. Flagg  
(*out of print*)
- Vol. 5 **Aquametry: A Treatise on Methods for the Determination of Water.** *Second Edition (in three parts).* By John Mitchell, Jr. and Donald Milton Smith
- Vol. 6 **Analysis of Insecticides and Acaricides.** By Francis A. Gunther and Roger C. Blinn (*out of print*)
- Vol. 7 **Chemical Analysis of Industrial Solvents.** By the late Morris B. Jacobs and Leopold Schetlan
- Vol. 8 **Colorimetric Determination of Nonmetals.** *Second Edition.* Edited by the late David F. Boltz and James A. Howell
- Vol. 9 **Analytical Chemistry of Titanium Metals and Compounds.** By Maurice Codell
- Vol. 10 **The Chemical Analysis of Air Pollutants.** By the late Morris B. Jacobs
- Vol. 11 **X-Ray Spectrochemical Analysis.** *Second Edition.* By L. S. Birks
- Vol. 12 **Systematic Analysis of Surface-Active Agents.** *Second Edition.* By Milton J. Rosen and Henry A. Goldsmith
- Vol. 13 **Alternating Current Polarography and Tensammetry.** By B. Breyer and H.H.Bauer
- Vol. 14 **Flame Photometry.** By R. Herrmann and J. Alkemade
- Vol. 15 **The Titration of Organic Compounds (in two parts).** By M. R. F. Ashworth
- Vol. 16 **Complexation in Analytical Chemistry: A Guide for the Critical Selection of Analytical Methods Based on Complexation Reactions.** By the late Anders Ringbom
- Vol. 17 **Electron Probe Microanalysis.** *Second Edition.* By L. S. Birks
- Vol. 18 **Organic Complexing Reagents: Structure, Behavior, and Application to Inorganic Analysis.** By D. D. Perrin
- Vol. 19 **Thermal Analysis.** *Third Edition.* By Wesley Wm.Wendlandt
- Vol. 20 **Amperometric Titrations.** By John T. Stock
- Vol. 21 **Reflectance Spectroscopy.** By Wesley Wm.Wendlandt and Harry G. Hecht
- Vol. 22 **The Analytical Toxicology of Industrial Inorganic Poisons.** By the late Morris B. Jacobs
- Vol. 23 **The Formation and Properties of Precipitates.** By Alan G.Walton
- Vol. 24 **Kinetics in Analytical Chemistry.** By Harry B. Mark, Jr. and Garry A. Rechnitz
- Vol. 25 **Atomic Absorption Spectroscopy.** *Second Edition.* By Morris Slavin
- Vol. 26 **Characterization of Organometallic Compounds (in two parts).** Edited by Minoru Tsutsui
- Vol. 27 **Rock and Mineral Analysis.** *Second Edition.* By Wesley M. Johnson and John A. Maxwell
- Vol. 28 **The Analytical Chemistry of Nitrogen and Its Compounds (in two parts).** Edited by C. A. Streuli and Philip R.Averell
- Vol. 29 **The Analytical Chemistry of Sulfur and Its Compounds (in three parts).** By J. H. Karchmer
- Vol. 30 **Ultramicro Elemental Analysis.** By Güther Toölg
- Vol. 31 **Photometric Organic Analysis (in two parts).** By Eugene Sawicki
- Vol. 32 **Determination of Organic Compounds: Methods and Procedures.** By Frederick T. Weiss
- Vol. 33 **Masking and Demasking of Chemical Reactions.** By D. D. Perrin

- Vol. 34. **Neutron Activation Analysis.** By D. De Soete, R. Gijbels, and J. Hoste
- Vol. 35. **Laser Raman Spectroscopy.** By Marvin C. Tobin
- Vol. 36. **Emission Spectrochemical Analysis.** By Morris Slavin
- Vol. 37. **Analytical Chemistry of Phosphorus Compounds.** Edited by M. Halmann
- Vol. 38. **Luminescence Spectrometry in Analytical Chemistry.** By J. D. Winefordner, S. G. Schulman, and T. C. O'Haver
- Vol. 39. **Activation Analysis with Neutron Generators.** By Sam S. Nargolwalla and Edwin P. Przybylowicz
- Vol. 40. **Determination of Gaseous Elements in Metals.** Edited by Lynn L. Lewis, Laben M. Melnick, and Ben D. Holt
- Vol. 41. **Analysis of Silicones.** Edited by A. Lee Smith
- Vol. 42. **Foundations of Ultracentrifugal Analysis.** By H. Fujita
- Vol. 43. **Chemical Infrared Fourier Transform Spectroscopy.** By Peter R. Griffiths
- Vol. 44. **Microscale Manipulations in Chemistry.** By T. S. Ma and V. Horak
- Vol. 45. **Thermometric Titrations.** By J. Barthel
- Vol. 46. **Trace Analysis: Spectroscopic Methods for Elements.** Edited by J. D. Winefordner
- Vol. 47. **Contamination Control in Trace Element Analysis.** By Morris Zief and James W. Mitchell
- Vol. 48. **Analytical Applications of NMR.** By D. E. Leyden and R. H. Cox
- Vol. 49. **Measurement of Dissolved Oxygen.** By Michael L. Hitchman
- Vol. 50. **Analytical Laser Spectroscopy.** Edited by Nicolo Omenetto
- Vol. 51. **Trace Element Analysis of Geological Materials.** By Roger D. Reeves and Robert R. Brooks
- Vol. 52. **Chemical Analysis by Microwave Rotational Spectroscopy.** By Ravi Varma and Lawrence W. Hrubesh
- Vol. 53. **Information Theory as Applied to Chemical Analysis.** By Karl Eckschlager and Vladimir Stepanek
- Vol. 54. **Applied Infrared Spectroscopy: Fundamentals, Techniques, and Analytical Problemsolving.** By A. Lee Smith
- Vol. 55. **Archaeological Chemistry.** By Zvi Goffer
- Vol. 56. **Immobilized Enzymes in Analytical and Clinical Chemistry.** By P. W. Carr and L. D. Bowers
- Vol. 57. **Photoacoustics and Photoacoustic Spectroscopy.** By Allan Rosenzweig
- Vol. 58. **Analysis of Pesticide Residues.** Edited by H. Anson Moye
- Vol. 59. **Affinity Chromatography.** By William H. Scouten
- Vol. 60. **Quality Control in Analytical Chemistry. Second Edition.** By G. Kateman and L. Buydens
- Vol. 61. **Direct Characterization of Fineparticles.** By Brian H. Kaye
- Vol. 62. **Flow Injection Analysis.** By J. Ruzicka and E. H. Hansen
- Vol. 63. **Applied Electron Spectroscopy for Chemical Analysis.** Edited by Hassan Windawi and Floyd Ho
- Vol. 64. **Analytical Aspects of Environmental Chemistry.** Edited by David F. S. Natusch and Philip K. Hopke
- Vol. 65. **The Interpretation of Analytical Chemical Data by the Use of Cluster Analysis.** By D. Luc Massart and Leonard Kaufman
- Vol. 66. **Solid Phase Biochemistry: Analytical and Synthetic Aspects.** Edited by William H. Scouten
- Vol. 67. **An Introduction to Photoelectron Spectroscopy.** By Pradip K. Ghosh
- Vol. 68. **Room Temperature Phosphorimetry for Chemical Analysis.** By Tuan Vo-Dinh
- Vol. 69. **Potentiometry and Potentiometric Titrations.** By E. P. Serjeant
- Vol. 70. **Design and Application of Process Analyzer Systems.** By Paul E. Mix
- Vol. 71. **Analysis of Organic and Biological Surfaces.** Edited by Patrick Echlin
- Vol. 72. **Small Bore Liquid Chromatography Columns: Their Properties and Uses.** Edited by Raymond P.W. Scott
- Vol. 73. **Modern Methods of Particle Size Analysis.** Edited by Howard G. Barth
- Vol. 74. **Auger Electron Spectroscopy.** By Michael Thompson, M. D. Baker, Alec Christie, and J. F. Tyson
- Vol. 75. **Spot Test Analysis: Clinical, Environmental, Forensic and Geochemical Applications.** By Ervin Jungreis
- Vol. 76. **Receptor Modeling in Environmental Chemistry.** By Philip K. Hopke

- Vol. 77 **Molecular Luminescence Spectroscopy: Methods and Applications** (*in three parts*). Edited by Stephen G. Schulman
- Vol. 78 **Inorganic Chromatographic Analysis**. Edited by John C. MacDonald
- Vol. 79 **Analytical Solution Calorimetry**. Edited by J. K. Grime
- Vol. 80 **Selected Methods of Trace Metal Analysis: Biological and Environmental Samples**. By Jon C. VanLoon
- Vol. 81 **The Analysis of Extraterrestrial Materials**. By Isidore Adler
- Vol. 82 **Chemometrics**. By Muhammad A. Sharaf, Deborah L. Illman, and Bruce R. Kowalski
- Vol. 83 **Fourier Transform Infrared Spectrometry**. By Peter R. Griffiths and James A. de Haseth
- Vol. 84 **Trace Analysis: Spectroscopic Methods for Molecules**. Edited by Gary Christian and James B. Callis
- Vol. 85 **Ultratrace Analysis of Pharmaceuticals and Other Compounds of Interest**. Edited by S. Ahuja
- Vol. 86 **Secondary Ion Mass Spectrometry: Basic Concepts, Instrumental Aspects, Applications and Trends**. By A. Benninghoven, F. G. Rüenauer, and H.W. Werner
- Vol. 87 **Analytical Applications of Lasers**. Edited by Edward H. Piepmeier
- Vol. 88 **Applied Geochemical Analysis**. By C. O. Ingamells and F. F. Pitard
- Vol. 89 **Detectors for Liquid Chromatography**. Edited by Edward S. Yeung
- Vol. 90 **Inductively Coupled Plasma Emission Spectroscopy: Part I: Methodology, Instrumentation, and Performance; Part II: Applications and Fundamentals**. Edited by J. M. Boumans
- Vol. 91 **Applications of New Mass Spectrometry Techniques in Pesticide Chemistry**. Edited by Joseph Rosen
- Vol. 92 **X-Ray Absorption: Principles, Applications, Techniques of EXAFS, SEXAFS, and XANES**. Edited by D. C. Konnigsberger
- Vol. 93 **Quantitative Structure-Chromatographic Retention Relationships**. By Roman Kaliszan
- Vol. 94 **Laser Remote Chemical Analysis**. Edited by Raymond M. Measures
- Vol. 95 **Inorganic Mass Spectrometry**. Edited by F. Adams, R. Gijbels, and R. Van Grieken
- Vol. 96 **Kinetic Aspects of Analytical Chemistry**. By Horacio A. Mottola
- Vol. 97 **Two-Dimensional NMR Spectroscopy**. By Jan Schraml and Jon M. Bellama
- Vol. 98 **High Performance Liquid Chromatography**. Edited by Phyllis R. Brown and Richard A. Hartwick
- Vol. 99 **X-Ray Fluorescence Spectrometry**. By Ron Jenkins
- Vol. 100 **Analytical Aspects of Drug Testing**. Edited by Dale G. Deustch
- Vol. 101 **Chemical Analysis of Polycyclic Aromatic Compounds**. Edited by Tuan Vo-Dinh
- Vol. 102 **Quadrupole Storage Mass Spectrometry**. By Raymond E. March and Richard J. Hughes (*out of print: see Vol. 165*)
- Vol. 103 **Determination of Molecular Weight**. Edited by Anthony R. Cooper
- Vol. 104 **Selectivity and Detectability Optimization in HPLC**. By Satinder Ahuja
- Vol. 105 **Laser Microanalysis**. By Lieselotte Moenke-Blankenburg
- Vol. 106 **Clinical Chemistry**. Edited by E. Howard Taylor
- Vol. 107 **Multielement Detection Systems for Spectrochemical Analysis**. By Kenneth W. Busch and Marianna A. Busch
- Vol. 108 **Planar Chromatography in the Life Sciences**. Edited by Joseph C. Touchstone
- Vol. 109 **Fluorometric Analysis in Biomedical Chemistry: Trends and Techniques Including HPLC Applications**. By Norio Ichinose, George Schwedt, Frank Michael Schnepel, and Kyoko Adochi
- Vol. 110 **An Introduction to Laboratory Automation**. By Victor Cerdá and Guillermo Ramis
- Vol. 111 **Gas Chromatography: Biochemical, Biomedical, and Clinical Applications**. Edited by Ray E. Clement
- Vol. 112 **The Analytical Chemistry of Silicones**. Edited by A. Lee Smith
- Vol. 113 **Modern Methods of Polymer Characterization**. Edited by Howard G. Barth and Jimmy W. Mays
- Vol. 114 **Analytical Raman Spectroscopy**. Edited by Jeanette Graselli and Bernard J. Bulkin
- Vol. 115 **Trace and Ultratrace Analysis by HPLC**. By Satinder Ahuja
- Vol. 116 **Radiochemistry and Nuclear Methods of Analysis**. By William D. Ehmann and Diane E. Vance

- Vol. 117 **Applications of Fluorescence in Immunoassays.** By Ilkka Hemmila
- Vol. 118 **Principles and Practice of Spectroscopic Calibration.** By Howard Mark
- Vol. 119 **Activation Spectrometry in Chemical Analysis.** By S. J. Parry
- Vol. 120 **Remote Sensing by Fourier Transform Spectrometry.** By Reinhard Beer
- Vol. 121 **Detectors for Capillary Chromatography.** Edited by Herbert H. Hill and Dennis McMinn
- Vol. 122 **Photochemical Vapor Deposition.** By J. G. Eden
- Vol. 123 **Statistical Methods in Analytical Chemistry.** By Peter C. Meier and Richard Züd
- Vol. 124 **Laser Ionization Mass Analysis.** Edited by Akos Vertes, Renaat Gijbels, and Fred Adams
- Vol. 125 **Physics and Chemistry of Solid State Sensor Devices.** By Andreas Mandelis and Constantinos Christofides
- Vol. 126 **Electroanalytical Stripping Methods.** By Khjena Z. Brainina and E. Neyman
- Vol. 127 **Air Monitoring by Spectroscopic Techniques.** Edited by Markus W. Sigrist
- Vol. 128 **Information Theory in Analytical Chemistry.** By Karel Eckschlager and Klaus Danzer
- Vol. 129 **Flame Chemiluminescence Analysis by Molecular Emission Cavity Detection.** Edited by David Stiles, Anthony Calokerinos, and Alan Townshend
- Vol. 130 **Hydride Generation Atomic Absorption Spectrometry.** Edited by Jiri Dedina and Dimiter L. Tsalev
- Vol. 131 **Selective Detectors: Environmental, Industrial, and Biomedical Applications.** Edited by Robert E. Sievers
- Vol. 132 **High-Speed Countercurrent Chromatography.** Edited by Yoichiro Ito and Walter D. Conway
- Vol. 133 **Particle-Induced X-Ray Emission Spectrometry.** By Sven A. E. Johansson, John L. Campbell, and Klas G. Malmqvist
- Vol. 134 **Photothermal Spectroscopy Methods for Chemical Analysis.** By Stephen E. Bialkowski
- Vol. 135 **Element Speciation in Bioinorganic Chemistry.** Edited by Sergio Caroli
- Vol. 136 **Laser-Enhanced Ionization Spectrometry.** Edited by John C. Travis and Gregory C. Turk
- Vol. 137 **Fluorescence Imaging Spectroscopy and Microscopy.** Edited by Xue Feng Wang and Brian Herman
- Vol. 138 **Introduction to X-Ray Powder Diffractometry.** By Ron Jenkins and Robert L. Snyder
- Vol. 139 **Modern Techniques in Electroanalysis.** Edited by Petr Vanýek
- Vol. 140 **Total-Reflection X-Ray Fluorescence Analysis.** By Reinhold Klockenkamper
- Vol. 141 **Spot Test Analysis: Clinical, Environmental, Forensic, and Geochemical Applications. Second Edition.** By Ervin Jungreis
- Vol. 142 **The Impact of Stereochemistry on Drug Development and Use.** Edited by Hassan Y. Aboul-Enein and Irving W. Wainer
- Vol. 143 **Macrocyclic Compounds in Analytical Chemistry.** Edited by Yuri A. Zolotov
- Vol. 144 **Surface-Launched Acoustic Wave Sensors: Chemical Sensing and Thin-Film Characterization.** By Michael Thompson and David Stone
- Vol. 145 **Modern Isotope Ratio Mass Spectrometry.** Edited by T. J. Platzner
- Vol. 146 **High Performance Capillary Electrophoresis: Theory, Techniques, and Applications.** Edited by Morteza G. Khaledi
- Vol. 147 **Solid Phase Extraction: Principles and Practice.** By E. M. Thurman
- Vol. 148 **Commercial Biosensors: Applications to Clinical, Bioprocess and Environmental Samples.** Edited by Graham Ramsay
- Vol. 149 **A Practical Guide to Graphite Furnace Atomic Absorption Spectrometry.** By David J. Butcher and Joseph Sneddon
- Vol. 150 **Principles of Chemical and Biological Sensors.** Edited by Dermot Diamond
- Vol. 151 **Pesticide Residue in Foods: Methods, Technologies, and Regulations.** By W. George Fong, H. Anson Moye, James N. Seiber, and John P. Toth
- Vol. 152 **X-Ray Fluorescence Spectrometry. Second Edition.** By Ron Jenkins
- Vol. 153 **Statistical Methods in Analytical Chemistry. Second Edition.** By Peter C. Meier and Richard E. Züd
- Vol. 154 **Modern Analytical Methodologies in Fat- and Water-Soluble Vitamins.** Edited by Won O. Song, Gary R. Beecher, and Ronald R. Eitenmiller
- Vol. 155 **Modern Analytical Methods in Art and Archaeology.** Edited by Enrico Ciliberto and Guiseppe Spoto



- Vol. 156 **Shpol'skii Spectroscopy and Other Site Selection Methods: Applications in Environmental Analysis, Bioanalytical Chemistry and Chemical Physics.** Edited by C. Gooijer, F. Ariese and J.W. Hofstraat
- Vol. 157 **Raman Spectroscopy for Chemical Analysis.** By Richard L. McCreery
- Vol. 158 **Large ( $C \geq 24$ ) Polycyclic Aromatic Hydrocarbons: Chemistry and Analysis.** By John C. Fetzer
- Vol. 159 **Handbook of Petroleum Analysis.** By James G. Speight
- Vol. 160 **Handbook of Petroleum Product Analysis.** By James G. Speight
- Vol. 161 **Photoacoustic Infrared Spectroscopy.** By Kirk H. Michaelian
- Vol. 162 **Sample Preparation Techniques in Analytical Chemistry.** Edited by Somenath Mitra
- Vol. 163 **Analysis and Purification Methods in Combination Chemistry.** Edited by Bing Yan
- Vol. 164 **Chemometrics: From Basics to Wavelet Transform.** By Foo-tim Chau, Yi-Zeng Liang, Junbin Gao, and Xue-guang Shao
- Vol. 165 **Quadrupole Ion Trap Mass Spectrometry. Second Edition.** By Raymond E. March and John F. J. Todd
- Vol. 166 **Handbook of Coal Analysis.** By James G. Speight
- Vol. 167 **Introduction to Soil Chemistry: Analysis and Instrumentation.** By Alfred R. Conklin, Jr.
- Vol. 168 **Environmental Analysis and Technology for the Refining Industry.** By James G. Speight
- Vol. 169 **Identification of Microorganisms by Mass Spectrometry.** Edited by Charles L. Wilkins and Jackson O. Lay, Jr.
- Vol. 170 **Archaeological Chemistry. Second Edition.** By Zvi Goffer
- Vol. 171 **Fourier Transform Infrared Spectrometry. Second Edition.** By Peter R. Griffiths and James A. de Haseth